Electromagnetic scattering from thin tubular objects and an application in electromagnetic chirality

Zur Erlangung des akademischen Grades eines

DOKTORS DER NATURWISSENSCHAFTEN

von der KIT-Fakultät für Mathematik des
Karlsruher Instituts für Technologie (KIT)
genehmigte

DISSERTATION

von

Marvin Knöller

Tag der mündlichen Prüfung: 21. Juni 2023

1. Referent: Prof. Dr. Roland Griesmaier
2. Referent: Prof. Dr. Willy Dörfler
3. Referent: Prof. Dr. Nuutti Hyvönen

Acknowledgement

I gratefully acknowledge funding by the Deutsche Forschungsgemeinschaft (DFG, German Research Foundation) – Project-ID 258734477 – SFB 1173
I continue in German.

An erster Stelle möchte ich mich bei Prof. Dr. Roland Griesmaier für seine hervorragende Betreuung und seine stetige Unterstützung bedanken. Seine vielen Verbesserungsvorschläge und die vielen Diskussionen mit ihm haben maßgeblich zum Gelingen dieser Arbeit beigetragen.
Weiterhin danke ich Prof. Dr. Willy Dörfler und Prof. Dr. Nuutti Hyvönen für das Begutachten dieser Arbeit.
Großer Dank gilt ebenfalls PD. Dr. Tilo Arens, PD. Dr. Frank Hettlich und Prof. Dr. Andreas Kirsch, welche mich durch ihre Vorlesungen bereits als Student für die inversen Probleme, Integralgleichungen und Streutheorie begeistern konnten. Als ich später Doktorand in der Arbeitsgruppe wurde standen ihre Türen immer offen und ich konnte mich stets auf ihre Expertise und Erfahrung verlassen.
Für die gute Zusammenarbeit und den regelmäßigen Austausch über das Forschungsprojekt C5 des Sonderforschungsbereichs bedanke ich mich bei meinen Kollegen aus der Physik Dr. Ivan Fernandez-Corbaton und Prof. Dr. Carsten Rockstuhl. Ebenfalls möchte ich mich bei meinem ehemaligen Kollegen Dr. Felix Hagemann bedanken, der mir als Vorgänger im Projekt C5 zu Beginn meiner Promotion viele Dinge zur elektromagnetischen Chiralität und zum Umgang mit Bempp erklärt hat. Ich bedanke mich bei Leonie Fink und Nasim Shafieeabyaneh für das Korrekturlesen von einigen Kapiteln dieser Arbeit.
Besonderer Dank gilt meinen Eltern, welche mich seit jeher bedingungslos unterstützen und die immer wussten, dass ich *das* schaffen werde.
Nicht zuletzt danke ich meiner Partnerin Lisa Schätzle für das Korrekturlesen, ihre Unterstützung, ihr Verständnis, und unsere schöne gemeinsame Zeit.

Contents

List of Figures

Abstract

Asymptotic perturbation formulas characterize the effective behavior of waves as the volume of the scattering object tends to zero. In this work, wave propagation is described by time-harmonic Maxwell's equations in free space and the corresponding scattering objects are thin tubular objects that feature a different electric permittivity and a different magnetic permeability than their surrounding medium. For this setting, we derive an asymptotic representation of the scattered electric field away from the thin tubular object and use the corresponding leading order term in a shape identification problem and for designing highly electromagnetically chiral objects. In inverse problems, the leading order term may be used to find the center curve of a thin wire that is supposed to emit a scattered field, which is reasonably close to a given measured field. For the optimal design of electromagnetically chiral structures, the representation formula provides an explicit formula for the leading order term of an asymptotic far field operator expansion. A chirality measure, usually requiring the far field operator, will now map aforementioned leading order term to a value between 0 and 1 dependent on the level of electromagnetic chirality of the thin tubular scatterer. This approximation greatly simplifies the challenge to maximize the chirality measure with respect to thin tubular objects. The fact that neither the evaluation of the leading order term nor the calculation of corresponding derivatives require a Maxwell system to be solved implies that the shape optimization scheme is highly efficient compared to shape optimization algorithms that use e.g. domain derivatives. In the visible range, the metallic nanowires obtained by our optimization scheme attain high values of electromagnetic chirality and even exceed those attained by traditional metallic helices.

Chapter 1

Introduction

1.1 Electromagnetic scattering from thin tubular structures

This thesis is about the interaction of time-harmonic electromagnetic waves with thin tubular scattering objects and the efficient shape optimization of these structures to obtain objects with large electromagnetic chirality.

The wave propagation is described by time-harmonic Maxwell's equations in three-dimensional space. An incident electric field $\boldsymbol{E}^i$ satisfying

$$\mathbf{curl}\,\mathbf{curl}\,\boldsymbol{E}^i - k^2\boldsymbol{E}^i = \mathbf{0} \quad \text{in } \mathbb{R}^3$$

illuminates the object and produces a scattered field $\boldsymbol{E}^s$. The wave number k is given by $k = \omega\sqrt{\varepsilon_0\mu_0}$, where ω denotes the angular frequency and ε_0 and μ_0 denote the electric permittivity and the magnetic permeability in free space, respectively. Inside the scattering object the electric permittivity and magnetic permeability distributions ε_ρ and μ_ρ differ from the free space by attaining the interior values ε_1 and μ_1. The interior permeability μ_1 is supposed to be positive, i.e. $\mu_1 > 0$, whereas we study permittivities with either $\varepsilon_1 > 0$ or $\varepsilon_1 \in \mathbb{C}$ with $\mathrm{Re}(\varepsilon_1) < 0$ and $\mathrm{Im}(\varepsilon_1) > 0$. The first case corresponds to a purely dielectric scatterer, whereas the second case covers metallic materials such as gold or silver for frequencies corresponding to the optical range. The full Maxwell system for the total field $\boldsymbol{E} = \boldsymbol{E}^i + \boldsymbol{E}^s$ is consequently given by the weak formulation of

$$\mathbf{curl}\,(\mu_\rho^{-1}\,\mathbf{curl}\,\boldsymbol{E}) - \omega^2\varepsilon_\rho\boldsymbol{E} = \mathbf{0} \quad \text{in } \mathbb{R}^3$$

and the Silver–Müller radiation condition for the scattered field $\boldsymbol{E}^s$.

We consider thin tubular scattering objects, which can be described by a non self-intersecting center curve $K \subset \mathbb{R}^3$ with finite length, a fixed cross-section $D'_\rho \subset \mathbb{R}^2$ and a twist rate that determines how the cross-section rotates as it is extruded along the center curve. Throughout this thesis such an object will be denoted by D_ρ and we call it a thin tubular scattering object. If its size is in the range of a few nanometers (nm), we call D_ρ a nanotube or nanowire. The cross-section is supposed to be given by $D'_\rho = \rho D'$, where D' is a bounded Lipschitz domain, which is orthogonal to the center curve's tangent vector for every point on K. The number $\rho > 0$ in the notations D_ρ and D'_ρ is called the radius of the cross-section. In particular, it holds that $|D_\rho| \to 0$ for $\rho \to 0$. An example of such a thin tubular scattering object is visualized in Figure 1.1. The non-circular cross-section D'_ρ that is also shown in the bottom right corner, twists along the tube's center curve K.

We aim to derive an asymptotic model for electromagnetic wave scattering for thin tubular scattering objects D_ρ in free space that holds true as the cross-section D'_ρ of D_ρ shrinks to the center curve K, i.e., as the radius ρ tends to zero. In our analysis we derive such an expansion for the scattered field $\boldsymbol{E}^s$ away from D_ρ as well as for the electric far field $\boldsymbol{E}^\infty$. The latter can be understood as the unique representation of the scattered field on the unit sphere. For this

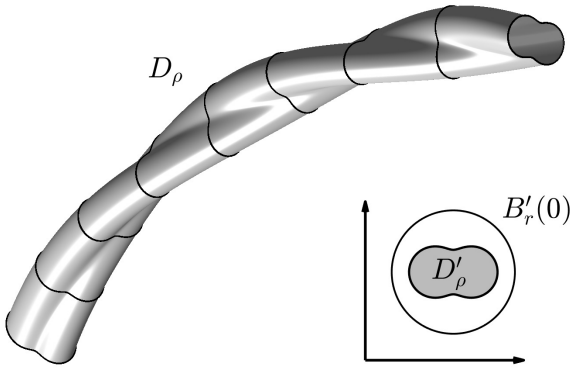

Figure 1.1: Sketch of the geometry of a thin tubular scattering object D_ρ.

asymptotic expansion, the goal is to study the leading order term that is supposed to effectively characterize the scattered electric field due to thin tubular scattering objects without solving the full Maxwell system. In the literature, various asymptotic perturbation formulas are available for electrostatic potentials (see e.g. [2, 29, 31, 56, 69]), elastic waves (see e.g. [11, 18, 20]) as well as for electromagnetic waves (see e.g. [12, 13, 68]). These formulas find applications in inverse problems such as the reconstruction of small inhomogeneities (see e.g. [9] and the references therein) or crack-identification in homogeneous material (see e.g. [19, 69]). However, the existing formulas for Maxwell's equations either consider different geometries for the scatterer, or are posed in a bounded set.

Here, we derive an asymptotic perturbation formula for scattered electric fields in free space away from the scattering object by extending the general low-volume asymptotic representation formula from [68] by using integral equation methods similar to [13]. We find that the leading order term of this expansion can be written as a (scaled) line integral over the spine curve K with an integrand featuring (i) the dyadic Green's function of time-harmonic Maxwell's equations in free space, (ii) the incident field $\boldsymbol{E}^i$ and (iii) the electric and magnetic polarization tensors denoted by $\mathbb{M}^\varepsilon$ and $\mathbb{M}^\mu$. The range of integration and the polarization tensors are the signatures of the scattering object, as they depend on the shape of both the curve K and the cross-section D'_ρ, on the twist rate of the cross-section around the curve, as well as on the material parameters inside and outside of the scatterer. The polarization tensors can be seen as a generalization to the particle polarizability α for a nano particle that relates the electric dipole moment $\boldsymbol{p}$ generated by a nanoparticle to the incoming field $\boldsymbol{E}^i$ via $\boldsymbol{p} = \alpha \boldsymbol{E}^i$ (see e.g. [1, pp. 152]). Similar as for the particle polarizability α, plasmonic resonances, i.e. collective surface charge-density oscillations on metallic nanoparticles are directly coupled to the polarization tensors. For simple cross-sections such as circles or ellipses, the condition for the appearance of plasmonic resonances is linked to poles in an explicit representation of $\mathbb{M}^\varepsilon$ and $\mathbb{M}^\mu$. More general cross-sections require to study the spectrum of the adjoint double layer potential, also called the Neumann–Poincaré operator.

For the particular choice of material parameters considered throughout this thesis and for thin tubular scatterers D_ρ we study the magnetic polarization tensor for positive and the electric polarization tensor for positive as well as for complex-valued interior permittivities having a negative real and a positive imaginary part. In both cases, we find that for $\gamma \in \{\varepsilon, \mu\}$ the tangent vector of the center curve K is an eigenvector of $\mathbb{M}^\gamma$ for a.e. point on the center curve K. In the orthogonal complement of the space spanned by the tangent vector, this is the plane in which the cross-section D'_ρ is located, the polarization tensors can be characterized by

using the two-dimensional polarization tensors m^γ corresponding to D'_ρ. This property does not come by surprise as it has been established in [19] for straight cylindrical scatterers with a sufficiently small but arbitrary cross-section. The asymptotic representation formula, as well as the characterization of the polarization tensors give a straightforward model for approximating scattered fields due to thin tubular scatterers. For the simple case, in which the cross-section is given by an ellipse, the two-dimensional polarization tensor is explicitly known and the lowest-order term in the asymptotic perturbation formula is explicitly computable.

We incorporate the leading order term in two efficient shape optimization algorithms, which are the reconstruction of thin tubular dielectric and metallic wires and the maximization of electromagnetic chirality.

1.2 Shape optimization of thin wires in electromagnetic chirality

A shape optimization problem can be understood as a minimization (or likewise maximization) problem, described as follows: Within the set of admissible shapes $\mathcal{U}_{\text{ad}}$, find the optimal structure $D^* \in \mathcal{U}_{\text{ad}}$, for which holds that

$$D^* = \operatorname*{arg\,min}_{D \in \mathcal{U}_{\text{ad}}} J(D)\,, \tag{1.1}$$

where $J : \mathcal{U}_{\text{ad}} \to \mathbb{R}$ is a shape functional. This objective function often incorporates the solution of a partial differential equation, for which $D \in \mathcal{U}_{\text{ad}}$ acts as (or changes) the domain, on which the partial differential equation is defined. Studies on the sensitivity of J with respect to variations in D may lead to shape derivatives (see e.g. [117]) or topological derivatives (see e.g. [101, 116]). Another approach in shape optimization (in particular in the context of thin wires) relies in adding thin ligaments to the domain and to study the shape functional as the ligaments thickness tends to zero (see [39]).

As a first shape optimization problem, we consider the inverse problem, which is to determine the center curve of a thin tubular scatterer with a circular cross-section, given the material parameters, a single incident plane wave and measurements of the corresponding electric far field. In the literature, derivative-based reconstruction schemes often make use of domain derivatives. For domain derivatives corresponding to the Helmholtz equation, we refer to e.g. [77, 78, 87], for Maxwell's equation see e.g. [72, 73, 74, 79]. In a different approach, the boundary integral equation for the solution of the scattering problem is differentiated with respect to variations of the domain. For the Helmholtz equation this has been done in e.g. [108, 110] and for Maxwell's equations in e.g. [71, 109]. Both of these approaches require an additional scattering problem to be solved for every variation of the domain. In a Newton-type algorithm every iteration requires several variations of an admissible shape (note that the current iterate is an admissible shape) to establish a gradient and therefore, several scattering problems need to be solved.

In our approach for a reconstruction scheme, we let the forward model map the center curve K of the wire to the leading order term of the asymptotic representation formula of the electric far field. We use this map to derive an inexpensive Gauß-Newton scheme which does not require a single Maxwell system to be solved. We introduce regularization terms for stabilizing the reconstructions and provide several numerical results. Starting from a given far field pattern, which is simulated independently by means of Bempp, both, dielectric as well as metallic thin tubes can be reconstructed when the initial guess is close enough to the true scattering object. A similar method for electrical impedance tomography has been considered in [69] (see also [19], where a similar inverse problem involving thin straight cylinders is studied).

Our motivation to study electromagnetic scattering from thin wires is electromagnetic chirality (em-chirality). The concept of em-chirality has been introduced to distinguish scattering objects, materials or metamaterials from one another based on different interactions with waves of opposite helicities. Helicity can be understood as an extension to circular polarization from

plane waves to general fields, which solve the homogeneous time-harmonic Maxwell's equations. More precisely, helicity of a monochromatic field is related to the eigenvalues and eigenvectors of the helicity operator $k^{-1}\,\mathbf{curl}$ (see also [49]). Since this operator has the eigenvalues ± 1, one distinguishes between fields of positive (+1) and negative (-1) helicities. A scattering object is said to be electromagnetically achiral (em-achiral), if, in some sense, all the information that is obtained upon illuminating the scattering object with fields of one helicity (either positive or negative) can be reproduced by fields of the opposite helicity. If this property is not given, the object is defined as electromagnetically chiral (em-chiral). The quantification of em-chirality is realized by using chirality measures, which were introduced in [49] and further studied in [15] in a mathematical framework involving the electric far field operator.

The far field operator can be associated to a scattering object and is mapped by the chirality measure to a scalar value, which lies between zero and the total interaction cross-section of the scattering object. An object attaining the lower bound (i.e. zero) would be em-achiral. This class includes objects that are achiral in the classical sense, i.e., objects that are symmetric with respect to a mirror plane. Examples include e.g. spheres, ellipsoids or tori. On the other hand, an object attaining the upper bound of the chirality measure (i.e. the total interaction cross-section) would be maximally em-chiral. Such an object would not scatter fields of one helicity at all, i.e. the scatterer would be invisible with respect to fields of one helicity. It is not clear, whether such a maximally em-chiral object exists. However, even scatterers that attain sufficiently large measures of em-chirality would enable interesting applications in photonic metamaterials, especially, when these chiral effects occur in the visible spectrum (see e.g. [41, 52, 60, 84, 105, 107, 112, 125]).

An approach for formulating a shape optimization scheme for finding highly em-chiral objects might be described as follows. The shape functional J in (1.1) would map the scattering object D to its electric far field operator and afterwards, by introducing a scaled chirality measure (i.e. dividing the original chirality measure by the total interaction cross-section), to a value between zero (em-achiral) and one (maximally em-chiral). This approach has a major drawback from the numerical perspective, as the numerical approximation of the electric far field operator corresponding to the scattering object under consideration requires the computation of several solutions corresponding to Maxwell's equations. To be precise, denoting by $N \in \mathbb{N}$ the degree of the multipole expansion that is used to approximate the incident and scattered field, the computation of the far field operator requires the solution of $2N(N+2)$ Maxwell systems. An optimization of em-chirality based on shape derivatives would require additional $2N(N+2)$ solutions to Maxwell systems for every variation of the domain, resulting in a tremendous computational effort.

In the literature, metallic helices are often studied for frequencies corresponding to the infrared regime. It has been observed in [60] that gold helices exhibit strong chiral effects as they show low transmittance for waves of one polarization handedness with a direction of propagation parallel to the helix axis, while allowing for a high transmittance of the other polarization handedness. Experimentally, an array of these helices has been observed to block fields of one helicity while transmitting the other one, thus, acting as a broadband circular polarizer for an exterior wavelength from around 4μm to 8μm. Further improvements on the design of such a helix were proposed in the literature such as tapered helices, intertwined helices or combinations of such. For an overview on these we refer to the review article [76] and the references therein. Using the chirality measure introduced in [49], the optimizations in [61, 62] focus on designing silver helices with a fixed circular cross-section at frequencies ranging from the infrared regime to the optical band. The shape optimization consequently results in optimizing four parameters that define the geometry of the helix: the radius, the pitch, the thickness and the number of turns. While the obtained optimized silver helices achieve high chirality measures in the infrared regime, their performance decreases significantly towards the optical frequency band (see [61, 62]).

Our approach to designing highly em-chiral objects relies on using the thin wire model for approximating the far field operator. In doing so, we go beyond the search for helices by establishing a simultaneous free-form optimization of both the center curve of the wire as well as the rotation of the cross-section around it. This enables us to cover a wide range of thin tubular scattering objects. In particular, we aim to design metallic nanowires for frequencies in the optical regime that attain high values of the (normalized) chirality measure. These optimized nano structures are supposed to serve as possible building blocks in novel three-dimensional metamaterials (see e.g. [52, 76, 84]).

The procedure in establishing the optimization algorithm can be described as follows: We use the leading order term of the asymptotic representation formula for approximating the electric far field operator, which provides the leading order term of a far field operator expansion. The shape functional J from (1.1) can now be understood as a function that first maps the thin tubular scatterer to its leading order term of this expansion and afterwards, to a normalized chirality value. By using this approximation, the effort to quantify em-chirality reduces significantly: Computationally expensive finite element or boundary element simulations are replaced by the computation of curve integrals over known integrands, which can be approximated within seconds. The shape derivative with respect to the center curve and the rotation of the thin tubular scatterer can be computed explicitly. A BFGS scheme for the shape optimization thus does not require a single Maxwell system to be solved, neither for the evaluation of the forward model, nor for the Fréchet derivative with respect to the center curve and rotation.

In our numerical examples we first focus on dielectric scattering objects with a circular cross-section. The shape optimization results in helix-shaped center curves with a relatively low value of em-chirality. Secondly, we study dual symmetric scatterers, i.e. objects, for which the electric and magnetic fields stay a solution to Maxwell's equation when they are transformed by a certain duality transform. Dual symmetry implies preservation of helicity, which is a necessary condition for an object to be maximally em-chiral. Our shape optimization yields similar structures as for the dielectric case and the chirality measure reaches approximately half of the (theoretically possible) upper bound. Finally, we focus on metallic nanowires with an elliptical cross-section. We study discrete frequencies in the optical band and obtain the largest chirality values, when both the shape of the center curve and the twist rate of the cross-section of the nanowire are suitably optimized simultaneously, and when the frequency, where the optimization is carried out is slightly below the plasmonic resonance frequency of the nanowire's cross-section. In these cases, our optimization scheme finds nanowires with non-intuitive shapes that attain more than 90% of the theoretically maximum of the chirality measure.

1.3 Outline of the thesis

In Chapter 2 we first introduce some preliminaries that we need throughout the whole thesis. This includes function spaces and traces for bounded Lipschitz domains. Afterwards we derive time-harmonic Maxwell's equations from Maxwell's equations in the time domain and study special solutions of time-harmonic Maxwell's equations. Then, we prove existence and uniqueness for the particular choice of material parameters that we consider throughout this thesis.

Chapter 3 is about the asymptotic representation formula for electric fields in free space. We give a precise definition for the scattering objects D_ρ and derive the previously mentioned formula rigorously from an asymptotic representation formula in a bounded domain. To study the leading order term of the representation formula we focus on the polarization tensor corresponding to a thin tubular scattering object in detail. For this purpose, we derive symmetry properties, bounds and finally establish an explicit characterization of the polarization tensors. Moreover, we study the two-dimensional polarization tensor of the thin tubes' cross-section and recall that its definition is linked to an elliptic transmission problem. We examine the plasmonic resonances and discuss the conditions under which this phenomenon occurs for thin metallic nanotubes.

Finally we perform numerical studies on the accuracy of the leading order term compared to a boundary element simulation. Here, we focus on dielectric thin tubular scatterers and metallic nanowires with a circular cross-section.

In Chapter 4 we discuss an inverse scattering problem for thin tubular objects with a circular cross-section. The challenge is to reconstruct the center curve of a thin tubular scattering object essentially, from observations of an electric far field pattern corresponding to a single incident plane wave. We establish an inexpensive Gauß-Newton algorithm that incorporates the leading order term of the asymptotic perturbation formula for the reconstruction. Furthermore, we provide numerical examples for the identification of the center curve for dielectric thin tubes and metallic nanowires.

Chapter 5 is about the maximization of electromagnetic chirality (em-chirality) for thin tubular scattering objects. First, we recall the definition and quantification of em-chirality for general three-dimensional scattering objects. Afterwards we focus on the quantification of em-chirality for thin tubular scatterers. By using the leading order term of the asymptotic perturbation formula we find an explicit representation of the leading order term of a far field operator expansion that is associated to the thin tubular scatterer. This implies a functional that maps the center curve and a potential rotation of the cross-section around the center curve to its chirality value. For this operator we rigorously derive the Fréchet derivative with respect to the center curve and the rotation and establish an efficient shape optimization algorithm for designing highly em-chiral structures and in particular, highly em-chiral metallic nanowires. We introduce penalization terms for the optimization and derive the corresponding Fréchet derivatives. Finally, we highlight numerical results achieved by the shape optimization algorithm. For dielectric, dual symmetric and metallic thin tubular scattering objects, we study shape optimizations and examine the final structures that the optimization scheme provides by performing various parameter scans. In Appendix A we study a few basic definitions from functional analysis.

In Appendix B we collect several useful estimates that are needed for the characterization of the polarization tensor in Chapter 3.

Moreover, we study in Appendix C the PMCHTW formulation that we need in order to simulate electromagnetic scattering using the boundary element library Bempp.

In Appendix D we compute derivatives of entire solutions of Maxwell's equations. These are needed for the shape optimization.

Prior publications

This thesis is based on the following works, in which I contributed as an author:

- [14], together with T. Arens and R. Griesmaier,
- [28], together with Y. Capdeboscq and R. Griesmaier,
- [50], together with I. Fernandez-Corbaton, R. Griesmaier and C. Rockstuhl.

Chapter 3 was originally published in [28] and [50]. In [28] we studied the derivation of the asymptotic perturbation formula in free space and the characterization of the polarization tensor for dielectric materials. We extended this to metallic materials in [50]. The reconstruction of thin tubular scattering objects in Chapter 4 was originally published in [28]. The shape optimization for thin em-chiral structures from Chapter 5 was published in [14] and [50]. In [14] we studied shape optimization for dielectric thin tubes with a circular cross-section and in [50] we extended these studies to metallic nanowires with an elliptical cross-section. Appendix B was published in [28] and Appendix D in [14].

Chapter 2

Time-harmonic Maxwell's equations: Well-posedness for dielectric and metallic objects

Maxwell's equations model electromagnetic wave propagation and serve as the governing partial differential equation for describing the scattering problems that we study in this work. In this chapter, we consider general bounded Lipschitz domains $D \subset \mathbb{R}^3$ as potential scattering objects. We first discuss preliminaries for studying Maxwell's equations. This includes special functions, spaces and traces. Afterwards, we derive time-harmonic Maxwell's equations and show existence and uniqueness for the particular coefficients considered in this thesis. For this aim, we use the procedure, ideas and results from [99].

2.1 Preliminaries

We shortly summarize the mathematical framework for studying time-harmonic Maxwell's equations. For an open set $\Omega \subset \mathbb{R}^d$ with $d = 2, 3$ we denote by $C^k(\Omega)$ and $C^k(\partial\Omega)$ the classical function spaces of k times continuously differentiable functions on Ω and $\partial\Omega$, respectively. The spaces $C_0^k(\Omega)$ and $C^k(\overline{\Omega})$ are constituted by functions in $C^k(\Omega)$ that have compact support in Ω and that have bounded and uniformly continuous derivatives up to order k on $\overline{\Omega}$, respectively. Let $B'_\alpha(0)$ denote the two-dimensional disc of radius α centered at the origin. Moreover, denote by $B_\alpha(0)$ the three-dimensional ball of radius α centered at the origin. We recall the definition of a three-dimensional Lipschitz domain from [88, Def. 5.1].

Definition 2.1. We define a domain $\Omega \subset \mathbb{R}^3$ to be a Lipschitz domain, if there exist a finite number of open cylinders U_j, $j = 1, \dots, m$, $m \in \mathbb{N}$ of the form

$$U_j \;=\; \{R_j \boldsymbol{x} + \boldsymbol{z}^{(j)} \,|\, \boldsymbol{x} \in B'_\alpha(0) \times (-2\beta_j, 2\beta_j)\}$$

with $\boldsymbol{z}^{(j)} \in \mathbb{R}^3$ and rotations $R_j \in \mathbb{R}^{3\times 3}$ and real-valued Lipschitz-continuous functions $\xi_j \in C(\overline{B'_\alpha(0)})$ with $|\xi_j(x_1, x_2)| \leq \beta_j$ for all $(x_1, x_2) \in \overline{B'_\alpha(0)}$ such that $\partial\Omega \subset \bigcup_{j=1}^m U_j$ and

$$\begin{aligned}
\partial\Omega \cap U_j \;&=\; \{R_j \boldsymbol{x} + \boldsymbol{z}^{(j)} \,|\, (x_1, x_2) \in B'_\alpha(0),\; x_3 \;=\; \xi_j(x_1, x_2)\}\,,\\
\Omega \cap U_j \;&=\; \{R_j \boldsymbol{x} + \boldsymbol{z}^{(j)} \,|\, (x_1, x_2) \in B'_\alpha(0),\; x_3 \;<\; \xi_j(x_1, x_2)\}\,,\\
U_j \setminus \overline{\Omega} \;&=\; \{R_j \boldsymbol{x} + \boldsymbol{z}^{(j)} \,|\, (x_1, x_2) \in B'_\alpha(0),\; x_3 \;>\; \xi_j(x_1, x_2)\}\,.
\end{aligned}$$

Two-dimensional Lipschitz domains can be defined similarly (see e.g. [97, Def. 3.28]). The Definition 2.1 requires the sets of cylinders U_j, $j = 1, \dots, m$ to cover the boundary $\partial\Omega$. The cross-section of the cylinder $B'_\alpha(0) \times \{0\}$ is mapped to a part of the boundary by using the map ξ_j. Assuming without loss of generality that the height of the cylinder β is larger than the radius α, we have $B_\alpha(0) \subset B'_\alpha(0) \times (-2\beta_j, 2\beta_j)$. Moreover, we define the transformations

$$\widetilde{\Psi_j}(\boldsymbol{x}) \;=\; R_j \begin{bmatrix} x_1 \\ x_2 \\ \xi_j(x_1, x_2) + x_3 \end{bmatrix} + \boldsymbol{z}^{(j)}, \quad \boldsymbol{x} \;=\; (x_1, x_2, x_3)^\top \in B_\alpha(0)\,,$$

as well as the restriction of $\widetilde{\Psi}_j$ to $B'_\alpha(0)$

$$\Psi_j(\widetilde{\boldsymbol{x}}) \;=\; R_j \begin{bmatrix} x_1 \\ x_2 \\ \xi_j(x_1,x_2) \end{bmatrix} + \boldsymbol{z}^{(j)}, \quad \widetilde{\boldsymbol{x}} \;=\; (x_1,x_2)^\top \in B'_\alpha(0) \tag{2.1}$$

(see [88, p. 228]). The functions Ψ_j are differentiable a.e. on $B'_\alpha(0)$ by the Rademacher theorem (see e.g. [45, Thm. 6, Sec. 5.8]). This implies the existence of a unit normal vector $\boldsymbol{\nu}$ a.e. on the boundary of Ω (see also [88, Rmk. A.8]). We define $U'_j = \widetilde{\Psi}_j(B_\alpha(0))$. Then, the boundary $\partial\Omega$ is still covered by these sets, i.e. $\partial\Omega \subset \bigcup_{j=1}^m U'_j$. Moreover,

$$\begin{aligned}
\partial\Omega \cap U'_j \;&=\; \{\widetilde{\Psi}_j(\boldsymbol{x}) \,|\, \boldsymbol{x} \in B_\alpha(0),\, x_3 \,=\, 0\} \;=\; \{\Psi_j(\widetilde{\boldsymbol{x}}) \,|\, \widetilde{\boldsymbol{x}} \in B'_\alpha(0)\}\,, \\
\Omega \cap U'_j \;&=\; \{\widetilde{\Psi}_j(\boldsymbol{x}) \,|\, \boldsymbol{x} \in B_\alpha(0),\, x_3 \,<\, 0\}\,, \\
U'_j \setminus \overline{\Omega} \;&=\; \{\widetilde{\Psi}_j(\boldsymbol{x}) \,|\, \boldsymbol{x} \in B_\alpha(0),\, x_3 \,>\, 0\}\,.
\end{aligned}$$

The transformation Ψ will be directly involved in the definition of (vector-valued) Sobolev spaces. From now on, let $\Omega \subset \mathbb{R}^3$ denote a Lipschitz domain as introduced in Definition 2.1. We denote by $L^p(\Omega)$ for $1 \le p \le \infty$ the standard Lebesgue space with norm

$$\|f\|_{L^p(\Omega)} \;=\; \begin{cases} \left(\int_\Omega |f(\boldsymbol{x})|^p \,\mathrm{d}\boldsymbol{x}\right)^{1/p} & \text{for } 1 \le p < \infty \\ \operatorname{ess\,sup}_{\boldsymbol{x}\in\Omega} |f(\boldsymbol{x})| & \text{for } p = \infty\,. \end{cases} \tag{2.2}$$

The space $L^2(\Omega)$ is a Hilbert space with scalar product[1]

$$\langle f, g\rangle_{L^2(\Omega)} \;=\; \int_\Omega f(\boldsymbol{x})\overline{g(\boldsymbol{x})} \,\mathrm{d}\boldsymbol{x} \quad \text{for } f, g \in L^2(\Omega)\,.$$

The Hilbert space $L^2(\partial\Omega)$ is defined analogously. For a locally integrable function u in Ω and a multi-index $\boldsymbol{\alpha} \in \mathbb{N}_0^3$ we say that a locally integrable function v is the $\boldsymbol{\alpha}$th weak derivative of u if it satisfies

$$\int_\Omega \phi(\boldsymbol{x}) v(\boldsymbol{x}) \,\mathrm{d}\boldsymbol{x} \;=\; (-1)^{|\boldsymbol{\alpha}|} \int_\Omega u(\boldsymbol{x})(D^{\boldsymbol{\alpha}}\phi)(\boldsymbol{x}) \,\mathrm{d}\boldsymbol{x} \quad \text{for all } \phi \in C_0^{|\boldsymbol{\alpha}|}(\Omega)$$

(see e.g. [63, Sec. 7.3.] or [45, Sec. 5.2]). Further, we denote by $W^k(\Omega)$ the space of k times weakly differentiable functions. Let $W^{k,p}(\Omega)$, for $1 \le p < \infty$, be defined by

$$W^{k,p}(\Omega) \;=\; \{u \in W^k(\Omega) \,|\, D^{\boldsymbol{\alpha}} u \in L^p(\Omega) \text{ for all } |\boldsymbol{\alpha}| \le k\}\,,$$

where the norm is given by

$$\|u\|_{W^{k,p}(\Omega)} \;=\; \Big(\int_\Omega \sum_{|\boldsymbol{\alpha}|\le k} \big|(D^{\boldsymbol{\alpha}} u)(\boldsymbol{x})\big|^p \,\mathrm{d}\boldsymbol{x}\Big)^{1/p}. \tag{2.3}$$

We denote by $W_0^{1,p}(\Omega)$ the closure of $C_0^1(\Omega)$ with respect to the norm in (2.3) for $k = 1$. For $p = 2$, $W^{k,p}(\Omega)$ and $W_0^{k,p}(\Omega)$ become Hilbert spaces and we denote these by $H^k(\Omega) = W^{k,2}(\Omega)$ and $H_0^1(\Omega) = W_0^{1,2}(\Omega)$, respectively. Often, we consider $H^1(\Omega)$, where the inner product is given by

$$\langle u, v\rangle_{H^1(\Omega)} \;=\; \langle u, v\rangle_{L^2(\Omega)} + \langle \nabla u, \nabla v\rangle_{L^2(\Omega)}\,. \tag{2.4}$$

In order to introduce Sobolev spaces on the boundary $\partial\Omega$ we first consider a space of periodic functions and declare the assignment of a function to this space by the decay of its Fourier

[1] In our notation, scalar products are always linear in the first and antilinear in the second component.

coefficients. This follows [88, Def. 5.5]. Let $Q_d = (-\pi,\pi)^d \subset \mathbb{R}^d$ denote the cube in $\mathbb{R}^d$ for $d = 2, 3$. For a scalar-valued function $v \in L^2(Q_d)$ the Fourier series $\sum_{\boldsymbol{n}\in\mathbb{Z}^d} v_{\boldsymbol{n}} e^{\mathrm{i}\boldsymbol{n}\cdot\boldsymbol{x}}$ with Fourier coefficients $(v_{\boldsymbol{n}})_{\boldsymbol{n}\in\mathbb{Z}^d} \subset \mathbb{C}$ converges to v with respect to the norm in (2.2) for $p = 2$. Therefore, we identify the function v with its Fourier series and write $v(\boldsymbol{x}) = \sum_{\boldsymbol{n}\in\mathbb{Z}^d} v_{\boldsymbol{n}} e^{\mathrm{i}\boldsymbol{n}\cdot\boldsymbol{x}}$. For any real-valued $s \geq 0$, let $H^s_{\mathrm{per}}(Q_d)$ be defined as

$$H^s_{\mathrm{per}}(Q_d) = \Big\{ v \in L^2(Q_d) \,\Big|\, \|v\|_{H^s_{\mathrm{per}}(Q_d)} < \infty \Big\}, \text{ with } \|v\|_{H^s_{\mathrm{per}}(Q_d)} = \Big(\sum_{\boldsymbol{n}\in\mathbb{Z}^d} (1+|\boldsymbol{n}|^2)^s |v_{\boldsymbol{n}}|^2 \Big)^{1/2}.$$

Indeed, $\|\cdot\|_{H^s_{\mathrm{per}}(Q_d)}$ is a norm (see [88, Def. 5.5]). The trace $\gamma_0 : H^1_{\mathrm{per}}(Q_3) \to H^{1/2}_{\mathrm{per}}(Q_2)$ is introduced as the extension of $\widetilde{\gamma_0} : \mathcal{P}(Q_3) \to \mathcal{P}(Q_2)$ defined by $\widetilde{\gamma_0}(u) = u|_{Q_2\times\{0\}}$, where $\mathcal{P}(Q_3)$ and $\mathcal{P}(Q_2)$ are the spaces of trigonometric polynomials defined on Q_3 and Q_2, respectively (see [88, Thm. 5.7]). In order to define the operator γ_0 for a Lipschitz boundary $\partial\Omega$ we need a partition of unity $\{\phi_j,\ j = 1,\dots,m\}$ (see Theorem A.1) and the transformations Ψ_j from (2.1). Let $f \in L^2(\partial\Omega)$. Then, using that $\left|\frac{\partial\Psi_j}{\partial x_1} \times \frac{\partial\Psi_j}{\partial x_2}\right| = (1+|\nabla\xi_j|^2)^{1/2}$ and the transformation rule gives

$$\begin{aligned} \|f\|^2_{L^2(\partial\Omega)} = \int_{\partial\Omega} |f(\boldsymbol{y})|^2 \,\mathrm{d}s &= \sum_{j=1}^m \int_{\partial\Omega\cap U'_j} \phi_j(\boldsymbol{y}) |f(\boldsymbol{y})|^2 \,\mathrm{d}s \\ &= \sum_{j=1}^m \int_{Q_2} |\widetilde{f}_j(\boldsymbol{x})|^2 (1+|\nabla\xi_j(\boldsymbol{x})|^2)^{1/2} \,\mathrm{d}\boldsymbol{x}\,, \end{aligned} \tag{2.5}$$

where

$$\widetilde{f}_j(\boldsymbol{x}) = \begin{cases} (\phi_j(\Psi_j(\boldsymbol{x}))^{1/2} f(\Psi_j(\boldsymbol{x})), & \boldsymbol{x} \in B'_\alpha(0)\,, \\ 0, & \boldsymbol{x} \in Q_2 \setminus B'_\alpha(0)\,, \end{cases} \tag{2.6}$$

(see [88, p. 236]). Using the inequality

$$1 \leq \Big(1+|\nabla\xi_j(\boldsymbol{x})|^2\Big)^{1/2} \leq \max_{j=1,\dots,m} \Big(1+\|\nabla\xi_j\|^2_{L^\infty(Q_2)}\Big)^{1/2}$$

and (2.5) shows that the norms $\|f\|_{L^2(\partial\Omega)}$ and $\Big(\sum_{j=1}^m \|\widetilde{f}_j\|^2_{L^2(Q_2)}\Big)^{1/2}$ are equivalent. Therefore, we find that $f \in L^2(\partial\Omega)$ if and only if $\widetilde{f}_j \in L^2(Q_2)$ for all $j = 1,\dots,m$ (see [88, p. 236]). This property is used to define the space $H^{1/2}(\partial\Omega)$, given by

$$H^{1/2}(\partial\Omega) = \{ f \in L^2(\partial\Omega) \,|\, \widetilde{f}_j \in H^{1/2}_{\mathrm{per}}(Q_2) \text{ for all } j = 1,\dots,m \}$$

with norm

$$\|f\|_{H^{1/2}(\partial\Omega)} = \Big(\sum_{j=1}^m \|\widetilde{f}_j\|^2_{H^{1/2}_{\mathrm{per}}(Q_2)} \Big)^{1/2} \tag{2.7}$$

(see [88, Def. 5.8]). The choice of the partition of unity, that is used in the definition of $\widetilde{f}_j$ in (2.6) does not matter, as different choices imply equivalent norms (2.7) (see [88, Cor. 5.15]). It turns out that the trace $\gamma_0 : C^1(\overline{\Omega}) \to C(\partial\Omega)$, $\gamma_0 u = u|_{\partial\Omega}$ can be extended to a bounded operator from $H^1(\Omega)$ to $H^{1/2}(\partial\Omega)$. Moreover, the trace operator γ_0 has a bounded right inverse that we denote by η (see [88, Thm. 5.10]). We denote by $H^{-1/2}(\partial\Omega)$ the dual space of $H^{1/2}(\partial\Omega)$. A vector field $\boldsymbol{v} \in (L^2(\Omega))^3$ has a variational (or weak) divergence in $L^2(\Omega)$ if there is a scalar-valued function $p \in L^2(\Omega)$ such that

$$\int_\Omega \boldsymbol{v}\cdot\nabla\varphi \,\mathrm{d}\boldsymbol{x} = -\int_\Omega p\varphi \,\mathrm{d}\boldsymbol{x} \quad \text{for all } \varphi \in C^\infty_0(\Omega)\,. \tag{2.8}$$

For the unique function p we write $\mathrm{div}\boldsymbol{v}$ (see [88, Def. 4.16]). The space of functions that possess a weak divergence in $L^2(\Omega)$ is denoted by $H(\mathrm{div},\Omega)$. For $\boldsymbol{u}\in(C^\infty(\Omega))^3$, the normal trace

$$\gamma_n\boldsymbol{u} \;=\; \boldsymbol{\nu}\cdot\boldsymbol{u}|_{\partial\Omega}\,, \tag{2.9}$$

where $\boldsymbol{\nu}$ denotes the exterior unit normal to $\partial\Omega$, can be extended to a continuous linear map from $H(\mathrm{div},\Omega)$ to $H^{-1/2}(\partial\Omega)$. Moreover, Green's theorem holds for functions $\boldsymbol{v}\in H(\mathrm{div},\Omega)$ and $\varphi\in H^1(\Omega)$, that is

$$\int_\Omega \boldsymbol{v}\cdot\nabla\varphi\,\mathrm{d}\boldsymbol{x}+\int_\Omega \mathrm{div}\boldsymbol{v}\varphi\,\mathrm{d}\boldsymbol{x} \;=\; \int_{\partial\Omega}\varphi\boldsymbol{\nu}\cdot\boldsymbol{v}\,\mathrm{d}s\,. \tag{2.10}$$

These results are found in [99, Thm. 3.24]. We emphasize that we interpret the right hand side of (2.10) as the dual pairing in $H^{1/2}(\partial\Omega)\times H^{-1/2}(\partial\Omega)$.

A vector field $\boldsymbol{v}\in(L^2(\Omega))^3$ has a variational (or weak) **curl** in $(L^2(\Omega))^3$, if there exists a vector field $\boldsymbol{w}\in(L^2(\Omega))^3$ such that

$$\int_\Omega \boldsymbol{v}\cdot\mathbf{curl}\,\boldsymbol{\psi}\,\mathrm{d}\boldsymbol{x} \;=\; \int_\Omega \boldsymbol{w}\cdot\boldsymbol{\psi}\,\mathrm{d}\boldsymbol{x}\quad\text{for all }\boldsymbol{\psi}\in(C_0^\infty(\Omega))^3\,.$$

For the unique function $\boldsymbol{w}$ we write $\mathbf{curl}\,\boldsymbol{v}$ (see [88, Def. 4.16]). The space of functions that possess a weak **curl** in $(L^2(\Omega))^3$ is denoted by $H(\mathbf{curl},\Omega)$, i.e.

$$H(\mathbf{curl},\Omega) \;=\; \left\{\boldsymbol{v}\in\left(L^2(\Omega)\right)^3 \;\middle|\; \mathbf{curl}\,\boldsymbol{v}\in\left(L^2(\Omega)\right)^3\right\}.$$

The inner product in $H(\mathbf{curl},\Omega)$ is defined by

$$\langle\boldsymbol{u},\boldsymbol{v}\rangle \;=\; \langle\mathbf{curl}\,\boldsymbol{u},\mathbf{curl}\,\boldsymbol{v}\rangle_{L^2(\Omega)}+\langle\boldsymbol{u},\boldsymbol{v}\rangle_{L^2(\Omega)}\,. \tag{2.11}$$

For an unbounded Ω we use the notation $H_{\mathrm{loc}}(\mathbf{curl},\Omega)$ for the space of functions, for which the function itself and its **curl** are locally in $(L^2(\Omega))^3$. More precisely, a function $\boldsymbol{v}$ is said to be in $H_{\mathrm{loc}}(\mathbf{curl},\Omega)$ if $\boldsymbol{v}|_{\widetilde{\Omega}}$ is in $H(\mathbf{curl},\widetilde{\Omega})$ for all open and bounded $\widetilde{\Omega}\subset\Omega$. The following theorem can be found in e.g. [88, Thm. 5.19].

Proposition 2.2. *If Ω is a bounded Lipschitz domain, then $(C^\infty(\overline{\Omega}))^3$ is dense in $H(\mathbf{curl},\Omega)$ with respect to the norm in (2.11).*

In order to introduce appropriate traces for functions in $H(\mathbf{curl},\Omega)$, we first describe periodic Sobolev spaces of vector-valued functions (see [88, Def. 5.20]). We recall that for $\boldsymbol{x}\in Q_d=(-\pi,\pi)^d$ and $\boldsymbol{v}\in(L^2(Q_d))^3$ the Fourier series $\sum_{\boldsymbol{n}\in\mathbb{Z}^d}\boldsymbol{v}_{\boldsymbol{n}}e^{\mathrm{i}\boldsymbol{n}\cdot\boldsymbol{x}}$, where $\boldsymbol{v}_{\boldsymbol{n}}\in\mathbb{C}^d$ denote the Fourier coefficients of $\boldsymbol{v}$, converges to $\boldsymbol{v}$ with respect to the norm in $(L^2(Q_d))^3$. Let

$$\mathcal{T}(Q_2) \;=\; \left\{\sum_{|\boldsymbol{m}|\le N}\boldsymbol{v}_{\boldsymbol{m}}e^{\mathrm{i}\boldsymbol{m}\cdot\boldsymbol{x}}\;\middle|\;\boldsymbol{x}\in Q_2,\,\boldsymbol{v}_{\boldsymbol{m}}\in\mathbb{C}^2,\,N\in\mathbb{N}\right\}$$

be the space of trigonometric vector polynomials. For any $s\in\mathbb{R}$ we introduce the spaces $H^s_{\mathrm{div,per}}(Q_2)$ and $H^s_{\mathrm{curl,per}}(Q_2)$ as the completion of $\mathcal{T}(Q_2)$ with respect to the norms

$$\|\boldsymbol{v}\|_{H^s_{\mathrm{div,per}}(Q_2)} \;=\; \Big(\sum_{\boldsymbol{m}\in\mathbb{Z}^2}(1+|\boldsymbol{m}|^2)^s\left(|\boldsymbol{v}_{\boldsymbol{m}}|^2+|\boldsymbol{m}\cdot\boldsymbol{v}_{\boldsymbol{m}}|^2\right)\Big)^{1/2},$$

$$\|\boldsymbol{v}\|_{H^s_{\mathrm{curl,per}}(Q_2)} \;=\; \Big(\sum_{\boldsymbol{m}\in\mathbb{Z}^2}(1+|\boldsymbol{m}|^2)^s\left(|\boldsymbol{v}_{\boldsymbol{m}}|^2+|\boldsymbol{m}\times\boldsymbol{v}_{\boldsymbol{m}}|^2\right)\Big)^{1/2},$$

respectively (see [88, Def. 5.20]). Here, $\boldsymbol{m}\times\boldsymbol{a}=m_1a_2-m_2a_1$ for $\boldsymbol{m},\boldsymbol{a}\in\mathbb{C}^2$. For a bounded Lipschitz domain Ω, let

$$L^2_t(\partial\Omega) \;=\; \left\{\boldsymbol{a}\in\left(L^2(\partial\Omega)\right)^3 \mid \boldsymbol{\nu}\cdot\boldsymbol{a}=0\ \text{ a.e. on }\partial\Omega\right\}.$$

The unit sphere in $\mathbb{R}^3$ is denoted by S^2 and often takes the role of $\partial\Omega$. Let $\{\phi_j \,|\, j = 1, \dots, m\}$ be a partition of unity (see Theorem A.1) and recall the transformation Ψ_j from (2.1). For $\boldsymbol{f} \in L_t^2(\partial\Omega)$ we define the functions

$$\widetilde{\boldsymbol{f}_j^t}(\widetilde{\boldsymbol{x}}) = \begin{cases} \zeta_j(\widetilde{\boldsymbol{x}})\,(\phi_j(\Psi_j(\widetilde{\boldsymbol{x}})))^{1/2}\, F_j^{-1}(\widetilde{\boldsymbol{x}})\boldsymbol{f}(\Psi_j(\widetilde{\boldsymbol{x}})), & \widetilde{\boldsymbol{x}} \in B'_\alpha(0)\,, \\ 0, & \widetilde{\boldsymbol{x}} \in Q_2 \setminus \overline{B'_\alpha(0)}\,, \end{cases}$$
$$\widetilde{\boldsymbol{f}_j^T}(\widetilde{\boldsymbol{x}}) = \begin{cases} \zeta_j(\widetilde{\boldsymbol{x}})\,(\phi_j(\Psi_j(\widetilde{\boldsymbol{x}})))^{1/2}\, F_j^{\top}(\widetilde{\boldsymbol{x}})\boldsymbol{f}(\Psi_j(\widetilde{\boldsymbol{x}})), & \widetilde{\boldsymbol{x}} \in B'_\alpha(0)\,, \\ 0, & \widetilde{\boldsymbol{x}} \in Q_2 \setminus \overline{B'_\alpha(0)}\,, \end{cases}$$

where

$$\zeta_j(\widetilde{\boldsymbol{x}}) = \left|\frac{\partial\Psi_j(\widetilde{\boldsymbol{x}})}{\partial x_1} \times \frac{\partial\Psi_j(\widetilde{\boldsymbol{x}})}{\partial x_2}\right| \quad \text{and} \quad F_j(\widetilde{\boldsymbol{x}}) = \left[\frac{\partial\Psi_j(\widetilde{\boldsymbol{x}})}{\partial x_1} \,\middle|\, \frac{\partial\Psi_j(\widetilde{\boldsymbol{x}})}{\partial x_2} \,\middle|\, \frac{\partial\Psi_j(\widetilde{\boldsymbol{x}})}{\partial x_1} \times \frac{\partial\Psi_j(\widetilde{\boldsymbol{x}})}{\partial x_2}\right]$$

for $\widetilde{\boldsymbol{x}} \in B'_\alpha(0)$. We define the space $H_{\mathrm{div}}^{-1/2}(\partial\Omega)$ and $H_{\mathrm{curl}}^{-1/2}(\partial\Omega)$ as the completion of the spaces

$$\left\{\boldsymbol{f} \in L_t^2(\partial\Omega) \,|\, \widetilde{\boldsymbol{f}_j^t} \in H_{\mathrm{div,per}}^{-1/2}(Q_2),\ j = 1, \dots, m\right\} \text{ and}$$
$$\left\{\boldsymbol{f} \in L_t^2(\partial\Omega) \,|\, \widetilde{\boldsymbol{f}_j^T} \in H_{\mathrm{curl,per}}^{-1/2}(Q_2),\ j = 1, \dots, m\right\}$$

with respect to the norms

$$\|\boldsymbol{f}\|_{H_{\mathrm{div}}^{-1/2}(\partial\Omega)} = \Big(\sum_{j=1}^m \|\widetilde{\boldsymbol{f}_j^t}\|^2_{H_{\mathrm{div,per}}^{-1/2}(Q_2)}\Big)^{1/2} \quad \text{and} \quad \|\boldsymbol{f}\|_{H_{\mathrm{curl}}^{-1/2}(\partial\Omega)} = \Big(\sum_{j=1}^m \|\widetilde{\boldsymbol{f}_j^T}\|^2_{H_{\mathrm{curl,per}}^{-1/2}(Q_2)}\Big)^{1/2},$$

respectively (see [88, Def. 5.23]). For $\boldsymbol{v} \in (C^\infty(\Omega))^3$ we consider the tangential trace γ_t and the projection on the tangential plane γ_T given by

$$\gamma_t(\boldsymbol{v}) = \boldsymbol{\nu} \times \boldsymbol{v}|_{\partial\Omega} \quad \text{and} \quad \gamma_T(\boldsymbol{v}) = (\boldsymbol{\nu} \times \boldsymbol{v}|_{\partial\Omega}) \times \boldsymbol{\nu}.$$

Both traces γ_t and γ_T can be extended to $H(\mathbf{curl}, \Omega)$ in such a way that the maps

$$\gamma_t : H(\mathbf{curl}, \Omega) \to H_{\mathrm{div}}^{-1/2}(\partial\Omega) \quad \text{and} \quad \gamma_T : H(\mathbf{curl}, \Omega) \to H_{\mathrm{curl}}^{-1/2}(\partial\Omega) \tag{2.12}$$

are both linear, continuous and surjective. Moreover, for both operators, there exists a bounded right inverse denoted by $\eta_t : H_{\mathrm{div}}^{-1/2}(\partial\Omega) \to H(\mathbf{curl}, \Omega)$ and $\eta_T : H_{\mathrm{curl}}^{-1/2}(\partial\Omega) \to H(\mathbf{curl}, \Omega)$ (see [88, Thm. 5.24]). Following [88, Def. 5.29], for $\boldsymbol{a} \in H_{\mathrm{div}}^{-1/2}(\partial\Omega)$ and $\boldsymbol{b} \in H_{\mathrm{curl}}^{-1/2}(\partial\Omega)$, we define the surface divergence $\mathrm{div}_{\partial\Omega}\boldsymbol{a} \in H^{-1/2}(\partial\Omega)$ and the surface curl $\mathrm{curl}_{\partial\Omega}\,\boldsymbol{b} \in H^{-1/2}(\partial\Omega)$ as the linear bounded functionals defined by

$$\int_{\partial\Omega} \mathrm{div}_{\partial\Omega}\boldsymbol{a}\psi \,\mathrm{d}s = -\int_{\partial\Omega} \boldsymbol{a} \cdot \left(\left(\boldsymbol{\nu} \times \nabla\widetilde{\psi}\right) \times \boldsymbol{\nu}|_{\partial\Omega}\right) \mathrm{d}s \quad \text{for all } \psi \in H^{1/2}(\partial\Omega)\,, \tag{2.13a}$$
$$\int_{\partial\Omega} \mathrm{curl}_{\partial\Omega}\,\boldsymbol{b}\psi \,\mathrm{d}s = -\int_{\partial\Omega} \left(\boldsymbol{\nu} \times \nabla\widetilde{\psi}|_{\partial\Omega}\right) \cdot \boldsymbol{b} \,\mathrm{d}s \quad \text{for all } \psi \in H^{1/2}(\partial\Omega)\,. \tag{2.13b}$$

Here, $\widetilde{\psi} \in H^1(\Omega)$ is any extension of ψ, which is defined as $\widetilde{\psi} = \eta\psi$, where η is the bounded right inverse of the trace γ_0. We emphasize that both left hand sides in (2.13) must be interpreted as the dual pairing in $H^{1/2}(\partial\Omega) \times H^{-1/2}(\partial\Omega)$ and the right hand sides as the dual pairing in $H_{\mathrm{div}}^{-1/2}(\partial\Omega) \times H_{\mathrm{curl}}^{-1/2}(\partial\Omega)$. By Proposition 2.2, for a bounded domain Ω, the space $(C^\infty(\overline{\Omega}))^3$ is dense in $H(\mathbf{curl}, \Omega)$. This implies that the space $\{\boldsymbol{\nu} \times \boldsymbol{u}|_{\partial\Omega} \,|\, \boldsymbol{u} \in (C^\infty(\overline{\Omega}))^3\}$ is dense in $H_{\mathrm{div}}^{-1/2}(\partial\Omega)$. For $\boldsymbol{a} \in H_{\mathrm{div}}^{-1/2}(\partial\Omega)$ we therefore find an expression for $\boldsymbol{a} \times \boldsymbol{\nu} \in H_{\mathrm{curl}}^{-1/2}(\partial\Omega)$ that we interpret as

$$\boldsymbol{a} \times \boldsymbol{\nu} = (\boldsymbol{\nu} \times \eta_t\boldsymbol{a}) \times \boldsymbol{\nu}|_{\partial\Omega}\,, \tag{2.14}$$

where η_t is the bounded right inverse of γ_t (see also [88, Proof of Lem. 5.61]).

We introduce spherical coordinates

$$\boldsymbol{x} = r\,[\sin(\theta)\cos(\varphi)\,|\,\sin(\theta)\sin(\varphi)\,|\,\cos(\theta)]^\top, \qquad r>0,\ \theta\in[0,\pi],\ \varphi\in[0,2\pi) \tag{2.15}$$

and define the spherical harmonics Y_n^m for $\widehat{\boldsymbol{x}} = \boldsymbol{x}/|\boldsymbol{x}| \in S^2$ by

$$Y_n^m(\widehat{\boldsymbol{x}}) = \sqrt{\frac{2n+1}{4\pi}\frac{(n-|m|)!}{(n+|m|)!}}P_n^{|m|}(\cos(\theta))\,\mathrm{e}^{\mathrm{i}m\varphi} \quad \text{for } m=-n,\ldots,n \text{ and } n=1,2,\ldots,$$

where $P_n^m(t) = (1-t^2)^{m/2}(\mathrm{d}/\mathrm{d}t)^m P_n(t)$ denote the associated Legendre polynomials. The functions P_n are the Legendre polynomials (see e.g. [34, pp. 26]). The functions Y_n^m form a complete orthonormal system in $L^2(S^2)$ (see e.g. [88, p. 41]). We denote by ∇_{S^2} the surface gradient on the unit sphere, which for a function $f\in C^1(S^2)$ can be defined in the spherical coordinates (2.15) by

$$\nabla_{S^2} f(\theta,\phi) = \frac{\partial f}{\partial\theta}(\theta,\phi)\widehat{\boldsymbol{\theta}} + \frac{1}{\sin(\theta)}\frac{\partial f}{\partial\phi}(\theta,\phi)\widehat{\boldsymbol{\varphi}},$$

with $\widehat{\boldsymbol{\theta}} = [\cos(\theta)\cos(\varphi)\,|\,\cos(\theta)\sin(\varphi)\,|\,-\sin(\theta)]^\top$ and $\widehat{\boldsymbol{\varphi}} = [-\sin(\varphi)\,|\,\cos(\varphi)\,|\,0]^\top$. We define the vector spherical harmonics by

$$\boldsymbol{U}_n^m(\widehat{\boldsymbol{x}}) = \frac{1}{\sqrt{n(n+1)}}\nabla_{S^2}Y_n^m(\widehat{\boldsymbol{x}}) \quad \text{and} \quad \boldsymbol{V}_n^m(\widehat{\boldsymbol{x}}) = \widehat{\boldsymbol{x}}\times\boldsymbol{U}_n^m(\widehat{\boldsymbol{x}}) \tag{2.16}$$

for $m=-n,\ldots,n$ and $n=1,2,\ldots$. These functions form a complete orthonormal system in $L_t^2(S^2)$ (see e.g. [88, Thm. 2.46]), i.e., every function $\boldsymbol{f}\in L_t^2(S^2)$ has an expansion of the form

$$\boldsymbol{f}(\widehat{\boldsymbol{x}}) = \sum_{n=1}^{\infty}\sum_{m=-n}^{n} a_n^m\boldsymbol{U}_n^m(\widehat{\boldsymbol{x}}) + b_n^m\boldsymbol{V}_n^m(\widehat{\boldsymbol{x}}), \quad \text{for } \widehat{\boldsymbol{x}}\in S^2. \tag{2.17}$$

Remark 2.3. For functions $\boldsymbol{a}\in H_{\mathrm{div}}^{-1/2}(\partial B_1(0))$ we interpret the expansion in (2.17) in the following sense. The function $\boldsymbol{a}$ can be extended to $H(\mathbf{curl}, B_1(0))$ by using the bounded right inverse η_t of the trace γ_t from (2.12). The extension $\boldsymbol{u} = \eta_t\boldsymbol{a}\in H(\mathbf{curl}, B_1(0))$ can be approximated by a sequence $(\boldsymbol{u}_N)_N \subset (C^\infty(\overline{B_1(0)}))^3$ (see Proposition 2.2) that we can write explicitly as

$$\boldsymbol{u}_N(r\widehat{\boldsymbol{x}}) = \sum_{n=1}^{N}\sum_{m=-n}^{n}\alpha_n^m(r)\boldsymbol{U}_n^m(\widehat{\boldsymbol{x}}) + \beta_n^m(r)\boldsymbol{V}_n^m(\widehat{\boldsymbol{x}}) + \gamma_n^m(r)Y_n^m(\widehat{\boldsymbol{x}})\widehat{\boldsymbol{x}},$$

for $0\le r<1$, $\widehat{\boldsymbol{x}}\in S^2$ (see [88, Thm. 5.36]). Applying the trace γ_t to $\boldsymbol{u}_N$ (note that $\boldsymbol{\nu} = \widehat{\boldsymbol{x}}$ on S^2), using the boundedness of γ_t and the fact that $\gamma_t\boldsymbol{u} = \boldsymbol{a}$ gives that

$$\boldsymbol{\nu}\times u_N|_{\partial B_1(0)}(\widehat{\boldsymbol{x}}) = \sum_{n=1}^{N}\sum_{m=-n}^{n}\alpha_n^m(1)\boldsymbol{V}_n^m(\widehat{\boldsymbol{x}}) - \beta_n^m(1)\boldsymbol{U}_n^m(\widehat{\boldsymbol{x}}) \to \boldsymbol{a} \quad \text{as } N\to\infty.$$

Similarly, we consider series expansions of $\boldsymbol{b}\in H_{\mathrm{curl}}^{-1/2}(\partial B_1(0))$.

2.2 Time-harmonic Maxwell's equations

We shortly outline how to derive time-harmonic Maxwell's equations from the time-dependent Maxwell's equations. We refer to the introductory chapters in [81, 88, 96]. Let $\mathcal{E}$ be the electric field in Volt/meter, $\mathcal{H}$ the magnetic field in Ampere/meter, $\mathcal{D}$ the electric displacement

in Coulomb/meter^2, $\mathcal{B}$ the magnetic flux density in Weber/meter^2, $\mathcal{J}$ the current density in Ampere/meter^2 and ρ the volume charge in Coulomb/meter^3. Maxwell's equations relate the fields $\mathcal{E}, \mathcal{H}, \mathcal{D}, \mathcal{B}, \mathcal{J}$ and the scalar function ρ via

$$\begin{aligned} \operatorname{div}\mathcal{D} &= \rho\,, \qquad & \mathbf{curl}\,\mathcal{H} &= \mathcal{J} + \frac{\partial \mathcal{D}}{\partial t}\,, \\ \operatorname{div}\mathcal{B} &= 0\,, \qquad & \mathbf{curl}\,\mathcal{E} + \frac{\partial \mathcal{B}}{\partial t} &= 0\,. \end{aligned}$$

All of these quantities in general depend on time and space. The four fields $\mathcal{E}, \mathcal{H}, \mathcal{D}, \mathcal{B}$ are further related via the equations

$$\mathcal{D} = \varepsilon_0 \mathcal{E} + \mathcal{P}\,, \qquad \mathcal{H} = \frac{1}{\mu_0}\mathcal{B} - \mathcal{M}\,, \tag{2.18}$$

where $\mathcal{P}$ and $\mathcal{M}$ denote the macroscopic polarization and magnetization, respectively. The parameters ε_0 and μ_0 denote the electric permittivity and magnetic permeability in free space and they are given by

$$\varepsilon_0 = 8.854 \times 10^{-12}\,\frac{\mathrm{F}}{\mathrm{m}}, \qquad \mu_0 = 4\pi \times 10^{-7}\,\frac{\mathrm{H}}{\mathrm{m}}. \tag{2.19}$$

As described in [102, Sec. 2.1], the relations in (2.18) are not restrictive, i.e. they can be stated for any medium. In this work, we consider linear and isotropic media. This means that the constitutive relations[2], i.e. the relations between $\mathcal{D}, \mathcal{E}$ and $\mathcal{B}, \mathcal{H}$ are linear and do not depend on the direction of $\mathcal{E}$ and $\mathcal{H}$. Thus,

$$\mathcal{D} = \varepsilon \mathcal{E}\,, \qquad \mathcal{B} = \mu \mathcal{H}\,, \tag{2.20}$$

where ε and μ are scalar-valued. The equations in (2.20) are often implicitly defined by using the electric and magnetic susceptibilities χ_e, χ_m that describe the relation between $\mathcal{P}$ and $\mathcal{E}$ and $\mathcal{M}$ and $\mathcal{H}$ from (2.18) in terms of

$$\mathcal{P} = \varepsilon_0 \chi_e \mathcal{E}, \qquad \mathcal{M} = \chi_m \mathcal{H} \tag{2.21}$$

(see e.g. [102, Sec. 2.3] and [96, p. 8]). Comparing (2.21), (2.20) and (2.18) gives that $\varepsilon = \varepsilon_0(1+\chi_e)$ and $\mu = \mu_0(1+\chi_m)$. According to Ohm's law, a linear approximation to the current density $\mathcal{J}$ is given by $\mathcal{J} = \sigma\mathcal{E} + \mathcal{J}_e$, where σ is the conductivity and $\mathcal{J}_e$ denotes external source densities. We always assume that $\mathcal{J}_e = 0$. If $\sigma = 0$, the material is called dielectric.

Our considerations restrict to time-harmonic fields, i.e. we consider an ansatz for the fields as $\mathcal{E}(\boldsymbol{x}, t) = \operatorname{Re}(\boldsymbol{E}(\boldsymbol{x})\mathrm{e}^{-\mathrm{i}\omega t})$, $\mathcal{H}(\boldsymbol{x}, t) = \operatorname{Re}(\boldsymbol{H}(\boldsymbol{x})\mathrm{e}^{-\mathrm{i}\omega t})$ etc.. The number $\omega > 0$ is the angular frequency. It is connected to the frequency f via $\omega = 2\pi f$. Using ε_0 and μ_0 as defined in (2.19), the wave number k in free space is given by $k = \omega\sqrt{\varepsilon_0\mu_0}$. The corresponding wavelength $\lambda > 0$ can be computed via $\lambda = 2\pi/k = c/f$, where $c = (\varepsilon_0\mu_0)^{-1/2}$ denotes the speed of light in meter/second. Thus, the time-harmonic Maxwell's equations read

$$\mathbf{curl}\,\boldsymbol{E} - \mathrm{i}\omega\mu\boldsymbol{H} = 0\,, \qquad \mathbf{curl}\,\boldsymbol{H} + \mathrm{i}\omega\left(\varepsilon + \frac{\mathrm{i}\sigma}{\omega}\right)\boldsymbol{E} = 0\,.$$

For convenience, we do not consider permittivity and conductivity separately. This means that instead of $\varepsilon + \mathrm{i}\sigma/\omega$ we only write ε, where $\varepsilon \in \mathbb{C}$. Accordingly, a medium is said to be dielectric, if $\operatorname{Im}(\varepsilon) = 0$. This is a common procedure in the literature (see e.g. [102, Sec. 2.8]).

Before we start with the introduction to the electromagnetic scattering problem, we provide an overview about special solutions of Maxwell's equations and the Helmholtz equation that we

[2] In the literature, instead of ε and μ in (2.20) one often finds $\varepsilon_0\tilde{\varepsilon}$ and $\mu_0\tilde{\mu}$, where $\tilde{\varepsilon}$ and $\tilde{\mu}$ denote a relative permittivity and permeability (see e.g. [102, Eq. (2.11)–(2.13)]).

use throughout this thesis. For a domain $\Omega \subset \mathbb{R}^3$ we consider isotropic time-harmonic Maxwell's equations, which read

$$\mathbf{curl}\, \boldsymbol{V} - \mathrm{i}\omega\mu_0 \boldsymbol{W} \;=\; 0, \qquad \mathbf{curl}\, \boldsymbol{W} + \mathrm{i}\omega\varepsilon_0 \boldsymbol{V} \;=\; 0 \quad \text{in } \Omega\,. \tag{2.22}$$

The following definition can be found in [34, p. 231] and [34, Def. 6.6]. Note the different scaling of time-harmonic Maxwell's equations that we consider here.

Definition 2.4. Let $(\boldsymbol{V}, \boldsymbol{W})$ be a pair of fields satisfying (2.22). On the one hand, for $\Omega = \mathbb{R}^3$ the pair $(\boldsymbol{V}, \boldsymbol{W})$ is called an entire solution of (2.22). On the other hand, let $\Omega = \mathbb{R}^3 \setminus \overline{B_R(0)}$ for some $R > 0$ in (2.22). If the pair $(\boldsymbol{V}, \boldsymbol{W})$ additionally satisfies one of the Silver–Müller radiation conditions

$$\lim_{|\boldsymbol{x}|\to\infty} |\boldsymbol{x}| \left(\sqrt{\varepsilon_0}\boldsymbol{V} \times \widehat{\boldsymbol{x}} + \sqrt{\mu_0}\boldsymbol{W}\right) \;=\; 0 \quad \text{or} \quad \lim_{|\boldsymbol{x}|\to\infty} |\boldsymbol{x}| \left(\sqrt{\mu_0}\boldsymbol{W} \times \widehat{\boldsymbol{x}} - \sqrt{\varepsilon_0}\boldsymbol{V}\right) \;=\; 0\,,$$

uniformly with respect to $\widehat{\boldsymbol{x}} = \boldsymbol{x}/|\boldsymbol{x}|$, then it is called a radiating solution of (2.22).

For $n \in \mathbb{N}$, $m = -n \ldots, n$, we define the fields

$$\boldsymbol{M}_n^m(\boldsymbol{x}) \;=\; -j_n(kr)\, \boldsymbol{V}_n^m(\widehat{\boldsymbol{x}})\,, \tag{2.23a}$$

$$\mathbf{curl}\, \boldsymbol{M}_n^m(\boldsymbol{x}) \;=\; \frac{\sqrt{n(n+1)}}{r}\, j_n(kr)\, Y_n^m(\widehat{\boldsymbol{x}})\, \widehat{\boldsymbol{x}} + \frac{1}{r}\left(j_n(kr) + kr\, j_n'(kr)\right) \boldsymbol{U}_n^m(\widehat{\boldsymbol{x}})\,, \tag{2.23b}$$

as well as

$$\boldsymbol{N}_n^m(\boldsymbol{x}) \;=\; -h_n^{(1)}(kr)\, \boldsymbol{V}_n^m(\widehat{\boldsymbol{x}})\,, \tag{2.24a}$$

$$\mathbf{curl}\, \boldsymbol{N}_n^m(\boldsymbol{x}) \;=\; \frac{\sqrt{n(n+1)}}{r}\, h_n^{(1)}(kr)\, Y_n^m(\widehat{\boldsymbol{x}})\, \widehat{\boldsymbol{x}} + \frac{1}{r}\left(h_n^{(1)}(kr) + kr\, h_n^{(1)\prime}(kr)\right) \boldsymbol{U}_n^m(\widehat{\boldsymbol{x}})\,, \tag{2.24b}$$

where j_n denote spherical Bessel functions of the first kind and degree n (see e.g. [34, Chap. 2.4]). Moreover, we denote by y_n spherical Bessel functions of the second kind and degree n. The spherical Hankel functions of the first kind of order n are defined by $h_n^{(1)} = j_n + \mathrm{i}y_n$. From [34, Thm. 6.26] we find that the pair $(\boldsymbol{M}_n^m, (\mathrm{i}\omega\mu_0)^{-1}\, \mathbf{curl}\, \boldsymbol{M}_n^m)$ is an entire solution to time-harmonic Maxwell's equations (2.22) and that the pair $(\boldsymbol{N}_n^m, (\mathrm{i}\omega\mu_0)^{-1}\, \mathbf{curl}\, \boldsymbol{N}_n^m)$ is a radiating solution to time-harmonic Maxwell's equations (2.22) in $\mathbb{R}^3 \setminus \{0\}$. Moreover, for $k > 0$, we introduce the fundamental solution of the Helmholtz equation given by

$$\Phi(\boldsymbol{x}, \boldsymbol{y}) \;=\; \frac{\mathrm{e}^{\mathrm{i}k|\boldsymbol{x}-\boldsymbol{y}|}}{4\pi|\boldsymbol{x}-\boldsymbol{y}|} \quad \text{for } \boldsymbol{x}, \boldsymbol{y} \in \mathbb{R}^3,\ \boldsymbol{x} \neq \boldsymbol{y}\,. \tag{2.25}$$

This function satisfies

$$\Delta_{\boldsymbol{x}} \Phi(\boldsymbol{x}, \boldsymbol{y}) + k^2 \Phi(\boldsymbol{x}, \boldsymbol{y}) \;=\; -\delta_{\boldsymbol{y}}(\boldsymbol{x}) \quad \text{for } \boldsymbol{x}, \boldsymbol{y} \in \mathbb{R}^3$$

together with the Sommerfeld radiation condition in the three-dimensional space that is

$$\lim_{|\boldsymbol{x}|\to\infty} |\boldsymbol{x}| \left(\widehat{\boldsymbol{x}} \cdot \nabla_{\boldsymbol{x}} \Phi(\boldsymbol{x}, \boldsymbol{y}) - \mathrm{i}k\Phi(\boldsymbol{x}, \boldsymbol{y})\right) \;=\; 0\,, \tag{2.26}$$

where the limit is uniform in $\widehat{\boldsymbol{x}} = \boldsymbol{x}/|\boldsymbol{x}| \in S^2$ and in $\boldsymbol{y} \in Y$ for every bounded subset $Y \subset \mathbb{R}^3$. The matrix-valued function

$$\mathbb{G}(\boldsymbol{x}, \boldsymbol{y}) \;=\; \Phi(\boldsymbol{x}, \boldsymbol{y})\mathbb{I}_3 + \frac{1}{k^2} \nabla_{\boldsymbol{x}} \mathrm{div}_{\boldsymbol{x}} \left(\Phi(\boldsymbol{x}, \boldsymbol{y})\mathbb{I}_3\right) \quad \text{for } \boldsymbol{x}, \boldsymbol{y} \in \mathbb{R}^3\,,\ \boldsymbol{x} \neq \boldsymbol{y}\,, \tag{2.27}$$

where $\mathbb{I}_3 \in \mathbb{R}^{3\times 3}$ is the identity matrix, is called the dyadic Green's function for Maxwell's equations (see e.g. [99, p. 303]) as it fulfills

$$\mathbf{curl}_{\mathrm{x}}\, \mathbf{curl}_{\mathrm{x}}\, \mathbb{G}(\boldsymbol{x}, \boldsymbol{y}) - k^2 \mathbb{G}(\boldsymbol{x}, \boldsymbol{y}) \;=\; \delta_{\boldsymbol{y}}(\boldsymbol{x})\mathbb{I}_3\,.$$

Here, the operators $\nabla_{\boldsymbol{x}}, \operatorname{div}_{\boldsymbol{x}}$ and $\mathbf{curl}_{\mathrm{x}}$ are applied columnwise. Furthermore, denoting a column of $\mathbb{G}$ by g_ℓ, $\ell = 1,2,3$, the pairs $(g_\ell(\cdot,\boldsymbol{y}), (\mathrm{i}\omega\mu_0)^{-1}\,\mathbf{curl}\, g_\ell(\cdot,\boldsymbol{y}))$ are radiating solutions of (2.22), where $\boldsymbol{y} \in Y$, for every bounded subset $Y \subset \mathbb{R}^3$.

It is well-known (see e.g. [34, Thm. 6.9]) that every radiating solution of (2.22) denoted by $(\boldsymbol{V}, \boldsymbol{W})$ has an asymptotic expansion of the form

$$\boldsymbol{V}(\boldsymbol{x}) = \frac{\mathrm{e}^{\mathrm{i}k|\boldsymbol{x}|}}{4\pi|\boldsymbol{x}|}\left(\boldsymbol{V}^\infty(\widehat{\boldsymbol{x}}) + \mathcal{O}\left(\frac{1}{|\boldsymbol{x}|}\right)\right), \qquad \boldsymbol{W}(\boldsymbol{x}) = \frac{\mathrm{e}^{\mathrm{i}k|\boldsymbol{x}|}}{4\pi|\boldsymbol{x}|}\left(\boldsymbol{W}^\infty(\widehat{\boldsymbol{x}}) + \mathcal{O}\left(\frac{1}{|\boldsymbol{x}|}\right)\right), \quad (2.28)$$

as $|\boldsymbol{x}| \to \infty$, where $\widehat{\boldsymbol{x}} = \boldsymbol{x}/|\boldsymbol{x}|$. The fields $\boldsymbol{V}^\infty, \boldsymbol{W}^\infty \in L_t^2(S^2)$ are called far field patterns. Similarly, it can be seen that also (scalar valued) solutions u^s of the Helmholtz equation

$$\Delta u^s + k^2 u^s = 0 \quad \text{in } \mathbb{R}^3 \setminus \overline{B_R(0)}$$

for some $R > 0$ that additionally satisfy the Sommerfeld radiation condition from (2.26), possess an expansion of the form

$$u^s(\boldsymbol{x}) = \frac{\mathrm{e}^{\mathrm{i}k|\boldsymbol{x}|}}{4\pi|\boldsymbol{x}|}\left(u^\infty(\widehat{\boldsymbol{x}}) + \mathcal{O}\left(\frac{1}{|\boldsymbol{x}|}\right)\right), \quad \text{as } |\boldsymbol{x}| \to \infty,$$

where $\widehat{\boldsymbol{x}} = \boldsymbol{x}/|\boldsymbol{x}|$. For the dyadic Green's function $\mathbb{G}$, we find that

$$\mathbb{G}^\infty(\widehat{\boldsymbol{x}}, \boldsymbol{y}) = \mathrm{e}^{-\mathrm{i}k\widehat{\boldsymbol{x}}\cdot\boldsymbol{y}}(\widehat{\boldsymbol{x}} \times (\mathbb{I}_3 \times \widehat{\boldsymbol{x}})), \qquad (\mathbf{curl}_{\mathrm{x}}\,\mathbb{G})^\infty(\widehat{\boldsymbol{x}}, \boldsymbol{y}) = \mathrm{i}k\mathrm{e}^{-\mathrm{i}k\widehat{\boldsymbol{x}}\cdot\boldsymbol{y}}(\widehat{\boldsymbol{x}} \times \mathbb{I}_3) \quad (2.29)$$

with the $\mathbf{curl}_{\mathrm{x}}$ operator for matrix valued functions, again, to be understood columnwise (see e.g. [99, Proof of Cor. 9.5]).

Now, we can introduce the electromagnetic scattering problem. Let the pair of incident fields $(\boldsymbol{E}^i, \boldsymbol{H}^i) \in H_{\mathrm{loc}}(\mathbf{curl}, \mathbb{R}^3)$ be entire solutions of time-harmonic Maxwell's equations in homogeneous space, i.e.

$$\mathbf{curl}\,\boldsymbol{E}^i - \mathrm{i}\omega\mu_0\boldsymbol{H}^i = 0, \quad \mathbf{curl}\,\boldsymbol{H}^i + \mathrm{i}\omega\varepsilon_0\boldsymbol{E}^i = 0 \quad \text{in } \mathbb{R}^3, \quad (2.30)$$

with angular frequency $\omega > 0$, and electric permittivity ε_0 and magnetic permeability μ_0 in free space defined as in (2.19). The incident fields are scattered by a bounded Lipschitz object D as defined in Definition 2.1, which we assume to be isotropic and homogeneous. We denote its material parameters by the constant electric permittivity ε_1 and the constant magnetic permeability μ_1. In this work, the magnetic permeability is assumed to be positive, i.e. $\mu_1 > 0$. For the electric permittivity we distinguish between two cases. In the first case we choose $\varepsilon_1 > 0$. For this choice, our setting models electromagnetic scattering from a purely dielectric object. In the second case let $\varepsilon_1 \in \mathbb{C}$ with $\operatorname{Re}(\varepsilon_1) < 0$ and $\operatorname{Im}(\varepsilon_1) > 0$. These electric permittivities are observed in the study of metallic scattering objects like silver and gold, in particular for wavelengths in the visible electromagnetic spectrum. We define the piecewise constant permittivity and permeability distributions ε and μ by

$$\varepsilon(\boldsymbol{x}) = \begin{cases} \varepsilon_1, & \boldsymbol{x} \in D, \\ \varepsilon_0, & \boldsymbol{x} \in \mathbb{R}^3 \setminus \overline{D} \end{cases} \qquad \text{and} \qquad \mu(\boldsymbol{x}) = \begin{cases} \mu_1, & \boldsymbol{x} \in D, \\ \mu_0, & \boldsymbol{x} \in \mathbb{R}^3 \setminus \overline{D}. \end{cases}$$

We also use the notation $\varepsilon_r = \varepsilon_1/\varepsilon_0 \in \mathbb{C}$ and $\mu_r = \mu_1/\mu_0 \in \mathbb{R}$ for the relative electric permittivity and the relative magnetic permeability, respectively. The scattering problem is to find the total fields $(\boldsymbol{E}, \boldsymbol{H}) = (\boldsymbol{E}^i + \boldsymbol{E}^s, \boldsymbol{H}^i + \boldsymbol{H}^s) \in (H_{\mathrm{loc}}(\mathbf{curl}, \mathbb{R}^3))^2$ satisfying

$$\mathbf{curl}\,\boldsymbol{E} - \mathrm{i}\omega\mu\boldsymbol{H} = 0, \quad \mathbf{curl}\,\boldsymbol{H} + \mathrm{i}\omega\varepsilon\boldsymbol{E} = 0 \quad \text{in } \mathbb{R}^3, \quad (2.31)$$

together with the Silver–Müller radiation condition for the scattered fields $(\boldsymbol{E}^s, \boldsymbol{H}^s)$, which is

$$\lim_{|\boldsymbol{x}|\to\infty} |\boldsymbol{x}|\,(\sqrt{\mu_0}\boldsymbol{H}^s(\boldsymbol{x}) \times \widehat{\boldsymbol{x}} - \sqrt{\varepsilon_0}\boldsymbol{E}^s(\boldsymbol{x})) = 0 \quad (2.32)$$

uniformly with respect to all directions $\widehat{\boldsymbol{x}} = \boldsymbol{x}/|\boldsymbol{x}| \in S^2$. From (2.28) we see that

$$\boldsymbol{E}^s(\boldsymbol{x}) = \frac{\mathrm{e}^{\mathrm{i}k|\boldsymbol{x}|}}{4\pi|\boldsymbol{x}|}\left(\boldsymbol{E}^\infty(\widehat{\boldsymbol{x}}) + \mathcal{O}\left(\frac{1}{|\boldsymbol{x}|}\right)\right), \qquad \boldsymbol{H}^s(\boldsymbol{x}) = \frac{\mathrm{e}^{\mathrm{i}k|\boldsymbol{x}|}}{4\pi|\boldsymbol{x}|}\left(\boldsymbol{H}^\infty(\widehat{\boldsymbol{x}}) + \mathcal{O}\left(\frac{1}{|\boldsymbol{x}|}\right)\right), \tag{2.33}$$

as $|\boldsymbol{x}| \to \infty$, where $\widehat{\boldsymbol{x}} = \boldsymbol{x}/|\boldsymbol{x}|$. The field $\boldsymbol{E}^\infty \in L_t^2(S^2)$ is called electric far field pattern, radiation pattern or simply far field of $\boldsymbol{E}^s$. The magnetic counterpart is the magnetic far field pattern $\boldsymbol{H}^\infty$. It is sufficient to work only with $\boldsymbol{E}^\infty$, since $Z_0\boldsymbol{H}^\infty = \widehat{\boldsymbol{x}} \times \boldsymbol{E}^\infty$, where $Z_0 = \sqrt{\mu_0/\varepsilon_0}$ denotes the impedance in free space (see e.g. [88, Thm. 3.30]). The Maxwell system (2.31) can be formulated in terms of the electric field $\boldsymbol{E}$ alone by

$$\mathbf{curl}\left(\frac{1}{\mu}\,\mathbf{curl}\,\boldsymbol{E}\right) - \omega^2\varepsilon\boldsymbol{E} = 0 \quad \text{in } \mathbb{R}^3, \tag{2.34}$$

whereas (2.32) becomes

$$\lim_{|\boldsymbol{x}|\to\infty} |\boldsymbol{x}|\left(\mathbf{curl}\,\boldsymbol{E}^s(\boldsymbol{x}) \times \widehat{\boldsymbol{x}} - \mathrm{i}k\boldsymbol{E}^s(\boldsymbol{x})\right) = 0, \tag{2.35}$$

with the limit to be understood uniformly with respect to all directions $\widehat{\boldsymbol{x}} = \boldsymbol{x}/|\boldsymbol{x}| \in S^2$.

Remark 2.5. In this work, Maxwell's equations for piecewise constant parameters always need to be understood in a weak sense. For example, $\boldsymbol{E} \in H_{\mathrm{loc}}(\mathbf{curl}, \mathbb{R}^3)$ is a solution to (2.34) if and only if

$$\int_{\mathbb{R}^3}\left(\frac{1}{\mu}\,\mathbf{curl}\,\boldsymbol{E}\cdot\mathbf{curl}\,\boldsymbol{V} - \omega^2\varepsilon\boldsymbol{E}\cdot\boldsymbol{V}\right)\mathrm{d}\boldsymbol{x} = 0 \qquad \text{for all } \boldsymbol{V} \in H_0(\mathbf{curl}, \mathbb{R}^3). \tag{2.36}$$

Here, $H_0(\mathbf{curl}, \mathbb{R}^3)$ denotes the space of functions that are in $H(\mathbf{curl}, \mathbb{R}^3)$ and have a compact support. Note that the Silver–Müller radiation condition in (2.35) is not included in (2.36) and must be prescribed additionally.

The radiation condition in (2.35) can be understood as a boundary condition at infinity. In fact, uniqueness of solutions to the scattering problem (2.34) together with (2.35) (see Proposition 2.14) follows from Rellich's lemma that we cite from [99, Lem. 9.28].

Lemma 2.6. *Suppose that $\boldsymbol{E}^s \in H_{\mathrm{loc}}(\mathbf{curl}, \mathbb{R}^3 \setminus \overline{B_R(0)})$ is a solution of Maxwell's equations*

$$\mathbf{curl}\,\mathbf{curl}\,\boldsymbol{E}^s - k^2\boldsymbol{E}^s = 0 \quad \text{in } \mathbb{R}^3 \setminus \overline{B_R(0)}$$

and suppose that $\boldsymbol{E}^s$ satisfies the Silver–Müller radiation condition (2.35). Furthermore, let $\boldsymbol{H}^s = (\mathrm{i}\omega\mu_0)^{-1}\,\mathbf{curl}\,\boldsymbol{E}^s$. If

$$\mathrm{Re}\left(\int_{\partial B_{R'}(0)} (\widehat{\boldsymbol{x}} \times \boldsymbol{E}^s)\cdot\overline{\boldsymbol{H}^s}\,\mathrm{d}s\right) \le 0$$

for all $R' > R$, then $\boldsymbol{E}^s = \boldsymbol{H}^s = 0$ in $\mathbb{R}^3 \setminus \overline{B_R(0)}$.

Remark 2.7. Electric permittivities ε_1 with $\mathrm{Re}(\varepsilon_1) < 0$ and $\mathrm{Im}(\varepsilon_1) > 0$ are also predicted by the Drude model. We present a short description of this model based on the works [96, 102]. We return to (2.18) and do not apply the constitutive relations in (2.20). Following the procedure in [102, Sec. 12.2], we denote by $\boldsymbol{r}$ the displacement of an electron, linked to a dipole moment $\boldsymbol{p}$ via $\boldsymbol{p} = e\boldsymbol{r}$, where e is the elementary charge. Then, the macroscopic polarization $\mathcal{P}$ from (2.18) is given by $\mathcal{P} = n\boldsymbol{p}$, where n is the electron density. This formula reflects the collective action of all electric dipoles generated by single electrons. The Drude model is based on a harmonic oscillator model. Thus, for the displacement $\boldsymbol{r}$, we consider Newton's equation of motion driven by the external field $\mathcal{E} = \boldsymbol{E}_0 e^{-\mathrm{i}\omega t}$, which reads

$$m_e\frac{\partial \boldsymbol{r}^2}{\partial t^2} + m_e\Gamma\frac{\partial \boldsymbol{r}}{\partial t} = e\boldsymbol{E}_0\mathrm{e}^{-\mathrm{i}\omega t},$$

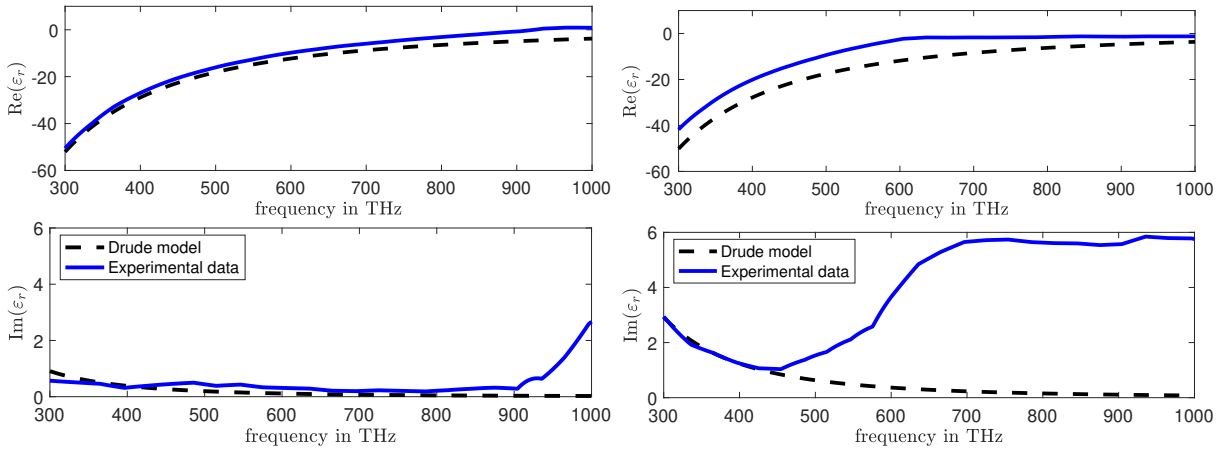

Figure 2.1: The relative permittivity of the Drude model $\varepsilon_{\text{Drude}}/\varepsilon_0$ compared to experimental data from [83]. Left column: Material parameters corresponding to silver. For the Drude model we used the values $\omega_p = 9.04\text{eV}$ and $\Gamma = 21.25\text{meV}$. Right column: Material parameters corresponding to gold. For the Drude model we used the values $\omega_p = 8.89\text{eV}$ and $\Gamma = 70.88\text{meV}$.

where m_e is the effective mass of the free electrons and Γ is a damping parameter (see e.g. [102, Eq. 12.16]). Using the time-harmonic ansatz $\boldsymbol{r}(t) = \boldsymbol{r}_0 e^{-\mathrm{i}\omega t}$ yields a solution to this differential equation given by

$$\boldsymbol{r}_0 \;=\; -\frac{e}{m_e(\omega^2 + \Gamma \mathrm{i}\omega)}\boldsymbol{E}_0.$$

Therefore,

$$\mathcal{P} \;=\; ne\boldsymbol{r} \;=\; -\frac{ne^2}{m_e(\omega^2 + \Gamma \mathrm{i}\omega)}\boldsymbol{E}_0 \mathrm{e}^{-\mathrm{i}\omega t}\,.$$

Using (2.18) now yields that $\mathcal{D} = \varepsilon_{\text{Drude}}(\omega)\mathcal{E}$, with

$$\varepsilon_{\text{Drude}}(\omega) \;=\; \varepsilon_0 \left(1 - \frac{\omega_p^2}{\omega^2 + \Gamma \mathrm{i}\omega}\right), \tag{2.37}$$

where the plasma frequency ω_p is given by $\omega_p = (ne^2/(\varepsilon_0 m_e))^{1/2}$. The permittivity $\varepsilon_{\text{Drude}}$ in (2.37) is also called the dielectric function of the free electron gas (see e.g. [96, p. 11]. Different material features different plasma frequencies ω_p and damping parameters Γ. Moreover, the values for ω_p and Γ vary in the literature. For silver, typical values are e.g. $\omega_p = 9.04\text{eV}$ and $\Gamma = 21.25\text{meV}$. For gold we further find e.g. $\omega_p = 8.89\text{eV}$ and $\Gamma = 70.88\text{meV}$ (see e.g. [124, Tab. 1]). To obtain corresponding values in $2\pi\text{Hz}$ we use the Planck relation $E = \hbar\omega$, where E denotes the photon energy, $\hbar$ denotes the reduced Planck constant and ω is the angular frequency. As explained in [102, Ch. 12.2.2] and [96, Ch. 1.2], the Drude model provides a good approximation to the electric permittivities of metals at low frequencies. However, at higher frequencies, the model becomes less accurate. For more details, we refer to [96, Chap. 1.4]. In Figure 2.1 we plot the complex dielectric function $\varepsilon_{\text{Drude}}/\varepsilon_0$ for silver and gold against experimental data from [83]. We find that the imaginary part of the experimental data for silver starts to deviate from the Drude model for frequencies higher than 900THz. For gold, this deviation already starts for frequencies around 450THz. Similar plots are also found in the literature, e.g. in [96, p. 14], [102, p. 375] or [65, Fig. 4.4].

In the next section, we establish unique solvability of the Maxwell system (2.31) and (2.32) following the techniques from [99, Chap. 4, 9, 10]. Doing so, we particularly consider the second case for the electric permittivity, namely that $\text{Re}(\varepsilon_1) < 0$ and $\text{Im}(\varepsilon_1) > 0$, since this case is

not explicitly covered by the techniques in [99]. However, we emphasize that this case does not involve new methods, except for the use of the slightly different version of the Lax-Milgram theorem from Appendix A.

2.3 The exterior Calderón operator

In order to reduce the scattering problem from (2.34) and (2.35) to a bounded domain, we study the exterior Calderón operator. Let $R > 0$ be such that $B_R(0)$, the ball centered at zero with radius R, satisfies $D \subset\subset B_R(0)$. For a given field on the boundary $\boldsymbol{f} \in H_{\mathrm{div}}^{-1/2}(\partial B_R(0))$, consider the exterior scattering problem

$$\begin{cases} \mathbf{curl}\, \boldsymbol{E}^s - \mathrm{i}\omega\mu_0 \boldsymbol{H}^s = 0, \\ \mathbf{curl}\, \boldsymbol{H}^s + \mathrm{i}\omega\varepsilon_0 \boldsymbol{E}^s = 0 \end{cases} \quad \text{in } \mathbb{R}^3 \setminus \overline{B_R(0)}, \qquad \boldsymbol{\nu} \times \boldsymbol{E}^s = \boldsymbol{f} \quad \text{on } \partial B_R(0) \tag{2.38}$$

together with the Silver–Müller radiation condition

$$\lim_{|\boldsymbol{x}|\to\infty} |\boldsymbol{x}| \left(\sqrt{\mu_0}\boldsymbol{H}^s(\boldsymbol{x}) \times \widehat{\boldsymbol{x}} - \sqrt{\varepsilon_0}\boldsymbol{E}^s(\boldsymbol{x})\right) = 0.$$

This problem has a unique solution (see e.g. [88, Thm. 5.64]). We cite the following well-known result about an expansion of the scattered fields from [99, Thm. 9.17]) without a proof.

Theorem 2.8. *Let $(\boldsymbol{E}^s, \boldsymbol{H}^s)$ be a pair of radiating solutions of Maxwell's equation's for $|\boldsymbol{x}| > R$ as introduced in Definition 2.4. Then, $(\boldsymbol{E}^s, \boldsymbol{H}^s)$ can be expanded using the radiating wave fields $\boldsymbol{N}_n^m$ and $\mathbf{curl}\, \boldsymbol{N}_n^m$ from (2.24). If $\boldsymbol{E}^s$ has the expansion*

$$\boldsymbol{E}^s(\boldsymbol{x}) = \sum_{n=1}^{\infty} \sum_{m=-n}^{n} a_n^m \boldsymbol{N}_n^m(\boldsymbol{x}) + b_n^m\, \mathbf{curl}\, \boldsymbol{N}_n^m(\boldsymbol{x}),$$

then

$$\boldsymbol{H}^s(\boldsymbol{x}) = \sum_{n=1}^{\infty} \sum_{m=-n}^{n} -\mathrm{i}\omega\varepsilon_0 b_n^m \boldsymbol{N}_n^m(\boldsymbol{x}) + \frac{1}{\mathrm{i}\omega\mu_0} a_n^m\, \mathbf{curl}\, \boldsymbol{N}_n^m(\boldsymbol{x}).$$

Moreover, both series (together with their classical derivatives) converge uniformly on compact subsets of $\mathbb{R}^3 \setminus \overline{B_R(0)}$.

Theorem 2.8 shows that for $|\boldsymbol{x}| > R$ the unique solution of (2.38) can be understood classically. We study the representations in the last theorem and find by using the definitions of $\boldsymbol{N}_n^m$ and $\mathbf{curl}\, \boldsymbol{N}_n^m$ from (2.24), the definitions of $\boldsymbol{U}_n^m$ and $\boldsymbol{V}_n^m$ from (2.16) as well as that on $\partial B_R(0)$ it holds that $\boldsymbol{\nu} = \widehat{\boldsymbol{x}}$ that

$$\begin{aligned} \boldsymbol{\nu} \times \boldsymbol{E}^s|_{\partial B_R(0)}(R\widehat{\boldsymbol{x}}) &= \sum_{n=1}^{\infty} \sum_{m=-n}^{n} h_n^{(1)}(kR) a_n^m \boldsymbol{U}_n^m(\widehat{\boldsymbol{x}}) + \frac{1}{R} \widetilde{h}_n(kR) b_n^m \boldsymbol{V}_n^m(\widehat{\boldsymbol{x}}), \\ \boldsymbol{\nu} \times \boldsymbol{H}^s|_{\partial B_R(0)}(R\widehat{\boldsymbol{x}}) &= -\mathrm{i}\omega\varepsilon_0 \left(\sum_{n=1}^{\infty} \sum_{m=-n}^{n} h_n^{(1)}(kR) b_n^m \boldsymbol{U}_n^m(\widehat{\boldsymbol{x}}) + \frac{1}{k^2 R} \widetilde{h}_n(kR) a_n^m \boldsymbol{V}_n^m(\widehat{\boldsymbol{x}}) \right), \end{aligned}$$

where $\widetilde{h}_n(kR) = h_n^{(1)}(kR) + kR\, h_n^{(1)\prime}(kR)$. Let the field on the boundary $\boldsymbol{f} \in H_{\mathrm{div}}^{-1/2}(\partial B_R(0))$ be given by

$$\boldsymbol{f}(R\widehat{\boldsymbol{x}}) = \sum_{n=1}^{\infty} \sum_{m=-n}^{n} \alpha_n^m \boldsymbol{U}_n^m(\widehat{\boldsymbol{x}}) + \beta_n^m \boldsymbol{V}_n^m(\widehat{\boldsymbol{x}}), \quad \widehat{\boldsymbol{x}} \in S^2 \tag{2.39}$$

(see also Remark 2.3). Then, the boundary condition $\boldsymbol{\nu} \times \boldsymbol{E}^s = \boldsymbol{f}$ on $\partial B_R(0)$ yields that

$$\boldsymbol{E}^s(\boldsymbol{x}) = \sum_{n=1}^{\infty} \sum_{m=-n}^{n} \frac{\alpha_n^m}{h_n^{(1)}(kR)} \boldsymbol{N}_n^m(\boldsymbol{x}) + \frac{\beta_n^m R}{\widetilde{h}_n(kR)} \operatorname{\mathbf{curl}} \boldsymbol{N}_n^m(\boldsymbol{x}), \tag{2.40a}$$

$$\boldsymbol{H}^s(\boldsymbol{x}) = \sum_{n=1}^{\infty} \sum_{m=-n}^{n} -\mathrm{i}\omega\varepsilon_0 \frac{\beta_n^m R}{\widetilde{h}_n(kR)} \boldsymbol{N}_n^m(\boldsymbol{x}) + \frac{1}{\mathrm{i}\omega\mu_0} \frac{\alpha_n^m}{h_n^{(1)}(kR)} \operatorname{\mathbf{curl}} \boldsymbol{N}_n^m(\boldsymbol{x}), \tag{2.40b}$$

for $\boldsymbol{x} \in \mathbb{R}^3 \setminus \overline{B_R(0)}$. We define the electric to magnetic Calderón operator

$$\Lambda : H_{\mathrm{div}}^{-1/2}(\partial B_R(0)) \to H_{\mathrm{div}}^{-1/2}(\partial B_R(0)), \qquad \Lambda \boldsymbol{f} = \boldsymbol{\nu} \times \boldsymbol{H}^s|_{\partial B_R(0)}, \tag{2.41}$$

where $\boldsymbol{H}^s \in H_{\mathrm{loc}}(\mathbf{curl}, \mathbb{R}^3 \setminus \overline{B_R(0)})$ is the magnetic field of the unique solution to (2.38), which is given by (2.40b). For $\boldsymbol{f} \in H_{\mathrm{div}}^{-1/2}(\partial B_R(0))$ expanded as in (2.39), we see by comparing coefficients that

$$\Lambda \boldsymbol{f} = \sum_{n=1}^{\infty} \sum_{m=-n}^{n} -\frac{\mathrm{i}\omega\varepsilon_0 \beta_n^m R}{\delta_n} \boldsymbol{U}_n^m + \frac{\alpha_n^m \delta_n}{\mathrm{i}\omega\mu_0 R} \boldsymbol{V}_n^m, \quad \text{where} \quad \delta_n = 1 + \frac{kR h_n^{(1)\prime}(kR)}{h_n^{(1)}(kR)}. \tag{2.42}$$

Remark 2.9. The functions $h_n^{(1)}(x)$ and $\widetilde{h}_n(x) = h_n^{(1)}(x) + x h_n^{(1)\prime}(x)$ that appear in (2.40) do not have roots on the positive real line. This is seen as follows. The Wronskian $W(j_n, y_n)$ satisfies

$$W(j_n, y_n)(z) = j_n(z) y_n'(z) - j_n'(z) y_n(z) = \frac{1}{z^2}$$

for all $z \in \mathbb{C} \setminus \{0\}$ and $n \in \mathbb{N} \cup \{0\}$ (see [88, Thm. 2.27]). As introduced earlier, j_n and y_n denote spherical Bessel functions of the first and second kind, respectively. Then, for real and positive t the identity

$$\begin{aligned} \frac{-2\mathrm{i}}{t^2} &= 2\mathrm{i}\big(y_n(t) j_n'(t) - j_n(t) y_n'(t)\big) \\ &= \big(j_n(t) + \mathrm{i} y_n(t)\big)\big(j_n'(t) - \mathrm{i} y_n'(t)\big) - \big(j_n(t) - \mathrm{i} y_n(t)\big)\big(j_n'(t) + \mathrm{i} y_n'(t)\big) \\ &= h_n^{(1)}(t) \overline{h_n^{(1)\prime}(t)} - \overline{h_n^{(1)}(t)} h_n^{(1)\prime}(t), \end{aligned}$$

which can be also found in [99, Eq. (9.51)], cannot hold true if either $h_n^{(1)}(t)$ or $\widetilde{h}_n(t)$ vanish.

We cite the next result from [99, Thm. 9.21] without a proof. This proposition shows the boundedness of the exterior Calderón operator Λ.

Proposition 2.10. *For a constant $C > 0$ it holds that*

$$\|\Lambda \boldsymbol{f}\|_{H_{\mathrm{div}}^{-1/2}(\partial B_R(0))} \leq C \|\boldsymbol{f}\|_{H_{\mathrm{div}}^{-1/2}(\partial B_R(0))} \quad \textit{for all } \boldsymbol{f} \in H_{\mathrm{div}}^{-1/2}(\partial B_R(0)).$$

Remark 2.11. The proof of Proposition 2.10 in [99, Proof of Thm. 9.21] uses that $c_1 n \leq |\delta_n| \leq c_2 n$ for constants $c_1, c_2 > 0$ (see [99, Lem. 9.20]) and the norm

$$\|\boldsymbol{f}\| = \left(\sum_{n=1}^{\infty} \sum_{m=-n}^{n} (1 + n(n+1))^{1/2} |\alpha_n^m|^2 + (1 + n(n+1))^{-1/2} |\beta_n^m|^2 \right)^{1/2}$$

where $\boldsymbol{f}$ is given as in (2.39). This norm is equivalent to $\|\cdot\|_{H_{\mathrm{div}}^{-1/2}(\partial B_R(0))}$ on balls (see e.g. [88, Thm. 5.38] and its proof).

We define

$$\widetilde{\delta}_n = 1 + \frac{\mathrm{i}Rh_n^{(1)\prime}(\mathrm{i}R)}{h_n^{(1)}(\mathrm{i}R)}, \tag{2.43}$$

recall the expansion of $\boldsymbol{f}$ from (2.39) and define the bounded operator

$$\widetilde{\Lambda} : H_{\mathrm{div}}^{-1/2}(\partial B_R(0)) \to H_{\mathrm{div}}^{-1/2}(\partial B_R(0)), \quad \widetilde{\Lambda}\boldsymbol{f} = \frac{\sqrt{\varepsilon_0}}{\sqrt{\mu_0}} \left(\sum_{n=1}^{\infty} \sum_{m=-n}^{n} \frac{R\beta_n^m}{\widetilde{\delta}_n} \boldsymbol{U}_n^m - \frac{\alpha_n^m \widetilde{\delta}_n}{R} \boldsymbol{V}_n^m \right). \tag{2.44}$$

This operator arises from replacing $k = \mathrm{i}$ or equivalently $\omega = \mathrm{i}/\sqrt{\mu_0\varepsilon_0}$ in the definition of Λ in (2.42). For this operator we cite [99, Lem. 9.22, 9.23], which we summarize in the following lemma.

Lemma 2.12. *For all $n \in \mathbb{N}$ it holds that $\widetilde{\delta}_n$ is real and strictly negative. Moreover,*

$$\int_{\partial B_R(0)} \widetilde{\Lambda}\boldsymbol{f} \cdot (\boldsymbol{f} \times \boldsymbol{\nu}) \, \mathrm{d}s < 0 \tag{2.45}$$

for any $\boldsymbol{f} \in H_{\mathrm{div}}^{-1/2}(\partial B_R(0))$, $\boldsymbol{f} \neq 0$.

We recall that we interpret the expression on the left hand side in (2.45) as the dual evaluation in $H_{\mathrm{div}}^{-1/2}(\partial B_R(0)) \times H_{\mathrm{curl}}^{-1/2}(\partial B_R(0))$ (see also (2.14) for the interpretation of $\boldsymbol{f} \times \boldsymbol{\nu}$). The fact that $\widetilde{\Lambda}$ is bounded can be seen similarly as outlined by Remark 2.11 by using that $-2n < \widetilde{\delta}_n < -n$ for n large enough (see [99, Proof of Lem. 9.22]). We define the space

$$H_{\mathrm{div},0}^{-1/2}(\partial B_R(0)) = \left\{ \boldsymbol{f} \in H_{\mathrm{div}}^{-1/2}(\partial B_R(0)) \;\middle|\; \boldsymbol{f} = \sum_{n=1}^{\infty} \sum_{m=-n}^{n} b_n^m \boldsymbol{V}_n^m \text{ for some } (b_n^m)_{n,m} \subset \mathbb{C} \right\}.$$

This space is of particular interest, as for $p \in H^1(B_R(0))$ we find that $\boldsymbol{\nu} \times \nabla p|_{\partial B_R(0)} \in H_{\mathrm{div},0}^{-1/2}(\partial B_R(0))$. We cite [99, Lem. 9.24] in our next lemma.

Lemma 2.13. *The operator*

$$\Lambda + \mathrm{i}k\widetilde{\Lambda} : H_{\mathrm{div},0}^{-1/2}(\partial B_R(0)) \to H_{\mathrm{div}}^{-1/2}(\partial B_R(0))$$

is linear, bounded and compact.

2.4 Reduction of the scattering problem to a bounded domain

The aim of this subsection is to transform the scattering problem (2.31) and (2.32) into an equivalent problem posed on a bounded domain. For this, we need the exterior Calderón operator that we introduced in the previous section. Subsequently, we use the Fredholm theory to prove existence and uniqueness of solutions to this problem. We consider the artificial computational domain $B_R(0)$ with $R > 0$ such that $D \subset\subset B_R(0)$. We repeat the proof of the general uniqueness theorem from [99, Thm. 10.1] and emphasize that it remains true for our choice of complex-valued ε_1.

Proposition 2.14. *Let $\varepsilon_1 > 0$ or $\varepsilon_1 \in \mathbb{C}$ with $\mathrm{Re}(\varepsilon_1) < 0$ and $\mathrm{Im}(\varepsilon_1) > 0$. Then there is at most one solution $\boldsymbol{E} = \boldsymbol{E}^i + \boldsymbol{E}^s \in H_{\mathrm{loc}}(\mathbf{curl}, \mathbb{R}^3)$ of*

$$\mathbf{curl}\left(\frac{1}{\mu}\,\mathbf{curl}\,\boldsymbol{E}\right) - \omega^2\varepsilon\boldsymbol{E} = 0 \quad \text{in } \mathbb{R}^3, \tag{2.46}$$

together with the Silver–Müller radiation condition

$$\lim_{|\boldsymbol{x}|\to\infty} |\boldsymbol{x}| \left(\mathbf{curl}\,\boldsymbol{E}^s(\boldsymbol{x}) \times \widehat{\boldsymbol{x}} - \mathrm{i}k\boldsymbol{E}^s(\boldsymbol{x})\right) = 0. \tag{2.47}$$

uniformly with respect to all directions $\widehat{\boldsymbol{x}} = \boldsymbol{x}/|\boldsymbol{x}|$.

Proof. Let $\boldsymbol{E}_1 = \boldsymbol{E}^i + \boldsymbol{E}_1^s, \boldsymbol{E}_2 = \boldsymbol{E}^i + \boldsymbol{E}_2^s \in H_{\mathrm{loc}}(\mathbf{curl}, \mathbb{R}^3)$ be two solutions of (2.46), where the scattered fields $\boldsymbol{E}_1^s$ and $\boldsymbol{E}_2^s$ both satisfy (2.47). Defining $\boldsymbol{E} = \boldsymbol{E}_1 - \boldsymbol{E}_2 \in H_{\mathrm{loc}}(\mathbf{curl}, \mathbb{R}^3)$, we find that $\boldsymbol{E}$ solves (2.46) and (2.47). The weak formulation of (2.46) in (2.36) with $\boldsymbol{V} = \psi\overline{\boldsymbol{E}}$, where $\psi \in C_0^\infty(\mathbb{R}^3)$ with $\psi = 1$ in $B_R(0)$ and $\psi = 0$ in $\mathbb{R}^3 \setminus \overline{B_{R'}(0)}$ with $R' > R$ implies that

$$0 = \int_{B_R(0)} \frac{1}{\mu} |\,\mathbf{curl}\,\boldsymbol{E}|^2 - \omega^2\varepsilon|\boldsymbol{E}|^2 \,\mathrm{d}\boldsymbol{x} + \int_{B_{R'}(0)\setminus B_R(0)} \frac{1}{\mu_0}\,\mathbf{curl}\,\boldsymbol{E}\cdot\mathbf{curl}(\psi\overline{\boldsymbol{E}}) - \omega^2\varepsilon_0\boldsymbol{E}\cdot\psi\overline{\boldsymbol{E}}\,\mathrm{d}\boldsymbol{x}\,.$$

Outside of $B_R(0)$ the field $\boldsymbol{E}$ is smooth and therefore partial integration and $\mathbf{curl}\,\boldsymbol{E} = \mathrm{i}\omega\mu_0\boldsymbol{H}$ yields

$$\int_{B_R(0)} \frac{1}{\mu} |\,\mathbf{curl}\,\boldsymbol{E}|^2 - \omega^2\varepsilon|\boldsymbol{E}|^2 \,\mathrm{d}\boldsymbol{x} - \mathrm{i}\omega \int_{\partial B_R(0)} (\boldsymbol{\nu}\times\overline{\boldsymbol{E}}|_{\partial B_R(0)})\cdot((\boldsymbol{\nu}\times\boldsymbol{H})\times\boldsymbol{\nu})|_{\partial B_R(0)}\,\mathrm{d}s = 0\,. \quad (2.48)$$

Taking the complex conjugate of both sides in (2.48) and considering the imaginary part gives that

$$\omega \int_{B_R(0)} \mathrm{Im}(\overline{\varepsilon})|\boldsymbol{E}|^2 \,\mathrm{d}\boldsymbol{x} = \mathrm{Re}\left(\int_{\partial B_R(0)} (\boldsymbol{\nu}\times\boldsymbol{E}|_{\partial B_R(0)})\cdot((\boldsymbol{\nu}\times\overline{\boldsymbol{H}})\times\boldsymbol{\nu})|_{\partial B_R(0)}\,\mathrm{d}s\right). \quad (2.49)$$

In both cases we have that $\mathrm{Im}(\overline{\varepsilon}) \le 0$ and therefore

$$\mathrm{Re}\left(\int_{\partial B_R(0)} (\boldsymbol{\nu}\times\boldsymbol{E}|_{\partial B_R(0)})\cdot((\boldsymbol{\nu}\times\overline{\boldsymbol{H}})\times\boldsymbol{\nu})|_{\partial B_R(0)}\,\mathrm{d}s\right) \le 0.$$

Since $(\boldsymbol{E}, \boldsymbol{H})$ are radiating solutions of the Maxwell system, Rellich's lemma 2.6 gives that $(\boldsymbol{E}, \boldsymbol{H})$ vanish in $\mathbb{R}^3 \setminus \overline{B_R(0)}$. Due to the unique continuation principle in [99, Thm. 4.13] (since $\varepsilon_0, \mu_0 > 0$) the fields $(\boldsymbol{E}, \boldsymbol{H})$ vanish in $\mathbb{R}^3 \setminus \overline{D}$. In particular, the right hand side of (2.49) vanishes.

Let us now assume that $\mathrm{Im}(\varepsilon) > 0$ in D. Then, the left hand side of (2.49) yields that $\boldsymbol{E} = 0$ in D. For $\mathrm{Im}(\varepsilon) = 0$ in D we proceed as in the proof of [99, Thm. 4.12]: Let $\boldsymbol{x}_0 \in \partial D$ and let $r > 0$ be sufficiently small such that the boundary ∂D divides $B_r(\boldsymbol{x}_0)$ into two disjoint parts. We find that $\boldsymbol{E}$ is a weak solution of

$$\mathbf{curl}\left(\frac{1}{\mu_1}\,\mathbf{curl}\,\boldsymbol{E}\right) - \omega^2\varepsilon_1\boldsymbol{E} = 0 \quad \text{in } D \cup B_r(\boldsymbol{x}_0)\,,$$

since in $B_r(\boldsymbol{x}_0) \cap D$, the field $\boldsymbol{E}$ is a solution of (2.46) and we have already shown that $\boldsymbol{E}$ vanishes in $B_r(\boldsymbol{x}_0) \cap (B_R(0) \setminus \overline{D})$. Recall that $\boldsymbol{E} \in H_{\mathrm{loc}}(\mathbf{curl}, \mathbb{R}^3)$ by definition. Now we use the unique continuation principle in [99, Thm. 4.13] to conclude that $\boldsymbol{E}$ must vanish in all $B_r(\boldsymbol{x}_0)$ and by the same argument in all of D. □

For $(\boldsymbol{E}, \boldsymbol{H}) = (\boldsymbol{E}^i + \boldsymbol{E}^s, \boldsymbol{H}^i + \boldsymbol{H}^s)$ we study the Maxwell system in the truncated domain $B_R(0)$, which is

$$\mathbf{curl}\,\boldsymbol{E} - \mathrm{i}\omega\mu\boldsymbol{H} = 0\,, \qquad \mathbf{curl}\,\boldsymbol{H} + \mathrm{i}\omega\varepsilon\boldsymbol{E} = 0 \quad \text{in } B_R(0)\,, \quad (2.50)$$

and introduce the nonlocal boundary condition on $\partial B_R(0)$ given by

$$\Lambda(\boldsymbol{\nu}\times\boldsymbol{E}^s|_{\partial B_R(0)}) = \boldsymbol{\nu}\times\boldsymbol{H}^s|_{\partial B_R(0)} \quad \text{on } \partial B_R(0)\,, \quad (2.51)$$

where Λ denotes the exterior Calderon operator introduced in (2.41). Again, the boundary value problem (2.50) with (2.51) has to be understood in a variational sense. The weak formulation is to find $\boldsymbol{E} \in H(\mathbf{curl}, B_R(0))$ such that

$$B(\boldsymbol{E}, \boldsymbol{V}) = F(\boldsymbol{V}) \quad \text{for all } \boldsymbol{V} \in H(\mathbf{curl}, B_R(0)) \quad (2.52)$$

with

$$B(\boldsymbol{E},\boldsymbol{V}) = \int_{B_R(0)} \frac{1}{\mu}\,\mathbf{curl}\,\boldsymbol{E}\cdot\overline{\mathbf{curl}\,\boldsymbol{V}} - \omega^2\varepsilon\boldsymbol{E}\cdot\overline{\boldsymbol{V}}\,\mathrm{d}\boldsymbol{x} + \mathrm{i}\omega\int_{\partial B_R(0)} \Lambda(\boldsymbol{\nu}\times\boldsymbol{E}|_{\partial B_R(0)})\cdot((\boldsymbol{\nu}\times\overline{\boldsymbol{V}})\times\boldsymbol{\nu})|_{\partial B_R(0)}\,\mathrm{d}s\,, \quad (2.53)$$

$$F(\boldsymbol{V}) = \mathrm{i}\omega\int_{\partial B_R(0)} \Lambda(\boldsymbol{\nu}\times\boldsymbol{E}^i|_{\partial B_R(0)})\cdot(\boldsymbol{\nu}\times\overline{\boldsymbol{V}})\times\boldsymbol{\nu}|_{\partial B_R(0)}\,\mathrm{d}s - \frac{1}{\mu_0}\int_{\partial B_R(0)} (\boldsymbol{\nu}\times\mathbf{curl}\,\boldsymbol{E}^i|_{\partial B_R(0)})\cdot((\boldsymbol{\nu}\times\overline{\boldsymbol{V}})\times\boldsymbol{\nu})|_{\partial B_R(0)}\,\mathrm{d}s\,. \quad (2.54)$$

The following lemma states that any (weak) solution of the scattering problem (2.31) with (2.32) can be reduced to a (weak) solution of (2.50) with (2.51). On the other hand, any (weak) solution to (2.50) with (2.51) can be uniquely extended to a (weak) solution of (2.31) with (2.32).

Lemma 2.15. *Let the entire incident fields $(\boldsymbol{E}^i,\boldsymbol{H}^i)$ be given. The problem in full space, which is to determine the total fields $(\boldsymbol{E},\boldsymbol{H}) = (\boldsymbol{E}^i+\boldsymbol{E}^s,\boldsymbol{H}^i+\boldsymbol{H}^s) \in (H_{\mathrm{loc}}(\mathbf{curl},\mathbb{R}^3))^2$ satisfying (2.31) and the Silver–Müller radiation condition (2.32) is equivalent to the problem to determine $(\boldsymbol{E},\boldsymbol{H}) = (\boldsymbol{E}^i+\boldsymbol{E}^s,\boldsymbol{H}^i+\boldsymbol{H}^s) \in (H(\mathbf{curl},B_R(0)))^2$ satisfying (2.50) and the nonlocal boundary condition (2.51).*

Proof. For $\boldsymbol{f} \in H^{-1/2}_{\mathrm{div}}(\partial B_R(0))$ we consider the exterior boundary value problem, which is to determine $(\boldsymbol{V},\boldsymbol{W}) \in (H_{\mathrm{loc}}(\mathbf{curl},\mathbb{R}^3\setminus\overline{B_R(0)}))^2$ such that

$$\begin{cases} \mathbf{curl}\,\boldsymbol{V} - \mathrm{i}\omega\mu_0\boldsymbol{W} = 0, \\ \mathbf{curl}\,\boldsymbol{W} + \mathrm{i}\omega\varepsilon_0\boldsymbol{V} = 0 \end{cases} \quad \text{in } \mathbb{R}^3\setminus\overline{B_R(0)}, \qquad \boldsymbol{\nu}\times\boldsymbol{V} = \boldsymbol{f} \quad \text{on } \partial B_R(0), \quad (2.55)$$

together with the Silver–Müller radiation condition

$$\lim_{|\boldsymbol{x}|\to\infty} |\boldsymbol{x}|\,(\sqrt{\mu_0}\boldsymbol{W}(\boldsymbol{x})\times\widehat{\boldsymbol{x}} - \sqrt{\varepsilon_0}\boldsymbol{V}(\boldsymbol{x})) = 0 \quad (2.56)$$

with the limit to be understood uniformly with respect to all directions $\widehat{\boldsymbol{x}} = \boldsymbol{x}/|\boldsymbol{x}| \in S^2$. Now let $(\boldsymbol{E},\boldsymbol{H}) \in (H_{\mathrm{loc}}(\mathbf{curl},\mathbb{R}^3))^2$ be a solution to (2.31) and (2.32), which, by Proposition 2.14, is uniquely determined. Then,

$$\widetilde{\boldsymbol{E}} = \boldsymbol{E}\big|_{B_R(0)} \quad \text{and} \quad \widetilde{\boldsymbol{H}} = \boldsymbol{H}\big|_{B_R(0)} \quad \text{satisfy } (\widetilde{\boldsymbol{E}},\widetilde{\boldsymbol{H}}) \in (H(\mathbf{curl},B_R(0)))^2 \quad (2.57)$$

and Maxwell's equations in $B_R(0)$. We define $\boldsymbol{f} = \boldsymbol{\nu}\times\widetilde{\boldsymbol{E}^s}|_{\partial B_R(0)} \in H^{-1/2}_{\mathrm{div}}(\partial B_R(0))$ with $\widetilde{\boldsymbol{E}^s} = \widetilde{\boldsymbol{E}} - \boldsymbol{E}^i|_{B_R(0)}$ and denote by $(\boldsymbol{V},\boldsymbol{W}) \in (H_{\mathrm{loc}}(\mathbf{curl},\mathbb{R}^3\setminus\overline{B_R(0)}))^2$ the unique radiating fields determined by (2.55) and (2.56). It holds that

$$\begin{aligned}\Lambda(\boldsymbol{\nu}\times\widetilde{\boldsymbol{E}^s}|_{\partial B_R(0)}) &= \Lambda(\boldsymbol{\nu}\times\boldsymbol{E}^s|^-_{\partial B_R(0)}) = \Lambda(\boldsymbol{\nu}\times\boldsymbol{E}^s|^+_{\partial B_R(0)}) = \Lambda(\boldsymbol{\nu}\times\boldsymbol{V}|^+_{\partial B_R(0)}) \\ &= \boldsymbol{\nu}\times\boldsymbol{W}|^+_{\partial B_R(0)} = \boldsymbol{\nu}\times\boldsymbol{H}^s|^+_{\partial B_R(0)} = \boldsymbol{\nu}\times\boldsymbol{H}^s|^-_{\partial B_R(0)} = \boldsymbol{\nu}\times\widetilde{\boldsymbol{H}^s}|_{\partial B_R(0)}\,.\end{aligned}$$

The first and the last equality hold due to (2.57). The second and the sixth equality is fulfilled since $(\boldsymbol{E},\boldsymbol{H}) \in (H_{\mathrm{loc}}(\mathbf{curl},\mathbb{R}^3))^2$ and hence the interior traces coincide with the exterior ones (see e.g. [99, Lem. 5.3]). The third and the fifth equality are satisfied since (due to the uniqueness of solutions) $\boldsymbol{V} = \boldsymbol{E}^s|_{\mathbb{R}^3\setminus\overline{B_R(0)}}$ and $\boldsymbol{W} = \boldsymbol{H}^s|_{\mathbb{R}^3\setminus\overline{B_R(0)}}$. The fourth equality holds by the definition of the exterior Calderón operator from (2.41).

On the other hand, let $(\boldsymbol{E}, \boldsymbol{H}) = (\boldsymbol{E}^i + \boldsymbol{E}^s, \boldsymbol{H}^i + \boldsymbol{H}^s) \in (H(\mathbf{curl}, B_R(0)))^2$ be a solution of (2.50) and (2.51). Again, we consider the auxiliary problem (2.55) with $\boldsymbol{f} = \boldsymbol{\nu} \times \boldsymbol{E}^s|_{\partial B_R(0)}$. As in (2.40), we can derive a series representation of the scattered fields $(\boldsymbol{V}, \boldsymbol{W})$. We define

$$\widetilde{\boldsymbol{E}^s} = \begin{cases} \boldsymbol{E}^s & \text{in } B_R(0), \\ \boldsymbol{V} & \text{in } \mathbb{R}^3 \setminus \overline{B_R(0)} \end{cases} \quad \text{and} \quad \widetilde{\boldsymbol{H}^s} = \begin{cases} \boldsymbol{H}^s & \text{in } B_R(0), \\ \boldsymbol{W} & \text{in } \mathbb{R}^3 \setminus \overline{B_R(0)}. \end{cases} \tag{2.58}$$

It holds that

$$\boldsymbol{\nu} \times \widetilde{\boldsymbol{E}^s}|^+_{\partial B_R(0)} = \boldsymbol{\nu} \times \boldsymbol{V}|_{\partial B_R(0)} = \boldsymbol{f} = \boldsymbol{\nu} \times \boldsymbol{E}^s|_{\partial B_R(0)} = \boldsymbol{\nu} \times \widetilde{\boldsymbol{E}^s}|^-_{\partial B_R(0)}\,. \tag{2.59}$$

Moreover, we find that

$$\begin{aligned} \boldsymbol{\nu} \times \widetilde{\boldsymbol{H}^s}|^+_{\partial B_R(0)} = \boldsymbol{\nu} \times \boldsymbol{W}|_{\partial B_R(0)} = \Lambda(\boldsymbol{\nu} \times \boldsymbol{V}|_{\partial B_R(0)}) &= \Lambda(\boldsymbol{\nu} \times \boldsymbol{E}^s|_{\partial B_R(0)}) \\ &= \boldsymbol{\nu} \times \boldsymbol{H}^s|_{\partial B_R(0)} = \boldsymbol{\nu} \times \widetilde{\boldsymbol{H}^s}|^-_{\partial B_R(0)}\,. \end{aligned}$$

The first and the last equality hold by the definition in (2.58). The second equality is fulfilled due to the definition of Λ in (2.41). The third one holds as seen in (2.59). The fourth equality is true due to (2.51). Using [99, Lem. 5.3], we conclude that $(\widetilde{\boldsymbol{E}}, \widetilde{\boldsymbol{H}}) = (\boldsymbol{E}^i + \widetilde{\boldsymbol{E}^s}, \boldsymbol{H}^i + \widetilde{\boldsymbol{H}^s}) \in (H_{\mathrm{loc}}(\mathbf{curl}, \mathbb{R}^3))^2$ solve (2.31). Furthermore, $(\widetilde{\boldsymbol{E}^s}, \widetilde{\boldsymbol{H}^s})$ is a radiating wave pair. Proposition 2.14 now yields that this series extension is unique. This completes the proof. □

In conclusion, once we proved that the problem to find $\boldsymbol{E} \in H(\mathbf{curl}, B_R(0))$ satisfying (2.52) has a unique solution and depends continuously on the right hand side, the scattering problem (2.31) with (2.32) is well-posed. The space $H(\mathbf{curl}, \mathbb{R}^3)$ is not compactly embedded in $(L^2(B_R(0)))^3$ and therefore, we need to study a Helmholtz decomposition for the space $H(\mathbf{curl}, B_R(0))$. This is a decomposition of $H(\mathbf{curl}, B_R(0))$ into two subspaces, which are orthogonal to each other with respect to the inner product in $H(\mathbf{curl}, B_R(0))$. On the one hand, in the first subspace, this is the **curl** free part of $H(\mathbf{curl}, B_R(0))$, the variational problem (2.52) is easy to solve, as we see next. On the other hand, the second subspace, this is the div free part of $H(\mathbf{curl}, B_R(0))$, is compactly embedded in $H(\mathbf{curl}, B_R(0))$. We first study the **curl** free space and define

$$\widetilde{S} = \left\{ q \in H^1(B_R(0)) \;\middle|\; \int_{\partial B_R(0)} q \, \mathrm{d}s = 0 \right\},$$

with the norm $\|\cdot\|_{H^1(B_R(0))}$ given by (2.3) for $k = 1$ and $p = 2$. Finding $p \in \widetilde{S}$ such that

$$B(\nabla p, \nabla \xi) = F(\nabla \xi) \qquad \text{for all } \xi \in \widetilde{S}$$

is equivalent to

$$a_1(p, \xi) + a_2(p, \xi) = F(\nabla \xi) \qquad \text{for all } \xi \in \widetilde{S} \tag{2.60}$$

with

$$\begin{aligned} a_1(p, \xi) = -\omega^2 \int_{B_R(0)} \varepsilon \nabla p \cdot \overline{\nabla \xi} \, \mathrm{d}\boldsymbol{x} \\ + \omega k \int_{\partial B_R(0)} \widetilde{\Lambda}(\boldsymbol{\nu} \times \nabla p|_{\partial B_R(0)}) \cdot (\boldsymbol{\nu} \times \overline{\nabla \xi}) \times \boldsymbol{\nu}|_{\partial B_R(0)} \, \mathrm{d}s\,, \end{aligned} \tag{2.61}$$

$$a_2(p, \xi) = \mathrm{i}\omega \int_{\partial B_R(0)} (\Lambda + \mathrm{i}k\widetilde{\Lambda})(\boldsymbol{\nu} \times \nabla p|_{\partial B_R(0)}) \cdot (\boldsymbol{\nu} \times \overline{\nabla \xi}) \times \boldsymbol{\nu}|_{\partial B_R(0)} \, \mathrm{d}s\,, \tag{2.62}$$

where $\widetilde{\Lambda}$ denotes the electric to magnetic Calderón operator with $k = \mathrm{i}$ from (2.44). For the space $\widetilde{S}$ we obtain a similar result as in [99, Thm. 10.2], that we state and prove below.

Proposition 2.16. *Let $\varepsilon_1 > 0$ or $\varepsilon_1 \in \mathbb{C}$ with $\operatorname{Re}(\varepsilon_1) < 0$ and $\operatorname{Im}(\varepsilon_1) > 0$. The sesquilinear form $a_1 : \widetilde{S} \times \widetilde{S} \to \mathbb{C}$ from (2.61) is bounded . Further, there is a $\zeta \in \mathbb{R}$ such that*

$$\operatorname{Re}\big(\mathrm{e}^{\mathrm{i}\zeta} a_1(p,p)\big) \geq c\|p\|_{H^1(B_R(0))} \quad \text{for all } p \in \widetilde{S}\,. \tag{2.63}$$

Moreover, there is a compact operator $A : \widetilde{S} \to \widetilde{S}$ with

$$a_1(Ap,\xi) = a_2(p,\xi) \quad \text{for all } p,\xi \in \widetilde{S}\,,$$

where $a_2 : \widetilde{S} \times \widetilde{S} \to \mathbb{C}$ is defined in (2.62).

The operator $I + A$ is an isomorphism from $\widetilde{S}$ onto itself. The problem to find $p \in \widetilde{S}$ with

$$B(\nabla p, \nabla \xi) = F(\nabla \xi) \quad \text{for all } \xi \in \widetilde{S}$$

is uniquely solvable in $\widetilde{S}$, where the sesquilinear form B and the antilinear functional F are defined in (2.53) and (2.54), respectively. The solution is given by

$$p = (I + A)^{-1} b\,,$$

where b is the unique solution to

$$a_1(b,\xi) = F(\nabla \xi) \quad \text{for all } \xi \in \widetilde{S}\,.$$

In particular, it holds that $\|p\|_{H^1(B_R(0))} \leq C\|F\|$.

Proof. The boundedness of a_1 follows from an application of the Cauchy–Schwarz inequality together with the boundedness of $\widetilde{\Lambda}$ and the traces γ_t and γ_T from (2.12) combined with the fact that $\mathbf{curl}(\nabla p) = 0$.

Let $\varepsilon_1 > 0$. We use the negative definiteness of $\widetilde{\Lambda}$ from Lemma 2.12 and the Poincaré inequality to find that

$$-a_1(p,p) \geq c \int_{B_R(0)} |\nabla p|^2 \,\mathrm{d}\boldsymbol{x} \geq c\,\|p\|_{H^1(B_R(0))}\,.$$

On the other hand, let $\varepsilon_1 \in \mathbb{C}$ with $\operatorname{Re}(\varepsilon_1) < 0$ and $\operatorname{Im}(\varepsilon_1) > 0$, i.e. we can write $\varepsilon_1 = |\varepsilon_1| e^{\mathrm{i}\alpha}$ with $\alpha \in (\pi/2, \pi)$. For $\beta = \alpha/2 \in (\pi/4, \pi/2)$ we find that

$$\begin{aligned}\operatorname{Re}\big(-\mathrm{e}^{-\mathrm{i}\beta} a_1(p,p)\big) &= \omega^2 \int_{B_R(0)} \operatorname{Re}\big(\mathrm{e}^{-\mathrm{i}\beta}\varepsilon\big)|\nabla p|^2 \,\mathrm{d}\boldsymbol{x} \\ &\quad - \omega k \operatorname{Re}\big(\mathrm{e}^{-\mathrm{i}\beta}\big) \int_{\partial B_R(0)} \widetilde{\Lambda}(\boldsymbol{\nu} \times \nabla p|_{\partial B_R(0)}) \cdot (\boldsymbol{\nu} \times \overline{\nabla p}) \times \boldsymbol{\nu}|_{\partial B_R(0)} \,\mathrm{d}s.\end{aligned}$$

Since $\beta \in (\pi/4, \pi/2)$ it holds that

$$-\omega k \operatorname{Re}\big(\mathrm{e}^{-\mathrm{i}\beta}\big) \int_{\partial B_R(0)} \widetilde{\Lambda}(\boldsymbol{\nu} \times \nabla p|_{\partial B_R(0)}) \cdot (\boldsymbol{\nu} \times \overline{\nabla p}) \times \boldsymbol{\nu}|_{\partial B_R(0)} \,\mathrm{d}s > 0$$

for $p \neq 0$ due to the negative definiteness of $\widetilde{\Lambda}$ from Lemma 2.12. Furthermore, we see that

$$\omega^2 \operatorname{Re}\big(\mathrm{e}^{-\mathrm{i}\beta}\varepsilon\big) > c > 0$$

for a constant $c > 0$. Using the Poincaré inequality once more gives that

$$\operatorname{Re}\big(-\mathrm{e}^{-\mathrm{i}\beta} a_1(p,p)\big) \geq c\,\|p\|_{H^1(B_R(0))}\,,$$

which shows (2.63). Due to the Lax-Milgram theorem A.4, the boundedness and coercivity of a_1 on $\widetilde{S}$ implies the existence of a linear and boundedly invertible operator $A_1 : \widetilde{S} \to \widetilde{S}$ such that

$$a_1(p,\xi) \;=\; \langle A_1 p, \xi\rangle_{H^1(B_R(0))} \quad \text{for all } p,\xi \in \widetilde{S}. \tag{2.64}$$

The inner product on the right hand side of (2.64) is given as in (2.4). Since the sesquilinear form a_2 from (2.62) is bounded as well there exists a linear and bounded operator $A_2 : \widetilde{S} \to \widetilde{S}$ such that

$$a_2(p,\xi) \;=\; \langle A_2 p, \xi\rangle_{H^1(B_R(0))} \quad \text{for all } p,\xi \in \widetilde{S}. \tag{2.65}$$

Furthermore, A_2 is compact. This can be seen as follows. Let $(p_n)_n \subset \widetilde{S}$ be a sequence, weakly converging to 0. We have to show that $(A_2 p_n)_n$ converges strongly to 0 since, by [33, Lem. 12.2], an operator $T : X \to Y$, for a reflexive Banach space X is compact if and only if it maps weakly convergent sequences in X to strongly convergent sequences in the Banach space Y. Accordingly,

$$\begin{aligned}\|A_2 p_n\|^2_{H^1(B_R(0))} \;&=\; a_2(p_n, A_2 p_n)\\ &\leq\; C\|(\Lambda + \mathrm{i}k\widetilde{\Lambda})(\boldsymbol{\nu}\times\nabla p_n|_{\partial B_R(0)})\|_{H^{-1/2}_{\mathrm{div}}(\partial B_R(0))}\|(\boldsymbol{\nu}\times\nabla\,(A_2 p_n))\times\boldsymbol{\nu}|_{\partial B_R(0)}\|_{H^{-1/2}_{\mathrm{curl}}(\partial B_R(0))}.\end{aligned}$$

Using the boundedness of the trace operator γ_T from (2.12) and noting that $\mathbf{curl}(\nabla(A_2 p_n)) = 0$ gives that

$$\|A_2 p_n\|_{H^1(B_R(0))} \leq C\|(\Lambda + \mathrm{i}k\widetilde{\Lambda})(\boldsymbol{\nu}\times\nabla p_n|_{\partial B_R(0)})\|_{H^{-1/2}_{\mathrm{div}}(\partial B_R(0))}. \tag{2.66}$$

The gradient ∇ is a linear and bounded operator from $H^1(B_R(0))$ to $H(\mathbf{curl}, B_R(0))$. Thus, for all functionals $\psi \in H(\mathbf{curl}, B_R(0))'$, the functional $\psi \circ \nabla$ is an element of $H^1(B_R(0))'$. Since $(p_n)_n$ converges weakly to 0 in $H^1(B_R(0))$, we therefore find that ∇p_n converges weakly to 0 in $H(\mathbf{curl}, B_R(0))$. Moreover, since γ_t is a bounded operator from $H(\mathbf{curl}, B_R(0))$ to $H^{-1/2}_{\mathrm{div}}(\partial B_R(0))$ we get that $(\boldsymbol{\nu}\times\nabla p_n|_{\partial B_R(0)})_n$ converges weakly to 0 in $H^{-1/2}_{\mathrm{div}}(\partial B_R(0))$. Finally, since $\Lambda + \mathrm{i}k\widetilde{\Lambda}$ is a compact operator by Lemma 2.13 we get that the right hand side of (2.66) converges to 0. This shows that A_2 is compact. We define $A = A_1^{-1}A_2 : \widetilde{S} \to \widetilde{S}$ and observe from (2.64) and (2.65) that

$$a_1(Ap,\xi) \;=\; a_2(p,\xi) \quad \text{for all } p,\xi \in \widetilde{S}.$$

Furthermore, A is compact, since A_2 is compact and compositions of compact and bounded operators are compact (see e.g. [33, Lem. 12.3]). By the Riesz representation theorem (see e.g. [122, p. 90]) there further exists a unique $\widetilde{b} \in \widetilde{S}$ such that $\langle \widetilde{b}, \xi\rangle_{H^1(B_R(0))} = F(\nabla\xi)$ with

$$\|\widetilde{b}\|_{H^1(B_R(0))} \;=\; \|F(\nabla\cdot)\|_{\widetilde{S}\to\mathbb{C}} \;\leq\; \|F\|_{H(\mathbf{curl},B_R(0))\to\mathbb{C}} \;=\; \|F\|\,, \tag{2.67}$$

where F has been defined in (2.54). For $b = A_1^{-1}\widetilde{b}$ we use (2.64) and see that

$$a_1(b,\xi) = F(\nabla\xi) \quad \text{for all } \xi \in \widetilde{S}\,.$$

Thus, equation (2.60) is equivalent to finding $p \in \widetilde{S}$ such that

$$a_1(p,\xi) + a_1(Ap,\xi) \;=\; a_1(b,\xi) \quad \text{for all } \xi \in \widetilde{S},$$

which is equivalent to the operator equation

$$(I + A)p \;=\; b. \tag{2.68}$$

The operator on the left hand side of (2.68) is an operator of Fredholm type and solvability of (2.68) is equivalent to uniqueness of solutions to (2.68) due to the Fredholm alternative (see e.g. [33, Lem. 13.4]). Therefore, we consider the case, in which $b = 0$. Then, (2.60) reduces to

$$-\omega^2 \int_{B_R(0)} \varepsilon \nabla p \cdot \overline{\nabla \xi} \, \mathrm{d}\boldsymbol{x} + \mathrm{i}\omega \int_{\partial B_R(0)} \Lambda(\boldsymbol{\nu} \times \nabla p|_{\partial B_R(0)}) \cdot (\boldsymbol{\nu} \times \overline{\nabla \xi}) \times \boldsymbol{\nu}|_{\partial B_R(0)} \, \mathrm{d}s \;=\; 0$$

for all $\xi \in \widetilde{S}$. Choosing $\xi = p$ yields that

$$\mathrm{i} \int_{\partial B_R(0)} \Lambda(\boldsymbol{\nu} \times \nabla p|_{\partial B_R(0)}) \cdot (\boldsymbol{\nu} \times \overline{\nabla p}) \times \boldsymbol{\nu}|_{\partial B_R(0)} \, \mathrm{d}s \;=\; \omega \int_{B_R(0)} \varepsilon |\nabla p|^2 \, \mathrm{d}\boldsymbol{x} \,.$$

For $\boldsymbol{f} = \boldsymbol{\nu} \times \nabla p$ denote by $(\boldsymbol{V}, \boldsymbol{W}) \in H_{\mathrm{loc}}(\mathbf{curl}, B_R(0))^2$ the unique radiating pair of fields solving (2.38). Then, $\boldsymbol{\nu} \times \boldsymbol{V} = \boldsymbol{\nu} \times \nabla p$ and $\Lambda(\boldsymbol{\nu} \times \nabla p) = \boldsymbol{\nu} \times \boldsymbol{W}$. We write γ_t and γ_T for abbreviating the traces $\boldsymbol{\nu} \times \cdot|_{\partial B_R(0)}$ and $((\boldsymbol{\nu} \times \cdot) \times \boldsymbol{\nu})|_{\partial B_R(0)}$, respectively and compute

$$\begin{aligned}\int_{\partial B_R(0)} (\gamma_t \boldsymbol{V}) \cdot (\gamma_T \overline{\boldsymbol{W}}) \, \mathrm{d}s &= -\int_{\partial B_R(0)} (\gamma_t \overline{\boldsymbol{W}}) \cdot (\gamma_T \nabla p) \, \mathrm{d}s = -\int_{\partial B_R(0)} \Lambda(\gamma_t \overline{\nabla p}) \cdot (\gamma_T \nabla p) \, \mathrm{d}s \\ &= -\overline{\int_{\partial B_R(0)} \Lambda\,(\gamma_t \nabla p) \cdot (\gamma_T \overline{\nabla p}) \, \mathrm{d}s} = -\mathrm{i}\omega \int_{B_R(0)} \overline{\varepsilon} |\nabla p|^2 \, \mathrm{d}\boldsymbol{x}. \quad (2.69)\end{aligned}$$

Therefore,

$$\mathrm{Re}\left(\int_{\partial B_R(0)} \left(\boldsymbol{\nu} \times \boldsymbol{V}|_{B_R(0)} \right) \cdot ((\boldsymbol{\nu} \times \overline{\boldsymbol{W}}) \times \boldsymbol{\nu}|_{\partial B_R(0)}) \, \mathrm{d}s \right) \;=\; \omega \int_{B_R(0)} \mathrm{Im}(\overline{\varepsilon}) |\nabla p|^2 \, \mathrm{d}\boldsymbol{x} \;\leq\; 0.$$

Rellich's lemma 2.6 now implies that $\boldsymbol{V}$ and $\boldsymbol{W}$ vanish in $\mathbb{R}^3 \setminus \overline{B_R(0)}$. Due to (2.69) it follows that ∇p vanishes in all $B_R(0)$, since the left hand side in (2.69) is zero. The Poincaré inequality now yields that $p = 0$ in $B_R(0)$, and we have shown uniqueness of solutions to (2.68). For the unique solution $p \in \widetilde{S}$ of (2.68) we obtain by using (2.67) that

$$\|p\|_{H^1(B_R(0))} \;\leq\; C\|b\|_{H^1(B_R(0))} \;\leq\; C\|\widetilde{b}\|_{H^1(B_R(0))} \;\leq\; C\|F\| \,.$$

□

The space $\nabla \widetilde{S}$ is the **curl** free part of a Helmholtz decomposition of $H(\mathbf{curl}, B_R(0))$. For the div free part we define the space

$$\begin{aligned}\widetilde{X}_0 &= \{\boldsymbol{u} \in H(\mathbf{curl}, B_R(0)) \mid B(\boldsymbol{u}, \nabla \xi) = 0 \text{ for all } \xi \in \widetilde{S}\} \\ &= \{\boldsymbol{u} \in H(\mathbf{curl}, B_R(0)) \mid \mathrm{div}(\varepsilon \boldsymbol{u}) = 0 \text{ in } B_R(0),\ \mathrm{i}\omega\varepsilon_0\gamma_n \boldsymbol{u} = \mathrm{div}_{\partial B_R(0)} \Lambda(\gamma_t \boldsymbol{u}) \text{ on } \partial B_R(0)\},\end{aligned}$$

where B is defined in (2.53). The operators div, γ_n and $\mathrm{div}_{\partial B_R(0)}$ denote the weak divergence, normal trace and surface divergence introduced in (2.8), (2.9) and (2.13a), respectively. If $B(\boldsymbol{u}, \nabla \xi) = 0$ for all $\xi \in \widetilde{S}$, then indeed $\mathrm{div}(\varepsilon \boldsymbol{u})$ exists, since $C_0^\infty(\overline{B_R(0)}) \subset \widetilde{S}$ and $\xi \in C_0^\infty(\overline{B_R(0)})$ implies that $\nabla \xi \in (C_0^\infty(\overline{B_R(0)}))^3 \subset \mathcal{N}(\gamma_T)$, where $\mathcal{N}(\gamma_T)$ denotes the kernel of γ_T (see [88, Thm. 5.25]). To see that the above mentioned sets are indeed the same, we consider $\boldsymbol{u} \in H(\mathbf{curl}, B_R(0))$ and apply Green's theorem in (2.10), which yields

$$\int_{B_R(0)} \mathrm{div}(\varepsilon \boldsymbol{u}) \overline{\xi} \, \mathrm{d}\boldsymbol{x} \;=\; -\int_{B_R(0)} \varepsilon \boldsymbol{u} \cdot \overline{\nabla \xi} \, \mathrm{d}\boldsymbol{x} + \int_{\partial B_R(0)} \varepsilon_0 \boldsymbol{\nu} \cdot \boldsymbol{u}|_{\partial B_R(0)} \overline{\xi}|_{\partial B_R(0)} \, \mathrm{d}s \qquad (2.70)$$

for all $\xi \in \widetilde{S}$. Let

$$B(\boldsymbol{u}, \nabla \xi) \;=\; 0 \text{ for all } \xi \in \widetilde{S} \,.$$

By using (2.70) and the definition of the surface divergence in (2.13a) this implies that

$$\int_{B_R(0)} \operatorname{div}(\varepsilon \boldsymbol{u})\overline{\xi}\,\mathrm{d}\boldsymbol{x} = \int_{\partial B_R(0)} \left(\frac{\mathrm{i}}{\omega}\operatorname{div}_{\partial B_R(0)}\Lambda(\boldsymbol{\nu}\times\boldsymbol{u}) + \varepsilon_0 \boldsymbol{\nu}\cdot\boldsymbol{u}|_{\partial B_R(0)}\right)\overline{\xi}|_{\partial B_R(0)}\,\mathrm{d}s$$

for all $\xi \in \widetilde{S}$. Since this equality holds for all $\xi \in \widetilde{S}$, it holds for $\xi \in H_0^1(B_R(0))$ in particular. Therefore, we find that

$$\operatorname{div}(\varepsilon\boldsymbol{u}) = 0 \quad \text{in } B_R(0) \quad \text{and} \quad \varepsilon_0\boldsymbol{\nu}\cdot\boldsymbol{u}|_{\partial B_R(0)} = -\frac{\mathrm{i}}{\omega}\operatorname{div}_{\partial B_R(0)}\Lambda(\boldsymbol{\nu}\times\boldsymbol{u}) \quad \text{on } \partial B_R(0).$$

We cite the next lemma from [99, Lem. 10.3]. The proof is omitted, as it can be done in the same way as in [99, Lem. 10.3].

Lemma 2.17. *The vector spaces $\nabla\widetilde{S}$ and $\widetilde{X}_0$ are closed subspaces of $H(\mathbf{curl}, B_R(0))$. The space $H(\mathbf{curl}, B_R(0))$ is the direct sum of the spaces $\nabla\widetilde{S}$ and $\widetilde{X}_0$, i.e. it holds that*

$$H(\mathbf{curl}, B_R(0)) = \nabla\widetilde{S} \oplus \widetilde{X}_0.$$

The orthogonal projections onto these spaces are bounded, i.e., there exist constants $C_1, C_2 > 0$ such that

$$C_1\|\boldsymbol{w}+\nabla p\|^2_{H(\mathbf{curl},B_R(0))} \le \|\boldsymbol{w}\|^2_{H(\mathbf{curl},B_R(0))} + \|\nabla p\|^2_{H(\mathbf{curl},B_R(0))} \le C_2\|\boldsymbol{w}+\nabla p\|^2_{H(\mathbf{curl},B_R(0))}$$

for all $\boldsymbol{w} \in \widetilde{X}_0$ and $p \in \widetilde{S}$.

The next lemma and proof are similar to [99, Lem. 10.4]. In our proof we make use of the second representation of $\widetilde{X}_0$ and refer to a compactness result from [75, Prop. B.3].

Lemma 2.18. *The space $\widetilde{X}_0$ is compactly embedded in $(L^2(B_R(0)))^3$.*

Proof. Let $(\boldsymbol{u}_n)_n \subset \widetilde{X}_0$ be a bounded sequence with respect to the norm $\|\cdot\|_{H(\mathbf{curl},B_R(0))}$. We show that this sequences converges with respect to the norm $\|\cdot\|_{L^2(B_R(0))^3}$. For every function $\boldsymbol{u}_n$, $n \in \mathbb{N}$, we consider $\boldsymbol{f}_n = \boldsymbol{\nu}\times\boldsymbol{u}_n|_{\partial B_R(0)}$ and denote by $(\boldsymbol{V}_n, \boldsymbol{W}_n) \in (H_{\mathrm{loc}}(\mathbf{curl}, \mathbb{R}^3 \setminus \overline{B_R(0)}))^2$ the unique radiating fields solving (2.38) with $\boldsymbol{f}_n$ taken as the boundary value. Then, the functions

$$\widetilde{\boldsymbol{u}}_n = \begin{cases} \boldsymbol{u}_n, & \boldsymbol{x} \in B_R(0) \\ \boldsymbol{V}_n, & \boldsymbol{x} \in \mathbb{R}^3 \setminus \overline{B_R(0)} \end{cases}$$

satisfy $\widetilde{\boldsymbol{u}}_n \in H_{\mathrm{loc}}(\mathbf{curl}, \mathbb{R}^3)$ for all $n \in \mathbb{N}$. Since $\boldsymbol{u}_n \in \widetilde{X}_0$ we find that

$$\mathrm{i}\omega\varepsilon_0\boldsymbol{\nu}\cdot\boldsymbol{u}_n|_{\partial B_R(0)} = \operatorname{div}_{\partial B_R(0)}\Lambda(\boldsymbol{\nu}\times\boldsymbol{u}_n|_{\partial B_R(0)}) \quad \text{for all } n \in \mathbb{N}. \tag{2.71}$$

From [99, Eq. (3.52)] we find that for $\boldsymbol{v} \in H(\mathbf{curl}, B_R(0))$ it holds that

$$\operatorname{div}_{\partial B_R(0)}(\boldsymbol{\nu}\times\boldsymbol{v}|_{\partial B_R(0)}) = -\boldsymbol{\nu}\cdot(\mathbf{curl}\,\boldsymbol{v})|_{\partial B_R(0)}. \tag{2.72}$$

By the definition of the exterior Calderón operator (see (2.41)) we find that

$$\Lambda(\boldsymbol{\nu}\times\boldsymbol{u}_n|_{\partial B_R(0)}) = \Lambda(\boldsymbol{f}_n) = \boldsymbol{\nu}\times\boldsymbol{W}_n|_{\partial B_R(0)} = \frac{1}{\mathrm{i}\omega\mu_0}\boldsymbol{\nu}\times\mathbf{curl}\,\boldsymbol{V}_n|_{\partial B_R(0)}$$

and combining this with (2.71) and (2.72) yields that

$$\mathrm{i}\omega\varepsilon_0\boldsymbol{\nu}\cdot\boldsymbol{u}_n|_{\partial B_R(0)} = \frac{1}{\mathrm{i}\omega\mu_0}\operatorname{div}_{\partial B_R(0)}(\boldsymbol{\nu}\times\mathbf{curl}\,\boldsymbol{V}_n|_{\partial B_R(0)}) = -\frac{1}{\mathrm{i}\omega\mu_0}\boldsymbol{\nu}\cdot(\mathbf{curl}^2\,\boldsymbol{V}_n)|_{\partial B_R(0)}$$

which gives that $\boldsymbol{\nu}\cdot\boldsymbol{u}_n|_{\partial B_R(0)} = \boldsymbol{\nu}\cdot\boldsymbol{V}_n|_{\partial B_R(0)}$. By [99, Lem. 5.3] and the definition of $\widetilde{X}_0$, we find that $\varepsilon\widetilde{\boldsymbol{u}}_n \in H(\mathrm{div},\mathbb{R}^3)$ and $\mathrm{div}(\varepsilon\widetilde{\boldsymbol{u}}_n) = 0$ in all $\mathbb{R}^3$. Let $R' > R$ and consider $\widetilde{\boldsymbol{u}}_n|_{B_{R'}(0)}$. Then, $\widetilde{\boldsymbol{u}}_n|_{B'_R(0)} \in H(\mathbf{curl}, B_{R'}(0))$, $\mathrm{div}(\varepsilon\widetilde{\boldsymbol{u}}_n|_{B'_R(0)}) = 0$ in $B_{R'}(0)$ and $\boldsymbol{\nu}\cdot(\varepsilon\widetilde{\boldsymbol{u}}_n|_{B'_R(0)})|_{\partial B_{R'}(0)} = \varepsilon_0\boldsymbol{\nu}\cdot\boldsymbol{V}_n|_{\partial B_{R'}(0)} \in C^\infty(\partial B_{R'}(0))$, since $(\boldsymbol{V}_n, \boldsymbol{W}_n)$ are analytic outside of $B_R(0)$ (see [34, Thm. 6.3] and Theorem 2.8). By [75, Prop. B.3], the space

$$M = \left\{\boldsymbol{u} \in H(\mathbf{curl}, B_{R'}(0)) \,\middle|\, \mathrm{div}(\boldsymbol{\xi}\boldsymbol{u}) \in L^2(B_{R'}(0)),\ \boldsymbol{\xi}\boldsymbol{u}\cdot\boldsymbol{\nu} \in L^2(\partial B_{R'}(0))\right\}, \tag{2.73}$$

with $\boldsymbol{\xi} \in L^\infty(B_{R'}(0))$ satisfying $\mathrm{Re}(\boldsymbol{\xi}) > \alpha$ is compactly embedded in $(L^2(B_{R'}(0))^3$. The set M in (2.73) does not change if either $\boldsymbol{\xi} = \varepsilon$ or $\boldsymbol{\xi} = e^{\mathrm{i}\beta}\varepsilon$, with β such that $\mathrm{Re}(e^{\mathrm{i}\beta}\varepsilon) > \alpha$ is chosen. Thus, there is a subsequence of $(\widetilde{\boldsymbol{u}}_n|_{B_{R'}(0)})_n$, still denoted by $(\widetilde{\boldsymbol{u}}_n|_{B_{R'}(0)})_n$ such that $(\widetilde{\boldsymbol{u}}_n|_{B_{R'}(0)})_n$ converges with respect to the norm in $(L^2(B_{R'}(0))^3$. Therefore, $(\widetilde{\boldsymbol{u}_n}|_{B_R(0)})_n = (\boldsymbol{u}_n)_n$ must converge in $(L^2(B_R(0))^3$. □

According to Lemma 2.17, any $\boldsymbol{E} \in H(\mathbf{curl}, B_R(0))$ has a unique decomposition $\boldsymbol{E} = \boldsymbol{w} + \nabla p$ with $\boldsymbol{w} \in \widetilde{X}_0$ and $p \in \widetilde{S}$. Following the definition of $\widetilde{X}_0$ it holds that

$$B(\boldsymbol{w}, \nabla\xi) = 0 \quad \text{for all } \xi \in \widetilde{S},$$

where B was defined in (2.53). Therefore, using for any $\boldsymbol{V} \in H(\mathbf{curl}, B_R(0))$ the decomposition $\boldsymbol{V} = \nabla\xi + \boldsymbol{\psi}$ with $\xi \in \widetilde{S}$ and $\boldsymbol{\psi} \in \widetilde{X}_0$ we find that the weak formulation in (2.52) is equivalent to

$$B(\nabla p, \nabla\xi) + B(\nabla p, \boldsymbol{\psi}) + B(\boldsymbol{w}, \boldsymbol{\psi}) = F(\nabla\xi) + F(\boldsymbol{\psi}) \quad \text{for all } \xi \in \widetilde{S} \text{ and } \boldsymbol{\psi} \in \widetilde{X}_0. \tag{2.74}$$

Setting $\boldsymbol{\psi} = 0$ gives that $p \in \widetilde{S}$ must satisfy

$$B(\nabla p, \nabla\xi) = F(\nabla\xi) \quad \text{for all } \xi \in \widetilde{S}.$$

Due to Proposition 2.16 we see that $p \in \widetilde{S}$ is uniquely defined by $(I + A)p = b$. Furthermore, p depends continuously on b. Now, in (2.74), we set $\xi = 0$. Therefore, it is left to show that there is a $\boldsymbol{w} \in \widetilde{X}_0$ with

$$B(\boldsymbol{w}, \boldsymbol{\psi}) = F(\boldsymbol{\psi}) - B(\nabla p, \boldsymbol{\psi}) \quad \text{for all } \boldsymbol{\psi} \in \widetilde{X}_0,$$

that is uniquely defined and continuously dependent on the data. We define the right hand side to be the antilinear and bounded functional

$$\widetilde{F}(\boldsymbol{\psi}) = F(\boldsymbol{\psi}) - B(\nabla p, \boldsymbol{\psi}) \quad \text{for all } \boldsymbol{\psi} \in \widetilde{X}_0. \tag{2.75}$$

Let $\boldsymbol{f} \in H^{-1/2}_{\mathrm{div}}(\partial B_R(0))$ be given by

$$\boldsymbol{f} = \sum_{n=1}^{\infty}\sum_{m=-n}^{n} \alpha_n^m \boldsymbol{U}_n^m + \beta_n^m \boldsymbol{V}_n^m, \tag{2.76}$$

with the vector spherical harmonics defined in (2.16). Using the expansion (2.42) we find that

$$\Lambda\boldsymbol{f} = \sum_{n=1}^{\infty}\sum_{m=-n}^{n} -\frac{\mathrm{i}\omega\varepsilon_0\beta_n^m R}{\delta_n}\boldsymbol{U}_n^m + \frac{\alpha_n^m(\delta_n - \widetilde{\delta}_n)}{\mathrm{i}\omega\mu_0 R}\boldsymbol{V}_n^m + \frac{\alpha_n^m\widetilde{\delta}_n}{\mathrm{i}\omega\mu_0 R}\boldsymbol{V}_n^m,$$

with $\widetilde{\delta}_n$ as in (2.43). Therefore, we define for $\boldsymbol{f} \in H^{-1/2}_{\mathrm{div}}(\partial B_R(0))$ as in (2.76) the bounded operators

$$\Lambda_1 : H^{-1/2}_{\mathrm{div}}(\partial B_R(0)) \to H^{-1/2}_{\mathrm{div}}(\partial B_R(0)), \quad \Lambda_1\boldsymbol{f} = \sum_{n=1}^{\infty}\sum_{m=-n}^{n} -\frac{\mathrm{i}\omega\varepsilon_0\beta_n^m R}{\delta_n}\boldsymbol{U}_n^m + \frac{\alpha_n^m(\delta_n - \widetilde{\delta}_n)}{\mathrm{i}\omega\mu_0 R}\boldsymbol{V}_n^m,$$

$$\Lambda_2 : H^{-1/2}_{\mathrm{div}}(\partial B_R(0)) \to H^{-1/2}_{\mathrm{div}}(\partial B_R(0)), \quad \Lambda_2\boldsymbol{f} = \sum_{n=1}^{\infty}\sum_{m=-n}^{n} \frac{\alpha_n^m\widetilde{\delta}_n}{\mathrm{i}\omega\mu_0 R}\boldsymbol{V}_n^m.$$

The boundedness of both Λ_1 and Λ_2 can be seen by using Remark 2.11 and $-2n < \widetilde{\delta_n} < -n$ (see [99, Proof of Lem. 9.22]). As before, the ansatz is to decompose the sesquilinear form B in such a way that the Riesz representation theorem yields an operator equation of the form $(I+K)\boldsymbol{w} = b$, where K is a compact operator. The compact operator results from the following observation about the first part of the Calderón map Λ_1, which we state in the following without proof (see [99, Lem. 10.5]).

Lemma 2.19. *The operator $\Lambda_1 \circ \gamma_t$ is compact from $\widetilde{X}_0$ into $H_{\mathrm{div}}^{-1/2}(\partial B_R(0))$.*

Now, we use the decomposition $B = b_1 + b_2$ with the sesquilinear forms $b_1, b_2 : \widetilde{X}_0 \times \widetilde{X}_0 \to \mathbb{C}$, defined by

$$b_1(\boldsymbol{u}, \boldsymbol{\psi}) = \int_{B_R(0)} \frac{1}{\mu} \operatorname{\mathbf{curl}} \boldsymbol{u} \cdot \overline{\operatorname{\mathbf{curl}} \boldsymbol{\psi}} \, \mathrm{d}\boldsymbol{x} + \omega^2 \int_{B_R(0)} \varepsilon \boldsymbol{u} \cdot \overline{\boldsymbol{v}} \, \mathrm{d}\boldsymbol{x} + \mathrm{i}\omega \int_{\partial B_R(0)} \Lambda_2(\boldsymbol{\nu} \times \boldsymbol{u}|_{\partial B_R(0)}) \cdot ((\boldsymbol{\nu} \times \overline{\boldsymbol{v}}) \times \boldsymbol{\nu}|_{\partial B_R(0)}) \, \mathrm{d}s \quad (2.77)$$

and

$$b_2(\boldsymbol{u}, \boldsymbol{\psi}) = -2\omega^2 \int_{B_R(0)} \varepsilon \boldsymbol{u} \cdot \overline{\boldsymbol{v}} \, \mathrm{d}\boldsymbol{x} + \mathrm{i}\omega \int_{\partial B_R(0)} \Lambda_1(\boldsymbol{\nu} \times \boldsymbol{u}|_{\partial B_R(0)}) \cdot ((\boldsymbol{\nu} \times \overline{\boldsymbol{v}}) \times \boldsymbol{\nu}|_{\partial B_R(0)}) \, \mathrm{d}s. \quad (2.78)$$

Using these two sesquilinear forms, we find the following proposition, which is similar to [99, Thm. 10.6].

Proposition 2.20. *Let $\varepsilon_1 > 0$ or $\varepsilon_1 \in \mathbb{C}$ with $\operatorname{Re}(\varepsilon_1) < 0$ and $\operatorname{Im}(\varepsilon_1) > 0$. The sesquilinear form $b_1 : \widetilde{X}_0 \times \widetilde{X}_0 \to \mathbb{C}$ from (2.77) is bounded. Further, there is a $\zeta \in \mathbb{R}$ such that*

$$\operatorname{Re}(\mathrm{e}^{\mathrm{i}\zeta} b_1(\boldsymbol{u}, \boldsymbol{u})) \geq c \|\boldsymbol{u}\|_{H^1(\Omega)} \quad \text{for all } \boldsymbol{u} \in \widetilde{X}_0.$$

There is a compact operator $A : \widetilde{X}_0 \to \widetilde{X}_0$ with

$$b_1(A\boldsymbol{u}, \boldsymbol{v}) = b_2(\boldsymbol{u}, \boldsymbol{v}) \quad \text{for all } \boldsymbol{u}, \boldsymbol{v} \in \widetilde{X}_0,$$

with $b_2 : \widetilde{X}_0 \times \widetilde{X}_0 \to \mathbb{C}$ defined as in (2.78).

The operator $I + A$ is an isomorphism from $\widetilde{X}_0$ onto itself. The variational formulation, which is to find $\boldsymbol{w} \in \widetilde{X}_0$ such that

$$B(\boldsymbol{w}, \boldsymbol{v}) = \widetilde{F}(\boldsymbol{v}) \quad \text{for all } \boldsymbol{v} \in \widetilde{X}_0$$

is uniquely solvable in $\widetilde{X}_0$, where the sesquilinear form B and the antilinear functional $\widetilde{F}$ are defined in (2.53) and (2.75), respectively. The solution is given by

$$\boldsymbol{w} = (I + A)^{-1} \boldsymbol{b},$$

where $\boldsymbol{b} \in \widetilde{X}_0$ is the unique solution to

$$b_1(\boldsymbol{b}, \xi) = \widetilde{F}(\boldsymbol{v}) \quad \text{for all } \boldsymbol{v} \in \widetilde{X}_0.$$

In particular, it holds that $\|\boldsymbol{w}\|_{H(\mathbf{curl}, (B_R(0))} \leq C \|\widetilde{F}\|$.

Proof. Boundedness of the sesquilinear form b_1 follows from an application of the Cauchy–Schwarz inequality, the boundedness of Λ_2 and the boundedness of the traces γ_t and γ_T. For $\boldsymbol{f} \in H_{\mathrm{div}}^{-1/2}(\partial B_R(0))$ defined as in (2.76) we find that

$$\boldsymbol{\nu} \times \boldsymbol{f} = \sum_{n=1}^{\infty} \sum_{m=-n}^{n} \alpha_n^m \boldsymbol{V}_n^m - \beta_n^m \boldsymbol{U}_n^m$$

and therefore

$$\mathrm{i}\omega \int_{\partial B_R(0)} \Lambda_2(\boldsymbol{\nu} \times \boldsymbol{f}) \cdot \overline{\boldsymbol{f}} \, \mathrm{d}s = -\frac{1}{R\mu_0} \sum_{n=1}^{\infty} \sum_{m=-n}^{n} |\beta_n^m| \widetilde{\delta}_n \geq 0 \,, \tag{2.79}$$

since $\widetilde{\delta}_n < 0$ (see Lemma 2.12). For $\varepsilon_1 > 0$, by using (2.79), we see that

$$b_1(\boldsymbol{u}, \boldsymbol{u}) \geq c \|\boldsymbol{u}\|_{H(\mathbf{curl}, B_R(0))} \quad \text{for all } \boldsymbol{u} \in \widetilde{X}_0 \,.$$

For $\varepsilon_1 \in \mathbb{C}$ with $\mathrm{Re}(\varepsilon_1) < 0$ and $\mathrm{Im}(\varepsilon_1) > 0$ we write $\varepsilon_1 = |\varepsilon_1| \mathrm{e}^{\mathrm{i}\alpha}$ with $\alpha \in (\pi/2, \pi)$. For $\beta = \alpha/2 \in (\pi/4, \pi/2)$ we have that $\mathrm{Re}(\mathrm{e}^{-\mathrm{i}\beta}\varepsilon) > 0$ and $\mathrm{Re}(\mathrm{e}^{-\mathrm{i}\beta}) > 0$. Therefore,

$$\begin{aligned}
\mathrm{Re}\big(\mathrm{e}^{-\mathrm{i}\beta} b_1(\boldsymbol{u}, \boldsymbol{u})\big) &= \mathrm{Re}\big(\mathrm{e}^{-\mathrm{i}\beta}\big) \int_{B_R(0)} \frac{1}{\mu} |\operatorname{\mathbf{curl}} \boldsymbol{u}|^2 \, \mathrm{d}\boldsymbol{x} + \omega^2 \int_{B_R(0)} \mathrm{Re}\big(\mathrm{e}^{-\mathrm{i}\beta}\varepsilon\big) |\boldsymbol{u}|^2 \, \mathrm{d}\boldsymbol{x} \\
&\quad + \mathrm{Re}\big(\mathrm{e}^{-\mathrm{i}\beta}\big) \mathrm{i}\omega \int_{\partial B_R(0)} \Lambda_2(\boldsymbol{\nu} \times \boldsymbol{u}|_{\partial B_R(0)}) \cdot ((\boldsymbol{\nu} \times \overline{\boldsymbol{u}}) \times \boldsymbol{\nu}|_{\partial B_R(0)}) \, \mathrm{d}s \\
&\geq c \|\boldsymbol{u}\|_{H(\mathbf{curl}, B_R(0))} \,.
\end{aligned}$$

The sesquilinear form b_2 from (2.78) is bounded as well. Therefore, we find a boundedly invertible operator A_1 and a bounded operator A_2, both mapping from $\widetilde{X}_0$ into itself, such that

$$b_1(\boldsymbol{u}, \boldsymbol{v}) = \langle A_1 \boldsymbol{u}, \boldsymbol{v} \rangle_{H(\mathbf{curl}, B_R(0))} \quad \text{and} \quad b_2(\boldsymbol{u}, \boldsymbol{v}) = \langle A_2 \boldsymbol{u}, \boldsymbol{v} \rangle_{H(\mathbf{curl}, B_R(0))} \quad \text{for all } \boldsymbol{u}, \boldsymbol{v} \in \widetilde{X}_0.$$

Defining $A = A_1^{-1} A_2$ gives that

$$b_1(A\boldsymbol{u}, \boldsymbol{v}) = b_2(\boldsymbol{u}, \boldsymbol{v}) \quad \text{for all } \boldsymbol{u}, \boldsymbol{v} \in \widetilde{X}_0 \,.$$

In order to show that the operator A is compact, we consider a sequence $(\boldsymbol{u}_n)_n$ in $\widetilde{X}_0$, weakly converging to 0, and show that $(A\boldsymbol{u}_n)_n$ converges strongly to 0. Then, by [33, Lem. 12.2], A is a compact operator. Since $(\boldsymbol{u}_n)_n$ converges weakly to 0 in $\widetilde{X}_0$, we find that $(\boldsymbol{\nu} \times \boldsymbol{u}_n)_n$ converges weakly to 0 in $H_{\mathrm{div}}^{-1/2}(\partial B_R(0))$, since the trace operator is a bounded operator. According to Lemma 2.19 we find that $\Lambda_1 \circ \gamma_t$ is compact and therefore, $(\Lambda_1(\boldsymbol{\nu} \times \boldsymbol{u}_n|_{\partial B_R(0)}))_n$ converges strongly to 0 in $H_{\mathrm{div}}^{-1/2}(\partial B_R(0))$. Moreover, due to Lemma 2.18, the sequence $(\boldsymbol{u}_n)_n$ converges strongly to 0 in $(L^2(B_R(0)))^3$. In what follows we use $\beta = 0$ for the case $\varepsilon_1 > 0$ and $\beta = \alpha/2$ for the case that $\varepsilon_1 = |\varepsilon_1| e^{\mathrm{i}\alpha}$ for $\alpha \in (\pi/2, \pi)$. We set

$$c = \min\{\mathrm{Re}(\mathrm{e}^{-\mathrm{i}\beta}\varepsilon), \mathrm{Re}(\mathrm{e}^{-\mathrm{i}\beta}\mu^{-1})\}$$

and find that

$$\begin{aligned}
&c \|A\boldsymbol{u}_n\|_{H(\mathbf{curl}, B_R(0))}^2 \leq \mathrm{Re}\left(\mathrm{e}^{-\mathrm{i}\beta} \left(\int_{B_R(0)} \frac{1}{\mu} |\operatorname{\mathbf{curl}} A\boldsymbol{u}_n|^2 \, \mathrm{d}\boldsymbol{x} + \int_{B_R(0)} \varepsilon |A\boldsymbol{u}_n|^2 \, \mathrm{d}\boldsymbol{x} \right) \right) \\
&\leq \mathrm{Re}\big(\mathrm{e}^{-\mathrm{i}\beta} b_1(A\boldsymbol{u}_n, A\boldsymbol{u}_n)\big) = \mathrm{Re}\big(\mathrm{e}^{-\mathrm{i}\beta} b_2(\boldsymbol{u}_n, A\boldsymbol{u}_n)\big) \leq |b_2(\boldsymbol{u}_n, A\boldsymbol{u}_n)| \\
&\leq C\big(\|A\boldsymbol{u}_n\|_{(L^2(B_R(0)))^3} \|\boldsymbol{u}_n\|_{(L^2(B_R(0)))^3} + \|\Lambda_1(\boldsymbol{\nu} \times \boldsymbol{u}_n|_{\partial B_R(0)})\|_{H_{\mathrm{div}}^{-1/2}(\partial B_R(0))} \|A\boldsymbol{u}_n\|_{H(\mathbf{curl}, B_R(0))}\big).
\end{aligned}$$

The second inequality holds true due to (2.79). This gives that

$$\|A\boldsymbol{u}_n\|_{H(\mathbf{curl}, \Omega)} \to 0 \quad \text{as } n \to \infty$$

and consequently that A is compact. Similar to the proof of Proposition 2.16, by the Riesz representation theorem (see e.g. [122, p. 90]), there exists a unique $\widetilde{\boldsymbol{b}} \in \widetilde{X}_0$ such that

$$\langle \widetilde{\boldsymbol{b}}, \boldsymbol{\psi} \rangle_{H(\mathbf{curl}, B_R(0))} = \widetilde{F}(\boldsymbol{\psi}) \quad \text{for all } \boldsymbol{\psi} \in \widetilde{X}_0 \qquad \text{with } \|\widetilde{\boldsymbol{b}}\|_{H(\mathbf{curl}, B_R(0))} = \|\widetilde{F}\|\,, \tag{2.80}$$

with $\widetilde{F}$ from (2.75). Thus, finding $\boldsymbol{w} \in \widetilde{X}_0$ such that $B(\boldsymbol{w}, \boldsymbol{\psi}) = \widetilde{F}(\boldsymbol{\psi})$ for all $\boldsymbol{\psi} \in \widetilde{X}_0$ is equivalent to the operator equation

$$(I + A)\boldsymbol{w} = \boldsymbol{b}\,,$$

where $\boldsymbol{b} = A_1^{-1}\widetilde{\boldsymbol{b}}$. It remains to show that $(I + A)\boldsymbol{w} = 0$ implies $\boldsymbol{w} = 0$. For such a $\boldsymbol{w} \in \widetilde{X}_0$, we have that

$$B(\boldsymbol{w}, \boldsymbol{\psi}) = b_1(\boldsymbol{w}, \boldsymbol{\psi}) + b_2(\boldsymbol{w}, \boldsymbol{\psi}) = b_1((I + A)\boldsymbol{w}, \boldsymbol{\psi}) = 0 \quad \text{for all } \boldsymbol{\psi} \in \widetilde{X}_0\,.$$

According to the definition of $\widetilde{X}_0$ we also have that

$$B(\boldsymbol{w}, \nabla\xi) = 0 \quad \text{for all } \xi \in \widetilde{S}.$$

Following the decomposition of $H(\mathbf{curl}, B_R(0))$ in Lemma 2.17 gives that

$$B(\boldsymbol{w}, \boldsymbol{z}) = 0 \quad \text{for all } \boldsymbol{z} \in H(\mathbf{curl}, B_R(0)).$$

This coincides with the weak formulation obtained in (2.52) if the pair of incoming fields $(\boldsymbol{E}^i, \boldsymbol{H}^i)$ vanishes identically in all $\mathbb{R}^3$. As established in the proof of Lemma 2.15, $\boldsymbol{w} \in \widetilde{X}_0$ can be extended to a function $\widetilde{\boldsymbol{E}}$ in the full space $\mathbb{R}^3$, where $\widetilde{\boldsymbol{E}}$ is a weak solution of Maxwell's equation (2.34) and $\widetilde{\boldsymbol{E}} - \boldsymbol{E}^i$ satisfies the Silver–Müller radiation condition. However, since the incident electric field is zero, the total field $\widetilde{\boldsymbol{E}}$, must be zero in all $\mathbb{R}^3$ due to the uniqueness result from Proposition 2.14. Consequently $\boldsymbol{w} = \widetilde{\boldsymbol{E}}|_{B_R(0)}$ must be zero as well. Since $(I + A)\boldsymbol{w} = 0$ implies $\boldsymbol{w} = 0$ and $(I + A)$ is an operator of Fredholm type, the Fredholm alternative (see e.g. [33, Lem. 13.4]) shows that $(I + A)\boldsymbol{w} = \boldsymbol{b}$ is uniquely solvable for every $\boldsymbol{b} \in \widetilde{X}_0$. Moreover, using (2.80), we obtain the bound

$$\|\boldsymbol{w}\|_{H(\mathbf{curl}, (B_R(0)))} \leq C\|\boldsymbol{b}\|_{H(\mathbf{curl}, (B_R(0)))} \leq C\|\widetilde{\boldsymbol{b}}\|_{H(\mathbf{curl}, (B_R(0)))} = C\|\widetilde{F}\|\,.$$

□

We summarize the main result of this chapter in the following theorem.

Theorem 2.21. *Let $\varepsilon_1 > 0$ or $\varepsilon_1 \in \mathbb{C}$ with $\mathrm{Re}(\varepsilon_1) < 0$ and $\mathrm{Im}(\varepsilon_1) > 0$ and let $\mu_1 > 0$. Moreover, let $(\boldsymbol{E}^i, \boldsymbol{H}^i)$ be entire wave fields satisfying (2.30). Then, the scattering problem, to find $(\boldsymbol{E}, \boldsymbol{H}) = (\boldsymbol{E}^i + \boldsymbol{E}^s, \boldsymbol{H}^i + \boldsymbol{H}^s) \in (H_{\mathrm{loc}}(\mathbf{curl}, \mathbb{R}^3))^2$ satisfying (2.31) together with the Silver–Müller radiation condition for $(\boldsymbol{E}^s, \boldsymbol{H}^s)$ in (2.32) is uniquely solvable and equivalent (by Lemma 2.15) to the problem to find $\boldsymbol{E} \in H(\mathbf{curl}, B_R(0))$ solving $B(\boldsymbol{E}, \boldsymbol{V}) = F(\boldsymbol{V})$ for all $\boldsymbol{V} \in H(\mathbf{curl}, B_R(0))$ with B and F defined in (2.53) and (2.54). Moreover, for this field $\boldsymbol{E}$ it holds that $\|\boldsymbol{E}\|_{H(\mathbf{curl}, B_R(0))} \leq C\|\boldsymbol{E}^i\|_{H(\mathbf{curl}, B_R(0))}$.*

Proof. According to Lemma 2.17, any fields $\boldsymbol{E}, \boldsymbol{V} \in H(\mathbf{curl}, B_R(0))$ can be uniquely decomposed via $\boldsymbol{E} = \nabla p + \boldsymbol{w}$ and $\boldsymbol{V} = \nabla\xi + \boldsymbol{\psi}$, where $p, \xi \in \widetilde{S}$ and $\boldsymbol{w}, \boldsymbol{\psi} \in \widetilde{X}_0$. The variational formulation to find $\boldsymbol{E} \in H(\mathbf{curl}, B_R(0))$ with $B(\boldsymbol{E}, \boldsymbol{V}) = F(\boldsymbol{V})$ is thus equivalent to find the unique $p \in \widetilde{S}$ and $\boldsymbol{w} \in \widetilde{X}_0$ such that

$$B(\nabla p, \nabla\xi) + B(\nabla p, \boldsymbol{\psi}) + B(\boldsymbol{w}, \nabla\xi) + B(\boldsymbol{w}, \boldsymbol{\psi}) = F(\nabla\xi) + F(\boldsymbol{\psi}) \text{ for all } \xi \in \widetilde{S}, \boldsymbol{\psi} \in \widetilde{X}_0\,. \tag{2.81}$$

By the definition of $\widetilde{X}_0$, we have that $B(\boldsymbol{w}, \nabla\xi) = 0$ for all $\xi \in \widetilde{S}$. If we set $\boldsymbol{\psi} = 0$ in (2.81), then, we obtain the problem to find $p \in \widetilde{S}$ such that

$$B(\nabla p, \nabla\xi) \;=\; F(\nabla\xi) \quad \text{for all } \xi \in \widetilde{S}\,. \tag{2.82}$$

From Proposition 2.16 we conclude that there is a uniquely determined $p \in \widetilde{S}$ solving (2.82) with $\|p\|_{H^1(B_R(0))} \leq \|F\|$. We use this p in (2.81), set $\xi = 0$ and find that $\boldsymbol{w} \in \widetilde{X}_0$ must satisfy

$$B(\boldsymbol{w}, \boldsymbol{\psi}) \;=\; F(\boldsymbol{\psi}) - B(\nabla p, \boldsymbol{\psi}) \;=\; \widetilde{F}(\boldsymbol{\psi}) \quad \text{for all } \xi \in \widetilde{X}_0\,. \tag{2.83}$$

According to Proposition 2.20 there is a uniquely determined $\boldsymbol{w} \in \widetilde{X}_0$ solving (2.83). Additionally, it holds that $\|\boldsymbol{w}\|_{H(\mathbf{curl},B_R(0))} \leq C\|\widetilde{F}\|$. Thus, $\boldsymbol{E} = \boldsymbol{w} + \nabla p$ is uniquely defined and it holds that

$$\|\boldsymbol{E}\|_{H(\mathbf{curl},B_R(0))} \;\leq\; \|\boldsymbol{w}\|_{H(\mathbf{curl},B_R(0))} + \|p\|_{H^1(B_R(0))} \;\leq\; C\|\boldsymbol{E}^i\|_{H(\mathbf{curl},B_R(0))}\,.$$

□

Chapter 3

An asymptotic perturbation formula for electromagnetic scattering by thin tubular structures

In the previous chapter, we established existence and uniqueness of solutions to time-harmonic Maxwell's equations for a scattering object $D \subset \mathbb{R}^3$ with a Lipschitz boundary ∂D. Beginning from this chapter on, our considerations concern thin tubular scattering objects exclusively. For this special class of three-dimensional objects, we study the behavior of scattered electric fields as the volume of the tubular cross-section shrinks to zero. The result is an asymptotic perturbation formula that provides a representation of the scattered electric field away from the scatterer via a leading order term plus terms of higher order, as the volume of the scatterer tends to zero. The leading order term features the electric and magnetic polarization tensors. As these terms carry essential properties of the thin tubular scattering object, they require detailed considerations, which are discussed in Section 3.3. In the next two chapters, the leading order term will be of particular interest, as it allows an approximation of solutions to the scattering problem (2.34) and (2.35) without a numerical computation of a solution corresponding to the full Maxwell system.

We start this chapter with a precise description of a family of thin tubular scattering objects. Afterwards, we present the asymptotic representation formula for electric fields in free space scattered by these objects. We continue with preliminary results for the proof of this theorem and finally prove it by extending the results from [68]. Afterwards, we study the polarization tensors, examine the two-dimensional polarization tensor of the thin tube's cross-section and draw connections to plasmon resonances. Finally, we perform our first numerical examples with the leading order term of the asymptotic perturbation formula.

3.1 Scattering from thin tubular structures

In this section we introduce a detailed description of (families of) thin tubular scattering objects, that we consider throughout the next chapters. For this purpose, let $B_R(0) \subset \mathbb{R}^3$ be a ball of radius $R > 0$ centered at the origin that is supposed to include all scatterers under consideration. Let $\Gamma \subset B_R(0)$ be a simple, i.e. non-self-intersecting but possibly closed curve with C^3 parametrization by arc-length $\boldsymbol{p}_\Gamma : (-L, L) \to \mathbb{R}^3$ equipped with a right handed rotation minimizing frame (RMF) $(\boldsymbol{t}_\Gamma, \boldsymbol{r}_\Gamma, \mathbf{s}_\Gamma)$. For the description of a rotation minimizing frame, we refer to [22, 36, 46, 121, 123]. For a list of possible applications consider e.g. the references in [36, Ch. 3]. In the RMF $(\boldsymbol{t}_\Gamma, \boldsymbol{r}_\Gamma, \mathbf{s}_\Gamma)$, the vector $\boldsymbol{t}_\Gamma = \boldsymbol{p}_\Gamma'$ denotes the tangent vector. The reference vector $\boldsymbol{r}_\Gamma$ is characterized as the solution of the ordinary differential equation

$$\boldsymbol{r}_\Gamma'(s) \;=\; f(s)\boldsymbol{t}_\Gamma(s), \quad \boldsymbol{r}_\Gamma(s) \cdot \boldsymbol{t}_\Gamma(s) \;=\; 0 \qquad \text{for all } s \in (-L, L) \tag{3.1}$$

for a function $f : (-L, L) \to \mathbb{R}$, together with some initial condition for $\boldsymbol{r}_\Gamma$ at $s = -L$. Having $\boldsymbol{r}_\Gamma$, the vector $\mathbf{s}_\Gamma$ is given by $\mathbf{s}_\Gamma = \boldsymbol{t}_\Gamma \times \boldsymbol{r}_\Gamma$. Using the linear combination

$$\boldsymbol{t}_\Gamma' \;=\; \kappa_1 \boldsymbol{r}_\Gamma + \kappa_2 \mathbf{s}_\Gamma \tag{3.2}$$

with functions $\kappa_1, \kappa_2 : (-L, L) \to \mathbb{R}$ as an ansatz, we find that

$$\mathbf{s}_\Gamma' = \boldsymbol{t}_\Gamma' \times \boldsymbol{r}_\Gamma + \boldsymbol{t}_\Gamma \times \boldsymbol{r}_\Gamma' = -\kappa_2 \boldsymbol{t}_\Gamma \quad \text{and} \quad \boldsymbol{r}_\Gamma' = -\kappa_1 \boldsymbol{t}_\Gamma \,. \tag{3.3}$$

The latter equality is found by using that $\boldsymbol{r}_\Gamma = \mathbf{s}_\Gamma \times \boldsymbol{t}_\Gamma$ and deriving as in the first equality. These differential equations were initially characterized by Bishop in [22]. Although, in his study, he named a normal field to a curve Γ satisfying (3.1) a relatively parallel frame. Therefore, the RMF is sometimes called the Bishop frame. In [22, Thm. 1] it is proven that for curves Γ as considered in this work, there exists a uniquely determined RMF $(\boldsymbol{t}_\Gamma, \boldsymbol{r}_\Gamma, \mathbf{s}_\Gamma)$ for a given initial value for $\boldsymbol{r}_\Gamma$ at $s = -L$. Moreover, for different initial values for $\boldsymbol{r}_\Gamma$ at $s = -L$, the two reference vectors corresponding to the uniquely determined frames keep a constant angle along the curve Γ (see also [121, p. 2:5]). We introduce the rotation function $\theta \in C^2([-L, L])$ and the rotation matrix

$$R_\theta(s) = \begin{bmatrix} \cos(\theta(s)) & -\sin(\theta(s)) \\ \sin(\theta(s)) & \cos(\theta(s)) \end{bmatrix} \in \mathbb{R}^{2\times 2}, \quad s \in (-L, L) \,. \tag{3.4}$$

For sufficiently small $r > 0$, the tubular neighborhood theorem (see e.g. [118, Thm. 20, p. 467]) shows that the map

$$\boldsymbol{q}_\Gamma : (-L, L) \times B_r'(0) \to \mathbb{R}^3, \qquad \boldsymbol{q}_\Gamma(s, \eta, \xi) = \boldsymbol{p}_\Gamma(s) + [\boldsymbol{r}_\Gamma(s) \,|\, \mathbf{s}_\Gamma(s)] \; R_\theta(s) \begin{bmatrix} \eta \\ \xi \end{bmatrix}, \tag{3.5}$$

where $B_r'(0) \subset \mathbb{R}^2$ is the disk of radius r centered at the origin, defines a local coordinate system around $\boldsymbol{p}_\Gamma$. We define its range by

$$\Omega_r = \{\boldsymbol{q}_\Gamma(s, \eta, \xi) \mid s \in (-L, L),\ (\eta, \xi) \in B_r'(0)\} \,. \tag{3.6}$$

For $0 < \ell < L$ and $0 < \rho < r/2$ we consider a cross-section $D_\rho' \subset B_\rho'(0)$ given by $D_\rho' = \rho D'$, where D' is supposed to be a simply connected Lipschitz domain. Thus, the rotation matrix in (3.4) that appears in the definition of the local coordinates in (3.5) incorporates rotations of the cross-section D_ρ' along the wire. Accordingly, we define the corresponding thin tubular scattering object by

$$D_\rho = \left\{\boldsymbol{q}_\Gamma(s, \eta, \xi) \mid s \in (-\ell, \ell),\ (\eta, \xi) \in D_\rho'\right\} \tag{3.7}$$

and call

$$K = \{\boldsymbol{p}_\Gamma(s) \mid s \in (-\ell, \ell)\}$$

the center curve of D_ρ. In Figure 3.1 we visualize an example of a thin tubular scattering object having a cloud-shaped cross-section D_ρ' that twists along the center curve K. Note that, as explained before, the center curve K of the scattering object is a subset of Γ. In the particular situation, in which the dimensions of D_ρ' are within the order of a few nanometers (nm), we call D_ρ a nanowire.

The parameter ρ is called the radius of the cross-section D_ρ' of D_ρ or sometimes just the radius of D_ρ. For the family of thin tubular scatterers $(D_\rho)_{\rho>0}$ let the electric permittivity and magnetic permeability distributions be defined by

$$\varepsilon_\rho(\boldsymbol{x}) = \begin{cases} \varepsilon_1 \,, & \boldsymbol{x} \in D_\rho \,, \\ \varepsilon_0 \,, & \boldsymbol{x} \in \mathbb{R}^3 \setminus \overline{D_\rho} \end{cases} \quad \text{and} \quad \mu_\rho(\boldsymbol{x}) = \begin{cases} \mu_1 \,, & \boldsymbol{x} \in D_\rho \,, \\ \mu_0 \,, & \boldsymbol{x} \in \mathbb{R}^3 \setminus \overline{D_\rho}. \end{cases} \tag{3.8}$$

The coefficients in (3.8) are supposed to satisfy the same properties as those from Chapter 2, i.e. $\mu_1 > 0$ and either $\varepsilon_1 > 0$ or $\varepsilon_1 \in \mathbb{C}$ with $\operatorname{Re}(\varepsilon_1) < 0$ and $\operatorname{Im}(\varepsilon_1) > 0$. We emphasize the

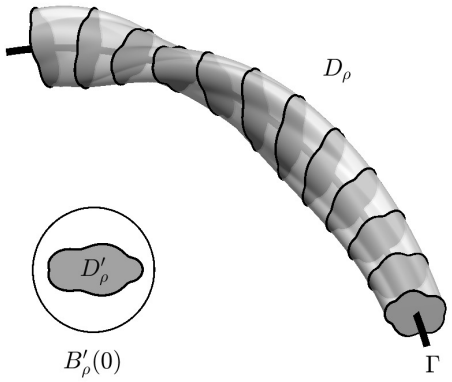

Figure 3.1: An example of a thin tubular scattering object with cross-section $D'_\rho \subset B'_\rho(0)$.

dependence of electric and magnetic fields on the cross-section D'_ρ by indexing them with $\rho > 0$. Accordingly, the electric field $\boldsymbol{E}_\rho = \boldsymbol{E}^i + \boldsymbol{E}^s_\rho$ must satisfy

$$\mathbf{curl}\left(\frac{1}{\mu_\rho}\,\mathbf{curl}\,\boldsymbol{E}_\rho\right) - \omega^2\varepsilon_\rho \boldsymbol{E}_\rho \;=\; 0 \quad \text{in } \mathbb{R}^3\,, \tag{3.9}$$

together with the Silver–Müller radiation condition

$$\lim_{|\boldsymbol{x}|\to\infty} |\boldsymbol{x}|\left(\mathbf{curl}\,\boldsymbol{E}^s_\rho(\boldsymbol{x}) \times \widehat{\boldsymbol{x}} - \mathrm{i}k\boldsymbol{E}^s_\rho(\boldsymbol{x})\right) \;=\; 0 \tag{3.10}$$

uniformly with respect to all directions $\widehat{\boldsymbol{x}} = \boldsymbol{x}/|\boldsymbol{x}| \in S^2$.

Remark 3.1. The results about the asymptotic perturbation formula and the polarization tensor that we describe in the next sections may be formulated for more general cross-sections D'_ρ than Lipschitz domains. In fact, one can assume that the cross-sections D'_ρ are just measurable and that $|D'_\rho|$ tends to zero as $\rho \to 0$. We do not consider this general setting and refer to the original work [28] instead.

3.2 The asymptotic perturbation formula

We establish and motivate the main result of this chapter, namely the asymptotic representation formula for electromagnetic fields scattered by thin tubular scattering objects. This formula reflects the behavior of the scattered electric field $\boldsymbol{E}^s_\rho$ away from the scattering object and the corresponding far field $\boldsymbol{E}^\infty_\rho$ as the radius of the cross-section D'_ρ of the scattering object D_ρ tends to zero. Asymptotic expansions of this type are available in the literature for time-harmonic electromagnetic fields. However, the existing results for Maxwell's equations are formulated either on bounded domains (see e.g. [2, 12, 68]) or for scattering problems on unbounded domains but with different geometrical assumptions on the scattering objects than considered in this work (see [13, 66]). In [12] the authors study an ensemble of diametrically small scatterers of the form $\boldsymbol{z}^{(j)} + \rho B_j$, for $j = 1, \dots, n$, where B_j is a C^∞ domain containing the origin. For a background medium with constant electric permittivity $\widetilde{\varepsilon}_0 \in \mathbb{C}$ with $\mathrm{Re}(\widetilde{\varepsilon}_0) > 0$ and $\mathrm{Im}(\widetilde{\varepsilon}_0) \geq 0$ and constant magnetic permeability $\widetilde{\mu}_0 > 0$ they derive an asymptotic perturbation formula for the magnetic field $\boldsymbol{H}$ inside a domain Ω with a smooth boundary $\partial\Omega$ under the assumption that the inclusions possess a constant electric permittivity and magnetic permeability. In [68] a general perturbation formula for measurable, low-volume defects in a homogeneous bounded

domain Ω with smooth boundary $\partial\Omega$ is derived. In fact, the perturbation formula from [12] can be derived from the one in [68]. In [2] the authors derive an asymptotic expansion for the electric and magnetic field for variable anisotropic permittivities and permeabilities inside and outside of the inclusions. In the work [13] a scattering problem for an ensemble of diametrically small inclusion is studied. Moreover, a representation formula for the scattered electric field subject to such a scattering object is derived. In [66] a similar setting is studied for layered media and an ensemble of perfectly conducting diametrically small scatterers. In the following we combine the general[1] perturbation formula for electromagnetic fields on bounded domains from [2, 68] (see also [29]) with an integral equation technique developed in [8, 13] to arrive at an asymptotic representation formula that applies to our setting.
In order to establish the asymptotic perturbation formula, we consider a sequence of radii $(\rho_n)_{n\in\mathbb{N}} \subset (0, r/2)$ converging to zero as $n \to \infty$. The corresponding sequence of cross-sections of Lipschitz domains is denoted by $D'_{\rho_n} = \rho_n D' \subset B'_{\rho_n}(0)$, $n \in \mathbb{N}$. We find the following property for the sequence of measures $(|D'_{\rho_n}|^{-1}\chi_{D'_{\rho_n}})_{n\in\mathbb{N}}$.

Lemma 3.2. *The sequence of measures $(|D'_{\rho_n}|^{-1}\chi_{D'_{\rho_n}})_{n\in\mathbb{N}}$ has the property that*

$$|D'_{\rho_n}|^{-1}\chi_{D'_{\rho_n}} \quad \text{converges in the sense of measures to } \mu' \text{ as } n \to \infty, \tag{3.11}$$

where μ' is the two-dimensional Dirac measure with support in 0.

Proof. By assumption, $D'_{\rho_n} \subset B'_r(0)$ for all $\rho_n < \rho'$ and a $\rho' > 0$. Thus, for all $\phi \in C(\overline{B'_r(0)})$ it holds that

$$|D'_{\rho_n}||D'_{\rho_n}|^{-1} \inf_{\boldsymbol{x}'\in\overline{D'_{\rho_n}}} \phi(\boldsymbol{x}') \le \int_{B'_r(0)} \chi_{D'_{\rho_n}} |D'_{\rho_n}|^{-1}\phi \, \mathrm{d}\boldsymbol{x}' \le |D'_{\rho_n}||D'_{\rho_n}|^{-1} \sup_{\boldsymbol{x}'\in\overline{D'_{\rho_n}}} \phi(\boldsymbol{x}') \,. \tag{3.12}$$

Since ϕ is a continuous function, the lower and the upper bound in (3.12) converge to $\phi(0)$ and so the middle term needs to converge to $\phi(0)$ as well. □

We need the Jacobian determinant of the local coordinates (3.5) in order to represent the gradient in these coordinates and to perform integral transformations. Recall that the two-dimensional parameter dependent rotation matrix $R_\theta \in C^2((-L, L), \mathbb{R}^{2\times 2})$ is defined as in (3.4).

Lemma 3.3. *The Jacobian determinant of the local coordinates $\boldsymbol{q}_\Gamma$ from (3.5) is given by*

$$J_\Gamma(s,\eta,\zeta) = \det D\boldsymbol{q}_\Gamma(s,\eta,\zeta) = 1 - \begin{bmatrix}\kappa_1(s)\\ \kappa_2(s)\end{bmatrix} \cdot R_\theta(s) \begin{bmatrix}\eta\\ \zeta\end{bmatrix} \tag{3.13}$$

for $s \in (-L, L)$ and $(\eta, \zeta) \in B'_r(0)$. The functions κ_1, κ_2 are introduced in (3.2).

Proof. By using the relations in (3.2) and (3.3) we find that the partial derivatives of $\boldsymbol{q}_\Gamma$ can be computed to

$$\begin{aligned}
\frac{\partial \boldsymbol{q}_\Gamma}{\partial s}(s,\eta,\zeta) &= \boldsymbol{t}_\Gamma(s)\left(1 - \begin{bmatrix}\kappa_1(s)\\ \kappa_2(s)\end{bmatrix} \cdot R_\theta(s) \begin{bmatrix}\eta\\ \zeta\end{bmatrix}\right) + \left[\boldsymbol{r}_\Gamma(s) \mid \mathbf{s}_\Gamma(s)\right] \frac{\partial R_\theta}{\partial s}(s) \begin{bmatrix}\eta\\ \zeta\end{bmatrix},\\
\frac{\partial \boldsymbol{q}_\Gamma}{\partial \eta}(s,\eta,\zeta) &= \left[\boldsymbol{r}_\Gamma(s) \mid \mathbf{s}_\Gamma(s)\right] R_\theta(s) \begin{bmatrix}1\\ 0\end{bmatrix},\\
\frac{\partial \boldsymbol{q}_\Gamma}{\partial \zeta}(s,\eta,\zeta) &= \left[\boldsymbol{r}_\Gamma(s) \mid \mathbf{s}_\Gamma(s)\right] R_\theta(s) \begin{bmatrix}0\\ 1\end{bmatrix}.
\end{aligned}$$

[1] Here, the word general refers to an arbitrary choice of scattering objects D_ρ with $|D_\rho| \to 0$.

The Jacobian of $\boldsymbol{q}_\Gamma$ is consequently given by $D\boldsymbol{q}_\Gamma$ with

$$D\boldsymbol{q}_\Gamma(s,\eta,\zeta) \;=\; [\boldsymbol{t}_\Gamma(s) \mid \boldsymbol{r}_\Gamma(s) \mid \mathbf{s}_\Gamma(s)] \left[\begin{array}{c|cc} 1 - \begin{bmatrix}\kappa_1(s)\\ \kappa_2(s)\end{bmatrix} \cdot R_\theta(s) \begin{bmatrix}\eta\\ \zeta\end{bmatrix} & 0 & 0 \\ \hline \frac{\partial R_\theta}{\partial s}(s) \begin{bmatrix}\eta\\ \zeta\end{bmatrix} & \multicolumn{2}{c}{R_\theta(s)} \end{array}\right]$$

and the Jacobian determinant is found to be

$$J_\Gamma(s,\eta,\zeta) \;=\; \det D\boldsymbol{q}_\Gamma(s,\eta,\zeta) \;=\; 1 - \begin{bmatrix}\kappa_1(s)\\ \kappa_2(s)\end{bmatrix} \cdot R_\theta(s) \begin{bmatrix}\eta\\ \zeta\end{bmatrix},$$

what ends the proof. □

Since the curvature κ is given by $\kappa = |\boldsymbol{p}_\Gamma''(s)|$ we find from (3.2) that $\kappa = \sqrt{\kappa_1^2 + \kappa_2^2}$. Furthermore, since Γ is a C^3 curve, we have that $\kappa_{\max} = \|\kappa\|_{C(-L,L)} < \infty$ and it has e.g. been shown in [95, Thm. 1] that the radius $r > 0$ from (3.5) must necessarily satisfy $r\kappa_{\max} < 1$ in order for the tubular neighborhood theorem to hold. Accordingly, the Jacobian determinant from (3.13) satisfies $|J_\Gamma| = J_\Gamma > 0$ in $(-L,L) \times B_r'(0)$. We introduce the notation

$$\nabla'_{\eta,\zeta} u \;=\; \left[\frac{\partial u}{\partial \eta} \;\middle|\; \frac{\partial u}{\partial \zeta}\right]^\top \quad \text{and} \quad \operatorname{div}'_{\eta,\zeta} \boldsymbol{v} \;=\; \frac{\partial \boldsymbol{v}_\eta}{\partial \eta} + \frac{\partial \boldsymbol{v}_\zeta}{\partial \zeta} \tag{3.14}$$

for the two-dimensional gradient and the two-dimensional divergence with respect to (η,ζ) and obtain the following representation of the three-dimensional gradient in local coordinates.

Lemma 3.4. *The gradient in the local coordinates $\boldsymbol{q}_\Gamma$ from (3.5) is given by*

$$\begin{aligned} \nabla u\left(\boldsymbol{q}_\Gamma(s,\eta,\zeta)\right) \;=\; & [\boldsymbol{r}_\Gamma(s) \mid \mathbf{s}_\Gamma(s)]\, R_\theta(s) \left(\nabla'_{\eta,\zeta} u \circ \boldsymbol{q}_\Gamma\right)(s,\eta,\zeta) \\ & + \left(J_\Gamma^{-1}(s,\eta,\zeta) \left(\frac{\partial u \circ \boldsymbol{q}_\Gamma}{\partial s}(s,\eta,\zeta) + \frac{\partial \theta}{\partial s}(s) \left(\nabla'_{\eta,\zeta} u \circ \boldsymbol{q}_\Gamma\right)(s,\eta,\zeta) \cdot \begin{bmatrix}\zeta\\ -\eta\end{bmatrix} \right) \right) \boldsymbol{t}_\Gamma(s), \end{aligned} \tag{3.15}$$

where $\nabla'_{\eta,\zeta} u$ denotes the two-dimensional gradient with respect to $(\eta,\zeta) \in B_r'(0)$ from (3.14).

Proof. We compute the partial derivatives of $\boldsymbol{q}_\Gamma$ as in the proof of Lemma 3.3 and find that an application of the chain rule gives that

$$\frac{\partial u \circ \boldsymbol{q}_\Gamma}{\partial s}(s,\eta,\zeta) \;=\; \nabla u(s,\eta,\zeta) \cdot \left(\boldsymbol{t}_\Gamma(s) J_\Gamma(s,\eta,\zeta) + [\boldsymbol{r}_\Gamma(s) \mid \mathbf{s}_\Gamma(s)] \frac{\partial R_\theta}{\partial s}(s) \begin{bmatrix}\eta\\ \zeta\end{bmatrix} \right), \tag{3.16a}$$

$$\frac{\partial u \circ \boldsymbol{q}_\Gamma}{\partial \eta}(s,\eta,\zeta) \;=\; \nabla u(s,\eta,\zeta) \cdot \left([\boldsymbol{r}_\Gamma(s) \mid \mathbf{s}_\Gamma(s)]\, R_\theta(s) \begin{bmatrix}1\\ 0\end{bmatrix} \right), \tag{3.16b}$$

$$\frac{\partial u \circ \boldsymbol{q}_\Gamma}{\partial \zeta}(s,\eta,\zeta) \;=\; \nabla u(s,\eta,\zeta) \cdot \left([\boldsymbol{r}_\Gamma(s) \mid \mathbf{s}_\Gamma(s)]\, R_\theta(s) \begin{bmatrix}0\\ 1\end{bmatrix} \right). \tag{3.16c}$$

Note that in (3.16a) we already used the representation of the Jacobian from (3.13). From (3.16b) and (3.16c) we find that the two-dimensional gradient with respect to (η,ζ) from (3.14) can be written as

$$\left(\nabla'_{\eta,\zeta} u \circ \boldsymbol{q}_\Gamma\right)^\top (s,\eta,\zeta) \;=\; \nabla u(s,\eta,\zeta) \cdot [\boldsymbol{r}_\Gamma(s) \mid \mathbf{s}_\Gamma(s)]\, R_\theta(s).$$

This implies that

$$\nabla u(s,\eta,\zeta) \cdot [\boldsymbol{r}_\Gamma(s) \mid \mathbf{s}_\Gamma(s)] \;=\; \left(\nabla'_{\eta,\zeta} u \circ \boldsymbol{q}_\Gamma\right)(s,\eta,\zeta) \cdot R_\theta^{-1}(s). \tag{3.17}$$

We rearrange the expression in (3.16a), use (3.17) and that

$$\frac{\partial R_\theta}{\partial s}(s) \;=\; \frac{\partial \theta}{\partial s}(s) R_\theta(s) \begin{bmatrix} 0 & -1 \\ 1 & 0 \end{bmatrix}$$

to see that

$$\nabla u(s,\eta,\zeta)\cdot \boldsymbol{t}_\Gamma(s) \;=\; J_\Gamma^{-1}(s,\eta,\zeta)\left(\frac{\partial u\circ \boldsymbol{q}_\Gamma}{\partial s}(s,\eta,\zeta) - \frac{\partial \theta}{\partial s}\left(\nabla'_{\eta,\zeta} u\circ \boldsymbol{q}_\Gamma\right)(s,\eta,\zeta)\cdot \begin{bmatrix} -\zeta \\ \eta \end{bmatrix}\right). \tag{3.18}$$

Finally, using the orthogonal decomposition

$$\nabla u(s,\eta,\zeta) \;=\; (\boldsymbol{t}_\Gamma(s)\cdot\nabla u(s,\eta,\zeta))\,\boldsymbol{t}_\Gamma(s) + (\boldsymbol{r}_\Gamma(s)\cdot\nabla u(s,\eta,\zeta))\,\boldsymbol{r}_\Gamma(s) + (\mathbf{s}_\Gamma(s)\cdot\nabla u(s,\eta,\zeta))\,\mathbf{s}_\Gamma(s)\,,$$

the fact that the last two summands can be written as

$$(\boldsymbol{r}_\Gamma\cdot\nabla u)\,\boldsymbol{r}_\Gamma + (\mathbf{s}_\Gamma\cdot\nabla u)\,\mathbf{s}_\Gamma \;=\; [\boldsymbol{r}_\Gamma \mid \mathbf{s}_\Gamma](\nabla u\cdot[\boldsymbol{r}_\Gamma \mid \mathbf{s}_\Gamma])^\top$$

as well as (3.17) and (3.18) gives that

$$\begin{aligned}\nabla u\left(\boldsymbol{q}_\Gamma(s,\eta,\zeta)\right) \;=\; & \left[\boldsymbol{r}_\Gamma(s) \mid \mathbf{s}_\Gamma(s)\right] R_\theta(s)\left(\nabla'_{\eta,\zeta} u\circ \boldsymbol{q}_\Gamma\right)(s,\eta,\zeta) \\ & + \left(J_\Gamma^{-1}(s,\eta,\zeta)\left(\frac{\partial u\circ \boldsymbol{q}_\Gamma}{\partial s}(s,\eta,\zeta) + \frac{\partial \theta}{\partial s}(s)\left(\nabla'_{\eta,\zeta} u\circ \boldsymbol{q}_\Gamma\right)(s,\eta,\zeta)\cdot\begin{bmatrix}\zeta\\ -\eta\end{bmatrix}\right)\right)\boldsymbol{t}_\Gamma(s)\,.\end{aligned}$$

□

Similar to Lemma 3.2, we can now derive a convergence property for the sequence of measures $(|D_{\rho_n}|^{-1}\chi_{D_{\rho_n}})_n$.

Lemma 3.5. *The sequence of measures $(|D_{\rho_n}|^{-1}\chi_{D_{\rho_n}})_{n\in\mathbb{N}}$ has the property that*

$$|D_{\rho_n}|^{-1}\chi_{D_{\rho_n}} \quad \textit{converges in the sense of measures to } \mu \textit{ as } n\to\infty, \tag{3.19}$$

where the Borel measure μ is defined by

$$\int_{B_R(0)} \psi \,\mathrm{d}\mu \;=\; \frac{1}{2\ell}\int_K \psi \,\mathrm{d}s. \tag{3.20}$$

Proof. We apply the particular formula for the Jacobian determinant in (3.13) and find that

$$|D_{\rho_n}| \;=\; \int_{-\ell}^{\ell}\int_{D'_{\rho_n}} J_\Gamma(s,\eta,\zeta)\,\mathrm{d}(\eta,\zeta)\,\mathrm{d}s \;=\; 2\ell|D'_{\rho_n}|\,(1+\mathcal{O}(\kappa_{\max}\rho_n))$$

as $n\to\infty$. Accordingly, for $\psi\in C(\overline{B_R(0)})$ it holds that

$$\begin{aligned}\int_{B_R(0)} \psi|D_{\rho_n}|^{-1}\chi_{D_{\rho_n}}\,\mathrm{d}\boldsymbol{x} \;&=\; \frac{|D'_{\rho_n}|}{|D_{\rho_n}|}\int_{-\ell}^{\ell}\frac{1}{|D'_{\rho_n}|}\int_{B'_r(0)}\chi_{D'_{\rho_n}}(\eta,\zeta)\psi(\boldsymbol{q}_\Gamma(s,\eta,\zeta))J_\Gamma(s,\eta,\zeta)\,\mathrm{d}(\eta,\zeta)\,\mathrm{d}s \\ &\to\; \frac{1}{2\ell}\int_{-\ell}^{\ell}\int_{B'_r(0)}\psi(\boldsymbol{q}_\Gamma(s,\eta,\zeta))\,\mathrm{d}\mu'(\eta,\zeta)\,\mathrm{d}s \;=\; \frac{1}{2\ell}\int_{-\ell}^{\ell}\psi(\boldsymbol{p}_\Gamma(s))\,\mathrm{d}s\end{aligned}$$

as $n\to\infty$. In the limit process we used the convergence property from (3.11). □

Using the fundamental solution of Maxwell's equation from (2.27) we state the main result of this chapter in the following theorem.

Theorem 3.6. *Let $K \subset\subset B_R(0)$ be a simple C^3 center curve and let $r > 0$ such that the local parametrization in (3.5) is well-defined. Let $(\rho_n)_{n\in\mathbb{N}} \subset (0, r/2)$ be a sequence of radii converging to zero and let $(D'_{\rho_n})_{n\in\mathbb{N}}$ be a sequence of Lipschitz cross-sections with $D'_{\rho_n} = \rho_n D' \subset B'_{\rho_n}(0)$ for all $n \in \mathbb{N}$. Suppose that $(D_{\rho_n})_{n\in\mathbb{N}} \subset B_R(0)$ is the corresponding sequence of thin tubular scattering objects as in (3.7), where the cross-section twists along the center curve subject to the parameter dependent rotation matrix $R_\theta \in C^2([-L, L], \mathbb{R}^{2\times 2})$ as in (3.4). Denoting by $(\varepsilon_{\rho_n})_{n\in\mathbb{N}}$ and $(\mu_{\rho_n})_{n\in\mathbb{N}}$ permittivity and permeability distributions as in (3.8), let $\boldsymbol{E}^s_{\rho_n}$ be the associated scattered electric field solving (3.9) for some incident electric field $\boldsymbol{E}^i$. Then, there exist matrix-valued functions $\mathbb{M}^\varepsilon \in L^2(K, \mathbb{C}^{3\times 3})$ and $\mathbb{M}^\mu \in L^2(K, \mathbb{R}^{3\times 3})$ called the electric and magnetic polarization tensor, respectively, such that*

$$\boldsymbol{E}^s_{\rho_n}(\boldsymbol{x}) = \frac{|D_{\rho_n}|}{2\ell}\Bigg(\int_K (\mu_r - 1)\, \mathbf{curl}_{\mathrm{x}}\, \mathbb{G}(\boldsymbol{x}, \boldsymbol{y}) \mathbb{M}^\mu(\boldsymbol{y})\, \mathbf{curl}\, \boldsymbol{E}^i(\boldsymbol{y})\, \mathrm{d}s(\boldsymbol{y}) + k^2 \int_K (\varepsilon_r - 1)\, \mathbb{G}(\boldsymbol{x}, \boldsymbol{y}) \mathbb{M}^\varepsilon(\boldsymbol{y}) \boldsymbol{E}^i(\boldsymbol{y})\, \mathrm{d}s(\boldsymbol{y}) \Bigg) + o\left(|D_{\rho_n}|\right) \tag{3.21}$$

for $\boldsymbol{x} \in \mathbb{R}^3 \setminus \overline{B_R(0)}$. Furthermore, the electric far field pattern satisfies

$$\boldsymbol{E}^\infty_{\rho_n}(\widehat{\boldsymbol{x}}) = \frac{|D_{\rho_n}|}{2\ell}\Bigg(\int_K (\mu_r - 1)\, \mathrm{i}k e^{-\mathrm{i}k\widehat{\boldsymbol{x}}\cdot\boldsymbol{y}} (\widehat{\boldsymbol{x}} \times \mathbb{I}_3)\, \mathbb{M}^\mu(\boldsymbol{y})\, \mathbf{curl}\, \boldsymbol{E}^i(\boldsymbol{y})\, \mathrm{d}s(\boldsymbol{y}) + k^2 \int_K (\varepsilon_r - 1)\, e^{-\mathrm{i}k\widehat{\boldsymbol{x}}\cdot\boldsymbol{y}} (\widehat{\boldsymbol{x}} \times (\mathbb{I}_3 \times \widehat{\boldsymbol{x}}))\, \mathbb{M}^\varepsilon(\boldsymbol{y}) \boldsymbol{E}^i(\boldsymbol{y})\, \mathrm{d}s(\boldsymbol{y}) \Bigg) + o\left(|D_{\rho_n}|\right) \tag{3.22}$$

for $\widehat{\boldsymbol{x}} \in S^2$. The sequence $(D_{\rho_n})_{n\in\mathbb{N}}$ and the polarization tensors $\mathbb{M}^\varepsilon$ and $\mathbb{M}^\mu$ are independent of the incident field $\boldsymbol{E}^i$. The terms $o\left(|D_{\rho_n}|\right)$ in (3.21) and (3.22) are such that for any $\widetilde{R} > R$,

$$\left\| o\left(|D_{\rho_n}|\right) \right\|_{L^\infty(\mathbb{R}^3 \setminus \overline{B_{\widetilde{R}}(0)})} / |D_{\rho_n}| \quad \text{and} \quad \left\| o\left(|D_{\rho_n}|\right) \right\|_{L^\infty(S^2)} / |D_{\rho_n}|$$

converge to zero uniformly for all $\boldsymbol{E}^i$ satisfying $\|\boldsymbol{E}^i\|_{H(\mathbf{curl}, B_R(0))} \leq C$ for some fixed $C > 0$.

Remark 3.7. For real-valued $\varepsilon_1 > 0$, the electric polarization tensor $\mathbb{M}^\varepsilon$ is real-valued as well.

The polarization tensors $\mathbb{M}^\varepsilon$ and $\mathbb{M}^\mu$ that appear in (3.21) and (3.22) carry essential information of the sequence of scattering object $(D_{\rho_n})_{n\in\mathbb{N}}$. Therefore, $\mathbb{M}^\varepsilon$ and $\mathbb{M}^\mu$ are studied in detail in the next section. Before we prove Theorem 3.6 we collect several results that we need for the proof. As stated before, our aim is to extend the general asymptotic representation formula for electromagnetic fields from [68] to free space. For this purpose, we recall the setting from [68] and repeat the results that we use. For $\boldsymbol{g} \in H^{-1/2}_{\mathrm{div}}(\partial B_R(0))$, we consider the boundary value problems

$$\mathbf{curl}\left(\frac{1}{\varepsilon_0}\, \mathbf{curl}\, \boldsymbol{h}_0\right) - \omega^2 \mu_0 \boldsymbol{h}_0 = 0 \ \text{ in } B_R(0), \qquad \frac{1}{\varepsilon_0}\, \mathbf{curl}\, \boldsymbol{h}_0 \times \boldsymbol{\nu} = \boldsymbol{g} \ \text{ on } \partial B_R(0), \tag{3.23}$$

$$\mathbf{curl}\left(\frac{1}{\varepsilon_{\rho_n}}\, \mathbf{curl}\, \boldsymbol{h}_{\rho_n}\right) - \omega^2 \mu_{\rho_n} \boldsymbol{h}_{\rho_n} = 0 \ \text{ in } B_R(0), \quad \frac{1}{\varepsilon_{\rho_n}}\, \mathbf{curl}\, \boldsymbol{h}_{\rho_n} \times \boldsymbol{\nu} = \boldsymbol{g} \ \text{ on } \partial B_R(0). \tag{3.24}$$

Throughout the rest of this section, we assume that k^2 is not an eigenvalue of the interior Maxwell problem (3.23). This is not a strict assumption as the set of eigenvalues of (3.23) is a discrete set in $\mathbb{R}_+$ (see [2, Prop. 3.17]). Consequently, for $\boldsymbol{g} \in H^{-1/2}_{\mathrm{div}}(\partial B_R(0))$, the problem (3.23) has a unique solution $\boldsymbol{h}_0 \in H(\mathbf{curl}, B_R(0))$. Assuming that $0 < \rho_n < \rho_0$ for a sufficiently small ρ_0, the problem (3.24) has a unique solution $\boldsymbol{h}_{\rho_n} \in H(\mathbf{curl}, B_R(0))$ as well. This can be shown by extending the results from [12] to Lipschitz domains (see also [68, Prop. 2.1]) as well as to the coefficients ε_r considered in this work by applying multiplications with $\mathrm{e}^{\mathrm{i}\zeta}$ similarly, as we did in Chapter 2. For these coefficients the asymptotic perturbation formula from [68, Thm. 2.2], that we cite next, can be derived in the same way.

Theorem 3.8. *Suppose that $(D_{\rho_n})_{n\in\mathbb{N}}$ is a sequence of thin tubular scattering objects as in (3.7) with Lipschitz cross-sections $D'_{\rho_n} = \rho_n D' \subset B'_{\rho_n}(0)$ and assume that $0 < \rho_n < \rho_0$, where $\rho_0 > 0$ is so small that (3.24) has a unique solution. Given $\boldsymbol{g} \in H^{-1/2}_{\mathrm{div}}(\partial B_R(0))$, let $\boldsymbol{h}_0$ and $\boldsymbol{h}_{\rho_n}$, $n \in \mathbb{N}$, denote the corresponding solutions of (3.23) and (3.24), respectively. Then, there exist matrix-valued functions $\mathbb{M}^\varepsilon \in L^2(K, \mathbb{C}^{3\times 3})$ and $\mathbb{M}^\mu \in L^2(K, \mathbb{R}^{3\times 3})$ such that*

$$\begin{aligned}
&\boldsymbol{\nu}(\boldsymbol{y}) \times (\boldsymbol{h}_{\rho_n}(\boldsymbol{y}) - \boldsymbol{h}_0(\boldsymbol{y})) - 2\int_{\partial B_R(0)} (\boldsymbol{\nu}(\boldsymbol{y}) \times \mathbf{curl}_{\mathrm{x}}\, \mathbb{G}(\boldsymbol{x},\boldsymbol{y}))\, (\boldsymbol{\nu}(\boldsymbol{x}) \times (\boldsymbol{h}_{\rho_n}(\boldsymbol{x}) - \boldsymbol{h}_0(\boldsymbol{x})))\, \mathrm{d}s(\boldsymbol{x}) \\
&\quad = 2\frac{|D_{\rho_n}|}{2\ell}\Big(-\int_K (\varepsilon_r - 1)\, (\boldsymbol{\nu}(\boldsymbol{y}) \times \mathbf{curl}_{\mathrm{x}}\, \mathbb{G}(\boldsymbol{x},\boldsymbol{y}))\, \mathbb{M}^\varepsilon(\boldsymbol{x})\, \mathbf{curl}\, \boldsymbol{h}_0(\boldsymbol{x})\, \mathrm{d}s(\boldsymbol{x}) \\
&\qquad - k^2 \int_K (1 - \mu_r)\, (\boldsymbol{\nu}(\boldsymbol{y}) \times \mathbb{G}(\boldsymbol{x},\boldsymbol{y}))\, \mathbb{M}^\mu(\boldsymbol{x}) \boldsymbol{h}_0(\boldsymbol{x})\, \mathrm{d}s(\boldsymbol{x})\Big) + o(|D_{\rho_n}|) \qquad (3.25)
\end{aligned}$$

for all $\boldsymbol{y} \in \partial B_R(0)$. The sequence $(D_{\rho_n})_{n\in\mathbb{N}}$ and the functions $\mathbb{M}^\varepsilon$ and $\mathbb{M}^\mu$ are independent of $\boldsymbol{g}$. The last term on the right hand side of (3.25) satisfies

$$\lim_{n\to\infty} \|o(|D_{\rho_n}|)\|_{L^\infty(\partial B_R(0))} / |D_{\rho_n}| = 0$$

for any $\boldsymbol{g} \in H^{-1/2}_{\mathrm{div}}(\partial B_R(0))$, uniformly on bounded subsets of $H^{-1/2}_{\mathrm{div}}(\partial B_R(0))$.

For later reference, we note that the proof of [68, Lem. 3.2] implies that there is a constant $C > 0$ such that, for any $\boldsymbol{g} \in H^{-1/2}_{\mathrm{div}}(\partial B_R(0))$ it holds that

$$\|\boldsymbol{h}_{\rho_n} - \boldsymbol{h}_0\|_{H(\mathbf{curl}, B_R(0))} \leq C|D_{\rho_n}|^{1/2}\, \|\boldsymbol{g}\|_{H^{-1/2}_{\mathrm{div}}(\partial B_R(0))}\,. \qquad (3.26)$$

We define the functions

$$\boldsymbol{e}_0 = \mathrm{i}/(\omega\varepsilon_0)\, \mathbf{curl}\, \boldsymbol{h}_0 \quad \text{and} \quad \boldsymbol{e}_{\rho_n} = \mathrm{i}/(\omega\varepsilon_{\rho_n})\, \mathbf{curl}\, \boldsymbol{h}_{\rho_n}\,,$$

and by using (3.23) and (3.24) we find that

$$\mathbf{curl}\, \boldsymbol{e}_0 = \mathrm{i}\omega\mu_0 \boldsymbol{h}_0 \quad \text{and} \quad \mathbf{curl}\, \boldsymbol{e}_{\rho_n} = \mathrm{i}\omega\mu_{\rho_n} \boldsymbol{h}_{\rho_n}\,.$$

Furthermore, $\boldsymbol{e}_0$ and $\boldsymbol{e}_{\rho_n}$ satisfy

$$\mathbf{curl}\left(\frac{1}{\mu_0}\, \mathbf{curl}\, \boldsymbol{e}_0\right) - \omega^2\varepsilon_0 \boldsymbol{e}_0 = 0 \quad \text{in } B_R(0)\,, \qquad \boldsymbol{\nu} \times \boldsymbol{e}_0 = \widetilde{\boldsymbol{g}} \quad \text{on } \partial B_R(0)\,, \qquad (3.27)$$

$$\mathbf{curl}\left(\frac{1}{\mu_{\rho_n}}\, \mathbf{curl}\, \boldsymbol{e}_{\rho_n}\right) - \omega^2\varepsilon_{\rho_n} \boldsymbol{e}_{\rho_n} = 0 \quad \text{in } B_R(0)\,, \qquad \boldsymbol{\nu} \times \boldsymbol{e}_{\rho_n} = \widetilde{\boldsymbol{g}} \quad \text{on } \partial B_R(0)\,, \qquad (3.28)$$

with $\widetilde{\boldsymbol{g}} = -\mathrm{i}/\omega \boldsymbol{g}$. As we see from (3.27), for $\boldsymbol{g} = \mathrm{i}\omega\boldsymbol{\nu} \times \boldsymbol{E}^i$ it holds that $\boldsymbol{e}_0 = \boldsymbol{E}^i$ in $B_R(0)$, where $\boldsymbol{E}^i$ denotes the incident field of the full scattering problem (3.9). In the next proposition we cite [88, Thm. 5.52] for part (a) and (b), which summarizes the mapping properties of the Maxwell single layer and Maxwell double layer potentials as well as their corresponding jump relations. Moreover, we show in part (c) a result about the representation of solutions to exterior scattering problems with boundary values in $H^{-1/2}_{\mathrm{div}}(\partial B_R(0))$ provided that k^2 is not an interior eigenvalue. This part is similar to [88, Thm. 3.36].

Proposition 3.9. *Let $Q \subset \mathbb{R}^3$ be a bounded domain such that $\partial B_R(0) \subset Q$.*

(a) The operators

$$(\widetilde{M}\boldsymbol{a})(\boldsymbol{x}) = \mathbf{curl}_{\mathrm{x}} \int_{\partial B_R(0)} \Phi(\boldsymbol{x},\boldsymbol{y}) \boldsymbol{a}(\boldsymbol{y})\, \mathrm{d}s(\boldsymbol{y})\,, \quad \boldsymbol{x} \in Q\,,$$

$$(\widetilde{N}\boldsymbol{a})(\boldsymbol{x}) = \mathbf{curl}^2_{\mathrm{x}} \int_{\partial B_R(0)} \Phi(\boldsymbol{x},\boldsymbol{y}) \boldsymbol{a}(\boldsymbol{y})\, \mathrm{d}s(\boldsymbol{y})\,, \quad \boldsymbol{x} \in Q\,,$$

are well-defined and bounded from $H^{-1/2}_{\mathrm{div}}(\partial B_R(0))$ into $H(\mathbf{curl}, Q)$.

(b) The traces

$$M = \frac{1}{2}\left(\boldsymbol{\nu} \times \widetilde{M}|^{+}_{\partial B_R(0)} + \boldsymbol{\nu} \times \widetilde{M}|^{-}_{\partial B_R(0)}\right), \qquad N = \boldsymbol{\nu} \times \widetilde{N}|_{\partial B_R(0)} \tag{3.29}$$

are bounded from $H^{-1/2}_{\mathrm{div}}(\partial B_R(0))$ *into itself. With* $\boldsymbol{u} = \widetilde{M}\boldsymbol{a}$ *and* $\boldsymbol{a} \in H^{-1/2}_{\mathrm{div}}(\partial B_R(0))$*, the jump relations read*

$$\boldsymbol{\nu} \times \boldsymbol{u}|^{\pm}_{\partial B_R(0)} = \pm\frac{1}{2}\boldsymbol{a} + M\boldsymbol{a}, \qquad \boldsymbol{\nu} \times \mathbf{curl}\, \boldsymbol{u}|^{\pm}_{\partial B_R(0)} = N\boldsymbol{a}. \tag{3.30}$$

(c) Consider the exterior scattering problem to find $\boldsymbol{v} \in H_{\mathrm{loc}}(\mathbf{curl}, \mathbb{R}^3 \setminus \overline{B_R(0)})$ *such that*

$$\mathbf{curl}\,\mathbf{curl}\,\boldsymbol{v} - k^2\boldsymbol{v} = 0 \quad \text{in } \mathbb{R}^3 \setminus \overline{B_R(0)}, \qquad \boldsymbol{\nu} \times \boldsymbol{v} = \boldsymbol{f} \quad \text{on } \partial B_R(0), \tag{3.31}$$

where $\boldsymbol{v}$ *is supposed to satisfy the Silver–Müller radiation condition. Let* $\boldsymbol{f} \in H^{-1/2}_{\mathrm{div}}(\partial B_R(0))$ *and assume that* $\boldsymbol{h}_0 = 0$ *is the unique solution to the interior boundary value problem* (3.23) *with* $\boldsymbol{g} = 0$*. Then,* (3.31) *has a unique solution given by* $\widetilde{M}\boldsymbol{a}$ *with* $\boldsymbol{a} \in H^{-1/2}_{\mathrm{div}}(\partial B_R(0))$ *given by* $(1/2I + M)\boldsymbol{a} = \boldsymbol{f}$*. In particular,* $(1/2I + M)^{-1}$ *exists and is bounded.*

Proof. For (a) and (b) we directly refer to the proof of [88, Thm. 5.52]. For part (c) we proceed similar to the proof of [88, Thm. 3.36]. Let $\boldsymbol{v} = \widetilde{M}\boldsymbol{a}$ for an $\boldsymbol{a} \in H^{-1/2}_{\mathrm{div}}(\partial B_R(0))$. Then, by [88, Thm. 5.52], $\boldsymbol{v}$ solves $\mathbf{curl}\,\mathbf{curl}\,\boldsymbol{v} - k^2\boldsymbol{v} = 0$ in $\mathbb{R}^3 \setminus \partial B_R(0)$ and satisfies the Silver–Müller radiation condition. Taking the trace from the exterior yields by (3.30) that $\boldsymbol{a}$ must satisfy $(1/2I + M)\,\boldsymbol{a} = \boldsymbol{f}$. By [27, Lem. 11] the operator M from $H^{-1/2}_{\mathrm{div}}(\partial B_R(0))$ into itself is compact. Note that this requires the boundary of the domain (in this case $\partial B_R(0)$) to be sufficiently regular. The Fredholm alternative (see e.g. [33, Lem. 13.4]) now yields that the operator $1/2I + M$ is injective if and only if it is surjective. Therefore, we study the case $\boldsymbol{f} = 0$ and denote by $\boldsymbol{a} \in H^{-1/2}_{\mathrm{div}}(\partial B_R(0))$ a solution to $(1/2I + M)\boldsymbol{a} = 0$. For this $\boldsymbol{a}$, let $\boldsymbol{v} = \widetilde{M}\boldsymbol{a}$. Then, $\boldsymbol{\nu} \times \boldsymbol{v}|^{+}_{\partial B_R(0)} = (1/2I + M)\boldsymbol{a} = 0$. The uniqueness theorem in [88, Thm. 5.59] yields that $\boldsymbol{v} = 0$ in $\mathbb{R}^3 \setminus \overline{B_R(0)}$. In particular, this implies that $\boldsymbol{\nu} \times \mathbf{curl}\, \boldsymbol{v}|^{+}_{\partial B_R(0)} = 0$. Again, by [88, Thm. 5.52] the field $\boldsymbol{v}$ satisfies $\boldsymbol{\nu} \times \mathbf{curl}\, \boldsymbol{v}|^{+}_{\partial B_R(0)} = \boldsymbol{\nu} \times \mathbf{curl}\, \boldsymbol{v}|^{-}_{\partial B_R(0)}$ and therefore, the interior trace satisfies $\boldsymbol{\nu} \times \mathbf{curl}\, \boldsymbol{v}|^{-}_{\partial B_R(0)} = 0$. Due to our assumption that k^2 is no interior eigenvalue of the problem (3.23), $\boldsymbol{v}$ must be 0 in $B_R(0)$. This also implies that $\boldsymbol{\nu} \times \boldsymbol{v}|^{-}_{\partial B_R(0)} = 0$. The jump relation in (3.30) now shows that $\boldsymbol{a} = \boldsymbol{\nu} \times \boldsymbol{v}_{\partial B_R(0)}|^{+} - \boldsymbol{\nu} \times \boldsymbol{v}_{\partial B_R(0)}|^{-} = 0$. This shows that $1/2I + M$ is injective and thus, by the Fredholm alternative, surjective. The open mapping theorem (see e.g. [122, p. 75] implies that the bijective operator $1/2I + M$ has a bounded inverse. □

Now, we can prove Theorem 3.6. In order to simplify notation, we suppress the dependency on the integral variable.

Proof of Theorem 3.6. The Stratton–Chu formula (see [88, Thm. 5.49]) applied to the incident field $\boldsymbol{E}^i$ gives that

$$\begin{aligned} &-\mathbf{curl}_{\mathrm{x}} \int_{\partial B_R(0)} \Phi(\boldsymbol{x}, \cdot)(\boldsymbol{\nu} \times \boldsymbol{E}^i|_{\partial B_R(0)})\, \mathrm{d}s \\ &\quad -\frac{1}{k^2}\mathbf{curl}^2_{\mathrm{x}} \int_{\partial B_R(0)} \Phi(\boldsymbol{x}, \cdot)(\boldsymbol{\nu} \times \mathbf{curl}\, \boldsymbol{E}^i|_{\partial B_R(0)})\, \mathrm{d}s = \begin{cases} \boldsymbol{E}^i(\boldsymbol{x}), & \boldsymbol{x} \in B_R(0) \\ 0, & \boldsymbol{x} \in \mathbb{R}^3 \setminus \overline{B_R(0)} \end{cases}. \end{aligned} \tag{3.32}$$

Furthermore, for the scattered field $\boldsymbol{E}^s_{\rho_n}$ the Stratton–Chu formula shows that

$$\begin{aligned} &\mathbf{curl}_{\mathrm{x}} \int_{\partial B_R(0)} \Phi(\boldsymbol{x}, \cdot)(\boldsymbol{\nu} \times \boldsymbol{E}^s_{\rho_n}|_{\partial B_R(0)})\, \mathrm{d}s \\ &\quad +\frac{1}{k^2}\mathbf{curl}^2_{\mathrm{x}} \int_{\partial B_R(0)} \Phi(\boldsymbol{x}, \cdot)(\boldsymbol{\nu} \times \mathbf{curl}\, \boldsymbol{E}^s_{\rho_n}|_{\partial B_R(0)})\, \mathrm{d}s = \begin{cases} 0, & \boldsymbol{x} \in B_R(0) \\ \boldsymbol{E}^s_{\rho_n}(\boldsymbol{x}), & \boldsymbol{x} \in \mathbb{R}^3 \setminus \overline{B_R(0)} \end{cases}. \end{aligned} \tag{3.33}$$

Subtracting (3.32) from (3.33) we conclude that

$$\boldsymbol{E}^s_{\rho_n}(\boldsymbol{x}) = \mathbf{curl}_{\mathrm{x}} \int_{\partial B_R(0)} \Phi(\boldsymbol{x},\cdot)(\boldsymbol{\nu} \times \boldsymbol{E}_{\rho_n}|_{\partial B_R(0)})\, \mathrm{d}s + \frac{1}{k^2}\, \mathbf{curl}^2_{\mathrm{x}} \int_{\partial B_R(0)} \Phi(\boldsymbol{x},\cdot)(\boldsymbol{\nu} \times \mathbf{curl}\, \boldsymbol{E}_{\rho_n}|_{\partial B_R(0)})\, \mathrm{d}s \quad (3.34)$$

for $\boldsymbol{x} \in \mathbb{R}^3 \setminus \overline{B_R(0)}$. Applying the tangential trace γ_t to (3.34) and noting the jump relations in (3.30) yields

$$\boldsymbol{\nu} \times \boldsymbol{E}^s_{\rho_n}|_{\partial B_R(0)} = \frac{1}{2}\boldsymbol{\nu} \times \boldsymbol{E}_{\rho_n}|_{\partial B_R(0)} + M(\boldsymbol{\nu} \times \boldsymbol{E}_{\rho_n}|_{\partial B_R(0)}) + \frac{1}{k^2} N(\boldsymbol{\nu} \times \mathbf{curl}\, \boldsymbol{E}_{\rho_n}|_{\partial B_R(0)})\,. \quad (3.35)$$

On the other hand, the same procedure applied to (3.32) gives

$$\boldsymbol{\nu} \times \boldsymbol{E}^i|_{\partial B_R(0)} = \frac{1}{2}\boldsymbol{\nu} \times \boldsymbol{E}^i|_{\partial B_R(0)} - M(\boldsymbol{\nu} \times \boldsymbol{E}^i|_{\partial B_R(0)}) - \frac{1}{k^2} N(\boldsymbol{\nu} \times \mathbf{curl}\, \boldsymbol{E}^i|_{\partial B_R(0)})\,. \quad (3.36)$$

Due to our assumption that k^2 is not an interior Maxwell eigenvalue for $B_R(0)$, we find that the boundary value problems (3.27) and (3.28) are uniquely solvable for every $\widetilde{\boldsymbol{g}} \in H^{-1/2}_{\mathrm{div}}(\partial B_R(0))$. Consequently, the interior Calderón operators

$$\Lambda_{\rho_n} : H^{-1/2}_{\mathrm{div}}(\partial B_R(0)) \to H^{-1/2}_{\mathrm{div}}(\partial B_R(0)), \quad \Lambda_{\rho_n}\widetilde{\boldsymbol{g}} = \frac{1}{k^2}\boldsymbol{\nu} \times \mathbf{curl}\, \boldsymbol{e}_{\rho_n}|_{\partial B_R(0)}\,,$$
$$\Lambda_0 : H^{-1/2}_{\mathrm{div}}(\partial B_R(0)) \to H^{-1/2}_{\mathrm{div}}(\partial B_R(0)), \quad \Lambda_0\widetilde{\boldsymbol{g}} = \frac{1}{k^2}\boldsymbol{\nu} \times \mathbf{curl}\, \boldsymbol{e}_0|_{\partial B_R(0)}\,,$$

are both well-defined and bounded. Furthermore, it holds that

$$\Lambda_{\rho_n}(\boldsymbol{\nu} \times \boldsymbol{E}_{\rho_n}) = \frac{1}{k^2}\boldsymbol{\nu} \times \mathbf{curl}\, \boldsymbol{E}_{\rho_n}|_{\partial B_R(0)} \quad \text{and} \quad \Lambda_0(\boldsymbol{\nu} \times \boldsymbol{E}^i) = \frac{1}{k^2}\boldsymbol{\nu} \times \mathbf{curl}\, \boldsymbol{E}^i|_{\partial B_R(0)}$$

on $\partial B_R(0)$. Next, we define the operators T_{ρ_n} and T_0 by

$$T_{\rho_n} : H^{-1/2}_{\mathrm{div}}(\partial B_R(0)) \to H^{-1/2}_{\mathrm{div}}(\partial B_R(0))\,, \quad T_{\rho_n} = \frac{1}{2}I - M - N\Lambda_{\rho_n}$$
$$T_0 : H^{-1/2}_{\mathrm{div}}(\partial B_R(0)) \to H^{-1/2}_{\mathrm{div}}(\partial B_R(0))\,, \quad T_0 = \frac{1}{2}I - M - N\Lambda_0\,.$$

The operator T_0 is the identity operator on $H^{-1/2}_{\mathrm{div}}(\partial B_R(0))$. This can be seen as follows. Let $\widetilde{\boldsymbol{g}} \in H^{-1/2}_{\mathrm{div}}(\partial B_R(0))$ and let $\boldsymbol{e}_0$ be the unique solution to (3.27). Then, the Stratton–Chu formula yields that

$$\boldsymbol{e}_0(\boldsymbol{x}) = -\mathbf{curl}_{\mathrm{x}} \int_{\partial B_R(0)} \Phi(\boldsymbol{x},\cdot)(\boldsymbol{\nu} \times \boldsymbol{e}_0|_{\partial B_R(0)})\, \mathrm{d}s - \frac{1}{k^2}\, \mathbf{curl}^2_{\mathrm{x}} \int_{\partial B_R(0)} \Phi(\boldsymbol{x},\cdot)(\boldsymbol{\nu} \times \mathbf{curl}\, \boldsymbol{e}_0|_{\partial B_R(0)})\, \mathrm{d}s \quad (3.37)$$

for $\boldsymbol{x} \in B_R(0)$. Applying the tangential trace γ_t to both sides of (3.37), using the jump conditions (3.30), the boundary condition of (3.27) and $\Lambda_0\widetilde{\boldsymbol{g}} = k^{-2}\boldsymbol{\nu} \times \mathbf{curl}\, \boldsymbol{e}_0|_{\partial B_R(0)}$ yields that

$$\begin{aligned}\widetilde{\boldsymbol{g}} = \boldsymbol{\nu} \times \boldsymbol{e}_0|_{\partial B_R(0)} &= \frac{1}{2}\boldsymbol{\nu} \times \boldsymbol{e}_0|_{\partial B_R(0)} - M(\boldsymbol{\nu} \times \boldsymbol{e}_0|_{\partial B_R(0)}) - \frac{1}{k^2} N(\boldsymbol{\nu} \times \mathbf{curl}\, \boldsymbol{e}_0|_{\partial B_R(0)}) \\ &= \frac{1}{2}\widetilde{\boldsymbol{g}} - M\widetilde{\boldsymbol{g}} - N\Lambda_0\widetilde{\boldsymbol{g}} = T_0\widetilde{\boldsymbol{g}}\,.\end{aligned}$$

Thus, (3.35) and (3.36) can be written as

$$T_{\rho_n}(\boldsymbol{\nu} \times \boldsymbol{E}_{\rho_n}|_{\partial B_R(0)}) = \boldsymbol{\nu} \times \boldsymbol{E}^i|_{\partial B_R(0)} \quad \text{and} \quad T_0(\boldsymbol{\nu} \times \boldsymbol{E}^i|_{\partial B_R(0)}) = \boldsymbol{\nu} \times \boldsymbol{E}^i|_{\partial B_R(0)}$$

on $\partial B_R(0)$. Accordingly, we have $T_{\rho_n}(\boldsymbol{\nu}\times\boldsymbol{E}_{\rho_n}|_{\partial B_R(0)}) - T_0(\boldsymbol{\nu}\times\boldsymbol{E}^i|_{\partial B_R(0)}) = 0$ and therefore

$$T_{\rho_n}(\boldsymbol{\nu}\times\boldsymbol{E}^s_{\rho_n}|_{\partial B_R(0)}) \;=\; -\,(T_{\rho_n}-T_0)\,(\boldsymbol{\nu}\times\boldsymbol{E}^i|_{\partial B_R(0)}) \;=\; N\big((\Lambda_{\rho_n}-\Lambda_0)\,(\boldsymbol{\nu}\times\boldsymbol{E}^i|_{\partial B_R(0)})\big) \tag{3.38}$$

on $\partial B_R(0)$. Changing the roles of $\boldsymbol{x}$ and $\boldsymbol{y}$ in (3.25), as well as noting that

$$\mathbb{G}(\boldsymbol{x},\boldsymbol{y}) \;=\; \mathbb{G}(\boldsymbol{y},\boldsymbol{x}), \quad \mathbf{curl}_{\mathrm{x}}\,\mathbb{G}(\boldsymbol{x},\boldsymbol{y}) \;=\; \mathbf{curl}_{\mathrm{x}}\,\mathbb{G}(\boldsymbol{y},\boldsymbol{x}), \quad \mathbf{curl}_{\mathrm{x}}\,\mathbb{G}(\boldsymbol{x},\boldsymbol{y}) \;=\; -\,\mathbf{curl}_{\mathrm{y}}\,\mathbb{G}(\boldsymbol{x},\boldsymbol{y})$$

turns the general asymptotic perturbation formula on bounded domains from (3.25) into

$$\begin{aligned}
&\boldsymbol{\nu}(\boldsymbol{x})\times(\boldsymbol{h}_{\rho_n}(\boldsymbol{x})-\boldsymbol{h}_0(\boldsymbol{x}))\,|_{\partial B_R(0)}\\
&\qquad + 2\int_{\partial B_R(0)}\Big(\boldsymbol{\nu}(\boldsymbol{x})\times\mathbf{curl}_{\mathrm{x}}\,\mathbb{G}(\boldsymbol{x},\cdot)|_{\partial B_R(0)}\Big)\Big(\boldsymbol{\nu}\times(\boldsymbol{h}_{\rho_n}-\boldsymbol{h}_0)\,|_{\partial B_R(0)}\Big)\,\mathrm{d}s\\
&\qquad = 2\frac{|D_{\rho_n}|}{2\ell}\Big(\int_K(\varepsilon_r-1)\Big(\boldsymbol{\nu}(\boldsymbol{x})\times\mathbf{curl}_{\mathrm{x}}\,\mathbb{G}(\boldsymbol{x},\cdot)|_{\partial B_R(0)}\Big)\mathbb{M}^{\varepsilon}\,\mathbf{curl}\,\boldsymbol{h}_0\,\mathrm{d}s\\
&\qquad\qquad + k^2\int_K(\mu_r-1)\Big(\boldsymbol{\nu}(\boldsymbol{x})\times\mathbb{G}(\boldsymbol{x},\cdot)|_{\partial B_R(0)}\Big)\mathbb{M}^{\mu}\boldsymbol{h}_0\,\mathrm{d}s\Big) + o(|D_{\rho_n}|)\,,
\end{aligned}\tag{3.39}$$

for $\boldsymbol{x}\in\partial B_R(0)$. As pointed out in the previous subsection, for $\widetilde{\boldsymbol{g}} = -\mathrm{i}/\omega\boldsymbol{g}$ the functions

$$\boldsymbol{h}_0 \;=\; \frac{1}{\mathrm{i}\omega\mu_0}\,\mathbf{curl}\,\boldsymbol{e}_0 \quad\text{and}\quad \boldsymbol{h}_{\rho_n} \;=\; \frac{1}{\mathrm{i}\omega\mu_{\rho_n}}\,\mathbf{curl}\,\boldsymbol{e}_{\rho_n} \tag{3.40}$$

solve (3.23) and (3.24), respectively. Using $\widetilde{\boldsymbol{g}} = \boldsymbol{\nu}\times\boldsymbol{E}^i|_{\partial B_R(0)}$ we find that $\boldsymbol{e}_0 = \boldsymbol{E}^i$ in $B_R(0)$ (but not that $\boldsymbol{e}_{\rho_n} = \boldsymbol{E}_{\rho_n}$ in $B_R(0)$). Since for this particular choice of $\widetilde{\boldsymbol{g}}$ it holds that

$$\Lambda_0(\widetilde{\boldsymbol{g}}) \;=\; \frac{1}{k^2}\boldsymbol{\nu}\times\mathbf{curl}\,\boldsymbol{e}_0|_{\partial B_R(0)} \;=\; \frac{1}{k^2}\boldsymbol{\nu}\times\mathbf{curl}\,\boldsymbol{E}^i|_{\partial B_R(0)}\,, \qquad \Lambda_{\rho_n}(\widetilde{\boldsymbol{g}}) \;=\; \frac{1}{k^2}\boldsymbol{\nu}\times\mathbf{curl}\,\boldsymbol{e}_{\rho_n}|_{\partial B_R(0)}\,,$$

equation (3.39) turns into

$$\begin{aligned}
&\Big(\frac{1}{2}I+M\Big)(\Lambda_{\rho_n}-\Lambda_0)(\boldsymbol{\nu}\times\boldsymbol{E}^i|_{\partial B_R(0)})(\boldsymbol{x})\\
&\qquad = \frac{|D_{\rho_n}|}{2\ell}\Big(\int_K(\mu_r-1)\Big(\boldsymbol{\nu}(\boldsymbol{x})\times\mathbb{G}(\boldsymbol{x},\cdot)|_{\partial B_R(0)}\Big)\mathbb{M}^{\mu}\,\mathbf{curl}\,\boldsymbol{E}^i\,\mathrm{d}s\\
&\qquad\qquad + \int_K(\varepsilon_r-1)\Big(\boldsymbol{\nu}(\boldsymbol{x})\times\mathbf{curl}_{\mathrm{x}}\,\mathbb{G}(\boldsymbol{x},\cdot)|_{\partial B_R(0)}\Big)\mathbb{M}^{\varepsilon}\boldsymbol{E}^i\,\mathrm{d}s\Big) + o(|D_{\rho_n}|)
\end{aligned}\tag{3.41}$$

for $\boldsymbol{x}\in\partial B_R(0)$. The proof of [68, Thm. 2.2.] and the smoothness of the dyadic Green's function $\mathbb{G}(\boldsymbol{x},\boldsymbol{y})$ for $\boldsymbol{x}\in\partial B_R(0)$ and $\boldsymbol{y}\in D_{\rho_n}$ shows that the remainder $o(|D_{\rho_n}|)$ on the right-hand side of (3.41) is such that $\|o(|D_{\rho_n}|)\|_{H^{-1/2}_{\mathrm{div}}(\partial B_R(0))}/|D_{\rho_n}|$ converges to zero uniformly for all $\boldsymbol{E}^i$ satisfying $\|\boldsymbol{\nu}\times\boldsymbol{E}^i|_{\partial B_R(0)}\|_{H^{-1/2}_{\mathrm{div}}(\partial B_R(0))}\leq C$ for some fixed $C\geq 0$.

In (3.31) we use the boundary data $\boldsymbol{f} = \boldsymbol{\nu}\times\mathbb{G}(\cdot,\boldsymbol{y})|_{\partial B_R(0)}$ (to be understood columnwise) for $\boldsymbol{y}\in B_R(0)$ away from the boundary, what yields that $\mathbb{G}(\cdot,\boldsymbol{y})$ is a solution to this problem. Further, using part (c) in Proposition 3.9 and the assumption that k^2 is not an eigenvalue of the interior Maxwell problem gives that $\mathbb{G}(\cdot,\boldsymbol{y})$ is the only solution to this problem and can be written as

$$\mathbb{G}(\boldsymbol{x},\boldsymbol{y}) \;=\; \mathbf{curl}_{\mathrm{x}}\int_{\partial B_R(0)}\boldsymbol{a}\Phi(\boldsymbol{x},\cdot)\,\mathrm{d}s\,, \tag{3.42}$$

where $\boldsymbol{a}$ is given by $\boldsymbol{a} = (1/2I+M)^{-1}\,(\boldsymbol{\nu}\times\mathbb{G}(\cdot,\boldsymbol{y})|_{\partial B_R(0)})$. Thus, using this particular $\boldsymbol{a}$, we find by applying $\boldsymbol{\nu}\times\mathbf{curl}$ to (3.42) and using (3.30) that

$$N\left(\frac{1}{2}I+M\right)^{-1}\Big(\boldsymbol{\nu}(\boldsymbol{x})\times\mathbb{G}(\boldsymbol{x},\boldsymbol{y})|_{\partial B_R(0)}\Big) \;=\; \boldsymbol{\nu}(\boldsymbol{x})\times\mathbf{curl}_{\mathrm{x}}\,\mathbb{G}(\boldsymbol{x},\boldsymbol{y})|_{\partial B_R(0)}$$

for $\boldsymbol{x} \in \partial B_R(0)$ and $\boldsymbol{y} \in K$. Similarly, one finds that

$$N\left(\frac{1}{2}I + M\right)^{-1}\left(\boldsymbol{\nu}(\boldsymbol{x}) \times \mathbf{curl}_{\mathrm{x}}\, \mathbb{G}(\boldsymbol{x},\boldsymbol{y})|_{\partial B_R(0)}\right) = k^2 \boldsymbol{\nu}(\boldsymbol{x}) \times \mathbb{G}(\boldsymbol{x},\boldsymbol{y})|_{\partial B_R(0)}\,.$$

for $\boldsymbol{x} \in \partial B_R(0)$ and $\boldsymbol{y} \in K$. Accordingly, applying $N(1/2I+M)^{-1}$ on both sides of (3.41) yields

$$\begin{aligned} &N\left(\Lambda_{\rho_n} - \Lambda_0\right)\left(\boldsymbol{\nu} \times \boldsymbol{E}^i|_{\partial B_R(0)}\right)(\boldsymbol{x}) \\ &\qquad = \frac{|D_{\rho_n}|}{2\ell}\Big(\int_K (\mu_r - 1)\left(\boldsymbol{\nu}(\boldsymbol{x}) \times \mathbf{curl}_{\mathrm{x}}\, \mathbb{G}(\boldsymbol{x},\cdot)|_{\partial B_R(0)}\right)\mathbb{M}^{\mu}\,\mathbf{curl}\,\boldsymbol{E}^i\,\mathrm{d}s \\ &\qquad\qquad + \int_K k^2\,(\varepsilon_r - 1)\left(\boldsymbol{\nu}(\boldsymbol{x}) \times \mathbb{G}(\boldsymbol{x},\cdot)|_{\partial B_R(0)}\right)\mathbb{M}^{\varepsilon}\boldsymbol{E}^i\,\mathrm{d}s\Big) + o(|D_{\rho_n}|) \end{aligned} \tag{3.43}$$

for $\boldsymbol{x} \in \partial B_R(0)$. Denoting

$$\begin{aligned} \widetilde{\boldsymbol{E}^s_{\rho_n}}(\boldsymbol{x}) = \frac{|D_{\rho_n}|}{2\ell}\Big(&\int_K (\mu_r - 1)\,\mathbf{curl}_{\mathrm{x}}\, \mathbb{G}(\boldsymbol{x},\cdot)\mathbb{M}^{\mu}\,\mathbf{curl}\,\boldsymbol{E}^i\,\mathrm{d}s \\ &+ \int_K k^2\,(\varepsilon_r - 1)\,\mathbb{G}(\boldsymbol{x},\cdot)\mathbb{M}^{\varepsilon}\boldsymbol{E}^i\,\mathrm{d}s\Big) \end{aligned} \tag{3.44}$$

for $\boldsymbol{x} \in \mathbb{R}^3 \setminus \overline{B_R(0)}$ and combining (3.43) with (3.38) leads to

$$T_{\rho_n}(\boldsymbol{\nu} \times \boldsymbol{E}^s_{\rho_n}|_{\partial B_R(0)}) = \boldsymbol{\nu} \times \widetilde{\boldsymbol{E}^s_{\rho_n}}|_{\partial B_R(0)} + o(|D_{\rho_n}|) \quad \text{on } \partial B_R(0)\,. \tag{3.45}$$

Due to (3.40) and (3.26) there is a constant $C > 0$ such that

$$\|(\Lambda_{\rho_n} - \Lambda_0)\,\widetilde{\boldsymbol{g}}\|_{H^{-1/2}_{\mathrm{div}}(\partial B_R(0))} \le C\,\|\boldsymbol{h}_{\rho_n} - \boldsymbol{h}_0\|_{H(\mathbf{curl},B_R(0))} \le C|D_{\rho_n}|^{1/2}\,\|\widetilde{\boldsymbol{g}}\|_{H^{-1/2}_{\mathrm{div}}(\partial B_R(0))}$$

for any $\widetilde{\boldsymbol{g}} \in H^{-1/2}_{\mathrm{div}}(\partial B_R(0))$. The boundedness of the operator N (see Proposition 3.9) further yields a constant $C > 0$ such that

$$\|T_{\rho_n} - T_0\| = \|N\,(\Lambda_{\rho_n} - \Lambda_0)\| \le C|D_{\rho_n}|^{1/2}.$$

Since $T_0 = I$, there is an $n_0 \in \mathbb{N}$ such that for all $n \ge n_0$, the operator T_{ρ_n} has a bounded inverse $T^{-1}_{\rho_n}$ and $\|T^{-1}_{\rho_n}\| \le C$, where $C > 0$ is independent of n for all $n \ge n_0$ (see e.g. [91, Thm. 10.1]). The identity (3.45) gives that

$$T_{\rho_n}\left(\boldsymbol{\nu} \times \boldsymbol{E}^s_{\rho_n}|_{\partial B_R(0)} - \boldsymbol{\nu} \times \widetilde{\boldsymbol{E}^s_{\rho_n}}|_{\partial B_R(0)}\right) = -\left(T_{\rho_n} - T_0\right)\left(\boldsymbol{\nu} \times \widetilde{\boldsymbol{E}^s_{\rho_n}}|_{\partial B_R(0)}\right) + o(|D_{\rho_n}|)\,.$$

Further, using (3.44) we find that $\|\boldsymbol{\nu} \times \widetilde{\boldsymbol{E}^s_{\rho_n}}|_{\partial B_R(0)}\|_{H^{-1/2}_{\mathrm{div}}(\partial B_R(0))} \le C|D_{\rho_n}|$. Thus,

$$\begin{aligned} &\|\boldsymbol{\nu} \times \boldsymbol{E}^s_{\rho_n}|_{\partial B_R(0)} - \boldsymbol{\nu} \times \widetilde{\boldsymbol{E}^s_{\rho_n}}|_{\partial B_R(0)}\|_{H^{-1/2}_{\mathrm{div}}(\partial B_R(0))} \\ &\qquad \le C\|T^{-1}_{\rho_n}\||D_{\rho_n}|^{1/2}\|\boldsymbol{\nu} \times \widetilde{\boldsymbol{E}^s_{\rho_n}}|_{\partial B_R(0)}\|_{H^{-1/2}_{\mathrm{div}}(\partial B_R(0))} + o(|D_{\rho_n}|) = o(|D_{\rho_n}|)\,. \end{aligned}$$

Accordingly, $\boldsymbol{E}^s_{\rho_n} \in H(\mathbf{curl}, \mathbb{R}^3 \setminus \overline{B_R(0)})$ is the radiating solution to

$$\begin{aligned} \mathbf{curl}\,\mathbf{curl}\,\boldsymbol{E}^s_{\rho_n} - k^2\boldsymbol{E}^s_{\rho_n} &= 0 \quad \text{in } \mathbb{R}^3 \setminus \overline{B_R(0)}\,, \\ \boldsymbol{\nu} \times \boldsymbol{E}^s_{\rho_n}|_{\partial B_R(0)} &= \boldsymbol{\nu} \times \widetilde{\boldsymbol{E}^s_{\rho_n}}|_{\partial B_R(0)} + o(|D_{\rho_n}|) \quad \text{on } \partial B_R(0)\,. \end{aligned}$$

As before, we use that $1/2I + M$ is invertible (see Proposition 3.9) and deduce that $\boldsymbol{E}^s_{\rho_n} - \widetilde{\boldsymbol{E}^s_{\rho_n}}$ can be written as

$$\boldsymbol{E}^s_{\rho_n}(\boldsymbol{x}) - \widetilde{\boldsymbol{E}^s_{\rho_n}}(\boldsymbol{x}) = \mathbf{curl}_{\mathrm{x}} \int_{\partial B_R(0)} \Phi(\boldsymbol{x},\cdot)\left(\frac{1}{2}I + M\right)^{-1}\left(\boldsymbol{\nu} \times \boldsymbol{E}^s_{\rho_n}|_{\partial B_R(0)} - \boldsymbol{\nu} \times \widetilde{\boldsymbol{E}^s_{\rho_n}}|_{\partial B_R(0)}\right)\mathrm{d}s$$

for $\boldsymbol{x} \in \mathbb{R}^3 \setminus \overline{B_R(0)}$). The right hand side is in $o(|D_{\rho_n}|)$, what shows (3.21). The asymptotic representation formula (3.22) follows by substituting the far field expansion of $\mathbb{G}(\cdot,\boldsymbol{y})$ and $\mathbf{curl}_{\mathrm{x}}\,\mathbb{G}(\cdot,\boldsymbol{y})$ from (2.29) into (3.21). □

Remark 3.10. The asymptotic representation formulas for the scattered field in (3.21) and for the far field in (3.22) can be extended to variable anisotropic permittivities and permeabilities in D_{ρ_n}, as well as in $\mathbb{R}^3 \setminus \overline{B_R(0)}$ by using the more general perturbation formula from [2, Thm. 4.4] instead of [68, Thm. 2.2].

3.3 Explicit characterization of the polarization tensor of a thin tubular scattering object

The leading order term of the asymptotic perturbation formula features two matrix-valued polarization tensors $\mathbb{M}^\varepsilon \in L^2(K, \mathbb{C}^{3\times 3})$ and $\mathbb{M}^\mu \in L^2(K, \mathbb{R}^{3\times 3})$. The definition of $\mathbb{M}^\varepsilon$ and $\mathbb{M}^\mu$ depend both on the material parameters and on the geometry of the scatterer and can therefore be seen as the fundamental parts in the leading order term of the perturbation formula. Our studies on the polarization tensors rely on the works [29, 30, 68].

To introduce the polarization tensor as in [68] (see also [29]) we consider $B_R(0) \subset \mathbb{R}^3$ including the scattering objects D_{ρ_n} for $0 < \rho_n < r/2$ as in Theorem 3.6. Further, let γ_{ρ_n} with $\gamma \in \{\varepsilon, \mu\}$ be as in (3.8). We consider the boundary value problems, which are to find $V^{(j)}, v_\rho^{(j)} \in H^1(B_R(0))$ for $j = 1, 2, 3$ with

$$\operatorname{div}\left(\gamma_0 \nabla V^{(j)}\right) = 0 \quad \text{in } B_R(0), \qquad \gamma_0 \frac{\partial V^{(j)}}{\partial \boldsymbol{\nu}} = \gamma_0 \nu_j \quad \text{on } \partial B_R(0)\,, \tag{3.46}$$

$$\operatorname{div}\left(\gamma_{\rho_n} \nabla v_{\rho_n}^{(j)}\right) = 0 \quad \text{in } B_R(0), \qquad \gamma_{\rho_n} \frac{\partial v_{\rho_n}^{(j)}}{\partial \boldsymbol{\nu}} = \gamma_0 \nu_j \quad \text{on } \partial B_R(0)\,, \tag{3.47}$$

together with the normalization conditions $\int_{\partial B_R(0)} V^{(j)}\, \mathrm{d}s = 0$ and $\int_{\partial B_R(0)} v_{\rho_n}^{(j)}\, \mathrm{d}s = 0$. The functions $\nu_j, 1 \le j \le 3$ denote the jth component of the exterior unit normal to $B_R(0)$. The solution of (3.46) is explicitly given by $V^{(j)} = x_j - |\partial B_R(0)|^{-1} \int_{\partial\Omega} x_j\, \mathrm{d}s$. Convergence results from [29, Lem. 1] are cited in the following lemma.

Lemma 3.11. *Let $V^{(j)}$ and $v_{\rho_n}^{(j)}$ be the unique solutions of (3.46) and (3.47), respectively. Then, there is a constant $C > 0$ such that*

$$\|V^{(j)} - v_{\rho_n}^{(j)}\|_{H^1(\Omega)} \le C |D_{\rho_n}|^{1/2}\,. \tag{3.48}$$

Moreover, there is a constant $C > 0$ such that

$$\|V^{(j)} - v_{\rho_n}^{(j)}\|_{L^2(\Omega)} \le C |D_{\rho_n}|^{3/4}\,. \tag{3.49}$$

For a sequence of Lipschitz domains $(D_{\rho_n})_{n\in\mathbb{N}}$ as in Theorem 3.6, and $\psi \in C(\overline{B_R(0)})$ the component M_{ij}^γ, $1 \le i, j \le 3$ of the polarization tensor $\mathbb{M}^\gamma$ is defined by

$$\int_{B_R(0)} M_{ij}^\gamma \psi\, \mathrm{d}\mu = \lim_{n\to\infty} \frac{1}{|D_{\rho_n}|} \int_{D_{\rho_n}} \frac{\partial v_{\rho_n}^{(j)}}{\partial x_i} \psi\, \mathrm{d}\boldsymbol{x}\,, \tag{3.50}$$

where μ denotes the measure from (3.20). Later in this chapter we use an equivalent definition of the polarization tensor. However, for the next two propositions, in which we study symmetry and bounds of the polarization tensor, this definition is favorable. The following proposition and proof follows along the lines of [29, Lem. 2]. We emphasize, that it remains valid also for complex-valued coefficients ε_1 with $\operatorname{Re}(\varepsilon_1) < 0$ and $\operatorname{Im}(\varepsilon_1) > 0$.

Proposition 3.12. *The polarization tensor $\mathbb{M}^\gamma$ for $\gamma \in \{\varepsilon, \mu\}$ is symmetric, i.e. $M_{ij}^\gamma = M_{ji}^\gamma$ for all $1 \le i, j \le 3$.*

Proof. The weak formulations of (3.46) and (3.47) imply that

$$\int_{B_R(0)} \gamma_{\rho_n} \nabla(v_{\rho_n}^{(i)} - V^{(i)}) \cdot \nabla(v_{\rho_n}^{(j)}\psi) \, \mathrm{d}\boldsymbol{x} = \int_{B_R(0)} (\gamma_0 - \gamma_{\rho_n}) \nabla V^{(i)} \cdot \nabla(v_{\rho_n}^{(j)}\psi) \, \mathrm{d}\boldsymbol{x} \tag{3.51}$$

and

$$\int_{B_R(0)} \gamma_0 \nabla(v_{\rho_n}^{(i)} - V^{(i)}) \cdot \nabla(V^{(j)}\psi) \, \mathrm{d}\boldsymbol{x} = \int_{B_R(0)} (\gamma_0 - \gamma_{\rho_n}) \nabla v_{\rho_n}^{(i)} \cdot \nabla(V^{(j)}\psi) \, \mathrm{d}\boldsymbol{x} \tag{3.52}$$

for all $\psi \in C(\overline{B_R(0)})$. Further, it holds that

$$\int_{B_R(0)} \gamma_{\rho_n} \nabla((v_{\rho_n}^{(i)} - V^{(i)})\psi) \cdot \nabla v_{\rho_n}^{(j)} \, \mathrm{d}\boldsymbol{x} = \int_{\partial B_R(0)} \gamma_0 \nu_j \psi (v_{\rho_n}^{(i)} - V^{(i)}) \, \mathrm{d}s \,. \tag{3.53}$$

Using the Cauchy–Schwarz inequality as well as (3.48) and (3.49) yields

$$\int_{B_R} \gamma_{\rho_n} \nabla(v_{\rho_n}^{(i)} - V^{(i)}) \cdot \nabla\psi v_{\rho_n}^{(j)} \, \mathrm{d}\boldsymbol{x} = \int_{B_R} \gamma_{\rho_n} \nabla(v_{\rho_n}^{(i)} - V^{(i)}) \cdot \nabla\psi V^{(j)} \, \mathrm{d}\boldsymbol{x} + o(|D_{\rho_n}|) \tag{3.54}$$

and

$$\int_{B_R(0)} \gamma_{\rho_n} (v_{\rho_n}^{(i)} - V^{(i)}) \nabla\psi \cdot \nabla v_{\rho_n}^{(j)} \, \mathrm{d}\boldsymbol{x} = \int_{B_R(0)} \gamma_{\rho_n} (v_{\rho_n}^{(i)} - V^{(i)}) \nabla\psi \cdot \nabla V^{(j)} \, \mathrm{d}\boldsymbol{x} + o(|D_{\rho_n}|) \,. \tag{3.55}$$

In the equality

$$\int_{B_R(0)} \gamma_{\rho_n} \nabla(v_{\rho_n}^{(i)} - V^{(i)}) \cdot \nabla(v_{\rho_n}^{(j)}\psi) \, \mathrm{d}\boldsymbol{x} = \int_{B_R(0)} \gamma_{\rho_n} \nabla(v_{\rho_n}^{(i)} - V^{(i)}) \cdot \left(\nabla v_{\rho_n}^{(j)}\psi + v_{\rho_n}^{(j)} \nabla\psi\right) \mathrm{d}\boldsymbol{x}$$

we apply (3.53) and (3.55) for the first summand and (3.54) for the second summand on the right hand side to see that

$$\begin{aligned} \int_{B_R(0)} \gamma_{\rho_n} \nabla(v_{\rho_n}^{(i)} - V^{(i)}) \cdot \nabla(v_{\rho_n}^{(j)}\psi) \, \mathrm{d}\boldsymbol{x} &= -\int_{B_R(0)} \gamma_{\rho_n} (v_{\rho_n}^{(i)} - V^{(i)}) \nabla\psi \cdot \nabla V^{(j)} \, \mathrm{d}\boldsymbol{x} \\ &+ \int_{\partial B_R(0)} \gamma_0 \nu_j \psi (v_{\rho_n}^{(i)} - V^{(i)}) \, \mathrm{d}s + \int_{B_R(0)} \gamma_0 \nabla(v_{\rho_n}^{(i)} - V^{(i)}) \cdot \nabla\psi V^{(j)} \, \mathrm{d}\boldsymbol{x} \\ &+ \int_{D_{\rho_n}} (\gamma_1 - \gamma_0) \nabla(v_{\rho_n}^{(i)} - V^{(i)}) \cdot \nabla\psi V^{(j)} \, \mathrm{d}\boldsymbol{x} + o(|D_{\rho_n}|) \,. \end{aligned} \tag{3.56}$$

Similarly, we find that

$$\begin{aligned} \int_{B_R(0)} \gamma_0 \nabla(v_{\rho_n}^{(i)} - V^{(i)}) \cdot \nabla(V^{(j)}\psi) \, \mathrm{d}\boldsymbol{x} &= -\int_{B_R(0)} \gamma_0 (v_{\rho_n}^{(i)} - V^{(i)}) \nabla\psi \cdot \nabla V^{(j)} \, \mathrm{d}\boldsymbol{x} \\ &+ \int_{\partial B_R(0)} \gamma_0 \nu_j \psi (v_{\rho_n}^{(i)} - V^{(i)}) \, \mathrm{d}s + \int_{B_R(0)} \gamma_0 \nabla(v_{\rho_n}^{(i)} - V^{(i)}) \cdot \nabla\psi V^{(j)} \, \mathrm{d}\boldsymbol{x} \,. \end{aligned} \tag{3.57}$$

Using (3.57) in (3.56), rearranging the terms and using (3.49) again gives that

$$\begin{aligned} \int_{B_R(0)} \gamma_{\rho_n} \nabla(v_{\rho_n}^{(i)} - V^{(i)}) \cdot \nabla(v_{\rho_n}^{(j)}\psi) \, \mathrm{d}\boldsymbol{x} &= \int_{B_R(0)} \gamma_0 \nabla(v_{\rho_n}^{(i)} - V^{(i)}) \cdot \nabla(V^{(j)}\psi) \, \mathrm{d}\boldsymbol{x} \\ &+ \int_{D_{\rho_n}} (\gamma_1 - \gamma_0) \nabla(v_{\rho_n}^{(i)} - V^{(i)}) \cdot \nabla\psi V^{(j)} \, \mathrm{d}\boldsymbol{x} + o(|D_{\rho_n}|) \,. \end{aligned} \tag{3.58}$$

In (3.58) we use the identities (3.51), (3.52) and (3.48) once more to obtain

$$\begin{aligned}
&\int_{B_R(0)} (\gamma_0 - \gamma_{\rho_n}) \nabla V^{(i)} \cdot \nabla (v_{\rho_n}^{(j)} \psi) \, \mathrm{d}\boldsymbol{x} \\
&= \int_{B_R(0)} (\gamma_0 - \gamma_{\rho_n}) \nabla v_{\rho_n}^{(i)} \cdot \nabla (V^{(j)} \psi) \, \mathrm{d}\boldsymbol{x} + \int_{D_{\rho_n}} (\gamma_1 - \gamma_0) \nabla (v_{\rho_n}^{(i)} - V^{(i)}) \cdot \nabla \psi V^{(j)} \, \mathrm{d}\boldsymbol{x} + o(|D_{\rho_n}|) \\
&= \int_{B_R(0)} (\gamma_0 - \gamma_{\rho_n}) \nabla v_{\rho_n}^{(i)} \cdot \nabla (V^{(j)} \psi) \, \mathrm{d}\boldsymbol{x} - \int_{D_{\rho_n}} (\gamma_0 - \gamma_1) \nabla v_{\rho_n}^{(i)} \cdot \nabla \psi V^{(j)} \, \mathrm{d}\boldsymbol{x} \\
&\quad + \int_{D_{\rho_n}} (\gamma_0 - \gamma_1) \nabla V^{(i)} \cdot \nabla \psi V^{(j)} \, \mathrm{d}\boldsymbol{x} + o(|D_{\rho_n}|) \\
&= \int_{B_R(0)} (\gamma_0 - \gamma_{\rho_n}) \nabla v_{\rho_n}^{(i)} \cdot \nabla V^{(j)} \psi \, \mathrm{d}\boldsymbol{x} + \int_{D_{\rho_n}} (\gamma_0 - \gamma_1) \nabla V^{(i)} \cdot \nabla \psi V^{(j)} \, \mathrm{d}\boldsymbol{x} + o(|D_{\rho_n}|) \\
&= \int_{B_R(0)} (\gamma_0 - \gamma_{\rho_n}) \nabla v_{\rho_n}^{(i)} \cdot \nabla V^{(j)} \psi \, \mathrm{d}\boldsymbol{x} + \int_{D_{\rho_n}} (\gamma_0 - \gamma_1) \nabla V^{(i)} \cdot \nabla \psi v_{\rho_n}^{(j)} \, \mathrm{d}\boldsymbol{x} + o(|D_{\rho_n}|) \, .
\end{aligned}$$

Another rearrangement gives that

$$\begin{aligned}
&|D_{\rho_n}|^{-1} \int_{B_R(0)} (\gamma_0 - \gamma_1) \chi_{D_{\rho_n}} \nabla V^{(i)} \cdot \nabla v_{\rho_n}^{(j)} \psi \, \mathrm{d}\boldsymbol{x} \\
&\qquad = |D_{\rho_n}|^{-1} \int_{B_R(0)} (\gamma_0 - \gamma_1) \chi_{D_{\rho_n}} \nabla v_{\rho_n}^{(i)} \cdot \nabla V^{(j)} \psi \, \mathrm{d}\boldsymbol{x} + o(1) \, .
\end{aligned}$$

Taking the limit on both sides gives that

$$\int_{B_R(0)} (\gamma_0 - \gamma_1) M_{ij}^{\gamma} \psi \, \mathrm{d}\mu = \int_{B_R(0)} (\gamma_0 - \gamma_1) M_{ji}^{\gamma} \psi \, \mathrm{d}\mu \, ,$$

for all $\psi \in C(\overline{B_R(0)})$, what shows that the polarization tensor $\mathbb{M}^{\gamma}$ is symmetric. □

In the next theorem, we establish bounds for the polarization tensors. For real γ_1, we refer to the results from [29, Ch. 4]. The proof that we provide here for ε_1 with $\mathrm{Re}(\varepsilon_1) < 0$ and $\mathrm{Im}(\varepsilon_1) > 0$ is similar to [29, Ch. 4].

Proposition 3.13. *Let $\boldsymbol{\xi} \in \mathbb{R}^3$. For $\gamma_1 > 0$, $\gamma \in \{\varepsilon, \mu\}$, it holds that*

$$\min\left\{1, \frac{\gamma_0}{\gamma_1}\right\} |\boldsymbol{\xi}|^2 \leq \boldsymbol{\xi} \cdot \mathbb{M}^{\gamma} \boldsymbol{\xi} \leq \max\left\{1, \frac{\gamma_0}{\gamma_1}\right\} |\boldsymbol{\xi}|^2$$

for μ−a.e. $x \in B_R(0)$. For ε_1 with $\mathrm{Re}(\varepsilon_1) < 0$ and $\mathrm{Im}(\varepsilon_1) > 0$ there is a $\beta \in (0, \pi/2)$ with $\mathrm{Re}(\mathrm{e}^{\mathrm{i}\beta}\overline{\varepsilon_{\rho_n}}) > 0$ and $\mathrm{Re}(\mathrm{e}^{\mathrm{i}\beta}(\overline{\varepsilon_1} - \varepsilon_0)) < 0$ such that the inequalities

$$\left(1 - \frac{|\varepsilon_0 - \overline{\varepsilon_1}|^2}{\mathrm{Re}(\mathrm{e}^{\mathrm{i}\beta}(\overline{\varepsilon_1} - \varepsilon_0)) \, \mathrm{Re}(\mathrm{e}^{\mathrm{i}\beta}\overline{\varepsilon_1})}\right) |\boldsymbol{\xi}|^2 \geq \frac{\boldsymbol{\xi} \cdot \mathrm{Re}(\mathrm{e}^{\mathrm{i}\beta}(\overline{\varepsilon_1} - \varepsilon_0)\mathbb{M}^{\varepsilon})\boldsymbol{\xi}}{\mathrm{Re}(\mathrm{e}^{\mathrm{i}\beta}(\overline{\varepsilon_1} - \varepsilon_0))} \geq |\boldsymbol{\xi}|^2, \tag{3.59a}$$

$$\left(1 - \frac{|\varepsilon_0 - \overline{\varepsilon_1}|^2}{\mathrm{Im}(\overline{\varepsilon_1})^2}\right) |\boldsymbol{\xi}|^2 \leq \frac{\boldsymbol{\xi} \cdot \mathrm{Im}((\overline{\varepsilon_1} - \varepsilon_0)\mathbb{M}^{\varepsilon})\boldsymbol{\xi}}{\mathrm{Im}\,(\overline{\varepsilon_1})} \leq |\boldsymbol{\xi}|^2 \tag{3.59b}$$

hold for μ−a.e. $x \in B_R(0)$.

Proof. We show the assertion for complex-valued ε_1 only. Let $\boldsymbol{\xi} \in \mathbb{R}^3$. As in [29, Chap. 4] it can be shown that

$$\begin{aligned}
&\sum_{1 \leq i,j \leq 3} \xi_i \xi_j \int_{B_R(0)} (\overline{\varepsilon_1} - \varepsilon_0) |D_{\rho_n}|^{-1} \chi_{D_{\rho_n}} \nabla v_{\rho_n}^{(j)} \cdot \nabla V^{(i)} \psi \, \mathrm{d}\boldsymbol{x} \\
&= |D_{\rho_n}|^{-1} \sum_{1 \leq i,j \leq 3} \xi_i \xi_j \int_{D_{\rho_n}} (\overline{\varepsilon_1} - \varepsilon_0) \nabla V^{(j)} \cdot \nabla V^{(i)} \psi \, \mathrm{d}\boldsymbol{x} \\
&\quad + |D_{\rho_n}|^{-1} \sum_{1 \leq i,j \leq 3} \xi_i \xi_j \int_{B_R(0)} \overline{\varepsilon_{\rho_n}} \nabla (v_{\rho_n}^{(j)} - V^{(j)}) \cdot \nabla \left(V^{(i)} - \overline{v_{\rho_n}^{(i)}}\right) \psi \, \mathrm{d}\boldsymbol{x} + o(1)
\end{aligned} \tag{3.60}$$

for all $\psi \in C(\overline{B_R(0)})$. We define the functions

$$V^{(\boldsymbol{\xi})} = \sum_{i=1}^{3} \xi_i V^{(i)} = \sum_{i=1}^{3} \xi_i \left(x_i - |\partial B_R(0)|^{-1} \int_{\partial B_R(0)} x_i \, \mathrm{d}s \right) \quad \text{and} \quad v_{\rho_n}^{(\boldsymbol{\xi})} = \sum_{i=1}^{3} \xi_i v_{\rho_n}^{(i)}$$

and conclude for $\rho_n \to 0$ in (3.60) that

$$\begin{aligned} \sum_{1 \le i,j \le 3} \int_{B_R(0)} (\overline{\varepsilon_1} - \varepsilon_0) M_{ij} \xi_i \xi_j \psi \, \mathrm{d}\mu \;=\; & |D_{\rho_n}|^{-1} \int_{D_{\rho_n}} (\overline{\varepsilon_1} - \varepsilon_0) \left| \nabla V^{(\boldsymbol{\xi})} \right|^2 \psi \, \mathrm{d}\boldsymbol{x} \\ & - |D_{\rho_n}|^{-1} \int_{B_R(0)} \overline{\varepsilon_{\rho_n}} \left| \nabla (v_{\rho_n}^{(\boldsymbol{\xi})} - V^{(\boldsymbol{\xi})}) \right|^2 \psi \, \mathrm{d}\boldsymbol{x} + o(1) \,. \end{aligned} \tag{3.61}$$

We consider (3.61) for real and positive ψ only and take the imaginary part on both sides. This gives that

$$\int_{B_R(0)} \boldsymbol{\xi} \cdot \mathrm{Im}\left((\overline{\varepsilon_1} - \varepsilon_0) \mathbb{M}^{\varepsilon} \right) \boldsymbol{\xi} \psi \, \mathrm{d}\mu \;\ge\; |D_{\rho_n}|^{-1} \int_{D_{\rho_n}} \mathrm{Im}\,(\overline{\varepsilon_1}) \left| \nabla V^{(\boldsymbol{\xi})} \right|^2 \psi \, \mathrm{d}\boldsymbol{x} + o(1) \,,$$

since $\mathrm{Im}(\overline{\varepsilon_{\rho_n}}) \le 0$. Further, we take the limit $\rho_n \to 0$ on the right hand side and see that

$$\mathrm{Im}\,(\overline{\varepsilon_1}) \, |\boldsymbol{\xi}|^2 \;\le\; \boldsymbol{\xi} \cdot \mathrm{Im}\left((\overline{\varepsilon_1} - \varepsilon_0) \mathbb{M}^{\varepsilon} \right) \boldsymbol{\xi} \,.$$

We write $\overline{\varepsilon_1} = |\varepsilon_1| \mathrm{e}^{\mathrm{i}\alpha}$ with $\alpha \in (\pi, 3\pi/2)$. We multiply both sides of (3.61) with $\mathrm{e}^{\mathrm{i}\beta}$, where $\beta = 3\pi/2 - \alpha + c$ and $c > 0$ is so small that $\mathrm{Re}(\mathrm{e}^{\mathrm{i}\beta} \overline{\varepsilon_{\rho_n}}) > 0$ and $\mathrm{Re}(\mathrm{e}^{\mathrm{i}\beta}(\overline{\varepsilon_1} - \varepsilon_0)) < 0$. This gives that

$$\int_{B_R(0)} \boldsymbol{\xi} \cdot \mathrm{Re}\big(\mathrm{e}^{\mathrm{i}\beta} ((\overline{\varepsilon_1} - \varepsilon_0) \mathbb{M}^{\varepsilon}) \big) \boldsymbol{\xi} \psi \, \mathrm{d}\mu \le |D_{\rho_n}|^{-1} \int_{D_{\rho_n}} \mathrm{Re}\big(\mathrm{e}^{\mathrm{i}\beta} (\overline{\varepsilon_1} - \varepsilon_0) \big) \left| \nabla V^{(\boldsymbol{\xi})} \right|^2 \psi \, \mathrm{d}\boldsymbol{x} + o(1)$$

and the limit $\rho_n \to 0$ shows that

$$\boldsymbol{\xi} \cdot \mathrm{Re}\big(\mathrm{e}^{\mathrm{i}\beta} (\overline{\varepsilon_1} - \varepsilon_0) \mathbb{M}^{\varepsilon} \big) \boldsymbol{\xi} \;\le\; \mathrm{Re}\big(\mathrm{e}^{\mathrm{i}\beta} \, (\overline{\varepsilon_1} - \varepsilon_0) \big) |\boldsymbol{\xi}|^2 \,.$$

We rearrange the terms in (3.60) and see that

$$\begin{aligned} & |D_{\rho_n}|^{-1} \int_{B_R(0)} \overline{\varepsilon_{\rho_n}} \left| \nabla (V^{(\boldsymbol{\xi})} - v_{\rho_n}^{(\boldsymbol{\xi})}) \right|^2 \psi \, \mathrm{d}\boldsymbol{x} \\ & \qquad = |D_{\rho_n}|^{-1} \int_{D_{\rho_n}} (\overline{\varepsilon_1} - \varepsilon_0) \nabla (V^{(\boldsymbol{\xi})} - v_{\rho_n}^{(\boldsymbol{\xi})}) \cdot \nabla V^{(\boldsymbol{\xi})} \psi \, \mathrm{d}\boldsymbol{x} + o(1) \,. \end{aligned}$$

As before, we consider real and positive ψ. We multiply both sides with -1 and take the imaginary part. This gives

$$\begin{aligned} & |D_{\rho_n}|^{-1} \int_{B_R(0)} \mathrm{Im}(-\overline{\varepsilon_{\rho_n}}) \left| \nabla (V^{(\boldsymbol{\xi})} - v_{\rho_n}^{(\boldsymbol{\xi})}) \right|^2 \psi \, \mathrm{d}\boldsymbol{x} \\ & \le |D_{\rho_n}|^{-1} \left| \int_{D_{\rho_n}} (\varepsilon_0 - \overline{\varepsilon_1}) \nabla (V^{(\boldsymbol{\xi})} - v_{\rho_n}^{(\boldsymbol{\xi})}) \cdot \nabla V^{(\boldsymbol{\xi})} \psi \, \mathrm{d}\boldsymbol{x} \right| + o(1) \\ & \le |D_{\rho_n}|^{-1} \left(\int_{D_{\rho_n}} \frac{|\varepsilon_0 - \overline{\varepsilon_1}|^2}{(-\mathrm{Im}(\overline{\varepsilon_1}))} \left| \nabla V^{(\boldsymbol{\xi})} \right|^2 \psi \, \mathrm{d}\boldsymbol{x} \right)^{1/2} \left(\int_{D_{\rho_n}} (-\mathrm{Im}(\overline{\varepsilon_1})) \left| \nabla (V^{(\boldsymbol{\xi})} - v_{\rho_n}^{(\boldsymbol{\xi})}) \right|^2 \psi \, \mathrm{d}\boldsymbol{x} \right)^{1/2} \\ & \quad + o(1) \,. \end{aligned}$$

The inequality $a^2 < ab + c$ implies that $a^2 < ab + c + (a-b)^2 = a^2 + c + b^2 - ab < b^2 + 2c$. This shows that

$$|D_{\rho_n}|^{-1} \int_{B_R(0)} \mathrm{Im}(\overline{\varepsilon_{\rho_n}}) \left| \nabla (V^{(\boldsymbol{\xi})} - v_{\rho_n}^{(\boldsymbol{\xi})}) \right|^2 \psi \, \mathrm{d}\boldsymbol{x} \;\ge\; |D_{\rho_n}|^{-1} \int_{D_{\rho_n}} \frac{|\varepsilon_0 - \overline{\varepsilon_1}|^2}{\mathrm{Im}(\overline{\varepsilon_1})} \left| \nabla V^{(\boldsymbol{\xi})} \right|^2 \psi \, \mathrm{d}\boldsymbol{x} + o(1) \,.$$

We consider the imaginary part of the identity (3.61) again, estimate the second term on the right hand side using the inequality above and apply the limit $\rho_n \to 0$ to get that

$$\boldsymbol{\xi} \cdot \operatorname{Im}\left((\overline{\varepsilon_1} - \varepsilon_0)\mathbb{M}^\varepsilon\right)\boldsymbol{\xi} \;\leq\; \left(\operatorname{Im}\left(\overline{\varepsilon_1}\right) - \frac{|\varepsilon_0 - \overline{\varepsilon_1}|^2}{\operatorname{Im}(\overline{\varepsilon_1})}\right)|\boldsymbol{\xi}|^2.$$

For the real part, we study a similar setting. We multiply both sides of (3.61) with $e^{\mathrm{i}\beta}$, where β is chosen as before, and consider the real part. We perform the same calculations as before, which yields that

$$|D_{\rho_n}|^{-1}\int_{B_R(0)} \operatorname{Re}\left(\mathrm{e}^{\mathrm{i}\beta}\overline{\varepsilon_{\rho_n}}\right)\left|\nabla(V^{(\boldsymbol{\xi})} - v_{\rho_n}^{(\boldsymbol{\xi})})\right|^2\psi\,\mathrm{d}\boldsymbol{x} \;\leq\; |D_{\rho_n}|^{-1}\int_{D_{\rho_n}} \frac{|\varepsilon_0 - \overline{\varepsilon_1}|^2}{\operatorname{Re}\left(\mathrm{e}^{\mathrm{i}\beta}\overline{\varepsilon_1}\right)}\left|\nabla V^{(\boldsymbol{\xi})}\right|^2\psi\,\mathrm{d}\boldsymbol{x} + o(1)\,.$$

Using this inequality, we finally deduce from (3.61) that

$$\left(\operatorname{Re}(\mathrm{e}^{\mathrm{i}\beta}(\overline{\varepsilon_1} - \varepsilon_0)) - \frac{|\varepsilon_0 - \overline{\varepsilon_1}|^2}{\operatorname{Re}(\mathrm{e}^{\mathrm{i}\beta}\overline{\varepsilon_1})}\right)|\boldsymbol{\xi}|^2 \;\leq\; \boldsymbol{\xi}\cdot\operatorname{Re}(\mathrm{e}^{\mathrm{i}\beta}(\overline{\varepsilon_1} - \varepsilon_0)\mathbb{M}^\varepsilon)\boldsymbol{\xi}\,.$$

□

Exactly as in the proof of Proposition 3.13 we introduce a vector $\boldsymbol{\xi} \in S^2$, define $V^{(\boldsymbol{\xi})} = \sum_{i=1}^3 \xi_i V^{(i)}$ and find that

$$\operatorname{div}\left(\gamma_0\nabla V^{(\boldsymbol{\xi})}\right) \;=\; 0 \quad \text{in } B_R(0), \qquad \gamma_0\frac{\partial V^{(\boldsymbol{\xi})}}{\partial \boldsymbol{\nu}} \;=\; \gamma_0\boldsymbol{\xi}\cdot\boldsymbol{\nu} \quad \text{on } \partial B_R(0)\,.$$

Moreover, defining $v_{\rho_n}^{(\boldsymbol{\xi})} = \sum_{i=1}^3 \xi_i v_{\rho_n}^{(i)}$ gives that

$$\operatorname{div}\left(\gamma_{\rho_n}\nabla v_{\rho_n}^{(\boldsymbol{\xi})}\right) \;=\; 0 \quad \text{in } B_R(0), \qquad \gamma_0\frac{\partial v_{\rho_n}^{(\boldsymbol{\xi})}}{\partial \boldsymbol{\nu}} \;=\; \gamma_0\boldsymbol{\xi}\cdot\boldsymbol{\nu} \quad \text{on } \partial B_R(0)\,.$$

Noting that $\nabla V^{(\boldsymbol{\xi})} = \boldsymbol{\xi}$ and using the definition from (3.50), we find that for all $\psi \in C(\overline{B_R(0)})$ it holds that

$$\frac{1}{2\ell}\int_K \boldsymbol{\xi}\cdot\mathbb{M}^\gamma\boldsymbol{\xi}\psi\,\mathrm{d}s \;=\; \int_{B_R(0)}\boldsymbol{\xi}\cdot\mathbb{M}^\gamma\boldsymbol{\xi}\psi\,\mathrm{d}\mu \;=\; \lim_{n\to\infty}\frac{1}{|D_{\rho_n}|}\int_{D_{\rho_n}}\nabla V^{(\boldsymbol{\xi})}\cdot\nabla v_{\rho_n}^{(\boldsymbol{\xi})}\psi\,\mathrm{d}\boldsymbol{x}\,. \tag{3.62}$$

Remark 3.14. As stated in [30, Lem. 1], the characterization of $\mathbb{M}^\gamma$ in (3.62) still holds true when $v_{\rho_n}^{(\boldsymbol{\xi})}$ is replaced by $\widetilde{v}_{\rho_n}^{(\boldsymbol{\xi})}$ on the right hand side, where $\widetilde{v}_{\rho_n}^{(\boldsymbol{\xi})} \in H^1(B_R(0))$ is the unique solution to

$$\operatorname{div}\left(\gamma_{\rho_n}\nabla\widetilde{v}_{\rho_n}^{(\boldsymbol{\xi})}\right) \;=\; 0 \quad \text{in } B_R(0), \qquad \widetilde{v}_{\rho_n}^{(\boldsymbol{\xi})} \;=\; V^{(\boldsymbol{\xi})} \quad \text{on } \partial B_R(0)\,. \tag{3.63}$$

Using $\widetilde{v}_{\rho_n}^{(\boldsymbol{\xi})}$ from (3.63), we define the corrector potential $W_{\rho_n}^{(\boldsymbol{\xi})} = \widetilde{v}_{\rho_n}^{(\boldsymbol{\xi})} - V^{(\boldsymbol{\xi})} \in H_0^1(B_R(0))$ satisfying

$$\operatorname{div}\left(\gamma_{\rho_n}\nabla W_{\rho_n}^{(\boldsymbol{\xi})}\right) \;=\; -\operatorname{div}\left((\gamma_{\rho_n} - \gamma_0)\,\boldsymbol{\xi}\right) \quad \text{in } B_R(0), \qquad W_{\rho_n}^{(\boldsymbol{\xi})} \;=\; 0 \quad \text{on } \partial B_R(0)\,. \tag{3.64}$$

Considering the sequence $(D_{\rho_n})_n$ from Theorem 3.6 and in view of (3.62), we find that the polarization tensor $\mathbb{M}^\gamma \in L^2(K, \mathbb{C}^{3\times 3})$ is uniquely defined by

$$\frac{1}{2\ell}\int_K \boldsymbol{\xi}\cdot\mathbb{M}^\gamma\boldsymbol{\xi}\psi\,\mathrm{d}s \;=\; \frac{1}{|D_{\rho_n}|}\int_{D_{\rho_n}}|\boldsymbol{\xi}|^2\psi\,\mathrm{d}\boldsymbol{x} + \frac{1}{|D_{\rho_n}|}\int_{D_{\rho_n}}\left(\boldsymbol{\xi}\cdot\nabla W_{\rho_n}^{(\boldsymbol{\xi})}\right)\psi\,\mathrm{d}\boldsymbol{x} + o(1) \tag{3.65}$$

for all $\psi \in C(\overline{B_R(0)})$ and $\boldsymbol{\xi} \in S^2$.

Similarly, we assign a two-dimensional polarization tensor $m^\gamma \in \mathbb{C}^{2\times 2}$ to the sequence of cross-sections $(D'_{\rho_n})_n$ of the scattering objects $(D_{\rho_n})_n$ as follows. As before, we denote by $r > 0$ the radius, such that the local parametrization in (3.5) is well-defined. Then, we set

$$\gamma'_{\rho_n}(\eta,\zeta) \;=\; \begin{cases} \gamma_1, & (\eta,\zeta) \in D'_{\rho_n}\,, \\ \gamma_0, & (\eta,\zeta) \in B'_r(0) \setminus \overline{D'_{\rho_n}}\,, \end{cases}$$

i.e. γ'_{ρ_n} is the electric permittivity or the magnetic permeability distribution associated to the cross-section D'_{ρ_n}. For each $\boldsymbol{\xi}' \in S^1$ we define the two-dimensional corrector potential $w_{\rho_n} \in H^1_0(B'_r(0))$ as the unique solution to

$$\mathrm{div}'_{\eta,\zeta}\left(\gamma'_{\rho_n}\nabla'_{\eta,\zeta} w^{(\boldsymbol{\xi}')}_{\rho_n}\right) \;=\; -\mathrm{div}'_{\eta,\zeta}((\gamma_1-\gamma_0)\,\chi_{D'_{\rho_n}}\boldsymbol{\xi}') \quad \text{in } B'_r(0), \quad w^{(\boldsymbol{\xi}')}_{\rho_n} \;=\; 0 \quad \text{on } \partial B'_r(0)\,. \tag{3.66}$$

The operators $\mathrm{div}'_{\eta,\zeta}$ and $\nabla'_{\eta,\zeta}$ denote the two-dimensional divergence and two-dimensional gradient with respect to the local coordinates of the cross-section (η,ζ), as introduced in (3.14). Recalling the measure μ' from (3.11), the two-dimensional polarization tensor $m^\gamma \in L^2\left(K,\mathbb{C}^{2\times 2}\right)$ is now defined by

$$\boldsymbol{\xi}'\cdot m^\gamma\boldsymbol{\xi}'\psi(0) \;=\; \frac{1}{|D'_{\rho_n}|}\int_{D'_{\rho_n}} |\boldsymbol{\xi}'|^2\psi\;\mathrm{d}\boldsymbol{x} + \frac{1}{|D'_{\rho_n}|}\int_{D'_{\rho_n}}\left(\boldsymbol{\xi}'\cdot\nabla'_{\eta,\zeta}w^{(\boldsymbol{\xi}')}_{\rho_n}\right)\psi\;\mathrm{d}\boldsymbol{x} + o(1) \tag{3.67}$$

for all $\psi \in C(\overline{B'_r(0)})$ and any $\boldsymbol{\xi}' \in S^1$.

Remark 3.15. The definition of the polarization tensor in (3.65) remains valid, if we replace the domain $B_R(0)$ in (3.64) by the tubular neighborhood Ω_r from (3.6) (see [30, Rmk. 1]). The regularity results that are used in the proof of [30, Rem. 1] are applicable because Ω_r is C^2 away from the ends of the tube and convex in a neighborhood of the ends of the tube. This will be used in the next proofs.

The following theorem characterizes the polarization tensor $\mathbb{M}^\varepsilon$ and $\mathbb{M}^\mu$ for thin tubular scattering objects as in (3.7).

Theorem 3.16. *Let $K \subset B_R(0)$ be a simple C^3 center curve, and let $r > 0$ be such that the local parametrization in (3.5) is well defined. Let $(\rho_n)_n \subset (0, r/2)$ be a sequence of radii converging to zero, and let $(D'_{\rho_n})_n$ be a sequence of Lipschitz cross-sections with $D'_{\rho_n} = \rho_n D' \subset B'_{\rho_n}(0)$ for all $n \in \mathbb{N}$. Suppose that $(D_{\rho_n})_n \subset B_R(0)$ is the corresponding sequence of thin tubular scattering objects as in (3.7), where the cross-section twists along the center curve subject to a parameter dependent rotation matrix $R_\theta \in C^2([-L,L],\mathbb{R}^{2\times 2})$. For $\gamma \in \{\varepsilon,\mu\}$, denoting by $(\gamma_{\rho_n})_n$ a parameter distribution as in (3.8), let $\mathbb{M}^\gamma$ be the polarization tensor corresponding to the thin tubular scattering objects $(D_{\rho_n})_n$ from (3.65). The following pointwise characterization of $\mathbb{M}^\gamma$ holds for a.e. $s \in (-\ell,\ell)$:*

(a) For the unit tangent vector $\boldsymbol{t}_\Gamma(s)$ it holds that

$$\boldsymbol{t}_\Gamma(s)\cdot\mathbb{M}^\gamma(\boldsymbol{p}_\Gamma(s))\boldsymbol{t}_\Gamma(s) \;=\; 1 \quad \text{for a.e. } s \in (-\ell,\ell)\,. \tag{3.68}$$

(b) Let $\boldsymbol{\xi}' \in S^1$, and let $\boldsymbol{\xi} \in C^1(K,S^2)$ be given by $\boldsymbol{\xi}(s) = \left[\boldsymbol{r}_\Gamma \,\middle|\, \mathbf{s}_\Gamma\right]\boldsymbol{\xi}' \in S^2$ for all $s \in (-\ell,\ell)$. Then

$$\boldsymbol{\xi}(s)\cdot\mathbb{M}^\gamma(\boldsymbol{p}_\Gamma(s))\boldsymbol{\xi}(s) \;=\; \boldsymbol{\xi}'\cdot(R_\theta(s)m^\gamma R_\theta^{-1}(s))\boldsymbol{\xi}' \quad \text{for a.e. } s \in (-\ell,\ell)\,. \tag{3.69}$$

Before we give a proof to Theorem 3.16 we outline its implications that we summarize in the following corollary.

Corollary 3.17. *Under the same assumptions as in Theorem 3.16, the polarization tensor* $\mathbb{M}^\gamma$ *can be written as*

$$\mathbb{M}^\gamma(s) \;=\; V(s) \left[\begin{array}{c|cc} 1 & 0 & 0 \\ \hline 0 & & \\ 0 & & R_\theta(s) m^\gamma R_\theta^{-1}(s) \end{array}\right] V(s)^\top \quad \text{for a.e. } s \in (-\ell, \ell)\,, \tag{3.70}$$

where $V(s) \in \mathbb{R}^{3\times 3}$ *for a.e.* $s \in (-\ell,\ell)$ *is the matrix that has the vectors* $\boldsymbol{t}_\Gamma(s), \boldsymbol{r}_\Gamma(s), \mathbf{s}_\Gamma(s)$ *as its columns.*

Proof. We distinguish between $\gamma_1 > 0$ and $\gamma_1 \in \mathbb{C}$ with $\mathrm{Re}(\gamma_1) < 0$ and $\mathrm{Im}(\gamma_1) > 0$. In the first case, the polarization tensor is real-valued and symmetric. Part (a) in Theorem 3.16, together with the bounds for the real polarization tensor in Proposition 3.13 directly imply that the tangent vector $\boldsymbol{t}_\Gamma(s)$ is an eigenvector for a.e. $s \in (-\ell,\ell)$ with corresponding (minimal or maximal) eigenvalue 1. Furthermore, there must be two more eigenvectors that lie in the orthogonal plane to $\boldsymbol{t}_\Gamma(s)$, the plane that is spanned by $\boldsymbol{r}_\Gamma(s)$ and $\mathbf{s}_\Gamma(s)$. Part (b) in Theorem 3.16 states, that in this plane, the polarization tensor coincides with the polarization tensor $R_\theta(s) m^\gamma R_\theta^{-1}(s)$ of the twisted two-dimensional cross-section. Thus, the representation of $\mathbb{M}^\varepsilon$ in (3.70) follows by (3.69).

For the case that $\gamma_1 \in \mathbb{C}$ with $\mathrm{Re}(\gamma_1) < 0$ and $\mathrm{Im}(\gamma_1) > 0$ the polarization tensor is not real-valued anymore (in particular it is not self-adjoint) and we need to apply the bounds for the complex-valued polarization tensor from Proposition 3.13 as follows. We replace γ by ε here, since μ is always real-valued. With $\beta \in (0, \pi/2)$ as in Proposition 3.13 we find that, for $\boldsymbol{\xi} \in S^2$,

$$\frac{\boldsymbol{\xi} \cdot \mathrm{Re}(e^{\mathrm{i}\beta}(\overline{\varepsilon_1} - \varepsilon_0)\mathbb{M}^\varepsilon)\boldsymbol{\xi}}{\mathrm{Re}(e^{\mathrm{i}\beta}(\overline{\varepsilon_1} - \varepsilon_0))} \;=\; \boldsymbol{\xi} \cdot \left(\mathrm{Re}(\mathbb{M}^\varepsilon) - \frac{\mathrm{Im}(e^{\mathrm{i}\beta}(\overline{\varepsilon_1} - \varepsilon_0))}{\mathrm{Re}(e^{\mathrm{i}\beta}(\overline{\varepsilon_1} - \varepsilon_0))} \mathrm{Im}(\mathbb{M}^\varepsilon) \right) \boldsymbol{\xi} \tag{3.71}$$

and

$$\frac{\boldsymbol{\xi} \cdot \mathrm{Im}\left((\overline{\varepsilon_1} - \varepsilon_0)\mathbb{M}^\varepsilon\right)\boldsymbol{\xi}}{\mathrm{Im}(\overline{\varepsilon_1})} \;=\; \boldsymbol{\xi} \cdot \left(\frac{\mathrm{Re}\,(\overline{\varepsilon_1} - \varepsilon_0)}{\mathrm{Im}(\overline{\varepsilon_1})} \mathrm{Im}(\mathbb{M}^\varepsilon) + \mathrm{Re}(\mathbb{M}^\varepsilon) \right) \boldsymbol{\xi}\,.$$

Therefore, we multiply (3.59a) with -1 and add it to (3.59b). This gives that

$$c_1 |\boldsymbol{\xi}|^2 \;\le\; c_2 \boldsymbol{\xi} \cdot \mathrm{Im}(\mathbb{M}^\varepsilon)\boldsymbol{\xi} \;\le\; 0 \tag{3.72}$$

with constants

$$c_1 \;=\; \frac{|\varepsilon_0 - \overline{\varepsilon_1}|^2}{\mathrm{Re}(e^{\mathrm{i}\beta}(\overline{\varepsilon_1} - \varepsilon_0))\,\mathrm{Re}(e^{\mathrm{i}\beta}\overline{\varepsilon_1})} - \frac{|\varepsilon_0 - \overline{\varepsilon_1}|^2}{\mathrm{Im}(\overline{\varepsilon_1})^2}\,, \qquad c_2 \;=\; \frac{\mathrm{Im}(e^{\mathrm{i}\beta}(\overline{\varepsilon_1} - \varepsilon_0))}{\mathrm{Re}(e^{\mathrm{i}\beta}(\overline{\varepsilon_1} - \varepsilon_0))} + \frac{\mathrm{Re}\,(\overline{\varepsilon_1} - \varepsilon_0)}{\mathrm{Im}(\overline{\varepsilon_1})}\,.$$

Due to our choice of β from Proposition 3.13 we find that

$$\mathrm{Re}(e^{\mathrm{i}\beta}(\overline{\varepsilon_1} - \varepsilon_0)) \;<\; 0\,,\; \mathrm{Im}(e^{\mathrm{i}\beta}(\overline{\varepsilon_1} - \varepsilon_0)) \;<\; 0\,,\; \mathrm{Re}(e^{\mathrm{i}\beta}\overline{\varepsilon_1}) \;>\; 0\,,\; \mathrm{Re}\,(\overline{\varepsilon_1} - \varepsilon_0) \;<\; 0\,,\; \mathrm{Im}(\overline{\varepsilon_1}) \;<\; 0$$

and therefore, $c_1 < 0$ and $c_2 > 0$. We consider (3.68) and compare the real and imaginary part on both sides, what gives that

$$\boldsymbol{t}_\Gamma(s) \cdot \mathrm{Re}(\mathbb{M}^\varepsilon)\boldsymbol{t}_\Gamma(s) \;=\; 1 \quad \text{and} \quad \boldsymbol{t}_\Gamma(s) \cdot \mathrm{Im}(\mathbb{M}^\varepsilon)\boldsymbol{t}_\Gamma(s) \;=\; 0 \quad \text{for a.e. } s \in (-\ell,\ell)\,. \tag{3.73}$$

Due to (3.72) we conclude that $\boldsymbol{t}_\Gamma(s)$ lies in the kernel of $\mathrm{Im}(\mathbb{M}^\varepsilon)$. From (3.59a) and (3.71), we find that

$$|\boldsymbol{\xi}|^2 \;\le\; \boldsymbol{\xi} \cdot A\boldsymbol{\xi} \;\le\; \left(1 - \frac{|\varepsilon_0 - \overline{\varepsilon_1}|^2}{\mathrm{Re}(e^{\mathrm{i}\beta}(\overline{\varepsilon_1} - \varepsilon_0))\,\mathrm{Re}(e^{\mathrm{i}\beta}\overline{\varepsilon_1})}\right) |\boldsymbol{\xi}|^2 \quad \text{for all } \boldsymbol{\xi} \in \mathbb{R}^3\,,$$

where

$$A = \mathrm{Re}(\mathbb{M}^\varepsilon) - \frac{\mathrm{Im}\big(e^{\mathrm{i}\beta}(\overline{\varepsilon_1} - \varepsilon_0)\big)}{\mathrm{Re}\big(e^{\mathrm{i}\beta}(\overline{\varepsilon_1} - \varepsilon_0)\big)} \mathrm{Im}(\mathbb{M}^\varepsilon) \quad \text{is self-adjoint} \quad \text{and} \quad \boldsymbol{t}_\Gamma(s) \cdot A\boldsymbol{t}_\Gamma(s) = 1$$

for a.e. $s \in (-\ell, \ell)$. The latter property follows by (3.73). This gives that $\boldsymbol{t}_\Gamma$ is an eigenvector of A with eigenvalue 1. However, as we have seen before, $\boldsymbol{t}_\Gamma$ is also an eigenvector of $\mathrm{Im}(\mathbb{M}^\varepsilon)$ with eigenvalue 0 and therefore,

$$\boldsymbol{t}_\Gamma = A\boldsymbol{t}_\Gamma = \left(\mathrm{Re}(\mathbb{M}^\varepsilon) - \frac{\mathrm{Im}\big(e^{\mathrm{i}\beta}(\overline{\varepsilon_1} - \varepsilon_0)\big)}{\mathrm{Re}\big(e^{\mathrm{i}\beta}(\overline{\varepsilon_1} - \varepsilon_0)\big)} \mathrm{Im}(\mathbb{M}^\varepsilon)\right) \boldsymbol{t}_\Gamma = \mathrm{Re}(\mathbb{M}^\varepsilon)\boldsymbol{t}_\Gamma\,,$$

i.e. $\boldsymbol{t}_\Gamma$ is an eigenvector of $\mathrm{Re}(\mathbb{M}^\varepsilon)$ with corresponding eigenvalue 1. The representation of $\mathbb{M}^\varepsilon$ in (3.70) follows by (3.69). □

The proof of Theorem 3.16 relies on the following proposition, which extends the characterization of the polarization tensor in (3.65) from constant vectors $\boldsymbol{\xi} \in \mathbb{R}^3$ to vector valued functions $\boldsymbol{\xi} \in C^1(\Omega_r, S^2)$.

Proposition 3.18. *Let $\boldsymbol{\xi} \in C^1(\Omega_r, S^2)$ and denote by $W_{\rho_n}^{(\boldsymbol{\xi})} \in H_0^1(\Omega_r)$ the solution to (3.64). Then, the polarization tensor satisfies*

$$\frac{1}{2\ell}\int_K \boldsymbol{\xi} \cdot \mathbb{M}^\gamma \boldsymbol{\xi}\psi \,\mathrm{d}s = \frac{1}{|D_{\rho_n}|}\int_{D_{\rho_n}} |\boldsymbol{\xi}|^2\psi \,\mathrm{d}\boldsymbol{x} + \frac{1}{|D_{\rho_n}|}\int_{D_{\rho_n}} \left(\boldsymbol{\xi} \cdot \nabla W_{\rho_n}^{(\boldsymbol{\xi})}\right)\psi \,\mathrm{d}\boldsymbol{x} + o(1) \tag{3.74}$$

for all $\psi \in C(\overline{\Omega_r})$.

Proof. Denote by $(\boldsymbol{e}_1, \boldsymbol{e}_2, \boldsymbol{e}_3)$ the standard basis of $\mathbb{R}^3$ and let $\boldsymbol{\xi} = \sum_{i=1}^3 \xi_i \boldsymbol{e}_i \in C^1(\Omega_r, S^2)$ with $\xi_i \in C^1(\Omega_r, \mathbb{R})$ for $1 \le i \le 3$. Let $W_{\rho_n}^{(\boldsymbol{\xi})} \in H_0^1(\Omega_r)$ be the solution to (3.64) and let $W_{\rho_n}^{(\boldsymbol{e}_j)}$, $1 \le j \le 3$, be the solution to (3.64) with $\boldsymbol{\xi} = \boldsymbol{e}_j$. Then, using (3.50), we find that

$$\begin{aligned}
&\frac{1}{2\ell}\int_K \boldsymbol{\xi}(\boldsymbol{x}) \cdot \mathbb{M}^\gamma(\boldsymbol{x})\boldsymbol{\xi}(\boldsymbol{x})\psi(\boldsymbol{x}) \,\mathrm{d}s(\boldsymbol{x}) \\
&= \sum_{i,j=1}^3 \frac{1}{|D_{\rho_n}|}\int_{D_{\rho_n}} \boldsymbol{e}_i \cdot \nabla v_{\rho_n}^{(\boldsymbol{e}_j)}(\boldsymbol{x}) \left(\xi_i\xi_j\psi\right)(\boldsymbol{x}) \,\mathrm{d}\boldsymbol{x} + o(1) \\
&= \sum_{i,j=1}^3 \frac{1}{|D_{\rho_n}|}\int_{D_{\rho_n}} \boldsymbol{e}_i \cdot \nabla \tilde{v}_{\rho_n}^{(\boldsymbol{e}_j)}(\boldsymbol{x}) \left(\xi_i\xi_j\psi\right)(\boldsymbol{x}) \,\mathrm{d}\boldsymbol{x} + o(1) \\
&= \frac{1}{|D_{\rho_n}|}\sum_{i,j=1}^3 \left(\int_{D_{\rho_n}} \boldsymbol{e}_i \cdot \nabla V^{(\boldsymbol{e}_j)} \left(\xi_i\xi_j\psi\right)(\boldsymbol{x}) \,\mathrm{d}\boldsymbol{x} + \int_{D_{\rho_n}} \boldsymbol{e}_i \cdot \nabla W_{\rho_n}^{(\boldsymbol{e}_j)}(\boldsymbol{x}) \left(\xi_i\xi_j\psi\right)(\boldsymbol{x}) \,\mathrm{d}\boldsymbol{x}\right) + o(1) \\
&= \frac{1}{|D_{\rho_n}|}\int_{D_{\rho_n}} |\boldsymbol{\xi}(\boldsymbol{x})|^2\psi(\boldsymbol{x}) \,\mathrm{d}\boldsymbol{x} + \frac{1}{|D_{\rho_n}|}\int_{D_{\rho_n}} \boldsymbol{\xi}(\boldsymbol{x}) \cdot \nabla W_{\rho_n}^{(\boldsymbol{\xi})}(\boldsymbol{x})\psi(\boldsymbol{x}) \,\mathrm{d}\boldsymbol{x} \\
&\quad - \frac{1}{|D_{\rho_n}|}\int_{D_{\rho_n}} \boldsymbol{\xi}(\boldsymbol{x}) \cdot \left(\nabla W_{\rho_n}^{(\boldsymbol{\xi})}(\boldsymbol{x}) - \sum_{j=1}^3 \xi_j(\boldsymbol{x}) \nabla W_{\rho_n}^{(\boldsymbol{e}_j)}(\boldsymbol{x})\right)\psi(\boldsymbol{x}) \,\mathrm{d}\boldsymbol{x} + o(1)
\end{aligned}$$

for all $\psi \in C(\overline{B_R(0)})$. An application of Hölder's inequality for the last integral gives that

$$\left|\int_{D_{\rho_n}} \boldsymbol{\xi} \cdot \left(\nabla W_{\rho_n}^{(\boldsymbol{\xi})} - \sum_{j=1}^3 \xi_j \nabla W_{\rho_n}^{(\boldsymbol{e}_j)}\right)\psi \,\mathrm{d}\boldsymbol{x}\right| \le C|D_{\rho_n}|^{1/2} \left\|\nabla W_{\rho_n}^{(\boldsymbol{\xi})} - \sum_{j=1}^3 \xi_j \nabla W_{\rho_n}^{(\boldsymbol{e}_j)}\right\|_{L^2(\Omega_r)}. \tag{3.75}$$

In order to show the assertion we prove that the right hand side of (3.75) is in $o(|D_{\rho_n}|)$ as $n \to \infty$. Using (3.64) we obtain

$$\begin{aligned}\operatorname{div}\left(\gamma_{\rho_n}\nabla\left(W_{\rho_n}^{(\boldsymbol{\xi})}-\sum_{j=1}^{3}\xi_j W_{\rho_n}^{(\boldsymbol{e}_j)}\right)\right)\\ = -\operatorname{div}\left(\left(\gamma_{\rho_n}-\gamma_0\right)\boldsymbol{\xi}\right)-\sum_{j=1}^{3}\operatorname{div}\left(\gamma_{\rho_n}\left(W_{\rho_n}^{(\boldsymbol{e}_j)}\nabla\xi_j+\nabla W_{\rho_n}^{(\boldsymbol{e}_j)}\xi_j\right)\right). \quad (3.76)\end{aligned}$$

Applying (3.64) once more, we find for the third term on the right hand side of (3.76) that

$$-\sum_{j=1}^{3}\operatorname{div}\left(\gamma_{\rho_n}\nabla W_{\rho_n}^{(\boldsymbol{e}_j)}\xi_j\right) = -\sum_{j=1}^{3}\gamma_{\rho_n}\nabla W_{\rho_n}^{(\boldsymbol{e}_j)}\cdot\nabla\xi_j+\sum_{j=1}^{3}\operatorname{div}\left(\left(\gamma_{\rho_n}-\gamma_0\right)\boldsymbol{e}_j\right)\xi_j\,.$$

With $\boldsymbol{\xi}=\sum_{j=1}^{3}\xi_j\boldsymbol{e}_j$, the first term on the right hand side of (3.76) can be written as

$$-\operatorname{div}\left(\left(\gamma_{\rho_n}-\gamma_0\right)\boldsymbol{\xi}\right) = -\sum_{j=1}^{3}\operatorname{div}\left(\left(\gamma_{\rho_n}-\gamma_0\right)\boldsymbol{e}_j\right)\xi_j-\sum_{j=1}^{3}\left(\gamma_{\rho_n}-\gamma_0\right)\boldsymbol{e}_j\cdot\nabla\xi_j\,.$$

Therefore, (3.76) turns into

$$\begin{aligned}\operatorname{div}\left(\gamma_{\rho_n}\nabla\left(W_{\rho_n}^{(\boldsymbol{\xi})}-\sum_{j=1}^{3}\xi_j W_{\rho_n}^{(e_j)}\right)\right)\\ = -\sum_{j=1}^{3}\left(\gamma_{\rho_n}-\gamma_0\right)e_j\cdot\nabla\xi_j-\sum_{j=1}^{3}\operatorname{div}\left(\gamma_{\rho_n}W_{\rho_n}^{(e_j)}\nabla\xi_j\right)-\sum_{j=1}^{3}\gamma_{\rho_n}\nabla W_{\rho_n}^{(e_j)}\cdot\nabla\xi_j. \quad (3.77)\end{aligned}$$

Considering (3.77), we define $r_{\rho_n}^{(1)}, r_{\rho_n}^{(2)}, r_{\rho_n}^{(3)} \in H_0^1(\Omega_r)$ as the unique solutions to

$$\operatorname{div}\left(\gamma_{\rho_n}\nabla r_{\rho_n}^{(1)}\right) = -\sum_{j=1}^{3}\operatorname{div}(\gamma_{\rho_n}W_{\rho_n}^{(\boldsymbol{e}_j)}\nabla\xi_j) \quad \text{in } \Omega_r\,, \qquad r_{\rho_n}^{(1)} = 0 \quad \text{on } \partial\Omega_r\,, \quad (3.78)$$

$$\operatorname{div}\left(\gamma_{\rho_n}\nabla r_{\rho_n}^{(2)}\right) = -\sum_{j=1}^{3}\gamma_{\rho_n}\nabla W_{\rho_n}^{(\boldsymbol{e}_j)}\cdot\nabla\xi_j \quad \text{in } \Omega_r\,, \qquad r_{\rho_n}^{(2)} = 0 \quad \text{on } \partial\Omega_r\,, \quad (3.79)$$

$$\operatorname{div}\left(\gamma_{\rho_n}\nabla r_{\rho_n}^{(3)}\right) = -\sum_{j=1}^{3}\left(\gamma_{\rho_n}-\gamma_0\right)\boldsymbol{e}_j\cdot\nabla\xi_j \quad \text{in } \Omega_r\,, \qquad r_{\rho_n}^{(3)} = 0 \quad \text{on } \partial\Omega_r\,. \quad (3.80)$$

The unique solutions to these Dirichlet problems imply that

$$W_{\rho_n}^{(\boldsymbol{\xi})}-\sum_{j=1}^{3}\xi_j W_{\rho_n}^{(\boldsymbol{e}_j)} = r_{\rho_n}^{(1)}+r_{\rho_n}^{(2)}+r_{\rho_n}^{(3)} \quad (3.81)$$

and we find the following estimates for $r_{\rho_n}^{(1)}, r_{\rho_n}^{(2)}$ and $r_{\rho_n}^{(3)}$. Using the well-posedness of (3.78) (see e.g. [63, Cor. 8.7]), together with (B.3) yields that

$$\begin{aligned}\|r_{\rho_n}^{(1)}\|_{H^1(\Omega_r)} \le \left\|\sum_{j=1}^{3}\gamma_{\rho_n}W_{\rho_n}^{(\boldsymbol{e}_j)}\nabla\xi_j\right\|_{L^2(\Omega_r)} &\le C\max_{j=1,2,3}\|\nabla\xi_j\|_{L^\infty(\Omega_r)}\|W_{\rho_n}^{(\boldsymbol{e}_j)}\|_{L^2(\Omega_r)}\\ &\le C\,\|\boldsymbol{\xi}\|_{C^1(\Omega_r)}\,|D_{\rho_n}|^{3/4}.\end{aligned}$$

Similarly, using the Poincaré inequality, the weak formulation of (3.79), Hölder's inequality, the Sobolev embedding theorem giving that $H^1_0(\Omega_r) \subset L^6(\Omega_r)$ (see e.g. [63, Thm. 7.10]) and (B.4), we find that

$$\begin{aligned}
\|r^{(2)}_{\rho_n}\|^2_{H^1(\Omega_r)} &\leq C \left| \int_{\Omega_r} \gamma_{\rho_n} \nabla r^{(2)}_{\rho_n} \cdot \nabla \overline{r^{(2)}_{\rho_n}} \, \mathrm{d}\boldsymbol{x} \right| \leq C \left| \int_{\Omega_r} \sum_{j=1}^{3} \gamma_{\rho_n} \left(\nabla W^{(\boldsymbol{e}_j)}_{\rho_n} \cdot \nabla \xi_j \right) \overline{r^{(2)}_{\rho_n}} \, \mathrm{d}\boldsymbol{x} \right| \\
&\leq C \left\| \sum_{j=1}^{3} \gamma_{\rho_n} \nabla W^{(\boldsymbol{e}_j)}_{\rho_n} \right\|_{L^{6/5}(\Omega_r)} \max_{j=1,2,3} \|\nabla \xi_j\|_{L^\infty(\Omega_r)} \, \|r^{(2)}_{\rho_n}\|_{L^6(\Omega_r)} \\
&\leq C |D_{\rho_n}|^{5/6} \, \|\boldsymbol{\xi}\|_{C^1(\Omega_r)} \, \|r^{(2)}_{\rho_n}\|_{H^1(\Omega_r)} \, .
\end{aligned}$$

For $r^{(3)}_{\rho_n}$ we apply the Poincaré inequality, the weak formulation of (3.80), Hölder's inequality and the Sobolev embedding theorem to see that

$$\begin{aligned}
\|r^{(3)}_{\rho_n}\|^2_{H^1(\Omega_r)} &\leq C \left| \int_{\Omega_r} \gamma_{\rho_n} \nabla r^{(3)}_{\rho_n} \cdot \nabla \overline{r^{(3)}_{\rho_n}} \, \mathrm{d}\boldsymbol{x} \right| = \left| \int_{\Omega_r} (\gamma_{\rho_n} - \gamma_0) \sum_{j=1}^{3} (e_j \cdot \nabla \xi_j) \, r^{(3)}_{\rho_n} \, \mathrm{d}\boldsymbol{x} \right| \\
&\leq C \, \|\gamma_{\rho_n} - \gamma_0\|_{L^{6/5}(\Omega_r)} \max_{j=1,2,3} \|\nabla \xi_j\|_{L^\infty(\Omega_r)} \, \|r^{(3)}_{\rho_n}\|_{L^6(\Omega_r)} \\
&\leq C \, |D_{\rho_n}|^{5/6} \, \|\boldsymbol{\xi}\|_{C^1(\Omega_r)} \, \|r^{(3)}_{\rho_n}\|_{H^1(\Omega_r)} \, .
\end{aligned}$$

Combining these estimates with (3.81), we find that

$$\left\| W^{(\boldsymbol{\xi})}_{\rho_n} - \sum_{j=1}^{3} \xi_j W^{(\boldsymbol{e}_j)}_{\rho_n} \right\|_{H^1(\Omega_r)} \leq C \, \|\boldsymbol{\xi}\|_{C^1(\Omega_r)} \, |D_{\rho_n}|^{3/4}$$

and using (B.3) again, finally gives

$$\begin{aligned}
\left\| \nabla W^{(\boldsymbol{\xi})}_{\rho_n} - \sum_{j=1}^{3} \xi_j \nabla W^{(\boldsymbol{e}_j)}_{\rho_n} \right\|_{L^2(\Omega_r)} &\leq \left\| \nabla \left(W^{(\boldsymbol{\xi})}_{\rho_n} - \sum_{j=1}^{3} \xi_j W^{(\boldsymbol{e}_j)}_{\rho_n} \right) \right\|_{L^2(\Omega_r)} + \sum_{j=1}^{3} \|W^{(\boldsymbol{e}_j)}_{\rho_n} \nabla \xi_j\|_{L^2(\Omega_r)} \\
&\leq C \, \|\boldsymbol{\xi}\|_{C^1(\Omega_r)} \, |D_{\rho_n}|^{3/4} + \max_{j=1,2,3} \|W^{(\boldsymbol{e}_j)}_{\rho_n}\|_{L^2(\Omega_r)} \, \|\nabla \xi_j\|_{L^\infty(\Omega_r)} \\
&\leq C \, \|\boldsymbol{\xi}\|_{C^1(\Omega_r)} \, |D_{\rho_n}|^{3/4} \, .
\end{aligned}$$

Inserting this estimate in (3.75) yields the assertion. □

We can now prove the first part of Theorem 3.16. The idea is to use $\boldsymbol{\xi} = \boldsymbol{t}_\Gamma$ in the representation (3.74). Then, combining the representation of the gradient ∇ in local coordinates as in (3.15) with partial integration, interior regularity estimates and the estimates from Appendix B, we find that the second term on the right hand side of (3.74) is in $o(1)$.

Proof of Theorem 3.16, (a). Let $\boldsymbol{\xi} \in C^1(\Omega_r)$ be given by $\boldsymbol{\xi}(\boldsymbol{x}) = \boldsymbol{t}_\Gamma(s)$ for any $\boldsymbol{x} = \boldsymbol{q}_\Gamma(s,\eta,\zeta) \in \Omega_r$. Using equation (3.74), we find that

$$\begin{aligned}
&\frac{1}{2\ell} \int_{-\ell}^{\ell} \boldsymbol{t}_\Gamma(s) \cdot \mathbb{M}^\gamma(\boldsymbol{p}_\Gamma(s)) \boldsymbol{t}_\Gamma(s) \psi(\boldsymbol{p}_\Gamma(s)) \, \mathrm{d}s \\
&\qquad = \frac{1}{|D_{\rho_n}|} \int_{D_{\rho_n}} \psi(\boldsymbol{x}) \, \mathrm{d}\boldsymbol{x} \quad + \frac{1}{|D_{\rho_n}|} \int_{D_{\rho_n}} \left(\boldsymbol{\xi}(\boldsymbol{x}) \cdot \nabla W^{(\boldsymbol{\xi})}_{\rho_n}(\boldsymbol{x}) \right) \psi(\boldsymbol{x}) \, \mathrm{d}\boldsymbol{x} + o(1) \qquad (3.82)
\end{aligned}$$

for any $\psi \in C^1(\overline{\Omega_r})$. Working in local coordinates (3.5) and recalling the determinant of the Jacobian in (3.13) and the ∇ operator in local coordinates from (3.15) gives that

$$
\begin{aligned}
&\left| \int_{D_{\rho n}} \left(\boldsymbol{\xi}(\boldsymbol{x}) \cdot \nabla W_{\rho_n}^{(\boldsymbol{\xi})}(\boldsymbol{x}) \right) \psi(\boldsymbol{x}) \, \mathrm{d}\boldsymbol{x} \right| \\
&= \left| \int_{-\ell}^{\ell} \int_{D'_{\rho n}} \left(\frac{\partial W_{\rho_n}^{(\boldsymbol{\xi})}}{\partial s} (\boldsymbol{q}_\Gamma(s,\eta,\zeta)) + \frac{\partial \theta}{\partial s}(s) \begin{bmatrix} \zeta \\ -\eta \end{bmatrix} \cdot \nabla'_{\eta,\zeta} W_{\rho_n}^{(\boldsymbol{\xi})}(\boldsymbol{q}_\Gamma(s,\eta,\zeta)) \right) \psi(\boldsymbol{q}_\Gamma(s,\eta,\zeta)) \, \mathrm{d}(\eta,\zeta) \, \mathrm{d}s \right| \\
&\leq \left| \left[\int_{D'_{\rho n}} W_{\rho_n}^{(\boldsymbol{\xi})}(\boldsymbol{q}_\Gamma(s,\eta,\zeta)) \psi(\boldsymbol{q}_\Gamma(s,\eta,\zeta)) \, \mathrm{d}(\eta,\zeta) \right]_{s=-\ell}^{\ell} \right| \\
&\quad + \left| \int_{-\ell}^{\ell} \int_{D'_{\rho n}} W_{\rho_n}^{(\boldsymbol{\xi})}(\boldsymbol{q}_\Gamma(s,\eta,\zeta)) \frac{\partial \psi}{\partial s} (\boldsymbol{q}_\Gamma(s,\eta,\zeta)) \, \mathrm{d}(\eta,\zeta) \, \mathrm{d}s \right| \\
&\quad + \left| \int_{-\ell}^{\ell} \int_{D'_{\rho n}} \frac{\partial \theta}{\partial s}(s) \begin{bmatrix} \zeta \\ -\eta \end{bmatrix} \cdot \nabla'_{\eta,\zeta} W_{\rho_n}^{(\boldsymbol{\xi})}(\boldsymbol{q}_\Gamma(s,\eta,\zeta)) \psi(\boldsymbol{q}_\Gamma(s,\eta,\zeta)) \, \mathrm{d}(\eta,\zeta) \, \mathrm{d}s \right| .
\end{aligned}
$$

Interior regularity estimates (see e.g. [63, Thm. 8.24]) and (B.3) give that

$$
\|W_{\rho_n}^{(\boldsymbol{\xi})}\|_{L^\infty(D_{\rho n})} \leq C \left(\|W_{\rho_n}^{(\boldsymbol{\xi})}\|_{L^2(\Omega_r)} + \| (\gamma_{\rho_n} - \gamma_0) \, \boldsymbol{\xi} \|_{L^4(\Omega_r)} \right) \leq C \, |D_{\rho_n}|^{1/4} .
$$

Using (B.2) and (B.3) now shows that

$$
\begin{aligned}
&\left| \int_{D_{\rho n}} \left(\boldsymbol{\xi}(\boldsymbol{x}) \cdot \nabla W_{\rho_n}^{(\boldsymbol{\xi})}(\boldsymbol{x}) \right) \psi(\boldsymbol{x}) \, \mathrm{d}\boldsymbol{x} \right| \\
&\leq C|D'_{\rho_n}| \|W_{\rho_n}^{(\boldsymbol{\xi})}\|_{L^\infty(D_{\rho n})} + C|D_{\rho_n}|^{1/2} \|W_{\rho_n}^{(\boldsymbol{\xi})}\|_{L^2(D_{\rho n})} + C\rho_n |D_{\rho_n}|^{1/2} \left\| \nabla W_{\rho_n}^{(\boldsymbol{\xi})} \right\|_{L^2(\Omega_r)} \\
&\leq C|D_{\rho_n}||D_{\rho_n}|^{1/4} + C|D_{\rho_n}|^{1/2}|D_{\rho_n}|^{3/4} + C\rho_n |D_{\rho_n}|^{1/2}|D_{\rho_n}|^{1/2} = o(|D_{\rho_n}|) .
\end{aligned}
$$

Inserting this estimate in (3.82), using (3.19) and (3.20) and letting $n \to \infty$ yields that

$$
\frac{1}{2\ell} \int_{-\ell}^{\ell} \boldsymbol{t}_\Gamma(s) \cdot \mathbb{M}^\gamma(\boldsymbol{p}_\Gamma(s)) \boldsymbol{t}_\Gamma(s) \psi(\boldsymbol{p}_\Gamma(s)) \, \mathrm{d}s = \frac{1}{2\ell} \int_{-\ell}^{\ell} \psi(\boldsymbol{p}_\Gamma(s)) \, \mathrm{d}s .
$$

Since $\psi \in C^1(\overline{\Omega_r})$ was arbitrary, this implies (3.68). □

The idea in proving the second part of Theorem 3.16 is to define $\boldsymbol{\xi} \in C^1(\Omega_r, \mathbb{R}^3)$ by

$$
\boldsymbol{\xi}(\boldsymbol{x}) = [\boldsymbol{r}_\Gamma(s) \mid \mathbf{s}_\Gamma(s)] \, \boldsymbol{\xi}' \quad \text{for any } \boldsymbol{x} = \boldsymbol{q}_\Gamma(s,\eta,\zeta) \in \Omega_r , \tag{3.83}
$$

where $\boldsymbol{\xi}' \in S^1$, and to use it in the representation (3.74). However, in contrast to the proof before, the second term in (3.74) is no longer in $o(1)$. Instead, it turns out that the second term in (3.74) minus the second term in (3.67) is in $o(1)$. Before we prove the second part of Theorem 3.16, we first consider some auxiliary functions. The idea is to approximate the function $\nabla W_{\rho_n}^{(\boldsymbol{\xi})}$ by the gradient of a product of functions involving the solution $w_{\rho_n}^{(R_\theta^{-1}\boldsymbol{\xi}')} \in H_0^1(B'_r(0))$ of (3.66) with $\boldsymbol{\xi}'$ replaced by $R_\theta^{-1}\boldsymbol{\xi}'$. To do so, we introduce a modified corrector potential $\widetilde{w}_{\rho_n}^{(R_\theta^{-1}\boldsymbol{\xi}')} \in H_0^1(B'_r(0))$ as the unique solution to

$$
\begin{aligned}
\operatorname{div}'_{\eta,\zeta} \left(\gamma'_{\rho_n} (\mathbb{I} + A) \, \nabla'_{\eta,\zeta} \widetilde{w}_{\rho_n}^{(R_\theta^{-1}\boldsymbol{\xi}')} \right) &= -\operatorname{div}'_{\eta,\zeta} ((\gamma_1 - \gamma_0) \, \chi_{D'_{\rho_n}} R_\theta^{-1} \boldsymbol{\xi}') \quad \text{in } B'_r(0) , \\
\widetilde{w}_{\rho_n}^{(R_\theta^{-1}\boldsymbol{\xi}')} &= 0 \quad \text{on } \partial B'_r(0) ,
\end{aligned} \tag{3.84}
$$

where for $s \in (-L, L)$ and $(\eta, \zeta) \in B_r'(0)$ we define

$$A(s,\eta,\zeta) \;=\; J_\Gamma^{-2} \left(\frac{\partial\theta}{\partial s}\right)^2 (s) \begin{bmatrix} \zeta^2 & -\eta\zeta \\ -\eta\zeta & \eta^2 \end{bmatrix}. \tag{3.85}$$

We note that the matrix A is symmetric and positive definite, i.e. there is a $c > 0$ such that

$$c^{-1}|\boldsymbol{\xi}|^2 \;\le\; \boldsymbol{\xi}' \cdot A(s,\eta,\zeta)\boldsymbol{\xi}' \;\le\; c|\boldsymbol{\xi}'|^2 \quad \text{for all } \boldsymbol{\xi}' \in \mathbb{R}^2,\ s \in (-L,L),\ (\eta,\zeta) \in B_r'(0)\,. \tag{3.86}$$

Therefore, (3.84) has a unique solution (see also the proof of Lemma B.2). Both $w_{\rho_n}^{(R_\theta^{-1}\boldsymbol{\xi}')}$ and $\widetilde{w}_{\rho_n}^{(R_\theta^{-1}\boldsymbol{\xi}')}$ depend on the parameter $s \in (-L, L)$, although this is not indicated through our notation. We define the function

$$\widetilde{W}_{\rho_n}^{(\boldsymbol{\xi})}\left(\boldsymbol{q}_\Gamma(s,\eta,\zeta)\right) \;=\; f_{\rho_n}(s) J_\Gamma^{-1}(s,\eta,\zeta) \widetilde{w}_{\rho_n}^{(R_\theta^{-1}\boldsymbol{\xi}')}(\eta,\zeta) \tag{3.87}$$

for $s \in (-L, L)$ and $(\eta, \zeta) \in B_r'(0)$, where $f_{\rho_n} \in C^1([-L, L])$ is a cutoff function satisfying

$$\begin{aligned} &0 \le f_{\rho_n} \le 1\,, \qquad f_{\rho_n}\chi_{(-\ell,\ell)} \;=\; \chi_{(-\ell,\ell)}\,, \\ &\left\| \frac{\partial f_{\rho_n}}{\partial s} \right\|_{L^2(-L,L)} \le C|D_{\rho_n}'|^{-1/8}\,, \qquad \|f_{\rho_n}(1-\chi_{(-\ell,\ell)})\|_{L^2(-L,L)} \le C|D_{\rho_n}'|^{1/8}\,. \end{aligned} \tag{3.88}$$

The existence of such a function is clarified in [19, Lem. 3.6]. Furthermore, for ρ_n small enough, we can choose f_{ρ_n} such that $f_{\rho_n}(-L) = f_{\rho_n}(L) = 0$. We can now prove the second part of Theorem 3.16

Proof of Theorem 3.16, (b). Let $\boldsymbol{\xi} \in C^1(\Omega_r, \mathbb{R}^3)$ and $\widetilde{W}_{\rho_n}^{(\boldsymbol{\xi})} \in H_0^1(\Omega_r)$ be defined as in (3.83) and (3.87), respectively, and let $\psi \in C^1(\Omega_r)$. Using (3.74), it holds that

$$\begin{aligned} \frac{1}{2\ell}\int_{-\ell}^{\ell} \boldsymbol{\xi}(s) \cdot \mathbb{M}^\gamma(\boldsymbol{p}_\Gamma(s))\boldsymbol{\xi}(s)\psi(\boldsymbol{p}_\Gamma(s))\,\mathrm{d}s \;=\; &\frac{1}{|D_{\rho_n}|}\int_{D_{\rho_n}} \psi\,\mathrm{d}\boldsymbol{x} + \frac{1}{|D_{\rho_n}|}\int_{D_{\rho_n}} \left(\boldsymbol{\xi}\cdot\nabla\widetilde{W}_{\rho_n}^{(\boldsymbol{\xi})}\right)\psi\,\mathrm{d}\boldsymbol{x} \\ &+ \frac{1}{|D_{\rho_n}|}\int_{D_{\rho_n}} \left(\boldsymbol{\xi}\cdot\left(\nabla W_{\rho_n}^{(\boldsymbol{\xi})} - \nabla\widetilde{W}_{\rho_n}^{(\boldsymbol{\xi})}\right)\right)\psi\,\mathrm{d}\boldsymbol{x} + o(1)\,. \end{aligned} \tag{3.89}$$

We consider the three integrals on the right hand side of (3.89) separately. For the second integral we use the definition of J_Γ from (3.13) and the gradient in local coordinates from (3.15) to see that

$$\begin{aligned} &\int_{D_{\rho_n}} \left(\boldsymbol{\xi}\cdot\nabla\widetilde{W}_{\rho_n}^{(\boldsymbol{\xi})}\right)\psi\,\mathrm{d}\boldsymbol{x} \\ &= \int_{-\ell}^{\ell}\int_{D_{\rho_n}'} \left(\boldsymbol{\xi}'\cdot\left(R_\theta\nabla_{\eta,\zeta}'(J_\Gamma^{-1}\widetilde{w}_{\rho_n}^{(R_\theta^{-1}\boldsymbol{\xi}')})\right)(s,\eta,\zeta)\right)\psi\left(\boldsymbol{q}_\Gamma(s,\eta,\zeta)\right)J_\Gamma(s,\eta,\zeta)\,\mathrm{d}(\eta,\zeta)\,\mathrm{d}s \\ &= \int_{-\ell}^{\ell}\int_{D_{\rho_n}'} \left((R_\theta^{-1}(s)\boldsymbol{\xi}')\cdot\nabla_{\eta,\zeta}'\widetilde{w}_{\rho_n}^{(R_\theta^{-1}\boldsymbol{\xi}')}(\eta,\zeta)\right)\psi\left(\boldsymbol{q}_\Gamma(s,\eta,\zeta)\right)\mathrm{d}(\eta,\zeta)\,\mathrm{d}s \\ &\quad + \mathcal{O}\left(|D_{\rho_n}|^{1/2}\|\widetilde{w}_{\rho_n}^{(R_\theta^{-1}\boldsymbol{\xi}')}\|_{L^2(D_{\rho_n}')}\right). \end{aligned}$$

Applying estimate (B.3) and Lemma B.2 gives

$$\begin{aligned} &\frac{1}{|D_{\rho_n}|}\int_{D_{\rho_n}} \left(\boldsymbol{\xi}\cdot\nabla\widetilde{W}_{\rho_n}^{(\boldsymbol{\xi})}\right)\psi\,\mathrm{d}\boldsymbol{x} \\ &= \int_{-\ell}^{\ell}\int_{D_{\rho_n}'} \left((R_\theta^{-1}(s)\boldsymbol{\xi}')\cdot\nabla_{\eta,\zeta}' w_{\rho_n}^{(R_\theta^{-1}\boldsymbol{\xi}')}(\eta,\zeta)\right)\psi\left(\boldsymbol{q}_\Gamma(s,\eta,\zeta)\right)\mathrm{d}(\eta,\zeta)\,\mathrm{d}s \\ &\quad + \mathcal{O}\left(|D_{\rho_n}|^{-1/2}\left\|\nabla_{\eta,\zeta}' w_{\rho_n}^{(R_\theta^{-1}\boldsymbol{\xi}')} - \nabla_{\eta,\zeta}'\widetilde{w}_{\rho_n}^{(R_\theta^{-1}\boldsymbol{\xi}')}\right\|_{L^2(D_{\rho_n}')}\right) + o(1) \\ &= \int_{-\ell}^{\ell}\int_{D_{\rho_n}'} \left((R_\theta^{-1}(s)\boldsymbol{\xi}')\cdot\nabla_{\eta,\zeta}' w_{\rho_n}^{(R_\theta^{-1}\boldsymbol{\xi}')}(\eta,\zeta)\right)\psi\left(\boldsymbol{q}_\Gamma(s,\eta,\zeta)\right)\mathrm{d}(\eta,\zeta)\,\mathrm{d}s + o(1)\,. \end{aligned}$$

Accordingly, using (3.67) we obtain for the first two terms in (3.89) that

$$\begin{aligned}
&\frac{1}{|D_{\rho_n}|}\int_{D_{\rho_n}}\psi\,\mathrm{d}\boldsymbol{x}+\frac{1}{|D_{\rho_n}|}\int_{D_{\rho_n}}\left(\boldsymbol{\xi}\cdot\nabla\widetilde{W}_{\rho_n}^{(\boldsymbol{\xi})}\right)\psi\,\mathrm{d}\boldsymbol{x}\;=\;\frac{1}{|D_{\rho_n}|}\int_{-\ell}^{\ell}\left(\int_{D'_{\rho_n}}\psi\left(\boldsymbol{q}_\Gamma\left(s,\eta,\zeta\right)\right)\mathrm{d}(\eta,\zeta)\right.\\
&\quad\left.+\int_{D'_{\rho_n}}\left((R_\theta^{-1}(s)\boldsymbol{\xi}')\cdot\nabla'_{\eta,\zeta}w_{\rho_n}^{(R_\theta^{-1}\boldsymbol{\xi}')}(\eta,\zeta)\right)\psi\left(\boldsymbol{q}_\Gamma\left(s,\eta,\zeta\right)\right)\mathrm{d}(\eta,\zeta)\right)\mathrm{d}s+o(1)\\
&\to\;\frac{1}{2\ell}\int_{-\ell}^{\ell}\boldsymbol{\xi}'\cdot(R_\theta(s)m^\gamma R_\theta^{-1}(s))\boldsymbol{\xi}'\psi(\boldsymbol{p}_\Gamma(s))\,\mathrm{d}s
\end{aligned}\tag{3.90}$$

as $n\to\infty$. For the last integral on the right hand side of (3.89) we apply Hölder's inequality and conclude that

$$\left|\int_{D_{\rho n}}\left(\boldsymbol{\xi}\cdot\left(\nabla W_{\rho_n}^{(\boldsymbol{\xi})}-\nabla\widetilde{W}_{\rho_n}^{(\boldsymbol{\xi})}\right)\right)\psi\,\mathrm{d}\boldsymbol{x}\right|\;\le\;C\,\|\boldsymbol{\xi}\|_{L^\infty(\Omega_r)}\,|D_{\rho_n}|^{1/2}\left\|\nabla W_{\rho_n}^{(\boldsymbol{\xi})}-\nabla\widetilde{W}_{\rho_n}^{(\boldsymbol{\xi})}\right\|_{L^2(\Omega_r)}.$$

To finish the proof, we will show that $\left\|\nabla W_{\rho_n}^{(\boldsymbol{\xi})}-\nabla\widetilde{W}_{\rho_n}^{(\boldsymbol{\xi})}\right\|_{L^2(\Omega_r)}$ is in $o(|D_{\rho_n}|^{1/2})$ as $n\to\infty$. Then, (3.69) follows from (3.89) and (3.90). This is done in Lemma 3.19 below. □

Lemma 3.19. *Let $\boldsymbol{\xi}'\in S^1$ and let $\boldsymbol{\xi}\in C^1(\Omega_r,\mathbb{R}^3)$ be given by*

$$\boldsymbol{\xi}(\boldsymbol{x})\;=\;\left[\boldsymbol{r}_\Gamma(s)\;\middle|\;\mathbf{s}_\Gamma(s)\right]\boldsymbol{\xi}'\quad\textit{for any }\boldsymbol{x}\;=\;\boldsymbol{q}_\Gamma(s,\eta,\zeta)\in\Omega_r\,.$$

Let $W_{\rho_n}^{(\boldsymbol{\xi})}\in H_0^1(\Omega_r)$ be the unique solution of (3.64) and define

$$\widetilde{W}_{\rho_n}^{(\boldsymbol{\xi})}\left(\boldsymbol{q}_\Gamma(s,\eta,\zeta)\right)\;=\;f_{\rho_n}(s)J_\Gamma^{-1}(s,\eta,\zeta)\widetilde{w}_{\rho_n}^{(R_\theta^{-1}\boldsymbol{\xi}')}(\eta,\zeta)$$

for $s\in(-L,L)$ and $(\eta,\zeta)\in B'_r(0)$, where $f_{\rho_n}\in C^1([-L,L])$ is a cut-off function satisfying (3.88), and $\widetilde{w}_{\rho_n}^{(R_\theta^{-1}\boldsymbol{\xi}')}\in H_0^1(B'_r(0))$ solves (3.84). Then,

$$\left\|\nabla W_{\rho_n}^{(\boldsymbol{\xi})}-\nabla\widetilde{W}_{\rho_n}^{(\boldsymbol{\xi})}\right\|_{L^2(\Omega_r)}\;=\;o(|D_{\rho_n}|^{1/2})\,.$$

For the proof of Lemma 3.19, we need the following technical result. The corresponding proof that we present here is similar to the proof of [19, Lem. 3.4].

Lemma 3.20. *Let $\boldsymbol{\xi}'\in S^1$ and let $\widetilde{w}_{\rho_n}^{(R_\theta^{-1}\boldsymbol{\xi}')}\in H_0^1(B'_r(0))$ be the unique solution to (3.84). Then, for a.e. $s\in(-\ell,\ell)$ it holds that*

$$\left\|\frac{\partial}{\partial s}\left(\nabla'_{\eta,\zeta}\widetilde{w}_{\rho_n}^{(R_\theta^{-1}\boldsymbol{\xi}')}\right)\right\|_{L^2(B'_r(0))}\;\le\;C|D'_{\rho_n}|^{1/2}\quad\textit{and}\quad\left\|\frac{\partial\widetilde{w}_{\rho_n}^{(R_\theta^{-1}\boldsymbol{\xi}')}}{\partial s}\right\|_{L^2(B'_r(0))}\;\le\;C|D'_{\rho_n}|^{3/4}.$$

Proof. We apply the operator $\frac{\partial}{\partial s}$ to both sides of the equation (3.84). The derivative on the right hand side exists and thus, the derivative on the left hand side must exist as well. We get that

$$\begin{aligned}
&\mathrm{div}'_{\eta,\zeta}\left(\frac{\partial}{\partial s}(\gamma'_{\rho_n}(\mathbb{I}+A))\nabla'_{\eta,\zeta}\widetilde{w}_{\rho_n}^{(R_\theta^{-1}\boldsymbol{\xi}')}\right)+\mathrm{div}'_{\eta,\zeta}\left((\gamma'_{\rho_n}(\mathbb{I}+A))\nabla'_{\eta,\zeta}\frac{\partial}{\partial s}\widetilde{w}_{\rho_n}^{(R_\theta^{-1}\boldsymbol{\xi}')}\right)\\
&\qquad=\;-\mathrm{div}'_{\eta,\zeta}\left((\gamma_1-\gamma_0)\,\chi_{D'_{\rho_n}}\frac{\partial}{\partial s}R_\theta^{-1}\boldsymbol{\xi}'\right).
\end{aligned}\tag{3.91}$$

This implies that

$$\frac{\partial}{\partial s}\widetilde{w}_{\rho_n}^{(R_\theta^{-1}\boldsymbol{\xi}')}\;=\;a_{\rho_n,1}+a_{\rho_n,2}\,,$$

where $a_{\rho_n,1}, a_{\rho_n,2} \in H^1_0(B'_r(0))$ are the unique solutions to

$$\begin{aligned}
\operatorname{div}'_{\eta,\zeta}\left(\gamma'_{\rho_n}\left(\mathbb{I}+A\right)\nabla'_{\eta,\zeta}a_{\rho_n,1}\right) &= -\operatorname{div}'_{\eta,\zeta}\left(\frac{\partial}{\partial s}(\gamma'_{\rho_n}\left(\mathbb{I}+A\right))\nabla'_{\eta,\zeta}\widetilde{w}_{\rho_n}^{(R_\theta^{-1}\boldsymbol{\xi}')}\right) && \text{in } B'_r(0)\,,\\
\operatorname{div}'_{\eta,\zeta}\left(\gamma'_{\rho_n}\left(\mathbb{I}+A\right)\nabla'_{\eta,\zeta}a_{\rho_n,2}\right) &= -\operatorname{div}'_{\eta,\zeta}\left((\gamma_1-\gamma_0)\,\chi_{D'_{\rho_n}}\frac{\partial}{\partial s}R_\theta^{-1}\boldsymbol{\xi}'\right) && \text{in } B'_r(0)\,,
\end{aligned}$$

together with homogeneous Dirichlet data on the boundary $\partial B'_r(0)$, respectively. Exactly as for the estimates in Lemma B.1, which are found in Appendix B, it can be seen that

$$\|a_{\rho_n,2}\|_{L^2(B'_r(0))} \leq C|D'_{\rho_n}|^{3/4} \quad \text{and} \quad \left\|\nabla'_{\eta,\zeta}a_{\rho_n,2}\right\|_{L^2(B'_r(0))} \leq C|D'_{\rho_n}|^{1/2}\,.$$

For $a_{\rho_n,1}$ we find that

$$\begin{aligned}
&\operatorname{div}'_{\eta,\zeta}\left(\gamma'_{\rho_n}\left(\mathbb{I}+A\right)\nabla'_{\eta,\zeta}a_{\rho_n,1}\right)\\
&= -\operatorname{div}'_{\eta,\zeta}\left(\frac{\partial}{\partial s}(\gamma'_{\rho_n}\left(\mathbb{I}+A\right))\nabla'_{\eta,\zeta}\widetilde{w}_{\rho_n}^{(R_\theta^{-1}\boldsymbol{\xi}')}\right)\\
&= -\operatorname{div}'_{\eta,\zeta}\left(\gamma'_{\rho_n}\left(\mathbb{I}+A\right)(\gamma'_{\rho_n}(\mathbb{I}+A))^{-1}\frac{\partial}{\partial s}(\gamma'_{\rho_n}(\mathbb{I}+A))\nabla'_{\eta,\zeta}\widetilde{w}_{\rho_n}^{(R_\theta^{-1}\boldsymbol{\xi}')}\right)\\
&= -\operatorname{div}'_{\eta,\zeta}\left(\gamma'_{\rho_n}\left(\mathbb{I}+A\right)\nabla'_{\eta,\zeta}\left((\gamma'_{\rho_n}(\mathbb{I}+A))^{-1}\frac{\partial}{\partial s}(\gamma'_{\rho_n}(\mathbb{I}+A))\widetilde{w}_{\rho_n}^{(R_\theta^{-1}\boldsymbol{\xi}')}\right)\right)\\
&\quad + \operatorname{div}'_{\eta,\zeta}\left(\gamma'_{\rho_n}\left(\mathbb{I}+A\right)\nabla'_{\eta,\zeta}\left((\gamma'_{\rho_n}(\mathbb{I}+A))^{-1}\frac{\partial}{\partial s}(\gamma'_{\rho_n}(\mathbb{I}+A))\right)\widetilde{w}_{\rho_n}^{(R_\theta^{-1}\boldsymbol{\xi}')}\right)
\end{aligned}$$

in $B'_r(0)$. This shows that

$$a_{\rho_n,1} = -(\gamma'_{\rho_n}(\mathbb{I}+A))^{-1}\frac{\partial}{\partial s}(\gamma'_{\rho_n}(\mathbb{I}+A))\widetilde{w}_{\rho_n}^{(R_\theta^{-1}\boldsymbol{\xi}')} + b_{\rho_n}\,, \tag{3.92}$$

where $b_{\rho_n} \in H^1_0(B'_r(0))$ denotes the unique solution to

$$\begin{aligned}
&\operatorname{div}'_{\eta,\zeta}\left(\gamma'_{\rho_n}\left(\mathbb{I}+A\right)\nabla'_{\eta,\zeta}b_{\rho_n}\right)\\
&\qquad = \operatorname{div}'_{\eta,\zeta}\left(\gamma'_{\rho_n}\left(\mathbb{I}+A\right)\nabla'_{\eta,\zeta}\left((\gamma'_{\rho_n}(\mathbb{I}+A))^{-1}\frac{\partial}{\partial s}(\gamma'_{\rho_n}(\mathbb{I}+A))\right)\widetilde{w}_{\rho_n}^{(R_\theta^{-1}\boldsymbol{\xi}')}\right)
\end{aligned} \tag{3.93}$$

in $B'_r(0)$ together with homogeneous Dirichlet data on the boundary $\partial B'_r(0)$. The weak formulation of (3.93) with test function b_{ρ_n} implies that

$$\begin{aligned}
&\int_{B'_r(0)} e^{\mathrm{i}\beta}\gamma'_{\rho_n}\left(\left(\mathbb{I}+A\right)\nabla'_{\eta,\zeta}b_{\rho_n}\right)\cdot\overline{\nabla'_{\eta,\zeta}b_{\rho_n}}\,\mathrm{d}\boldsymbol{x}\\
&\quad = \int_{B'_r(0)} e^{\mathrm{i}\beta}\gamma'_{\rho_n}\left(\left(\mathbb{I}+A\right)\nabla'_{\eta,\zeta}\left((\gamma'_{\rho_n}(\mathbb{I}+A))^{-1}\frac{\partial}{\partial s}(\gamma'_{\rho_n}(\mathbb{I}+A))\right)\right)\cdot\overline{\nabla'_{\eta,\zeta}b_{\rho_n}}\,\widetilde{w}_{\rho_n}^{(R_\theta^{-1}\boldsymbol{\xi}')}\,\mathrm{d}\boldsymbol{x}\,,
\end{aligned}$$

with β chosen such that $\operatorname{Re}(e^{\mathrm{i}\beta}\gamma'_{\rho_n}) \geq c_1 > 0$. Without loss of generality, let $c_1 = \min\{\operatorname{Re}(e^{\mathrm{i}\beta}\gamma'_{\rho_n})\}$. Due to the positive definiteness of $\mathbb{I}+A$ (see also (3.86)) it holds that

$$\begin{aligned}
\|\nabla'_{\eta,\zeta}b_{\rho_n}\|^2_{L^2(B'_r(0))} &\leq C\int_{B'_r(0)}\left(\left(\mathbb{I}+A\right)\nabla'_{\eta,\zeta}b_{\rho_n}\right)\cdot\overline{\nabla'_{\eta,\zeta}b_{\rho_n}}\,\mathrm{d}(\eta,\zeta)\\
&\leq \frac{C}{c_1}\operatorname{Re}\left(\int_{B'_r(0)} e^{\mathrm{i}\beta}\gamma'_{\rho_n}\left(\left(\mathbb{I}+A\right)\nabla'_{\eta,\zeta}b_{\rho_n}\right)\cdot\overline{\nabla'_{\eta,\zeta}b_{\rho_n}}\,\mathrm{d}(\eta,\zeta)\right)\\
&\leq C\|\nabla'_{\eta,\zeta}b_{\rho_n}\|_{L^2(B'_r(0))}\|\widetilde{w}_{\rho_n}^{(R_\theta^{-1}\boldsymbol{\xi}')}\|_{L^2(B'_r(0))}\,.
\end{aligned} \tag{3.94}$$

Using the Poincaré inequality, (3.94) and (B.3) we see that

$$\|b_{\rho_n}\|_{L^2(B_r'(0))} \leq C \left\|\nabla'_{\eta,\zeta} b_{\rho_n}\right\|_{L^2(B_r'(0))} \leq C\|\widetilde{w}_{\rho_n}^{(R_\theta^{-1}\boldsymbol{\xi}')}\|_{L^2(B_r'(0))} \leq C|D'_{\rho_n}|^{3/4}. \tag{3.95}$$

Thus, by using (3.92), (3.95) and (B.2), we find that

$$\|a_{\rho_n,1}\|_{L^2(B_r'(0))} \leq C|D'_{\rho_n}|^{3/4} \quad \text{and} \quad \left\|\nabla'_{\eta,\zeta} a_{\rho_n,1}\right\|_{L^2(B_r'(0))} \leq C|D'_{\rho_n}|^{1/2},$$

what ends the proof. □

Remark 3.21. The regularity assumption that $\boldsymbol{p}_\Gamma \in C^3((-L,L),\mathbb{R}^3)$ and $R_\theta \in C^2((-L,L),\mathbb{R}^{2\times 2})$ imply the existence of $\frac{\partial}{\partial s}(\gamma'_{\rho_n}(\mathbb{I}+A))$ in (3.91). This further implies the existence of $\frac{\partial}{\partial s}\widetilde{w}_{\rho_n}^{(R_\theta^{-1}\boldsymbol{\xi}')}$. In our analysis, this is the only time, where we need the existence of the third derivative of $\boldsymbol{p}_\Gamma$ and of the second derivative of θ.

We can now prove Lemma 3.19.

Proof of Lemma 3.19. The weak formulation of (3.64) implies that $W_{\rho_n}^{(\boldsymbol{\xi})} \in H_0^1(\Omega_r)$ fulfills

$$\int_{\Omega_r} \gamma_{\rho_n} \nabla W_{\rho_n}^{(\boldsymbol{\xi})} \cdot \nabla\psi \,\mathrm{d}\boldsymbol{x} = -\int_{\Omega_r} (\gamma_{\rho_n} - \gamma_0)\,\boldsymbol{\xi}\cdot\nabla\psi \,\mathrm{d}\boldsymbol{x} \tag{3.96}$$

for all $\psi \in H_0^1(\Omega_r)$. On the other hand, for the modified potential $\widetilde{W}_{\rho_n}^{(\boldsymbol{\xi})}$ from (3.87), we find by using the gradient in local coordinates from (3.15), (3.88) and the product rule that

$$\begin{aligned}
&\int_{\Omega_r} \gamma_{\rho_n} \nabla \widetilde{W}_{\rho_n}^{(\boldsymbol{\xi})} \cdot \nabla\psi \,\mathrm{d}\boldsymbol{x} \\
&= \int_{-L}^{L}\int_{B_r'(0)} \gamma_{\rho_n}\left(\nabla'_{\eta,\zeta}\widetilde{W}_{\rho_n}^{(\boldsymbol{\xi})}\cdot\nabla'_{\eta,\zeta}\psi + \left(\boldsymbol{t}_\Gamma\cdot\nabla\widetilde{W}_{\rho_n}^{(\boldsymbol{\xi})}\right)(\boldsymbol{t}_\Gamma\cdot\nabla\psi)\right) J_\Gamma \,\mathrm{d}(\eta,\zeta)\,\mathrm{d}s \\
&= \int_{-L}^{L}\int_{B_r'(0)} \gamma_{\rho_n}\Bigg(\chi_{(-\ell,\ell)}\left(\widetilde{w}_{\rho_n}^{(R_\theta^{-1}\boldsymbol{\xi}')}\nabla'_{\eta,\zeta}J_\Gamma^{-1} + J_\Gamma^{-1}\nabla'_{\eta,\zeta}\widetilde{w}_{\rho_n}^{(R_\theta^{-1}\boldsymbol{\xi}')}\right)\cdot\nabla'_{\eta,\zeta}\psi \\
&\quad + (1-\chi_{(-\ell,\ell)})f_{\rho_n}\left(\widetilde{w}_{\rho_n}^{(R_\theta^{-1}\boldsymbol{\xi}')}\nabla'_{\eta,\zeta}J_\Gamma^{-1} + J_\Gamma^{-1}\nabla'_{\eta,\zeta}\widetilde{w}_{\rho_n}^{(R_\theta^{-1}\boldsymbol{\xi}')}\right)\cdot\nabla'_{\eta,\zeta}\psi \\
&\quad + \left(\widetilde{w}_{\rho_n}^{(R_\theta^{-1}\boldsymbol{\xi}')}\left(\boldsymbol{t}_\Gamma\cdot\nabla(f_{\rho_n}J_\Gamma^{-1})\right) + f_{\rho_n}J_\Gamma^{-1}\left(\boldsymbol{t}_\Gamma\cdot\nabla\widetilde{w}_{\rho_n}^{(R_\theta^{-1}\boldsymbol{\xi}')}\right)\right)(\boldsymbol{t}_\Gamma\cdot\nabla\psi)\Bigg) J_\Gamma \,\mathrm{d}(\eta,\zeta)\,\mathrm{d}s\,.
\end{aligned} \tag{3.97}$$

Using the gradient in local coordinates once more gives a decomposition of the last term on the right hand side of (3.97), which reads

$$\begin{aligned}
\left(\boldsymbol{t}_\Gamma\cdot\nabla\widetilde{w}_{\rho_n}^{(R_\theta^{-1}\boldsymbol{\xi}')}\right)(\boldsymbol{t}_\Gamma\cdot\nabla\psi) &= J_\Gamma^{-2}\frac{\partial\widetilde{w}_{\rho_n}^{(R_\theta^{-1}\boldsymbol{\xi}')}}{\partial s}\frac{\partial\psi}{\partial s} + A\,\nabla'_{\eta,\zeta}\widetilde{w}_{\rho_n}^{(R_\theta^{-1}\boldsymbol{\xi}')}\cdot\nabla'_{\eta,\zeta}\psi \\
&\quad + \frac{\partial\widetilde{w}_{\rho_n}^{(R_\theta^{-1}\boldsymbol{\xi}')}}{\partial s}\left(\boldsymbol{d}'\cdot\nabla'_{\eta,\zeta}\psi\right) + \frac{\partial\psi}{\partial s}\left(\boldsymbol{d}'\cdot\nabla'_{\eta,\zeta}\widetilde{w}_{\rho_n}^{(R_\theta^{-1}\boldsymbol{\xi}')}\right),
\end{aligned}$$

where A has been defined in (3.85) and

$$\boldsymbol{d}'(s,\eta,\zeta) = \frac{\partial\theta}{\partial s}(s)J_\Gamma^{-2}(s,\eta,\zeta)\begin{bmatrix}\zeta\\-\eta\end{bmatrix}, \quad s\in[-L,L], \quad (\eta,\zeta)\in B_r'(0)\,.$$

Thus,

$$
\begin{aligned}
&\int_{\Omega_r} \gamma_{\rho_n} \nabla \widetilde{W}_{\rho_n}^{(\boldsymbol{\xi})} \cdot \nabla \psi \, \mathrm{d}\boldsymbol{x} \\
&= \int_{-\ell}^{\ell} \int_{B_r'(0)} \gamma_{\rho_n} \left(\widetilde{w}_{\rho_n}^{(R_\theta^{-1}\boldsymbol{\xi}')} \nabla'_{\eta,\zeta} J_\Gamma^{-1} + J_\Gamma^{-1} \nabla'_{\eta,\zeta} \widetilde{w}_{\rho_n}^{(R_\theta^{-1}\boldsymbol{\xi}')} \right) \cdot \nabla'_{\eta,\zeta} \psi \, J_\Gamma \, \mathrm{d}(\eta,\zeta) \, \mathrm{d}s \\
&\quad + \int_{-L}^{L} \int_{B_r'(0)} \gamma_{\rho_n} (1 - \chi_{(-\ell,\ell)}) f_{\rho_n} \left(\widetilde{w}_{\rho_n}^{(R_\theta^{-1}\boldsymbol{\xi}')} \nabla'_{\eta,\zeta} J_\Gamma^{-1} + J_\Gamma^{-1} \nabla'_{\eta,\zeta} \widetilde{w}_{\rho_n}^{(R_\theta^{-1}\boldsymbol{\xi}')} \right) \cdot \nabla'_{\eta,\zeta} \psi \, J_\Gamma \\
&\qquad + \gamma_{\rho_n} \widetilde{w}_{\rho_n}^{(R_\theta^{-1}\boldsymbol{\xi}')} \left(\boldsymbol{t}_\Gamma \cdot \nabla (f_{\rho_n} J_\Gamma^{-1}) \right) (\boldsymbol{t}_\Gamma \cdot \nabla \psi) \, J_\Gamma \\
&\qquad + \gamma_{\rho_n} f_{\rho_n} \Bigg(J_\Gamma^{-2} \frac{\partial \widetilde{w}_{\rho_n}^{(R_\theta^{-1}\boldsymbol{\xi}')}}{\partial s} \frac{\partial \psi}{\partial s} + A \, \nabla'_{\eta,\zeta} \widetilde{w}_{\rho_n}^{(R_\theta^{-1}\boldsymbol{\xi}')} \cdot \nabla'_{\eta,\zeta} \psi \\
&\qquad\quad + \frac{\partial \widetilde{w}_{\rho_n}^{(R_\theta^{-1}\boldsymbol{\xi}')}}{\partial s} \left(\boldsymbol{d}' \cdot \nabla'_{\eta,\zeta} \psi \right) + \frac{\partial \psi}{\partial s} \left(\boldsymbol{d}' \cdot \nabla'_{\eta,\zeta} \widetilde{w}_{\rho_n}^{(R_\theta^{-1}\boldsymbol{\xi}')} \right) \Bigg) \, \mathrm{d}(\eta,\zeta) \, \mathrm{d}s \\
&= \int_{-\ell}^{\ell} \int_{B_r'(0)} \gamma_{\rho_n} \left(\mathbb{I} + A \right) \nabla'_{\eta,\zeta} \widetilde{w}_{\rho_n}^{(R_\theta^{-1}\boldsymbol{\xi}')} \cdot \nabla'_{\eta,\zeta} \psi \, \mathrm{d}(\eta,\zeta) \, \mathrm{d}s \\
&\quad + \int_{-L}^{L} \int_{B_r'(0)} \gamma_{\rho_n} \Bigg(\chi_{(-\ell,\ell)} \, \widetilde{w}_{\rho_n}^{(R_\theta^{-1}\boldsymbol{\xi}')} \, \nabla'_{\eta,\zeta} J_\Gamma^{-1} \cdot \nabla'_{\eta,\zeta} \psi \\
&\qquad + (1 - \chi_{(-\ell,\ell)}) f_{\rho_n} \left(\widetilde{w}_{\rho_n}^{(R_\theta^{-1}\boldsymbol{\xi}')} \, \nabla'_{\eta,\zeta} J_\Gamma^{-1} + J_\Gamma^{-1} \left(\mathbb{I} + A \right) \nabla'_{\eta,\zeta} \widetilde{w}_{\rho_n}^{(R_\theta^{-1}\boldsymbol{\xi}')} \right) \cdot \nabla'_{\eta,\zeta} \psi \\
&\qquad + \widetilde{w}_{\rho_n}^{(R_\theta^{-1}\boldsymbol{\xi}')} \left(\boldsymbol{t}_\Gamma \cdot \nabla (f_{\rho_n} J_\Gamma^{-1}) \right) (\boldsymbol{t}_\Gamma \cdot \nabla \psi) + f_{\rho_n} \Bigg(J_\Gamma^{-3} \frac{\partial \widetilde{w}_{\rho_n}^{(R_\theta^{-1}\boldsymbol{\xi}')}}{\partial s} \frac{\partial \psi}{\partial s} \\
&\qquad\quad + J_\Gamma^{-1} \Bigg(\frac{\partial \widetilde{w}_{\rho_n}^{(R_\theta^{-1}\boldsymbol{\xi}')}}{\partial s} \left(\boldsymbol{d}' \cdot \nabla'_{\eta,\zeta} \psi \right) + \frac{\partial \psi}{\partial s} \left(\boldsymbol{d}' \cdot \nabla'_{\eta,\zeta} \widetilde{w}_{\rho_n}^{(R_\theta^{-1}\boldsymbol{\xi}')} \right) \Bigg) \Bigg) \Bigg) J_\Gamma \, \mathrm{d}(\eta,\zeta) \, \mathrm{d}s \,. \qquad (3.98)
\end{aligned}
$$

Let $v \in H_0^1(B_r'(0))$ be the unique solution to

$$
\mathrm{div}'_{\eta,\zeta} \left(\gamma'_{\rho_n} \left(\mathbb{I} + A \right) \nabla'_{\eta,\zeta} v \right) = -\mathrm{div}'_{\eta,\zeta} (J_\Gamma (\gamma'_{\rho_n} - \gamma'_0)(R_\theta^{-1}\boldsymbol{\xi}')) \quad \text{in } B_r'(0) \,. \qquad (3.99)
$$

Then, using (3.13) we find that

$$
\begin{aligned}
\mathrm{div}'_{\eta,\zeta} \left(\gamma'_{\rho_n} \left(\mathbb{I} + A \right) \nabla'_{\eta,\zeta} v \right) &= -\mathrm{div}'_{\eta,\zeta} ((\gamma'_{\rho_n} - \gamma'_0)(R_\theta^{-1}\boldsymbol{\xi}')) \\
&\quad + \mathrm{div}'_{\eta,\zeta} \left(\begin{bmatrix} \kappa_1 \\ \kappa_2 \end{bmatrix} \cdot R_\theta(s) \begin{bmatrix} \eta \\ \zeta \end{bmatrix} (\gamma'_{\rho_n} - \gamma'_0)(R_\theta^{-1}\boldsymbol{\xi}') \right) .
\end{aligned}
$$

Uniqueness of the solution to the Dirichlet problem implies that $\widetilde{w}_{\rho_n}^{(R_\theta^{-1}\boldsymbol{\xi}')} = v + v_1$, where $v_1 \in H_0^1(B_r'(0))$ satisfies

$$
\mathrm{div}'_{\eta,\zeta} \left(\gamma'_{\rho_n} \left(\mathbb{I} + A \right) \nabla'_{\eta,\zeta} v_1 \right) = -\mathrm{div}'_{\eta,\zeta} \left(\begin{bmatrix} \kappa_1 \\ \kappa_2 \end{bmatrix} \cdot R_\theta(s) \begin{bmatrix} \eta \\ \zeta \end{bmatrix} (\gamma'_{\rho_n} - \gamma'_0)(R_\theta^{-1}\boldsymbol{\xi}') \right) .
$$

Using estimate (B.2) yields that

$$
\left\| \nabla'_{\eta,\zeta} v_1 \right\|_{L^2(B_r'(0))} \leq C \kappa_{\max} \rho_n |D_{\rho_n}|^{1/2} \,.
$$

Thus, (3.99) and the representation of the gradient in local coordinates in (3.15) give that

$$\begin{aligned}
&\int_{-\ell}^{\ell}\int_{B_r'(0)} \gamma_{\rho_n}\,(\mathbb{I}+A)\,\nabla'_{\eta,\zeta}\widetilde{w}_{\rho_n}^{(R_\theta^{-1}\boldsymbol{\xi}')}\cdot\nabla'_{\eta,\zeta}\psi\;\mathrm{d}(\eta,\zeta)\;\mathrm{d}s\\
&=\int_{-\ell}^{\ell}\int_{B_r'(0)} \gamma_{\rho_n}\,(\mathbb{I}+A)\,\nabla'_{\eta,\zeta}v\cdot\nabla'_{\eta,\zeta}\psi\;\mathrm{d}(\eta,\zeta)\;\mathrm{d}s+o(|D_{\rho_n}|^{1/2}\,\|\nabla\psi\|_{L^2(\Omega_r)})\\
&=-\int_{-\ell}^{\ell}\int_{B_r'(0)} J_\Gamma\,(\gamma_{\rho_n}-\gamma_0)\,(R_\theta^{-1}\boldsymbol{\xi}')\cdot\nabla'_{\eta,\zeta}\psi\;\mathrm{d}(\eta,\zeta)\;\mathrm{d}s+o(|D_{\rho_n}|^{1/2}\,\|\nabla\psi\|_{L^2(\Omega_r)})\\
&=-\int_{\Omega_r}(\gamma_{\rho_n}-\gamma_0)\,\boldsymbol{\xi}\cdot\nabla\psi\;\mathrm{d}\boldsymbol{x}+o(|D_{\rho_n}|^{1/2}\,\|\nabla\psi\|_{L^2(\Omega_r)})\,. \qquad (3.100)
\end{aligned}$$

Combining (3.96) with (3.100) and applying (3.98) yields that for all $\psi\in H_0^1(\Omega_r)$,

$$\begin{aligned}
\int_{\Omega_r}\gamma_{\rho_n}\left(\nabla W_{\rho_n}^{(\boldsymbol{\xi})}-\nabla\widetilde{W}_{\rho_n}^{(\boldsymbol{\xi})}\right)\cdot\nabla\psi\;\mathrm{d}\boldsymbol{x}\;=\;&-\int_{-L}^{L}\int_{B_r'(0)}\gamma_{\rho_n}\Bigg(\chi_{(-\ell,\ell)}\,\widetilde{w}_{\rho_n}^{(R_\theta^{-1}\boldsymbol{\xi}')}\,\nabla'_{\eta,\zeta}J_\Gamma^{-1}\cdot\nabla'_{\eta,\zeta}\psi\\
&+(1-\chi_{(-\ell,\ell)})f_{\rho_n}\left(\widetilde{w}_{\rho_n}^{(R_\theta^{-1}\boldsymbol{\xi}')}\,\nabla'_{\eta,\zeta}J_\Gamma^{-1}+J_\Gamma^{-1}\,(\mathbb{I}+A)\,\nabla'_{\eta,\zeta}\widetilde{w}_{\rho_n}^{(R_\theta^{-1}\boldsymbol{\xi}')}\right)\cdot\nabla'_{\eta,\zeta}\psi\\
&+\widetilde{w}_{\rho_n}^{(R_\theta^{-1}\boldsymbol{\xi}')}\left(\boldsymbol{t}_\Gamma\cdot\nabla(f_{\rho_n}J_\Gamma^{-1})\right)(\boldsymbol{t}_\Gamma\cdot\nabla\psi)+f_{\rho_n}\Bigg(J_\Gamma^{-3}\frac{\partial\widetilde{w}_{\rho_n}^{(R_\theta^{-1}\boldsymbol{\xi}')}}{\partial s}\frac{\partial\psi}{\partial s}\\
&+J_\Gamma^{-1}\left(\frac{\partial\widetilde{w}_{\rho_n}^{(R_\theta^{-1}\boldsymbol{\xi}')}}{\partial s}\left(\boldsymbol{d}'\cdot\nabla'_{\eta,\zeta}\psi\right)+\frac{\partial\psi}{\partial s}\left(\boldsymbol{d}'\cdot\nabla'_{\eta,\zeta}\widetilde{w}_{\rho_n}^{(R_\theta^{-1}\boldsymbol{\xi}')}\right)\right)\Bigg)\Bigg)J_\Gamma\;\mathrm{d}(\eta,\zeta)\;\mathrm{d}s\\
&+o(|D_{\rho_n}|^{1/2}\,\|\nabla\psi\|_{L^2(\Omega_r)})\,. \qquad (3.101)
\end{aligned}$$

As pointed out in the definition of f_{ρ_n} in (3.88), we assume that $|D_{\rho_n}|$ is so small that $f_{\rho_n}(-L)=f_{\rho_n}(L)=0$. Accordingly, we find that

$$\begin{aligned}
&-\int_{-L}^{L}\int_{B_r'(0)}\gamma_{\rho_n}f_{\rho_n}\frac{\partial\psi}{\partial s}\left(\boldsymbol{d}'\cdot\nabla'_{\eta,\zeta}\widetilde{w}_{\rho_n}^{(R_\theta^{-1}\boldsymbol{\xi}')}\right)\mathrm{d}(\eta,\zeta)\;\mathrm{d}s\\
&\qquad=\int_{-L}^{L}\int_{B_r'(0)}\psi\frac{\partial}{\partial s}\left(\gamma_{\rho_n}f_{\rho_n}\left(\boldsymbol{d}'\cdot\nabla'_{\eta,\zeta}\widetilde{w}_{\rho_n}^{(R_\theta^{-1}\boldsymbol{\xi}')}\right)\right)\mathrm{d}(\eta,\zeta)\;\mathrm{d}s\,.
\end{aligned}$$

Combining this with (3.101) and choosing $\psi=\overline{W_{\rho_n}^{(\boldsymbol{\xi})}-\widetilde{W}_{\rho_n}^{(\boldsymbol{\xi})}}$ implies that

$$\begin{aligned}
&\left\|\nabla W_{\rho_n}^{(\boldsymbol{\xi})}-\nabla\widetilde{W}_{\rho_n}^{(\boldsymbol{\xi})}\right\|_{L^2(\Omega_r)}^2\\
&\le C\Bigg(\left\|\chi_{(-\ell,\ell)}\widetilde{w}_{\rho_n}^{(R_\theta^{-1}\boldsymbol{\xi}')}\nabla'_{\eta,\zeta}J_\Gamma^{-1}\right\|_{L^2(\Omega_r)}+\left\|(1-\chi_{(-\ell,\ell)})f_{\rho_n}\widetilde{w}_{\rho_n}^{(R_\theta^{-1}\boldsymbol{\xi}')}\nabla'_{\eta,\zeta}J_\Gamma^{-1}\right\|_{L^2(\Omega_r)}\\
&\quad+\left\|(1-\chi_{(-\ell,\ell)})f_{\rho_n}J_\Gamma^{-1}\,(\mathbb{I}+A)\,\nabla'_{\eta,\zeta}\widetilde{w}_{\rho_n}^{(R_\theta^{-1}\boldsymbol{\xi}')}\right\|_{L^2(\Omega_r)}\\
&\quad+\left\|\widetilde{w}_{\rho_n}^{(R_\theta^{-1}\boldsymbol{\xi}')}\left(\boldsymbol{t}_\Gamma\cdot\nabla(f_{\rho_n}J_\Gamma^{-1})\right)\right\|_{L^2(\Omega_r)}+\left\|f_{\rho_n}J_\Gamma^{-3}\frac{\partial\widetilde{w}_{\rho_n}^{(R_\theta^{-1}\boldsymbol{\xi}')}}{\partial s}\right\|_{L^2(\Omega_r)}\\
&\quad+\left\|f_{\rho_n}J_\Gamma^{-1}\frac{\partial\widetilde{w}_{\rho_n}^{(R_\theta^{-1}\boldsymbol{\xi}')}}{\partial s}\right\|_{L^2(\Omega_r)}\Bigg)\left\|\nabla W_{\rho_n}^{(\boldsymbol{\xi})}-\nabla\widetilde{W}_{\rho_n}^{(\boldsymbol{\xi})}\right\|_{L^2(\Omega_r)}\\
&\quad+C\left\|\frac{\partial}{\partial s}\left(\gamma_{\rho_n}f_{\rho_n}\left(\boldsymbol{d}'\cdot\nabla'_{\eta,\zeta}\widetilde{w}_{\rho_n}^{(R_\theta^{-1}\boldsymbol{\xi}')}\right)\right)\right\|_{L^2(\Omega_r)}\|W_{\rho_n}^{(\boldsymbol{\xi})}-\widetilde{W}_{\rho_n}^{(\boldsymbol{\xi})}\|_{L^2(\Omega_r)}\\
&\quad+o\left(|D_{\rho_n}|^{1/2}\left\|\nabla W_{\rho_n}^{(\boldsymbol{\xi})}-\nabla\widetilde{W}_{\rho_n}^{(\boldsymbol{\xi})}\right\|_{L^2(\Omega_r)}\right)\,. \qquad (3.102)
\end{aligned}$$

From (3.64), (3.87), (3.84) and (B.3) we get that

$$\|W_{\rho_n}^{(\boldsymbol{\xi})} - \widetilde{W}_{\rho_n}^{(\boldsymbol{\xi})}\|_{L^2(\Omega_r)} \leq C|D_{\rho_n}|^{3/4}.$$

Next, we estimate the remaining terms on the right hand side of (3.102) separately. For the first term we conclude by using (B.3) that

$$\left\|\chi_{(-\ell,\ell)}\widetilde{w}_{\rho_n}^{(R_\theta^{-1}\boldsymbol{\xi}')}\nabla'_{\eta,\zeta}J_\Gamma^{-1}\right\|^2_{L^2(\Omega_r)} \leq C\|\widetilde{w}_{\rho_n}^{(R_\theta^{-1}\boldsymbol{\xi}')}\|^2_{L^2(\Omega_r)} \leq C|D_{\rho_n}|^{3/2}.$$

Using (3.88) and (B.3), the second term can be estimated similarly, i.e.

$$\left\|\left(1-\chi_{(-\ell,\ell)}\right)f_{\rho_n}\widetilde{w}_{\rho_n}^{(R_\theta^{-1}\boldsymbol{\xi}')}\nabla'_{\eta,\zeta}J_\Gamma^{-1}\right\|^2_{L^2(\Omega_r)} \leq C\|\widetilde{w}_{\rho_n}^{(R_\theta^{-1}\boldsymbol{\xi}')}\|^2_{L^2(\Omega_r)} \leq C|D_{\rho_n}|^{3/2}.$$

For the third term we use again (3.88) and (B.2) to see that

$$\begin{aligned}
&\left\|(1-\chi_{(-\ell,\ell)})f_{\rho_n}J_\Gamma^{-1}\left(\mathbb{I}+A\right)\nabla'_{\eta,\zeta}\widetilde{w}_{\rho_n}^{(R_\theta^{-1}\boldsymbol{\xi}')}\right\|^2_{L^2(\Omega_r)}\\
&\quad\leq C\|(1-\chi_{(-\ell,\ell)})f_{\rho_n}\|^2_{L^2(-L,L)}\left\|\nabla'_{\eta,\zeta}\widetilde{w}_{\rho_n}^{(R_\theta^{-1}\boldsymbol{\xi}')}\right\|^2_{L^2(\Omega_r)} \leq C|D_{\rho_n}|^{1/4}|D_{\rho_n}| \leq C|D_{\rho_n}|^{5/4}.
\end{aligned}$$

For the fourth term we use the product rule, the representation of the gradient in local coordinates (3.15), (3.88) and (B.3) to get that

$$\begin{aligned}
&\left\|\widetilde{w}_{\rho_n}^{(R_\theta^{-1}\boldsymbol{\xi}')}\left(\boldsymbol{t}_\Gamma\cdot\nabla(f_{\rho_n}J_\Gamma^{-1})\right)\right\|^2_{L^2(\Omega_r)}\\
&= \int_{-L}^{L}\int_{B'_r(0)}|\widetilde{w}_{\rho_n}^{(R_\theta^{-1}\boldsymbol{\xi}')}|^2\left|J_\Gamma^{-2}\frac{\partial f_{\rho_n}}{\partial s}+f_{\rho_n}\left(\boldsymbol{t}_\Gamma\cdot\nabla J_\Gamma^{-1}\right)\right|^2 J_\Gamma\,\mathrm{d}(\eta,\zeta)\,\mathrm{d}s\\
&\leq C\int_{-L}^{L}\|\widetilde{w}_{\rho_n}^{(R_\theta^{-1}\boldsymbol{\xi}')}\|^2_{L^2(B'_r(0))}\left(C+\left|\frac{\partial f_{\rho_n}}{\partial s}\right|\right)^2\mathrm{d}s \leq C|D'_{\rho_n}|^{3/2}|D'_{\rho_n}|^{-1/4} \leq C|D_{\rho_n}|^{5/4}.
\end{aligned}$$

Using Lemma 3.20 we obtain for the fifth and sixth term on the right hand side of (3.102) that

$$\left\|f_{\rho_n}J_\Gamma^{-3}\frac{\partial\widetilde{w}_{\rho_n}^{(R_\theta^{-1}\boldsymbol{\xi}')}}{\partial s}\right\|^2_{L^2(\Omega_r)} \leq C|D_{\rho_n}|^{3/2} \quad\text{and}\quad \left\|f_{\rho_n}J_\Gamma^{-1}\frac{\partial\widetilde{w}_{\rho_n}^{(R_\theta^{-1}\boldsymbol{\xi}')}}{\partial s}\right\|^2_{L^2(\Omega_r)} \leq C|D_{\rho_n}|^{3/2}.$$

Finally, we combine (3.88) with (B.2) and use Lemma 3.20 to get that

$$\begin{aligned}
&\left\|\frac{\partial}{\partial s}\left(\gamma_{\rho_n}f_{\rho_n}\left(\boldsymbol{d}'\cdot\nabla'_{\eta,\zeta}\widetilde{w}_{\rho_n}^{(R_\theta^{-1}\boldsymbol{\xi}')}\right)\right)\right\|^2_{L^2(\Omega_r)}\\
&\leq C\Bigg(\int_{-L}^{L}\int_{B'_r(0)}\left|\frac{\partial}{\partial s}\left(\gamma_{\rho_n}f_{\rho_n}\right)\right|^2\left|\boldsymbol{d}'\cdot\nabla'_{\eta,\zeta}\widetilde{w}_{\rho_n}^{(R_\theta^{-1}\boldsymbol{\xi}')}\right|^2 J_\Gamma\,\mathrm{d}(\eta,\zeta)\,\mathrm{d}s\\
&\qquad+\int_{-L}^{L}\int_{B'_r(0)}|\gamma_{\rho_n}f_{\rho_n}|^2\left|\frac{\partial}{\partial s}\left(\boldsymbol{d}'\cdot\nabla'_{\eta,\zeta}\widetilde{w}_{\rho_n}^{(R_\theta^{-1}\boldsymbol{\xi}')}\right)\right|^2 J_\Gamma\,\mathrm{d}(\eta,\zeta)\,\mathrm{d}s\Bigg)\\
&\leq C\left(\left\|\frac{\partial f_{\rho_n}}{\partial s}\right\|^2_{L^2(-L,L)}\left\|\nabla'_{\eta,\zeta}\widetilde{w}_{\rho_n}^{(R_\theta^{-1}\boldsymbol{\xi}')}\right\|^2_{L^2(B'_r(0)}+\left\|\frac{\partial}{\partial s}\left(\boldsymbol{d}'\cdot\nabla'_{\eta,\zeta}\widetilde{w}_{\rho_n}^{(R_\theta^{-1}\boldsymbol{\xi}')}\right)\right\|^2_{L^2(\Omega_r)}\right)\\
&\leq C(|D'_{\rho_n}|^{-1/4}|D'_{\rho_n}|+|D'_{\rho_n}|) \leq C|D'_{\rho_n}|^{3/4}.
\end{aligned}$$

Taking the square root on both sides gives that

$$\left\|\frac{\partial}{\partial s}\left(\gamma_{\rho_n}f_{\rho_n}\left(\boldsymbol{d}'\cdot\nabla'_{\eta,\zeta}\widetilde{w}_{\rho_n}^{(R_\theta^{-1}\boldsymbol{\xi}')}\right)\right)\right\|_{L^2(\Omega_r)} \leq C|D_{\rho_n}|^{3/8}.$$

We estimated every single term on the right hand side of (3.102) separately. This finishes the proof. □

3.4 The cross-section's polarization tensor and plasmonic resonances

Theorem 3.16 and the subsequent Corollary 3.17 induce a characterization of the three-dimensional polarization tensor $\mathbb{M}^\gamma$ for $\gamma \in \{\varepsilon, \mu\}$. If there is knowledge of the two-dimensional polarization tensor m^γ corresponding to the two-dimensional cross-section of the scattering objects $(D'_{\rho_n})_{n\in\mathbb{N}}$, then the polarization tensor $\mathbb{M}^\gamma$ has an explicit representation in terms of

$$\mathbb{M}^\gamma(s) = V(s) \left[\begin{array}{c|cc} 1 & 0 & 0 \\ \hline 0 & \multicolumn{2}{c}{\multirow{2}{*}{$R_\theta(s) m^\gamma R_\theta^{-1}(s)$}} \\ 0 & & \end{array}\right] V(s)^\top \quad \text{for a.e. } s \in (-\ell, \ell)\,.$$

Here, as before, $V(s)$ for a.e. $s \in (-\ell, \ell)$ is the matrix having the pairwise orthogonal vectors $\boldsymbol{t}_\Gamma(s), \boldsymbol{r}_\Gamma(s), \mathbf{s}_\Gamma(s)$ as its columns. In order to study $m^\gamma \in \mathbb{C}^{2\times 2}$, we first consider an equivalent definition to the one provided in (3.67), which is analogous to the definition of $\mathbb{M}^\gamma$ in (3.50). Using the measure μ' from (3.11) (which is simply the Dirac measure in 0), the sequence $D'_{\rho_n} = \rho_n D'$, where D' is a Lipschitz domain, satisfies

$$m^\gamma_{ij}\psi(0) = \int_{B'_r(0)} m^\gamma_{ij}\psi \, \mathrm{d}\mu' = \lim_{n\to\infty} \frac{1}{|D'_{\rho_n}|} \int_{D'_{\rho_n}} \frac{\partial z^{(j)}_{\rho_n}}{\partial x_i} \psi \, \mathrm{d}\boldsymbol{x} \tag{3.103}$$

for all $\psi \in C(\overline{B'_r(0)})$. The function $z^{(j)}_{\rho_n} \in H^1(B'_r(0))$ is the unique solution to

$$\operatorname{div}\left(\gamma'_{\rho_n} \nabla z^{(j)}_{\rho_n}\right) = 0 \quad \text{in } B'_r(0), \qquad \gamma'_{\rho_n} \frac{\partial z^{(j)}_{\rho_n}}{\partial \boldsymbol{\nu}} = \gamma_0 \nu_j \quad \text{on } \partial B'_r(0) \tag{3.104}$$

together with the normalization condition $\int_{\partial B'_r(0)} z^{(j)}_{\rho_n} = 0$. As in (3.46) and (3.47), the functions ν_j, $j = 1, 2$ denote the jth component of the exterior unit normal to $B'_r(0)$. In addition to (3.104) we also study the unperturbed problem, which is to find $z^{(j)} \in H^1(B'_r(0))$ such that

$$\Delta z^{(j)} = 0 \quad \text{in } B'_r(0), \qquad \gamma_0 \frac{\partial z^{(j)}}{\partial \boldsymbol{\nu}} = \gamma_0 \nu_j \quad \text{on } \partial B'_r(0) \tag{3.105}$$

together with the normalization condition $\int_{\partial B'_r(0)} z^{(j)} \, \mathrm{d}s = 0$. The solution of (3.105) is explicitly given by $z^{(j)} = x_j - |\partial B'_r(0)|^{-1} \int_{\partial B'_r(0)} x_j \, \mathrm{d}s$.

Remark 3.22. The definitions of m from (3.103) and (3.67) are equivalent. In fact, defining $\boldsymbol{\xi}' = (\xi_1, \xi_2)^\top \in S^1$, $z^{(\boldsymbol{\xi}')}_{\rho_n} = \xi_1 z^{(1)}_{\rho_n} + \xi_2 z^{(2)}_{\rho_n}$ and $z^{(\boldsymbol{\xi}')} = \xi_1 z^{(1)} + \xi_2 z^{(2)}$ implies by using (3.103) that

$$\int_{B'_r(0)} (m\boldsymbol{\xi}') \cdot \boldsymbol{\xi}' \psi \, \mathrm{d}\mu' = \lim_{n\to\infty} \frac{1}{|D'_{\rho_n}|} \int_{D'_{\rho_n}} \nabla z^{(\boldsymbol{\xi}')}_{\rho_n} \cdot \boldsymbol{\xi}' \psi \, \mathrm{d}\boldsymbol{x}\,. \tag{3.106}$$

By [30, Lem. 1], the characterization in (3.106) still holds true, when the function $z^{(\boldsymbol{\xi}')}_{\rho_n}$ on the right hand side of (3.106) is replaced with $\tilde{z}^{(\boldsymbol{\xi}')}_{\rho_n} \in H^1(B'_r(0))$, the unique solution to

$$\operatorname{div}\left(\gamma'_{\rho_n} \nabla \tilde{z}^{(\boldsymbol{\xi}')}_{\rho_n}\right) = 0 \quad \text{in } B'_r(0), \qquad \tilde{z}^{(\boldsymbol{\xi}')}_{\rho_n} = z^{(\boldsymbol{\xi}')} \quad \text{on } \partial B'_r(0)\,.$$

Then, the function $w^{(\boldsymbol{\xi}')}_{\rho_n} \in H^1_0(B'_r(0))$ from (3.66) is given by $w^{(\boldsymbol{\xi}')}_{\rho_n} = \tilde{z}^{(\boldsymbol{\xi}')}_{\rho_n} - z^{(\boldsymbol{\xi}')}$.

The following observations are simplified versions of the results in [31], since here, the interior material parameter γ_1 is constant. By considering the variational formulations of (3.104) and (3.105) it can be seen that

$$\int_{B'_r(0)} \gamma'_{\rho_n} \nabla(z^{(j)}_{\rho_n} - z^{(j)}) \cdot \nabla\overline{\psi} \, \mathrm{d}\boldsymbol{x} = \int_{D'_{\rho_n}} (\gamma_0 - \gamma_1) \nabla z^{(j)} \cdot \nabla\overline{\psi} \, \mathrm{d}\boldsymbol{x} \quad \text{for all } \psi \in H^1(B'_r(0))\,. \tag{3.107}$$

We perform the variable transformation

$$\phi : B'_{r/\rho_n}(0) \to B'_r(0), \quad \boldsymbol{x} \mapsto \boldsymbol{y} = \rho_n \boldsymbol{x}\,.$$

In order to relate the gradients to the new variable $\boldsymbol{y}$ we find that for $\boldsymbol{x} = \rho_n \boldsymbol{y}$ with $\boldsymbol{y} \in B'_{r/\rho_n}(0)$, it holds that

$$\nabla_{\boldsymbol{x}} V(\boldsymbol{x}) = \nabla_{\boldsymbol{x}} V(\rho_n \boldsymbol{y}) = \frac{1}{\rho_n} \nabla_{\boldsymbol{y}} V(\rho_n \boldsymbol{y})\,.$$

For (3.107) we therefore find that

$$\begin{aligned}\int_{B'_{r/\rho_n}(0)} \gamma'_{\rho_n}(\rho_n \boldsymbol{y})\, \nabla_{\boldsymbol{y}}(z^{(j)}_{\rho_n}(\rho_n \boldsymbol{y}) - z^{(j)}(\rho_n \boldsymbol{y})) \cdot \nabla_{\boldsymbol{y}} \overline{\psi}(\rho_n \boldsymbol{y})\, \mathrm{d}\boldsymbol{y} \\ = (\gamma_0 - \gamma_1)\, \rho_n \int_{\partial D'} \nu_j(\boldsymbol{y}) \overline{\psi}(\rho_n \boldsymbol{y})\, \mathrm{d}\boldsymbol{y} \quad \text{for all } \psi \in H^1(B'_r(0))\,. \end{aligned} \tag{3.108}$$

We define $\widetilde{w}_j \in H^1_{\mathrm{loc}}(\mathbb{R}^2)$ as the weak solution to

$$\begin{aligned} \Delta \widetilde{w}_j &= 0 \quad \text{in } \mathbb{R}^2 \setminus \partial D'\,, \\ \widetilde{w}_j|^+ - \widetilde{w}_j|^- &= 0 \quad \text{on } \partial D'\,, \\ \gamma_0 \frac{\partial \widetilde{w}_j}{\partial \boldsymbol{\nu}}\Big|^+ - \gamma_1 \frac{\partial \widetilde{w}_j}{\partial \boldsymbol{\nu}}\Big|^- &= -(\gamma_0 - \gamma_1)\nu_j \quad \text{on } \partial D'\,, \\ \widetilde{w}_j(\boldsymbol{x}) &\to 0 \quad \text{as } |\boldsymbol{x}| \to \infty\,. \end{aligned} \tag{3.109}$$

Indeed, $\widetilde{w}_j$ is uniquely determined. This is seen by using a single layer ansatz for the function $\widetilde{w}_j$, using jump relations to derive an integral equation and by studying the spectrum of the corresponding boundary integral operator (details on this follow later in this section). Moreover, using the weak formulation of (3.109) it holds that

$$\begin{aligned}&\int_{B'_{r/\rho_n}(0)} \gamma'_{\rho_n}(\rho_n \boldsymbol{y})\, \nabla_{\boldsymbol{y}} \widetilde{w}_j(\boldsymbol{y}) \cdot \nabla_{\boldsymbol{y}} \overline{\psi}(\rho_n \boldsymbol{y})\, \mathrm{d}\boldsymbol{y} \\ &= \int_{D'} \gamma_1 \nabla_{\boldsymbol{y}} \widetilde{w}_j(\boldsymbol{y}) \cdot \nabla_{\boldsymbol{y}} \overline{\psi}(\rho_n \boldsymbol{y})\, \mathrm{d}\boldsymbol{y} \quad + \int_{B'_{r/\rho_n}(0) \setminus \overline{D'}} \gamma_0 \nabla_{\boldsymbol{y}} \widetilde{w}_j(\boldsymbol{y}) \cdot \nabla_{\boldsymbol{y}} \overline{\psi}(\rho_n \boldsymbol{y})\, \mathrm{d}\boldsymbol{y} \\ &= (\gamma_0 - \gamma_1) \int_{\partial D'} \nu_j \overline{\psi}(\rho_n \boldsymbol{y})\, \mathrm{d}s(\boldsymbol{y}) + \gamma_0 \int_{\partial B'_{r/\rho_n}(0)} \frac{\partial \widetilde{w}_j}{\partial \boldsymbol{\nu}_{\boldsymbol{y}}}\Big|^-(\boldsymbol{y})\, \overline{\psi}(\rho_n \boldsymbol{y})\, \mathrm{d}s(\boldsymbol{y})\,. \end{aligned} \tag{3.110}$$

for all $\psi \in H^1(B'_r(0))$. We define

$$w_j(\boldsymbol{y}) = z^{(j)}_{\rho_n}(\rho_n \boldsymbol{y}) - z^{(j)}(\rho_n \boldsymbol{y}) - \rho_n \widetilde{w}_j(\boldsymbol{y}) - c_j\,, \tag{3.111}$$

where c_j is chosen in such a way that $\int_{\partial B'_{r/\rho_n}(0)} w_j \, \mathrm{d}s = 0$. A combination of (3.108) and (3.110) yields that for $\psi = w_j$ we have that

$$\int_{B'_{r/\rho_n}(0)} \gamma'_{\rho_n}(\rho_n \boldsymbol{y})\, |\nabla_{\boldsymbol{y}} w_j(\boldsymbol{y})|^2\, \mathrm{d}\boldsymbol{y} = -\rho_n \gamma_0 \int_{\partial B'_{r/\rho_n}(0)} \frac{\partial \widetilde{w}_j}{\partial \boldsymbol{\nu}_{\boldsymbol{y}}}(\boldsymbol{y}) \overline{w}_j(\boldsymbol{y})\, \mathrm{d}s(\boldsymbol{y})\,.$$

This gives that

$$\|\nabla w_j\|^2_{L^2(B'_{r/\rho_n}(0))} \leq C \rho_n \left| \int_{\partial B'_{r/\rho_n}(0)} \frac{\partial \widetilde{w}_j}{\partial \boldsymbol{\nu}_{\boldsymbol{y}}}(\boldsymbol{y}) \overline{w}_j(\boldsymbol{y})\, \mathrm{d}s(\boldsymbol{y}) \right|. \tag{3.112}$$

We rescale the integral on the right hand side to get that

$$\int_{\partial B'_{r/\rho_n}(0)} \frac{\partial \widetilde{w}_j}{\partial \boldsymbol{\nu}_{\boldsymbol{y}}}(\boldsymbol{y}) \overline{w}_j(\boldsymbol{y})\, \mathrm{d}s(\boldsymbol{y}) = \frac{1}{\rho_n} \int_{\partial B'_r(0)} \frac{\partial \widetilde{w}_j}{\partial \boldsymbol{\nu}_{\boldsymbol{y}}}\left(\frac{\boldsymbol{x}}{\rho_n}\right) \overline{w}_j\left(\frac{\boldsymbol{x}}{\rho_n}\right) \mathrm{d}s(\boldsymbol{x})\,.$$

We apply [55, Prop. 2.75] and find that

$$\left|\frac{\partial \widetilde{w}_j}{\partial \boldsymbol{\nu}}(\boldsymbol{x})\right| = \mathcal{O}(|\boldsymbol{x}|^{-2}) \quad \text{as } |\boldsymbol{x}| \to \infty\,, \quad \text{which implies} \quad \left\|\frac{\partial \widetilde{w}_j}{\partial \boldsymbol{\nu}}\left(\frac{\cdot}{\rho_n}\right)\right\|_{L^\infty(\partial B'_r(0))} \leq C{\rho_n}^2\,,$$

as $n \to \infty$. Further, we use the boundedness of the trace $\gamma : H^1(B'_r(0)) \to H^{1/2}(\partial B'_r(0))$, $\gamma u = u|_{\partial B'_r(0)}$ (see e.g. [97, Thm. 3.38]) and the Poincaré inequality and find that

$$\begin{aligned}\left|\int_{\partial B'_{r/\rho_n}(0)} \frac{\partial \widetilde{w}_j}{\partial \boldsymbol{\nu}_{\boldsymbol{y}}}(\boldsymbol{y})\overline{w}_j(\boldsymbol{y})\,\mathrm{d}s(\boldsymbol{y})\right| &\leq \frac{1}{\rho_n}\left\|\frac{\partial \widetilde{w}_j}{\partial \boldsymbol{\nu}}\left(\frac{\cdot}{\rho_n}\right)\right\|_{L^\infty(\partial B'_r(0))}\left\|w_j\left(\frac{\cdot}{\rho_n}\right)\right\|_{H^{1/2}(\partial B'_r(0))}\\ &\leq C\rho_n \left\|\nabla w_j\right\|_{L^2(B'_{r/\rho_n}(0))}\,.\end{aligned}$$

Combining this inequality with (3.112) yields that

$$\left\|\nabla w_j\right\|_{L^2(B'_{r/\rho_n}(0))} \leq C{\rho_n}^2\,. \tag{3.113}$$

Thus, returning to the definition of m_{ij}^γ in (3.103), we find with another rescaling that

$$\begin{aligned}\frac{1}{|D'_{\rho_n}|}\int_{D'_{\rho_n}} \frac{\partial z_{\rho_n}^{(j)}}{\partial x_i}\psi\,\mathrm{d}\boldsymbol{x} &= \frac{1}{|D'|}\int_{D'}\frac{1}{\rho_n}\frac{\partial z_{\rho_n}^{(j)}}{\partial y_i}(\rho_n\boldsymbol{y})\psi(\rho_n\boldsymbol{y})\,\mathrm{d}\boldsymbol{y}\\ &= \frac{1}{|D'|}\int_{D'}\frac{1}{\rho_n}\left(\frac{\partial z_{\rho_n}^{(j)}}{\partial y_i}(\rho_n\boldsymbol{y}) - \rho_n\delta_{ij} - \rho_n\frac{\partial \widetilde{w}_j}{\partial y_i}\right)\psi\left(\rho_n\boldsymbol{y}\right)\,\mathrm{d}\boldsymbol{y}\\ &\quad + \frac{1}{|D'|}\int_{D'}\left(\delta_{ij} + \frac{\partial \widetilde{w}_j}{\partial y_i}\right)\psi\left(\rho_n\boldsymbol{y}\right)\,\mathrm{d}\boldsymbol{y}\,.\end{aligned} \tag{3.114}$$

for all $\psi \in C(\overline{B'_r\,(0)})$. For the first integral on the right hand side of (3.114) we use (3.111) and (3.113) to find that

$$\left|\frac{1}{|D'|}\int_{D'}\frac{1}{\rho_n}\left(\frac{\partial z_{\rho_n}^{(j)}}{\partial y_i}(\rho_n\boldsymbol{y}) - \rho_n\delta_{ij} - \rho_n\frac{\partial \widetilde{w}_j}{\partial y_i}\right)\psi\left(\rho_n\boldsymbol{y}\right)\,\mathrm{d}\boldsymbol{y}\right| \leq C\rho_n\,.$$

Therefore, we deduce for the second term by using (3.103) that

$$\frac{1}{|D'|}\int_{D'}\left(\delta_{ij} + \frac{\partial \widetilde{w}_j}{\partial y_i}\right)\mathrm{d}\boldsymbol{y}\psi(0) = \int_{B'_r(0)} m_{ij}^\gamma\psi\,\mathrm{d}\mu' \quad \text{for all } \psi \in H^1(B'_r\,(0))\,.$$

Consequently,

$$m_{ij}^\gamma = \delta_{ij} + \frac{1}{|D'|}\int_{D'}\frac{\partial \widetilde{w}_j}{\partial y_i}\,\mathrm{d}\boldsymbol{y} = \delta_{ij} + \frac{1}{|D'|}\int_{\partial D'} y_i\frac{\partial \widetilde{w}_j}{\partial \boldsymbol{\nu}}\Big|_{\partial D'}^-\,\mathrm{d}s(\boldsymbol{y})\,.$$

We summarize these observations in the following lemma.

Lemma 3.23. *Let the two-dimensional cross-section D'_{ρ_n} be given by $D'_{\rho_n} = \rho_n D'$, where $D' \subset \mathbb{R}^2$ is a simply connected Lipschitz domain and $(\rho_n)_n \subset (0,\infty)$ is a sequence converging to zero. Further, let $\widetilde{w}_j \in H^1_{loc}(\mathbb{R}^2)$ be the unique solution to (3.109). Then, for the two-dimensional polarization tensor $m^\gamma = (m_{ij}^\gamma)$ corresponding to $(D'_{\rho_n})_{n\in\mathbb{N}}$ it holds that*

$$m_{ij}^\gamma = \delta_{ij} + \frac{1}{|D'|}\int_{D'}\frac{\partial \widetilde{w}_j}{\partial y_i}\,\mathrm{d}\boldsymbol{y} = \delta_{ij} + \frac{1}{|D'|}\int_{\partial D'} y_i\frac{\partial \widetilde{w}_j}{\partial \boldsymbol{\nu}}\Big|_{\partial D'}^-\,\mathrm{d}s(\boldsymbol{y})\,.$$

Explicit formulas for m^γ are e.g. available when D' is an ellipse. If the semi axes of the ellipse are aligned with the coordinate axes, the semi axis in x_1-direction has length a and the semi axis in x_2-direction has length b, then the polarization tensor m^γ has the form (see e.g. [10, Prop. 4.6], [25])

$$m^\gamma = \begin{bmatrix} \frac{a+b}{a+\gamma_r b} & 0 \\ 0 & \frac{a+b}{b+\gamma_r a} \end{bmatrix}. \tag{3.115}$$

In order to approximate a solution to (3.109) for more general cross-sections $D'_{\rho_n} = \rho_n D'$ one uses a single layer ansatz. One aims to find a density $a_j \in H^{1/2}(\partial D')$ such that

$$w_j(\boldsymbol{x}) = \int_{\partial D'} a_j(\boldsymbol{y}) \widetilde{\Phi}(\boldsymbol{x}, \boldsymbol{y}) \, \mathrm{d}s(\boldsymbol{y}) \,,$$

where $\widetilde{\Phi}$ is the fundamental solution of the two-dimensional Laplace equation given by

$$\widetilde{\Phi}(\boldsymbol{x}, \boldsymbol{y}) = \frac{1}{2\pi} \log\left(\frac{1}{|\boldsymbol{x}-\boldsymbol{y}|}\right) \quad \text{for } \boldsymbol{x} \neq \boldsymbol{y} \,. \tag{3.116}$$

Applying the jump relations for the normal derivative to (3.116) (see e.g. [97, Thm. 6.11]) and considering the boundary condition for the normal derivative in (3.109) gives that the density a_j must satisfy

$$\left(\frac{1}{2}\left(\frac{1+\gamma_r}{1-\gamma_r}\right) I - K^*_{\partial D'}\right) a_j \;=\; \nu_j \quad \text{on } \partial D' \,. \tag{3.117}$$

Here, $K^*_{\partial D'} : H^{-1/2}(\partial D') \to H^{-1/2}(\partial D')$ is the adjoint double layer potential, also known as the Neumann–Poincaré operator, defined by

$$\left(K^*_{\partial D'} a_j\right)(\boldsymbol{x}) \;=\; \int_{\partial D'} \frac{\partial \widetilde{\Phi}(\boldsymbol{x}, \boldsymbol{y})}{\partial \boldsymbol{\nu}(\boldsymbol{x})} a_j(\boldsymbol{y}) \, \mathrm{d}s(\boldsymbol{y}) \,, \quad \boldsymbol{x} \in \partial D' \,.$$

In what follows, we focus on the case, in which $\gamma_r = \varepsilon_r = \varepsilon_1/\varepsilon_0$ with $\mathrm{Re}(\varepsilon_r) < 0$ and $\mathrm{Im}(\varepsilon_r) > 0$. As described in Chapter 2, electric permittivities in this range are observed for metallic scattering objects, in particular for frequencies in the optical regime. Electric permittivities with $\mathrm{Re}(\varepsilon_r) < 0$ and $\mathrm{Im}(\varepsilon_r) > 0$ are also predicted by the Drude model that we studied in Remark 2.7. We put the concept of localized surface plasmons in a more general context and motivate this phenomenon first for general three-dimensional metallic nanoparticles. Especially, we recall results from the literature, where balls and ellipsoids are studied. Then, we relate this to two-dimensional cross-sections of a thin metallic nanowire and thus, obtain conditions for the appearance of a plasmon resonance for a thin metallic nanowire D_ρ as in (3.7).

Consider an electromagnetic field (e.g. an incident plane wave) illuminating a three-dimensional sub-wavelength metallic nanoparticle. In more detail, this is an object of characteristic size $\rho > 0$ (e.g. the radius of a ball), for which $\rho \ll \lambda$, where λ denotes the wavelength of the exterior electromagnetic field. As described in [85], the metal's free conduction electrons perform a collective oscillation as the nanoparticle is illuminated by an electric field (see also [85, Fig. 1] for a visualization). On the one hand, the metal's plasma, i.e. the gas of charged electrons, is displaced due to the external field, which drives the negatively charged electrons away from the positively charged nuclei. On the other hand, by Coulomb's law, oppositely charged particles, i.e., the negatively charged electrons and the positively charged nuclei, attract each other. This means that, on the one side, electrons and nuclei are driven apart, but on the other hand, a restoring force acts to bring them back together. This results in a collective surface charge-density oscillation, what is called a localized surface plasmon (see e.g. [1, p. 152], [102, p. 369], [96, p. 65]). As stated in e.g. [1, pp. 152], the optical response of a plasmon is characterized via $\boldsymbol{p} = \alpha \boldsymbol{E}_0$,

where $\boldsymbol{p}$ is the electric dipole moment, $\boldsymbol{E}_0$ is the incident field and α is the polarizability of the nanoparticle. The occurrence of a localized surface plasmon resonance is related to roots in the denominator of the polarizability α, with respect to the frequency-dependent material parameter $\varepsilon_r(\omega)$ (see [1, p. 153]). In many textbooks and articles, localized plasmon resonances are studied first for the case of a sub-wavelength metallic sphere with radius $a > 0$ (see e.g. [1, p. 154], [23, Ch. 5], [81, Sec. 9.2], [85], [96, Sec. 5.1], [102, pp. 398]). The polarizability can be written in this case as (see [1, Eq. (5.3)])

$$\alpha \;=\; 4\pi\varepsilon_0 a^3 \frac{\varepsilon_r - 1}{\varepsilon_r + 2}\,. \tag{3.118}$$

In [96, p. 68] it is pointed out that the polarizability for a sphere in (3.118) possesses the same representation as the Clausius-Mossoti relation found in e.g. [82, Eq. 4.70]. The polarization α from (3.118) has a pole for $\varepsilon_r = -2$. The frequency, for which this condition is met is sometimes called the Fröhlich frequency (see e.g. [23, p. 327], [96, p. 68]). We emphasize that this electric permittivity is not attained by the experimental data from [83] or by the Drude model from Remark 2.7, since $\mathrm{Im}(\varepsilon_r) > 0$. However, one expects a great increase of $|\alpha|$ if $\mathrm{Re}(\varepsilon_r) = -2$ and $\mathrm{Im}(\varepsilon_r)$ is small. Using the experimental data from [83], we find that the condition $\mathrm{Re}(\varepsilon_r) = -2$ is met at approximately 846.51THz ($\varepsilon_r = -2 + 0.28$) for silver and 620.32THz ($\varepsilon_r = -2 + 4.31\mathrm{i}$) for gold (see also Figure 2.1). For the Drude model, the condition $\mathrm{Re}(\varepsilon_r) = -2$ can be solved for the angular frequency explicitly: Using (2.37), we find that $\mathrm{Re}(\varepsilon_r) = -2$ if and only if $\omega = (\omega_p^2/3 - \Gamma^2)^{1/2}$, where ω_p is the plasma frequency. In the literature, one often suppresses the damping parameter Γ in this equation (since it is relatively small) and obtains the resonance frequency at $\omega = \omega_p/\sqrt{3}$ (see e.g. [1, p. 155]). Using the same parameters for ω_p for silver and gold as those in Remark 2.7 suggests that for silver, the plasmon resonance occurs approximately at 1262THz ($\varepsilon_{r,\mathrm{Drude}} = -2 + 0.01\mathrm{i}$) and for gold at 1241THz ($\varepsilon_{r,\mathrm{Drude}} = -2 + 0.04\mathrm{i}$). This simple study reminds us again that the Drude model does not provide a good model for the relative electric permittivity at optical or even higher frequencies. In [85] the authors consider a spheroid with ratio of major and minor axis r ranging from $r = 1$ (sphere) to $r = 10$ (oblate spheroid) and observe a red-shift of the plasmon resonance as r increases. In [23, Ch. 12.2.1] the polarizability for an ellipsoid is studied. It is shown that if an incident wave has a direction of propagation that coincides with one of the principal axis of the ellipsoid, then, the polarizability is given by

$$\alpha \;=\; v\varepsilon_0 \frac{\varepsilon_r - 1}{1 + L(\varepsilon_r - 1)}\,, \tag{3.119}$$

where v denotes the volume of the ellipsoid and the parameter L is a scalar that depends on the shape of the ellipsoid and lies between 0 and 1. Thus, the condition for a vanishing denominator is $\varepsilon_r = 1 - 1/L$. For a sphere, one obtains $L = 1/3$ (see [23, p. 146]) and thus, a plasmon resonance occurs at the Fröhlich frequency.

Polarization tensors for ellipsoids, similarly defined as polarization tensors for thin tubular scattering objects in (3.50), are studied in [10, Sec. 4.2]. Up to a constant, these formulas coincide with those in (3.118) and (3.119).

A direct implication of a localized plasmon resonance is the strong enhancement of the electromagnetic field near the boundary of the scattering object. Applications include e.g. surface enhanced Raman scattering and optical sensing (see e.g. [96, Ch. 9, 10]).

We return to the two-dimensional polarization tensor corresponding to an ellipse in (3.115). In analogy to the previously studied conditions, we find that the resonance condition in (3.115) is met if and only if the real part of a denominator vanishes. Thus, the frequency ω is said to be a plasmonic resonance frequency for an ellipse with semi axis lengths a and b if either

$$-\frac{a}{b} \;=\; \mathrm{Re}(\varepsilon_r(\omega)) \quad \text{or} \quad -\frac{b}{a} \;=\; \mathrm{Re}(\varepsilon_r(\omega))\,. \tag{3.120}$$

For a circle, i.e. for $a = b$ we therefore see that the resonance condition is fulfilled if and only if $\mathrm{Re}(\varepsilon_r) = -1$. This resonance condition is found e.g. in [102, Sec. 12.4.1] in the study of transverse plasmon resonances of a thin wire. For a general two-dimensional simply connected Lipschitz domain D' the two-dimensional polarization tensor m^ε cannot be computed explicitly and poles in m^ε cannot be studied as we did before. The authors in [6, 43] consider the integral equation (3.117) and define ω to be a (dielectric) plasmonic resonance frequency, if

$$\mathrm{Re}\left(\frac{1+\varepsilon_r(\omega)}{2(1-\varepsilon_r(\omega))}\right) \text{ lies in the spectrum of } K^*_{\partial D'}\,. \tag{3.121}$$

Based on this definition, the optimal design of two-dimensional shapes that resonate at particular frequencies has been considered in [5]. Furthermore, an inverse problem that uses the occurrence of plasmon resonances is studied in [43]. In [86, Sec. 8.3] it is shown that the spectrum of $K^*_{\partial D'}$ corresponding to an ellipse D' with eccentricity $q = (a-b)/(a+b)$ is given by

$$\sigma(K^*_{\partial D'}) = \left\{\pm\frac{1}{2}q^k \,\middle|\, k \geq 1\right\} \cup \left\{0, \frac{1}{2}\right\}.$$

Since

$$\frac{1+\varepsilon_r(\omega)}{2(1-\varepsilon_r(\omega))} = \frac{1-\mathrm{Re}(\varepsilon_r)^2-\mathrm{Im}(\varepsilon_r)^2}{2((1-\mathrm{Re}(\varepsilon_r))^2+\mathrm{Im}(\varepsilon_r)^2)} + \frac{2\,\mathrm{Im}(\varepsilon_r)}{(1-\mathrm{Re}(\varepsilon_r))^2+\mathrm{Im}(\varepsilon_r)^2}\mathrm{i}$$

and the spectrum of $K^*_{\partial D'}$ is real-valued, the integral equation (3.117) becomes singular if and only if ω is a dielectric plasmonic resonance and $\mathrm{Im}(\varepsilon_r) = 0$. In this case, it holds that

$$\mathrm{Re}\left(\frac{1+\varepsilon_r(\omega)}{2(1-\varepsilon_r(\omega))}\right) = \pm\frac{a-b}{2(a+b)} \quad \text{if and only if} \quad \mathrm{Re}(\varepsilon_r(\omega)) \in \left\{-\frac{a}{b}, -\frac{b}{a}\right\},$$

giving the condition for plasmonic resonances that we observed by studying the poles of m^ε from (3.115) in (3.120).

Based on these observations, and by using Corollary 3.17 we can apply the definition of (dielectric) plasmonic resonances to thin tubular scattering objects D_ρ with a cross-section $D'_\rho = \rho D'$, where D' is a simply connected Lipschitz domain.

Definition 3.24. Let D_ρ be a thin tubular scattering object as in (3.7) with cross-section $D'_\rho = \rho D'$, where D' is a simply connected and bounded Lipschitz domain. A frequency ω (or equivalently f) is defined to be a dielectric plasmonic resonance frequency of D_ρ if and only if the condition (3.121) for the cross-section is fulfilled. If D' is an ellipse with semi axes lengths a and b, then the frequency ω (or equivalently f) is a plasmonic resonance frequency if (3.120) is fulfilled.

Similar as in [85], where the tuning of the major and minor axis of a spheroids leads to the appearance of plasmon resonances at different frequencies, the tuning of the elliptical cross-section of a thin nanowire D_ρ can be used to shift the appearance of plasmonic resonances across the optical band. We apply this tuning in the shape optimizations for highly electromagnetically chiral structures in Chapter 5.

3.5 Numerical experiments on the accuracy of the leading order term of the asymptotic representation formula

The asymptotic representation formula from Theorem 3.6 together with the characterization of the polarization tensor from Theorem 3.16 provide an efficient way to approximate the electric scattered field away from the scattering object or the electric far field pattern corresponding to a thin tubular scattering object. The approximation relies in evaluating the leading order term

of the asymptotic perturbation formula in (3.21) or (3.22) and to neglect terms of higher order in $o(|D_\rho|)$. Consequently, the quality of the approximation is determined by the norm of the terms of higher order. As we do not provide any bounds on this norm, we perform numerical experiments for several scattering objects made from dielectric and metallic material.

In the following, we denote the leading order term of the electric far field pattern expansion from (3.22) by $\widetilde{\boldsymbol{E}_\rho^\infty}$, i.e.

$$\widetilde{\boldsymbol{E}_\rho^\infty}(\widehat{\boldsymbol{x}}) = \frac{|D_{\rho_n}|}{2\ell}\Bigg(\int_K (\mu_r - 1)\, \mathrm{i}k e^{-\mathrm{i}k\widehat{\boldsymbol{x}}\cdot\boldsymbol{y}}\, (\widehat{\boldsymbol{x}} \times \mathbb{I}_3)\, \mathbb{M}^\mu(\boldsymbol{y})\, \mathbf{curl}\, \boldsymbol{E}^i(\boldsymbol{y})\, \mathrm{d}s(\boldsymbol{y}) \\ + k^2 \int_K (\varepsilon_r - 1)\, e^{-\mathrm{i}k\widehat{\boldsymbol{x}}\cdot\boldsymbol{y}}\, (\widehat{\boldsymbol{x}} \times (\mathbb{I}_3 \times \widehat{\boldsymbol{x}}))\, \mathbb{M}^\varepsilon(\boldsymbol{y}) \boldsymbol{E}^i(\boldsymbol{y})\, \mathrm{d}s(\boldsymbol{y}) \Bigg), \quad \widehat{\boldsymbol{x}} \in S^2. \tag{3.122}$$

Moreover, we consider far field data $\boldsymbol{E}_\rho^\infty$ accurately computed by using the boundary element library Bempp (see [115]). In order to approximate a solution with Bempp, one transforms the transmission problem for the Maxwell's equation from (2.34) into an integral equation on the boundary of the scattering object. The corresponding integral equation is based on the multitrace operator. An explanation on this is found in Appendix C. We stress that although in our simulations $\boldsymbol{E}_\rho^\infty$ takes the role of a reference solution, and is also denoted as such, it is still a numerical approximation, where errors arise e.g. from the boundary element mesh size, H-matrix compression or the use of an iterative solver to approximate the solution of the linear system of equations. In our Bempp simulations, we apply the GMRES method to approximate the linear system of equations that results from the discretization of the Calderón operator (see Appendix C). The tolerance is set to 10^{-5} and we do not use any restarts of the GMRES method.

In order to quantify the error of the leading order term in (3.122) to the reference solution $\boldsymbol{E}_\rho^\infty$, we consider the relative difference of the far field, measured in the L^2 norm, i.e.

$$\texttt{RelDiff} = \frac{\|\widetilde{\boldsymbol{E}_\rho^\infty} - \boldsymbol{E}_\rho^\infty\|_{L_t^2(S^2)}}{\|\boldsymbol{E}_\rho^\infty\|_{L_t^2(S^2)}}. \tag{3.123}$$

To approximate the norms we fix $N \in \mathbb{N}$ and consider $2N(N-1)$ points on S^2 given by

$$\boldsymbol{y}_{jl} = [\sin(\theta_j)\cos(\varphi_l),\ \sin(\theta_j)\sin(\varphi_l),\ \cos(\theta_j)]^\top, \qquad j = 1, \dots, N-1, \quad l = 1, \dots, 2N,$$

where $\theta_j = j\pi/N$ and $\varphi_l = (l-1)\pi/N$. Using the composite trapezoidal rule in both directions the quantity `RelDiff` is approximated via

$$\texttt{RelDiff} \approx \left(\frac{\sum_{l=1}^{2N} \sum_{j=1}^{N-1} \sin(\theta_j)\, |(\widetilde{\boldsymbol{E}_\rho^\infty} - \boldsymbol{E}_\rho^\infty)(\boldsymbol{y}_{jl})|^2}{\sum_{l=1}^{2N} \sum_{j=1}^{N-1} \sin(\theta_j)\, |\boldsymbol{E}_\rho^\infty(\boldsymbol{y}_{jl})|^2} \right)^{1/2}.$$

In this section the first numerical examples of this thesis are simulated. For simulating scattering from thin metallic nanowires, we can always use a scaling in such a way that we can perform the simulation with the computational wave number k_c, which is often chosen to be $k_c = 1$. Details on upscaling and downscaling of scattering objects are collected in the following remark.

Remark 3.25. Let $\alpha > 0$ be a scaling parameter that is supposed to enlarge ($\alpha > 1$) or shrink ($\alpha < 1$) the scattering object. Effectively, this means that the original scattering object D is transformed to αD. We define the scaled electric permittivity distribution ε_c and magnetic permeability distribution μ_c by $\varepsilon_c(\boldsymbol{x}) = \varepsilon(\alpha^{-1}\boldsymbol{x})$ and $\mu_c(\boldsymbol{x}) = \mu(\alpha^{-1}\boldsymbol{x})$. Furthermore, we define the scaled electric and magnetic fields by $\boldsymbol{E}_c(\boldsymbol{x}) = \boldsymbol{E}(\alpha^{-1}\boldsymbol{x})$ and $\boldsymbol{H}_c(\boldsymbol{x}) = \boldsymbol{H}(\alpha^{-1}\boldsymbol{x})$. The subscript c stands for computational, as these quantities will be used in numerical simulations later. The variable transform $\boldsymbol{y} = \alpha^{-1}\boldsymbol{x}$ yields that $\boldsymbol{V}_c(\boldsymbol{x}) = \boldsymbol{V}(\alpha^{-1}\boldsymbol{x}) = \boldsymbol{V}(\boldsymbol{y})$ and

$$\mathbf{curl}_{\mathrm{y}}\, \boldsymbol{V}(\boldsymbol{y}) = \mathbf{curl}_{\mathrm{y}}\, \boldsymbol{V}(\alpha^{-1}\boldsymbol{x}) = \alpha\, \mathbf{curl}_{\mathrm{x}}\, \boldsymbol{V}(\alpha^{-1}\boldsymbol{x}) = \alpha\, \mathbf{curl}_{\mathrm{x}}\, \boldsymbol{V}_c(\boldsymbol{x}).$$

With B and F from (2.53) and (2.54), we see that $\boldsymbol{E} \in H(\mathbf{curl}, B_R(0))$ satisfies

$$B(\boldsymbol{E}, \boldsymbol{V}) \;=\; F(\boldsymbol{V}) \quad \text{for all } \boldsymbol{V} \in H(\mathbf{curl}, B_R(0))$$

if and only if $\boldsymbol{E}_c \in H(\mathbf{curl}, B_{\alpha R}(0))$ satisfies

$$B_c(\boldsymbol{E}_c, \boldsymbol{V}) \;=\; F_c(\boldsymbol{V}) \quad \text{for all } \boldsymbol{V} \in H(\mathbf{curl}, B_{\alpha R}(0))\,.$$

Here, B_c and F_c differ from B and F by replacing ε and μ by ε_c and μ_c and ω by $\omega_c = \alpha^{-1}\omega$. Moreover, the integration domains changed from $B_R(0)$ and $\partial B_R(0)$ to $B_{\alpha R}(0)$ and $\partial B_{\alpha R}(0)$. Both $\boldsymbol{E}^s = \boldsymbol{E} - \boldsymbol{E}^i$ and $\boldsymbol{E}_c^s = \boldsymbol{E}_c - \boldsymbol{E}_c^i$ possess a far field as in (2.33) given by

$$\boldsymbol{E}^s(\boldsymbol{x}) \;=\; \frac{e^{\mathrm{i}k|\boldsymbol{x}|}}{4\pi|\boldsymbol{x}|}\left(\boldsymbol{E}^\infty(\widehat{\boldsymbol{x}}) + \mathcal{O}\left(\frac{1}{|\boldsymbol{x}|}\right)\right) \quad \text{and} \quad \boldsymbol{E}_c^s(\boldsymbol{x}) \;=\; \frac{e^{\mathrm{i}k_c|\boldsymbol{x}|}}{4\pi|\boldsymbol{x}|}\left(\boldsymbol{E}_c^\infty(\widehat{\boldsymbol{x}}) + \mathcal{O}\left(\frac{1}{|\boldsymbol{x}|}\right)\right),$$

as $|\boldsymbol{x}| \to \infty$, where $k_c = \omega_c\sqrt{\varepsilon_0\mu_0}$. Due to the equality $\boldsymbol{E}_c(\boldsymbol{x}) = \boldsymbol{E}(\alpha^{-1}\boldsymbol{x})$ we see that

$$\boldsymbol{E}_c^s(\boldsymbol{x}) \;=\; \boldsymbol{E}^s(\alpha^{-1}\boldsymbol{x}) \;=\; \frac{e^{\mathrm{i}k_c|\boldsymbol{x}|}}{4\pi|\boldsymbol{x}|}\left(\alpha\boldsymbol{E}^\infty(\widehat{\boldsymbol{x}}) + \mathcal{O}\left(\frac{1}{|\boldsymbol{x}|}\right)\right)$$

giving that

$$\boldsymbol{E}_c^\infty \;=\; \alpha\boldsymbol{E}^\infty\,. \tag{3.124}$$

When we are interested in the norm of the far field (this will later be the case when studying the total interaction cross-section) we use (3.124) to recover the original far field. In the following, we provide an example on how we scale a metallic nanowire.

Example 3.26. Let the exterior wavelength be given by $\lambda = 400\text{nm} = 0.4\mu\text{m}$ (i.e. the frequency is $f = 750\text{THz}$ and the wave number is $k = 2\pi/(0.4\times10^{-6})\text{m}^{-1}$) and consider the material parameters for silver from [83] giving $\mu_r = 1$ and $\varepsilon_r = -4.42 + 0.21\mathrm{i}$. Let the scatterer be a thin helix with two turns defined by the center curve parametrized by

$$p_1(s) \;=\; R\cos(4\pi s), \quad p_2(s) \;=\; R\sin(4\pi s), \quad p_3(s) \;=\; hs \qquad \text{for } s \in [0,1]$$

with radius $R = 63.66\text{nm}$ and total height $h = 381.97\text{nm}$. Further, let the radius of the circular cross-section of the thin wire be given by $\rho = 12.73\text{nm}$. We scale the object in such a way that we can use the exterior wave number $k_c = 1\text{m}^{-1}$ in our numerical simulation, giving that $\lambda_c = 2\pi\text{m}$. For this, define $\alpha = 2\pi/(0.4\times10^{-6}) \approx 1.57\times10^7$ as the scaling parameter. Indeed, from Remark 3.25 we find that $k_c = \alpha^{-1}k = 1\text{m}^{-1}$ giving $\lambda_c = 2\pi\text{m}$. The scaled exterior radius R_c, height h_c and inner radius ρ_c are given by

$$R_c \;=\; 63.66\alpha\times10^{-9}\text{m} \;\approx\; 1\text{m}, \quad h_c \;=\; 381.97\alpha\times10^{-9}\text{m} \;\approx\; 6\text{m}, \quad \rho_c \;=\; 12.73\alpha\times10^{-9}\text{m} \;\approx\; 0.2\text{m}$$

To summarize, we compute the far field $\boldsymbol{E}_c^\infty$ corresponding to the double helix with radius $R_c = 1\text{m}$, height $h_c = 6\text{m}$, cross-section radius $\rho_c = 0.2\text{m}$ and wave number $k_c = 1\text{m}^{-1}$ and obtain the far field in the original units $\boldsymbol{E}^\infty$ by setting $\boldsymbol{E}^\infty = \alpha^{-1}\boldsymbol{E}_c^\infty$.

Remark 3.27. This scaling is reasonable for computational purposes only, since in practice, the modification of the exterior wavelength changes the electric permittivity ε of a metallic nanowire.

In order to approximate the center curve of the scattering object under consideration, we use cubic splines with the not-a-knot condition at the end points of the splines. Given a non-uniform partition

$$\triangle \;=\; \{0 = t_1 < t_2 < \cdots < t_n = 1\} \;\subset\; [0,1]\,, \tag{3.125}$$

we denote a corresponding not-a-knot spline by $\boldsymbol{p}_\triangle$ (see e.g. [40, p. 44]). Note that for numerical simulations, in order to integrate over the spine curve, we always consider the interval $[0,1]$ instead of $(-\ell,\ell)$ as we did in the definition of D_ρ in (3.7). The reason for this is that a parametrization by arc length for the spine curve is difficult to realize numerically. We summarize the generation of spline curves from given spatial points $\boldsymbol{x}^{(j)} \in \mathbb{R}^3$, $j = 1,\dots,n$, as well as the discretization of curve integrals in the following technical remark.

Remark 3.28. For $n \in \mathbb{N}$ nodal points $\boldsymbol{x}^{(j)} \in \mathbb{R}^3$, $j = 1,\dots,n$, in space we consider the determination of the parameter values t_j defining the partition $\triangle$ from (3.125) by chord length (see [106, pp. 364-365]). We denote by d the total chord length defined by

$$d \;=\; \sum_{j=1}^{n-1} |\boldsymbol{x}^{(j+1)} - \boldsymbol{x}^{(j)}|$$

and set

$$t_1 \;=\; 0, \quad t_n \;=\; 1, \quad t_j \;=\; t_{j-1} + \frac{|\boldsymbol{x}^{(j+1)} - \boldsymbol{x}^{(j)}|}{d} \quad \text{for } j = 2,\dots,n-1\,.$$

Note that this usually leads to a non-uniform partition $\triangle$ from (3.125). Now, we can compute the interpolating cubic not-a-knot spline $\boldsymbol{p}_\triangle$ (see e.g. [40, p. 44]) satisfying $\boldsymbol{p}_\triangle(t_j) = \boldsymbol{x}^{(j)}$. Denoting by $\boldsymbol{p}_{\triangle,j}$ the cubic polynomial defined on the segment $[t_j, t_{j+1}]$ for $j = 1,\cdots,n-1$, the not-a-knot condition reads $\boldsymbol{p}'''_{\triangle,1}(t_2) = \boldsymbol{p}'''_{\triangle,2}(t_2)$ and $\boldsymbol{p}'''_{\triangle,n-2}(t_{n-1}) = \boldsymbol{p}'''_{\triangle,n-1}(t_{n-1})$. Thus, the knots $\boldsymbol{x}^{(2)}$ and $\boldsymbol{x}^{(n-1)}$ behave as if they were no knots, since the piecewise defined cubic polynomials have matching derivatives of arbitrary order at these spatial points. For every segment $[t_j, t_{j+1}]$, $j = 1,\dots,n-1$, we define the odd number $M \in \mathbb{N}$, $M \geq 3$, and consider M uniformly distributed points in $[t_j, t_{j+1}]$ including t_j and t_{j+1}. For every segment, we denote the discretization length by $h_j = (t_{j+1} - t_j)/(M-1)$, $j = 1,\dots,n-1$. This gives a total amount of $T = (M-1)(n-1)+1$ non-repeating points that we denote by $\boldsymbol{x}_\tau$ for $\tau = 1,\dots,T$. We use these in order to approximate curve integrals as described next. Let $f : \mathbb{R}^3 \to \mathbb{C}$ be an integrable function such as e.g. a component of the integrand of the leading order term of (3.22). It holds that

$$\begin{aligned}\int_0^1 f(\boldsymbol{x})\,\mathrm{d}\boldsymbol{x} \;=\; \sum_{j_1=1}^{n-1} \int_{t_{j_1}}^{t_{j_1+1}} f(\boldsymbol{x})\,\mathrm{d}\boldsymbol{x} \;&\approx\; \sum_{j_1=1}^{n-1} \sum_{j_2=(M-1)(j_1-1)+1}^{(M-1)j_1+1} w_{j_2} f(\boldsymbol{x}_{j_2}) \\ &=\; \sum_{j_1=1}^{n-1} \sum_{j_2=1}^{M} w_{j_2+(M-1)(j_1-1)} f\big(\boldsymbol{x}_{j_2+(M-1)(j_1-1)}\big)\,,\end{aligned}$$

where the approximation is done by using the composite Simpson's rule with equidistant discretization length h_{j_1} (see e.g. [91, Thm. 12.2]). By rearranging the last sums in such a way that

$$\int_0^1 f(\boldsymbol{x})\,\mathrm{d}\boldsymbol{x} \;\approx\; \sum_{j=1}^{T} \widetilde{w_j} f(\boldsymbol{x}_j)$$

we find that

$$\widetilde{w_j} \;=\; \begin{cases} \frac{1}{3}h_1\,, & j = 1, \\ \frac{1}{3}h_{n-1}\,, & j = T, \\ \frac{4}{3}h_k\,, & j \text{ even, } (M-1)(k-1)+1 < j < (M-1)k+1 \text{ for a } k = 1,\dots,n-1, \\ \frac{2}{3}h_k\,, & j \text{ odd, } j \neq (M-1)(k-1)+1 \text{ for all } k = 2,\dots,n-1, \\ \frac{1}{3}h_k + \frac{1}{3}h_{k+1}\,, & j \text{ odd, } j = (M-1)(k-1)+1 \text{ for a } k = 2,\dots,n-1\,. \end{cases}$$

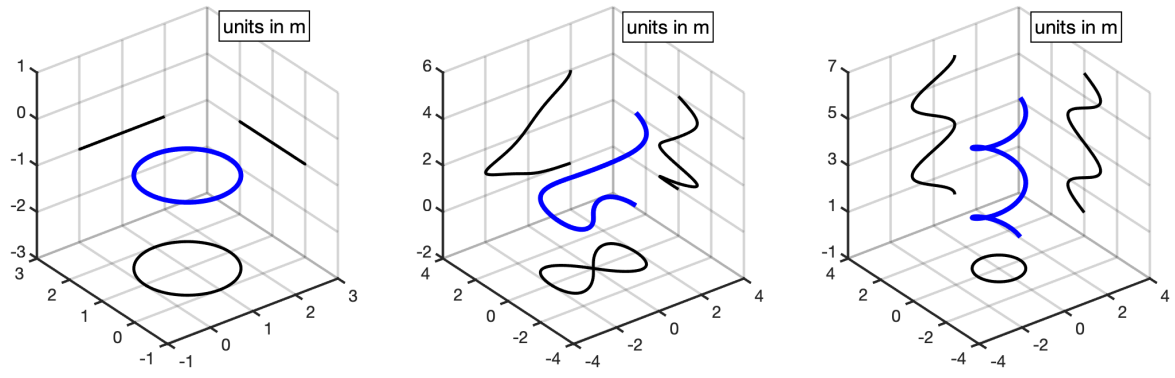

Figure 3.2: The three center curves from Example 3.29 - Example 3.31, together with their projection onto the surrounding coordinate planes, respectively. The unit of length in all plots is meter.

In our simulations we pick $M = 11$ points in each subsegment for approximating the integral in (3.122) by using the composite Simpson's rule. We return to the study of the relative difference `RelDiff` from (3.123) and discuss the following two questions:

1. How many spline points are sufficient in the approximation of the center curve K that is used to evaluate $\widetilde{\boldsymbol{E}_\rho^\infty}$ numerically, to obtain a reasonably good approximation of $\widetilde{\boldsymbol{E}_\rho^\infty}$?
2. How small does the radius $\rho > 0$ of the thin tubular scattering object D_ρ have to be such that the leading order term $\widetilde{\boldsymbol{E}_\rho^\infty}$ in the asymptotic perturbation formula (3.22) is a sufficiently good approximation of $\boldsymbol{E}_\rho^\infty$?

The first question is a study on the accuracy of the cubic spline interpolation.The second question is more important for our applications in Chapter 4 and 5 as it indicates a range of radii, for which the leading order term of the asymptotic perturbation formula from (3.122) is a reasonable approximation to the electric far field. We first discuss both Questions 1 and 2 for dielectric scattering objects.

3.5.1 Numerical examples for dielectric scattering objects

For our numerical experiments, we study three different scattering objects with corresponding center curves K, parametrized by $\boldsymbol{p} : [0,1] \to \mathbb{R}^3$. These are given in the next examples. The center curves are also shown in Figure 3.2. Each plot features the center curve in blue surrounded by the three shifted coordinate planes, in which we plotted the projections of the center curve in black. The material parameters ε_r, μ_r that we use in the examples are not intended to describe a realistic material. We study these parameters as a matter of interest and to test the leading order term from (3.122).

Example 3.29. The center curve is a closed ring parametrized by

$$p_1(s) = \cos(2\pi s) + 1, \quad p_2(s) = \sin(2\pi s) + 1, \quad p_3(s) = -1 \qquad \text{for } s \in [0,1]\,,$$

as shown in Figure 3.2 (left). The unit of length is given in m. With a two-dimensional circular cross-section D_ρ' with radius $\rho > 0$, the corresponding scattering object D_ρ becomes a torus. We consider the material parameters $\varepsilon_r = 2.5$ and $\mu_r = 1.6$.

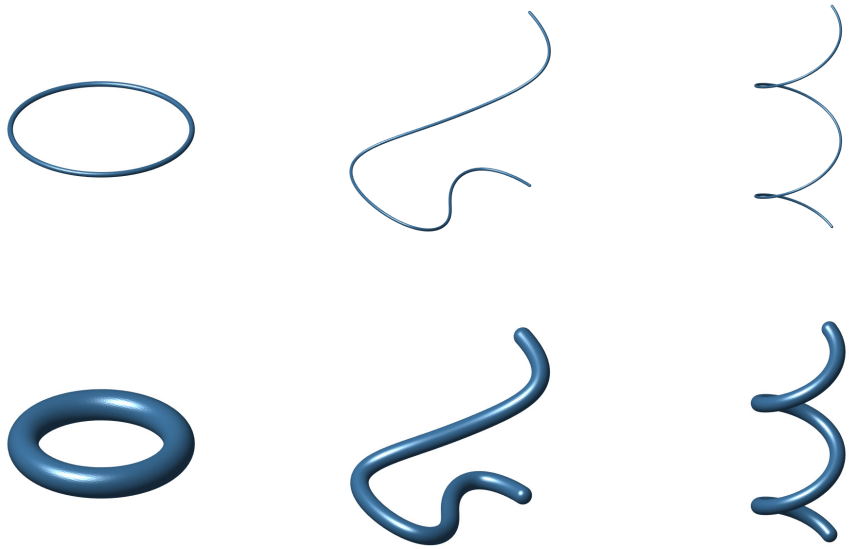

Figure 3.3: The three-dimensional scattering objects corresponding to Example 3.29 - 3.31. Top row: The radius of the circular cross-sections D'_ρ is $\rho = 0.03$m. Bottom row: The radius of the circular cross-sections D'_ρ is $\rho = 0.2$m.

Example 3.30. We consider the center curve parametrized by

$$p_1(s) = 2\frac{\cos(2\pi s)}{1+\sin(2\pi s)^2}, \quad p_2(s) = 4\frac{\cos(2\pi s)\sin(2\pi s)}{1+2\sin(2\pi s)^2}, \quad p_3(s) = 4s^2 \qquad \text{for } s \in [0,1]\,,$$

as shown in Figure 3.2 (center). The unit of length is given in m. The cross-section D'_ρ is a disc of radius $\rho > 0$. The projection onto the xy-plane of the center curve depicts an infinity sign. Here, we choose the material parameters $\varepsilon_r = 1$ and $\mu_r = 2.1$.

Example 3.31. Finally, we consider a helix with two turns parametrized by

$$p_1(s) = \cos(4\pi s), \quad p_2(s) = \sin(4\pi s), \quad p_3(s) = 6s \qquad \text{for } s \in [0,1]\,,$$

as shown in Figure 3.2 (right). The unit of length is given in m. The cross-section D'_ρ is a disc of radius $\rho > 0$. Here, let the material parameters be given by $\varepsilon_r = 2.1$ and $\mu_r = 1.0$.

In all examples, the incoming field is a plane wave, i.e.

$$\boldsymbol{E}^i(\boldsymbol{x}) = \boldsymbol{A}\mathrm{e}^{\mathrm{i}k\boldsymbol{\theta}\cdot\boldsymbol{x}}$$

with polarization $\boldsymbol{A} = [-1,\, 1\mathrm{i},\, 1+1\mathrm{i}]^\top$ and direction of propagation $\boldsymbol{\theta} = 1/\sqrt{3}[1,\,-1,\,1]^\top$. Note that $\boldsymbol{A}\cdot\boldsymbol{\theta} = 0$. In all examples the frequency is given by 100MHz. Accordingly, the wave number in all simulations is $k = \omega\sqrt{\varepsilon_0\mu_0} \approx 2.1\mathrm{m}^{-1}$. Here, ε_0 and μ_0 denote the electric permittivity and magnetic permeability in free space given as in (2.19). The wavelength in the exterior is thus given by $\lambda = 2\pi/k \approx 3$m. Concerning the first numerical study, we consider the radius $\rho = 0.03$m for the circular cross-section in all simulations. The corresponding thin tubular scattering objects are visualized in the top row of Figure 3.3. Using different numbers of nodes $n \in \mathbb{N}$ we consider partitions $\triangle$ as in (3.125) and approximate the curves given by the parametrization $\boldsymbol{p}$ by using the cubic spline $\boldsymbol{p}_\triangle$. Due to the asymptotic character of the expansion (3.22) and due to numerical errors in the approximation $\boldsymbol{E}_\rho^\infty$ obtained by Bempp,

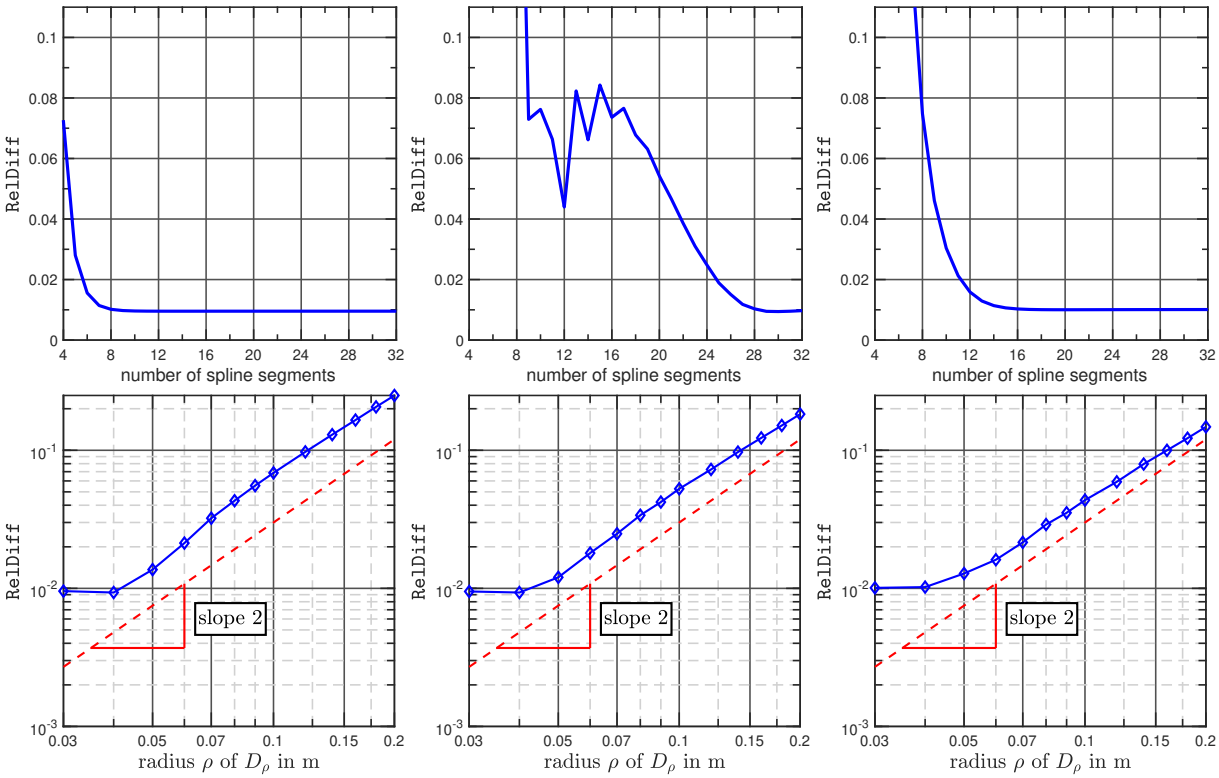

Figure 3.4: Dielectric scattering objects. Top row: Relative difference `RelDiff` between $\boldsymbol{E}_\rho^\infty$ and the leading order term $\widetilde{\boldsymbol{E}_\rho^\infty}$ in (3.123) as a function of the number of subsegments in the spline approximation $\boldsymbol{p}_\triangle$ of the center curve K for Examples 3.29 (left), 3.30 (center), and 3.31 (right) with radius $\rho = 0.03$. Bottom row: Relative difference `RelDiff` (solid blue) between $\boldsymbol{E}_\rho^\infty$ and the leading order term $\widetilde{\boldsymbol{E}_\rho^\infty}$ in (3.123) as a function of the radius $\rho > 0$ of the cross-section D'_ρ for Examples 3.29 (left), 3.30 (center), and 3.31 (right). For comparison, the plot contains a line of slope 2 (dashed red).

we do not expect the relative difference in (3.123) to decay to zero. The result is visualized in the top row of Figure 3.4. In each case, the relative difference from (3.123) falls below 2% for a relatively low number of spline segments $n \in \mathbb{N}$ that approximate the center curve. For the torus in Example 3.29 this is the case for $n \geq 6$, for the curve in Example 3.30 for $n \geq 26$ and for the double-turn helix in Example 3.31 for $n \geq 12$.

Concerning the second numerical study, we simulate reference solutions for different radii $\rho > 0$ for the center curves from Example 3.29-3.31 and evaluate the relative difference in (3.123). Here, we consider 13 Bempp simulations, respectively, with the radius in the range

$$\rho \in \{0.03,\ 0.04,\ 0.05,\ 0.06,\ 0.07,\ 0.08,\ 0.09,\ 0.1,\ 0.12,\ 0.14,\ 0.16,\ 0.18,\ 0.2\}\,\mathrm{m}\,. \tag{3.126}$$

Since the exterior wavelength is $\lambda \approx 3$m, the radius ρ varies in a range of around 1% to 6.7% of the exterior wavelength. We gather information about the convergence of the GMRES method in Table 3.1. We find that in all cases, the GMRES method converges with a relative low number of iterations. In Figure 3.3 we visualize the scattering objects for $\rho = 0.03$ in the top row and for $\rho = 0.2$ in the bottom row. For decreasing ρ we use increasingly fine triangulations of the boundary of scatterers ∂D_ρ. On the other hand, for evaluating $\widetilde{\boldsymbol{E}_\rho^\infty}$ we approximate the center curves using $n = 30$ nodes for the spline representation $\boldsymbol{p}_\triangle$, respectively. We present our numerical study in the bottom row of Figure 3.4. Each plot features the relative difference `RelDiff` from (3.123) as a function of the radius ρ (solid blue). The diamonds indicate the positions, for which we evaluate the relative difference. Moreover, the plots show a reference line of slope 2 (dashed red). For all examples, the relative difference decays approximately

Example 3.29, $\varepsilon_r = 2.5$, $\mu_r = 1.6$							
ρ [cm]	3	4	5	6	7	8	9
#DOFs	80094	54216	69708	56958	64992	66006	67644
#iter	5	5	5	5	5	5	5
ρ [cm]	10	12	14	16	18	20	
#DOFs	67266	67146	60912	54852	61974	59226	
#iter	5	6	6	7	7	8	

Example 3.30, $\varepsilon_r = 1.0$, $\mu_r = 2.1$							
ρ [cm]	3	4	5	6	7	8	9
#DOFs	186348	186348	186348	189420	189420	147012	147012
#iter	9	6	6	7	6	6	6
ρ [cm]	10	12	14	16	18	20	
#DOFs	146724	146724	141756	141756	132108	132108	
#iter	6	8	9	6	6	6	

Example 3.31, $\varepsilon_r = 2.5$, $\mu_r = 1.6$							
ρ [cm]	3	4	5	6	7	8	9
#DOFs	186348	186348	186348	189420	189420	147012	147012
#iter	5	5	6	5	5	5	5
ρ [cm]	10	12	14	16	18	20	
#DOFs	146724	146724	141756	141756	132108	132108	
#iter	6	6	6	6	6	6	

Table 3.1: The number of degrees of freedom (DOFs) and the number of GMRES iterations (iter) for different radii ρ corresponding to Example 3.29-3.31.

of order ρ^2. However, note that our theoretical results in Theorem 3.6 do not predict any convergence rates. In all examples the relative error `RelDiff` from (3.123) stays below 10% if the radius ρ is below 0.12m. This corresponds to a radius, which is below 4% of the exterior wavelength.

3.5.2 Numerical examples for metallic nanowires

We study scattering of visible light from silver nanowires for two different sizes of the scattering objects. In all cases, let the exterior wavelength be given by $\lambda = 400$nm. The material coefficients for silver corresponding to this wavelength are thus given by $\varepsilon_r \approx -4.42 + 0.21\mathrm{i}$ and $\mu_r = 1$ (see [83]). We study the same overall shape of the scattering objects from Example 3.29-3.31, however, the scattering objects are much smaller as we point out in the following examples. Each example covers two different parametrizations of center curves that feature coefficients dependent on $j = 1, 2$.

Example 3.32. The center curve is a closed ring parametrized by

$$p_1(s) = R_j \cos(2\pi s) + R_j, \quad p_2(s) = R_j \sin(2\pi s) + R_j, \quad p_3(s) = -z_j \qquad \text{for } s \in [0,1]\,.$$

With a two-dimensional circular cross-section D'_ρ with $\rho > 0$, the corresponding scattering object D_ρ becomes a torus. For $j = 1$, on the one hand, the exterior radius of the torus is defined to be $R_1 = 133.69$nm and the offset in z direction is also defined as $z_1 = 133.69$nm. For $j = 2$, on the other hand, we choose $R_2 = z_2 = 63.66$nm.

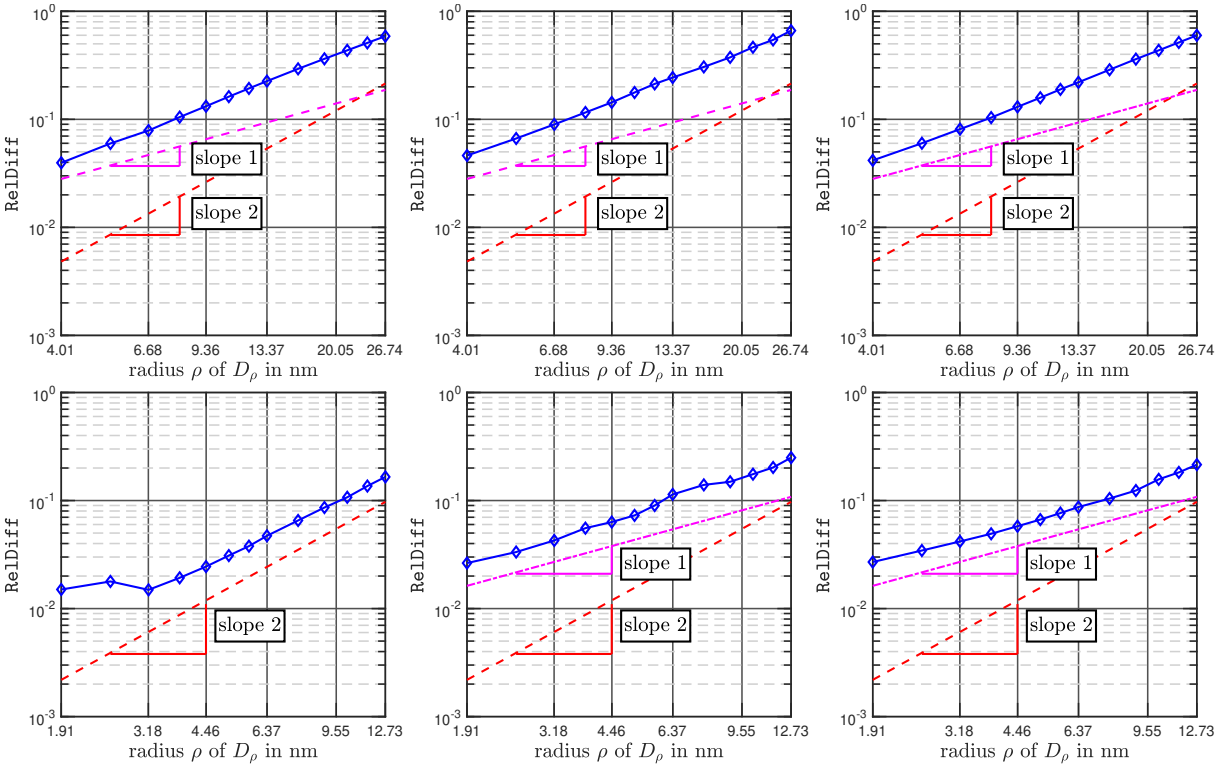

Figure 3.5: Relative difference `RelDiff` (solid blue) between $\boldsymbol{E}_\rho^\infty$ and the leading order term $\widetilde{\boldsymbol{E}_\rho^\infty}$ in (3.123) as a function of the radius $\rho > 0$ of the cross-section D'_ρ for Examples 3.32 (left), 3.33 (center), and 3.34 (right). For comparison, the plots contain a line of slope 1 (dashed magenta) and a line of slope 2 (dashed red). Top row: $j = 1$. Bottom row: $j = 2$.

Example 3.33. We consider the center curve parametrized by

$$p_1(s) = R_j \frac{\cos(2\pi s)}{1+\sin(2\pi s)^2}, \quad p_2(s) = S_j \frac{\cos(2\pi s)\sin(2\pi s)}{1+2\sin(2\pi s)^2}, \quad p_3(s) = h_j s^2 \qquad \text{for } s \in [0,1]\,.$$

The cross-section D'_ρ is a disc of radius $\rho > 0$. For $j = 1$, let the parameters be given by $R_1 = 534.76$nm, $S_1 = 267.38$nm and $h_1 = 534.76$nm. For $j = 2$ we define the parameters to be $R_2 = 254.65$nm, $S_2 = 127.32$nm and $h_2 = 254.65$nm.

Example 3.34. We consider a nano-helix with two turns parametrized by the center curve

$$p_1(s) = R_j \cos(4\pi s), \quad p_2(s) = R_j \sin(4\pi s), \quad p_3(s) = h_j s \qquad \text{for } s \in [0,1]\,.$$

The cross-section D'_ρ is a disc of radius $\rho > 0$. In the first case, i.e. for $j = 1$, let the exterior radius of the helix and the total height be given by $R_1 = 133.69$nm and $h_1 = 802.14$nm. In the second case, we consider $R_2 = 63.66$nm and $h_2 = 381.97$nm.

For $j = 1$ we consider radii within the range

$$\rho \in \{4.01,\ 5.35,\ 6.68,\ 8.02,\ 9.36,\ 10.7,\ 12.03,\ 13.37,\ 16.04,\ 18.72,\ 21.39,\ 24.06,\ 26.74\}\,\text{nm}\,.$$

On the other hand, for $j = 2$, let the radii lie in the range

$$\rho \in \{1.91,\ 2.55,\ 3.18,\ 3.82,\ 4.46,\ 5.09,\ 5.73,\ 6.37,\ 7.64,\ 8.91,\ 10.19,\ 11.46,\ 12.73\}\,\text{nm}\,.$$

The results for first numerical study are similar to those for the dielectric examples found in the top row of Figure 3.4. Therefore, we focus on the second question and study the relative error

Example 3.32, $j = 1$, $\varepsilon_r = -4.42 + 0.21\mathrm{i}$, $\mu_r = 1.0$							
ρ [nm]	4.01	5.35	6.68	8.02	9.36	10.7	12.03
#DOFs	80094	54216	69708	56958	64992	66006	67644
#iter	122	160	104	93	123	104	86
ρ [nm]	13.37	16.04	18.72	21.39	24.06	26.74	
#DOFs	67266	67146	60912	54852	61974	59226	
#iter	73	86	85	99	112	77	

Example 3.33, $j = 1$, $\varepsilon_r = -4.42 + 0.21\mathrm{i}$, $\mu_r = 1.0$							
ρ [nm]	4.01	5.35	6.68	8.02	9.36	10.7	12.03
#DOFs	186348	186348	186348	189420	189420	147012	147012
#iter	319	309	313	329	333	351	366
ρ [nm]	13.37	16.04	18.72	21.39	24.06	26.74	
#DOFs	146724	146724	141756	141756	132108	132108	
#iter	381	403	416	427	448	451	

Example 3.34, $j = 1$, $\varepsilon_r = -4.42 + 0.21\mathrm{i}$, $\mu_r = 1.0$							
ρ [nm]	4.01	5.35	6.68	8.02	9.36	10.7	12.03
#DOFs	186348	186348	186348	189420	189420	147012	147012
#iter	313	317	324	334	340	358	364
ρ [nm]	13.37	16.04	18.72	21.39	24.06	26.74	
#DOFs	146724	146724	141756	141756	132108	132108	
#iter	375	390	406	416	428	423	

Table 3.2: The number of degrees of freedom (DOFs) and the number of GMRES iterations (iter) for different radii ρ corresponding to Example 3.32-3.34 for $j = 1$.

`RelDiff` for a fixed center curve and a circular cross-section D'_ρ as $\rho \to 0$. First, we consider the case $j = 1$. In this case, we scale the objects from Example 3.32-3.34 in such a way that we can perform the numerical experiments with the (computational) exterior wave number $k_c = 2.1\mathrm{m}^{-1}$ (see also Remark 3.25). In order to do so, we use the scaling parameter $\alpha_1 = 2\pi/(2.1(0.4 \times 10^{-6})) \approx 7.48 \times 10^6$ and multiply each of the parametrizations from Example 3.32-3.34 by α_1. It turns out that the computational units for the scattering objects from Example 3.32-3.34 are given by the parametrizations found in Example 3.29-3.31. The curves in Figure 3.2 represent the center curves of the nanowires in computational units. Moreover, the radii in computational units are given by those in (3.126). Therefore, in order to compute a reference solution using Bempp, we use the same grids that we studied before. Note however, that the material parameters ε_r, μ_r are completely different to those treated in Example 3.29-3.31. The results on this study are found in the top row of Figure 3.5. In all plots we show a reference line of slope 2 (dashed red) and a reference line of slope 1 (dashed magenta). For all examples we find that the relative error decreases, as ρ gets smaller, however, the relative error (3.123) does not decay as fast as in the dielectric case (bottom row of Figure 3.4). We leave this numerical result as an observation and do not analyze why the relative difference decays slower in the metallic case than in the dielectric case, as ρ decreases. We note however, that the GMRES method for approximating the linear system of equations that arises by the discretization of the Calderón preconditioned PMCHWT integral formulation in (C.9) requires significantly more steps as listed in Table 3.2. We stress that this only affects the computation of the Bempp reference solution since the evaluation of the leading order term in (3.122) does not require a linear system of equations to be solved. In this series of examples, we find that the relative error `RelDiff` stays below 10% if the radius is below 6.68nm. This is approximately 1.7% of the

Example 3.32, $j = 2$, $\varepsilon_r = -4.42 + 0.21\mathrm{i}$, $\mu_r = 1.0$							
ρ [nm]	1.91	2.55	3.18	3.82	4.46	5.09	5.73
#DOFs	80094	54216	69708	56958	64992	66006	67644
#iter	136	227	111	100	118	153	122
ρ [nm]	6.37	7.64	8.91	10.19	11.46	12.73	
#DOFs	67266	67146	60912	54852	61974	59226	
#iter	65	44	47	75	40	40	

Example 3.33, $j = 2$, $\varepsilon_r = -4.42 + 0.21\mathrm{i}$, $\mu_r = 1.0$							
ρ [nm]	1.91	2.55	3.18	3.82	4.46	5.09	5.73
#DOFs	186348	186348	186348	189420	189420	147012	147012
#iter	557	343	311	534	348	333	341
ρ [nm]	6.37	7.64	8.91	10.19	11.46	12.73	
#DOFs	146724	146724	141756	141756	132108	132108	
#iter	354	445	593	391	407	417	

Example 3.34, $j = 2$, $\varepsilon_r = -4.42 + 0.21\mathrm{i}$, $\mu_r = 1.0$							
ρ [nm]	1.91	2.55	3.18	3.82	4.46	5.09	5.73
#DOFs	186348	186348	186348	189420	189420	147012	147012
#iter	315	342	365	331	330	344	347
ρ [nm]	6.37	7.64	8.91	10.19	11.46	12.73	
#DOFs	146724	146724	141756	141756	132108	132108	
#iter	357	373	371	376	386	395	

Table 3.3: The number of degrees of freedom (DOFs) and the number of GMRES iterations (iter) for different radii ρ corresponding to Example 3.32-3.34 for $j = 2$.

exterior wavelength. We note, that the overall size of the curves parametrized in Example 3.32-3.34 for $j = 1$ varies approximately between 2/3 (Example 3.32) to 2 (Example 3.34) times the size of the exterior wavelength.

For $j = 2$ we proceed similarly as before. First, we scale the curves from Example 3.32-3.34 in such a way that the (computational) exterior wave number $k_c = 1$ (see Remark 3.25) may be considered. Therefore, we define the scaling parameter $\alpha_2 = 2\pi/(0.4 \times 10^{-6}) \approx 1.57 \times 10^7$ and multiply each of the parametrizations from Example 3.32-3.34 by α_2. It turns out that the computational units for the scattering objects from Example 3.32-3.34 are given by the parametrizations found in Example 3.29-3.31. The radii in computational units are given by those in (3.126). For Example 3.34, $j = 2$ and $\rho = 12.73$nm the scaling to exterior wave number $k_c = 1$ is done in detail in Example 3.26. Again, note that although we consider the same grids as for the dielectric case in order to simulate the Bempp reference solutions, the material parameters are completely different here. The results on this study are found in the bottom row of Figure 3.5. Further, the number of degrees of freedom together with the number of iterations of the GMRES method is found in Table 3.3. Again, we find that comparably many steps are required for GMRES to stop. For Example 3.33, $j = 2$, and $\rho = 8.91$nm the number of iterations reaches a maximum with 593 iterations.

Comparing Example 3.32 for $j = 2$ (bottom-left) with $j = 1$ (top-left) shows that the relative error decays faster for $j = 2$. Again, we leave this as an observation that is not analyzed further. For the other two examples the decay of the error is similar. The relative error `RelDiff` stays below 10% if the radius is below 6.3nm, i.e. if the radius is less than 1.6% of the exterior wavelength. This is comparable to the situation for $j = 1$ before.

Our conclusion of this section is that the leading order term of the asymptotic representation

formula provides a relatively good approximation to the electric far field if the radius of the cross-section is at most a few percent of the exterior wavelength. In the dielectric Examples 3.29-3.31 we found a relative error `RelDiff` from (3.123) less than 10%, when the total size of the scattering object is between approximately 2/3 (Example 3.29) to 2 (Example 3.31) times the size of the exterior wavelength and the radius of the thin scatterer ρ is below 4% of the exterior wavelength. For metallic scattering objects our numerical examples indicate that the leading order term provides an approximation with a relative error `RelDiff`, which is less than 10%, if the radius of the nanowire ρ is below 1.6% of the exterior wavelength.

Remark 3.35. The numerical evaluation of the leading order term in (3.122) requires only a few seconds, whereas computations by means of Bempp can take hours or days, dependent on how many iterations are needed for GMRES to stop. In the next two chapters we establish, implement and test efficient shape optimization algorithms, in which we will benefit from these rapid approximations: We first study a reconstruction scheme for thin tubular scattering objects in Chapter 4 and afterwards, we focus on the design of highly electromagnetically chiral tubular objects in Chapter 5.

Chapter 4

Reconstructing thin tubular scattering objects

In this chapter we discuss an inverse scattering problem, which is the reconstruction of scattering objects given measurements of scattered fields or far fields. We assume given a priori information on the material of the scatterer ε_r, μ_r, the incident electric field $\boldsymbol{E}^i$ and the corresponding (measured) far field pattern $\boldsymbol{E}^\infty$. The challenge is to reconstruct the shape of the scattering object D that generates the far field $\boldsymbol{E}^\infty$ as it is illumined by $\boldsymbol{E}^i$. We introduce the nonlinear operator $\widetilde{F} : \mathcal{X} \to L_t^2(S^2)$ that maps scattering objects to its far field for a given incident field. The inverse problem is to find the object $D \in \mathcal{X}$, where $\mathcal{X}$ is a set of suitable objects, such that D satisfies

$$\widetilde{F}(D) \;=\; \boldsymbol{E}^\infty . \tag{4.1}$$

The nonlinear operator equation (4.1) is a starting point for derivative-based reconstruction schemes such as e.g. a shape optimization based on domain derivatives. These were initially studied for the Helmholtz equation. The domain derivative corresponding to sound-soft obstacles was introduced in [87]. For sound-hard obstacles, Robin boundary conditions and for the transmission problem domain derivatives were studied in [77, 78]. Fréchet derivatives based on boundary integral equations are studied for sound-soft obstacles in [108] and for sound-hard obstacles in [110]. In the context of Maxwell's equations domain derivatives for the perfect conductor are studied in [72, 74]. For penetrable scattering objects domain derivatives are considered in [72, 79]. An inverse problem for obstacles with generalized impedance boundary conditions is studied in [32].

Asymptotic representation formulas have been used in the literature to detect and reconstruct inhomogeneities of small volume. For an overview we refer to [9] and the references therein. For thin tubular objects, a reconstruction algorithm for a single inclusion for a two-dimensional conductivity problem is studied in [3], and extended to several inclusions in [4]. A uniqueness result for the inverse problem is provided in both works. In [69] an iterative optimization scheme is applied in order to reconstruct thin tubular inhomogeneities in electrical impedance tomography. Moreover, an inverse uniqueness result is proven. A similar inverse problem is studied in [67]. Here, a non-iterative method based on a factorization of an asymptotic perturbation formula is established that generates an indicator function taking the value zero outside the inhomogeneity and the value one inside. In [19] the authors use an algorithm to reconstruct the end points of a straight conductivity inclusion in a three-dimensional domain. Furthermore, they provide an inverse uniqueness result.

Our aim is to reconstruct the shape of a thin tubular scattering object D_ρ as in (3.7) from observations of a single electric far field pattern $\boldsymbol{E}_\rho^\infty$ due to an incident field $\boldsymbol{E}^i$. We restrict our discussion to the special case, when the cross-section of the scatterer is of the form $D'_\rho = \rho D'$, where $D' = B'_1(0)$ is the unit disk. The algorithm that we study here is similar to [69]. The central building block for our study is the asymptotic representation formula from Theorem 3.6. The nonlinear operator in (4.1) is approximated by using the leading order term of the asymptotic representation formula from (3.22). Our intention is to find out whether the leading order term

of the asymptotic representation formula provides enough information to reconstruct a thin tubular scattering object given measurements of a single electric far field. We assume that the radius $\rho > 0$ is small and that the material parameters of the scattering object ε_1, μ_1 are known a priori. In this case the explicit formulas for the polarization tensors $m^\varepsilon, m^\mu \in \mathbb{C}^{2\times 2}$ of the cross-sections from (3.115) can be used in the reconstruction algorithm. A possible twisting of the cross-section along the spine curve does not have to be taken into account. Accordingly, the inverse problem reduces to reconstructing the center curve K of the scattering object D_ρ from observations of the electric far field pattern $\boldsymbol{E}_\rho^\infty$. The governing nonlinear operator equation is ill-posed and therefore, in order to reconstruct a solution, a regularization method is needed. We suppose that the incident field $\boldsymbol{E}^i$ is a plane wave, i.e.

$$\boldsymbol{E}^i(\boldsymbol{x}) \;=\; \boldsymbol{A}\mathrm{e}^{\mathrm{i}k\boldsymbol{\theta}\cdot\boldsymbol{x}}, \qquad \boldsymbol{x}\in\mathbb{R}^3, \tag{4.2}$$

with direction of propagation $\boldsymbol{\theta} \in S^2$ and polarization $\boldsymbol{A} \in \mathbb{C}^3 \setminus \{0\}$, for which holds that $\boldsymbol{A}\cdot\boldsymbol{\theta} = 0$.

The solution to the direct problem is to compute the nonlinear forward map

$$F_\rho \;:\; K \mapsto \boldsymbol{E}_\rho^\infty\,, \tag{4.3}$$

which maps the center curve K of the scattering object D_ρ to the electric far field pattern $\boldsymbol{E}_\rho^\infty$. For the inverse problem we assume that the electric far field pattern $\boldsymbol{E}_\rho^\infty$ is given. In this case the challenge consists in solving the nonlinear and ill-posed equation

$$F_\rho(K) = \boldsymbol{E}_\rho^\infty \tag{4.4}$$

for the unknown center curve K. In practice, $\boldsymbol{E}_\rho^\infty$ would be accessible through measurements that carry additional noise. Therefore, one usually considers a noisy right hand side $\boldsymbol{E}_\rho^{\infty,\delta}$ instead of $\boldsymbol{E}_\rho^\infty$, where $\delta > 0$ is an a-priori information on the noise level satisfying

$$\|\boldsymbol{E}_\rho^{\infty,\delta} - \boldsymbol{E}_\rho^\infty\|_{L_t^2(S^2)} \le \delta\,.$$

In what follows, we develop a regularized Newton scheme in order to reconstruct the curve K given the measurement $\boldsymbol{E}_\rho^\infty$ numerically. For this purpose, we first introduce the set of admissible parametrizations,

$$\mathcal{P} \;=\; \Big\{\boldsymbol{p}\in C^3([0,1],\mathbb{R}^3) \;\big|\; \boldsymbol{p}\,([0,1]) \text{ is simple and } \boldsymbol{p}'(t)\neq 0 \text{ for all } t\in[0,1]\Big\}$$

and identify curves K with their parametrization $\boldsymbol{p} \in \mathcal{P}$. Using the parametrization $\boldsymbol{p}$ in the leading order term of the asymptotic perturbation formula from (3.22) gives

$$\begin{aligned}\widetilde{\boldsymbol{E}_\rho^\infty}\,(\widehat{\boldsymbol{x}}) \;=\; (k\rho)^2\,\pi\Big(&-\int_0^1 (\mu_r-1)\,\mathrm{e}^{\mathrm{i}k(\boldsymbol{\theta}-\widehat{\boldsymbol{x}})\cdot\boldsymbol{p}(s)}\,(\widehat{\boldsymbol{x}}\times\mathbb{I}_3)\,\mathbb{M}_{\boldsymbol{p}}^\mu(s)\,(\boldsymbol{\theta}\times\boldsymbol{A})\,|\boldsymbol{p}'(s)|\,\mathrm{d}s\\ &+\int_0^1 (\varepsilon_r-1)\,\mathrm{e}^{\mathrm{i}k(\boldsymbol{\theta}-\widehat{\boldsymbol{x}})\cdot\boldsymbol{p}(s)}\,(\widehat{\boldsymbol{x}}\times(\mathbb{I}_3\times\widehat{\boldsymbol{x}}))\,\mathbb{M}_{\boldsymbol{p}}^\varepsilon(s)\boldsymbol{A}\,|\boldsymbol{p}'(s)|\,\mathrm{d}s\Big), \qquad \widehat{\boldsymbol{x}}\in S^2.\end{aligned} \tag{4.5}$$

For this representation we combined (3.22) with (4.2) and with the identity

$$\mathbf{curl}\,\boldsymbol{E}^i\,(\boldsymbol{x}) \;=\; \mathrm{i}k\,(\boldsymbol{\theta}\times\boldsymbol{A})\,\mathrm{e}^{\mathrm{i}k\boldsymbol{\theta}\cdot\boldsymbol{x}}.$$

Here, $\mathbb{M}_{\boldsymbol{p}}^\gamma = \mathbb{M}^\gamma\circ\boldsymbol{p}$ for $\gamma\in\{\varepsilon,\mu\}$ is the parametrized version of the polarization tensor. The parametrized unit tangent vector $\boldsymbol{t}_{\boldsymbol{p}} = \boldsymbol{p}'/|\boldsymbol{p}'|$ can always be completed to an orthonormal frame $(\boldsymbol{t}_{\boldsymbol{p}}, \boldsymbol{r}_{\boldsymbol{p}}, \mathbf{s}_{\boldsymbol{p}})$. For generating a rotation minimizing frame for the curve K one can use e.g. the double reflection method (see [121]). The characterization of $\mathbb{M}_{\boldsymbol{p}}^\gamma$ from Theorem 3.16 together with (3.115) shows that for $\gamma\in\{\varepsilon,\mu\}$ it holds that

$$\mathbb{M}_{\boldsymbol{p}}^\gamma(s) \;=\; V_{\boldsymbol{p}}(s)M^\gamma V_{\boldsymbol{p}}(s)^\top, \qquad s\in[0,1]\,,$$

where $M^\gamma = \operatorname{diag}(1, 2/(\gamma_r+1), 2/(\gamma_r+1)) \in \mathbb{C}^{3\times 3}$ and the matrix-valued function $V_{\boldsymbol{p}} = [\boldsymbol{t}_{\boldsymbol{p}} \,|\, \boldsymbol{r}_{\boldsymbol{p}} \,|\, \mathbf{s}_{\boldsymbol{p}}] \in C^1([0,1], \mathbb{R}^{3\times 3})$ contains the components of the orthogonal frame $(\boldsymbol{t}_{\boldsymbol{p}}, \boldsymbol{r}_{\boldsymbol{p}}, \mathbf{s}_{\boldsymbol{p}})$ as its columns that we introduced in the beginning of Chapter 3.

Remark 4.1. Instead of using a rotation minimizing frame it is also possible to use the Frenet-Serret frame as in the original work [28]. For this, one assumes that $\boldsymbol{p}'(t) \times \boldsymbol{p}''(t)$ vanishes at most at isolated points. Then, the Frenet-Serret frame $(\boldsymbol{t}_{\boldsymbol{p}}, \boldsymbol{n}_{\boldsymbol{p}}, \boldsymbol{b}_{\boldsymbol{p}})$ reads

$$\boldsymbol{t}_{\boldsymbol{p}} = \frac{\boldsymbol{p}'}{|\boldsymbol{p}'|}, \qquad \boldsymbol{n}_{\boldsymbol{p}} = \frac{(\boldsymbol{p}' \times \boldsymbol{p}'') \times \boldsymbol{p}'}{|\,(\boldsymbol{p}' \times \boldsymbol{p}'') \times \boldsymbol{p}'|}, \qquad \boldsymbol{b}_{\boldsymbol{p}} = \boldsymbol{t}_{\boldsymbol{p}} \times \boldsymbol{n}_{\boldsymbol{p}}.$$

Note that the orientation of this frame might flip when passing an inflection point (i.e. a point $\boldsymbol{y} = \boldsymbol{p}(s)$ for which $\boldsymbol{p}''(s) = 0$ for an $s \in (0,1)$) of the parametrization of the curve. Therefore, the use of this frame is only reasonable when considering a circular cross-section.

We assume that the radius $\rho > 0$ of the thin tubular scattering object D_ρ is sufficiently small such that the terms of higher order on the right hand side of (3.22) can be neglected, we approximate the nonlinear operator F_ρ from (4.3) by the nonlinear operator

$$T_\rho : \mathcal{P} \to L^2_t(S^2), \qquad T_\rho(\boldsymbol{p}) = \widetilde{\boldsymbol{E}^\infty_\rho}, \tag{4.6}$$

with $\widetilde{\boldsymbol{E}^\infty_\rho}$ from (4.5). Accordingly, we consider the nonlinear minimization problem

$$\frac{\|T_\rho(\boldsymbol{p}) - \boldsymbol{E}^\infty_\rho\|^2_{L^2_t(S^2)}}{\|\boldsymbol{E}^\infty_\rho\|^2_{L^2_t(S^2)}} \to \min \tag{4.7}$$

to approximate a solution to the inverse problem (4.4). We note that due to the asymptotic character of (3.22) the minimum of (4.7) will be nonzero even for exact far field data. Below we apply a Gauss–Newton method to a regularized version of (4.7). Thus, we need access to the Fréchet derivative of the operator T_ρ.

4.1 The Fréchet derivative of T_ρ

For the operator $T_\rho : \mathcal{P} \to L^2_t(S^2)$, we aim to derive the Fréchet derivative denoted by $T'_\rho[\boldsymbol{p}] : C^3([0,1], \mathbb{R}^3) \to L^2(S^2, \mathbb{C}^3)$. This operator satisfies

$$\frac{1}{\|\boldsymbol{h}\|_{C^3([0,1],\mathbb{R}^3)}} \|T_\rho(\boldsymbol{p}+\boldsymbol{h}) - T_\rho(\boldsymbol{p}) - T'_\rho[\boldsymbol{p}]\boldsymbol{h}\|_{L^2(S^2)} \to 0 \quad \text{as } \|\boldsymbol{h}\|_{C^3([0,1],\mathbb{R}^3)} \to 0. \tag{4.8}$$

From the representation of $\widetilde{\boldsymbol{E}^\infty_\rho}$ from (4.5) we observe that variations of the parametrization $\boldsymbol{p}$ affect three terms in each of both integrals. In particular, it affects the polarization tensors $\mathbb{M}^\gamma$ with $\gamma \in \{\varepsilon, \mu\}$. The following lemma concerning the Fréchet derivative of the mapping $\boldsymbol{p} \mapsto \mathbb{M}^\gamma_{\boldsymbol{p}}$ has been established in [69, Lem. 4.1].

Lemma 4.2. *The mapping $\mathbb{M}^\gamma : \mathcal{P} \to C([0,1], \mathbb{C}^{3\times 3})$, $\gamma \in \{\varepsilon, \mu\}$ with*

$$\mathbb{M}^\gamma_{\boldsymbol{p}}(s) = \mathbb{M}^\gamma(\boldsymbol{p})(s) = V_{\boldsymbol{p}} M^\gamma V_{\boldsymbol{p}}(s)^\top$$

is Fréchet differentiable. Its Fréchet derivative at $\boldsymbol{p} \in \mathcal{P}$ is given by

$$(\mathbb{M}^\gamma_{\boldsymbol{p}})' : \mathcal{P} \to C([0,1], \mathbb{C}^{3\times 3}), \quad (\mathbb{M}^\gamma_{\boldsymbol{p},\boldsymbol{h}})' = (\mathbb{M}^\gamma_{\boldsymbol{p}})'\boldsymbol{h} = V'_{\boldsymbol{p},\boldsymbol{h}} M^\gamma V_{\boldsymbol{p}}^\top + V_{\boldsymbol{p}} M^\gamma (V'_{\boldsymbol{p},\boldsymbol{h}})^\top,$$

where the matrix-valued function $V'_{\boldsymbol{p},\boldsymbol{h}}$ is defined columnwise by

$$V'_{\boldsymbol{p},\boldsymbol{h}} = \frac{1}{|\boldsymbol{p}'|}\left[(\boldsymbol{h}' \cdot \boldsymbol{n}_{\boldsymbol{p}})\boldsymbol{n}_{\boldsymbol{p}} + (\boldsymbol{h}' \cdot \boldsymbol{b}_{\boldsymbol{p}})\boldsymbol{b}_{\boldsymbol{p}} \,|\, -(\boldsymbol{h}' \cdot \boldsymbol{n}_{\boldsymbol{p}})\boldsymbol{t}_{\boldsymbol{p}} \,|\, -(\boldsymbol{h}' \cdot \boldsymbol{b}_{\boldsymbol{p}})\boldsymbol{t}_{\boldsymbol{p}}\right].$$

The proof of Lemma 4.2 is omitted since we study a similar theorem involving an additional rotation of a non-circular cross-section in Section 5.3. This is done in Theorem 5.14. We note that the proof of [69, Lem. 4.1] constructs an explicit orthonormal frame $(\boldsymbol{t}_{\boldsymbol{p}+\boldsymbol{h}}, \boldsymbol{r}_{\boldsymbol{p}+\boldsymbol{h}}, \mathbf{s}_{\boldsymbol{p}+\boldsymbol{h}})$ for $\boldsymbol{p}+\boldsymbol{h}$, given an orthonormal frame for $\boldsymbol{p}$, denoted by $(\boldsymbol{t}_{\boldsymbol{p}}, \boldsymbol{r}_{\boldsymbol{p}}, \mathbf{s}_{\boldsymbol{p}})$. This frame reads

$$\boldsymbol{t}_{\boldsymbol{p}+\boldsymbol{h}} = \frac{\boldsymbol{p}'+\boldsymbol{h}'}{|\boldsymbol{p}'+\boldsymbol{h}'|}, \tag{4.9a}$$

$$\boldsymbol{r}_{\boldsymbol{p}+\boldsymbol{h}} = (\boldsymbol{t}_{\boldsymbol{p}}\cdot\boldsymbol{t}_{\boldsymbol{p}+\boldsymbol{h}})\,\boldsymbol{r}_{\boldsymbol{p}} - \frac{\mathbf{s}_{\boldsymbol{p}}\cdot\boldsymbol{t}_{\boldsymbol{p}+\boldsymbol{h}}}{1+\boldsymbol{t}_{\boldsymbol{p}}\cdot\boldsymbol{t}_{\boldsymbol{p}+\boldsymbol{h}}}(\boldsymbol{t}_{\boldsymbol{p}}\times\boldsymbol{t}_{\boldsymbol{p}+\boldsymbol{h}}) - (\boldsymbol{r}_{\boldsymbol{p}}\cdot\boldsymbol{t}_{\boldsymbol{p}+\boldsymbol{h}})\,\boldsymbol{t}_{\boldsymbol{p}}, \tag{4.9b}$$

$$\mathbf{s}_{\boldsymbol{p}+\boldsymbol{h}} = (\boldsymbol{t}_{\boldsymbol{p}}\cdot\boldsymbol{t}_{\boldsymbol{p}+\boldsymbol{h}})\,\mathbf{s}_{\boldsymbol{p}} + \frac{\boldsymbol{r}_{\boldsymbol{p}}\cdot\boldsymbol{t}_{\boldsymbol{p}+\boldsymbol{h}}}{1+\boldsymbol{t}_{\boldsymbol{p}}\cdot\boldsymbol{t}_{\boldsymbol{p}+\boldsymbol{h}}}(\boldsymbol{t}_{\boldsymbol{p}}\times\boldsymbol{t}_{\boldsymbol{p}+\boldsymbol{h}}) - (\mathbf{s}_{\boldsymbol{p}}\cdot\boldsymbol{t}_{\boldsymbol{p}+\boldsymbol{h}})\,\boldsymbol{t}_{\boldsymbol{p}}. \tag{4.9c}$$

Remark 4.3. In our shape optimization for em-chiral structures in Section 5.3, we study a similar update formula as the one in (4.9) involving an additional rotation of a non-circular cross-section. For this more general update formula we show in Lemma 5.12 that the updated frame is an orthonormal frame to the curve parametrized by $\boldsymbol{p}+\boldsymbol{h}$.

Next we consider the Fréchet derivative of the mapping T_ρ. The proof that is similar to the proof of [69, Thm. 4.2], relies in computing the Fréchet derivatives of the terms in the leading order term separately and assembling the full Fréchet derivative by using the product rule.

Theorem 4.4. *The operator $T_\rho : \mathcal{P} \to L^2(S^2,\mathbb{C}^3)$ from (4.6) is Fréchet differentiable and its Fréchet derivative at $\boldsymbol{p}\in\mathcal{P}$ is given by $T'_\rho[\boldsymbol{p}] : C^3([0,1],\mathbb{R}^3) \to L^2(S^2,\mathbb{C}^3)$,*

$$T'_\rho[\boldsymbol{p}]\boldsymbol{h} = (k\rho)^2\pi\Big(-(\mu_r-1)\sum_{j=1}^{3} T'_{\rho,\mu,j}[\boldsymbol{p}]\boldsymbol{h} + (\varepsilon_r-1)\sum_{j=1}^{3} T'_{\rho,\varepsilon,j}[\boldsymbol{p}]\boldsymbol{h}\Big) \tag{4.10}$$

with

$$T'_{\rho,\mu,1}[\boldsymbol{p}]\boldsymbol{h} = \int_0^1 \mathrm{i}k((\boldsymbol{\theta}-\widehat{\boldsymbol{x}})\cdot\boldsymbol{h}(s))(\widehat{\boldsymbol{x}}\times\mathbb{I}_3)\mathbb{M}^\mu_{\boldsymbol{p}}(s)(\boldsymbol{\theta}\times\boldsymbol{A})e^{\mathrm{i}k(\boldsymbol{\theta}-\widehat{\boldsymbol{x}})\cdot\boldsymbol{p}(s)}|\boldsymbol{p}'(s)|\,\mathrm{d}s, \tag{4.11a}$$

$$T'_{\rho,\mu,2}[\boldsymbol{p}]\boldsymbol{h} = \int_0^1 (\widehat{\boldsymbol{x}}\times\mathbb{I}_3)(\mathbb{M}^\mu_{\boldsymbol{p},\boldsymbol{h}})'(s)(\boldsymbol{\theta}\times\boldsymbol{A})e^{\mathrm{i}k(\boldsymbol{\theta}-\widehat{\boldsymbol{x}})\cdot\boldsymbol{p}(s)}|\boldsymbol{p}'(s)|\,\mathrm{d}s, \tag{4.11b}$$

$$T'_{\rho,\mu,3}[\boldsymbol{p}]\boldsymbol{h} = \int_0^1 (\widehat{\boldsymbol{x}}\times\mathbb{I}_3)\mathbb{M}^\mu_{\boldsymbol{p}}(s)(\boldsymbol{\theta}\times\boldsymbol{A})e^{\mathrm{i}k(\boldsymbol{\theta}-\widehat{\boldsymbol{x}})\cdot\boldsymbol{p}(s)}\frac{\boldsymbol{p}'(s)\cdot\boldsymbol{h}'(s)}{|\boldsymbol{p}'(s)|}\,\mathrm{d}s \tag{4.11c}$$

and

$$T'_{\rho,\varepsilon,1}[\boldsymbol{p}]\boldsymbol{h} = \int_0^1 \mathrm{i}k((\boldsymbol{\theta}-\widehat{\boldsymbol{x}})\cdot\boldsymbol{h}(s))(\widehat{\boldsymbol{x}}\times(\mathbb{I}_3\times\widehat{\boldsymbol{x}}))\mathbb{M}^\varepsilon_{\boldsymbol{p}}(s)\boldsymbol{A}e^{\mathrm{i}k(\boldsymbol{\theta}-\widehat{\boldsymbol{x}})\cdot\boldsymbol{p}(s)}|\boldsymbol{p}'(s)|\,\mathrm{d}s, \tag{4.12a}$$

$$T'_{\rho,\varepsilon,2}[\boldsymbol{p}]\boldsymbol{h} = \int_0^1 (\widehat{\boldsymbol{x}}\times(\mathbb{I}_3\times\widehat{\boldsymbol{x}}))(\mathbb{M}^\varepsilon_{\boldsymbol{p},\boldsymbol{h}})'(s)\boldsymbol{A}e^{\mathrm{i}k(\boldsymbol{\theta}-\widehat{\boldsymbol{x}})\cdot\boldsymbol{p}(s)}|\boldsymbol{p}'(s)|\,\mathrm{d}s, \tag{4.12b}$$

$$T'_{\rho,\varepsilon,3}[\boldsymbol{p}]\boldsymbol{h} = \int_0^1 (\widehat{\boldsymbol{x}}\times(\mathbb{I}_3\times\widehat{\boldsymbol{x}}))\mathbb{M}^\varepsilon_{\boldsymbol{p}}(s)\boldsymbol{A}e^{\mathrm{i}k(\boldsymbol{\theta}-\widehat{\boldsymbol{x}})\cdot\boldsymbol{p}(s)}\frac{\boldsymbol{p}'(s)\cdot\boldsymbol{h}'(s)}{|\boldsymbol{p}'(s)|}\,\mathrm{d}s. \tag{4.12c}$$

Proof. Let $\boldsymbol{p}\in\mathcal{P}$, $\delta>0$ and $\boldsymbol{h}\in C^3([0,1],\mathbb{R}^3)$ such that $\|\boldsymbol{h}\|_{C^3([0,1],\mathbb{R}^3)}<\delta$. In particular, let $\|\boldsymbol{h}\|_{C^3}=\|\boldsymbol{h}\|_{C^3([0,1],\mathbb{R}^3)}$ be so small that the curve parametrized by $\boldsymbol{p}+\boldsymbol{h}$ is simple. We have to show (4.8) with $T'_\rho[\boldsymbol{p}]\boldsymbol{h}$ from (4.10). We note that $T_\rho(\boldsymbol{p}+\boldsymbol{h})-T_\rho(\boldsymbol{p})$ can be written as

$$\begin{aligned} T_\rho(\boldsymbol{p}+\boldsymbol{h})-T_\rho(\boldsymbol{p}) = (k\rho)^2\pi(&-(\mu_r-1)(T_{\rho,\mu}(\boldsymbol{p}+\boldsymbol{h})-T_{\rho,\mu}(\boldsymbol{p})) \\ &+(\varepsilon_r-1)(T_{\rho,\varepsilon}(\boldsymbol{p}+\boldsymbol{h})-T_{\rho,\varepsilon}(\boldsymbol{p}))) \end{aligned}$$

with

$$\begin{aligned} T_{\rho,\mu}(\boldsymbol{p}+\boldsymbol{h}) - T_{\rho,\mu}(\boldsymbol{p}) &= \int_0^1 \mathrm{e}^{\mathrm{i}k(\boldsymbol{\theta}-\widehat{\boldsymbol{x}})\cdot(\boldsymbol{p}+\boldsymbol{h})(s)} \, (\widehat{\boldsymbol{x}} \times \mathbb{I}_3) \, \mathbb{M}^{\mu}_{\boldsymbol{p}+\boldsymbol{h}}(s) \, (\boldsymbol{\theta} \times \boldsymbol{A}) \, |(\boldsymbol{p}'+\boldsymbol{h}')(s)| \, \mathrm{d}s \\ &\quad - \int_0^1 \mathrm{e}^{\mathrm{i}k(\boldsymbol{\theta}-\widehat{\boldsymbol{x}})\cdot\boldsymbol{p}(s)} \, (\widehat{\boldsymbol{x}} \times \mathbb{I}_3) \, \mathbb{M}^{\mu}_{\boldsymbol{p}}(s) \, (\boldsymbol{\theta} \times \boldsymbol{A}) \, |\boldsymbol{p}'(s)| \, \mathrm{d}s \,, \\ T_{\rho,\varepsilon}(\boldsymbol{p}+\boldsymbol{h}) - T_{\rho,\varepsilon}(\boldsymbol{p}) &= \int_0^1 \mathrm{e}^{\mathrm{i}k(\boldsymbol{\theta}-\widehat{\boldsymbol{x}})\cdot(\boldsymbol{p}+\boldsymbol{h})(s)} \, (\widehat{\boldsymbol{x}} \times (\mathbb{I}_3 \times \widehat{\boldsymbol{x}})) \, \mathbb{M}^{\varepsilon}_{\boldsymbol{p}+\boldsymbol{h}}(s) \boldsymbol{A} \, |(\boldsymbol{p}'+\boldsymbol{h}')(s)| \, \mathrm{d}s \\ &\quad - \int_0^1 \mathrm{e}^{\mathrm{i}k(\boldsymbol{\theta}-\widehat{\boldsymbol{x}})\cdot\boldsymbol{p}(s)} \, (\widehat{\boldsymbol{x}} \times (\mathbb{I}_3 \times \widehat{\boldsymbol{x}})) \, \mathbb{M}^{\varepsilon}_{\boldsymbol{p}}(s) \boldsymbol{A} \, |\boldsymbol{p}'(s)| \, \mathrm{d}s \,. \end{aligned}$$

We study $T_{\rho,\mu}(\boldsymbol{p}+\boldsymbol{h}) - T_{\rho,\mu}(\boldsymbol{p})$ in detail and show that

$$\frac{1}{\|\boldsymbol{h}\|_{C^3}} \Big\| T_{\rho,\mu}(\boldsymbol{p}+\boldsymbol{h}) - T_{\rho,\mu}(\boldsymbol{p}) - \sum_{j=1}^{3} T'_{\rho,\mu,j}[\boldsymbol{p}]\boldsymbol{h} \Big\|_{L^2(S^2)} \to 0 \quad \text{as } \|\boldsymbol{h}\|_{C^3} \to 0 \,, \tag{4.13}$$

with $T'_{\rho,\mu,j}[\boldsymbol{p}]\boldsymbol{h}$, $1 \le j \le 3$, defined in (4.11). The same techniques can then be used to see that (4.13) holds with μ replaced by ε and the terms in (4.12). We write $T_{\rho,\mu}(\boldsymbol{p}+\boldsymbol{h}) - T_{\rho,\mu}(\boldsymbol{p})$ as

$$T_{\rho,\mu}(\boldsymbol{p}+\boldsymbol{h}) - T_{\rho,\mu}(\boldsymbol{p}) = T_{\rho,\mu,1}(\boldsymbol{p},\boldsymbol{h}) + T_{\rho,\mu,2}(\boldsymbol{p},\boldsymbol{h}) + T_{\rho,\mu,3}(\boldsymbol{p},\boldsymbol{h}) \,, \tag{4.14}$$

where

$$\begin{aligned} T_{\rho,\mu,1}(\boldsymbol{p},\boldsymbol{h}) &= \int_0^1 \left(\mathrm{e}^{\mathrm{i}k(\boldsymbol{\theta}-\widehat{\boldsymbol{x}})\cdot(\boldsymbol{p}+\boldsymbol{h})(s)} - \mathrm{e}^{\mathrm{i}k(\boldsymbol{\theta}-\widehat{\boldsymbol{x}})\cdot\boldsymbol{p}(s)} \right) (\widehat{\boldsymbol{x}} \times \mathbb{I}_3) \, \mathbb{M}^{\mu}_{\boldsymbol{p}+\boldsymbol{h}}(s) \, (\boldsymbol{\theta} \times \boldsymbol{A}) \, |(\boldsymbol{p}'+\boldsymbol{h}')(s)| \, \mathrm{d}s \,, \\ T_{\rho,\mu,2}(\boldsymbol{p},\boldsymbol{h}) &= \int_0^1 \mathrm{e}^{\mathrm{i}k(\boldsymbol{\theta}-\widehat{\boldsymbol{x}})\cdot\boldsymbol{p}(s)} \, (\widehat{\boldsymbol{x}} \times \mathbb{I}_3) \left(\mathbb{M}^{\mu}_{\boldsymbol{p}+\boldsymbol{h}}(s) - \mathbb{M}^{\mu}_{\boldsymbol{p}}(s) \right) (\boldsymbol{\theta} \times \boldsymbol{A}) \, |(\boldsymbol{p}'+\boldsymbol{h}')(s)| \, \mathrm{d}s \,, \\ T_{\rho,\mu,3}(\boldsymbol{p},\boldsymbol{h}) &= \int_0^1 \mathrm{e}^{\mathrm{i}k(\boldsymbol{\theta}-\widehat{\boldsymbol{x}})\cdot\boldsymbol{p}(s)} \, (\widehat{\boldsymbol{x}} \times \mathbb{I}_3) \, \mathbb{M}^{\mu}_{\boldsymbol{p}}(s) \, (\boldsymbol{\theta} \times \boldsymbol{A}) \left(|(\boldsymbol{p}'+\boldsymbol{h}')(s)| - |\boldsymbol{p}'(s)| \right) \mathrm{d}s \,. \end{aligned}$$

We will show that

$$\left\| T_{\rho,\mu,j}(\boldsymbol{p},\boldsymbol{h}) - T'_{\rho,\mu,j}[\boldsymbol{p}]\boldsymbol{h} \right\|_{C(S^2)} \le C \, \|\boldsymbol{h}\|^2_{C^3} \tag{4.15}$$

for all $1 \le j \le 3$. Then, (4.13) follows by the continuous embedding of $C(S^2)$ into $L^2(S^2)$ and the triangle inequality. All functions that appear in (4.14) are smooth. Thus, we use Taylor's theorem and Lemma 4.2 to see that

$$\left\| \mathrm{e}^{\mathrm{i}k(\boldsymbol{\theta}-\widehat{\boldsymbol{x}})\cdot(\boldsymbol{p}+\boldsymbol{h})(\cdot)} - \mathrm{e}^{\mathrm{i}k(\boldsymbol{\theta}-\widehat{\boldsymbol{x}})\cdot\boldsymbol{p}(\cdot)} - \mathrm{i}k((\boldsymbol{\theta}-\widehat{\boldsymbol{x}})\cdot\boldsymbol{h}(\cdot))\mathrm{e}^{\mathrm{i}k(\boldsymbol{\theta}-\widehat{\boldsymbol{x}})\cdot\boldsymbol{p}(\cdot)} \right\|_{C([0,1],\mathbb{C})} \le C \, \|\boldsymbol{h}\|^2_{C^3} \,, \tag{4.16a}$$

$$\left\| |(\boldsymbol{p}'+\boldsymbol{h}')(\cdot)| - |\boldsymbol{p}'(\cdot)| - \frac{\boldsymbol{p}'(\cdot)\cdot\boldsymbol{h}'(\cdot)}{|\boldsymbol{p}'(\cdot)|} \right\|_{C([0,1],\mathbb{R})} \le C \, \|\boldsymbol{h}\|^2_{C^3} \,, \tag{4.16b}$$

$$\left\| \mathbb{M}^{\mu}_{\boldsymbol{p}+\boldsymbol{h}}(\cdot) - \mathbb{M}^{\mu}_{\boldsymbol{p}}(\cdot) - (\mathbb{M}^{\mu}_{\boldsymbol{p},\boldsymbol{h}})'(\cdot) \right\|_{C([0,1],\mathbb{R}^{3\times 3})} \le C \, \|\boldsymbol{h}\|^2_{C^3} \,. \tag{4.16c}$$

For $j = 3$, (4.15) follows directly by (4.16b). For $j = 2$ we proceed as in the proof of [69, Thm. 4.2] and write (we omit the integration variable)

$$\begin{aligned} T_{\rho,\mu,2}(\boldsymbol{p},\boldsymbol{h}) - T'_{\rho,\mu,2}[\boldsymbol{p}]\boldsymbol{h} &= \int_0^1 \mathrm{e}^{\mathrm{i}k(\boldsymbol{\theta}-\widehat{\boldsymbol{x}})\cdot\boldsymbol{p}} \, (\widehat{\boldsymbol{x}} \times \mathbb{I}_3) \left(\mathbb{M}^{\mu}_{\boldsymbol{p}+\boldsymbol{h}} - \mathbb{M}^{\mu}_{\boldsymbol{p}} - (\mathbb{M}^{\mu}_{\boldsymbol{p},\boldsymbol{h}})' \right) (\boldsymbol{\theta} \times \boldsymbol{A}) \, |\boldsymbol{p}'| \, \mathrm{d}s \\ &\quad + \int_0^1 \mathrm{e}^{\mathrm{i}k(\boldsymbol{\theta}-\widehat{\boldsymbol{x}})\cdot\boldsymbol{p}} \, (\widehat{\boldsymbol{x}} \times \mathbb{I}_3) \left(\mathbb{M}^{\mu}_{\boldsymbol{p}+\boldsymbol{h}} - \mathbb{M}^{\mu}_{\boldsymbol{p}} \right) (\boldsymbol{\theta} \times \boldsymbol{A}) \left(|(\boldsymbol{p}'+\boldsymbol{h}')| - |\boldsymbol{p}'| \right) \mathrm{d}s \,. \end{aligned} \tag{4.17}$$

By (4.16c), the first term on the right hand side of (4.17) is in $O(\|\boldsymbol{h}\|^2_{C^3})$. Again, by Taylor's theorem,

$$\left\| \mathbb{M}^{\mu}_{\boldsymbol{p}+\boldsymbol{h}}(\cdot) - \mathbb{M}^{\mu}_{\boldsymbol{p}}(\cdot) \right\|_{C([0,1],\mathbb{R}^{3\times 3})} \le C \, \|\boldsymbol{h}\|_{C^3} \,, \qquad \big\| |(\boldsymbol{p}'(\cdot)+\boldsymbol{h}'(\cdot))| - |\boldsymbol{p}'(\cdot)| \big\|_{C([0,1],\mathbb{R})} \le C \, \|\boldsymbol{h}\|_{C^3}$$

and therefore, the second term in (4.17) is in $O(\|\boldsymbol{h}\|^2_{C^3})$. For $j = 1$, (4.15) can be shown similarly by using (4.16a). □

4.2 Discretization, regularization and the reconstruction

In the reconstruction algorithm we use interpolating cubic splines with the not-a-knot conditions at the end points of the spline to discretize center curves K parametrized by $\boldsymbol{p} \in \mathcal{P}$. Given a non-uniform partition

$$\triangle \;=\; \{0 = t_1 < t_2 < \cdots < t_n = 1\} \subset [0,1]$$

we denote corresponding not-a-knot splines by $\boldsymbol{p}_\triangle$ (see also Remark 3.28). The space of all three-dimensional not-a-knot splines with respect to $\triangle$ is denoted by $\mathcal{P}_\triangle$. We note that $\mathcal{P}_\triangle \not\subseteq \mathcal{P}$, although, functions in $\mathcal{P}_\triangle$ are piecewise C^∞. Since the inverse problem (4.4) is ill-posed, we add two regularization terms to stabilize the minimization of (4.7). The functional $\Psi_1 : \mathcal{P}_\triangle \to \mathbb{R}$ is defined by

$$\Psi_1(\boldsymbol{p}_\triangle) \;=\; \int_0^1 \kappa^2(s)|\boldsymbol{p}'(s)|\,\mathrm{d}s\,, \tag{4.18}$$

where

$$\kappa(s) \;=\; \frac{|\boldsymbol{p}'_\triangle(s) \times \boldsymbol{p}''_\triangle(s)|}{|\boldsymbol{p}'_\triangle(s)|^3}\,, \qquad s \in [0,1]\,, \tag{4.19}$$

denotes the curvature of the curve parametrized by $\boldsymbol{p}_\triangle$. We add $\alpha_1^2\Psi_1$ with a regularization parameter $\alpha_1 > 0$ as a penalty term to the left hand side of (4.7) to prevent minimizers from being too strongly entangled. Furthermore, we define another functional $\Psi_2 : \mathcal{P}_\triangle \to \mathbb{R}$ by

$$\Psi_2(\boldsymbol{p}_\triangle) \;=\; \sum_{j=1}^{n-1} \Big| \frac{1}{n-1} \int_0^1 |\boldsymbol{p}'_\triangle(s)|\,\mathrm{d}s - \int_{t_j}^{t_{j+1}} |\boldsymbol{p}'_\triangle(s)|\,\mathrm{d}s \Big|^2 .$$

Adding $\alpha_2^2\Psi_2$ with a regularization parameter $\alpha_2 > 0$ as a penalty term to the left hand side of (4.7) promotes uniformly distributed control points along the spline and therefore prevents clustering of control points during the minimization process. Adding both quadratic regularization terms $\alpha_1^2\Psi_1$ and $\alpha_2^2\Psi_2$ to the left hand side of (4.7) gives the regularized nonlinear output least squares functional

$$\Phi :\, \mathcal{P}_\triangle \to \mathbb{R}\,, \qquad \Phi(\boldsymbol{p}_\triangle) \;=\; \frac{\big\|T_\rho(\boldsymbol{p}_\triangle) - \boldsymbol{E}_\rho^\infty\big\|^2_{L_t^2(S^2)}}{\big\|\boldsymbol{E}_\rho^\infty\big\|^2_{L_t^2(S^2)}} + \alpha_1^2\psi_1(\boldsymbol{p}_\triangle) + \alpha_2^2\psi_2(\boldsymbol{p}_\triangle)\,, \tag{4.20}$$

which we will minimize iteratively.

We assume that $2N(N-1)$ observations of the far field $\boldsymbol{E}_\rho^\infty \in C^\infty(S^2, \mathbb{C}^3)$ are available on an equiangular grid of points

$$\boldsymbol{y}_{jl} \;=\; \big[\sin\theta_j \cos\varphi_l,\, \sin\theta_j \sin\varphi_l,\, \cos\theta_j\big]^\top \in S^2\,, \qquad j = 1, ..., N-1\,,\; l = 1, ..., 2N\,, \tag{4.21}$$

with $\theta_j = j\pi/N$ and $\varphi_l = (l-1)\pi/N$ for some $N \in \mathbb{N}$. Accordingly, we approximate the $L^2(S^2)$-norms in the cost functional Φ from (4.20) using a composite trapezoid rule in horizontal and vertical direction. This yields an approximation Φ_N that is given by

$$\Phi_N(\boldsymbol{p}_\triangle) \;=\; \frac{\sum_{j=1}^{N-1}\sum_{l=1}^{2N} \frac{\pi^2}{N^2}\sin(\theta_j)\big|(T_\rho(\boldsymbol{p}_\triangle) - \boldsymbol{E}_\rho^\infty)(\boldsymbol{y}_{jl})\big|^2}{\sum_{j=1}^{N-1}\sum_{l=1}^{2N} \frac{\pi^2}{N^2}\sin(\theta_j)\big|\boldsymbol{E}_\rho^\infty(\boldsymbol{y}_{jl})\big|^2} + \alpha_1^2\Psi_1(\boldsymbol{p}_\triangle) + \alpha_2^2\Psi_2(\boldsymbol{p}_\triangle)\,. \tag{4.22}$$

We denote by $\vec{\boldsymbol{x}} \in \mathbb{R}^{3n}$ the vector that contains the coordinates of the control points $\boldsymbol{x}^{(1)}, \ldots, \boldsymbol{x}^{(n)}$ of a not-a-knot spline $\boldsymbol{p}_\triangle$. We approximate all integrals over the parameter range $[0,1]$ of $\boldsymbol{p}_\triangle$ in (4.22) using a composite Simpson's rule with odd $M \in \mathbb{N}$ nodes on each subinterval of the partition $\triangle$. This is explained in Remark 3.28. Accordingly, we can rewrite Φ_N in the form

$$\Phi_N(\boldsymbol{p}_\triangle) \;=\; |P_N(\vec{\boldsymbol{x}})|^2\,, \tag{4.23}$$

Algorithm 1 Reconstruction of a thin tubular scatterer D_ρ with circular cross-section

Suppose that $\boldsymbol{E}^i$ (i.e., k, $\boldsymbol{\theta}$, $\boldsymbol{A}$), ρ, ε_r, μ_r, and $\boldsymbol{E}_\rho^\infty$ are given.

1: Choose an initial guess $\vec{\boldsymbol{x}}_0 = [\boldsymbol{x}^{(1)}, \dots, \boldsymbol{x}^{(n)}]$ for the control points of a cubic not-a-knot spline $\boldsymbol{p}_{\triangle,0} \in \mathcal{P}_\triangle$ approximating the unknown center curve K of D_ρ.
2: Initialize the regularization parameters $\alpha_1, \alpha_2 > 0$, a maximal step size $s_{\max} > 0$ for the line search and the tolerance $\texttt{tol} > 0$.
3: **for** $\ell = 0, 1, ..., \ell_{\max}$ **do**
4: Use the Fréchet derivatives T_ρ', ψ_1', $\psi_{2,1}', \dots, \psi_{2,n-1}'$ in (4.10), (4.25) and (4.26) to evaluate the Jacobian J_{P_N} of P_N from (4.23), which is then used to compute the Gauß–Newton search direction

$$\boldsymbol{\Delta}_\ell \;=\; -\Big(J_{P_N}^\top(\vec{\boldsymbol{x}}_\ell) J_{P_N}(\vec{\boldsymbol{x}}_\ell)\Big)^{-1} J_{P_N}^\top(\vec{\boldsymbol{x}}_\ell) P_N(\vec{\boldsymbol{x}}_\ell)\,.$$

5: Use the golden section line search to compute

$$s_\ell^* \;=\; \operatorname*{arg\,min}_{s\in[0,s_{\max}]} \Phi_N(\vec{\boldsymbol{x}}_\ell + s\boldsymbol{\Delta}_\ell)$$

and evaluate $\texttt{Mov}$ from (4.29).
6: **if** $\texttt{Mov} \geq \texttt{tol}$ **then**
7: Update the reconstruction, i.e. compute

$$\vec{\boldsymbol{x}}_{\ell+1} \;=\; \vec{\boldsymbol{x}}_\ell + s_\ell^* \boldsymbol{\Delta}_\ell \qquad \text{and} \qquad \ell \;=\; \ell + 1\,.$$

8: **else if** ($\texttt{Mov} < \texttt{tol}$) **and** the value of $|P(\vec{\boldsymbol{x}}_\ell)|^2$ is dominated by the contribution of $\alpha_j^2 \Psi_j(\boldsymbol{p}_{\triangle,\ell})$, $j \in \{1, 2\}$, in (4.22) **then**
9: Reduce the corresponding regularization parameter, i.e. set

$$\alpha_j \;=\; \alpha_j/2\,.$$

10: **else if** ($\texttt{Mov} < \texttt{tol}$) **and** the value of $|P(\vec{\boldsymbol{x}}_\ell)|^2$ is dominated by the residual term in (4.22) **then**
return
11: **end if**
12: **end for**
13: The entries of $\vec{\boldsymbol{x}}_\ell$ are the coefficients of the reconstruction $\boldsymbol{p}_{\triangle,\ell}$ of the unknown center curve K of D_ρ.

where $P_N : \mathbb{R}^{3n} \to \mathbb{R}^Q$ and $Q = 12N(N-1) + 3((M-1)(n-1)+1) + (n-1)$. Storing real and imaginary parts separately, $12N(N-1)$ entries of $P_N(\vec{\boldsymbol{x}})$ correspond to the normalized residual term in (4.22), $3((M-1)(n-1)+1)$ entries correspond to the penalty term Ψ_1, and $n-1$ entries correspond to the penalty term Ψ_2. Consequently, we obtain a real-valued nonlinear least squares problem, which is solved numerically using the Gauß–Newton algorithm with a golden section line search (see, e.g. [104, pp. 115]). In addition to the Fréchet derivative of the operator T_ρ this also requires appropriate Fréchet derivatives corresponding to the penalty terms in (4.20). Note that after a discretization of the integral in the definition of Ψ_1 from (4.18) we have

$$\Psi_1(\boldsymbol{p}_\triangle) \;\approx\; \sum_{j=1}^{T} w_j |\kappa(s_j)|^2 |\boldsymbol{p}'(s_j)|\,, \tag{4.24}$$

where $T = (M-1)(n-1)+1$ and w_j are the weights corresponding to the composite Simpson's

rule defined in Remark 3.28. Accordingly, in the vector P_N, we store a vector of size $3T$ at the appropriate position, which yields the value on the right hand side of (4.24), when the norm of P_N is squared as required in (4.23). In the following lemma we suppress the dependency on the variable s.

Lemma 4.5. *It holds that*

$$\kappa^2 |\boldsymbol{p}'| \;=\; \left| \frac{\boldsymbol{p}''}{|\boldsymbol{p}'|^{3/2}} - \frac{\boldsymbol{p}' \cdot \boldsymbol{p}''}{|\boldsymbol{p}'|^{7/2}} \boldsymbol{p}' \right|^2 .$$

The Fréchet derivatives of the mappings $\psi_1 : \mathcal{P} \to \mathbb{R}^3$,

$$\psi_1(\boldsymbol{p}) \;=\; \frac{\boldsymbol{p}''}{|\boldsymbol{p}'|^{3/2}} - \frac{\boldsymbol{p}' \cdot \boldsymbol{p}''}{|\boldsymbol{p}'|^{7/2}} \boldsymbol{p}'$$

and $\psi_{2,j} : \mathcal{P} \to \mathbb{R}$,

$$\psi_{2,j}(\boldsymbol{p}) \;=\; \frac{1}{n-1} \int_0^1 |\boldsymbol{p}'| \, \mathrm{d}s - \int_{t_j}^{t_{j+1}} |\boldsymbol{p}'| \, \mathrm{d}s \,, \qquad j = 1, \ldots, n-1 \,,$$

are given by $\psi_1'(\boldsymbol{p}) : C^3([0,1], \mathbb{R}^3) \to \mathbb{R}^3$,

$$\psi_1'(\boldsymbol{p})\boldsymbol{h} \;=\; \frac{\boldsymbol{h}''}{|\boldsymbol{p}'|^{3/2}} - \frac{3}{2} \frac{\boldsymbol{p}' \cdot \boldsymbol{h}'}{|\boldsymbol{p}'|^{7/2}} \boldsymbol{p}'' - \frac{\boldsymbol{p}'' \cdot \boldsymbol{p}'}{|\boldsymbol{p}'|^{7/2}} \boldsymbol{h}' - \left(\frac{\boldsymbol{p}'' \cdot \boldsymbol{h}'}{|\boldsymbol{p}'|^{7/2}} + \frac{\boldsymbol{h}'' \cdot \boldsymbol{p}'}{|\boldsymbol{p}'|^{7/2}} - \frac{7}{2} \frac{(\boldsymbol{p}'' \cdot \boldsymbol{p}')(\boldsymbol{p}' \cdot \boldsymbol{h}')}{|\boldsymbol{p}'|^{11/2}} \right) \boldsymbol{p}' \tag{4.25}$$

and by $\psi_2'(\boldsymbol{p}) : C^3([0,1], \mathbb{R}^3) \to \mathbb{R}$,

$$\psi_{2,j}'(\boldsymbol{p})\boldsymbol{h} \;=\; \frac{1}{n-1} \int_0^1 \frac{\boldsymbol{p}' \cdot \boldsymbol{h}'}{|\boldsymbol{p}'|} \, \mathrm{d}s - \int_{t_j}^{t_{j+1}} \frac{\boldsymbol{p}' \cdot \boldsymbol{h}'}{|\boldsymbol{p}'|} \, \mathrm{d}s \,, \qquad j = 1, \ldots, n-1 \,, \tag{4.26}$$

respectively.

Proof. Let $\boldsymbol{p} \in \mathcal{P}$ and let $\delta > 0$ be so small that $\boldsymbol{p} + \boldsymbol{h} \in \mathcal{P}$ for all $\boldsymbol{h} \in C^3([0,1], \mathbb{R}^3)$ with $\|\boldsymbol{h}\|_{C^3} < \delta$. First, we note that the curvature from (4.19) can be written as

$$\kappa(s) \;=\; \frac{|\boldsymbol{t}_{\boldsymbol{p}}'(s)|}{|\boldsymbol{p}'(s)|} \;=\; \left| \frac{\boldsymbol{p}''(s)}{|\boldsymbol{p}'(s)|^2} - \frac{(\boldsymbol{p}'(s) \cdot \boldsymbol{p}''(s))}{|\boldsymbol{p}'(s)|^4} \boldsymbol{p}'(s) \right| ,$$

where $\boldsymbol{t}_{\boldsymbol{p}}$ denotes the tangent vector (see e.g. [119, Prop. 1.34]). Therefore,

$$\kappa^2(s) |\boldsymbol{p}'(s)| \;=\; \left| \frac{\boldsymbol{p}''(s)}{|\boldsymbol{p}'(s)|^{3/2}} - \frac{(\boldsymbol{p}'(s) \cdot \boldsymbol{p}''(s))}{|\boldsymbol{p}'(s)|^{7/2}} \boldsymbol{p}'(s) \right|^2 .$$

Using Taylor's theorem we find that for $\alpha > 0$ it holds that

$$\frac{1}{|\boldsymbol{p}' + \boldsymbol{h}'|^{\alpha}} \;=\; \frac{1}{|\boldsymbol{p}'|^{\alpha}} - \frac{\alpha}{|\boldsymbol{p}'|^{\alpha+2}} (\boldsymbol{p}' \cdot \boldsymbol{h}') + O(\|\boldsymbol{h}\|_{C^3}^2). \tag{4.27}$$

Consequently,

$$\begin{aligned}
\psi_1(\boldsymbol{p} + \boldsymbol{h}) \;=\; & (\boldsymbol{p}'' + \boldsymbol{h}'') \left(\frac{1}{|\boldsymbol{p}'|^{3/2}} - \frac{3}{2} \frac{\boldsymbol{p}' \cdot \boldsymbol{h}'}{|\boldsymbol{p}'|^{7/2}} \right) \\
& - \left((\boldsymbol{p}' \cdot \boldsymbol{p}'') \boldsymbol{p}' + (\boldsymbol{p}' \cdot \boldsymbol{h}'') \boldsymbol{p}' + (\boldsymbol{h}' \cdot \boldsymbol{p}'') \boldsymbol{p}' + (\boldsymbol{p}' \cdot \boldsymbol{p}'') \boldsymbol{h}' \right) \left(\frac{1}{|\boldsymbol{p}'|^{7/2}} - \frac{7}{2} \frac{\boldsymbol{p}' \cdot \boldsymbol{h}'}{|\boldsymbol{p}'|^{11/2}} \right) \\
& + O(\|\boldsymbol{h}\|_{C^3}^2) \\
= \; & \frac{\boldsymbol{p}''}{|\boldsymbol{p}'|^{3/2}} - \frac{\boldsymbol{p}' \cdot \boldsymbol{p}''}{|\boldsymbol{p}'|^{7/2}} \boldsymbol{p}' + \frac{\boldsymbol{h}''}{|\boldsymbol{p}'|^{3/2}} - \frac{3}{2} \frac{\boldsymbol{p}' \cdot \boldsymbol{h}'}{|\boldsymbol{p}'|^{7/2}} \boldsymbol{p}'' - \frac{\boldsymbol{p}'' \cdot \boldsymbol{p}'}{|\boldsymbol{p}'|^{7/2}} \boldsymbol{h}' \\
& - \left(\frac{\boldsymbol{p}'' \cdot \boldsymbol{h}'}{|\boldsymbol{p}'|^{7/2}} + \frac{\boldsymbol{h}'' \cdot \boldsymbol{p}'}{|\boldsymbol{p}'|^{7/2}} - \frac{7}{2} \frac{(\boldsymbol{p}'' \cdot \boldsymbol{p}')(\boldsymbol{p}' \cdot \boldsymbol{h}')}{|\boldsymbol{p}'|^{11/2}} \right) \boldsymbol{p}' + O(\|\boldsymbol{h}\|_{C^3}^2).
\end{aligned}$$

This yields that

$$\frac{1}{\|\boldsymbol{h}\|_{C^3}}|\psi_1(\boldsymbol{p}+\boldsymbol{h})-\psi_1(\boldsymbol{p})-\psi_1'(\boldsymbol{p})\boldsymbol{h}| \to 0 \qquad \text{as } \|\boldsymbol{h}\|_{C^3} \to 0.$$

For the Fréchet derivative of $\psi_{2,j}$ we use Taylor's theorem again and find that

$$|\boldsymbol{p}'+\boldsymbol{h}'| = |\boldsymbol{p}'| + \frac{\boldsymbol{p}'\cdot\boldsymbol{h}'}{|\boldsymbol{p}'|} + O(\|\boldsymbol{h}\|_{C^3}^2). \tag{4.28}$$

This already shows that $\psi_{2,j}'$ from (4.26) is the Fréchet derivative of $\psi_{2,j}$. □

In Algorithm 1 we describe the optimization scheme that is used to minimize $|P_N|^2$ from (4.23). Here we denote the Jacobian of P_N by J_{P_N}. The algorithm uses the following heuristic stopping criterion. If the optimal step size s_ℓ^* determined by the line search in the current iteration is zero or if the (potential) relative movement[1] of the iterate defined by

$$\texttt{Mov} = \frac{\|s_\ell^*\boldsymbol{\Delta}_\ell\|}{\|\vec{\boldsymbol{x}}_\ell\|} \tag{4.29}$$

is smaller than a tolerance $\texttt{tol} > 0$ and additionally, if the value of the objective functional $|P(\vec{\boldsymbol{x}}_\ell)|^2$ is dominated by the normalized residual term in (4.22), then the algorithm stops. However, if the optimal step size s_ℓ^* determined by the line search is zero but the value of the objective functional $|P(\vec{\boldsymbol{x}}_\ell)|^2$ is dominated by the contribution of one of the two regularization terms $\alpha_j^2\Psi_j(\boldsymbol{p}_{\triangle,\ell})$, $j\in\{1,2\}$, then we conclude that in order to further improve the reconstruction, the corresponding regularization parameter should be reduced. In this case we replace α_j by $\frac{\alpha_j}{2}$ and restart the iteration using the current iterate for the initial guess. The fact that not a single Maxwell system has to be solved during the reconstruction process makes this algorithm extremely efficient, when compared to traditional iterative shape reconstruction methods for inverse scattering problems for Maxwell's equations (see e.g. [71, 72, 73, 79, 109]).

4.3 Numerical results

For our numerical reconstructions we study, as in Section 3.5, dielectric and metallic scattering objects separately. In both cases, the far field data $\boldsymbol{E}_\rho^\infty$ is computed by using the PMCHWT formulation described in Appendix C together with Bempp. This reduces the possibility of inverse crimes: The data generated by the forward solver (i.e. by Bempp) is more or less independent from the inverse solver (see also [34, p. 179]). In all our examples we consider the construction of cubic not-a-knot splines from given spatial points and approximate integrals using the composite Simpson's rule. We rigorously described this in Remark 3.28. For metallic objects, we further refer to Remark 3.25, which enables us to upscale and downscale scattering objects in order to perform simulations in computational units.

4.3.1 Reconstructions of dielectric thin tubes

For our numerical reconstructions of dielectric scattering objects we consider the three center curves from Example 3.29-3.31 in Section 3.5 for the radius $\rho = 0.03$, embedded in free space. For this particular radius the three-dimensional scattering object is also visualized in the top row of Figure 3.3. The corresponding center curves can be found in Figure 3.2. The material parameters corresponding to each example are as in the dielectric case of Section 3.5, i.e. $\varepsilon_r = 2.5$ and $\mu_r = 1.6$ for Example 3.29, $\varepsilon_r = 1$ and $\mu_r = 2.1$ for Example 3.30 and $\varepsilon_r = 2.1$ and $\mu_r = 1.0$ in Example 3.31. For these parameters we do not have a specific material in mind. We study

[1] Note that $s_\ell^*\boldsymbol{\Delta}_\ell = \vec{\boldsymbol{x}}_{\ell+1} - \vec{\boldsymbol{x}}_\ell$. Thus, we call the expression in (4.29) the relative movement of the iterate.

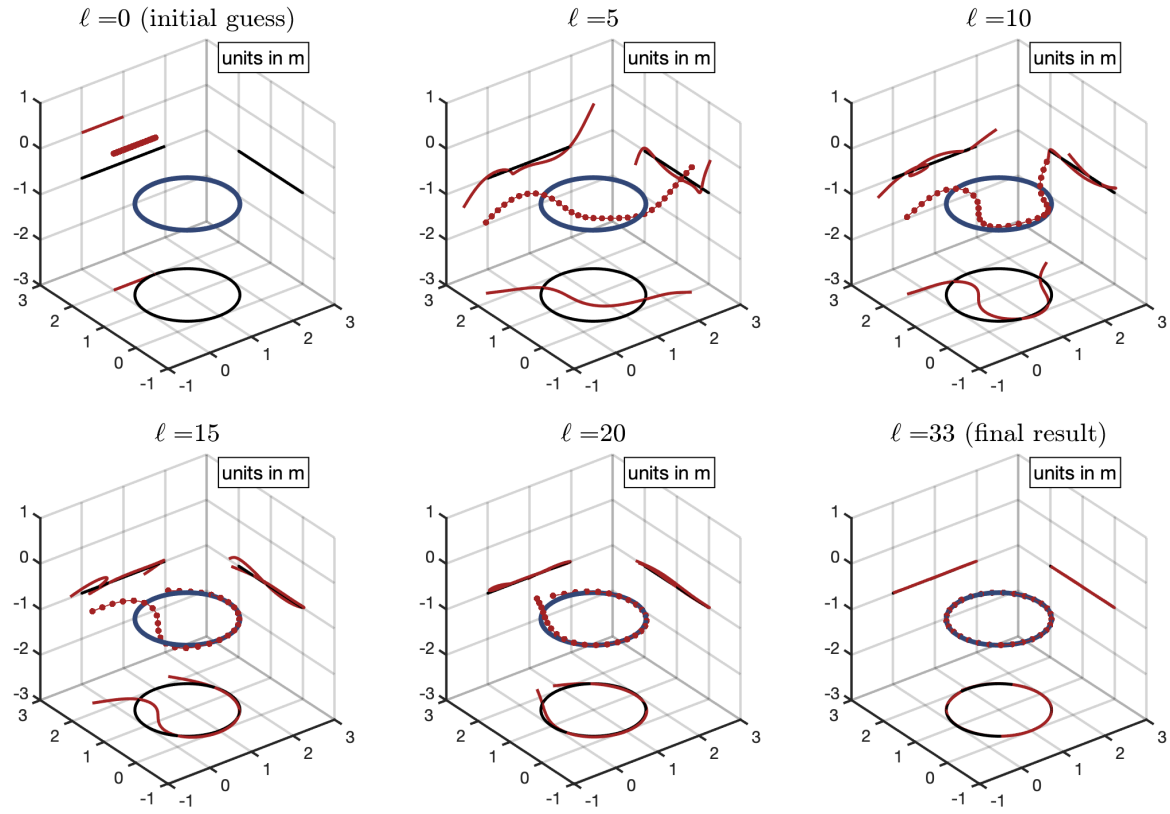

Figure 4.1: Reconstruction of the toroidal scatterer from Example 3.29. The top-left plot shows the initial guess, and the bottom-right plot shows the final reconstruction.

these coefficients as a matter of interest and to test the basis of the reconstruction algorithm, that is, the leading order term of the asymptotic perturbation formula. We simulate the far field data $\boldsymbol{E}_\rho^\infty$ for each of the three examples using the PMCHWT formulation described in Appendix C together with Bempp, where we use triangulations of the boundaries of the tubes ∂D_ρ with 26698 triangles for Example 3.29, 62116 triangles for Example 3.30, and 62116 triangles for Example 3.31. This corresponds to 80094, 186348 and 186348 degrees of freedom, respectively (see also Table 3.1). The values of $\boldsymbol{E}_\rho^\infty$ are evaluated on the equiangular grid on S^2 from (4.21) with $N = 10$. As in Section 3.5, the incident field is a plane wave with polarization $\boldsymbol{A} = [-1, 1\mathrm{i}, 1+1\mathrm{i}]^\top$ and direction of propagation $\boldsymbol{\theta} = 1/\sqrt{3}[1, -1, 1]^\top$. As the operating frequency we consider $f = 100\mathrm{MHz}$. With the electric permittivity ε_0 and the magnetic permeability μ_0 in free space from (2.19) the wave number is given by $k = \omega\sqrt{\varepsilon_0\mu_0} \approx 2.1\mathrm{m}^{-1}$, where $\omega = 2\pi f$ is the angular frequency. The corresponding wavelength in the exterior is $\lambda = 2\pi/k \approx 3\mathrm{m}$. Section 3.5 showed that the leading order term $\widetilde{\boldsymbol{E}_\rho^\infty}$ is a good approximation to the reference far field $\boldsymbol{E}_\rho^\infty$ in this regime. We choose the following parameters in Algorithm 1:

- Let the number of nodes of the cubic not-a-knot spline be given by $n = 30$.
- In order to approximate integrals using the composite Simpson's rule, let the number of elements on each spline segment be given by $M = 11$.
- Let the regularization parameters in step 2 by given by $\alpha_1 = 0.06$ and $\alpha_2 = 0.9$.
- We choose $s_{\max} = 1$ in the golden section line search in step 5 and we terminate each line search after a fixed number of 10 steps.
- We choose the tolerance $\texttt{tol} = 5 \times 10^{-3}$ in step 2 of the algorithm.

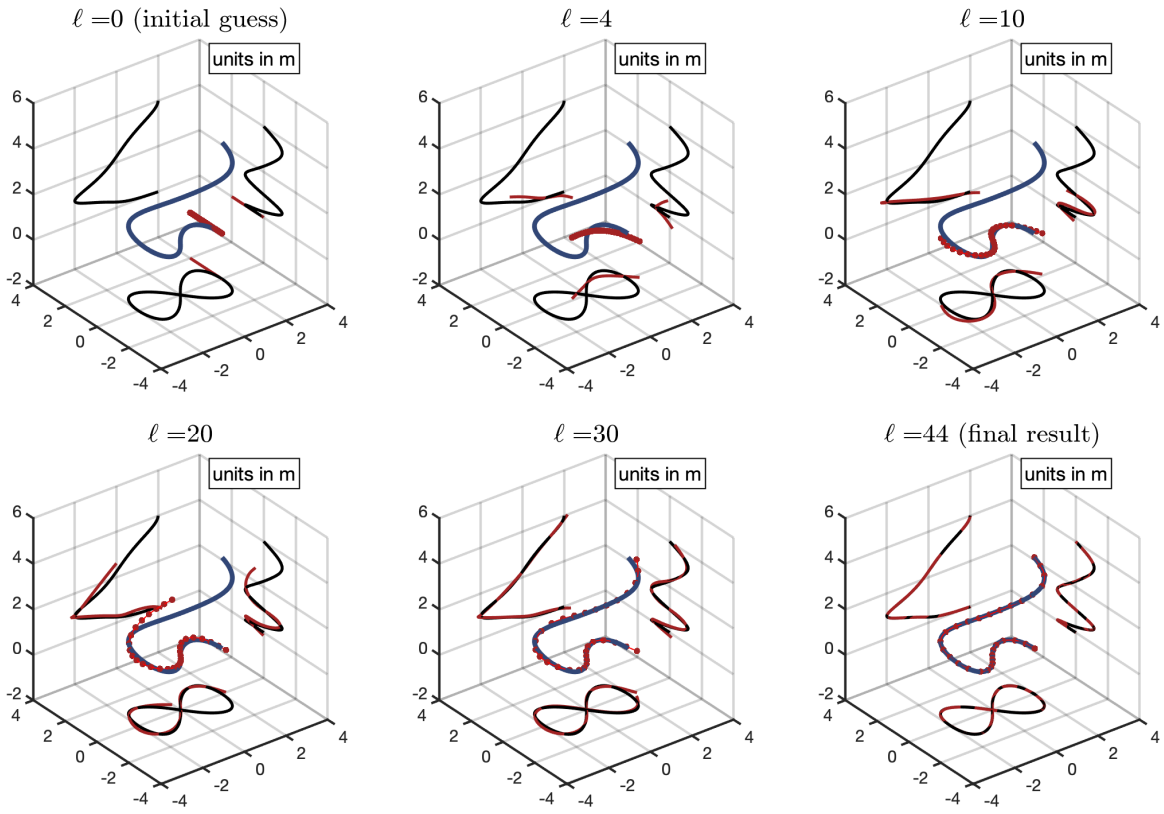

Figure 4.2: Reconstruction of the thin tubular scatterer from Example 3.30. The top-left plot shows the initial guess, and the bottom-right plot shows the final reconstruction.

The results are shown in Figure 4.1 - 4.3. Here, the top-left plots show the initial guess, and the bottom-right plots show the final reconstruction. The remaining four plots show intermediate approximations of the iterative reconstruction procedure. Each plot contains the exact center curve K (solid blue) and the current approximation $\boldsymbol{p}_{\triangle,\ell}$ of the reconstruction algorithm after ℓ iterations (solid red with dots). Furthermore, we have included projections of these curves onto the three coordinate planes to enhance the three-dimensional perspective.

Example 4.6. We consider the setting from Example 3.29. The initial guess is a straight line segment connecting the points $[0,2,0]^\top$ and $[1,2,0]^\top$. The reconstruction algorithm stops after 33 iterations. The initial guess, some intermediate steps and the final result of the reconstruction algorithm are shown in Figure 4.1. The final reconstruction is very close to the exact center curve K.

Example 4.7. We consider the setting from Example 3.30. The initial guess is a straight line segment connecting the points $[2,0,0]^\top$ and $[2,2,0]^\top$. The reconstruction algorithm stops after 44 iterations. The initial guess, some intermediate steps and the final result of the reconstruction algorithm are shown in Figure 4.2. Again, the final reconstruction is very close to the exact center curve K.

Example 4.8. We consider the setting from Example 3.31. The initial guess is a straight line segment connecting the points $[0,-1,1]^\top$ and $[0,-2,1]^\top$. The reconstruction algorithm stops after 45 iterations. The initial guess, some intermediate steps and the final result of the reconstruction algorithm are shown in Figure 4.3. As in the previous examples, the final reconstruction is very close to the exact center curve K.

In all three examples Algorithm 1 provides accurate approximations to the center curve K of the unknown scattering object D_ρ. However, a suitable choice of the regularization parameters

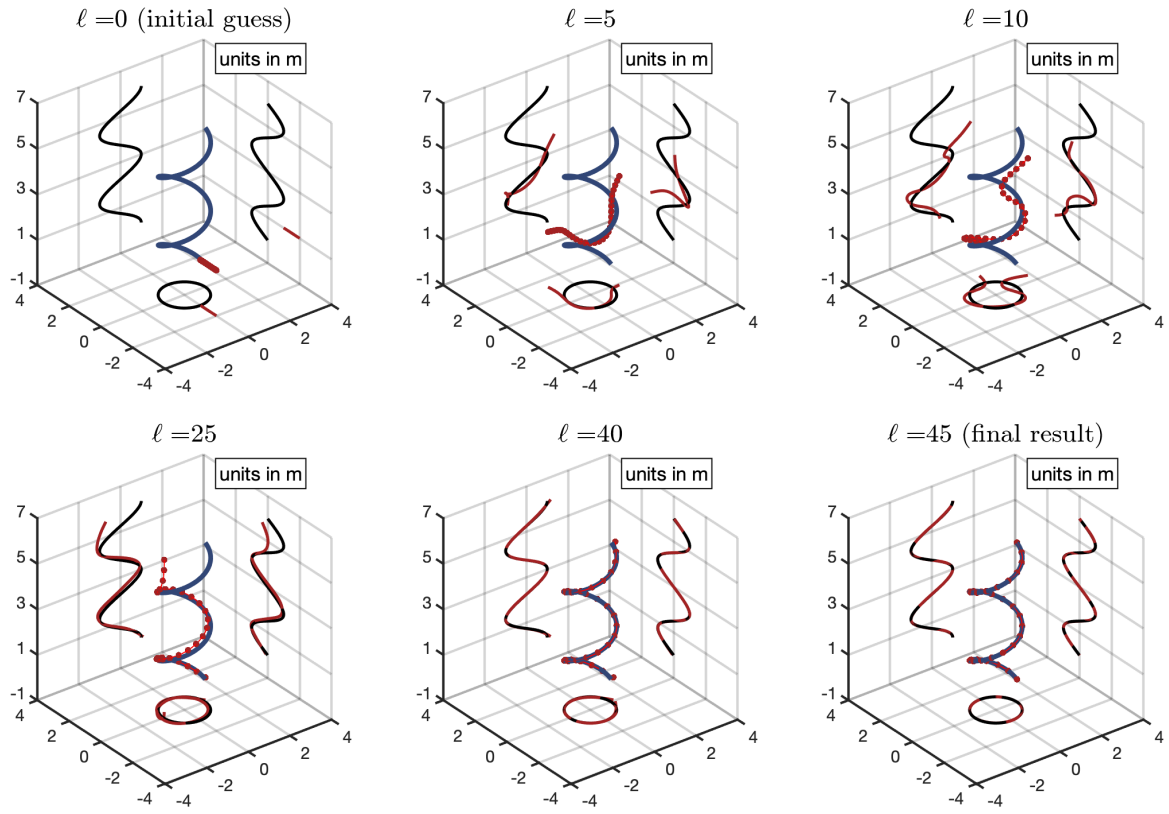

Figure 4.3: Reconstruction of the helical scatterer from Example 3.31. The top-left plot shows the initial guess, and the bottom-right plot shows the final reconstruction.

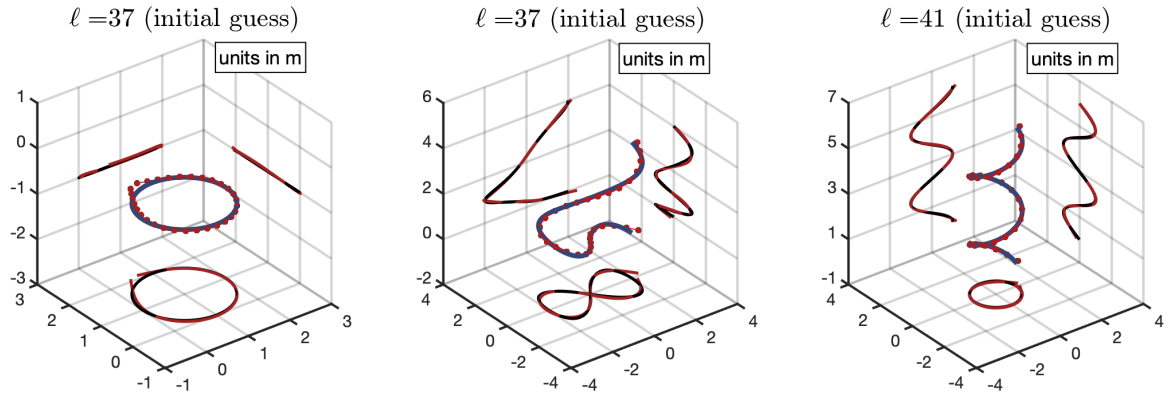

Figure 4.4: Reconstructions from noisy data with 30% uniformly distributed additive noise.

α_1 and α_2 and an initial guess for $\boldsymbol{p}_\triangle$ sufficiently close to the unknown center curve K are crucial for a successful reconstruction. In our next example we study the sensitivity of the reconstruction algorithm to noise in the far field data.

Example 4.9. We repeat the previous computations but we add 30% complex-valued uniformly distributed error to the electric far field patterns $\boldsymbol{E}_\rho^\infty$ that have been simulated using Bempp. Precisely, we define the error level $\delta = 0.3$ and set $\text{err}(\boldsymbol{y}_{jl}) = \text{rand}_1(\boldsymbol{y}_{jl}) + \text{rand}_2(\boldsymbol{y}_{jl})\text{i}$, where $\text{rand}_1(\boldsymbol{y}_{jl}), \text{rand}_2(\boldsymbol{y}_{jl})$ denote randomly generated numbers between -0.5 and 0.5 with $\boldsymbol{y}_{jl} \in S^2$ from (4.21). These are the points for which observations of the far field $\boldsymbol{E}_\rho^\infty$ are available. Then,

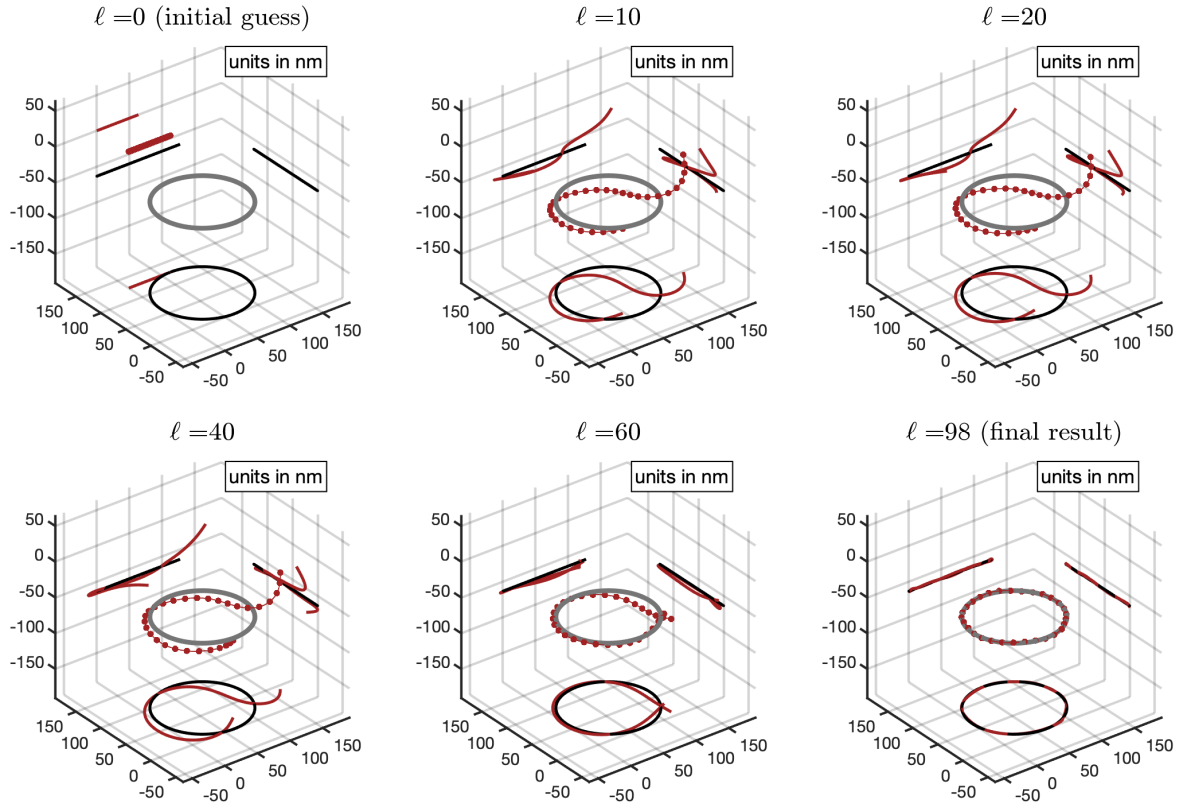

Figure 4.5: Reconstruction of the silver torus from Example 3.32 and $j = 2$. The top-left plot shows the initial guess, and the bottom-right plot shows the final reconstruction.

we define the noisy given far field $\boldsymbol{E}^{\infty}_{\rho,n}$ by

$$\boldsymbol{E}^{\infty}_{\rho,n}(\boldsymbol{y}_{jl}) \;=\; \frac{\mathrm{err}(\boldsymbol{y}_{jl})}{\|\mathrm{err}\|_{L^2_t(S^2)}}\delta\|\boldsymbol{E}^{\infty}_{\rho}\|_{L^2_t(S^2)} + \boldsymbol{E}^{\infty}_{\rho}(\boldsymbol{y}_{jl})\,. \tag{4.30}$$

We use the same initial guesses and the same initial values for the regularization parameters α_1 and α_2 as in Examples 4.6 - 4.8. The three plots in Figure 4.4 show the exact center curves (solid blue), the final reconstructions (solid red with dots), and the projections of these curves onto the coordinate planes. The reconstruction algorithm stops after 37 iterations for Example 4.6, after 37 iterations for Example 4.7 and after 41 iterations for Example 4.8, respectively. Despite the relatively high noise level, the final reconstructions are still very close to the exact center curves K. In the first and second case we find that essentially the end segments of the reconstruction distinguish from the true curve.

We note that Algorithm 1 incorporates all available a priori information about the radius ρ, the shape of the cross-section of the unknown scatterer and its material parameters ε_r and μ_r. Furthermore, it reconstructs a relatively low number of nodes corresponding to the spline approximation $\boldsymbol{p}_{\triangle}$ of the center curve K of the unknown thin tubular scattering object D_ρ. We also have carefully regularized the output least squares functional Φ in (4.20). This might explain the good performance of the reconstruction algorithm even for rather noisy far field data.

4.3.2 Reconstructions of metallic nanowires

We aim to reconstruct thin silver nanowires that possess the center curves described in Examples 3.32 - 3.34 for $j = 2$ together with a circular cross-section with radius $\rho = 1.91$nm. As in the

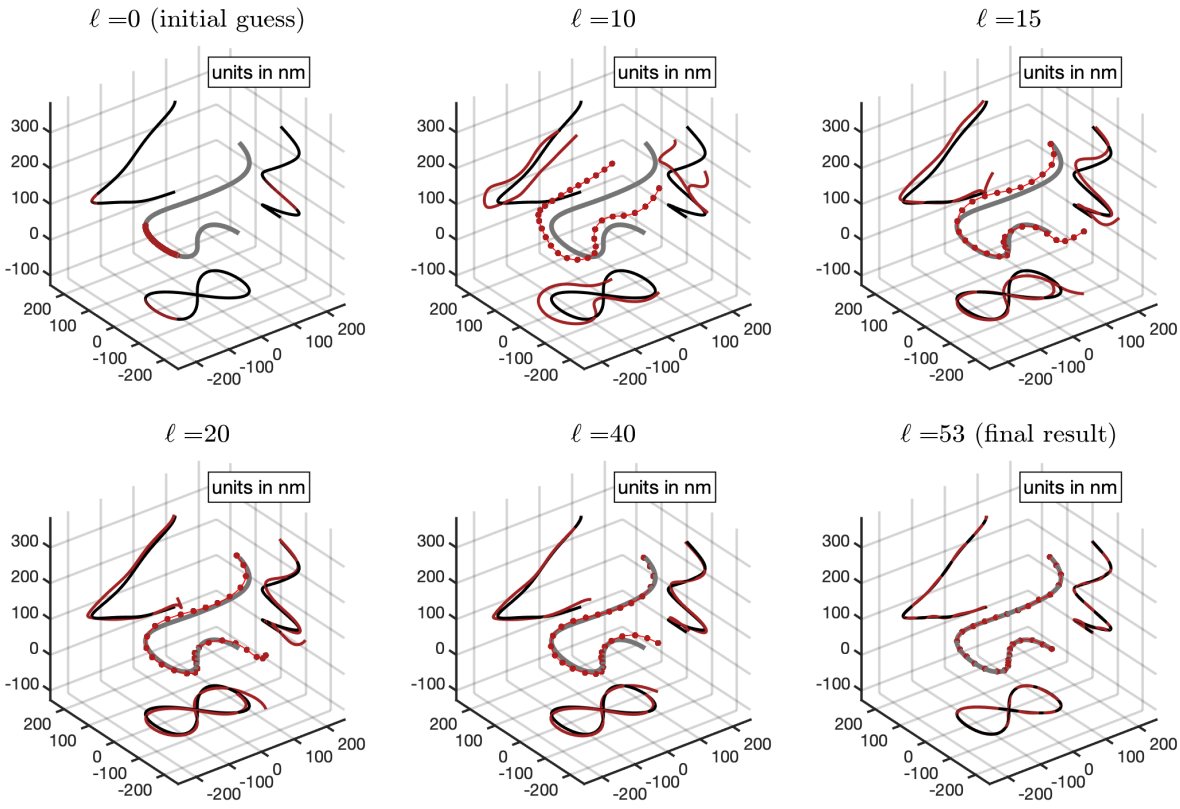

Figure 4.6: Reconstruction of the silver nanowire from Example 3.33 and $j = 2$. The top-left plot shows the initial guess, and the bottom-right plot shows the final reconstruction.

previous subsection, we simulate the far field data $\boldsymbol{E}_\rho^\infty$ for each of these three examples using the PMCHWT formulation described in Appendix C together with Bempp, where we use triangulations of the boundaries of the tubes ∂D_ρ with 26698 triangles for Example 3.29, 62116 triangles for Example 3.30, and 62116 triangles for Example 3.31. This corresponds to 80094, 186348 and 186348 degrees of freedom, respectively (see also Table 3.3). The values of $\boldsymbol{E}_\rho^\infty$ are evaluated on the equiangular grid on S^2 from (4.21) with $N = 10$. The incident field is a plane wave with polarization $\boldsymbol{A} = [-1, 1\mathrm{i}, 1 + 1\mathrm{i}]^\top$ and direction of propagation $\boldsymbol{\theta} = 1/\sqrt{3}[1, -1, 1]^\top$. The wavelength of the incident field is $\lambda = 400\mathrm{nm}$, what corresponds to the frequency $f \approx 750\mathrm{THz}$. The material parameters for silver for this wavelength are given by $\varepsilon_r \approx -4.42 + 0.21\mathrm{i}$ and $\mu_r = 1$ (see [83]). We recall that for computational purposes, we scale the scattering objects in such a way that the exterior computational wave number $k_c = 1$ may be used, although the actual wave number is given by $k = 2\pi/(0.4 \times 10^{-6})\mathrm{m}^{-1}$ in all examples (see Remark 3.25). In an application, one would measure the far field $\boldsymbol{E}_\rho^\infty$ corresponding to a thin metallic nanowire on the equiangular grid (4.21). As the incident wavelength $\lambda = 400\mathrm{nm}$ is known, the scaled far field, that we use as the given data for the reconstruction, is given by $\boldsymbol{E}_{\rho,c}^\infty = \alpha \boldsymbol{E}_\rho^\infty$ with the scaling parameter $\alpha = k$. Afterwards, the reconstruction algorithm in Algorithm 1 is supposed to find the thin tubular scatterer corresponding to the computational wavelength $k_c = 1$. Finally, the nanowire in real units will be given by scaling the reconstructed wire by α^{-1}. We choose the following parameters in Algorithm 1:

- Let the number of nodes of the cubic not-a-knot spline be given by $n = 30$.
- In order to approximate integrals using the composite Simpson's rule, let the number of elements on each spline segment be given by $M = 11$.
- Let the regularization parameters in step 2 by given by $\alpha_1 = 0.09$ and $\alpha_2 = 0.6$.

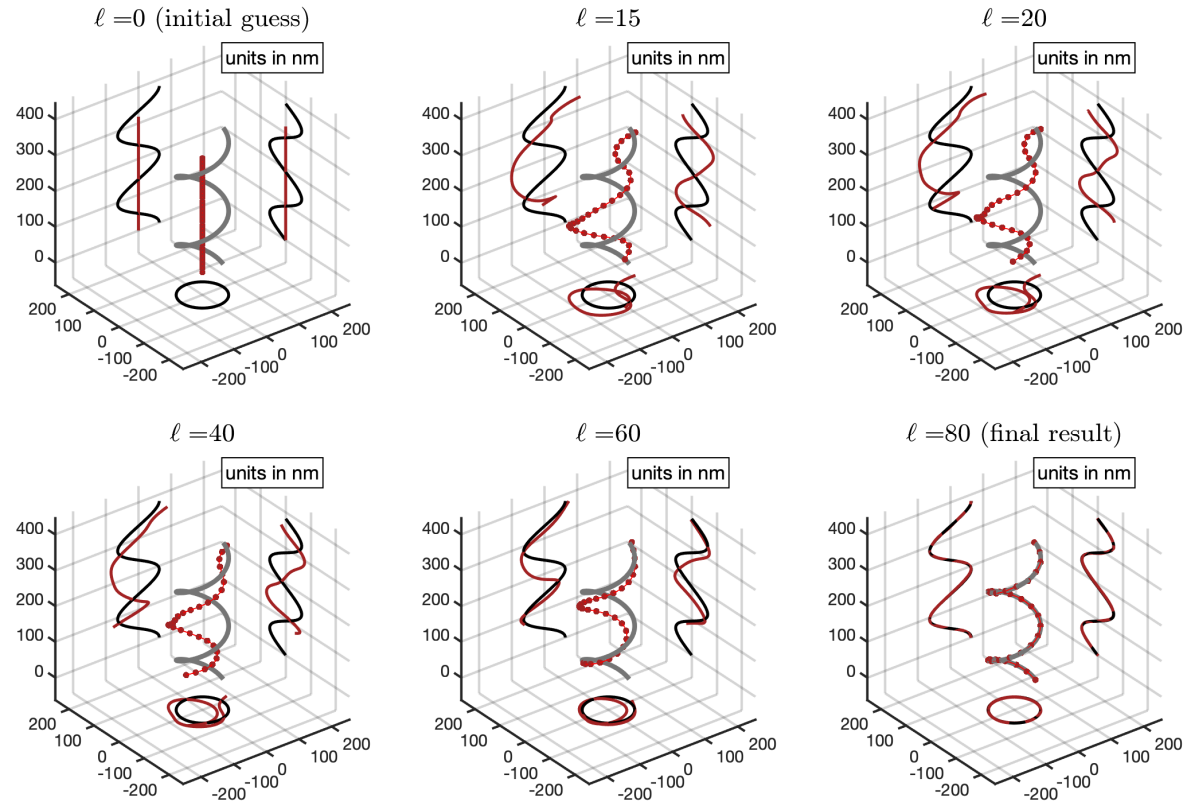

Figure 4.7: Reconstruction of the silver helix with two turns from Example 3.34 and $j = 2$. The top-left plot shows the initial guess, and the bottom-right plot shows the final reconstruction.

- We choose $s_{\max} = 1$ in the golden section line search in step 5 and we terminate each line search after a fixed number of 10 steps.
- We choose the tolerance $\texttt{tol} = 5 \times 10^{-3}$ in step 2 of the algorithm.

The results are shown in Figure 4.5 - 4.7. Again, the top-left plots show the initial guess, and the bottom-right plots show the final reconstruction. The remaining four plots show intermediate approximations of the iterative reconstruction procedure. Each plot contains the exact center curve K (solid silver) and the current approximation $\boldsymbol{p}_{\triangle,\ell}$ of the reconstruction algorithm after ℓ iterations (solid red with dots). Furthermore, we have included projections of these curves onto the three coordinate planes to enhance the three-dimensional perspective.

Example 4.10. We consider the setting from Example 3.32. The initial guess is a straight line segment connecting the points $[0, 127.32, 0]^\top$nm and $[63.66, 127.32, 0]^\top$nm. In computational units, this is the same initial guess as the one for the dielectric scattering objects from Example 4.6. The initial guess, some intermediate steps and the final result of the reconstruction algorithm are shown in Figure 4.5. The reconstruction algorithm stops after 98 iterations. Compared to the dielectric coefficients considered in Example 4.6, Algorithm 1 requires 46 more steps to stop (see Figure 4.1). As in the dielectric case, the final reconstruction is very close to the exact center curve K.

Example 4.11. We consider the setting from Example 3.33. The initial guess is a curve segment that lies exactly on the center curve of the true scatterer. This corresponds to an additional a-priori information about the nanowire that we want to reconstruct. For this initial guess, the algorithm stops after 53 iterations. The initial guess, some intermediate steps and the final result of the reconstruction algorithm are shown in Figure 4.6. The final reconstruction is very close

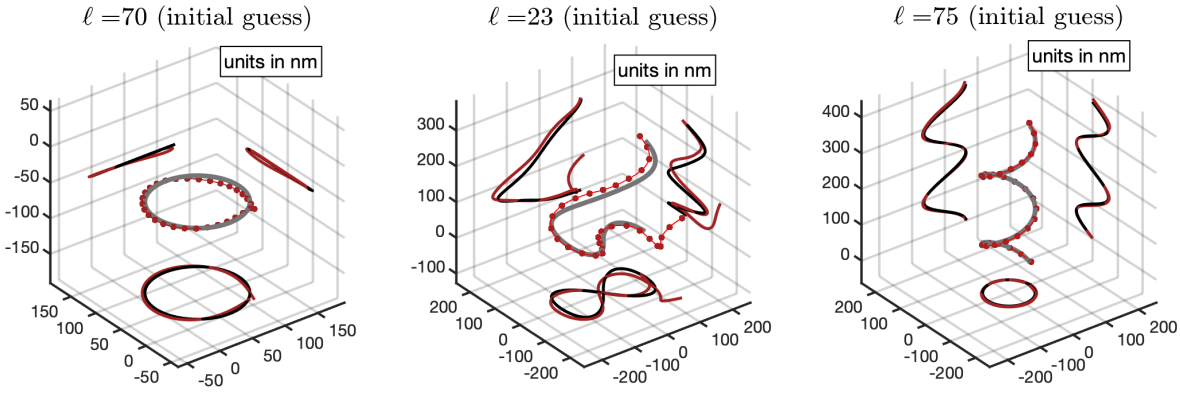

Figure 4.8: Reconstructions from noisy data with 30% uniformly distributed additive noise.

to the exact center curve K. We point out that for this example, the reconstruction appears to be more challenging than for the dielectric counterpart in Example 3.30. Using the same initial guess as in Example 3.30 (in computational units) does not lead to a satisfying reconstruction of the center curve. In fact, we found that a different initial guess often leads to a failure in the reconstruction.

Example 4.12. We consider the setting from Example 3.34. The initial guess is a straight line segment connecting the points $[0,0,0]^\top$nm and $[0,0,318]^\top$nm. The reconstruction algorithm stops after 80 iterations. The initial guess, some intermediate steps and the final result of the reconstruction algorithm are shown in Figure 4.7. The final reconstruction is very close to the exact center curve K. Again, the reconstruction is more challenging than in the dielectric case in Example 3.31: Different initial guesses often lead to a failure in the reconstruction.

In all examples, we find that the reconstruction algorithm provides a good approximation to the true scattering object. As we already pointed out, an appropriate initial guess of the algorithm is essential for a successful reconstruction. In our final example we add additional noise to the given Bempp far field as we did for dielectric scattering objects in Example 4.9.

Example 4.13. We repeat the computations from Example 4.10 - 4.12, but we add 30% complex-valued uniformly distributed error to the electric far field patterns $\boldsymbol{E}_\rho^\infty$ that have been simulated using Bempp as in (4.30). We use the same initial guesses and the same initial values for the regularization parameters α_1 and α_2 as in Example 4.10 - 4.12. The three plots in Figure 4.8 show the exact center curves (solid silver), the final reconstructions (solid red with dots), and the projections of these curves onto the coordinate planes. The reconstruction algorithm stops after 70 iterations for Example 4.10, after 23 iterations for Example 4.11 and after 75 iterations for Example 4.12, respectively. For the curves from Example 3.32 and 3.34 for $j = 2$, the reconstructions from noisy data are still very close to the exact center curves K. For Example 3.33 however, the reconstructed center curve is off from the true curve. In particular, one end of the curve strongly deviates from the scatterer's true position.

Remark 4.14. By using Algorithm 1 we reconstructed dielectric and metallic thin tubular scattering objects from given far field data corresponding to a single incident plane wave. We observe that for an initial guess that is sufficiently close to the true scatterer's center curve, the algorithm provides a nice approximation to the true object. Our numerical examples hence imply that the leading order term is well-suited for a derivative based reconstruction scheme. Therefore, it should also provide a promising basis for a derivative-based shape optimization method for designing highly electromagnetically chiral structures.

Chapter 5

Shape optimization for thin em-chiral structures

Electromagnetic chirality (em-chirality) describes the property of a scattering object to interact differently with electromagnetic waves of different polarization handedness, called helicity. Scatterers made of isotropic materials emitting a highly em-chiral effect are being considered as possible building blocks of novel chiral metamaterials that exhibit effective chiral material parameters many orders of magnitude larger than what is found in natural substances (see e.g. [52, 76, 84]). Metamaterials with large em-chirality have potential applications in angle-insensitive circular polarizers, which are materials that transmit one circular polarization of light and that reflect and/or absorb the opposite handedness nearly completely (see e.g. [59, 60]).

In Section 3.5, we found that the leading order term of the electric far field in (3.22) provides a good approximation to a reference solution computed by solving a boundary integral equation, if the radius ρ of the scatterer is sufficiently small. Moreover, we found in Chapter 4 that the leading order term can be used in an inexpensive Gauß-Newton algorithm that is able to reconstruct thin tubular dielectric or metallic scattering objects from measurements of a single electric far field pattern.

Our purpose in this chapter is to use the leading order term of the asymptotic perturbation formula from Theorem 3.6 to establish an inexpensive shape optimization algorithm that maximizes em-chirality for thin tubes. By means of this algorithm we want to design highly em-chiral thin tubular scatterers and in particular, metallic nanowires for frequencies in the optical regime. For this purpose, we proceed in the next sections as follows. We start this chapter with the definition of em-chirality based on the work [49]. In this context we review scalar-valued em-chirality measures. These measures quantify the degree of em-chirality of a scattering object in terms of the singular values of suitable projections of the associated far field operator onto subspaces of left and right circularly polarized fields. Our idea is to use the asymptotic perturbation formula in (3.22) to find an asymptotic expansion of the far field operator via a leading order term that is straightforward to evaluate plus terms of higher order. Hence, we consider the operator $\mathcal{T}_{D_\rho}$ that maps the thin tubular scatterer D_ρ to its corresponding leading order term of the far field operator expansion. Afterwards, the chirality measure uses only this leading order term to quantify em-chirality. In order to establish a derivative-based optimization scheme we require the shape derivative of the operator $\mathcal{T}_{D_\rho}$. We compute this derivative and provide remarks on its implementation. Afterwards we set up the optimization scheme and apply it in order to find optimal designs of em-chiral tubes and nanowires.

5.1 Definition of em-chirality

We first recall the definition of em-chirality, as introduced in [49]. In particular, we follow the exposition in [15], in which the notion of em-chirality is described in terms of the electric far field operator. We first discuss helicity, i.e. the handedness of an electromagnetic field. For a

motivating example, we consider a plane wave $(\boldsymbol{E}^i, \boldsymbol{H}^i)$ that solves (2.30) and which is given by

$$\boldsymbol{E}^i(\boldsymbol{x}) \;=\; \boldsymbol{A}\mathrm{e}^{\mathrm{i}k\boldsymbol{\theta}\cdot\boldsymbol{x}}, \qquad \boldsymbol{H}^i(\boldsymbol{x}) \;=\; \frac{1}{Z_0}\,(\boldsymbol{\theta}\times\boldsymbol{A})\,\mathrm{e}^{\mathrm{i}k\boldsymbol{\theta}\cdot\boldsymbol{x}}\,. \tag{5.1}$$

Here, $\boldsymbol{\theta}\in S^2$ is the direction of propagation, $\boldsymbol{A}\in\mathbb{C}^3\setminus\{0\}$ with $\boldsymbol{A}\cdot\boldsymbol{\theta}=0$ is the polarization and $Z_0=\sqrt{\mu_0/\varepsilon_0}$ denotes the impedance in free space. In physics literature (see e.g. [82, Chap. 7.2]) the polarization of a plane wave is introduced as the direction of the oscillation of the wave. For a given direction of propagation $\boldsymbol{\theta}\in S^2$, a general time-dependent plane wave can be written as

$$\boldsymbol{E}^i(\boldsymbol{x},t) \;=\; (\boldsymbol{a}_1E_1+\boldsymbol{a}_2E_2)e^{\mathrm{i}(k\boldsymbol{\theta}\cdot\boldsymbol{x}-\omega t)}\,, \tag{5.2}$$

where $(\boldsymbol{a}_1,\boldsymbol{a}_2,\boldsymbol{\theta})$ constitute an orthonormal system of $\mathbb{R}^3$ and E_1 and E_2 are complex numbers (see [82, Eq. 7.19]). Dependent on the phases, i.e. the arguments of E_1 and E_2, the plane wave in (5.2) shows different polarizations for variable times t. If both E_1 and E_2 have the same phase, then the plane wave is linearly polarized. For different phases of E_1 and E_2, the plane wave is in general elliptically polarized. For the special case that $|E_1|=|E_2|$ and the phases differ by $\pm\pi/2$, the wave is defined as circularly polarized. In this case, (5.2) can be written as

$$\boldsymbol{E}^i(\boldsymbol{x},t) \;=\; |E_1|(\boldsymbol{a}_1\pm\mathrm{i}\boldsymbol{a}_2)e^{\mathrm{i}(k\boldsymbol{\theta}\cdot\boldsymbol{x}-\omega t+\alpha)}\,, \tag{5.3}$$

for a fixed $\alpha\in[0,2\pi)$. The physical wave is obtained by studying the real part of (5.3), which gives that

$$\mathrm{Re}\left(\boldsymbol{E}^i(\boldsymbol{x},t)\right) \;=\; |E_1|(\boldsymbol{a}_1\cos(k\boldsymbol{\theta}\cdot\boldsymbol{x}-\omega t+\alpha)\mp\boldsymbol{a}_2\sin(k\boldsymbol{\theta}\cdot\boldsymbol{x}-\omega t+\alpha))\,. \tag{5.4}$$

Thus, for a fixed point in space $\boldsymbol{x}\in\mathbb{R}^3$ and varying times t the magnitude of $\mathrm{Re}\left(\boldsymbol{E}^i(\boldsymbol{x},t)\right)$ is constant and equals $|E_1|$ and the orientation of the vector performs a circular motion in the plane spanned by $\boldsymbol{e}_1$ and $\boldsymbol{e}_2$. Equivalently, one may consider a fixed time t, a point in space $\boldsymbol{x}$ and move a quarter wavelength, i.e. $\lambda/4$, forward in space into the direction of propagation $\boldsymbol{\theta}$. This gives that

$$\mathrm{Re}\left(\boldsymbol{E}^i(\boldsymbol{x}+\lambda/4\boldsymbol{\theta},t)\right) \;=\; |E_1|(\boldsymbol{a}_1\sin(k\boldsymbol{\theta}\cdot\boldsymbol{x}-\omega t+\alpha)\pm\boldsymbol{a}_2\cos(k\boldsymbol{\theta}\cdot\boldsymbol{x}-\omega t+\alpha))\,. \tag{5.5}$$

Comparing (5.4) and (5.5) implies that the orientation of the polarization has changed by $\pi/2$. This observation is independent of the time t and therefore, we return to the time-independent plane waves from (5.1). We distinguish between left and right circular polarization, dependent on the direction, in which the real part of the amplitude moves along the direction of propagation. Since $\mathrm{Re}(\boldsymbol{E}^i),\mathrm{Re}(\boldsymbol{H}^i)$ and $\boldsymbol{\theta}$ are pairwise orthogonal, $|\boldsymbol{E}^i|/|\boldsymbol{H}^i| = Z_0$ and $\mathrm{Re}(\boldsymbol{E}^i)\times\mathrm{Re}(\boldsymbol{H}^i)$ points in the direction $\boldsymbol{\theta}$, we find that the waves perform a anticlockwise/clockwise motion along the direction of propagation $\boldsymbol{\theta}$ (when viewed from the sender), if $\boldsymbol{E}^i(\boldsymbol{x}+\lambda/4\boldsymbol{\theta})$ coincides with $\mp Z_0\boldsymbol{H}^i(\boldsymbol{x})$ for all $\boldsymbol{x}\in\mathbb{R}^3$. This gives that

$$\mp\,(\boldsymbol{\theta}\times\boldsymbol{A})\,\mathrm{e}^{\mathrm{i}k\boldsymbol{\theta}\cdot\boldsymbol{x}} \;=\; \mp Z_0\boldsymbol{H}^i(\boldsymbol{x}) \;=\; \boldsymbol{E}^i\left(\boldsymbol{x}+\lambda/4\boldsymbol{\theta}\right) \;=\; \mathrm{i}\boldsymbol{A}\mathrm{e}^{\mathrm{i}k\boldsymbol{\theta}\cdot\boldsymbol{x}}. \tag{5.6}$$

This introductory example reveals that the polarization $\boldsymbol{A}$ corresponding to a circularly polarized plane wave must satisfy $\boldsymbol{A}=\pm\mathrm{i}\,(\boldsymbol{\theta}\times\boldsymbol{A})$. An example of such a case can be found in Figure 5.1. Here, the solid blue line shows the real part of the plane wave $\boldsymbol{E}^i(\boldsymbol{x})$ as in (5.1) with direction of propagation $\boldsymbol{\theta}=[0,\ 1,\ 0]^\top$ and polarization $\boldsymbol{A}=[1,\ 0,\ \mathrm{i}]^\top$ for $\boldsymbol{x}=[0,\ s,\ 0]^\top$, where $s\in[0,4\lambda]$. From the perspective of the sender, the real part of $\boldsymbol{E}^i$ performs an anticlockwise motion. This is visualized by the solid blue arrows. The solid red arrows, on the other hand, show the real part of the magnetic field $\boldsymbol{H}^i$. If we consider the orthogonal plane to $\boldsymbol{\theta}$ at a fixed spatial point and track the evolution of $\mathrm{Re}(\boldsymbol{E}^i\mathrm{e}^{-\mathrm{i}\omega t})$ for $t>0$, then this field performs a clockwise motion from the perspective of the sender.

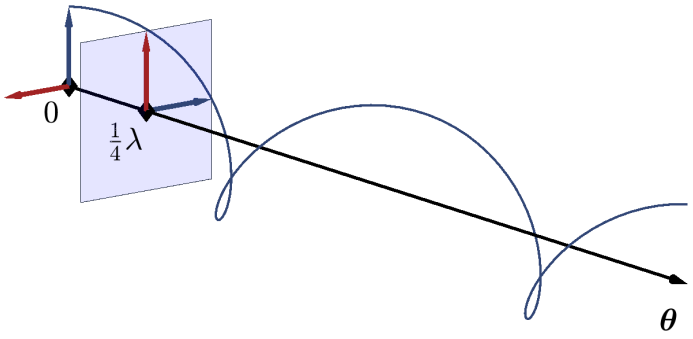

Figure 5.1: Visualization of a circularly polarized plane wave with direction of propagation $\boldsymbol{\theta} = [0,\ 1,\ 0]^\top$ and polarization $\boldsymbol{A} = [1,\ 0,\ \mathrm{i}]^\top$. From the perspective of the sender, the wave performs an anticlockwise motion.

From now on, let $\boldsymbol{A} \in L_t^2(S^2)$. A Herglotz wave with density $\boldsymbol{A}$ is a linear superposition of plane waves, for which we can write the electric field as

$$\boldsymbol{E}^i[\boldsymbol{A}](\boldsymbol{x}) = \int_{S^2} \boldsymbol{A}(\boldsymbol{\theta})\, \mathrm{e}^{\mathrm{i}k\boldsymbol{\theta}\cdot\boldsymbol{x}}\, \mathrm{d}s(\boldsymbol{\theta}), \qquad \boldsymbol{x} \in \mathbb{R}^3. \tag{5.7}$$

Let D be a bounded Lipschitz domain. One might already think of D as a thin tubular object D_ρ as in (3.7) for a fixed radius $\rho > 0$. Let D be the scattering object in the Maxwell system (2.34) together with (2.35) (or (3.9) together with (3.10) in the case $D = D_\rho$). If the incident field in the Maxwell system is given by $\boldsymbol{E}^i[\boldsymbol{A}]$ from (5.7), then we denote the corresponding scattered and total fields by $\boldsymbol{E}^s[\boldsymbol{A}]$ and $\boldsymbol{E}[\boldsymbol{A}]$, respectively. The electric far field patterns $\boldsymbol{E}^\infty[\boldsymbol{A}]$ excited by Herglotz waves as incident fields are fully described by the electric far field operator $\mathcal{F}_D : L_t^2(S^2) \to L_t^2(S^2)$, which is defined by

$$(\mathcal{F}_D \boldsymbol{A})(\widehat{\boldsymbol{x}}) = \int_{S^2} \boldsymbol{E}^\infty(\widehat{\boldsymbol{x}}; \boldsymbol{\theta})\, \boldsymbol{A}(\boldsymbol{\theta})\, \mathrm{d}s(\boldsymbol{\theta}). \tag{5.8}$$

For later reference, we note that $\mathcal{F}_D$ is an integral operator with a smooth kernel (see e.g. [34, Thm. 6.9]) and thus, $\mathcal{F}_D$ is compact. By linearity we have that $\boldsymbol{E}^\infty[\boldsymbol{A}] = \mathcal{F}_D \boldsymbol{A}$. For a Herglotz field as in (5.7) we cite from [15, Def. 2.1] the following property of the density $\boldsymbol{A} \in L_t^2(S^2)$ that characterizes helicity of the field $\boldsymbol{E}^i[\boldsymbol{A}]$.

Definition 5.1. A Herglotz wave field $\boldsymbol{E}^i[\boldsymbol{A}]$ as in (5.7) with $\boldsymbol{A} \in L_t^2(S^2)$ is called left (or right) circularly polarized if $\boldsymbol{A}$ is an eigenfunction for the eigenvalue $+1$ (or -1, respectively) of the operator $\mathcal{C} : L_t^2(S^2) \to L_t^2(S^2)$ with

$$\mathcal{C}\boldsymbol{A}(\boldsymbol{\theta}) = \mathrm{i}\,(\boldsymbol{\theta} \times \boldsymbol{A}(\boldsymbol{\theta})), \qquad \boldsymbol{\theta} \in S^2. \tag{5.9}$$

From (5.6) we found that a plane wave as in (5.1) has helicity ± 1 if and only if the polarization $\boldsymbol{A} \in \mathbb{C}^3 \setminus \{0\}$ satisfies $\boldsymbol{A} = \pm\mathrm{i}\,(\boldsymbol{\theta} \times \boldsymbol{A})$. Therefore, the eigenvalue problem to find $\boldsymbol{A} \in L_t^2(S^2)$ satisfying $\mathcal{C}\boldsymbol{A}(\boldsymbol{\theta}) = \pm\boldsymbol{A}$ with $\mathcal{C}$ from (5.9) is a generalization of helicity to Herglotz waves. The eigenspaces of the operator $\mathcal{C}$ corresponding to the eigenvalues ± 1 are given by

$$V^\pm = \{\boldsymbol{A} \pm \mathcal{C}\boldsymbol{A} \mid \boldsymbol{A} \in L_t^2(S^2)\} \tag{5.10}$$

(see [15, Rmk. 2.2]). This can be seen from the calculation

$$\mathcal{C}(\boldsymbol{A} \pm \mathcal{C}\boldsymbol{A})(\boldsymbol{\theta}) = \mathcal{C}\boldsymbol{A}(\boldsymbol{\theta}) \pm \mathcal{C}^2\boldsymbol{A}(\boldsymbol{\theta}) = \mathcal{C}\boldsymbol{A}(\boldsymbol{\theta}) \mp (\boldsymbol{\theta} \times (\boldsymbol{\theta} \times \boldsymbol{A}(\boldsymbol{\theta}))) = \mathcal{C}\boldsymbol{A}(\boldsymbol{\theta}) \pm \boldsymbol{A}(\boldsymbol{\theta}).$$

Moreover, the decomposition

$$\boldsymbol{A} \;=\; \frac{1}{2}\left(\boldsymbol{A}+\mathcal{C}\boldsymbol{A}\right)+\frac{1}{2}\left(\boldsymbol{A}-\mathcal{C}\boldsymbol{A}\right)$$

and the straightforward calculation

$$\int_{S^2}\left(\boldsymbol{A}+\mathcal{C}\boldsymbol{A}\right)\cdot\overline{\left(\boldsymbol{A}-\mathcal{C}\boldsymbol{A}\right)}\,\mathrm{d}s \;=\; 0$$

shows that

$$L_t^2(S^2) \;=\; V^+\oplus V^-$$

(see [15, p. 561]). The corresponding orthogonal projections onto the spaces $V^{\pm}$ are given by $\mathcal{P}^{\pm}\boldsymbol{A} \;=\; 1/2\left(\boldsymbol{A}\pm\mathcal{C}\boldsymbol{A}\right)$. These observations imply a decomposition of a Herglotz wave $\boldsymbol{E}^i[\boldsymbol{A}]$ in fields of pure positive and negative helicity. This is summarized in the following corollary.

Corollary 5.2. *A Herglotz wave field $\boldsymbol{E}^i[\boldsymbol{A}]$ as in (5.7) with $\boldsymbol{A}\in L_t^2(S^2)$ can be uniquely decomposed in fields of pure positive and negative helicity. The decomposition is done by projecting the density $\boldsymbol{A}$ to the spaces V^+ (positive helicity) and V^- (negative helicity) using the orthogonal projections*

$$\mathcal{P}^{\pm}\boldsymbol{A} \;=\; \frac{1}{2}\left(\boldsymbol{A}\pm\mathcal{C}\boldsymbol{A}\right). \tag{5.11}$$

The decomposition of fields in different helicities from Corollary 5.2 based on the density $\boldsymbol{A}$ and was established in [15]. To work directly with the corresponding electric fields, we note that for a Herglotz field $\boldsymbol{E}^i\left[\boldsymbol{A}\right]$ with density $\boldsymbol{A}$ the condition $\mathcal{C}\boldsymbol{A} \;=\; \pm\boldsymbol{A}$ with $\mathcal{C}$ from (5.9) is equivalent to

$$k^{-1}\,\mathbf{curl}\,\boldsymbol{E}^i\left[\boldsymbol{A}\right]=\pm\boldsymbol{E}^i\left[\boldsymbol{A}\right]. \tag{5.12}$$

This is seen by using [99, Lem. 14.11], which states that $\boldsymbol{E}^i[\boldsymbol{A}]=0$ is equivalent to $\boldsymbol{A}=0$. The property in Equation (5.12) is used to describe helicity for more general fields. Let $\Omega\subset\mathbb{R}^3$ be a bounded domain. A solution to

$$\mathbf{curl}\,\mathbf{curl}\,\boldsymbol{U}-k^2\boldsymbol{U} \;=\; 0 \qquad \text{in } \Omega \tag{5.13}$$

is said to have helicity ±1, if $\boldsymbol{U}$ is an eigenfunction of the operator $k^{-1}\,\mathbf{curl}$ for the eigenvalue ±1, respectively. Using the two subspaces of Beltrami fields[1]

$$W^{\pm}\left(\Omega\right) \;=\; \left\{\boldsymbol{U}\in H\left(\mathbf{curl},\Omega\right)\;\middle|\;k^{-1}\,\mathbf{curl}\,\boldsymbol{U} \;=\; \pm\boldsymbol{U}\right\}, \tag{5.14}$$

we find that every solution to (5.13) can be decomposed into a sum of two fields of helicity $+1$ and -1, respectively (see also [15, Rmk. 2.3]). To see this, let $\boldsymbol{E}$ denote a solution to (5.13) and define $\boldsymbol{H}=(\mathrm{i}\omega\mu_0)^{-1}\,\mathbf{curl}\,\boldsymbol{E}$. Then, we set

$$\boldsymbol{E}^+ \;=\; \boldsymbol{E}+\mathrm{i}Z_0\boldsymbol{H}\in W^+(\Omega) \quad\text{and}\quad \boldsymbol{E}^- \;=\; \boldsymbol{E}-\mathrm{i}Z_0\boldsymbol{H}\in W^-(\Omega)$$

and see that $\boldsymbol{E}=1/2\left(\boldsymbol{E}^++\boldsymbol{E}^-\right)$. Using straightforward calculations it can be seen that $\boldsymbol{E}^+$ and $\boldsymbol{E}^-$ are orthogonal with respect to the inner product

$$\langle\boldsymbol{u},\boldsymbol{v}\rangle \;=\; \int_{\Omega}\mathbf{curl}\,\boldsymbol{u}\cdot\mathbf{curl}\,\overline{\boldsymbol{v}}+k^2\boldsymbol{u}\cdot\overline{\boldsymbol{v}}\;\mathrm{d}\boldsymbol{x}\,.$$

The fields $\boldsymbol{E}^+$ and $\boldsymbol{E}^-$ are called the Riemann-Silberstein linear combinations (see e.g. [21]).

The definition of helicity for fields satisfying (5.13) also applies for the scattered field $\boldsymbol{E}^s[\boldsymbol{A}]$ in $\mathbb{R}^3\setminus\overline{D}$. In order to characterize helicity for $\boldsymbol{E}^s[\boldsymbol{A}]$ using the spaces $V^{\pm}$, we cite the following theorem from [15, Thm. 2.4].

[1] This is a field $\boldsymbol{U}$ satisfying $\mathbf{curl}\,\boldsymbol{U}=\sigma\boldsymbol{U}$ for $\sigma\neq0$ (see e.g. [92, §1.3])

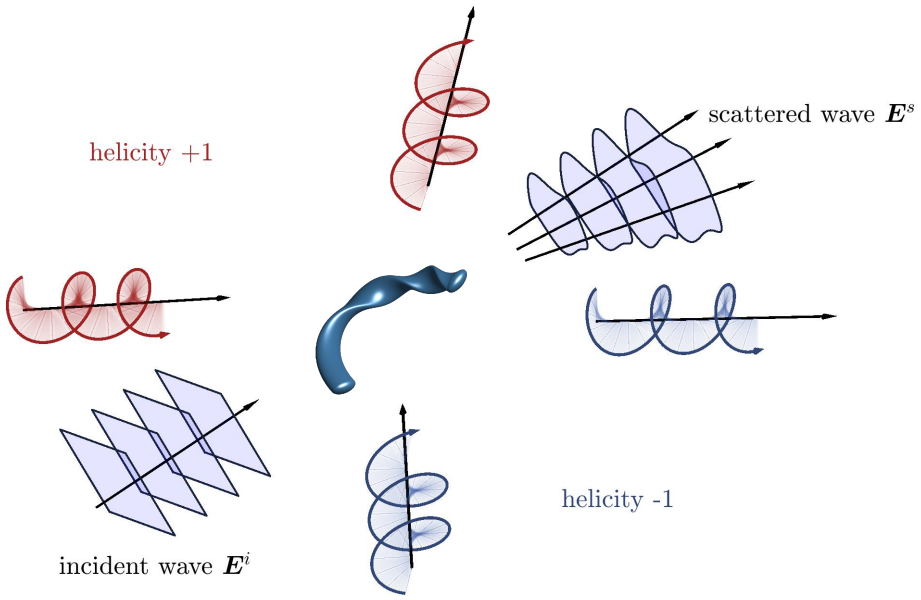

Figure 5.2: Visualization of the scattering problem concerning em-chirality. The incident field $\boldsymbol{E}^i$ (bottom-left) and the scattered field $\boldsymbol{E}^s$ (top-right) are both decomposed in fields with helicity $+1$ (red) and fields with helicity -1 (blue).

Theorem 5.3. *The far field pattern $\boldsymbol{E}^\infty[\boldsymbol{A}]$ is an element of $V^\pm$ if and only if for any open and bounded set $\Omega \subset \mathbb{R}^3 \setminus \overline{D}$ we have $\boldsymbol{E}^s[\boldsymbol{A}] \in W^\pm(\Omega)$.*

To conclude, we have that

$$\begin{aligned} \boldsymbol{E}^i[\boldsymbol{A}] \text{ has helicity } \pm 1 \quad &\text{if and only if} \quad \boldsymbol{A} \in V^\pm, \\ \boldsymbol{E}^s[\boldsymbol{A}]|_{\mathbb{R}^3\setminus\overline{D}} \text{ has helicity } \pm 1 \quad &\text{if and only if} \quad \boldsymbol{E}^\infty[\boldsymbol{A}] \in V^\pm. \end{aligned}$$

A visualization of the wave decomposition is found in Figure 5.2. Here, the incident field, visualized by a plane wave in the bottom-left and the scattered field in the top-right are both decomposed in fields with helicity $+1$ (red) and -1 (blue).

Electromagnetic chirality describes the difference in the interaction of a scattering object with fields of opposite helicities. Using the projections $\mathcal{P}^\pm : L_t^2(S^2) \to V^\pm$ from (5.11), we can decompose the electric far field operator $\mathcal{F}_D$ via

$$\mathcal{F}_D = \mathcal{F}_D^{++} + \mathcal{F}_D^{+-} + \mathcal{F}_D^{-+} + \mathcal{F}_D^{--}. \tag{5.15}$$

Here, for $p, q \in \{+,-\}$, the helicity contribution of the q incoming field to the p scattered field is given by $\mathcal{F}_D^{pq} = \mathcal{P}^p \mathcal{F}_D \mathcal{P}^q$. We note that $\mathcal{F}_D^{pq}$ is a composition of a compact operator with two bounded operators and therefore, it is compact. It has been proven in [15, 49] that if a scatterer is geometrically achiral, then there exists a unitary operator $\mathcal{U} : L_t^2(S^2) \to L_t^2(S^2)$ such that

$$\mathcal{C}\mathcal{U} = -\mathcal{U}\mathcal{C} \qquad \text{and} \qquad \mathcal{F}_D\mathcal{U} = \mathcal{U}\mathcal{F}_D\,. \tag{5.16}$$

The first condition ensures that the unitary transformation $\mathcal{U}$ swaps helicity, as with $\boldsymbol{A} \pm \mathcal{C}\boldsymbol{A} \in V^\pm$ the property $\mathcal{C}\mathcal{U} = -\mathcal{U}\mathcal{C}$ gives that $\mathcal{U}(\boldsymbol{A} \pm \mathcal{C}\boldsymbol{A}) \in V^\mp$. Thus, geometrical achirality of an object D can be understood as the equivalence of the far field operator $\mathcal{F}_D$ to itself by means of a unitary transform that swaps helicity. An immediate consequence of (5.16) is that $\mathcal{F}_D^{++} = \mathcal{U}\mathcal{F}_D^{--}\mathcal{U}^*$ and $\mathcal{F}_D^{-+} = \mathcal{U}\mathcal{F}_D^{+-}\mathcal{U}^*$. The first equality can be seen by using the computation

$$\mathcal{U}\mathcal{F}_D^{--}\mathcal{U}^* = \mathcal{U}\left(\frac{1}{2}I - \mathcal{C}\right)\mathcal{F}_D\left(\frac{1}{2}I - \mathcal{C}\right)\mathcal{U}^* = \left(\frac{1}{2}I + \mathcal{C}\right)\mathcal{U}\mathcal{F}_D\mathcal{U}^*\left(\frac{1}{2}I + \mathcal{C}\right) = \mathcal{F}_D^{++}$$

where we used the definitions of $\mathcal{F}_D^{++}$ and $\mathcal{F}_D^{--}$, the definition of $\mathcal{P}^{\pm}$ from (5.11) and the definition of the unitary transform that swaps helicity in (5.16). In the exact same way one shows that (5.16) implies $\mathcal{F}_D^{-+} = \mathcal{U}\mathcal{F}_D^{+-}\mathcal{U}^*$. Based on this observation, the following more general definition of electromagnetic chirality was introduced in [15, Def. 2.5].

Definition 5.4. A scattering object D is called electromagnetically achiral (em-achiral) if there exist unitary operators $\mathcal{U}^{(j)} : L_t^2(S^2) \to L_t^2(S^2)$ satisfying $\mathcal{U}^{(j)}\mathcal{C} = -\mathcal{C}\mathcal{U}^{(j)}$, $j = 1, \dots, 4$, such that

$$\mathcal{F}_D^{++} = \mathcal{U}^{(1)}\mathcal{F}_D^{--}\mathcal{U}^{(2)} \quad \text{and} \quad \mathcal{F}_D^{-+} = \mathcal{U}^{(3)}\mathcal{F}_D^{+-}\mathcal{U}^{(4)}\,. \tag{5.17}$$

If this is not the case, we call the scattering object D electromagnetically chiral (em-chiral).

The property for em-achirality in (5.17) immediately implies that the singular values of $\mathcal{F}^{++}$ and $\mathcal{F}^{--}$ as well as those of $\mathcal{F}^{+-}$ and $\mathcal{F}^{-+}$ coincide (see also [15, p. 565]). Let us denote the singular values of the operator $\mathcal{F}^{pq}$ by $(\sigma_j^{pq})_{j\in\mathbb{N}} \in \ell^2$, where $p, q \in \{+, -\}$. The quantification of em-chirality of a scattering object D relies in measuring the distance between the corresponding sequences of the singular values (see also the definitions in Appendix A). In fact, following [49], we define the chirality measure χ_2 of a scatterer D associated to the far field operator $\mathcal{F}_D$ as

$$\chi_2\left(\mathcal{F}_D\right) = \left(\left\|(\sigma_j^{++})_{j\in\mathbb{N}} - (\sigma_j^{--})_{j\in\mathbb{N}}\right\|_{\ell^2}^2 + \left\|(\sigma_j^{+-})_{j\in\mathbb{N}} - (\sigma_j^{-+})_{j\in\mathbb{N}}\right\|_{\ell^2}^2\right)^{1/2}. \tag{5.18}$$

The far field operator $\mathcal{F}_D$ is an integral operator and its kernel is smooth. As a consequence, the singular values decay exponentially (see e.g. [91, Thm. 15.20]) and the chirality measure χ_2 in (5.18) is well-defined. In particular, $\mathcal{F}_D$ is a Hilbert-Schmidt operator since every integral operator from $L_t^2(S^2)$ to $L_t^2(S^2)$ with a kernel in L^2 is a Hilbert-Schmidt operator (see e.g. [44, Chap. XI.6]). Moreover, using (5.18) and that the singular values are non-negative, it holds that

$$\chi_2\left(\mathcal{F}_D\right)^2 = \|\mathcal{F}_D\|_{\mathrm{HS}}^2 - 2\sum_{j\in\mathbb{N}}(\sigma_j^{++}\sigma_j^{--} + \sigma_j^{-+}\sigma_j^{+-}) \le \|\mathcal{F}_D\|_{\mathrm{HS}}^2\,. \tag{5.19}$$

If $\mathcal{F}_D^{++} = \mathcal{F}_D^{-+} = 0$ or $\mathcal{F}_D^{--} = \mathcal{F}_D^{+-} = 0$, i.e. if fields of either positive or negative helicity are not scattered, then the upper bound in (5.19) is attained. Thus, invisibility of an object with respect to fields of one helicity implies $\chi_2(\mathcal{F}_D) = \|\mathcal{F}_D\|_{\mathrm{HS}}$. If in addition, the reciprocity principle[2] holds, which is the case for the setting considered here, (see e.g. [34, Thm. 9.6]), then the implication is also valid in the other direction (see [15, Lem. 4.3]). In particular, the proof of [15, Lem. 4.3] shows that for a reciprocal scatterer, it holds that $\mathcal{F}_D^{+-} = 0$ if and only if $\mathcal{F}_D^{-+} = 0$. The squared Hilbert-Schmidt norm $\|\mathcal{F}_D\|_{\mathrm{HS}}^2$ of the far field operator is sometimes called the total interaction cross section of the scattering object D.

Remark 5.5. A scattering object that preserves helicity satisfies $\mathcal{F}_D^{+-} = \mathcal{F}_D^{-+} = 0$. Therefore, preservation of helicity is a necessary condition for the chirality measure χ_2 from (5.18) to attain its upper bound. A dual symmetric scatterer D is a scattering object for which the solution $(\boldsymbol{E}, \boldsymbol{H})$ to Maxwell's equations (2.31) in some $\Omega \subset \mathbb{R}^3$ stays a solution, when it is transformed by the duality transform

$$\boldsymbol{E}_\theta = \boldsymbol{E}\cos(\theta) - Z_0\boldsymbol{H}\sin(\theta)\,, \qquad Z_0\boldsymbol{H}_\theta = \boldsymbol{E}\sin(\theta) + Z_0\boldsymbol{H}\cos(\theta) \tag{5.20}$$

(see e.g. [47, 48, 53]), where again, $Z_0 = \sqrt{\mu_0/\varepsilon_0}$ is the impedance in free space. For the incident fields $(\boldsymbol{E}^i, \boldsymbol{H}^i)$ satisfying (2.30), the transformed fields in (5.20) remain a solution to time-harmonic Maxwell's equations in all $\mathbb{R}^3$ (this is also found in e.g. [82, Eq. 6.151]). However, the presence of a scatterer D in general breaks this property (see e.g. [51]). In [47, Sec. 2.7] and [53] it is shown that $\varepsilon_r = \mu_r$ is the condition for duality symmetry for the macroscopic Maxwell's equations (2.31) and that this implies preservation of helicity independent from the shape of the scatterer D.

[2] A scatterer is said to be reciprocal if $\boldsymbol{E}^\infty(\widehat{\boldsymbol{x}}, \boldsymbol{\theta}) = (\boldsymbol{E}^\infty(-\boldsymbol{\theta}, -\widehat{\boldsymbol{x}}))^\top$ for all $\widehat{\boldsymbol{x}}, \boldsymbol{\theta} \in S^2$ (see [34, Eq. 6.87]).

The previous discussion motivates the following definition.

Definition 5.6. A scattering object D is said to be maximally em-chiral if $\chi_2(\mathcal{F}_D) = \|\mathcal{F}_D\|_{\mathrm{HS}}$.

If the scattering object in the center of Figure 5.2 was maximally em-chiral, then either the $+1$ or the -1 helicity contribution in the scattered field would vanish.

In [72, Sec. 5.2] a relaxation for χ_2 was introduced. We denote it by χ_{HS} with

$$\begin{aligned}\chi_{\mathrm{HS}}(\mathcal{F}_D) &= \Big(\big(\|\mathcal{F}_D^{++}\|_{\mathrm{HS}} - \|\mathcal{F}_D^{--}\|_{\mathrm{HS}}\big)^2 + \big(\|\mathcal{F}_D^{-+}\|_{\mathrm{HS}} - \|\mathcal{F}_D^{+-}\|_{\mathrm{HS}}\big)^2 \Big)^{1/2} \\ &= \Big(\|\mathcal{F}_D\|_{\mathrm{HS}}^2 - 2\big(\|\mathcal{F}_D^{++}\|_{\mathrm{HS}}\|\mathcal{F}_D^{--}\|_{\mathrm{HS}} + \|\mathcal{F}_D^{-+}\|_{\mathrm{HS}}\|\mathcal{F}_D^{+-}\|_{\mathrm{HS}}\big) \Big)^{1/2} .\end{aligned} \tag{5.21}$$

The Cauchy–Schwarz inequality in ℓ^2 shows that

$$\begin{aligned}\sum_{j\in\mathbb{N}} \sigma_j^{++}\sigma_j^{--} &\leq \|(\sigma_j^{++})_{j\in\mathbb{N}}\|_{\ell^2}\|(\sigma_j^{--})_{j\in\mathbb{N}}\|_{\ell^2} = \|\mathcal{F}_D^{++}\|_{\mathrm{HS}}\|\mathcal{F}_D^{--}\|_{\mathrm{HS}} , \\ \sum_{j\in\mathbb{N}} \sigma_j^{-+}\sigma_j^{+-} &\leq \|\mathcal{F}_D^{-+}\|_{\mathrm{HS}}\|\mathcal{F}_D^{+-}\|_{\mathrm{HS}} .\end{aligned}$$

Therefore, it holds that

$$\chi_{\mathrm{HS}}(\mathcal{F}_D) \leq \chi_2(\mathcal{F}_D) \tag{5.22}$$

and comparing (5.19) and (5.22) yields that

$$\chi_{\mathrm{HS}}(\mathcal{F}_D) = \|\mathcal{F}_D\|_{\mathrm{HS}} \quad \text{if and only if} \quad \chi_2(\mathcal{F}) = \|\mathcal{F}_D\|_{\mathrm{HS}} .$$

The relaxation χ_{HS} is indeed smooth. The computation of the Fréchet derivative of χ_{HS} with respect to its argument is studied in Section 5.5.

5.2 Quantifying em-chirality for thin tubular scattering objects

In the literature, thin helical structures have been proposed as candidates for highly em-chiral scatterers (see e.g. [7, 49, 60]). In this section we use the results from Chapter 3 and consider the quantification of em-chirality for thin tubular scattering objects. Let D_ρ denote a thin tubular scattering object as in (3.7). Let the cross-section of the scattering object D_ρ be given by $D'_\rho = \rho D'$ with a Lipschitz domain $D' \subset \mathbb{R}^2$, that possibly twists around the spine curve K. The support D_ρ of a nanowire is uniquely determined by a parametrization $\boldsymbol{p}$ of the spine curve K and an associated geometry adapted frame $(\boldsymbol{t}_{\boldsymbol{p}}, \boldsymbol{r}_{\boldsymbol{p},\theta}, \mathbf{s}_{\boldsymbol{p},\theta})$, defined by

$$[\boldsymbol{r}_{\boldsymbol{p},\theta}(s) \,|\, \mathbf{s}_{\boldsymbol{p},\theta}(s)] = [\boldsymbol{r}_{\boldsymbol{p}}(s) \,|\, \mathbf{s}_{\boldsymbol{p}}(s)]\, R_\theta(s) . \tag{5.23}$$

Therefore, we define a set of admissible parametrizations for supports of thin nanowires by

$$\begin{aligned}\mathcal{U}_{\mathrm{ad}} = \Big\{ &(\boldsymbol{p}, V_{\boldsymbol{p},\theta}) \in C^3([0,1],\mathbb{R}^3) \times C^2([0,1],\mathrm{SO}(3)) \,| \\ &\boldsymbol{p}([0,1]) \text{ is simple, } \boldsymbol{p}'(s) \neq 0, \text{ and } V_{\boldsymbol{p},\theta}(s)\boldsymbol{e}_1 = \boldsymbol{p}'(s)/|\boldsymbol{p}'(s)| \text{ for all } s \in [0,1] \Big\} .\end{aligned} \tag{5.24}$$

Here, $\boldsymbol{e}_1 = (1,0,0)^\top$ denotes the first standard basis vector in $\mathbb{R}^3$. Measuring em-chirality, i.e. evaluating (5.18) (or (5.21)) for a given thin tubular object D_ρ, requires the evaluation of the corresponding far field operator. We denote the far field operator corresponding to D_ρ by $\mathcal{F}_{D_\rho}$

as in (5.8). Recalling the asymptotic representation formula for electric far fields from (3.22), we define the operator $\mathcal{T}_{D_\rho} : L_t^2(S^2) \to L_t^2(S^2)$ by

$$(\mathcal{T}_{D_\rho}\boldsymbol{A})(\widehat{\boldsymbol{x}}) = (k\rho)^2|D'|\bigg(\int_K (\mu_r - 1)\, e^{-\mathrm{i}k\widehat{\boldsymbol{x}}\cdot\boldsymbol{y}}\, (\widehat{\boldsymbol{x}} \times \mathbb{I}_3)\, \mathbb{M}^\mu(\boldsymbol{y}) \left(\frac{\mathrm{i}}{k}\, \mathbf{curl}\, \boldsymbol{E}^i[\boldsymbol{A}](\boldsymbol{y})\right) \mathrm{d}s(\boldsymbol{y}) + \int_K (\varepsilon_r - 1)\, e^{-\mathrm{i}k\widehat{\boldsymbol{x}}\cdot\boldsymbol{y}}\, (\widehat{\boldsymbol{x}} \times (\mathbb{I}_3 \times \widehat{\boldsymbol{x}}))\, \mathbb{M}^\varepsilon(\boldsymbol{y}) \boldsymbol{E}^i[\boldsymbol{A}](\boldsymbol{y})\, \mathrm{d}s(\boldsymbol{y})\bigg). \quad (5.25)$$

We choose the support of the thin nanowire D_ρ to be parametrized by $(\boldsymbol{p}, V_{\boldsymbol{p},\theta}) \in \mathcal{U}_{\mathrm{ad}}$. Then, Theorem 3.16 gives that the polarization tensors $\mathbb{M}^\gamma$, $\gamma \in \{\varepsilon, \mu\}$, are given by

$$\mathbb{M}^\gamma(\boldsymbol{p}(s)) = V_{\boldsymbol{p},\theta} M^\gamma V_{\boldsymbol{p},\theta}^\top \quad \text{for a.e. } s \in [0,1] \text{ and } \gamma \in \{\varepsilon, \mu\}\,, \quad (5.26)$$

where the matrix M^γ is given by

$$M^\gamma = \left[\begin{array}{c|cc} 1 & 0 & 0 \\ \hline 0 & & \\ 0 & & m^\gamma \end{array}\right] \in \mathbb{C}^{3\times 3}\,,$$

where m^γ denotes the two-dimensional polarization tensor corresponding to the cross-sections $(D'_{\rho_n})_{n\in\mathbb{N}}$. Note that here, compared to the representation of the polarization tensor in (3.70), the rotation is included in the geometry adapted frame (i.e. in $V_{\boldsymbol{p},\theta}$). From Theorem 3.6, we find that

$$\mathcal{F}_{D_\rho} = \mathcal{T}_{D_\rho} + o((k\rho)^2) \quad \text{as } \rho \to 0. \quad (5.27)$$

The remainder $o((k\rho)^2)$ is such that $\|o((k\rho)^2)\|_{\mathrm{HS}}/(k\rho)^2$ converges to 0 as $\rho \to 0$. The incident field $\boldsymbol{E}^i[\boldsymbol{A}]$ that appears in (5.25) is a Herglotz wave field with density $\boldsymbol{A}$ as in (5.7). We recall the vector spherical harmonics $\boldsymbol{U}_n^m$ and $\boldsymbol{V}_n^m$ from (2.16) and define the circularly polarized vector spherical harmonics by

$$\boldsymbol{A}_n^m = \frac{1}{\sqrt{2}}(\boldsymbol{U}_n^m + \mathrm{i}\boldsymbol{V}_n^m) \quad \text{and} \quad \boldsymbol{B}_n^m = \frac{1}{\sqrt{2}}(\boldsymbol{U}_n^m - \mathrm{i}\boldsymbol{V}_n^m) \quad (5.28)$$

for $m = -n, \dots, n$ and $n = 1, 2, \dots$. Since $\boldsymbol{U}_n^m$ and $\boldsymbol{V}_n^m$ form an orthonormal basis of $L_t^2(S^2)$, we find that $\boldsymbol{A}_n^m$ and $\boldsymbol{B}_n^m$ form an orthonormal basis of V^+ and V^- from (5.10), respectively. We refer to these bases as the helicity bases. Especially, it holds that

$$\mathrm{i}\boldsymbol{\theta} \times \boldsymbol{A}_n^m(\boldsymbol{\theta}) = \boldsymbol{A}_n^m(\boldsymbol{\theta}) \quad \text{and} \quad \mathrm{i}\boldsymbol{\theta} \times \boldsymbol{B}_n^m(\boldsymbol{\theta}) = -\boldsymbol{B}_n^m(\boldsymbol{\theta}), \qquad \boldsymbol{\theta} \in S^2.$$

Further, recalling the entire wave fields from (2.23), we find that the Beltrami fields corresponding to $\boldsymbol{A}_n^m$ and $\boldsymbol{B}_n^m$ as described in (5.14) are given by

$$\boldsymbol{P}_n^m(\boldsymbol{x}) = \boldsymbol{M}_n^m + k^{-1}\, \mathbf{curl}\, \boldsymbol{M}_n^m \quad \text{and} \quad \boldsymbol{Q}_n^m(\boldsymbol{x}) = \boldsymbol{M}_n^m - k^{-1}\, \mathbf{curl}\, \boldsymbol{M}_n^m \quad (5.29)$$

for $m = -n, \dots, n$ and $n = 1, 2, \dots$. In fact, the Beltrami fields $\boldsymbol{P}_n^m$, $\boldsymbol{Q}_n^m$ are linked to $\boldsymbol{A}_n^m, \boldsymbol{B}_n^m$ via $\boldsymbol{E}^i[\boldsymbol{A}_n^m] = \sqrt{8}\pi\mathrm{i}^{n-1}\boldsymbol{P}_n^m$ and $\boldsymbol{E}^i[\boldsymbol{B}_n^m] = -\sqrt{8}\pi\mathrm{i}^{n-1}\boldsymbol{Q}_n^m$. This is derived in detail in the proof of the next lemma and is found in (5.38). Since

$$\mathbf{curl}\, \boldsymbol{P}_n^m = k\boldsymbol{P}_n^m \quad \text{and} \quad \mathbf{curl}\, \boldsymbol{Q}_n^m = -k\boldsymbol{Q}_n^m \quad (5.30)$$

we have that $\boldsymbol{P}_n^m \in W^+$ and $\boldsymbol{Q}_n^m \in W^-$. The asymptotic expansions in (5.27) is now used to approximate $\mathcal{F}_{D_\rho}$ by $\mathcal{T}_{D_\rho}$ in order to quantify em-chirality for thin nanowires. It turns out that the representation of $\mathcal{T}_{D_\rho}$ in the helicity bases $\boldsymbol{A}_n^m$ and $\boldsymbol{B}_n^m$ can be written down by using the Beltrami fields $\boldsymbol{P}_n^m, \boldsymbol{Q}_n^m$. This is the result of the following lemma.

Lemma 5.7. *Let* $\boldsymbol{A} \in L_t^2(S^2)$ *with*

$$\boldsymbol{A} = \sum_{n=1}^{\infty} \sum_{m=-n}^{n} (a_n^m \boldsymbol{A}_n^m + b_n^m \boldsymbol{B}_n^m). \tag{5.31}$$

Then,

$$\mathcal{T}_{D_\rho} \boldsymbol{A} = \sum_{n=1}^{\infty} \sum_{m=-n}^{n} (c_n^m \boldsymbol{A}_n^m + d_n^m \boldsymbol{B}_n^m) \tag{5.32}$$

with

$$c_n^m = \sum_{n'=1}^{\infty} \sum_{m'=-n'}^{n'} \left(a_{n'}^{m'} \langle \mathcal{T}_{D_\rho} \boldsymbol{A}_{n'}^{m'}, \boldsymbol{A}_n^m \rangle_{L_t^2(S^2)} + b_{n'}^{m'} \langle \mathcal{T}_{D_\rho} \boldsymbol{B}_{n'}^{m'}, \boldsymbol{A}_n^m \rangle_{L_t^2(S^2)} \right) \tag{5.33a}$$

$$d_n^m = \sum_{n'=1}^{\infty} \sum_{m'=-n'}^{n'} \left(a_{n'}^{m'} \langle \mathcal{T}_{D_\rho} \boldsymbol{A}_{n'}^{m'}, \boldsymbol{B}_n^m \rangle_{L_t^2(S^2)} + b_{n'}^{m'} \langle \mathcal{T}_{D_\rho} \boldsymbol{B}_{n'}^{m'}, \boldsymbol{B}_n^m \rangle_{L_t^2(S^2)} \right). \tag{5.33b}$$

Introducing, for any $\boldsymbol{U}, \boldsymbol{V} \in C(K, \mathbb{C}^3)$*, the expressions*

$$\mathcal{J}^{\pm}(\boldsymbol{U}, \boldsymbol{V}) = 8(\pi k \rho)^2 |D'| \int_K \left(\pm (\varepsilon_r - 1) \overline{\boldsymbol{V}} \cdot \mathbb{M}^{\varepsilon} \boldsymbol{U} + (\mu_r - 1) \overline{\boldsymbol{V}} \cdot \mathbb{M}^{\mu} \boldsymbol{U} \right) \mathrm{d}s,$$

we have

$$\langle \mathcal{T}_{D_\rho} \boldsymbol{A}_{n'}^{m'}, \boldsymbol{A}_n^m \rangle_{L_t^2(S^2)} = \mathrm{i}^{n'-n} \mathcal{J}^{+}(\boldsymbol{P}_{n'}^{m'}, \boldsymbol{P}_n^m), \tag{5.34a}$$

$$\langle \mathcal{T}_{D_\rho} \boldsymbol{B}_{n'}^{m'}, \boldsymbol{A}_n^m \rangle_{L_t^2(S^2)} = \mathrm{i}^{n'-n} \mathcal{J}^{-}(\boldsymbol{Q}_{n'}^{m'}, \boldsymbol{P}_n^m), \tag{5.34b}$$

$$\langle \mathcal{T}_{D_\rho} \boldsymbol{A}_{n'}^{m'}, \boldsymbol{B}_n^m \rangle_{L_t^2(S^2)} = \mathrm{i}^{n'-n} \mathcal{J}^{-}(\boldsymbol{P}_{n'}^{m'}, \boldsymbol{Q}_n^m), \tag{5.34c}$$

$$\langle \mathcal{T}_{D_\rho} \boldsymbol{B}_{n'}^{m'}, \boldsymbol{B}_n^m \rangle_{L_t^2(S^2)} = \mathrm{i}^{n'-n} \mathcal{J}^{+}(\boldsymbol{Q}_{n'}^{m'}, \boldsymbol{Q}_n^m). \tag{5.34d}$$

Proof. The expansions (5.32) and (5.33) follow by linearity. In order to prove the expansions in (5.34), we first cite a series representation for the fundamental solution of the Helmholtz equation Φ from (2.25) (see e.g. [34, Thm. 6.29, Eq. (6.83)]). For $\boldsymbol{p} \in \mathbb{C}^3$ it holds that

$$\begin{aligned} \Phi(\boldsymbol{x}, \boldsymbol{y}) \boldsymbol{p} = {} & \mathrm{i}k \sum_{n=1}^{\infty} \sum_{m=-n}^{n} \overline{\boldsymbol{M}_n^m(\boldsymbol{x})} \boldsymbol{N}_n^m(\boldsymbol{y}) \cdot \boldsymbol{p} \\ & + \frac{\mathrm{i}}{k} \sum_{n=1}^{\infty} \sum_{m=-n}^{n} \overline{\operatorname{\mathbf{curl}} \boldsymbol{M}_n^m(\boldsymbol{x})} \operatorname{\mathbf{curl}} \boldsymbol{N}_n^m(\boldsymbol{y}) \cdot \boldsymbol{p} + \frac{\mathrm{i}}{k} \sum_{n=1}^{\infty} \sum_{m=-n}^{n} \overline{\nabla u_n^m(\boldsymbol{x})} \nabla v_n^m(\boldsymbol{y}) \cdot \boldsymbol{p}, \end{aligned} \tag{5.35}$$

where u_n^m and v_n^m denote spherical wave functions (see e.g. [34, Thm. 2.10]) that can be written in spherical coordinates (2.15) as

$$u_n^m(\boldsymbol{x}) = j_n(kr) Y_n^m(\widehat{\boldsymbol{x}}) \quad \text{for } \boldsymbol{x} \in \mathbb{R}^3 \quad \text{and} \quad v_n^m(\boldsymbol{x}) = h_n^{(1)} Y_n^m(\widehat{\boldsymbol{x}}) \quad \text{for } \boldsymbol{x} \in \mathbb{R}^3 \setminus \{0\}.$$

The series expansion in (5.35) and its term by term derivatives both converge uniformly on compact subsets of $|\boldsymbol{y}| > |\boldsymbol{x}|$. Using the asymptotic behavior of the Hankel function (see e.g. [34, Eq. 2.42]) yields that the far fields of $\boldsymbol{N}_n^m$ and $\operatorname{\mathbf{curl}} \boldsymbol{N}_n^m$ from (2.24) are given by

$$(\boldsymbol{N}_n^m)^{\infty}(\widehat{\boldsymbol{x}}) = -\frac{4\pi}{\mathrm{i}^{n+1} k} \boldsymbol{V}_n^m(\widehat{\boldsymbol{x}}) \quad \text{and} \quad (\operatorname{\mathbf{curl}} \boldsymbol{N}_n^m)^{\infty}(\widehat{\boldsymbol{x}}) = \frac{4\pi}{\mathrm{i}^n} \boldsymbol{U}_n^m(\widehat{\boldsymbol{x}}). \tag{5.36}$$

Splitting the gradient into its tangential and radial part yields

$$\nabla v_n^m(\boldsymbol{x}) = h_n^{(1)\prime}(kr) k Y_n^m(\widehat{\boldsymbol{x}}) \widehat{\boldsymbol{x}} + \frac{h_n^{(1)}(kr)}{r} \nabla_{S^2} Y_n^m(\widehat{\boldsymbol{x}}),$$

from which we find by using [34, Eq. 2.42] once more, that

$$(\nabla v_n^m)^\infty(\widehat{\boldsymbol{x}}) = \frac{4\pi}{\mathrm{i}^n} Y_n^m(\widehat{\boldsymbol{x}})\widehat{\boldsymbol{x}}\,.$$

The far field of the expansion (5.35) now reads

$$\begin{aligned} e^{-\mathrm{i}k\widehat{\boldsymbol{y}}\cdot\boldsymbol{x}}\boldsymbol{p} = &-4\pi\sum_{n=1}^{\infty}(-\mathrm{i})^n\sum_{m=-n}^{n}\overline{\boldsymbol{M}_n^m(\boldsymbol{x})}\boldsymbol{V}_n^m(\widehat{\boldsymbol{y}})\cdot\boldsymbol{p}\\ &+\frac{4\pi}{k}\sum_{n=1}^{\infty}(-\mathrm{i})^{n-1}\sum_{m=-n}^{n}\Big(\overline{\mathbf{curl}\,\boldsymbol{M}_n^m(\boldsymbol{x})}\boldsymbol{U}_n^m(\widehat{\boldsymbol{y}})\cdot\boldsymbol{p}+\overline{\nabla u_n^m(\boldsymbol{x})}Y_n^m(\widehat{\boldsymbol{y}})\widehat{\boldsymbol{y}}\cdot\boldsymbol{p}\Big)\,. \end{aligned}$$

Using the orthogonality of the vector spherical harmonics, it follows that

$$\langle \mathrm{e}^{-\mathrm{i}k\widehat{\boldsymbol{y}}\cdot\boldsymbol{x}}, \boldsymbol{U}_n^m(\widehat{\boldsymbol{y}})\rangle_{L^2(S^2)} = \frac{4\pi}{k}(-\mathrm{i})^{n-1}\overline{\mathbf{curl}\,\boldsymbol{M}_n^m(\boldsymbol{x})}\,, \tag{5.37a}$$

$$\langle \mathrm{e}^{-\mathrm{i}k\widehat{\boldsymbol{y}}\cdot\boldsymbol{x}}, \boldsymbol{V}_n^m(\widehat{\boldsymbol{y}})\rangle_{L^2(S^2)} = -4\pi(-\mathrm{i})^n\overline{\boldsymbol{M}_n^m(\boldsymbol{x})} \tag{5.37b}$$

with the scalar product between a scalar and a vector understood to be taken componentwise. Recalling (5.28) and (5.29) we find that

$$\begin{aligned} \langle \mathrm{e}^{-\mathrm{i}k\widehat{\boldsymbol{y}}\cdot\boldsymbol{x}}, \boldsymbol{A}_n^m(\widehat{\boldsymbol{y}})\rangle_{L^2(S^2)} &= \sqrt{8}\pi(-\mathrm{i})^{n-1}\overline{\boldsymbol{P}_n^m(\boldsymbol{x})}\,,\\ \langle \mathrm{e}^{-\mathrm{i}k\widehat{\boldsymbol{y}}\cdot\boldsymbol{x}}, \boldsymbol{B}_n^m(\widehat{\boldsymbol{y}})\rangle_{L^2(S^2)} &= -\sqrt{8}\pi(-\mathrm{i})^{n-1}\overline{\boldsymbol{Q}_n^m(\boldsymbol{x})}\,. \end{aligned}$$

Thus,

$$\boldsymbol{E}^i[\boldsymbol{A}_n^m](\boldsymbol{x}) = \langle \mathrm{e}^{\mathrm{i}k\widehat{\boldsymbol{y}}\cdot\boldsymbol{x}}, \overline{\boldsymbol{A}_n^m(\widehat{\boldsymbol{y}})}\rangle_{L^2(S^2)} = \sqrt{8}\pi\mathrm{i}^{n-1}\boldsymbol{P}_n^m(\boldsymbol{x})\,, \tag{5.38a}$$

$$\boldsymbol{E}^i[\boldsymbol{B}_n^m](\boldsymbol{x}) = \langle \mathrm{e}^{\mathrm{i}k\widehat{\boldsymbol{y}}\cdot\boldsymbol{x}}, \overline{\boldsymbol{B}_n^m(\widehat{\boldsymbol{y}})}\rangle_{L^2(S^2)} = -\sqrt{8}\pi\mathrm{i}^{n-1}\boldsymbol{Q}_n^m(\boldsymbol{x}) \tag{5.38b}$$

and applying (5.30) gives

$$\mathbf{curl}\,\boldsymbol{E}^i[\boldsymbol{A}_n^m](\boldsymbol{x}) = \sqrt{8}\pi k\mathrm{i}^{n-1}\boldsymbol{P}_n^m(\boldsymbol{x})\,, \tag{5.39a}$$

$$\mathbf{curl}\,\boldsymbol{E}^i[\boldsymbol{B}_n^m](\boldsymbol{x}) = \sqrt{8}\pi k\mathrm{i}^{n-1}\boldsymbol{Q}_n^m(\boldsymbol{x})\,. \tag{5.39b}$$

In order to derive the scalar products that are needed for the representation of the far field operator in the helicity bases $\boldsymbol{A}_n^m$ and $\boldsymbol{B}_n^m$, we note that the fundamental solution of time-harmonic Maxwell's equation satisfies

$$\mathbb{G}^\infty(\boldsymbol{x},\widehat{\boldsymbol{y}})\boldsymbol{p} = \frac{1}{k^2}\left(\mathbf{curl}_{\mathrm{y}}\,\mathbf{curl}_{\mathrm{y}}\,\Phi(\boldsymbol{x},\cdot)\boldsymbol{p}\right)^\infty(\widehat{\boldsymbol{y}}) \quad\text{and}\quad \mathbf{curl}_{\mathrm{y}}\,\mathbb{G}^\infty(\boldsymbol{x},\widehat{\boldsymbol{y}}) = \mathbf{curl}_{\mathrm{y}}\left(\Phi(\boldsymbol{x},\cdot)\boldsymbol{p}\right)^\infty(\widehat{\boldsymbol{y}})\,.$$

Again, using [34, Thm. 6.29] and the foregoing discussion, gives that

$$\begin{aligned} &\frac{1}{k^2}\,\mathbf{curl}_{\mathrm{y}}\,\mathbf{curl}_{\mathrm{y}}\left(\Phi(\boldsymbol{x},\boldsymbol{y})\boldsymbol{p}\right)\\ &\qquad = \mathrm{i}k\sum_{n=1}^{\infty}\sum_{m=-n}^{n}\boldsymbol{N}_n^m(\boldsymbol{y})\overline{\boldsymbol{M}_n^m(\boldsymbol{x})}\cdot\boldsymbol{p}+\frac{\mathrm{i}}{k}\sum_{n=1}^{\infty}\sum_{m=-n}^{n}\mathbf{curl}\,\boldsymbol{N}_n^m(\boldsymbol{y})\overline{\mathbf{curl}\,\boldsymbol{M}_n^m(\boldsymbol{x})}\cdot\boldsymbol{p} \end{aligned}$$

and an alternative version to (5.35), which reads

$$\begin{aligned} \Phi(\boldsymbol{x},\boldsymbol{y})\boldsymbol{p} = &\,\mathrm{i}k\sum_{n=1}^{\infty}\sum_{m=-n}^{n}\boldsymbol{N}_n^m(\boldsymbol{y})\overline{\boldsymbol{M}_n^m(\boldsymbol{x})}\cdot\boldsymbol{p}\\ &+\frac{\mathrm{i}}{k}\sum_{n=1}^{\infty}\sum_{m=-n}^{n}\mathbf{curl}\,\boldsymbol{N}_n^m(\boldsymbol{y})\overline{\mathbf{curl}\,\boldsymbol{M}_n^m(\boldsymbol{x})}\cdot\boldsymbol{p}+\frac{\mathrm{i}}{k}\sum_{n=1}^{\infty}\sum_{m=-n}^{n}\nabla v_n^m(\boldsymbol{y})\overline{\nabla u_n^m(\boldsymbol{x})}\cdot\boldsymbol{p}\,. \end{aligned}$$

Using (5.36) and (2.29) yields

$$\begin{aligned}
&\mathrm{e}^{-\mathrm{i}k\widehat{\boldsymbol{y}}\cdot\boldsymbol{x}}\,(\widehat{\boldsymbol{y}}\times\mathbb{I}_3)\times\widehat{\boldsymbol{y}})\,\boldsymbol{p}\\
&\quad= -4\pi\sum_{n=1}^{\infty}(-\mathrm{i})^n\sum_{m=-n}^{n}\boldsymbol{V}_n^m(\widehat{\boldsymbol{y}})\overline{\boldsymbol{M}_n^m(\boldsymbol{x})}\cdot\boldsymbol{p}+\frac{4\pi}{k}\sum_{n=1}^{\infty}(-\mathrm{i})^{n-1}\sum_{m=-n}^{n}\boldsymbol{U}_n^m(\widehat{\boldsymbol{y}})\overline{\mathbf{curl}\,\boldsymbol{M}_n^m(\boldsymbol{x})}\cdot\boldsymbol{p}
\end{aligned}$$

and

$$\begin{aligned}
\mathrm{e}^{-\mathrm{i}k\widehat{\boldsymbol{y}}\cdot\boldsymbol{x}}\,(\widehat{\boldsymbol{y}}\times\mathbb{I}_3)\,\boldsymbol{p} &= \frac{1}{\mathrm{i}k}\left(\mathbf{curl}_{\mathrm{y}}\left(\Phi(\boldsymbol{x},\cdot)\boldsymbol{p}\right)\right)^{\infty}(\widehat{\boldsymbol{y}})\\
&= 4\pi\sum_{n=1}^{\infty}(-\mathrm{i})^n\sum_{m=-n}^{n}\boldsymbol{U}_n^m(\widehat{\boldsymbol{y}})\overline{\boldsymbol{M}_n^m(\boldsymbol{x})}\cdot\boldsymbol{p}-\frac{4\pi}{k}\sum_{n=1}^{\infty}(-\mathrm{i})^{n+1}\sum_{m=-n}^{n}\boldsymbol{V}_n^m(\widehat{\boldsymbol{y}})\overline{\mathbf{curl}\,\boldsymbol{M}_n^m(\boldsymbol{x})}\cdot\boldsymbol{p}\,.
\end{aligned}$$

Hence, we obtain that

$$\langle\mathrm{e}^{-\mathrm{i}k\widehat{\boldsymbol{y}}\cdot\boldsymbol{x}}\,(\widehat{\boldsymbol{y}}\times\mathbb{I}_3)\times\widehat{\boldsymbol{y}})\,,\boldsymbol{A}_n^m(\widehat{\boldsymbol{y}})\rangle_{L_t^2(S^2)} = \sqrt{8}\pi(-\mathrm{i})^{n-1}\overline{\boldsymbol{P}_n^m(\boldsymbol{x})}^{\top}, \tag{5.40a}$$

$$\langle\mathrm{e}^{-\mathrm{i}k\widehat{\boldsymbol{y}}\cdot\boldsymbol{x}}\,(\widehat{\boldsymbol{y}}\times\mathbb{I}_3)\times\widehat{\boldsymbol{y}})\,,\boldsymbol{B}_n^m(\widehat{\boldsymbol{y}})\rangle_{L_t^2(S^2)} = -\sqrt{8}\pi(-\mathrm{i})^{n-1}\overline{\boldsymbol{Q}_n^m(\boldsymbol{x})}^{\top}, \tag{5.40b}$$

$$\langle\mathrm{e}^{-\mathrm{i}k\widehat{\boldsymbol{y}}\cdot\boldsymbol{x}}\,(\widehat{\boldsymbol{y}}\times\mathbb{I}_3)\,,\boldsymbol{A}_n^m(\widehat{\boldsymbol{y}})\rangle_{L_t^2(S^2)} = \sqrt{8}\pi(-\mathrm{i})^{n}\overline{\boldsymbol{P}_n^m(\boldsymbol{x})}^{\top}, \tag{5.40c}$$

$$\langle\mathrm{e}^{-\mathrm{i}k\widehat{\boldsymbol{y}}\cdot\boldsymbol{x}}\,(\widehat{\boldsymbol{y}}\times\mathbb{I}_3)\,,\boldsymbol{B}_n^m(\widehat{\boldsymbol{y}})\rangle_{L_t^2(S^2)} = \sqrt{8}\pi(-\mathrm{i})^{n}\overline{\boldsymbol{Q}_n^m(\boldsymbol{x})}^{\top}, \tag{5.40d}$$

with the scalar product between a matrix and a vector understood to be taken column by column. Now, we can combine (5.38), (5.39) and (5.40) with the representation of the operator $\mathcal{T}_{D_\rho}$ in (5.25) to end up with the terms in (5.34). □

Remark 5.8. The circularly polarized vector spherical harmonics $\boldsymbol{A}_n^m$ and $\boldsymbol{B}_n^m$, $m=-n,\dots,n$, $n=1,2,\dots$, in (5.28) have been constructed in such a way that they span the subspaces V^+ and V^-, respectively. Thus, the expansion in Lemma 5.7 immediately gives corresponding basis representations of the projected operators $\mathcal{T}_{D_\rho}^{pq}$ for $p,q\in\{+,-\}$, that yield a decomposition of $\mathcal{T}_{D_\rho}$ similar to (5.15).

Remark 5.9. In numerical implementations the series over n in (5.31) and (5.32) has to be truncated at some $N\in\mathbb{N}$. In [70] the authors studied the singular value decomposition of the linear operator that maps current densities supported in the ball $B_R(0)$ of radius R around the origin to their radiated far field patterns and showed that for all practically relevant source distributions the radiated far field pattern is well approximated by a vector spherical harmonics expansion of order $N\gtrsim kR$. Thus, we choose the truncation index N in the series representations in (5.31) and (5.32) such that $N\gtrsim kR$, where $B_R(0)$ denotes the smallest ball around the origin that includes the scattering object D_ρ. We further note that the truncation at index N yields a discretization of $\mathcal{T}_{D_\rho}$ denoted by $\mathcal{T}_{\rho,N}$, which is given by

$$\mathcal{T}_{\rho,N} = \begin{bmatrix}\boldsymbol{AA} & \boldsymbol{BA}\\ \boldsymbol{AB} & \boldsymbol{BB}\end{bmatrix} \tag{5.41}$$

with

$$\boldsymbol{XY} = \begin{bmatrix}
\langle\mathcal{T}_{D_\rho}\boldsymbol{X}_1^{-1},\boldsymbol{Y}_1^{-1}\rangle & \langle\mathcal{T}_{D_\rho}\boldsymbol{X}_1^{0},\boldsymbol{Y}_1^{-1}\rangle & \cdots & \cdots & \langle\mathcal{T}_{D_\rho}\boldsymbol{X}_N^{N},\boldsymbol{Y}_1^{-1}\rangle\\
\langle\mathcal{T}_{D_\rho}\boldsymbol{X}_1^{-1},\boldsymbol{Y}_1^{0}\rangle & \langle\mathcal{T}_{D_\rho}\boldsymbol{X}_1^{0},\boldsymbol{Y}_1^{0}\rangle & \ddots & & \vdots\\
\vdots & \ddots & \ddots & & \\
 & & & \ddots & \langle\mathcal{T}_{D_\rho}\boldsymbol{X}_N^{N},\boldsymbol{Y}_N^{N-1}\rangle\\
\langle\mathcal{T}_{D_\rho}\boldsymbol{X}_1^{-1},\boldsymbol{Y}_N^{N}\rangle & \cdots & \cdots & \langle\mathcal{T}_{D_\rho}\boldsymbol{X}_N^{N-1},\boldsymbol{Y}_N^{N}\rangle & \langle\mathcal{T}_{D_\rho}\boldsymbol{X}_N^{N},\boldsymbol{Y}_N^{N}\rangle
\end{bmatrix} \tag{5.42}$$

for $\boldsymbol{X},\boldsymbol{Y}\in\{\boldsymbol{A},\boldsymbol{B}\}$. The scalar products in (5.42) are given by (5.34). A single block $\boldsymbol{XY}$ has dimension $Q'\times Q'$ with $Q'=N(N+2)$, and consequently, $\mathcal{T}_{\rho,N}\in\mathbb{C}^{2Q'\times 2Q'}$.

Before we continue with the computation of the Fréchet derivative of $\mathcal{T}_{D_\rho}$, we study the link of the far field operator to the T-matrix. This is done in the next remark.

Remark 5.10. In the work [49] the definition and quantification of em-chirality is defined in terms of the transition matrix T, which is usually referred to as the T-matrix (see e.g. [98, Chap. 5]). Let $R > 0$ be so large that $D_\rho \subset B_R(0)$. For an incident field $\boldsymbol{E}^i$ and its corresponding scattered field $\boldsymbol{E}^s$, we consider the representations

$$\boldsymbol{E}^i = \sum_{n=1}^{\infty} \sum_{m=-n}^{n} a_n^m k^{-1} \operatorname{\mathbf{curl}} \boldsymbol{M}_n^m + b_n^m \boldsymbol{M}_n^m \quad \text{in } \mathbb{R}^3\,, \tag{5.43a}$$

$$\boldsymbol{E}^s = \sum_{n=1}^{\infty} \sum_{m=-n}^{n} c_n^m k^{-1} \operatorname{\mathbf{curl}} \boldsymbol{N}_n^m + d_n^m \boldsymbol{N}_n^m \quad \text{in } \mathbb{R}^3 \setminus \overline{B_R(0)} \tag{5.43b}$$

(see e.g. [57, Eq. (2)–(6)], [98, Eq. (5.2)–(5.3), App. C]), where $\boldsymbol{M}_n^m, \operatorname{\mathbf{curl}} \boldsymbol{M}_n^m$ and $\boldsymbol{N}_n^m, \operatorname{\mathbf{curl}} \boldsymbol{N}_n^m$ are defined in (2.23) and (2.24), respectively. Note that in (5.43), we added the factor k^{-1} in front of $\operatorname{\mathbf{curl}} \boldsymbol{M}_n^m$ and $\operatorname{\mathbf{curl}} \boldsymbol{N}_n^m$ in order to correct the different scaling compared to the work [57]. By the linearity of the scattering problem, we define the T-matrix T in such a way that

$$\begin{bmatrix} \boldsymbol{c} \\ \boldsymbol{d} \end{bmatrix} = T \begin{bmatrix} \boldsymbol{a} \\ \boldsymbol{b} \end{bmatrix}.$$

Here, the vectors $\boldsymbol{a}, \boldsymbol{b}, \boldsymbol{c}, \boldsymbol{d}$ contain the coefficients $a_n^m, b_n^m, c_n^m, d_n^m$ in succession for $m = -n, \dots, n$, $n = 1, 2, \dots$. In what follows, we study the entries of T in detail. Similar computations for the representation of the T-matrix were done in [58]. For a scattering object D, we denote by $\mathcal{S}$ the linear operator, that maps an incident field $\boldsymbol{E}^i$ to its corresponding scattered field $\boldsymbol{E}^s$ outside of D. With $\boldsymbol{E}^i, \boldsymbol{E}^s$ from (5.43) it therefore holds that $\mathcal{S}(\boldsymbol{E}^i) = \boldsymbol{E}^s$. Developing the function $\mathcal{S}(k^{-1} \operatorname{\mathbf{curl}} \boldsymbol{M}_n^m)$ and $\mathcal{S}(\boldsymbol{M}_n^m)$ as in (5.43) yields

$$\mathcal{S}(k^{-1} \operatorname{\mathbf{curl}} \boldsymbol{M}_n^m) = \sum_{n'=1}^{\infty} \sum_{m'=-n'}^{n'} t^{(1)}_{n'm',nm} k^{-1} \operatorname{\mathbf{curl}} \boldsymbol{N}_{n'}^{m'} + t^{(2)}_{n'm',nm} \boldsymbol{N}_{n'}^{m'} \quad \text{in } \mathbb{R}^3 \setminus \overline{B_R(0)}\,, \tag{5.44a}$$

$$\mathcal{S}(\boldsymbol{M}_n^m) = \sum_{n'=1}^{\infty} \sum_{m'=-n'}^{n'} t^{(3)}_{n'm',nm} k^{-1} \operatorname{\mathbf{curl}} \boldsymbol{N}_{n'}^{m'} + t^{(4)}_{n'm',nm} \boldsymbol{N}_{n'}^{m'} \quad \text{in } \mathbb{R}^3 \setminus \overline{B_R(0)}\,. \tag{5.44b}$$

Using these representations with $\boldsymbol{E}^i$ from (5.43) and changing the order of summation gives

$$\begin{aligned} \mathcal{S}(\boldsymbol{E}^i) = \sum_{n'=1}^{\infty} \sum_{m'=-n'}^{n'} \Bigg(& k^{-1} \operatorname{\mathbf{curl}} \boldsymbol{N}_{n'}^{m'} \left(\sum_{n=1}^{\infty} \sum_{m=-n}^{n} t^{(1)}_{n'm',nm} a_n^m + t^{(3)}_{n'm',nm} b_n^m \right) \\ & + \boldsymbol{N}_{n'}^{m'} \left(\sum_{n=1}^{\infty} \sum_{m=-n}^{n} t^{(2)}_{n'm',nm} a_n^m + t^{(4)}_{n'm',nm} b_n^m \right) \Bigg) \quad \text{in } \mathbb{R}^3 \setminus \overline{B_R(0)}\,. \end{aligned}$$

Comparing coefficients with $\boldsymbol{E}^s$ in (5.43) yields that

$$c_{n'}^{m'} = \sum_{n=1}^{\infty} \sum_{m=-n}^{n} t^{(1)}_{n'm',nm} a_n^m + t^{(3)}_{n'm',nm} b_n^m \quad \text{and} \quad d_{n'}^{m'} = \sum_{n=1}^{\infty} \sum_{m=-n}^{n} t^{(2)}_{n'm',nm} a_n^m + t^{(4)}_{n'm',nm} b_n^m\,.$$

Thus, the entries of the T-matrix T are determined by $t^{(j)}_{n'm',nm}$, $1 \le j \le 4$. For the expressions in (5.44) we extract the far field on both sides, respectively. On the left hand sides, we obtain the far fields corresponding to the incident field $k^{-1} \operatorname{\mathbf{curl}} \boldsymbol{M}_n^m$ and $\boldsymbol{M}_n^m$, respectively. By (5.37), these functions are Herglotz waves as in (5.7) with densities $(4\pi \mathrm{i}^{n-1})^{-1} \boldsymbol{U}_n^m$ and $-(4\pi \mathrm{i}^n)^{-1} \boldsymbol{V}_n^m$, respectively. The far field corresponding to a Herglotz wave is, by linearity, given by the far field

operator with the corresponding density. On the right hand sides of (5.44) we use the expression for the far field from (5.36). Then we find due to the orthogonality of $\boldsymbol{U}_n^m$ and $\boldsymbol{V}_n^m$ that

$$t^{(1)}_{n'm',nm} = \frac{\mathrm{i}k}{16\pi^2}\mathrm{i}^{n'-n}\langle \mathcal{F}_D\boldsymbol{U}_n^m, \boldsymbol{U}_{n'}^{m'}\rangle_{L_t^2(S^2)}, \qquad t^{(3)}_{n'm',nm} = \frac{\mathrm{i}k}{16\pi^2}\mathrm{i}^{n'-n+1}\langle \mathcal{F}_D\boldsymbol{V}_n^m, \boldsymbol{U}_{n'}^{m'}\rangle_{L_t^2(S^2)},$$
$$t^{(2)}_{n'm',nm} = \frac{\mathrm{i}k}{16\pi^2}\mathrm{i}^{n'-n-1}\langle \mathcal{F}_D\boldsymbol{U}_n^m, \boldsymbol{V}_{n'}^{m'}\rangle_{L_t^2(S^2)}, \qquad t^{(4)}_{n'm',nm} = \frac{\mathrm{i}k}{16\pi^2}\mathrm{i}^{n'-n}\langle \mathcal{F}_D\boldsymbol{V}_n^m, \boldsymbol{V}_{n'}^{m'}\rangle_{L_t^2(S^2)}.$$

For $\boldsymbol{A} \in L_t^2(S^2)$ we use the basis representations

$$\boldsymbol{A} = \sum_{n=1}^{\infty}\sum_{m=-n}^{n} e_n^m\boldsymbol{U}_n^m + f_n^m\boldsymbol{V}_n^m \quad \text{and} \quad \mathcal{F}_D\boldsymbol{A} = \sum_{n=1}^{\infty}\sum_{m=-n}^{n} g_n^m\boldsymbol{U}_n^m + h_n^m\boldsymbol{V}_n^m.$$

In the same way as above, it can be seen that

$$g_{n'}^{m'} = \sum_{n=1}^{\infty}\sum_{m=-n}^{n} \langle \mathcal{F}_D\boldsymbol{U}_n^m, \boldsymbol{U}_{n'}^{m'}\rangle_{L_t^2(S^2)}e_n^m + \langle \mathcal{F}_D\boldsymbol{V}_n^m, \boldsymbol{U}_{n'}^{m'}\rangle_{L_t^2(S^2)}f_n^m,$$
$$h_{n'}^{m'} = \sum_{n=1}^{\infty}\sum_{m=-n}^{n} \langle \mathcal{F}_D\boldsymbol{U}_n^m, \boldsymbol{V}_{n'}^{m'}\rangle_{L_t^2(S^2)}e_n^m + \langle \mathcal{F}_D\boldsymbol{V}_n^m, \boldsymbol{V}_{n'}^{m'}\rangle_{L_t^2(S^2)}f_n^m$$

Truncating all series representations at $N \in \mathbb{N}$, we therefore find that

$$T_N = \frac{\mathrm{i}k}{16\pi^2}\Sigma^* F_N \Sigma.$$

Here, $T_N, F_N \in \mathbb{C}^{Q\times Q}$ with $Q = 2N(N+2)$ denote the discretized operators T and $\mathcal{F}_D$, respectively, and $\Sigma \in \mathbb{C}^{Q\times Q}$ is the diagonal matrix with entries

$$\Sigma_{j,j} = \begin{cases} -(-\mathrm{i})^n, & n^2 \le j \le n(n+2), \\ -\mathrm{i}(-\mathrm{i})^n, & N(N+2)+n^2 \le j \le +N(N+2)+n(n+2), \end{cases} \qquad n = 1,\dots,N.$$

Thus, the T-matrix is obtained by applying a scaling and a unitary transformation to the far field operator.

5.3 The shape derivative of $\mathcal{T}_{D_\rho}$

In the previous section we discussed the asymptotic behavior of the far field operator $\mathcal{F}_{D_\rho}$ corresponding to a thin tubular scattering object D_ρ with a cross-section $D'_\rho = \rho D'$ that possibly rotates around the fixed spine curve, as the radius tends to 0. In this section, we fix the radius $\rho > 0$ and discuss the Fréchet differentiability of the leading order term $\mathcal{T}_{D_\rho}$ in the asymptotic expansion (5.27) with respect to the center curve K and to the rotation θ. We recall the set of admissible parametrizations $\mathcal{U}_{\mathrm{ad}}$ from (5.24) and define the nonlinear operator $\boldsymbol{T}_\rho : \mathcal{U}_{\mathrm{ad}} \to \mathrm{HS}(L_t^2(S^2))$ that maps admissible parametrizations of supports of thin nanowires D_ρ to the leading order term $\mathcal{T}_{D_\rho}$ of the associated far field operator $\mathcal{F}_{D_\rho}$ in (5.8), by

$$\boldsymbol{T}_\rho(\boldsymbol{p}, V_{\boldsymbol{p},\theta}) = \mathcal{T}_{D_\rho}, \qquad (\boldsymbol{p}, V_{\boldsymbol{p},\theta}) \in \mathcal{U}_{\mathrm{ad}}. \tag{5.45}$$

Here, D_ρ is a thin tubular scattering object as in (3.7). The set of admissible parametrizations $\mathcal{U}_{\mathrm{ad}}$ in (5.24) is not a vector space, but $\mathcal{U}_{\mathrm{ad}}$ can be parametrized locally around any admissible $(\boldsymbol{p}, V_{\boldsymbol{p},\theta}) \in \mathcal{U}_{\mathrm{ad}}$ with $V_{\boldsymbol{p},\theta} = [\boldsymbol{t}_{\boldsymbol{p}}(s) \,|\, \boldsymbol{r}_{\boldsymbol{p},\theta}(s) \,|\, \mathbf{s}_{\boldsymbol{p},\theta}(s)]$ as follows. Suppose that $\delta_{\boldsymbol{p}}, \delta_\theta > 0$ are sufficiently small. Then, an open neighborhood of $(\boldsymbol{p}, V_{\boldsymbol{p},\theta})$ in $\mathcal{U}_{\mathrm{ad}}$ is given by

$$\Big\{(\boldsymbol{p}+\boldsymbol{h}, V_{\boldsymbol{p}+\boldsymbol{h},\theta+\phi}) \mid \boldsymbol{h} \in C^3([0,1],\mathbb{R}^3),\ \|\boldsymbol{h}\|_{C^3} < \delta_{\boldsymbol{p}},\ \phi \in C^2([0,1],\mathbb{R}),\ \|\phi\|_{C^2} < \delta_\theta\Big\}, \tag{5.46}$$

where $V_{\boldsymbol{p}+\boldsymbol{h},\theta+\phi} = [\boldsymbol{t}_{\boldsymbol{p}+\boldsymbol{h}} \,|\, \boldsymbol{r}_{\boldsymbol{p}+\boldsymbol{h},\theta+\phi} \,|\, \mathbf{s}_{\boldsymbol{p}+\boldsymbol{h},\theta+\phi}] \in C^2([0,1],\mathrm{SO}(3))$ with

$$\boldsymbol{t}_{\boldsymbol{p}+\boldsymbol{h}} = \frac{\boldsymbol{p}'+\boldsymbol{h}'}{|\boldsymbol{p}'+\boldsymbol{h}'|}\,, \tag{5.47a}$$

$$\boldsymbol{r}_{\boldsymbol{p}+\boldsymbol{h},\theta+\phi} = (\boldsymbol{t}_{\boldsymbol{p}}\cdot\boldsymbol{t}_{\boldsymbol{p}+\boldsymbol{h}})\boldsymbol{r}_{\boldsymbol{p},\theta+\phi} - \frac{\mathbf{s}_{\boldsymbol{p},\theta+\phi}\cdot\boldsymbol{t}_{\boldsymbol{p}+\boldsymbol{h}}}{1+\boldsymbol{t}_{\boldsymbol{p}}\cdot\boldsymbol{t}_{\boldsymbol{p}+\boldsymbol{h}}}(\boldsymbol{t}_{\boldsymbol{p}}\times\boldsymbol{t}_{\boldsymbol{p}+\boldsymbol{h}}) - (\boldsymbol{r}_{\boldsymbol{p},\theta+\phi}\cdot\boldsymbol{t}_{\boldsymbol{p}+\boldsymbol{h}})\boldsymbol{t}_{\boldsymbol{p}}\,, \tag{5.47b}$$

$$\mathbf{s}_{\boldsymbol{p}+\boldsymbol{h},\theta+\phi} = (\boldsymbol{t}_{\boldsymbol{p}}\cdot\boldsymbol{t}_{\boldsymbol{p}+\boldsymbol{h}})\mathbf{s}_{\boldsymbol{p},\theta+\phi} + \frac{\boldsymbol{r}_{\boldsymbol{p},\theta+\phi}\cdot\boldsymbol{t}_{\boldsymbol{p}+\boldsymbol{h}}}{1+\boldsymbol{t}_{\boldsymbol{p}}\cdot\boldsymbol{t}_{\boldsymbol{p}+\boldsymbol{h}}}(\boldsymbol{t}_{\boldsymbol{p}}\times\boldsymbol{t}_{\boldsymbol{p}+\boldsymbol{h}}) - (\mathbf{s}_{\boldsymbol{p},\theta+\phi}\cdot\boldsymbol{t}_{\boldsymbol{p}+\boldsymbol{h}})\boldsymbol{t}_{\boldsymbol{p}} \tag{5.47c}$$

and

$$[\boldsymbol{r}_{\boldsymbol{p},\theta+\phi} \,|\, \mathbf{s}_{\boldsymbol{p},\theta+\phi}] = [\cos(\phi)\boldsymbol{r}_{\boldsymbol{p},\theta} + \sin(\phi)\mathbf{s}_{\boldsymbol{p},\theta} \,|\, -\sin(\phi)\boldsymbol{r}_{\boldsymbol{p},\theta} + \cos(\phi)\mathbf{s}_{\boldsymbol{p},\theta}]\,. \tag{5.48}$$

Remark 5.11. The formulas in (5.47) apply first an update of the rotation and in a second step an update of the spine curve. It is easy to see that changing the order of these steps results in the same overall update.

Whenever an admissible $(\boldsymbol{p}, V_{\boldsymbol{p},\theta}) \in \mathcal{U}_{\mathrm{ad}}$ is deformed by a sufficiently small $\boldsymbol{h}$ and ϕ, we apply the update formulas in (5.47) and (5.48). The next lemma shows that this updated frame is an admissible frame for the curve parametrized by $\boldsymbol{p}+\boldsymbol{h}$.

Lemma 5.12. *Let $(\boldsymbol{p}, V_{\boldsymbol{p},\theta}) \in \mathcal{U}_{\mathrm{ad}}$ and let $\boldsymbol{h} \in C^3([0,1],\mathbb{R}^3)$ with $\|\boldsymbol{h}\|_{C^3} < \delta_{\boldsymbol{p}}$ and $\phi \in C^2([0,1],\mathbb{R})$ with $\|\phi\|_{C^2} < \delta_\theta$ for sufficiently small $\delta_{\boldsymbol{p}}, \delta_\theta > 0$. Then, the update formulas from (5.47), (5.48) define an admissible frame $V_{\boldsymbol{p}+\boldsymbol{h},\theta+\phi}$ for the center curve parametrized by $\boldsymbol{p}+\boldsymbol{h}$.*

Proof. We prove the assertion by showing that the vectors $\boldsymbol{t}_{\boldsymbol{p}+\boldsymbol{h}}, \boldsymbol{r}_{\boldsymbol{p}+\boldsymbol{h},\theta+\phi}$ and $\mathbf{s}_{\boldsymbol{p}+\boldsymbol{h},\theta+\phi}$ are normalized and pairwise orthogonal. We first note that $\boldsymbol{t}_{\boldsymbol{p}+\boldsymbol{h}}$ is the tangent vector of $\boldsymbol{p}+\boldsymbol{h}$. Moreover, for the rotated reference vector $\boldsymbol{r}_{\boldsymbol{p},\theta+\phi}$ from (5.48), it holds that

$$|\boldsymbol{r}_{\boldsymbol{p},\theta+\phi}|^2 = |\cos(\phi)\boldsymbol{r}_{\boldsymbol{p},\theta} + \sin(\phi)\mathbf{s}_{\boldsymbol{p},\theta}|^2 = \cos^2(\phi)|\boldsymbol{r}_{\boldsymbol{p},\theta}|^2 + \sin^2(\phi)|\mathbf{s}_{\boldsymbol{p},\theta}|^2 = 1,$$

since $\boldsymbol{r}_{\boldsymbol{p}}$ and $\mathbf{s}_{\boldsymbol{p}}$ are normalized and orthogonal. In the same way, it can be seen that $|\mathbf{s}_{\boldsymbol{p},\theta+\phi}| = 1$. The pairwise orthogonality of $\boldsymbol{t}_{\boldsymbol{p}}, \boldsymbol{r}_{\boldsymbol{p},\theta}$ and $\mathbf{s}_{\boldsymbol{p},\theta}$ immediately implies the pairwise orthogonality of $\boldsymbol{t}_{\boldsymbol{p}}, \boldsymbol{r}_{\boldsymbol{p},\theta+\phi}$ and $\mathbf{s}_{\boldsymbol{p},\theta+\phi}$. For computing $|\boldsymbol{r}_{\boldsymbol{p}+\boldsymbol{h},\theta+\phi}|$ we use that $\boldsymbol{r}_{\boldsymbol{p},\theta+\phi}$ and $\boldsymbol{t}_{\boldsymbol{p}}$ are orthogonal, $\boldsymbol{r}_{\boldsymbol{p},\theta+\phi}\cdot(\boldsymbol{t}_{\boldsymbol{p}}\times\boldsymbol{t}_{\boldsymbol{p}+\boldsymbol{h}}) = -\mathbf{s}_{\boldsymbol{p},\theta+\phi}\cdot\boldsymbol{t}_{\boldsymbol{p}+\boldsymbol{h}}$ together with $|\boldsymbol{t}_{\boldsymbol{p}}\times\boldsymbol{t}_{\boldsymbol{p}+\boldsymbol{h}}|^2 = 1-(\boldsymbol{t}_{\boldsymbol{p}}\cdot\boldsymbol{t}_{\boldsymbol{p}+\boldsymbol{h}})^2$ and Parseval's identity. Thus, we compute

$$\begin{aligned}
|\boldsymbol{r}_{\boldsymbol{p}+\boldsymbol{h},\theta+\phi}|^2 &= (\boldsymbol{t}_{\boldsymbol{p}}\cdot\boldsymbol{t}_{\boldsymbol{p}+\boldsymbol{h}})^2 - 2\frac{\mathbf{s}_{\boldsymbol{p},\theta+\phi}\cdot\boldsymbol{t}_{\boldsymbol{p}+\boldsymbol{h}}}{1+\boldsymbol{t}_{\boldsymbol{p}}\cdot\boldsymbol{t}_{\boldsymbol{p}+\boldsymbol{h}}}(\boldsymbol{t}_{\boldsymbol{p}}\cdot\boldsymbol{t}_{\boldsymbol{p}+\boldsymbol{h}})(\boldsymbol{r}_{\boldsymbol{p},\theta+\phi}\cdot(\boldsymbol{t}_{\boldsymbol{p}}\times\boldsymbol{t}_{\boldsymbol{p}+\boldsymbol{h}})) \\
&\quad + \left(\frac{\mathbf{s}_{\boldsymbol{p},\theta+\phi}\cdot\boldsymbol{t}_{\boldsymbol{p}+\boldsymbol{h}}}{1+\boldsymbol{t}_{\boldsymbol{p}}\cdot\boldsymbol{t}_{\boldsymbol{p}+\boldsymbol{h}}}\right)^2 |\boldsymbol{t}_{\boldsymbol{p}}\times\boldsymbol{t}_{\boldsymbol{p}+\boldsymbol{h}}|^2 + (\boldsymbol{r}_{\boldsymbol{p},\theta+\phi}\cdot\boldsymbol{t}_{\boldsymbol{p}+\boldsymbol{h}})^2 \\
&= (\boldsymbol{t}_{\boldsymbol{p}}\cdot\boldsymbol{t}_{\boldsymbol{p}+\boldsymbol{h}})^2 + 2\frac{\mathbf{s}_{\boldsymbol{p},\theta+\phi}\cdot\boldsymbol{t}_{\boldsymbol{p}+\boldsymbol{h}}}{1+\boldsymbol{t}_{\boldsymbol{p}}\cdot\boldsymbol{t}_{\boldsymbol{p}+\boldsymbol{h}}}(\boldsymbol{t}_{\boldsymbol{p}}\cdot\boldsymbol{t}_{\boldsymbol{p}+\boldsymbol{h}})(\mathbf{s}_{\boldsymbol{p},\theta+\phi}\cdot\boldsymbol{t}_{\boldsymbol{p}+\boldsymbol{h}}) \\
&\quad + \left(\frac{\mathbf{s}_{\boldsymbol{p},\theta+\phi}\cdot\boldsymbol{t}_{\boldsymbol{p}+\boldsymbol{h}}}{1+\boldsymbol{t}_{\boldsymbol{p}}\cdot\boldsymbol{t}_{\boldsymbol{p}+\boldsymbol{h}}}\right)^2 (1-(\boldsymbol{t}_{\boldsymbol{p}}\cdot\boldsymbol{t}_{\boldsymbol{p}+\boldsymbol{h}})^2) + (\boldsymbol{r}_{\boldsymbol{p},\theta+\phi}\cdot\boldsymbol{t}_{\boldsymbol{p}+\boldsymbol{h}})^2 \\
&= (\boldsymbol{t}_{\boldsymbol{p}}\cdot\boldsymbol{t}_{\boldsymbol{p}+\boldsymbol{h}})^2 + (\boldsymbol{r}_{\boldsymbol{p},\theta+\phi}\cdot\boldsymbol{t}_{\boldsymbol{p}+\boldsymbol{h}})^2 + (\mathbf{s}_{\boldsymbol{p},\theta+\phi}\cdot\boldsymbol{t}_{\boldsymbol{p}+\boldsymbol{h}})^2 = 1.
\end{aligned}$$

In a similar fashion it can be seen that $|\mathbf{s}_{\boldsymbol{p}+\boldsymbol{h},\theta+\phi}| = 1$. For computing $\boldsymbol{r}_{\boldsymbol{p}+\boldsymbol{h},\theta+\phi}\cdot\mathbf{s}_{\boldsymbol{p}+\boldsymbol{h},\theta+\phi}$ we use the bilinearity of the dot product and the identities $\boldsymbol{t}_{\boldsymbol{p}}\times\boldsymbol{r}_{\boldsymbol{p},\theta+\phi} = \mathbf{s}_{\boldsymbol{p},\theta+\phi}$, $\mathbf{s}_{\boldsymbol{p},\theta+\phi}\times\boldsymbol{t}_{\boldsymbol{p}} = \boldsymbol{r}_{\boldsymbol{p},\theta+\phi}$

and $|\boldsymbol{t}_{\boldsymbol{p}} \times \boldsymbol{t}_{\boldsymbol{p}+\boldsymbol{h}}|^2 = 1 - (\boldsymbol{t}_{\boldsymbol{p}} \cdot \boldsymbol{t}_{\boldsymbol{p}+\boldsymbol{h}})^2$. This yields

$$
\begin{aligned}
&\boldsymbol{r}_{\boldsymbol{p}+\boldsymbol{h},\theta+\phi} \cdot \mathbf{s}_{\boldsymbol{p}+\boldsymbol{h},\theta+\phi} \\
&= \frac{\boldsymbol{t}_{\boldsymbol{p}} \cdot \boldsymbol{t}_{\boldsymbol{p}+\boldsymbol{h}}}{1 + \boldsymbol{t}_{\boldsymbol{p}} \cdot \boldsymbol{t}_{\boldsymbol{p}+\boldsymbol{h}}} \left((\boldsymbol{r}_{\boldsymbol{p},\theta+\phi} \cdot \boldsymbol{t}_{\boldsymbol{p}+\boldsymbol{h}})(\boldsymbol{r}_{\boldsymbol{p},\theta+\phi} \cdot (\boldsymbol{t}_{\boldsymbol{p}} \times \boldsymbol{t}_{\boldsymbol{p}+\boldsymbol{h}})) - (\mathbf{s}_{\boldsymbol{p},\theta+\phi} \cdot \boldsymbol{t}_{\boldsymbol{p}+\boldsymbol{h}})(\mathbf{s}_{\boldsymbol{p},\theta+\phi} \cdot (\boldsymbol{t}_{\boldsymbol{p}} \times \boldsymbol{t}_{\boldsymbol{p}+\boldsymbol{h}})) \right) \\
&\quad - \frac{(\mathbf{s}_{\boldsymbol{p},\theta+\phi} \cdot \boldsymbol{t}_{\boldsymbol{p}+\boldsymbol{h}})(\boldsymbol{r}_{\boldsymbol{p},\theta+\phi} \cdot \boldsymbol{t}_{\boldsymbol{p}+\boldsymbol{h}})}{(1 + \boldsymbol{t}_{\boldsymbol{p}} \cdot \boldsymbol{t}_{\boldsymbol{p}+\boldsymbol{h}})^2} |\boldsymbol{t}_{\boldsymbol{p}} \times \boldsymbol{t}_{\boldsymbol{p}+\boldsymbol{h}}|^2 + (\mathbf{s}_{\boldsymbol{p},\theta+\phi} \cdot \boldsymbol{t}_{\boldsymbol{p}+\boldsymbol{h}})(\boldsymbol{r}_{\boldsymbol{p},\theta+\phi} \cdot \boldsymbol{t}_{\boldsymbol{p}+\boldsymbol{h}}) \\
&= -2 \frac{\boldsymbol{t}_{\boldsymbol{p}} \cdot \boldsymbol{t}_{\boldsymbol{p}+\boldsymbol{h}}}{1 + \boldsymbol{t}_{\boldsymbol{p}} \cdot \boldsymbol{t}_{\boldsymbol{p}+\boldsymbol{h}}} (\boldsymbol{r}_{\boldsymbol{p},\theta+\phi} \cdot \boldsymbol{t}_{\boldsymbol{p}+\boldsymbol{h}})(\mathbf{s}_{\boldsymbol{p},\theta+\phi} \cdot \boldsymbol{t}_{\boldsymbol{p}+\boldsymbol{h}}) \\
&\quad - \frac{(\mathbf{s}_{\boldsymbol{p},\theta+\phi} \cdot \boldsymbol{t}_{\boldsymbol{p}+\boldsymbol{h}})(\boldsymbol{r}_{\boldsymbol{p},\theta+\phi} \cdot \boldsymbol{t}_{\boldsymbol{p}+\boldsymbol{h}})}{1 + \boldsymbol{t}_{\boldsymbol{p}} \cdot \boldsymbol{t}_{\boldsymbol{p}+\boldsymbol{h}}} (1 - \boldsymbol{t}_{\boldsymbol{p}} \cdot \boldsymbol{t}_{\boldsymbol{p}+\boldsymbol{h}}) + \frac{(\mathbf{s}_{\boldsymbol{p},\theta+\phi} \cdot \boldsymbol{t}_{\boldsymbol{p}+\boldsymbol{h}})(\boldsymbol{r}_{\boldsymbol{p},\theta+\phi} \cdot \boldsymbol{t}_{\boldsymbol{p}+\boldsymbol{h}})}{1 + \boldsymbol{t}_{\boldsymbol{p}} \cdot \boldsymbol{t}_{\boldsymbol{p}+\boldsymbol{h}}} (1 + \boldsymbol{t}_{\boldsymbol{p}} \cdot \boldsymbol{t}_{\boldsymbol{p}+\boldsymbol{h}}) \\
&= 0.
\end{aligned}
$$

The pairwise orthogonality of $\boldsymbol{t}_{\boldsymbol{p}+\boldsymbol{h}}$ with both vectors $\boldsymbol{r}_{\boldsymbol{p}+\boldsymbol{h},\theta+\phi}$ and $\mathbf{s}_{\boldsymbol{p}+\boldsymbol{h},\theta+\phi}$ follows straightforwardly. □

Remark 5.13. The update formulas in (5.47) and (5.48) do not guarantee that the new frame possesses a minimal rotation.

Before we establish the Fréchet derivative of $\boldsymbol{T}_\rho$, we discuss the Fréchet differentiability of the polarization tensor $\mathbb{M}^\gamma, \gamma \in \{\varepsilon, \mu\}$, with respect to the center curve K and to the rotation θ. For this, we use the explicit representation of $\mathbb{M}^\gamma$ from (5.26).

Theorem 5.14. *The mapping* $\mathbb{M}^\gamma : \mathcal{U}_{\text{ad}} \to C([0,1], \mathbb{C}^{3\times 3})$, $\gamma \in \{\varepsilon, \mu\}$, *defined by*

$$\mathbb{M}^\gamma(\boldsymbol{p}, V_{\boldsymbol{p},\theta}) = \mathbb{M}^\gamma_{\boldsymbol{p},V_{\boldsymbol{p},\theta}} = V_{\boldsymbol{p},\theta} M^\gamma V_{\boldsymbol{p},\theta}^\top$$

is Fréchet differentiable. Its Fréchet derivative at $(\boldsymbol{p}, V_{\boldsymbol{p},\theta}) \in \mathcal{U}_{\text{ad}}$ *with respect to the local parametrization of* $\mathcal{U}_{\text{ad}}$ *in* (5.46)–(5.48) *is given by*

$$(M^\gamma_{\boldsymbol{p},V_{\boldsymbol{p},\theta}})' : C^3([0,1], \mathbb{R}^3) \times C^2([0,1], \mathbb{R}) \to C([0,1], \mathbb{C}^{3\times 3})$$

with

$$(M^\gamma_{\boldsymbol{p},V_{\boldsymbol{p},\theta}})' = V'_{\boldsymbol{p},\theta}(\boldsymbol{h}, \phi) M^\gamma V_{\boldsymbol{p},\theta}^\top + V_{\boldsymbol{p},\theta} M^\gamma (V'_{\boldsymbol{p},\theta}(\boldsymbol{h}, \phi))^\top, \tag{5.49}$$

where the matrix-valued function $V'_{\boldsymbol{p},\theta}(\boldsymbol{h}, \phi)$ *satisfies*

$$V'_{\boldsymbol{p},\theta}(\boldsymbol{h}, \phi) = \left[\frac{\boldsymbol{h}' \cdot \boldsymbol{r}_{\boldsymbol{p},\theta}}{|\boldsymbol{p}'|} \boldsymbol{r}_{\boldsymbol{p},\theta} + \frac{\boldsymbol{h}' \cdot \mathbf{s}_{\boldsymbol{p},\theta}}{|\boldsymbol{p}'|} \mathbf{s}_{\boldsymbol{p},\theta} \,\middle|\, - \frac{\boldsymbol{h}' \cdot \boldsymbol{r}_{\boldsymbol{p},\theta}}{|\boldsymbol{p}'|} \boldsymbol{t}_{\boldsymbol{p}} + \phi \mathbf{s}_{\boldsymbol{p},\theta} \,\middle|\, - \frac{\boldsymbol{h}' \cdot \mathbf{s}_{\boldsymbol{p},\theta}}{|\boldsymbol{p}'|} \boldsymbol{t}_{\boldsymbol{p}} - \phi \boldsymbol{r}_{\boldsymbol{p},\theta} \right].$$

Proof. Using Taylor's theorem we find that

$$\boldsymbol{t}_{\boldsymbol{p}+\boldsymbol{h}} = \boldsymbol{t}_{\boldsymbol{p}} + \frac{1}{|\boldsymbol{p}'|} \left((\boldsymbol{h}' \cdot \boldsymbol{r}_{\boldsymbol{p},\theta}) \, \boldsymbol{r}_{\boldsymbol{p},\theta} + (\boldsymbol{h}' \cdot \mathbf{s}_{\boldsymbol{p},\theta}) \, \mathbf{s}_{\boldsymbol{p},\theta} \right) + O(\|\boldsymbol{h}\|^2_{C^2([0,1],\mathbb{R}^3)}) \tag{5.50}$$

and

$$\boldsymbol{r}_{\boldsymbol{p},\theta+\phi} = \boldsymbol{r}_{\boldsymbol{p},\theta} + \phi \mathbf{s}_{\boldsymbol{p},\theta} + O(\|\phi\|^2_{C^2([0,1],\mathbb{R})}), \tag{5.51a}$$

$$\mathbf{s}_{\boldsymbol{p},\theta+\phi} = \mathbf{s}_{\boldsymbol{p},\theta} - \phi \boldsymbol{r}_{\boldsymbol{p},\theta} + O(\|\phi\|^2_{C^2([0,1],\mathbb{R})}). \tag{5.51b}$$

Substituting (5.50) in (5.47), we find that

$$\boldsymbol{r}_{\boldsymbol{p}+\boldsymbol{h},\theta} = \boldsymbol{r}_{\boldsymbol{p},\theta} - \frac{1}{|\boldsymbol{p}'|} \left(\boldsymbol{h}' \cdot \boldsymbol{r}_{\boldsymbol{p},\theta} \right) \boldsymbol{t}_{\boldsymbol{p}} + O(\|\boldsymbol{h}\|^2_{C^2([0,1],\mathbb{R}^3)}), \tag{5.52a}$$

$$\mathbf{s}_{\boldsymbol{p}+\boldsymbol{h},\theta} = \mathbf{s}_{\boldsymbol{p},\theta} - \frac{1}{|\boldsymbol{p}'|} \left(\boldsymbol{h}' \cdot \mathbf{s}_{\boldsymbol{p},\theta} \right) \boldsymbol{t}_{\boldsymbol{p}} + O(\|\boldsymbol{h}\|^2_{C^2([0,1],\mathbb{R}^3)}). \tag{5.52b}$$

Thus, the partial derivatives

$$\partial_{\boldsymbol{p}} V_{\boldsymbol{p},\theta}(\boldsymbol{h}) = \frac{1}{|\boldsymbol{p}'|}\left[(\boldsymbol{h}'\cdot\boldsymbol{r}_{\boldsymbol{p},\theta})\,\boldsymbol{r}_{\boldsymbol{p},\theta} + (\boldsymbol{h}'\cdot\mathbf{s}_{\boldsymbol{p},\theta})\,\mathbf{s}_{\boldsymbol{p},\theta}\,|\,-(\boldsymbol{h}'\cdot\boldsymbol{r}_{\boldsymbol{p},\theta})\,\boldsymbol{t}_{\boldsymbol{p}}\,|\,-(\boldsymbol{h}'\cdot\mathbf{s}_{\boldsymbol{p},\theta})\,\boldsymbol{t}_{\boldsymbol{p}}\right], \tag{5.53a}$$

$$\partial_\theta V_{\boldsymbol{p},\theta}(\phi) = \phi\,[0\,|\,\mathbf{s}_{\boldsymbol{p},\theta}\,|\,-\boldsymbol{r}_{\boldsymbol{p},\theta}] \tag{5.53b}$$

satisfy

$$\|V_{\boldsymbol{p}+\boldsymbol{h},\theta} - V_{\boldsymbol{p},\theta} - \partial_{\boldsymbol{p}} V_{\boldsymbol{p},\theta}(\boldsymbol{h})\|_{C([0,1],\mathbb{R}^{3\times3})} \le C\,\|\boldsymbol{h}\|^2_{C^2([0,1],\mathbb{R}^3)}, \tag{5.54a}$$

$$\|V_{\boldsymbol{p},\theta+\phi} - V_{\boldsymbol{p},\theta} - \partial_\theta V_{\boldsymbol{p},\theta}(\phi)\|_{C([0,1],\mathbb{R}^{3\times3})} \le C\,\|\phi\|^2_{C^2([0,1],\mathbb{R})}. \tag{5.54b}$$

Accordingly, we find that

$$\begin{aligned}
&\|V_{\boldsymbol{p}+\boldsymbol{h},\theta+\phi} - V_{\boldsymbol{p},\theta} - V'_{\boldsymbol{p},\theta}(\boldsymbol{h},\phi)\|_{C([0,1],\mathbb{R}^{3\times3})}\\
&\le \|V_{\boldsymbol{p}+\boldsymbol{h},\theta+\phi} - V_{\boldsymbol{p}+\boldsymbol{h},\theta} - \partial_\theta V_{\boldsymbol{p},\theta}(\phi)\|_{C([0,1],\mathbb{R}^{3\times3})} + \|V_{\boldsymbol{p}+\boldsymbol{h},\theta} - V_{\boldsymbol{p},\theta} - \partial_{\boldsymbol{p}} V_{\boldsymbol{p},\theta}(\boldsymbol{h})\|_{C([0,1],\mathbb{R}^{3\times3})}\\
&\le \|V_{\boldsymbol{p}+\boldsymbol{h},\theta+\phi} - V_{\boldsymbol{p}+\boldsymbol{h},\theta} - \partial_\theta V_{\boldsymbol{p}+\boldsymbol{h},\theta}(\phi)\|_{C([0,1],\mathbb{R}^{3\times3})} + \|\partial_\theta V_{\boldsymbol{p}+\boldsymbol{h},\theta}(\phi) - \partial_\theta V_{\boldsymbol{p},\theta}(\phi)\|_{C([0,1],\mathbb{R}^{3\times3})}\\
&\quad + \|V_{\boldsymbol{p}+\boldsymbol{h},\theta} - V_{\boldsymbol{p},\theta} - \partial_{\boldsymbol{p}} V_{\boldsymbol{p},\theta}(\boldsymbol{h})\|_{C([0,1],\mathbb{R}^{3\times3})}.
\end{aligned}$$

Due to (5.54), the first and the third term on the right hand side can be estimated by $\|\boldsymbol{h}\|^2_{C^2([0,1],\mathbb{R}^3)} + \|\phi\|^2_{C^2([0,1],\mathbb{R})}$. For the second term, we note from (5.53) and (5.52), that

$$\begin{aligned}
\|\partial_\theta V_{\boldsymbol{p}+\boldsymbol{h},\theta}(\phi) - \partial_\theta V_{\boldsymbol{p},\theta}(\phi)\|_{C([0,1],\mathbb{R}^{3\times3})} &= \left\|\frac{\phi}{|\boldsymbol{p}'|}\left[0\,|\,(\boldsymbol{h}'\cdot\boldsymbol{r}_{\boldsymbol{p},\theta})\boldsymbol{t}_{\boldsymbol{p}}\,|\,(\boldsymbol{h}'\cdot\mathbf{s}_{\boldsymbol{p},\theta})\boldsymbol{t}_{\boldsymbol{p}}\right]\right\|_{C([0,1],\mathbb{R}^{3\times3})}\\
&\quad + C\,\|\boldsymbol{h}\|^2_{C^2([0,1],\mathbb{R}^3)}\\
&\le C\,\|\phi\|_{C^2([0,1],\mathbb{R})}\,\|\boldsymbol{h}\|_{C^2([0,1],\mathbb{R}^3)} + C\,\|\boldsymbol{h}\|^2_{C^2([0,1],\mathbb{R}^3)}\\
&\le C(\|\boldsymbol{h}\|^2_{C^2([0,1],\mathbb{R}^3)} + \|\phi\|^2_{C^2([0,1],\mathbb{R})}).
\end{aligned}$$

The Fréchet differentiability of the polarization tensor and (5.49) are now a consequence of the product rule. □

In the next theorem we establish the Fréchet derivative of $\boldsymbol{T}_\rho$ at $(\boldsymbol{p}, V_{\boldsymbol{p},\theta}) \in \mathcal{U}_{\mathrm{ad}}$.

Theorem 5.15. *The nonlinear map $\boldsymbol{T}_\rho$ from (5.45) is Fréchet differentiable from $\mathcal{U}_{\mathrm{ad}}$ to $\mathrm{HS}(L^2_t(S^2))$. The Fréchet derivative at $(\boldsymbol{p}, V_{\boldsymbol{p},\theta}) \in \mathcal{U}_{\mathrm{ad}}$ with respect to the local parametrization of $\mathcal{U}_{\mathrm{ad}}$ in (5.46)-(5.48) is given by $\boldsymbol{T}'_\rho[\boldsymbol{p}, V_{\boldsymbol{p},\theta}] : C^3([0,1],\mathbb{R}^3)\times C^2([0,1],\mathbb{R}) \to \mathrm{HS}(L^2_t(S^2))$ with*

$$\begin{aligned}
&\boldsymbol{T}'_\rho[\boldsymbol{p}, V_{\boldsymbol{p},\theta}](\boldsymbol{h},\phi)\\
&\quad = (k\rho)^2|D'|\Big((\varepsilon_r - 1)\sum_{j=1}^4 \boldsymbol{T}'_{\rho,\varepsilon,j}[\boldsymbol{p}, V_{\boldsymbol{p},\theta}](\boldsymbol{h},\phi) + (\mu_r - 1)\sum_{j=1}^4 \boldsymbol{T}'_{\rho,\mu,j}[\boldsymbol{p}, V_{\boldsymbol{p},\theta}](\boldsymbol{h},\phi)\Big),
\end{aligned} \tag{5.55}$$

where, for any $\boldsymbol{A} \in L^2_t(S^2)$,

$$((\boldsymbol{T}'_{\rho,\varepsilon,1}[\boldsymbol{p}, V_{\boldsymbol{p},\theta}](\boldsymbol{h},\phi))\boldsymbol{A})(\widehat{\boldsymbol{x}}) = -\int_0^1 \mathrm{i}k(\widehat{\boldsymbol{x}}\cdot\boldsymbol{h})\mathrm{e}^{-\mathrm{i}k\widehat{\boldsymbol{x}}\cdot\boldsymbol{p}}\,\mathbb{P}_{3,\widehat{\boldsymbol{x}}}\mathbb{M}^\varepsilon_{\boldsymbol{p},V_{\boldsymbol{p},\theta}}\boldsymbol{E}^i[\boldsymbol{A}](\boldsymbol{p})|\boldsymbol{p}'|\,\mathrm{d}t, \tag{5.56a}$$

$$((\boldsymbol{T}'_{\rho,\varepsilon,2}[\boldsymbol{p}, V_{\boldsymbol{p},\theta}](\boldsymbol{h},\phi))\boldsymbol{A})(\widehat{\boldsymbol{x}}) = \int_0^1 \mathrm{e}^{-\mathrm{i}k\widehat{\boldsymbol{x}}\cdot\boldsymbol{p}}\,\mathbb{P}_{3,\widehat{\boldsymbol{x}}}(\mathbb{M}^\varepsilon_{\boldsymbol{p},V_{\boldsymbol{p},\theta}})'(\boldsymbol{h},\phi)\boldsymbol{E}^i[\boldsymbol{A}](\boldsymbol{p})|\boldsymbol{p}'|\,\mathrm{d}t, \tag{5.56b}$$

$$((\boldsymbol{T}'_{\rho,\varepsilon,3}[\boldsymbol{p}, V_{\boldsymbol{p},\theta}](\boldsymbol{h},\phi))\boldsymbol{A})(\widehat{\boldsymbol{x}}) = \int_0^1 \mathrm{e}^{-\mathrm{i}k\widehat{\boldsymbol{x}}\cdot\boldsymbol{p}}\,\mathbb{P}_{3,\widehat{\boldsymbol{x}}}\mathbb{M}^\varepsilon_{\boldsymbol{p},V_{\boldsymbol{p},\theta}}\,(\boldsymbol{E}^i[\boldsymbol{A}])'[\boldsymbol{p}, V_{\boldsymbol{p},\theta}](\boldsymbol{h},\phi)\,|\boldsymbol{p}'|\,\mathrm{d}t, \tag{5.56c}$$

$$((\boldsymbol{T}'_{\rho,\varepsilon,4}[\boldsymbol{p}, V_{\boldsymbol{p},\theta}](\boldsymbol{h},\phi))\boldsymbol{A})(\widehat{\boldsymbol{x}}) = \int_0^1 \mathrm{e}^{-\mathrm{i}k\widehat{\boldsymbol{x}}\cdot\boldsymbol{p}}\,\mathbb{P}_{3,\widehat{\boldsymbol{x}}}\mathbb{M}^\varepsilon_{\boldsymbol{p},V_{\boldsymbol{p},\theta}}\,\boldsymbol{E}^i[\boldsymbol{A}](\boldsymbol{p})\,\frac{\boldsymbol{p}'\cdot\boldsymbol{h}'}{|\boldsymbol{p}'|}\,\mathrm{d}t \tag{5.56d}$$

and

$$\left((\boldsymbol{T}'_{\rho,\mu,1}[\boldsymbol{p},V_{\boldsymbol{p},\theta}](\boldsymbol{h},\phi))\boldsymbol{A}\right)(\widehat{\boldsymbol{x}}) \;=\; -\int_0^1 \mathrm{i}k(\widehat{\boldsymbol{x}}\cdot\boldsymbol{h})\mathrm{e}^{-\mathrm{i}k\widehat{\boldsymbol{x}}\cdot\boldsymbol{p}}(\widehat{\boldsymbol{x}}\times\mathbb{I}_3)\mathbb{M}^{\mu}_{\boldsymbol{p},V_{\boldsymbol{p},\theta}}\widetilde{\boldsymbol{H}^i}[\boldsymbol{A}](\boldsymbol{p})|\boldsymbol{p}'|\,\mathrm{d}t\,, \tag{5.57a}$$

$$\left((\boldsymbol{T}'_{\rho,\mu,2}[\boldsymbol{p},V_{\boldsymbol{p},\theta}](\boldsymbol{h},\phi))\boldsymbol{A}\right)(\widehat{\boldsymbol{x}}) \;=\; \int_0^1 \mathrm{e}^{-\mathrm{i}k\widehat{\boldsymbol{x}}\cdot\boldsymbol{p}}(\widehat{\boldsymbol{x}}\times\mathbb{I}_3)(\mathbb{M}^{\mu}_{\boldsymbol{p},V_{\boldsymbol{p},\theta}})'(\boldsymbol{h},\phi)\widetilde{\boldsymbol{H}^i}[\boldsymbol{A}](\boldsymbol{p})|\boldsymbol{p}'|\,\mathrm{d}t\,, \tag{5.57b}$$

$$\left((\boldsymbol{T}'_{\rho,\mu,3}[\boldsymbol{p},V_{\boldsymbol{p},\theta}](\boldsymbol{h},\phi))\boldsymbol{A}\right)(\widehat{\boldsymbol{x}}) \;=\; \int_0^1 \mathrm{e}^{-\mathrm{i}k\widehat{\boldsymbol{x}}\cdot\boldsymbol{p}}(\widehat{\boldsymbol{x}}\times\mathbb{I}_3)\mathbb{M}^{\mu}_{\boldsymbol{p},V_{\boldsymbol{p},\theta}}(\widetilde{\boldsymbol{H}^i}[\boldsymbol{A}])'[\boldsymbol{p},V_{\boldsymbol{p},\theta}](\boldsymbol{h},\phi)|\boldsymbol{p}'|\,\mathrm{d}t\,, \tag{5.57c}$$

$$\left((\boldsymbol{T}'_{\rho,\mu,4}[\boldsymbol{p},V_{\boldsymbol{p},\theta}](\boldsymbol{h},\phi))\boldsymbol{A}\right)(\widehat{\boldsymbol{x}}) \;=\; \int_0^1 \mathrm{e}^{-\mathrm{i}k\widehat{\boldsymbol{x}}\cdot\boldsymbol{p}}(\widehat{\boldsymbol{x}}\times\mathbb{I}_3)\,\mathbb{M}^{\mu}_{\boldsymbol{p},V_{\boldsymbol{p},\theta}}\widetilde{\boldsymbol{H}^i}[\boldsymbol{A}](\boldsymbol{p})\,\frac{\boldsymbol{p}'\cdot\boldsymbol{h}'}{|\boldsymbol{p}'|}\,\mathrm{d}t\,. \tag{5.57d}$$

Here, we used the notation $\mathbb{P}_{3,\widehat{\boldsymbol{x}}} = (\widehat{\boldsymbol{x}}\times\mathbb{I}_3)\times\widehat{\boldsymbol{x}}$ *and* $\widetilde{\boldsymbol{H}^i}[\boldsymbol{A}] = \frac{\mathrm{i}}{k}\,\mathbf{curl}\,\boldsymbol{E}^i[\boldsymbol{A}]$ *for abbreviation.*

Proof. Let $(\boldsymbol{p},V_{\boldsymbol{p},\theta})\in\mathcal{U}_{\mathrm{ad}}$. Further, let $\delta_{\boldsymbol{p}},\delta_\theta>0$ be such that the open neighborhood of $(\boldsymbol{p},V_{\boldsymbol{p},\theta})$ as in (5.46) is well-defined. We have to show that

$$\left\|\boldsymbol{T}_\rho\left(\boldsymbol{p}+\boldsymbol{h},V_{\boldsymbol{p}+\boldsymbol{h},\theta+\phi}\right)-\boldsymbol{T}_\rho\left(\boldsymbol{p},V_{\boldsymbol{p},\theta}\right)-\boldsymbol{T}'_\rho[\boldsymbol{p},V_{\boldsymbol{p},\theta}](\boldsymbol{h},\phi)\right\|_{\mathrm{HS}} \;=\; o\left(\|(\boldsymbol{h},\phi)\|_{C^3\times C^2}\right) \tag{5.58}$$

as $\|(\boldsymbol{h},\phi)\|_{C^3\times C^2}\to 0$. Here,

$$\|(\boldsymbol{h},\phi)\|_{C^3\times C^2} \;=\; (\|\boldsymbol{h}\|^2_{C^3([0,1],\mathbb{R}^3)}+\|\phi\|^2_{C^2([0,1],\mathbb{R})})^{1/2}.$$

Using (5.25), (5.55)-(5.57) and (5.7), the Hilbert-Schmidt operators $\boldsymbol{T}_\rho\left(\boldsymbol{p}+\boldsymbol{h},V_{\boldsymbol{p}+\boldsymbol{h},\theta+\phi}\right)$, $\boldsymbol{T}_\rho\left(\boldsymbol{p},V_{\boldsymbol{p},\theta}\right)$ and $\boldsymbol{T}'_\rho[\boldsymbol{p},V_{\boldsymbol{p},\theta}](\boldsymbol{h},\phi)$ can be written as integral operators such that for any $\boldsymbol{A}\in L^2_t(S^2)$,

$$\left(\boldsymbol{T}_\rho\left(\boldsymbol{p}+\boldsymbol{h},V_{\boldsymbol{p}+\boldsymbol{h},\theta+\phi}\right)\boldsymbol{A}\right)(\widehat{\boldsymbol{x}}) \;=\; \int_{S^2} K_{\boldsymbol{p}+\boldsymbol{h},\theta+\phi}(\widehat{\boldsymbol{x}},\boldsymbol{\zeta})\boldsymbol{A}(\boldsymbol{\zeta})\,\mathrm{d}s(\boldsymbol{\zeta})\,, \tag{5.59a}$$

$$\left(\boldsymbol{T}_\rho\left(\boldsymbol{p},V_{\boldsymbol{p},\theta}\right)\boldsymbol{A}\right)(\widehat{\boldsymbol{x}}) \;=\; \int_{S^2} K_{\boldsymbol{p},\theta}(\widehat{\boldsymbol{x}},\boldsymbol{\zeta})\boldsymbol{A}(\boldsymbol{\zeta})\,\mathrm{d}s(\boldsymbol{\zeta})\,, \tag{5.59b}$$

$$\left(\boldsymbol{T}'_\rho[\boldsymbol{p},V_{\boldsymbol{p},\theta}](\boldsymbol{h},\phi)\boldsymbol{A}\right)(\widehat{\boldsymbol{x}}) \;=\; \int_{S^2} K'_{\boldsymbol{p},\theta;\boldsymbol{h},\phi}(\widehat{\boldsymbol{x}},\boldsymbol{\zeta})\boldsymbol{A}(\boldsymbol{\zeta})\,\mathrm{d}s(\boldsymbol{\zeta})\,, \tag{5.59c}$$

with smooth kernels $K_{\boldsymbol{p}+\boldsymbol{h},\theta+\phi}$, $K_{\boldsymbol{p},\theta}$ and $K'_{\boldsymbol{p},\theta;\boldsymbol{h},\phi}$ in $L^2(S^2\times S^2,\mathbb{C}^{3\times 3})$. In detail, we find that $K_{\boldsymbol{p},\theta}$ from (5.59b) is given by

$$K_{\boldsymbol{p},\theta}(\widehat{\boldsymbol{x}},\boldsymbol{\zeta}) \;=\; (k\rho)^2|D'|\Big(\int_K -(\mu_r-1)\mathrm{e}^{-\mathrm{i}k\widehat{\boldsymbol{x}}\cdot\boldsymbol{y}}(\widehat{\boldsymbol{x}}\times\mathbb{I}_3)\mathbb{M}^{\mu}_{\boldsymbol{p},V_{\boldsymbol{p},\theta}}\mathrm{e}^{\mathrm{i}k\boldsymbol{\zeta}\cdot\boldsymbol{y}}\,\mathrm{d}s(\boldsymbol{y})\boldsymbol{\zeta}\times\cdot$$
$$\int_K(\varepsilon_r-1)\mathrm{e}^{-\mathrm{i}k\widehat{\boldsymbol{x}}\cdot\boldsymbol{y}}((\widehat{\boldsymbol{x}}\times\mathbb{I}_3)\times\widehat{\boldsymbol{x}})\mathbb{M}^{\varepsilon}_{\boldsymbol{p},V_{\boldsymbol{p},\theta}}\mathrm{e}^{\mathrm{i}k\boldsymbol{\zeta}\cdot\boldsymbol{y}}\,\mathrm{d}s(\boldsymbol{y})\Big)\,.$$

The representation of $K_{\boldsymbol{p}+\boldsymbol{h},\theta+\phi}(\widehat{\boldsymbol{x}},\boldsymbol{\zeta})$ from (5.59a) is obtained by replacing $\boldsymbol{p}$ and $V_{\boldsymbol{p},\theta}$ by $\boldsymbol{p}+\boldsymbol{h}$ and $V_{\boldsymbol{p}+\boldsymbol{h},\theta+\phi}$, respectively. Moreover, $K'_{\boldsymbol{p},\theta;\boldsymbol{h},\phi}$ from (5.59c) is given by

$$K'_{\boldsymbol{p},\theta;\boldsymbol{h},\phi}(\widehat{\boldsymbol{x}},\boldsymbol{\zeta}) \;=\; (k\rho)^2|D'|\Big(-(\mu_r-1)\sum_{j=1}^4 {K^{(j),\mu}_{\boldsymbol{p},\theta;\boldsymbol{h},\phi}}'(\widehat{\boldsymbol{x}},\boldsymbol{\zeta})\boldsymbol{\zeta}\times\cdot+(\varepsilon_r-1)\sum_{j=1}^4 {K^{(j),\varepsilon}_{\boldsymbol{p},\theta;\boldsymbol{h},\phi}}'(\widehat{\boldsymbol{x}},\boldsymbol{\zeta})\Big) \tag{5.60}$$

with

$${K^{(1),\mu}_{\boldsymbol{p},\theta;\boldsymbol{h},\phi}}'(\widehat{\boldsymbol{x}},\boldsymbol{\zeta}) \;=\; \int_0^1 -\mathrm{i}k(\widehat{\boldsymbol{x}}\cdot\boldsymbol{h}(t)\mathrm{e}^{-\mathrm{i}k\widehat{\boldsymbol{x}}\cdot\boldsymbol{p}(t)}(\widehat{\boldsymbol{x}}\times\mathbb{I}_3)\mathbb{M}^{\mu}_{\boldsymbol{p},V_{\boldsymbol{p},\theta}}\mathrm{e}^{\mathrm{i}k\boldsymbol{\zeta}\cdot\boldsymbol{p}(t)}|\boldsymbol{p}'(t)|\,\mathrm{d}t\,, \tag{5.61a}$$

$${K^{(2),\mu}_{\boldsymbol{p},\theta;\boldsymbol{h},\phi}}'(\widehat{\boldsymbol{x}},\boldsymbol{\zeta}) \;=\; \int_0^1 \mathrm{e}^{-\mathrm{i}k\widehat{\boldsymbol{x}}\cdot\boldsymbol{p}(t)}(\widehat{\boldsymbol{x}}\times\mathbb{I}_3)(\mathbb{M}^{\mu}_{\boldsymbol{p},V_{\boldsymbol{p},\theta}})'\mathrm{e}^{\mathrm{i}k\boldsymbol{\zeta}\cdot\boldsymbol{p}(t)}|\boldsymbol{p}'(t)|\,\mathrm{d}t\,, \tag{5.61b}$$

$${K^{(3),\mu}_{\boldsymbol{p},\theta;\boldsymbol{h},\phi}}'(\widehat{\boldsymbol{x}},\boldsymbol{\zeta}) \;=\; \int_0^1 \mathrm{e}^{-\mathrm{i}k\widehat{\boldsymbol{x}}\cdot\boldsymbol{p}(t)}(\widehat{\boldsymbol{x}}\times\mathbb{I}_3)\mathbb{M}^{\mu}_{\boldsymbol{p},V_{\boldsymbol{p},\theta}}\mathrm{i}k(\boldsymbol{\zeta}\cdot\boldsymbol{h}(t))\mathrm{e}^{\mathrm{i}k\boldsymbol{\zeta}\cdot\boldsymbol{p}(t)}|\boldsymbol{p}'(t)|\,\mathrm{d}t\,, \tag{5.61c}$$

$${K^{(4),\mu}_{\boldsymbol{p},\theta;\boldsymbol{h},\phi}}'(\widehat{\boldsymbol{x}},\boldsymbol{\zeta}) \;=\; \int_0^1 \mathrm{e}^{-\mathrm{i}k\widehat{\boldsymbol{x}}\cdot\boldsymbol{p}(t)}(\widehat{\boldsymbol{x}}\times\mathbb{I}_3)\mathbb{M}^{\mu}_{\boldsymbol{p},V_{\boldsymbol{p},\theta}}\mathrm{e}^{\mathrm{i}k\boldsymbol{\zeta}\cdot\boldsymbol{p}(t)}\frac{\boldsymbol{p}'(t)\cdot\boldsymbol{h}'(t)}{|\boldsymbol{p}'(t)|}\,\mathrm{d}t \tag{5.61d}$$

and

$$K^{(1),\varepsilon}_{\boldsymbol{p},\theta;\boldsymbol{h},\phi}{}'(\widehat{\boldsymbol{x}},\boldsymbol{\zeta}) = \int_0^1 -\mathrm{i}k(\widehat{\boldsymbol{x}}\cdot\boldsymbol{h}(t)\mathrm{e}^{-\mathrm{i}k\widehat{\boldsymbol{x}}\cdot\boldsymbol{p}(t)}((\widehat{\boldsymbol{x}}\times\mathbb{I}_3)\times\widehat{\boldsymbol{x}})\mathbb{M}^{\varepsilon}_{\boldsymbol{p},V_{\boldsymbol{p},\theta}}\mathrm{e}^{\mathrm{i}k\boldsymbol{\zeta}\cdot\boldsymbol{p}(t)}|\boldsymbol{p}'(t)|\,\mathrm{d}t\,, \tag{5.62a}$$

$$K^{(2),\varepsilon}_{\boldsymbol{p},\theta;\boldsymbol{h},\phi}{}'(\widehat{\boldsymbol{x}},\boldsymbol{\zeta}) = \int_0^1 \mathrm{e}^{-\mathrm{i}k\widehat{\boldsymbol{x}}\cdot\boldsymbol{p}(t)}((\widehat{\boldsymbol{x}}\times\mathbb{I}_3)\times\widehat{\boldsymbol{x}})(\mathbb{M}^{\varepsilon}_{\boldsymbol{p},V_{\boldsymbol{p},\theta}})'\mathrm{e}^{\mathrm{i}k\boldsymbol{\zeta}\cdot\boldsymbol{p}(t)}|\boldsymbol{p}'(t)|\,\mathrm{d}t\,, \tag{5.62b}$$

$$K^{(3),\varepsilon}_{\boldsymbol{p},\theta;\boldsymbol{h},\phi}{}'(\widehat{\boldsymbol{x}},\boldsymbol{\zeta}) = \int_0^1 \mathrm{e}^{-\mathrm{i}k\widehat{\boldsymbol{x}}\cdot\boldsymbol{p}(t)}((\widehat{\boldsymbol{x}}\times\mathbb{I}_3)\times\widehat{\boldsymbol{x}})\mathbb{M}^{\varepsilon}_{\boldsymbol{p},V_{\boldsymbol{p},\theta}}\mathrm{i}k(\boldsymbol{\zeta}\cdot\boldsymbol{h}(t))\mathrm{e}^{\mathrm{i}k\boldsymbol{\zeta}\cdot\boldsymbol{p}(t)}|\boldsymbol{p}'(t)|\,\mathrm{d}t\,, \tag{5.62c}$$

$$K^{(4),\varepsilon}_{\boldsymbol{p},\theta;\boldsymbol{h},\phi}{}'(\widehat{\boldsymbol{x}},\boldsymbol{\zeta}) = \int_0^1 \mathrm{e}^{-\mathrm{i}k\widehat{\boldsymbol{x}}\cdot\boldsymbol{p}(t)}((\widehat{\boldsymbol{x}}\times\mathbb{I}_3)\times\widehat{\boldsymbol{x}})\mathbb{M}^{\varepsilon}_{\boldsymbol{p},V_{\boldsymbol{p},\theta}}\mathrm{e}^{\mathrm{i}k\boldsymbol{\zeta}\cdot\boldsymbol{p}(t)}\frac{\boldsymbol{p}'(t)\cdot\boldsymbol{h}'(t)}{|\boldsymbol{p}'(t)|}\,\mathrm{d}t\,. \tag{5.62d}$$

In what follows, we denote by $K^{i,:}$ the ith row of the kernel K. Using the complete orthonormal system of vector spherical harmonics from (2.16), we obtain that

$$\begin{aligned}
&\|\boldsymbol{T}_\rho(\boldsymbol{p}+\boldsymbol{h},V_{\boldsymbol{p}+\boldsymbol{h},\theta+\phi})-\boldsymbol{T}_\rho(\boldsymbol{p},V_{\boldsymbol{p},\theta})-\boldsymbol{T}'_\rho[\boldsymbol{p},V_{\boldsymbol{p},\theta}](\boldsymbol{h},\phi)\|^2_{\mathrm{HS}}\\
&=\sum_{n=1}^{\infty}\sum_{m=-n}^{n}\Big(\|(\boldsymbol{T}_\rho(\boldsymbol{p}+\boldsymbol{h},V_{\boldsymbol{p}+\boldsymbol{h},\theta+\phi})-\boldsymbol{T}_\rho(\boldsymbol{p},V_{\boldsymbol{p},\theta})-\boldsymbol{T}'_\rho[\boldsymbol{p},V_{\boldsymbol{p},\theta}](\boldsymbol{h},\phi))\boldsymbol{U}^m_n\|^2_{(L^2(S^2))^3}\\
&\qquad+\|(\boldsymbol{T}_\rho(\boldsymbol{p}+\boldsymbol{h},V_{\boldsymbol{p}+\boldsymbol{h},\theta+\phi})-\boldsymbol{T}_\rho(\boldsymbol{p},V_{\boldsymbol{p},\theta})-\boldsymbol{T}'_\rho[\boldsymbol{p},V_{\boldsymbol{p},\theta}](\boldsymbol{h},\phi))\boldsymbol{V}^m_n\|^2_{(L^2(S^2))^3}\Big)\\
&=\int_{S^2}\sum_{n=1}^{\infty}\sum_{m=-n}^{n}\Big(\Big|\int_{S^2}(K_{\boldsymbol{p}+\boldsymbol{h},\theta+\phi}-K_{\boldsymbol{p},\theta}-K'_{\boldsymbol{p},\theta;\boldsymbol{h},\phi})(\boldsymbol{\zeta},\widehat{\boldsymbol{x}})\boldsymbol{U}^m_n(\widehat{\boldsymbol{x}})\,\mathrm{d}s(\widehat{\boldsymbol{x}})\Big|^2\\
&\qquad+\Big|\int_{S^2}(K_{\boldsymbol{p}+\boldsymbol{h},\theta+\phi}-K_{\boldsymbol{p},\theta}-K'_{\boldsymbol{p},\theta;\boldsymbol{h},\phi})(\boldsymbol{\zeta},\widehat{\boldsymbol{x}})\boldsymbol{V}^m_n(\widehat{\boldsymbol{x}})\,\mathrm{d}s(\widehat{\boldsymbol{x}})\Big|^2\Big)\,\mathrm{d}s(\boldsymbol{\zeta})\\
&=\int_{S^2}\sum_{n=1}^{\infty}\sum_{m=-n}^{n}\sum_{i=1}^{3}\Big(\Big|\Big\langle(K^{i,:}_{\boldsymbol{p}+\boldsymbol{h},\theta+\phi}-K^{i,:}_{\boldsymbol{p},\theta}-K'^{i,:}_{\boldsymbol{p},\theta;\boldsymbol{h},\phi})^\top(\boldsymbol{\zeta},\cdot),\overline{\boldsymbol{U}^m_n}\Big\rangle_{(L^2(S^2))^3}\Big|^2\\
&\qquad+\Big|\Big\langle(K^{i,:}_{\boldsymbol{p}+\boldsymbol{h},\theta+\phi}-K^{i,:}_{\boldsymbol{p},\theta}-K'^{i,:}_{\boldsymbol{p},\theta;\boldsymbol{h},\phi})^\top(\boldsymbol{\zeta},\cdot),\overline{\boldsymbol{V}^m_n}\Big\rangle_{(L^2(S^2))^3}\Big|^2\Big)\,\mathrm{d}s(\boldsymbol{\zeta})\\
&\le\int_{S^2}\sum_{i=1}^{3}\|(K^{i,:}_{\boldsymbol{p}+\boldsymbol{h},\theta+\phi}-K^{i,:}_{\boldsymbol{p},\theta}-K'^{i,:}_{\boldsymbol{p},\theta;\boldsymbol{h},\phi})^\top(\boldsymbol{\zeta},\cdot)\|^2_{(L^2(S^2))^3}\,\mathrm{d}s(\boldsymbol{\zeta})\\
&=\int_{S^2}\int_{S^2}\|(K_{\boldsymbol{p}+\boldsymbol{h},\theta+\phi}-K_{\boldsymbol{p},\theta}-K'_{\boldsymbol{p},\theta;\boldsymbol{h},\phi})(\boldsymbol{\zeta},\widehat{\boldsymbol{x}})\|^2_F\,\mathrm{d}s(\widehat{\boldsymbol{x}})\,\mathrm{d}s(\boldsymbol{\zeta})\,.
\end{aligned}$$

Here, $\|\cdot\|_F$ denotes the Frobenius norm on $\mathbb{C}^{3\times3}$. The inequality in the computation above arises since the rows in the kernels are not tangential. In the same way as in the proof of Theorem 4.4, i.e. by applying Taylor's theorem as in (4.16a) and (4.16b) and by using Theorem 5.14, we find by using (5.60) - (5.62) that

$$\|(K_{\boldsymbol{p}+\boldsymbol{h},\theta+\phi}-K_{\boldsymbol{p},\theta}-K'_{\boldsymbol{p},\theta;\boldsymbol{h},\phi})(\boldsymbol{\zeta},\widehat{\boldsymbol{x}})\|_F\le C\,\|(\boldsymbol{h},\phi)\|^2_{C^3\times C^2}\,.$$

This implies (5.58). □

In Lemma 5.7 we gave an explicit representation of the operator $\mathcal{T}_{D_\rho}$ in terms of the circularly polarized vector spherical harmonics $\boldsymbol{A}^m_n$ and $\boldsymbol{B}^m_n$, $m=-n,\dots,m$, $n=1,2,\dots$, from (5.28). In the following remark we establish a similar representation for the Fréchet derivative $\boldsymbol{T}'_\rho[\boldsymbol{p},V_{\boldsymbol{p},\theta}](\boldsymbol{h},\phi)$.

Remark 5.16. Let $\boldsymbol{A}\in L^2_t(S^2)$ with

$$\boldsymbol{A}=\sum_{n=1}^{\infty}\sum_{m=-n}^{n}(a^m_n\boldsymbol{A}^m_n+b^m_n\boldsymbol{B}^m_n)\,.$$

Then, we find that

$$(\boldsymbol{T}'_\rho[\boldsymbol{p}, V_{\boldsymbol{p},\theta}](\boldsymbol{h},\phi))\boldsymbol{A} = \sum_{n=1}^{\infty}\sum_{m=-n}^{n}(c_n^m \boldsymbol{A}_n^m + d_n^m \boldsymbol{B}_n^m)\,. \tag{5.63}$$

with

$$c_n^m = \sum_{n'=1}^{\infty}\sum_{m'=-n'}^{n'}\Big(a_{n'}^{m'}\langle(\boldsymbol{T}'_\rho[\boldsymbol{p}, V_{\boldsymbol{p},\theta}](\boldsymbol{h},\phi))\boldsymbol{A}_{n'}^{m'}, \boldsymbol{A}_n^m\rangle_{L_t^2(S^2)} + b_{n'}^{m'}\langle(\boldsymbol{T}'_\rho[\boldsymbol{p}, V_{\boldsymbol{p},\theta}](\boldsymbol{h},\phi))\boldsymbol{B}_{n'}^{m'}, \boldsymbol{A}_n^m\rangle_{L_t^2(S^2)}\Big)\,, \tag{5.64a}$$

$$d_n^m = \sum_{n'=1}^{\infty}\sum_{m'=-n'}^{n'}\Big(a_{n'}^{m'}\langle(\boldsymbol{T}'_\rho[\boldsymbol{p}, V_{\boldsymbol{p},\theta}](\boldsymbol{h},\phi))\boldsymbol{A}_{n'}^{m'}, \boldsymbol{B}_n^m\rangle_{L_t^2(S^2)} + b_{n'}^{m'}\langle(\boldsymbol{T}'_\rho[\boldsymbol{p}, V_{\boldsymbol{p},\theta}](\boldsymbol{h},\phi))\boldsymbol{B}_{n'}^{m'}, \boldsymbol{B}_n^m\rangle_{L_t^2(S^2)}\Big)\,. \tag{5.64b}$$

The inner products in (5.64) can be evaluated explicitly using (5.56)-(5.57), the identities (5.38), (5.39), (5.40) and the terms

$$(\boldsymbol{E}^i[\boldsymbol{A}_n^m])'(\boldsymbol{x}) = \sqrt{8}\pi \mathrm{i}^{n-1}(\boldsymbol{P}_n^m)'(\boldsymbol{x})\,, \tag{5.65a}$$
$$(\boldsymbol{E}^i[\boldsymbol{B}_n^m])'(\boldsymbol{x}) = -\sqrt{8}\pi \mathrm{i}^{n-1}(\boldsymbol{Q}_n^m)'(\boldsymbol{x})\,, \tag{5.65b}$$
$$(\mathbf{curl}\,\boldsymbol{E}^i[\boldsymbol{A}_n^m])'(\boldsymbol{x}) = \sqrt{8}\pi k \mathrm{i}^{n-1}(\boldsymbol{P}_n^m)'(\boldsymbol{x})\,, \tag{5.65c}$$
$$(\mathbf{curl}\,\boldsymbol{E}^i[\boldsymbol{B}_n^m])'(\boldsymbol{x}) = \sqrt{8}\pi k \mathrm{i}^{n-1}(\boldsymbol{Q}_n^m)'(\boldsymbol{x}) \tag{5.65d}$$

and

$$\langle \mathrm{i}k(\widehat{\boldsymbol{x}}\cdot\boldsymbol{h})\,\mathrm{e}^{-\mathrm{i}k\widehat{\boldsymbol{y}}\cdot\boldsymbol{x}}(\widehat{\boldsymbol{y}}\times\mathbb{I}_3)\times\widehat{\boldsymbol{y}}), \boldsymbol{A}_n^m(\widehat{\boldsymbol{y}})\rangle_{L_t^2(S^2)} = \sqrt{8}\pi(-\mathrm{i})^{n-1}\overline{(\boldsymbol{P}_n^m)'(\boldsymbol{x})\boldsymbol{h}}^{\top}, \tag{5.66a}$$
$$\langle \mathrm{i}k(\widehat{\boldsymbol{x}}\cdot\boldsymbol{h})\,\mathrm{e}^{-\mathrm{i}k\widehat{\boldsymbol{y}}\cdot\boldsymbol{x}}(\widehat{\boldsymbol{y}}\times\mathbb{I}_3)\times\widehat{\boldsymbol{y}}), \boldsymbol{B}_n^m(\widehat{\boldsymbol{y}})\rangle_{L_t^2(S^2)} = -\sqrt{8}\pi(-\mathrm{i})^{n-1}\overline{(\boldsymbol{Q}_n^m)'(\boldsymbol{x})\boldsymbol{h}}^{\top}, \tag{5.66b}$$
$$\langle \mathrm{i}k(\widehat{\boldsymbol{x}}\cdot\boldsymbol{h})\,\mathrm{e}^{-\mathrm{i}k\widehat{\boldsymbol{y}}\cdot\boldsymbol{x}}(\widehat{\boldsymbol{y}}\times\mathbb{I}_3), \boldsymbol{A}_n^m(\widehat{\boldsymbol{y}})\rangle_{L_t^2(S^2)} = \sqrt{8}\pi(-\mathrm{i})^{n}\overline{(\boldsymbol{P}_n^m)'(\boldsymbol{x})\boldsymbol{h}}^{\top}, \tag{5.66c}$$
$$\langle \mathrm{i}k(\widehat{\boldsymbol{x}}\cdot\boldsymbol{h})\,\mathrm{e}^{-\mathrm{i}k\widehat{\boldsymbol{y}}\cdot\boldsymbol{x}}(\widehat{\boldsymbol{y}}\times\mathbb{I}_3), \boldsymbol{B}_n^m(\widehat{\boldsymbol{y}})\rangle_{L_t^2(S^2)} = \sqrt{8}\pi(-\mathrm{i})^{n}\overline{(\boldsymbol{Q}_n^m)'(\boldsymbol{x})\boldsymbol{h}}^{\top}. \tag{5.66d}$$

Explicit formulas for the derivatives $(\boldsymbol{P}_n^m)'$ and $(\boldsymbol{Q}_n^m)'$ of the circularly polarized spherical vector wave functions $(\boldsymbol{P}_n^m)$ and $(\boldsymbol{Q}_n^m)$, $m = -n,\dots,n$, $n = 1,2,\dots$, from (5.29) can be found in Appendix D.

Remark 5.17. As for $\boldsymbol{T}_\rho$ we choose the maximal degree of vector spherical harmonics $N \in \mathbb{N}$ in such a way that $N \gtrsim kR$, where $B_R(0)$ denotes the smallest ball around the origin that includes the scattering object D_ρ (see Remark 5.9). This gives a discretization of the Fréchet derivative $\boldsymbol{T}'_{\rho,N} = \boldsymbol{T}'_{\rho,N}[\boldsymbol{p}, V_{\boldsymbol{p},\theta}](\boldsymbol{h},\phi)$, which is given by

$$\boldsymbol{T}'_{\rho,N} = \begin{bmatrix}(\boldsymbol{A}\boldsymbol{A})' & (\boldsymbol{B}\boldsymbol{A})'\\ (\boldsymbol{A}\boldsymbol{B})' & (\boldsymbol{B}\boldsymbol{B})'\end{bmatrix} \tag{5.67}$$

with

$$(\boldsymbol{X}\boldsymbol{Y})' = \begin{bmatrix}\langle\boldsymbol{T}'_{\rho,N}\boldsymbol{X}_1^{-1},\boldsymbol{Y}_1^{-1}\rangle & \langle\boldsymbol{T}'_{\rho,N}\boldsymbol{X}_1^{0},\boldsymbol{Y}_1^{-1}\rangle & \cdots & \cdots & \langle\boldsymbol{T}'_{\rho,N}\boldsymbol{X}_N^{N},\boldsymbol{Y}_1^{-1}\rangle\\ \langle\boldsymbol{T}'_{\rho,N}\boldsymbol{X}_1^{-1},\boldsymbol{Y}_1^{0}\rangle & \langle\boldsymbol{T}'_{\rho,N}\boldsymbol{X}_1^{0},\boldsymbol{Y}_1^{0}\rangle & \ddots & \iddots & \vdots\\ \vdots & \ddots & \ddots & \iddots & \\ & \iddots & \iddots & \ddots & \langle\boldsymbol{T}'_{\rho,N}\boldsymbol{X}_N^{N},\boldsymbol{Y}_N^{N-1}\rangle\\ \langle\boldsymbol{T}'_{\rho,N}\boldsymbol{X}_1^{-1},\boldsymbol{Y}_N^{N}\rangle & \cdots & \cdots & \langle\boldsymbol{T}'_{\rho,N}\boldsymbol{X}_N^{N-1},\boldsymbol{Y}_N^{N}\rangle & \langle\boldsymbol{T}'_{\rho,N}\boldsymbol{X}_N^{N},\boldsymbol{Y}_N^{N}\rangle\end{bmatrix} \tag{5.68}$$

for $\boldsymbol{X}, \boldsymbol{Y} \in \{\boldsymbol{A}, \boldsymbol{B}\}$. The scalar products in (5.68) are explicitly given by combining (5.55)-(5.57) with (5.65) and (5.66). A single block $(\boldsymbol{XY})'$ has dimension $Q' \times Q'$ with $Q' = N(N+2)$ and consequently, $\boldsymbol{T}'_{\rho,N} \in \mathbb{C}^{2Q' \times 2Q'}$.

5.4 Remarks on the implementation

We discuss the implementation of the discretized operators $\boldsymbol{T}'_{\rho,N}$ from (5.67). The matrix $\mathcal{T}_{\rho,N}$ from (5.41) can be implemented by using the same techniques. Considering the structure of $\boldsymbol{T}'_{\rho,N}$ shows that the matrix consists of four blocks $(\boldsymbol{XY})'$ for $\boldsymbol{X}, \boldsymbol{Y} \in \{\boldsymbol{A}, \boldsymbol{B}\}$, where $\boldsymbol{A}_n^m$ and $\boldsymbol{B}_n^m$ denote the circularly polarized vector spherical harmonics from (5.28). The block $(\boldsymbol{XY})'$ corresponds to evaluations of (5.55) using the incoming field $\boldsymbol{E}^i[\boldsymbol{X}_n^m]$, $m = -n, \dots, n$, $n = 1, 2, \dots$, together with the field $\boldsymbol{Y}_{n'}^{m'}$ in the scalar product, where $m' = -n', \dots, n'$, $n' = 1, 2, \dots$. Moreover, the block $(\boldsymbol{XY})'$ can be split up via

$$(\boldsymbol{XY})' = (\boldsymbol{XY})'_1 + (\boldsymbol{XY})'_2,$$

where $(\boldsymbol{XY})'_1$ results from the ε-terms and $(\boldsymbol{XY})'_2$ results from the μ-terms in (5.55). Once more, these blocks can be split up into 4 blocks, respectively, using the terms from (5.56) and (5.57). This gives that

$$(\boldsymbol{XY})'_j = \sum_{\ell=1}^{4} (\boldsymbol{XY})'_{j,\ell} \quad \text{for } j = 1, 2.$$

The entries of the matrix $(\boldsymbol{XY})'_{j,\ell}$, $j = 1, 2$, consist of a scalar product of the integrals in (5.56) and (5.57), together with circularly polarized vector spherical harmonics. A single integral term consists of four parts. Disregarding derivatives, these four parts are a scalar product term $\mathcal{S}$, a polarization tensor $\mathcal{P}$, an incoming field $\mathcal{I}$ and the norm of the derivative of the parametrization. For discretizing curves and applying the composite Simpson's rule for approximating integrals we refer to Remark 3.28. In the following we recall this approach. We use $n \in \mathbb{N}$ points to represent the curves by a cubic spline with the not-a-knot condition at the end points. For a partition $\triangle$ as in (3.125), we define the corresponding cubic not-a-knot spline by $\boldsymbol{p}_\triangle$. To compute the integrals in (5.56) and (5.57) we further define the odd number $M \in \mathbb{N}$, $M \geq 3$, and discretize each interval $[t_j, t_{j+1}]$ defined by the partition (3.125) in M equidistant points, including the end points. Loosely speaking, the number n determines the accuracy of the discretized curve, M on the other hand determines the accuracy of the quadrature formula, which we use to approximate the integrals. Altogether, to evaluate an integral from (5.56) or (5.57), we take the weighted sum over $T = (n-1)(M-1)+1$ non-repeating points. We arrange these points on the spline in the order, in which they are passed through as we go from the start to the end of the spline and denote the points by $\boldsymbol{x}_\tau = \boldsymbol{p}_\triangle(t_\tau)$ for $\tau = 1, \dots, T$. This means that the first point of the spline, which is denoted by $\boldsymbol{x}_1 = \boldsymbol{x}^{(1)}$, is the start of the spline, $\boldsymbol{x}_T = \boldsymbol{x}^{(n)}$ on the other hand, corresponds to the end. In what follows, we consider the implementation of a single $(\boldsymbol{XY})'_{j,\ell}$ in detail. We abbreviate by $\mathcal{S}, \mathcal{P}$ and $\mathcal{I}$ the functions corresponding to the scalar product, the polarization tensor and the incoming field, respectively. In our implementation, we handle these functions as tensors

$$\mathcal{S} \in \mathbb{C}^{Q \times 3 \times T}, \quad \mathcal{P} \in \mathbb{C}^{3 \times 3 \times T}, \quad \mathcal{I} \in \mathbb{C}^{3 \times Q \times T}.$$

Here, the number $Q = N(N+2)$ is the total number of entire wave field functions in each block. We define the mapping

$$\star : \mathbb{R}^{\alpha \times \beta \times \gamma} \times \mathbb{R}^{\beta \times \delta \times \gamma} \to \mathbb{R}^{\alpha \times \delta \times \gamma}, \quad (\mathcal{A} \star \mathcal{B})_{ijk} = \sum_{z=1}^{\beta} a_{izk} b_{zjk},$$

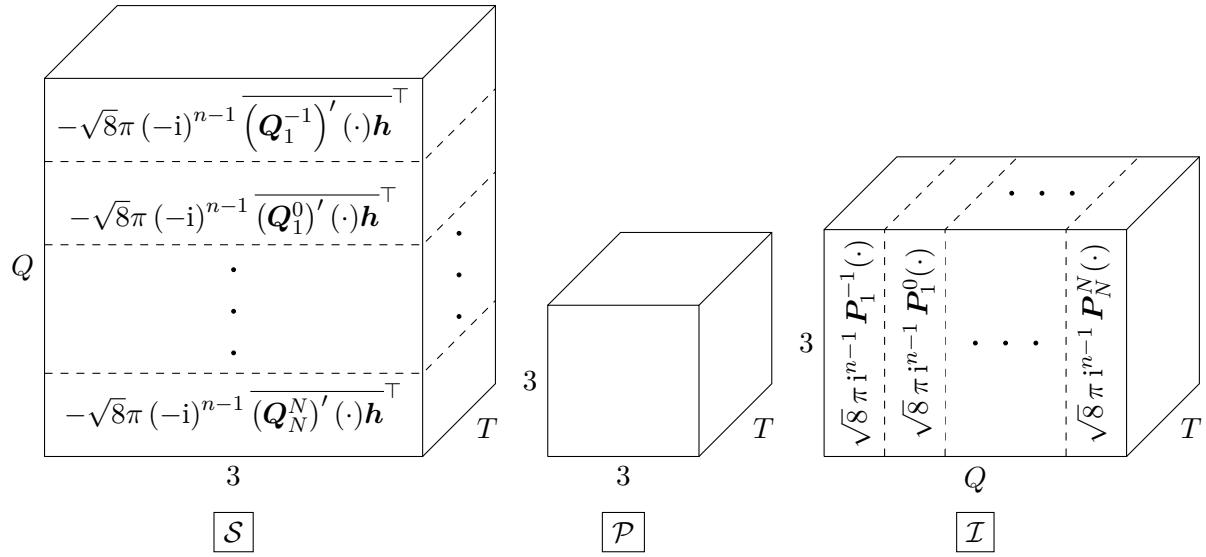

Figure 5.3: Sketch of the structure of the blocks $\mathcal{S}, \mathcal{P}$ and $\mathcal{I}$ that are required to implement the matrix $(\boldsymbol{AB})'_{1,1}$. The third dimension T corresponds to the number of points, including the quadrature points, that represent the cubic spline.

which is the usual matrix product along every slice in the third dimension. Combining the weights of the quadrature formula from Remark 3.28 with the norm of the derivative in the vector W gives that an integral in (5.56) or (5.57) can be approximated blockwise by

$$\sum_{\tau=1}^{T} W(\tau)\,(\mathcal{S} \star \mathcal{P} \star \mathcal{I})_{ij\tau} \quad \text{for } i,j = 1,\dots,Q.$$

For a better overview about the structure of $\mathcal{S}, \mathcal{P}$ and $\mathcal{I}$ we consider the sketch in Figure 5.3, where we visualized the assignment of the blocks $\mathcal{S}, \mathcal{I}$ for the matrix $(\boldsymbol{AB})'_{1,1}$. For this example, as we have to evaluate the entries $\langle (\boldsymbol{T}'_{\rho,\varepsilon,1}[\boldsymbol{p}, V_{\boldsymbol{p},\theta}](\boldsymbol{h},\phi))\boldsymbol{A}_n^m, \boldsymbol{B}_{n'}^{m'} \rangle$ for $m = -n,\dots,n$, $n = 1,2,\dots$, and $m' = -n',\dots,n'$, $n' = 1,2,\dots$ according to (5.66b) and (5.38a), we define

$$\mathcal{S}(q,:,\tau) = -\sqrt{8}\pi\,(-\mathrm{i})^{n-1}\,\overline{(\boldsymbol{Q}_n^m)'(\boldsymbol{x}_\tau)\boldsymbol{h}}^{\top}, \quad \mathcal{P}(:,:,\tau) = \mathbb{M}^{\varepsilon}_{\boldsymbol{p},V_{\boldsymbol{p},\theta}}(\boldsymbol{x}_\tau), \quad \mathcal{I}(:,q,\tau) = \sqrt{8}\pi\mathrm{i}^{n-1}\boldsymbol{P}_n^m(\boldsymbol{x}_\tau),$$

where $q = n(n+1)+m$.

5.5 The BFGS scheme for the regularized optimization problem

In the last sections the quantification of em-chirality for a scatterer D_ρ as in (3.7) based on the leading order term of the asymptotic perturbation formula is discussed (see Lemma 5.7). Moreover, the shape derivative of the curve and rotation to leading order term map is established (see Theorem 5.15). Now, we combine these results to construct a BFGS method for an efficient shape optimization. As for the reconstruction algorithm in Chapter 4, we emphasize that the optimization scheme does not require a single Maxwell system to be solved.

We develop a shape optimization scheme to determine dielectric and metallic thin tubular scattering objects D_ρ as in (3.7) that exhibit comparatively large measures of em-chirality χ_{HS} at a given frequency. In addition to the frequency, we also fix the material parameters ε_r, μ_r and the length $|K|$ of the center curve K of D_ρ before we start the optimization process. Furthermore, we assume that the radius $\rho > 0$ of the cross-section $D'_\rho = \rho D'$ is sufficiently small with respect to the wavelength of the incident fields, such that the leading order term $\boldsymbol{T}_\rho$ of the asymptotic expansion (5.45) gives a good approximation of the far field operator $\mathcal{F}_{D_\rho}$ (see also Section 3.5).

Combining (5.19) with (5.22) gives that the smooth relaxation χ_{HS} of the chirality measure χ_2 satisfies

$$\chi_{\mathrm{HS}}(\mathcal{G}) \leq \|\mathcal{G}\|_{\mathrm{HS}} \quad \text{for any } \mathcal{G} \in \mathrm{HS}(L^2_t(S^2)).$$

Accordingly, recalling the definition of the nonlinear operator $\boldsymbol{T}_\rho$ in (5.45), we normalize the smooth relaxiation χ_{HS} and consider the bounded objective functional $J_{\mathrm{HS}} : \mathcal{U}_{\mathrm{ad}} \to [0,1]$, which is given by

$$J_{\mathrm{HS}}(\boldsymbol{p}_\Gamma, \theta) = \frac{\chi_{\mathrm{HS}}\left(\boldsymbol{T}_\rho(\boldsymbol{p}_\Gamma, V_{\boldsymbol{p},\theta})\right)}{\|\boldsymbol{T}_\rho(\boldsymbol{p}_\Gamma, V_{\boldsymbol{p},\theta})\|_{\mathrm{HS}}}. \tag{5.69}$$

Furthermore, we introduce the relative chirality measure

$$J_2(\boldsymbol{p}_\Gamma, \theta) = \frac{\chi_2(\boldsymbol{T}_\rho(\boldsymbol{p}_\Gamma, V_{\boldsymbol{p},\theta}))}{\|\boldsymbol{T}_\rho(\boldsymbol{p}_\Gamma, V_{\boldsymbol{p},\theta})\|_{\mathrm{HS}}}, \tag{5.70}$$

which uses the original chirality measure χ_2 from (5.18) instead of χ_{HS}. Both functionals, J_2 and J_{HS} attain their maximal value 1 for a maximally em-chiral nanowire and their minimal value 0 for an em-achiral object. Since J_2 is not differentiable and hence less suitable for a gradient based optimization, we focus on maximizing the nonlinear functional J_{HS} in the following. Accordingly, the optimization problem is to

$$\text{find} \quad \operatorname*{arg\,min}_{(\boldsymbol{p},V_{\boldsymbol{p},\theta})\in\mathcal{U}_{\mathrm{ad}}} \left(-J_{\mathrm{HS}}(\boldsymbol{p}, V_{\boldsymbol{p},\theta})\right) \quad \text{subject to} \quad |K| = L \tag{5.71}$$

at some prescribed frequency f_{opt}, for some fixed rescaled cross-section $D' = D'_\rho/\rho \subset B'_1(0) \subset \mathbb{R}^2$, and for some prescribed length $L > 0$ of the thin tubular object. In all our numerical experiments, we present the values of J_2 for comparison (e.g. with the results from [62]).

Remark 5.18. It is important to observe that for $\boldsymbol{A} \in L^2_t(S^2)$ the electric far field pattern $\mathcal{T}_{D_\rho}\boldsymbol{A}$ from (5.25) is homogeneous with respect to the squared radius ρ^2 of the cross-section $D'_\rho = \rho D'$ of the support of the thin nanowire. Thus, the same is true for $\chi_2(\boldsymbol{T}_\rho(\boldsymbol{p}, V_{\boldsymbol{p},\theta}))$, $\chi_{\mathrm{HS}}(\boldsymbol{T}_\rho(\boldsymbol{p}, V_{\boldsymbol{p},\theta}))$ and $\|\boldsymbol{T}_\rho(\boldsymbol{p}, V_{\boldsymbol{p},\theta})\|_{\mathrm{HS}}$ with $(\boldsymbol{p}, V_{\boldsymbol{p},\theta}) \in \mathcal{U}_{\mathrm{ad}}$. In particular, the rescaled em-chirality measures $J_2(\boldsymbol{p}, V_{\boldsymbol{p},\theta})$ and $J_{\mathrm{HS}}(\boldsymbol{p}, V_{\boldsymbol{p},\theta})$ from (5.70) and (5.69) are independent of ρ. This means that the specific value of ρ does not affect the result of the optimization procedure considered below. However, in order for the leading order term $\mathcal{T}_{D_\rho}$ in (5.25) to be an acceptable approximation of $\mathcal{F}_{D_\rho}$, the radius ρ of the cross-section D'_ρ of the thin nanowire has to be sufficiently small.

It has been shown in [72, Lem. 5.15] that the smooth relaxation χ_{HS} is differentiable on

$$X = \left\{ \mathcal{G} \in \mathrm{HS}(L^2_t(S^2)) \mid \chi_{\mathrm{HS}}(\mathcal{G}) \neq 0 \text{ and } \|\mathcal{G}^{pq}\|_{\mathrm{HS}} > 0,\ p,q \in \{+,-\} \right\}. \tag{5.72}$$

We derive the Fréchet derivative in the next lemma.

Lemma 5.19. *For a given $\mathcal{G} \in X$, the Fréchet derivative of χ_{HS} from (5.21) is given by $(\chi_{\mathrm{HS}})'[\mathcal{G}] : \mathrm{HS}(L^2_t(S^2)) \to \mathbb{R}$ with*

$$(\chi_{\mathrm{HS}})'[\mathcal{G}]\,\mathcal{H} = \frac{\mathrm{Re}\langle \mathcal{G}, \mathcal{H}\rangle_{\mathrm{HS}} - \sum_{p,q\in\{+,-\}} \mathrm{Re}\langle \mathcal{G}^{pq}, \mathcal{H}^{pq}\rangle_{\mathrm{HS}} \frac{\|\mathcal{G}^{\overline{pq}}\|_{\mathrm{HS}}}{\|\mathcal{G}^{pq}\|_{\mathrm{HS}}}}{\chi_{\mathrm{HS}}(\mathcal{G})}, \tag{5.73}$$

where $\overline{p} = -p$ and $\overline{q} = -q$. Accordingly, the Fréchet derivative of the objective functional J_{HS} satisfies

$$\begin{aligned} J'_{\mathrm{HS}}[\boldsymbol{p}, V_{\boldsymbol{p},\theta}](\boldsymbol{h},\phi) = {} & \frac{(\chi_{\mathrm{HS}})'\left[\boldsymbol{T}_\rho(\boldsymbol{p}, V_{\boldsymbol{p},\theta})\right](\boldsymbol{T}'_\rho[\boldsymbol{p}, V_{\boldsymbol{p},\theta}](\boldsymbol{h},\phi))}{\|\boldsymbol{T}_\rho(\boldsymbol{p}, V_{\boldsymbol{p},\theta})\|_{\mathrm{HS}}} \\ & - \frac{\chi_{\mathrm{HS}}\left(\boldsymbol{T}_\rho(\boldsymbol{p}, V_{\boldsymbol{p},\theta})\right) \mathrm{Re}\langle \boldsymbol{T}_\rho(\boldsymbol{p}, V_{\boldsymbol{p},\theta}), \boldsymbol{T}'_\rho[\boldsymbol{p}, V_{\boldsymbol{p},\theta}](\boldsymbol{h},\phi)\rangle_{\mathrm{HS}}}{\|\boldsymbol{T}_\rho(\boldsymbol{p}, V_{\boldsymbol{p},\theta})\|^3_{\mathrm{HS}}}, \end{aligned} \tag{5.74}$$

where $\boldsymbol{T}'_\rho[\boldsymbol{p}, V_{\boldsymbol{p},\theta}](\boldsymbol{h},\phi)$ denotes the Fréchet derivative of the operator $\boldsymbol{T}_\rho$ at $(\boldsymbol{p}, V_{\boldsymbol{p},\theta}) \in \mathcal{U}_{\mathrm{ad}}$ from (5.63).

Proof. The Fréchet derivative of the map $X_0 : X \to \mathbb{R}$, $X_0(\mathcal{G}) = \|\mathcal{G}\|_{\mathrm{HS}}^2$ is given by

$$X_0'[\mathcal{G}] : \mathrm{HS}(L_t^2(S^2)) \to \mathbb{R}\,, \quad X_0'[\mathcal{G}]\mathcal{H} \;=\; 2\,\mathrm{Re}\langle \mathcal{G}, \mathcal{H}\rangle_{\mathrm{HS}}\,, \tag{5.75}$$

since the space $\mathrm{HS}\,(L_t^2(S^2))$ is a Hilbert space. Moreover, we recall that the operators $\mathcal{G}^{pq}$ for $p, q \in \{+,-\}$ are given by $\mathcal{G}^{pq} = \mathcal{P}^p \mathcal{G} \mathcal{P}^q$ (see (5.15) and (5.11)). Hence, it can be seen in the same way that the Fréchet derivative of the map $X_{pq} : X \to \mathbb{R}$, $X_{pq}(\mathcal{G}) = \|\mathcal{G}^{pq}\|_{\mathrm{HS}}^2$ is given by

$$X_{pq}'[\mathcal{G}] : \mathrm{HS}(L_t^2(S^2)) \to \mathbb{R}\,, \quad X_{pq}'[\mathcal{G}]\mathcal{H} \;=\; 2\,\mathrm{Re}\langle \mathcal{G}^{pq}, \mathcal{H}^{pq}\rangle_{\mathrm{HS}}\,. \tag{5.76}$$

We use the chain and the product rule and find that the Fréchet derivative of χ_{HS} is given by

$$(\chi_{\mathrm{HS}})'\,[\mathcal{G}]\,\mathcal{H} \;=\; \frac{1}{2\chi_{\mathrm{HS}}(\mathcal{G})}\Big(X_0'[\mathcal{G}]\mathcal{H} - 2 \sum_{p,q\in\{+,-\}} \frac{X_{pq}'[\mathcal{G}]\mathcal{H}}{2(X_{pq}(\mathcal{G}))^{1/2}} (X_{\overline{pq}}(\mathcal{G}))^{1/2} \Big)\,,$$

where $\overline{p} = -p$ and $\overline{q} = -q$. Using (5.75) and (5.76) implies the representation in (5.73). The Fréchet derivative of J_{HS} in (5.74) is obtained by applying the chain and product rule, as before. □

Before we establish the optimization scheme we study a simple example to varify the correctness of the shape derivative from (5.74) numerically and to provide an insight of the functionals J_2 from (5.70) and J_{HS} from (5.69).

Example 5.20. Let the frequency be given by $f = 700\mathrm{THz}$, i.e., the exterior wavelength is $\lambda = 428\mathrm{nm}$. We consider a family of thin metallic nanowires with a circular cross-section and center curves given by the parametrizations $\boldsymbol{p} = (p_1, p_2, p_3)^\top$ with

$$p_1(s) \;=\; R\cos(4\pi s), \quad p_2(s) \;=\; R\sin(4\pi s), \quad p_3(s) \;=\; hs - \frac{h}{2} \qquad \text{for } s \in [0,1]\,, \tag{5.77}$$

where the radius of the cross-section is given by $\rho = 4\mathrm{nm}$. At first, we consider the material parameter for silver, which, by [83], is given by $\varepsilon_r = -5.94 + 0.20\mathrm{i}$ (see also Figure 2.1). In (5.77), we study a fixed exterior radius $R = 30\mathrm{nm}$ and variable height $h \in [100, 600]\mathrm{nm}$. Since h is variable, we denote the corresponding parametrizations from (5.77) by $\boldsymbol{p}_h$. Using J_{HS} from (5.69), we define the operator

$$X_{\mathrm{HS},1} : [100, 600] \to [0,1]\,, \quad X_{\mathrm{HS},1}(h) \;=\; J_{\mathrm{HS}}(\boldsymbol{p}_h)\,, \tag{5.78}$$

which maps the height of the helix parametrized by (5.77) to the values of the relative smooth relaxation. We suppress the dependency on the twist function θ in the definition (5.78) since we consider a circular cross-section for the nanowire and thus, rotations of the cross-section do not change the tubular scatterer. By the chain rule, the derivative of $X_{\mathrm{HS},1}$ is given by

$$X_{\mathrm{HS},1}'(h) \;=\; J_{\mathrm{HS}}'[\boldsymbol{p}_h](\partial_h \boldsymbol{p}_h)\,, \tag{5.79}$$

where J_{HS}' is defined in (5.74) and $\partial_h \boldsymbol{p}_h$ is given by the curve with the parametrization

$$\partial_h p_{h,1}(s) \;=\; 0, \quad \partial_h p_{h,2}(s) \;=\; 0, \quad \partial_h p_{h,3}(s) \;=\; s - \frac{1}{2} \qquad \text{for } s \in [0,1]\,.$$

Note that $\partial_h \boldsymbol{p}_h$ replaces $\boldsymbol{h}$ in (5.74). For $h_j = 100 + 1/2j$, $j = 1, \dots, 1000$, we evaluate the functional $X_{\mathrm{HS},1}$ from (5.78). Moreover, we study the functional $X_{2,1}$, which is defined as in (5.78) with J_{HS} replaced by J_2 from (5.70), where we used the maximal degree of vector spherical harmonics $N = 5$. One the one hand, we study the derivative of $X_{\mathrm{HS},1}$ as in (5.79) for h_j, $j = 1, \dots, 1000$. On the other hand, we apply finite differences to $X_{\mathrm{HS},1}$. We find the result of this simulation in the top-row of Figure 5.4. In the top-left plot we find a visualization of

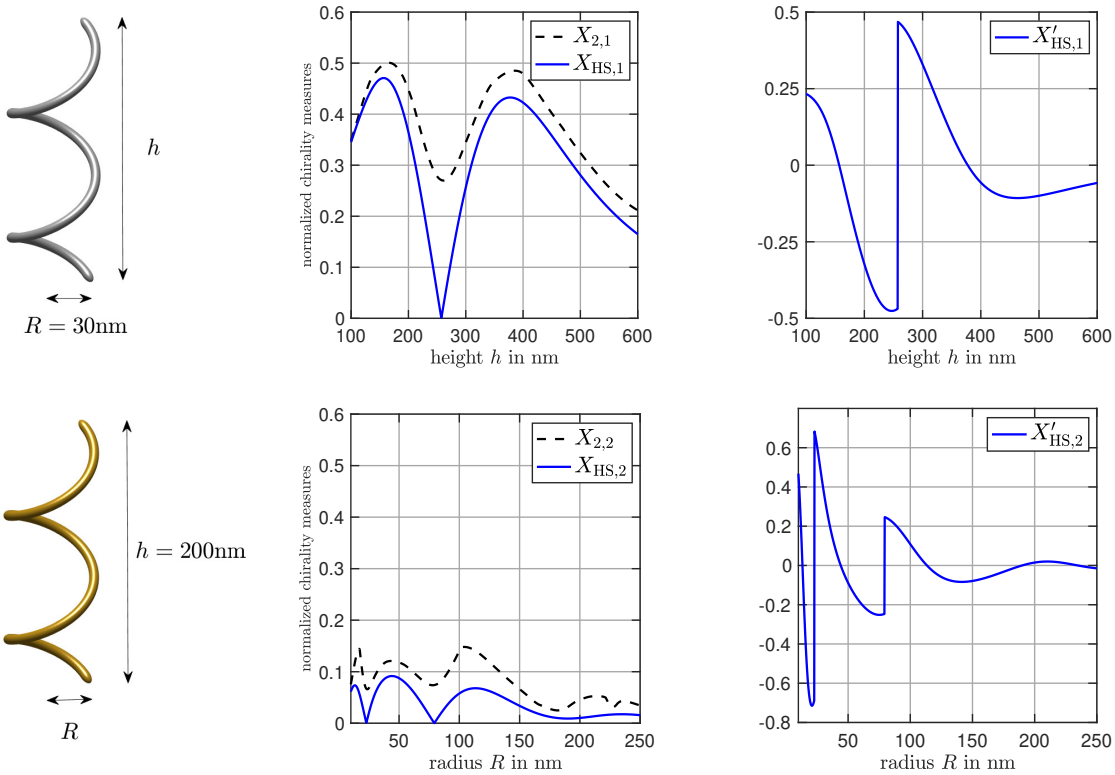

Figure 5.4: Numerical results from Example 5.20. Top-row: Numerical examples corresponding to the silver helix. The top-left plot visualizes the helices having the radius $R = 30\text{nm}$ and a variable height. The top-middle and top-right plots show the functions $X_{2,1}, X_{\mathrm{HS},1}$ and $X'_{\mathrm{HS},1}$, respectively. Bottom-row: Numerical examples corresponding to the gold helix. The bottom-left plot visualizes the helices having the height $R = 200\text{nm}$ and a variable radius. The bottom-middle and bottom-right plots show the functions $X_{2,2}, X_{\mathrm{HS},2}$ and $X'_{\mathrm{HS},2}$, respectively.

the families of thin tubular silver scatterers, which have a fixed exterior radius R, a fixed wire radius ρ and a variable height h. In the top-middle plot we find both functions $X_{2,1}$ and $X_{\mathrm{HS},1}$. The top-right plot features the derivative of $X_{\mathrm{HS},1}$. We find that the function $X_{\mathrm{HS},1}$ vanishes near $h = 257\text{nm}$ although $X_{2,1}$ does not vanish. Moreover, $X_{\mathrm{HS},1}$ is seen to be non-smooth at this point. Note that this does not contradict the smoothness of χ_{HS} in X from (5.72). In the top-right plot we find a jump of the derivative at this point. Excluding this jump point in the comparison of $X'_{\mathrm{HS},1}$ from (5.79) with finite differences gives a relative error of 0.004%.

We return to the parametrization of the double turn helix in (5.77) and consider a second example. Now we use the material parameter corresponding to gold from [83], which is given by $\varepsilon_r = -1.69 + 5.66\mathrm{i}$. We fix the height of the helix to be $h = 200\text{nm}$ and choose the radius R to be variable in the range $R \in [10, 250]\text{nm}$. We study the functions $X_{\mathrm{HS},2}, X_{2,2} : [10, 250] \to [0, 1]$, which differ from $X_{\mathrm{HS},1}, X_{2,1}$ insofar as they map the radius (instead of the height) to the parametrization in (5.77). The results are shown in the bottom-row of Figure 5.4. We observe again, that there are two points (around $R = 23\text{nm}$ and $R = 79\text{nm}$) for which $X_{\mathrm{HS},2}$ vanishes and the derivative jumps. Excluding both jump points in the comparison of $X'_{\mathrm{HS},2}$ with finite differences gives a relative error of 0.21%.

In what follows we rewrite the optimization problem (5.71) as an unconstrained optimization problem and apply a quasi-Newton method to approximate a (local) minimizer. As before, we consider the partition

$$\triangle \;=\; \{0 = t_1 < t_2 < \cdots t_n = 1\} \subset [0, 1].$$

We denote by $\mathcal{S}_\triangle$ and $(\mathcal{S}_\triangle)^3$ the space of one-dimensional and three-dimensional cubic not-a-knot splines with respect to this partition, respectively (see also Remark 3.28).

To evaluate local minimizers of the constrained optimization problem (5.71), we approximate the latter by an unconstrained optimization problem, where we include the length constraint $|K| = L$ via the penalty term

$$\Psi_1 : \mathcal{U}_{\mathrm{ad}} \to \mathbb{R}\,, \qquad \Psi_1(\boldsymbol{p}, V_{\boldsymbol{p},\theta}) \;=\; \sum_{j=1}^{n-1} \left| \frac{1}{n-1} - \frac{1}{L} \int_{t_j}^{t_{j+1}} |\boldsymbol{p}'(t)| \,\mathrm{d}t \right|^2 . \tag{5.80}$$

Besides enforcing the length constraint, this term will also promote uniformly distributed nodes along the spline representing the spine curve during the optimization process.

We use two further regularization terms to stabilize the optimization. The functional

$$\Psi_2 : \mathcal{U}_{\mathrm{ad}} \to \mathbb{R}\,, \qquad \Psi_2(\boldsymbol{p}, V_{\boldsymbol{p},\theta}) \;=\; \frac{1}{L} \int_0^1 \kappa^2(t) |\boldsymbol{p}'(t)| \,\mathrm{d}t\,, \tag{5.81}$$

where κ is the curvature of K parametrized by $\boldsymbol{p}$ given by

$$\kappa(t) \;=\; \frac{|\boldsymbol{p}'(t) \times \boldsymbol{p}''(t)|}{|\boldsymbol{p}'(t)|^3} \;=\; \frac{1}{|\boldsymbol{p}'(t)|} \left| \frac{\boldsymbol{p}''(t)}{|\boldsymbol{p}'(t)|} - \frac{\boldsymbol{p}'(t) \cdot \boldsymbol{p}''(t)}{|\boldsymbol{p}'(t)|^3} \boldsymbol{p}'(t) \right|, \quad t \in [0,1]\,, \tag{5.82}$$

prevents the optimal nanowire from being too strongly entangled. Similarly, the term

$$\Psi_3 : \mathcal{U}_{\mathrm{ad}} \to \mathbb{R}\,, \qquad \Psi_3(\boldsymbol{p}, V_{\boldsymbol{p},\theta}) \;=\; \frac{1}{L} \int_0^1 \beta^2(t) |\boldsymbol{p}'(t)| \,\mathrm{d}t\,, \tag{5.83}$$

where β is the twist rate of the geometry adapted frame $(\boldsymbol{t}_{\boldsymbol{p}}, \boldsymbol{r}_{\boldsymbol{p},\theta}, \mathbf{s}_{\boldsymbol{p},\theta})$ parametrized by $(\boldsymbol{p}, V_{\boldsymbol{p},\theta})$ given by

$$\beta(t) \;=\; \boldsymbol{r}'_{\boldsymbol{p},\theta}(t) \cdot \mathbf{s}_{\boldsymbol{p},\theta}(t), \quad t \in [0,1]\,, \tag{5.84}$$

penalizes strong twisting of the cross-section of the optimal nanowire along its spine curve.

Adding $\alpha_1\Psi_1$, $\alpha_2\Psi_2$, and $\alpha_3\Psi_3$ with some suitable regularization parameters $\alpha_1, \alpha_2, \alpha_3 > 0$ to the objective functional in (5.71), we obtain the regularized objective functional $\Phi : \mathcal{U}_{\mathrm{ad}} \to \mathbb{R}$ given by

$$\Phi(\boldsymbol{p}, V_{\boldsymbol{p},\theta}) \;=\; -J_{\mathrm{HS}}(\boldsymbol{p}, V_{\boldsymbol{p},\theta}) + \alpha_1\Psi_1(\boldsymbol{p}, V_{\boldsymbol{p},\theta}) + \alpha_2\Psi_2(\boldsymbol{p}, V_{\boldsymbol{p},\theta}) + \alpha_3\Psi_3(\boldsymbol{p}, V_{\boldsymbol{p},\theta})\,. \tag{5.85}$$

Accordingly, we consider the unconstrained optimization problem

$$\text{find} \qquad \operatorname*{arg\,min}_{(\boldsymbol{p}, V_{\boldsymbol{p},\theta}) \in \mathcal{U}_{\mathrm{ad}}} \Phi(\boldsymbol{p}, V_{\boldsymbol{p},\theta}). \tag{5.86}$$

Below we apply a quasi-Newton scheme to solve a finite dimensional approximation of (5.86) numerically. In the next lemma we collect the Fréchet derivatives of the penalty terms Ψ_1, Ψ_2, and Ψ_3, which are required by this algorithm.

Lemma 5.21. *The penalty terms Ψ_1, Ψ_2, and Ψ_3 from (5.80)–(5.83) are Fréchet differentiable. Their Fréchet derivatives at $(\boldsymbol{p}, V_{\boldsymbol{p},\theta}) \in \mathcal{U}_{\mathrm{ad}}$ with respect to the local parametrization of $\mathcal{U}_{\mathrm{ad}}$ in (5.46)–(5.48) are given by $\Psi_1'[\boldsymbol{p}, V_{\boldsymbol{p},\theta}] : C^3([0,1], \mathbb{R}^3) \times C^2([0,1], \mathbb{R}) \to \mathbb{R}$ with*[3]

$$\Psi_1'[\boldsymbol{p}, V_{\boldsymbol{p},\theta}](\boldsymbol{h}, \phi) \;=\; \partial_{\boldsymbol{p}}\Psi_1[\boldsymbol{p}, V_{\boldsymbol{p},\theta}](\boldsymbol{h}) \;=\; -\frac{2}{L^2} \sum_{j=1}^{n-1} \left(\int_{t_j}^{t_{j+1}} \frac{\boldsymbol{p}' \cdot \boldsymbol{h}'}{|\boldsymbol{p}'|} \,\mathrm{d}t \right) \left(\frac{L}{n-1} - \int_{t_j}^{t_{j+1}} |\boldsymbol{p}'| \,\mathrm{d}t \right), \tag{5.87}$$

[3] We corrected a $1/L$ term that was missing in the original publication [50].

by $\Psi_2'[\boldsymbol{p}, V_{\boldsymbol{p},\theta}] : C^3([0,1],\mathbb{R}^3) \times C^2([0,1],\mathbb{R}) \to \mathbb{R}$ *with*

$$\Psi_2'[\boldsymbol{p}, V_{\boldsymbol{p},\theta}](\boldsymbol{h},\phi) = \partial_{\boldsymbol{p}}\Psi_2[\boldsymbol{p}, V_{\boldsymbol{p},\theta}](\boldsymbol{h}) = \frac{1}{L}\int_0^1 \Bigg(2\frac{\boldsymbol{p}''\cdot\boldsymbol{h}''}{|\boldsymbol{p}'|^3} - 3\frac{|\boldsymbol{p}''|^2(\boldsymbol{p}'\cdot\boldsymbol{h}')}{|\boldsymbol{p}'|^5} - 2\frac{(\boldsymbol{p}'\cdot\boldsymbol{h}''+\boldsymbol{p}''\cdot\boldsymbol{h}')(\boldsymbol{p}'\cdot\boldsymbol{p}'')}{|\boldsymbol{p}'|^5} + 5\frac{(\boldsymbol{p}'\cdot\boldsymbol{h}')(\boldsymbol{p}'\cdot\boldsymbol{p}'')^2}{|\boldsymbol{p}'|^7}\Bigg)\,\mathrm{d}t\,, \tag{5.88}$$

and by $\Psi_3'[\boldsymbol{p}, V_{\boldsymbol{p},\theta}] : C^3([0,1],\mathbb{R}^3) \times C^2([0,1],\mathbb{R}) \to \mathbb{R}$ *with*[4]

$$\Psi_3'[\boldsymbol{p}, V_{\boldsymbol{p},\theta}](\boldsymbol{h},\phi) = \partial_{\boldsymbol{p}}\Psi_3[\boldsymbol{p}, V_{\boldsymbol{p},\theta}](\boldsymbol{h}) + \partial_\theta\Psi_3[\boldsymbol{p}, V_{\boldsymbol{p},\theta}](\phi)\,,$$

where

$$\partial_{\boldsymbol{p}}\Psi_3[\boldsymbol{p}, V_{\boldsymbol{p},\theta}](\boldsymbol{h}) = \frac{1}{L}\int_0^1 \Big(-2(\boldsymbol{r}_{\boldsymbol{p},\theta}'\cdot\mathbf{s}_{\boldsymbol{p},\theta})((\boldsymbol{h}'\cdot\mathbf{s}_{\boldsymbol{p},\theta})(\boldsymbol{r}_{\boldsymbol{p},\theta}'\cdot\boldsymbol{t}_{\boldsymbol{p}}) + (\boldsymbol{h}'\cdot\boldsymbol{r}_{\boldsymbol{p},\theta})(\boldsymbol{t}_{\boldsymbol{p}}'\cdot\mathbf{s}_{\boldsymbol{p},\theta})) + (\boldsymbol{r}_{\boldsymbol{p},\theta}'\cdot\mathbf{s}_{\boldsymbol{p},\theta})^2\frac{\boldsymbol{p}'\cdot\boldsymbol{h}'}{|\boldsymbol{p}'|}\Big)\,\mathrm{d}t\,, \tag{5.89a}$$

$$\partial_\theta\Psi_3[\boldsymbol{p}, V_{\boldsymbol{p},\theta}](\phi) = \frac{2}{L}\int_0^1 (\boldsymbol{r}_{\boldsymbol{p},\theta}'\cdot\mathbf{s}_{\boldsymbol{p},\theta})\phi'|\boldsymbol{p}'|\,\mathrm{d}t\,. \tag{5.89b}$$

Proof. The penalty term ψ_1 in (5.80) is given by

$$\Psi_1(\boldsymbol{p}, V_{\boldsymbol{p},\theta}) = \sum_{j=1}^{n-1}\left|\widetilde{\Psi}_1(\boldsymbol{p}, V_{\boldsymbol{p},\theta})\right|^2 \quad\text{with}\quad \widetilde{\Psi}_1(\boldsymbol{p}, V_{\boldsymbol{p},\theta}) = \frac{1}{n-1} - \frac{1}{L}\int_{t_j}^{t_{j+1}}|\boldsymbol{p}'|\,\mathrm{d}t\,.$$

Therefore, the Fréchet derivative of Ψ_1 is given by

$$\Psi_1'[\boldsymbol{p}, V_{\boldsymbol{p},\theta}](\boldsymbol{h},\phi) = 2\sum_{j=1}^{n-1}\widetilde{\Psi}_1'[\boldsymbol{p}, V_{\boldsymbol{p},\theta}](\boldsymbol{h},\phi)\widetilde{\Psi}_1(\boldsymbol{p}, V_{\boldsymbol{p},\theta})\,. \tag{5.90}$$

Using Taylor's theorem as in (4.28) shows that

$$\widetilde{\Psi}_1'[\boldsymbol{p}, V_{\boldsymbol{p},\theta}](\boldsymbol{h},\phi) = \frac{1}{L}\int_{t_j}^{t_{j+1}}\frac{\boldsymbol{p}'\cdot\boldsymbol{h}'}{|\boldsymbol{p}'|}\,\mathrm{d}t$$

and thus, the representation of $\Psi_1[\boldsymbol{p}, V_{\boldsymbol{p},\theta}](\boldsymbol{h},\phi)$ as in (5.87) follows by (5.90). For Ψ_2 we use the second representation of the curvature κ in (5.82) and find that

$$\Psi_2(\boldsymbol{p}, V_{\boldsymbol{p},\theta}) = \frac{1}{L}\int_0^1 \widetilde{\Psi}_2(\boldsymbol{p}, V_{\boldsymbol{p},\theta})\cdot\widetilde{\Psi}_2(\boldsymbol{p}, V_{\boldsymbol{p},\theta})\,\mathrm{d}t \quad\text{with}\quad \widetilde{\Psi}_2(\boldsymbol{p}, V_{\boldsymbol{p},\theta}) = \frac{\boldsymbol{p}''}{|\boldsymbol{p}'|^{3/2}} - \frac{(\boldsymbol{p}'\cdot\boldsymbol{p}'')\boldsymbol{p}'}{|\boldsymbol{p}'|^{7/2}}\,.$$

Therefore,

$$\Psi_2'[\boldsymbol{p}, V_{\boldsymbol{p},\theta}](\boldsymbol{h},\phi) = \frac{2}{L}\int_0^1 \widetilde{\Psi}_2'[\boldsymbol{p}, V_{\boldsymbol{p},\theta}](\boldsymbol{h},\phi)\cdot\widetilde{\Psi}_2(\boldsymbol{p}, V_{\boldsymbol{p},\theta})\,\mathrm{d}t\,. \tag{5.91}$$

We use Taylor's theorem as in (4.27) and find that

$$\begin{aligned}\widetilde{\Psi}_2(\boldsymbol{p}+\boldsymbol{h}, V_{\boldsymbol{p}+\boldsymbol{h},\theta+\phi}) &= \frac{\boldsymbol{p}''+\boldsymbol{h}''}{|\boldsymbol{p}'+\boldsymbol{h}'|^{3/2}} - \frac{((\boldsymbol{p}'+\boldsymbol{h}')\cdot(\boldsymbol{p}''+\boldsymbol{h}''))(\boldsymbol{p}'+\boldsymbol{h}')}{|\boldsymbol{p}'+\boldsymbol{h}'|^{7/2}}\\ &= -((\boldsymbol{p}'+\boldsymbol{h}')\cdot(\boldsymbol{p}''+\boldsymbol{h}''))\left(\frac{1}{|\boldsymbol{p}'|^{7/2}} - \frac{7(\boldsymbol{p}'\cdot\boldsymbol{h}')}{2|\boldsymbol{p}'|^{11/2}}\right)(\boldsymbol{p}'+\boldsymbol{h}')\end{aligned}$$

[4] We corrected errors in $\partial_{\boldsymbol{p}}\Psi_3[\boldsymbol{p}, V_{\boldsymbol{p},\theta}]$ that appear in the original publication [50].

$$
\begin{aligned}
&+ (\boldsymbol{p}'' + \boldsymbol{h}'') \left(\frac{1}{|\boldsymbol{p}'|^{3/2}} - \frac{3(\boldsymbol{p}' \cdot \boldsymbol{h}')}{2|\boldsymbol{p}'|^{7/2}} \right) + O(\|\boldsymbol{h}\|_{C^3([0,1],\mathbb{R}^3)}) \\
&= -((\boldsymbol{p}' \cdot \boldsymbol{p}'') + (\boldsymbol{p}' \cdot \boldsymbol{h}'') + (\boldsymbol{h}' \cdot \boldsymbol{p}'')) \left(\frac{\boldsymbol{p}'}{|\boldsymbol{p}'|^{7/2}} - \frac{7(\boldsymbol{p}' \cdot \boldsymbol{h}')\boldsymbol{p}'}{|\boldsymbol{p}'|^{11/2}} + \frac{\boldsymbol{h}'}{|\boldsymbol{p}'|^{7/2}} \right) \\
&\quad + \frac{\boldsymbol{p}''}{|\boldsymbol{p}'|^{3/2}} + \frac{\boldsymbol{h}''}{|\boldsymbol{p}'|^{3/2}} - \frac{3(\boldsymbol{p}' \cdot \boldsymbol{h}')\boldsymbol{p}''}{2|\boldsymbol{p}'|^{7/2}} + O(\|\boldsymbol{h}\|_{C^3([0,1],\mathbb{R}^3)}) \\
&= \frac{\boldsymbol{p}''}{|\boldsymbol{p}'|^{3/2}} - \frac{(\boldsymbol{p}' \cdot \boldsymbol{p}'')\boldsymbol{p}'}{|\boldsymbol{p}'|^{7/2}} + \frac{\boldsymbol{h}''}{|\boldsymbol{p}'|^{3/2}} - \frac{3(\boldsymbol{p}' \cdot \boldsymbol{h}')\boldsymbol{p}''}{2|\boldsymbol{p}'|^{7/2}} - \frac{(\boldsymbol{h}' \cdot \boldsymbol{p}'')\boldsymbol{p}'}{|\boldsymbol{p}'|^{7/2}} \\
&\quad + \frac{7(\boldsymbol{p}' \cdot \boldsymbol{p}'')(\boldsymbol{p}' \cdot \boldsymbol{h}')\boldsymbol{p}'}{2|\boldsymbol{p}'|^{11/2}} - \frac{(\boldsymbol{p}' \cdot \boldsymbol{p}'')\boldsymbol{h}'}{|\boldsymbol{p}'|^{7/2}} - \frac{(\boldsymbol{p}' \cdot \boldsymbol{h}'')\boldsymbol{p}'}{|\boldsymbol{p}'|^{7/2}} + O(\|\boldsymbol{h}\|_{C^3([0,1],\mathbb{R}^3)}) \,.
\end{aligned}
$$

Thus,

$$
\begin{aligned}
&\widetilde{\Psi_2}'[\boldsymbol{p}, V_{\boldsymbol{p},\theta}](\boldsymbol{h}, \phi) \\
&\quad = \frac{\boldsymbol{h}''}{|\boldsymbol{p}'|^{3/2}} - \frac{3(\boldsymbol{p}' \cdot \boldsymbol{h}')\boldsymbol{p}''}{2|\boldsymbol{p}'|^{7/2}} + \frac{7(\boldsymbol{p}' \cdot \boldsymbol{p}'')(\boldsymbol{p}' \cdot \boldsymbol{h}')\boldsymbol{p}'}{2|\boldsymbol{p}'|^{11/2}} - \frac{(\boldsymbol{p}' \cdot \boldsymbol{p}'')\boldsymbol{h}'}{|\boldsymbol{p}'|^{7/2}} - \frac{(\boldsymbol{p}' \cdot \boldsymbol{h}'')\boldsymbol{p}'}{|\boldsymbol{p}'|^{7/2}} - \frac{(\boldsymbol{h}' \cdot \boldsymbol{p}'')\boldsymbol{p}'}{|\boldsymbol{p}'|^{7/2}} \,.
\end{aligned}
$$

The representation of $\Psi_2'[\boldsymbol{p}, V_{\boldsymbol{p},\theta}](\boldsymbol{h}, \phi)$ as in (5.88) now follows by (5.91). For Ψ_3 we first consider variations with respect to $\boldsymbol{p}$. Using (5.52) and that $\boldsymbol{t}_{\boldsymbol{p}}, \boldsymbol{r}_{\boldsymbol{p},\theta}, \mathbf{s}_{\boldsymbol{p},\theta}$ are normalized and pairwise orthogonal, we find that

$$
\begin{aligned}
\boldsymbol{r}'_{\boldsymbol{p}+\boldsymbol{h},\theta} \cdot \mathbf{s}_{\boldsymbol{p}+\boldsymbol{h},\theta} &= \left(\boldsymbol{r}'_{\boldsymbol{p},\theta} - \left(\frac{1}{|\boldsymbol{p}'|} \right)' (\boldsymbol{h}' \cdot \boldsymbol{r}_{\boldsymbol{p},\theta}) \boldsymbol{t}_{\boldsymbol{p}} - \frac{1}{|\boldsymbol{p}'|} ((\boldsymbol{h}' \cdot \boldsymbol{r}_{\boldsymbol{p},\theta})' \boldsymbol{t}_{\boldsymbol{p}} + (\boldsymbol{h}' \cdot \boldsymbol{r}_{\boldsymbol{p},\theta}) \boldsymbol{t}'_{\boldsymbol{p}}) \right) \\
&\quad \cdot \left(\mathbf{s}_{\boldsymbol{p},\theta} - \frac{1}{|\boldsymbol{p}'|} (\boldsymbol{h}' \cdot \mathbf{s}_{\boldsymbol{p},\theta}) \boldsymbol{t}_{\boldsymbol{p}} \right) + O(\|\boldsymbol{h}\|_{C^3([0,1],\mathbb{R}^3)}) \\
&= \boldsymbol{r}'_{\boldsymbol{p},\theta} \cdot \mathbf{s}_{\boldsymbol{p},\theta} - \frac{(\boldsymbol{h}' \cdot \mathbf{s}_{\boldsymbol{p},\theta})(\boldsymbol{r}'_{\boldsymbol{p},\theta} \cdot \boldsymbol{t}_{\boldsymbol{p}})}{|\boldsymbol{p}'|} - \frac{(\boldsymbol{h}' \cdot \boldsymbol{r}_{\boldsymbol{p},\theta})(\boldsymbol{t}'_{\boldsymbol{p}} \cdot \mathbf{s}_{\boldsymbol{p},\theta})}{|\boldsymbol{p}'|} + O(\|\boldsymbol{h}\|_{C^3([0,1],\mathbb{R}^3)}) \,.
\end{aligned}
$$

With $\beta = \boldsymbol{r}'_{\boldsymbol{p},\theta} \cdot \mathbf{s}_{\boldsymbol{p},\theta}$ as in (5.84) we therefore find that

$$
\partial_{\boldsymbol{p}} \beta^2 = 2(\partial_{\boldsymbol{p}} \beta)\beta = -\frac{2}{|\boldsymbol{p}'|} ((\boldsymbol{h}' \cdot \mathbf{s}_{\boldsymbol{p},\theta})(\boldsymbol{r}'_{\boldsymbol{p},\theta} \cdot \boldsymbol{t}_{\boldsymbol{p}}) + (\boldsymbol{h}' \cdot \boldsymbol{r}_{\boldsymbol{p},\theta})(\boldsymbol{t}'_{\boldsymbol{p}} \cdot \mathbf{s}_{\boldsymbol{p},\theta}))(\boldsymbol{r}'_{\boldsymbol{p},\theta} \cdot \mathbf{s}_{\boldsymbol{p},\theta}) \,,
$$

what yields that

$$
\partial_{\boldsymbol{p}} (\beta^2 |\boldsymbol{p}'|) = -2((\boldsymbol{h}' \cdot \mathbf{s}_{\boldsymbol{p},\theta})(\boldsymbol{r}'_{\boldsymbol{p},\theta} \cdot \boldsymbol{t}_{\boldsymbol{p}}) + (\boldsymbol{h}' \cdot \boldsymbol{r}_{\boldsymbol{p},\theta})(\boldsymbol{t}'_{\boldsymbol{p}} \cdot \mathbf{s}_{\boldsymbol{p},\theta}))(\boldsymbol{r}'_{\boldsymbol{p},\theta} \cdot \mathbf{s}_{\boldsymbol{p},\theta}) + (\boldsymbol{r}'_{\boldsymbol{p},\theta} \cdot \mathbf{s}_{\boldsymbol{p},\theta})^2 \frac{\boldsymbol{p}' \cdot \boldsymbol{h}'}{|\boldsymbol{p}'|} \,.
$$

This implies the representation in (5.89a). The formula for the derivative in (5.89b) follows by using (5.51a) and again, by the fact that $\boldsymbol{t}_{\boldsymbol{p}}, \boldsymbol{r}_{\boldsymbol{p},\theta}, \mathbf{s}_{\boldsymbol{p},\theta}$ are normalized and pairwise orthogonal. □

We apply a BFGS scheme with an inexact Armijo-type line search and a cautious update rule as described in [94] to approximate a local solution to (5.86). We start with an initial approximation for the spine curve of the nanowire and for the geometry adapted frame. As in Section 4.2, let $\mathcal{P}_\triangle$ denote the space of all three-dimensional cubic not-a-knot splines. Furthermore, denote by $\mathcal{S}_\triangle$ the space of all one-dimensional cubic not-a-knot splines. Let $\boldsymbol{p}^{(0)} \in \mathcal{P}_\triangle$ be a three-dimensional cubic not-a-knot spline describing the initial guess for the spine curve. Accordingly, we compute a rotation minimizing frame $(\boldsymbol{t}_{\boldsymbol{p}^{(0)}}, \boldsymbol{r}_{\boldsymbol{p}^{(0)}}, \mathbf{s}_{\boldsymbol{p}^{(0)}})$ along this spline using the double reflection method from [121]. Then we choose a one-dimensional cubic not-a-knot spline $\theta^{(0)} \in \mathcal{S}_\triangle$ that describes the rotation function of the initial guess for the geometry adapted frame $(\boldsymbol{t}_{\boldsymbol{p}^{(0)}}, \boldsymbol{r}_{\boldsymbol{p}^{(0)},\theta^{(0)}}, \mathbf{s}_{\boldsymbol{p}^{(0)},\theta^{(0)}})$ as in (5.23). A visualization of $\boldsymbol{p}^{(0)}$ with $\boldsymbol{r}_{\boldsymbol{p}^{(0)}}$ and $\boldsymbol{r}_{\boldsymbol{p}^{(0)},\theta^{(0)}}$, respectively, is found in Figure 5.5. As before, we write $V_{\boldsymbol{p}^{(0)},\theta^{(0)}} = [\boldsymbol{t}_{\boldsymbol{p}^{(0)}} \,|\, \boldsymbol{r}_{\boldsymbol{p}^{(0)},\theta^{(0)}} \,|\, \mathbf{s}_{\boldsymbol{p}^{(0)},\theta^{(0)}}]$. We store the coordinates of the knots of $\boldsymbol{p}^{(0)}$ and $\theta^{(0)}$ in a vector $\vec{\boldsymbol{x}}_0 \in \mathbb{R}^{4n}$, where the first $3n$ components are

Figure 5.5: Visualization of the creation of the initial curve. Left: The initial cubic spline $\boldsymbol{p}^{(0)}$ together with the reference vectors $\boldsymbol{r}_{\boldsymbol{p}^{(0)}}$ from the double reflection method. Right: The initial cubic spline $\boldsymbol{p}^{(0)}$ together with the geometry adapted reference vector $\boldsymbol{r}_{\boldsymbol{p}^{(0)},\theta^{(0)}}$.

associated to $\boldsymbol{p}\{\vec{\boldsymbol{x}}_0\} = \boldsymbol{p}^{(0)}$ and the last n components correspond to $\theta\{\vec{\boldsymbol{x}}_0\} = \theta^{(0)}$. The vector $\vec{\boldsymbol{x}}_0$ is the initial guess for the BFGS-scheme. Let $\vec{\boldsymbol{x}}_\ell \in \mathbb{R}^{4n}$ denote the ℓ-th iterate of the BFGS-scheme. The ℓ-th spine curve $\boldsymbol{p}^{(\ell)} = \boldsymbol{p}\{\vec{\boldsymbol{x}}_\ell\} \in \mathcal{P}_\triangle$ is the three-dimensional cubic not-a-knot spline determined by the knots stored in the first $3n$ components of $\vec{\boldsymbol{x}}_\ell$. Denoting by $\theta^{(\ell)} = \theta\{\vec{\boldsymbol{x}}_\ell\} \in \mathcal{S}_\triangle$ the one-dimensional spline described by the knots stored in the last n components of $\vec{\boldsymbol{x}}_\ell$, the ℓ-th geometry adapted frame $(\boldsymbol{t}_{\boldsymbol{p}^{(\ell)}}, \boldsymbol{r}_{\boldsymbol{p}^{(\ell)},\theta^{(\ell)}}, \mathbf{s}_{\boldsymbol{p}^{(\ell)},\theta^{(\ell)}})$ is obtained from the $(\ell-1)$-th geometry adapted frame $(\boldsymbol{t}_{\boldsymbol{p}^{(\ell-1)}}, \boldsymbol{r}_{\boldsymbol{p}^{(\ell-1)},\theta^{(\ell-1)}}, \mathbf{s}_{\boldsymbol{p}^{(\ell-1)},\theta^{(\ell-1)}})$ using the formulas (5.47)–(5.48) with $\boldsymbol{h} = \boldsymbol{p}^{(\ell)} - \boldsymbol{p}^{(\ell-1)}$ and $\phi = \theta^{(\ell)} - \theta^{(\ell-1)}$. We write $V_{\boldsymbol{p}^{(\ell)},\theta^{(\ell)}} = V_{\boldsymbol{p},\theta}\{\vec{\boldsymbol{x}}_\ell\} = [\boldsymbol{t}_{\boldsymbol{p}^{(\ell)}} | \boldsymbol{r}_{\boldsymbol{p}^{(\ell)},\theta^{(\ell)}} | \mathbf{s}_{\boldsymbol{p}^{(\ell)},\theta^{(\ell)}}]$. After these discretizations the minimization problem from (5.86) becomes the finite dimensional optimization problem

$$\text{find} \qquad \operatorname*{arg\,min}_{\vec{\boldsymbol{x}} \in \mathbb{R}^{4n}} \Phi(\boldsymbol{p}\{\vec{\boldsymbol{x}}_\ell\}, V_{\boldsymbol{p},\theta}\{\vec{\boldsymbol{x}}_\ell\})\,.$$

For an iterate $\vec{\boldsymbol{x}}_\ell \in \mathbb{R}^{4n}$, $\ell \in \mathbb{N}_0$, the classical Newton's method for unconstrained optimization is to determine the descent direction $\vec{\boldsymbol{d}}_\ell \in \mathbb{R}^{4n}$ by solving

$$\nabla^2 \Phi[\boldsymbol{p}\{\vec{\boldsymbol{x}}_\ell\}, V_{\boldsymbol{p},\theta}\{\vec{\boldsymbol{x}}_\ell\}]\vec{\boldsymbol{d}}_\ell \;=\; -\nabla \Phi\,[\boldsymbol{p}\{\vec{\boldsymbol{x}}_\ell\}, V_{\boldsymbol{p},\theta}\{\vec{\boldsymbol{x}}_\ell\}] \tag{5.92}$$

and to update the iterate according to

$$\vec{\boldsymbol{x}}_{\ell+1} \;=\; \vec{\boldsymbol{x}}_\ell + \vec{\boldsymbol{d}}_\ell\,. \tag{5.93}$$

This procedure is simply the Newton's method for finding roots of the function $\nabla\Phi : \mathbb{R}^{4n} \to \mathbb{R}^{4n}$. Thus, it shares the same advantages and disadvantages as the classical Newton's method that are summarized in e.g. [42, Tab. 5.1.2]: The algorithm is q-quadratically convergent to a local minimum $\vec{\boldsymbol{x}}^*$ from a starting guess that is sufficiently close to $\vec{\boldsymbol{x}}^*$, if $\nabla^2\Phi[\boldsymbol{p}\{\vec{\boldsymbol{x}}^*\}, V_{\boldsymbol{p},\theta}\{\vec{\boldsymbol{x}}^*\}]$ is nonsingular (see e.g. [42, Thm. 5.2.1]). Here q-quadratically means that there exists a constant $c \geq 0$ and $\hat{\ell} \in \mathbb{N}$ such that $(\vec{\boldsymbol{x}}_\ell)_{\ell \in \mathbb{N}_0}$ converges to $\vec{\boldsymbol{x}}^*$ and for all $\ell > \hat{\ell}$ it holds that

$$|\vec{\boldsymbol{x}}_{\ell+1} - \vec{\boldsymbol{x}}^*| \leq c|\vec{\boldsymbol{x}}_\ell - \vec{\boldsymbol{x}}^*|^2,$$

see e.g. [42, Eq. 2.3.3]. The disadvantages are however that in each step ℓ, a possibly singular or ill-conditioned system of linear equations involving the Hessian $\nabla^2\Phi[\boldsymbol{p}\{\vec{\boldsymbol{x}}_\ell\}, V_{\boldsymbol{p},\theta}\{\vec{\boldsymbol{x}}_\ell\}]$ has to be solved and that there is no guarantee for the algorithm to converge, when starting with a starting guess that is not close to a local optimum. In particular, this means that in each step, the full Hessian $\nabla^2\Phi[\boldsymbol{p}\{\vec{\boldsymbol{x}}_\ell\}, V_{\boldsymbol{p},\theta}\{\vec{\boldsymbol{x}}_\ell\}]$ needs to be assembled, implying an immense computational effort. In fact, even if the iteration in (5.92) and (5.93) converges, it is not clear whether it

converges to a local maximum, minimum or to a saddle point as all of these points necessarily possess a vanishing gradient. Accordingly, instead of a Newton's method, we apply a quasi-Newton's method. Precisely, this will be the BFGS method with the cautious update rule from [94]. BFGS stands for Broyden, Fletcher, Goldfarb and Shanno, who discovered the BFGS update formula independently in 1970 (see [24, 54, 64, 114]). A quasi-Newton scheme requires only the gradient of the objective functional and replaces the Hessian $\nabla^2\Phi[\boldsymbol{p}\{\vec{\boldsymbol{x}}_\ell\}, V_{\boldsymbol{p},\theta}\{\vec{\boldsymbol{x}}_\ell\}]$ on the left hand side of (5.92) by an approximation $H_\ell \in \mathbb{R}^{4n\times 4n}$, which is updated, and thus refined, in each iteration step. Given $\vec{\boldsymbol{x}}_\ell$, the $(\ell+1)$-th iterate of the BFGS scheme is defined by

$$\vec{\boldsymbol{x}}_{\ell+1} \,=\, \vec{\boldsymbol{x}}_\ell + \lambda_\ell \vec{\boldsymbol{d}}_\ell\,, \tag{5.94}$$

where $\vec{\boldsymbol{d}}_\ell$ is a solution to the linear system

$$H_\ell \vec{\boldsymbol{d}}_\ell \,=\, -\nabla\Phi\big[\boldsymbol{p}\{\vec{\boldsymbol{x}}_\ell\}, V_{\boldsymbol{p},\theta}\{\vec{\boldsymbol{x}}_\ell\}\big]\,,$$

and $\lambda_\ell > 0$ determines the stepsize, which is chosen in such a way that certain line search conditions (e.g. the Wolfe conditions or the Armijo condition) are fulfilled. The gradient $\nabla\Phi[\boldsymbol{p}\{\vec{\boldsymbol{x}}_\ell\}, V_{\boldsymbol{p},\theta}\{\vec{\boldsymbol{x}}_\ell\}]$ of the regularized objective functional Φ from (5.85) with respect to $\vec{\boldsymbol{x}}_\ell$ is obtained by evaluating the Fréchet derivative of $\boldsymbol{T}_\rho$ from Theorem 5.15 and the Fréchet derivatives of the penalty terms Ψ_1, Ψ_2, and Ψ_3 from Lemma 5.21 in $(\boldsymbol{p}\{\vec{\boldsymbol{x}}_\ell\}, V_{\boldsymbol{p},\theta}\{\vec{\boldsymbol{x}}_\ell\})$ in the directions corresponding to the components of $\vec{\boldsymbol{x}}_\ell$. The classical BFGS update formula for the Hessian $H_{\ell+1}$ is defined by setting

$$H_{\ell+1} \,=\, H_\ell - \frac{H_\ell \vec{\mathbf{s}}_\ell \vec{\mathbf{s}}_\ell^{\,\top} H_\ell}{\vec{\mathbf{s}}_\ell^{\,\top} H_\ell \vec{\mathbf{s}}_\ell} + \frac{\vec{\boldsymbol{y}}_\ell \vec{\boldsymbol{y}}_\ell^{\,\top}}{\vec{\boldsymbol{y}}_\ell^{\,\top} \vec{\mathbf{s}}_\ell}\,, \tag{5.95}$$

where

$$\vec{\mathbf{s}}_\ell \,=\, \vec{\boldsymbol{x}}_{\ell+1} - \vec{\boldsymbol{x}}_\ell\,, \qquad \vec{\boldsymbol{y}}_\ell \,=\, \nabla\Phi\big[\boldsymbol{p}\{\vec{\boldsymbol{x}}_{\ell+1}\}, V_{\boldsymbol{p},\theta}\{\vec{\boldsymbol{x}}_{\ell+1}\}\big] - \nabla\Phi\big[\boldsymbol{p}\{\vec{\boldsymbol{x}}_\ell\}, V_{\boldsymbol{p},\theta}\{\vec{\boldsymbol{x}}_\ell\}\big]\,,$$

see e.g. [100, Alg. 6.1]. As described in [100, pp. 137], in order for the new approximation to the Hessian from (5.95) to be positive definite, the curvature condition $\vec{\mathbf{s}}_\ell \cdot \vec{\boldsymbol{y}}_\ell > 0$ needs to be satisfied. This condition is automatically satisfied for strongly convex objective functionals. However, there is no reason to believe that this is the case here (see Example 5.20 and Figure 5.4). As a consequence, the curvature condition $\vec{\mathbf{s}}_\ell \cdot \vec{\boldsymbol{y}}_\ell > 0$ is incorporated in the cautious update rule from [94]. Starting with the initial guess $H_0 = \mathbb{I}_{4n}$ (i.e. the first update direction corresponds to the direction of steepest descent), we use the cautious update rule

$$H_{\ell+1} \,=\, \begin{cases} H_\ell - \frac{H_\ell \vec{\mathbf{s}}_\ell \vec{\mathbf{s}}_\ell^{\,\top} H_\ell}{\vec{\mathbf{s}}_\ell^{\,\top} H_\ell \vec{\mathbf{s}}_\ell} + \frac{\vec{\boldsymbol{y}}_\ell \vec{\boldsymbol{y}}_\ell^{\,\top}}{\vec{\boldsymbol{y}}_\ell^{\,\top} \vec{\mathbf{s}}_\ell}\,, & \text{if } \frac{\vec{\boldsymbol{y}}_\ell^{\,\top} \vec{\mathbf{s}}_\ell}{|\vec{\mathbf{s}}_\ell|^2} \,>\, \varepsilon \big|\nabla\Phi\big[\boldsymbol{p}\{\vec{\boldsymbol{x}}_\ell\}, V_{\boldsymbol{p},\theta}\{\vec{\boldsymbol{x}}_\ell\}\big]\big|\,, \\ H_\ell\,, & \text{otherwise}\,. \end{cases} \tag{5.96}$$

Here, as in the classical BFGS scheme,

$$\vec{\mathbf{s}}_\ell \,=\, \vec{\boldsymbol{x}}_{\ell+1} - \vec{\boldsymbol{x}}_\ell\,, \qquad \vec{\boldsymbol{y}}_\ell \,=\, \nabla\Phi\big[\boldsymbol{p}\{\vec{\boldsymbol{x}}_{\ell+1}\}, V_{\boldsymbol{p},\theta}\{\vec{\boldsymbol{x}}_{\ell+1}\}\big] - \nabla\Phi\big[\boldsymbol{p}\{\vec{\boldsymbol{x}}_\ell\}, V_{\boldsymbol{p},\theta}\{\vec{\boldsymbol{x}}_\ell\}\big]\,, \tag{5.97}$$

and $\varepsilon > 0$ is a parameter. The update formula in (5.96) performs the regular BFGS update if a stronger curvature condition is satisfied. Otherwise, it simply skips the update. This ensures positive definiteness of H_ℓ throughout the BFGS iteration. It should be noted that some textbooks (see e.g. [100, p. 143]) do not recommend such a skip, as one might miss to capture important curvature information for the update. Instead, an inexact line search satisfying the Wolfe conditions

$$\begin{aligned} \Phi(\boldsymbol{p}\{\vec{\boldsymbol{x}}_\ell + \alpha_\ell \vec{\boldsymbol{d}}_\ell\}, V_{\boldsymbol{p},\theta}\{\vec{\boldsymbol{x}}_\ell + \alpha_\ell \vec{\boldsymbol{d}}_\ell\}) &\le \Phi(\boldsymbol{p}\{\vec{\boldsymbol{x}}_\ell\}, V_{\boldsymbol{p},\theta}\{\vec{\boldsymbol{x}}_\ell\}) + c_1\alpha_\ell \nabla\Phi\big[\boldsymbol{p}\{\vec{\boldsymbol{x}}_\ell\}, V_{\boldsymbol{p},\theta}\{\vec{\boldsymbol{x}}_\ell\}\big] \cdot \vec{\boldsymbol{d}}_\ell\,, \\ \nabla\Phi\big[\boldsymbol{p}\{\vec{\boldsymbol{x}}_\ell + \alpha_\ell \vec{\boldsymbol{d}}_\ell\}, V_{\boldsymbol{p},\theta}\{\vec{\boldsymbol{x}}_\ell + \alpha_\ell \vec{\boldsymbol{d}}_\ell\}\big] \cdot \vec{\boldsymbol{d}}_\ell &\ge c_2 \nabla\Phi\big[\boldsymbol{p}\{\vec{\boldsymbol{x}}_\ell\}, V_{\boldsymbol{p},\theta}\{\vec{\boldsymbol{x}}_\ell\}\big] \cdot \vec{\boldsymbol{d}}_\ell\,, \end{aligned}$$

with $0 < c_1 < c_2 < 1$, or a damped BFGS update is proposed. In order to satisfy the Wolfe conditions, each line search might require the evaluation of several Fréchet derivatives (see e.g. [42, Alg. A6.3.1mod]), what would consume a vast amount of time. Moreover, we note that the BFGS method with line searches that satisfy the Wolfe conditions may fail for non-convex functions (see [37, 38]). We expect a damped BFGS method to give similar results in a comparable amount of time, since the case, in which the second case in (5.96) is chosen, occurs rarely.

We use an inexact Armijo-type line search to determine the stepsize λ_ℓ in (5.94). Choosing parameters $\sigma \in (0,1)$ and $\delta \in (0,1)$, we identify the smallest integer $j = 0, 1, \dots$ such that δ^j satisfies

$$\Phi(\boldsymbol{p}\{\vec{\boldsymbol{x}}_\ell + \delta^j \vec{\boldsymbol{d}}_\ell\}, V_{\boldsymbol{p},\theta}\{\vec{\boldsymbol{x}}_\ell + \delta^j \vec{\boldsymbol{d}}_\ell\}) \leq \Phi(\boldsymbol{p}\{\vec{\boldsymbol{x}}_\ell\}, V_{\boldsymbol{p},\theta}\{\vec{\boldsymbol{x}}_\ell\}) + \sigma\delta^j \nabla\Phi[\boldsymbol{p}\{\vec{\boldsymbol{x}}_\ell\}, V_{\boldsymbol{p},\theta}\{\vec{\boldsymbol{x}}_\ell\}] \cdot \vec{\boldsymbol{d}}_\ell \,. \quad (5.98)$$

Then, we set $\lambda_\ell = \delta^j$. We note that the update of H_ℓ in (5.96) together with (5.98) is a modification of the BFGS method. The global convergence result in [94] cannot be applied here, since the level sets

$$\Omega = \{\vec{\boldsymbol{x}} \in \mathbb{R}^{4n} \,|\, \Phi(\boldsymbol{p}\{\vec{\boldsymbol{x}}\}, V_{\boldsymbol{p},\theta}\{\vec{\boldsymbol{x}}\}) \leq \Phi(\boldsymbol{p}\{\vec{\boldsymbol{x}}_0\}, V_{\boldsymbol{p},\theta}\{\vec{\boldsymbol{x}}_0\})\}$$

are not bounded: As described in [15], translations of the center curve do not change the chirality measure. Also, they do not change the values of the penalty terms. In our numerical examples, we did not encounter any non-convergence when all the spline curves $\boldsymbol{p}^{(\ell)}$ stayed within a ball of radius R with $kR < N$ (see Remark 5.9). In all examples, that we consider later, this is automatically fulfilled, when we choose the maximal degree of spherical harmonics N to be sufficiently large. In our numerical examples in the next chapter, we use the parameters $\varepsilon = 10^{-5}$, $\sigma = 10^{-4}$ and $\delta = 0.9$ in (5.96) and (5.98). We approximate all line integrals over K (i.e. over the parameter range $[0,1]$) using a composite Simpson rule with $M = 2m + 1$ nodes on each subinterval (see also Remark 3.28). We stop the BFGS iteration when $|\vec{\boldsymbol{x}}_{\ell+1} - \vec{\boldsymbol{x}}_\ell| / |\vec{\boldsymbol{x}}_\ell| < 10^{-4}$. In Algorithm 2 we describe the scheme that is used to design highly em-chiral objects.

5.6 Highly em-chiral thin tubular scatterers

In this chapter we present numerical examples from the previously described Algorithm 2 for finding highly em-chiral thin tubular scattering objects. We distinguish between three cases for our examples. In our first series of examples, we consider dielectric scattering objects with $\varepsilon_r > 1$, $\mu_r = 1$. Secondly, we consider the case, where $\varepsilon_r = \mu_r$. This property implies duality symmetry, i.e. the components $\mathcal{F}^{+-}_{D_\rho}$ and $\mathcal{F}^{-+}_{D_\rho}$ in the decomposition of the far field operator from (5.15) vanish (see also Remark 5.5). For the third type of examples, we study shape optimization for metallic nanowires. Here, we focus on silver and gold and consider frequencies corresponding to the optical spectrum. In this situation, scattering is modeled with material parameters $\varepsilon_r \in \mathbb{C}$ with $\mathrm{Im}(\varepsilon_r) > 0$, $\mathrm{Re}(\varepsilon_r) < 0$ and $\mu_r = 1$. As already pointed out in Remark 5.18, the scaling parameter $\rho > 0$ that determines the thickness of the thin scatterer D_ρ does not affect the outcome of the shape optimization. Accordingly, the results that we present in this section are valid for any $\rho > 0$ that is small enough such that the leading order term $\mathcal{T}_{D_\rho}$ in (5.25) constitutes an acceptable approximation of the far field operator $\mathcal{F}_{D_\rho}$. In Section 3.5 we compared the leading order term of the perturbation formula $\widetilde{\boldsymbol{E}^\infty_\rho}$ for circular cross-sections with radius ρ with a reference solution that has been computed using the C++ boundary element library Bempp [115] for a whole range of values for ρ. In the dielectric case (see Figure 3.4) the study suggests that $\widetilde{\boldsymbol{E}^\infty_\rho}$ is an accurate approximation to $\boldsymbol{E}^\infty_\rho$ within a relative error of less than 5% when the radius of the thin tube D_ρ is less than 1.5% of the wavelength of the incident field, i.e., when $k\rho \lesssim 0.1$. For metallic scattering objects however (see Figure 3.5), the condition $k\rho = 0.1$ is expected to lead to approximations that possess a relative error around

Algorithm 2 Optimization of thin tubes with elliptical cross-sections

Choose ε_r, μ_r and k. ▷ scattering problem parameters
Define $n \in \mathbb{N}$ and an initial spline $\boldsymbol{p}^{(0)}$ by the nodes $\boldsymbol{x}^{(1)}, \dots, \boldsymbol{x}^{(n)}$. Denote by $\vec{\boldsymbol{x}}_{0,\boldsymbol{p}} \in \mathbb{R}^{3n}$ the vector containing $\boldsymbol{x}^{(1)}, \dots, \boldsymbol{x}^{(n)}$ in succession.
Set $M \in \mathbb{N}$ as the number of intermediate points in each line segment.
Choose the semi-axis lengths $a > b$ for the elliptical cross-section.
Perform the double reflection method from [121] to generate an approximation to a RMF on all points including the intermediate points.
Define a spline $\theta^{(0)}$ by the nodes $\theta_1, \dots, \theta_n$ and rotate the frame according to (5.23). Denote by $\vec{\boldsymbol{x}}_{0,\theta} \in \mathbb{R}^n$ the zero vector (the rotation is included in the frame).
Set $\vec{\boldsymbol{x}}_0 \in \mathbb{R}^{4n}$ as the vector defined by concatenating $\vec{\boldsymbol{x}}_{0,\boldsymbol{p}}$ and $\vec{\boldsymbol{x}}_{0,\theta}$.
▷ initial tube defined
Choose $N \in \mathbb{N}$ satisfying $kR < N$, where $R > 0$ such that $B_R(0)$ includes the initial tube.
Initialize regularization parameters $\alpha_1, \alpha_2, \alpha_3 > 0$, the parameters for the line search $\sigma, \delta > 0$ and $H_0 \in \mathbb{R}^{4n \times 4n}$, $\varepsilon > 0$ for the BFGS update.
Set $\Phi_0 = \Phi(\boldsymbol{p}\{\vec{\boldsymbol{x}}_0\}, V_{\boldsymbol{p},\theta}\{\vec{\boldsymbol{x}}_0\})$.
for $\ell = 0, 1, \dots$ **do**
    Evaluate the Fréchet derivative of Φ from (5.85) with respect to $\boldsymbol{p}$ and θ using (5.74) and Lemma 5.21. Define

$$\Phi_0' \;=\; \nabla\Phi[\boldsymbol{p}\{\vec{\boldsymbol{x}}_\ell\}, V_{\boldsymbol{p},\theta}\{\vec{\boldsymbol{x}}_\ell\}] \quad \text{and solve} \quad H_\ell \boldsymbol{d}_\ell = -\Phi_0' \,.$$

    Define $\boldsymbol{r}_{\boldsymbol{p}} \in \mathbb{R}^3$ as the entries of $\boldsymbol{d}_\ell$ from 1 to $3n$ and $\boldsymbol{\varphi}_\theta$ as the entries of $\boldsymbol{d}_\ell$ from $3n+1$ to $4n$
    Set $j = -1$
    repeat
        Set j = j+1
        Set $\vec{\boldsymbol{x}}_{\ell+1,\boldsymbol{p}} = \vec{\boldsymbol{x}}_{\ell,\boldsymbol{p}} + \delta^j \boldsymbol{r}_{\boldsymbol{p}}$ and $\theta_{\ell+1} = \delta^j \boldsymbol{\varphi}_\theta$ and denote by $\boldsymbol{p}^{(\ell+1)}$ the spline corresponding to $\vec{\boldsymbol{x}}_{\ell+1,\boldsymbol{p}}$ and by $\theta^{(\ell+1)}$ the spline corresponding to $\theta_{\ell+1}$.
        Generate a frame for the tuple $(\boldsymbol{p}^{(\ell+1)}, \theta^{(\ell+1)})$ using (5.47).
        Set $\vec{\boldsymbol{x}}_{\ell+1}$ as the vector defined by concatenating $\vec{\boldsymbol{x}}_{\ell+1,\boldsymbol{p}}$ and $\theta_{\ell+1}$.
        Set $\Phi_1 = \Phi(\boldsymbol{p}\{\vec{\boldsymbol{x}}_{\ell+1}\}, V_{\boldsymbol{p},\theta}\{\vec{\boldsymbol{x}}_{\ell+1}\})$.
    until $\Phi_1 \le \Phi_0 + \sigma\delta^j \Phi_0' \cdot \boldsymbol{d}_\ell$ ▷ line search ended
    Evaluate the Fréchet derivative of Φ from (5.85) with respect to $\boldsymbol{p}$ and θ using (5.74) and Lemma 5.21 and define

$$\Phi_1' \;=\; \nabla\Phi[\boldsymbol{p}\{\vec{\boldsymbol{x}}_{\ell+1}\}, V_{\boldsymbol{p},\theta}\{\vec{\boldsymbol{x}}_{\ell+1}\}]$$

    Define $\vec{\mathbf{s}}_\ell$, $\vec{\boldsymbol{y}}_\ell$ from (5.97) via $\vec{\mathbf{s}}_\ell = \vec{\boldsymbol{x}}_{\ell+1} - \vec{\boldsymbol{x}}_\ell$ and $\vec{\boldsymbol{y}}_\ell = \Phi_1' - \Phi_0'$ and update the Hessian according to (5.96).
    Set $\Phi_0 = \Phi_1$, $\Phi_0' = \Phi_1'$ and set the components from $3n+1$ to $4n$ of $\vec{\boldsymbol{x}}_{\ell+1}$ to zero ▷ the rotation is included in the frame.
end for

10% in the worst case. In the following numerical experiments, we often show a thin tubular scattering object D_ρ together with the projections of its center curve K onto the three coordinate planes that surround D_ρ. We use the colors blue, magenta and gold or silver for dielectric, dual symmetric and metallic scatterers, respectively, to visualize the corresponding three dimensional scattering object.

5.6.1 Dielectric scatterers

In this subsection we examine scattering objects measuring several meters in length. Fixing this unit of length is artificial, since we do not intend to model a realistic scattering object here. We note however, that a relatively low relative permittivity (e.g. $2 < \varepsilon_r < 5$) can be associated to permittivities corresponding to some optical glass (see e.g. [93, Tab. 5.3]).

Example 5.22. In the first example we consider scattering objects with a circular cross-section. Thus, we do not consider variations with respect to the rotation θ. This is also reflected in our notation, as the dependency on θ is suppressed. Further note that different choices for $V_{\boldsymbol{p}}$ do not change the scattering object under consideration. The material parameters are set to $\varepsilon_r = 5$ and $\mu_r = 1$. Moreover, we use the wave number $k = 1\mathrm{m}^{-1}$ and pick $\alpha_1 = 5$, $\alpha_2 = 0.0005$ and $\alpha_3 = 0$ for the regularization parameters in (5.85) and the length constraint is chosen to be $L = 6\mathrm{m}$. As an initial guess $\vec{\boldsymbol{x}}_0$ we consider $n = 20$ equidistant nodes on the straight line segment between $[0, 0, -3]^\top$ and $[0, 0, 3]^\top$, and then, we slightly perturb the first two components of each node by adding random numbers between $-0.02\mathrm{m}$ and $0.02\mathrm{m}$. We note that the nodes cannot be exactly on the straight line segment, because then the thin tubular scattering object with center curve $\boldsymbol{p}_\triangle[\vec{\boldsymbol{x}}_0]$ would be geometrically achiral and thus, em-achiral. The objective functional Φ from (5.85) would not be differentiable at this initial guess (see also Example 5.20). Moreover, we pick $M = 11$ on each spline segment to approximate integrals over K using the composite Simpson rule. As outlined in Remark 5.9 and Remark 5.17, the maximal degree of vector spherical harmonics $N \in \mathbb{N}$ that is used in the representation of the operator $\boldsymbol{T}_\rho(\boldsymbol{p}_\triangle, V_{\boldsymbol{p}_\triangle})$ from (5.45) and of its Fréchet derivative $\boldsymbol{T}'_\rho[\boldsymbol{p}_\triangle, V_{\boldsymbol{p}_\triangle}]\boldsymbol{h}_\triangle$ from (5.55) must be chosen in such a way that N is greater than R, where $B_R(0)$ is the smallest ball centered at the origin that contains the scattering object D_ρ. In this example, we use $N = 5$. In Figure 5.6 we show the convergence history for this example. The initial guess is plotted in the top-left plot, some intermediate results that are obtained after $\ell = 10, 30, 50, 70$ are plotted in between and the final result after $\ell = 102$ steps of the BFGS method is in the bottom-right plot. Starting with an almost straight line in the top-left plot of Figure 5.6, the center curve winds up during the optimization process and finally becomes a helix. The orientation of the helix in space and whether it is left or right turning depends on the orientation of the initial curve $\boldsymbol{p}\{\vec{\boldsymbol{x}}_0\}$, thus, in particular on the values of the random perturbation that is used to construct the initial curve. In each plot we feature the relative chirality measure J_2 from (5.70) and the relative smooth relaxation J_{HS} from (5.69) in a table next to the center curve $\boldsymbol{p}\{\vec{\boldsymbol{x}}_\ell\}$. We find that both measures increase by several orders of magnitude. We track the evolution of both measures among the iteration steps ℓ in the left plot in Figure 5.7. Moreover, we perform a sensitivity analysis with respect to ε_r and k for the final result of the optimization scheme. For this purpose, we vary either ε_r or k and fix all the remaining parameters. The center plot in Figure 5.7 shows the sensitivity analysis with respect to $\varepsilon_r \in [1, 50]$ and the right plot in Figure 5.7 features the sensitivity analysis with respect to $k \in [0.01, 2]$. The vertical lines in both plots (dotted magenta) indicate the values of ε_r and k that have been used for the optimization ($\varepsilon_r = 5$ and $k = 1$). We see that both measures increase, when the relative electric permittivity ε_r increases. However, both measures seem to converge to a value which is around 0.23 for J_2 and 0.11 for J_{HS}. On the other hand, J_{HS} reaches a local maximum at the wave number $k = 1$ that has been used in the shape optimization, and there is a local maximum of J_2 close to this wave number. In order to study the dependency of the optimized center curve on the length constraint L in (5.71) we repeat the shape optimization with initial curves having the length $L = 4\mathrm{m}$ and $L = 8\mathrm{m}$ instead of $L = 6\mathrm{m}$. For the construction of the initial curves for $L = 4, 8\mathrm{m}$, we took the same random numbers as for the length constraint $L = 6\mathrm{m}$. The initial curves having length $L = 4, 6, 8\mathrm{m}$ can be found in the top-left, top-middle, and top-right plot of Figure 5.8, respectively. As before, we pick the maximal degree of vector spherical harmonics $N \in \mathbb{N}$ in such a way that N is larger than R, where $B_R(0)$ includes the scattering objects. Thus, for $L = 4\mathrm{m}$ we pick $N = 4$ and for $L = 8\mathrm{m}$, we pick $N = 6$. In the bottom-left and bottom-right plot in Figure 5.8 we show

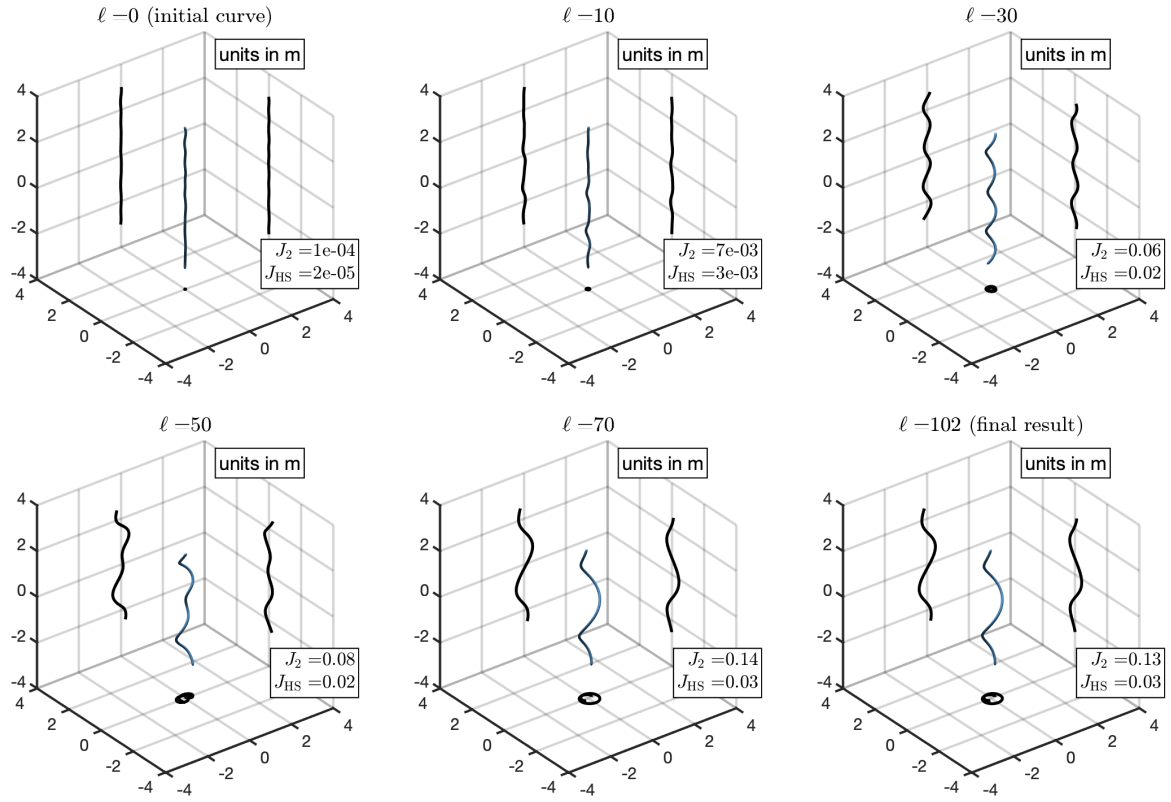

Figure 5.6: Convergence history for the dielectric scatterers from Example 5.22. Top-left: Initial guess. Bottom-right: Final result.

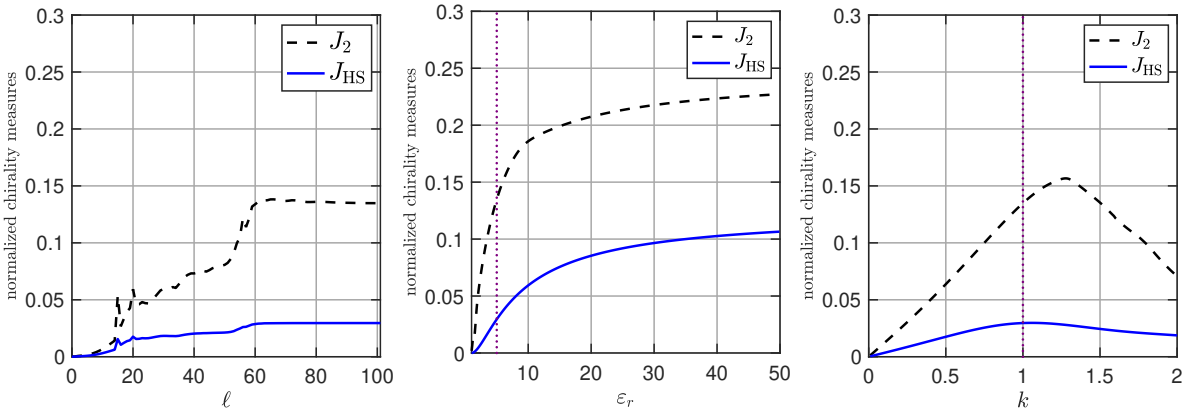

Figure 5.7: The relative measures J_{HS} and J_2 for Example 5.22 corresponding to the length constraint $L = 6$m. Left: Evolution of both measures for increasing iterations ℓ. Center: Sensitivity with respect to the relative electric permittivity ε_r. Right: Sensitivity with respect to the wave number k.

the final results that are obtained by the optimization scheme after 72 iteration steps and 122 iteration steps of the BFGS scheme, respectively. The bottom-middle plot features the final center curve for $L = 6$m for comparison. It is interesting to note that the diameter and the pitch of the helix is basically the same among the different values of L, while with an increasing length, also the number of turns increases. Both measures essentially attain the same value for the final structures, however, the total interaction cross section increases with increasing values of L. This is not shown in our figures. The orientation of the helix remains the same among the different lengths constraints since we used the same random numbers for perturbing the initial

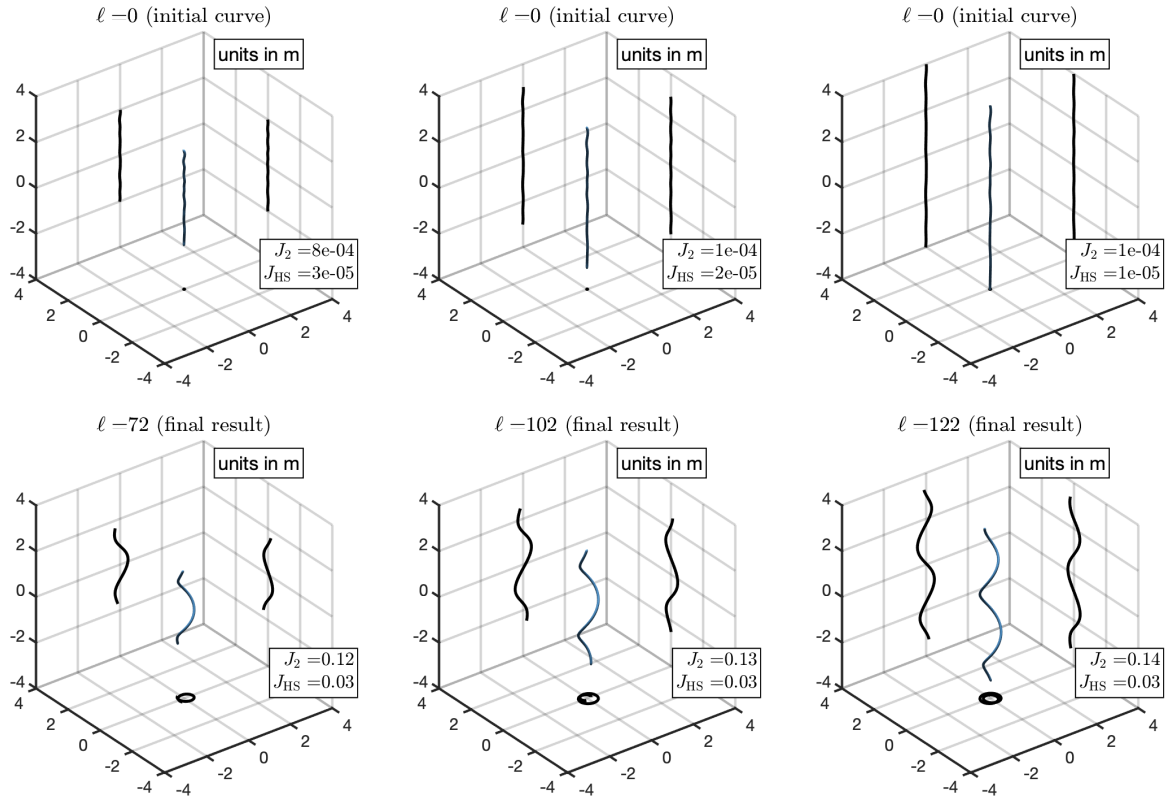

Figure 5.8: Optimized structures for the different length constraints $L = 4, 6, 8$m (left to right) from Example 5.22. Top row: Initial guesses. Bottom row: Final results.

straight curve.

Example 5.23. For the second example, we focus again on a dielectric thin tubular scattering object with a circular cross-section. Now, we choose the coefficients $k = 1\text{m}^{-1}$, $\varepsilon_r = 30$ and $\mu_r = 1$. This means that the permittivity contrast is much larger than in Example 5.22. We further pick the regularization parameters $\alpha_1 = 10$, $\alpha_2 = 0.005$ and, as in Example 5.22, $\alpha_3 = 0$ for the penalized objective function in (5.85). Since we consider circular cross-sections, rotations of those cross-sections do not change the scattering object and consequently, do not affect the optimization. The length constraint is set to $L = 20$m. We construct the initial guess of the optimization by using two parallel vertical lines connected by a half circle. The distance of the vertical lines is 2. Each of these has length 8 and is discretized by 20 nodes. The half circle on the other hand is discretized by 5 nodes, resulting in $n = 45$, which is the total number of nodes. As before, we slightly perturb the nodes on the vertical lines by adding random numbers between -0.02m and 0.02m to the x and y components. The unperturbed initial curve would be geometrically achiral and thus, the functional (5.85) would not be differentiable. We further pick $M = 11$ on each spline segment to approximate integrals over K using the composite Simpson rule. The total length of the initial curve is approximately 19.16m which is around 4% off the length constraint. In accordance with Remark 5.9 and Remark 5.17 we use $N = 6$ for the maximal degree of vector spherical harmonics that is used in the basis representation of the operator $\boldsymbol{T}_\rho(\boldsymbol{p}_\triangle, V_{\boldsymbol{p}_\triangle})$ from (5.45) and of its Fréchet derivative $\boldsymbol{T}'_\rho[\boldsymbol{p}_\triangle, V_{\boldsymbol{p}_\triangle}]\boldsymbol{h}_\triangle$ from (5.55).

In Figure 5.9 we visualize the evolution of the scattering objects by showing the initial guess (top-left), some intermediate results obtained after $\ell = 10, 30, 50, 70$ iterations, and the final result obtained after $\ell = 162$ steps (bottom-right). The optimization turns the U-shaped initial guess in an intertwined double helix. Both measures increase by several orders of magnitude, respectively, starting from an almost em-achiral object.

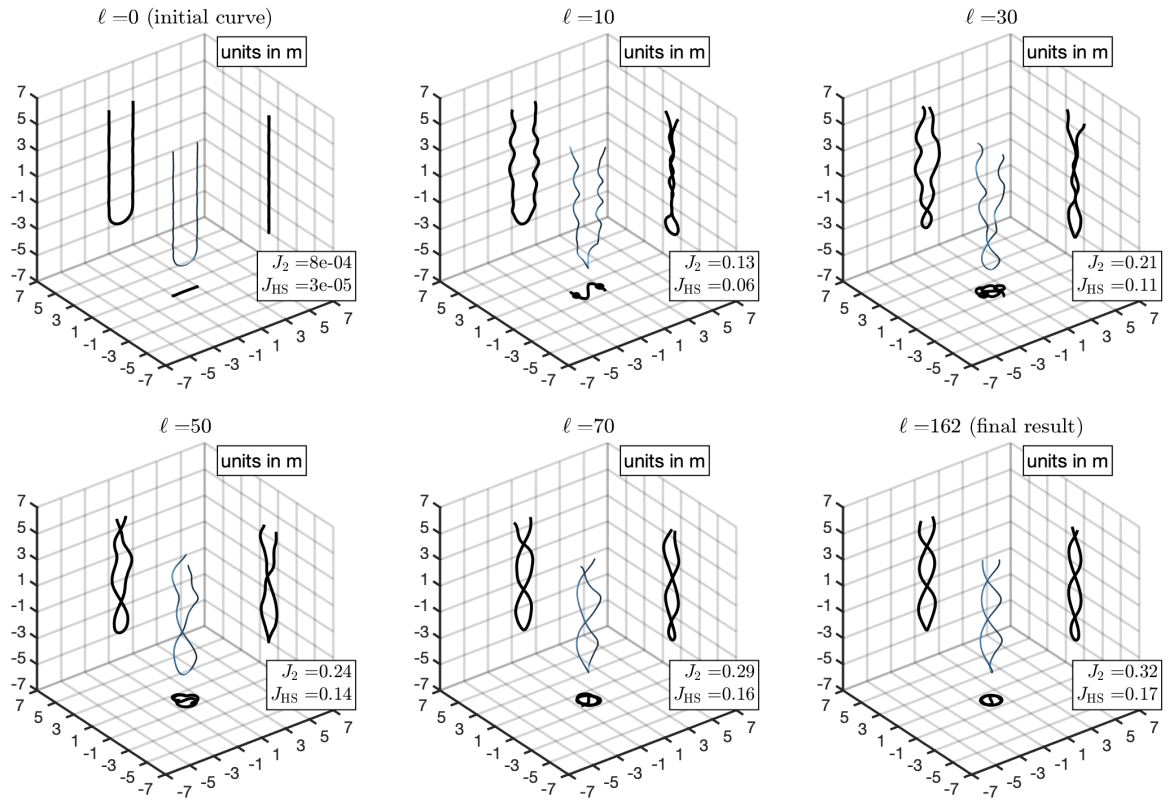

Figure 5.9: Convergence history for the dielectric scatterers from Example 5.23. Top-left: Initial guess. Bottom-right: Final result.

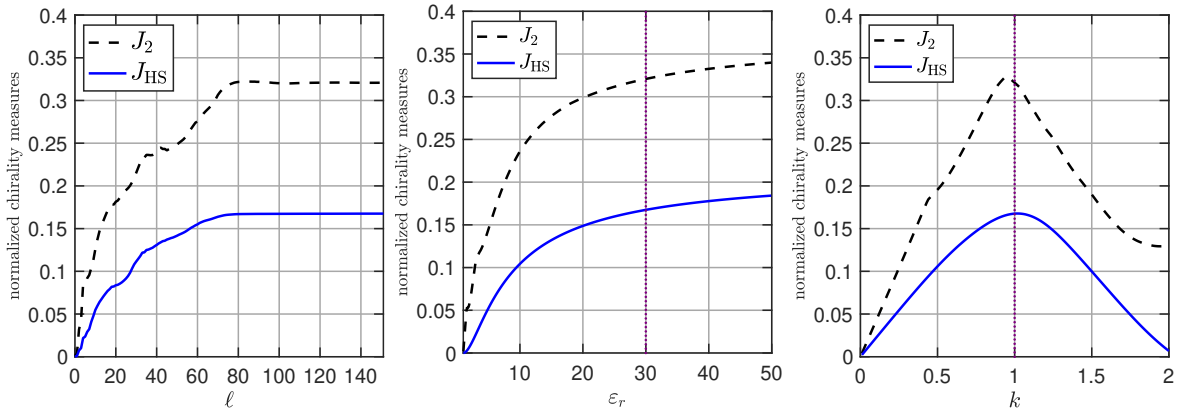

Figure 5.10: The relative measures J_{HS} and J_2 for Example 5.23 corresponding to the length constraint $L = 20$. Left: Evolution of both measures for increasing iterations ℓ. Center: Sensitivity with respect to the relative electric permittivity ε_r. Right: Sensitivity with respect to the wave number k.

In Figure 5.10 (left) we track the evolution of the chirality measure J_2 and the smooth relaxation J_{HS}, respectively. Figure 5.10 (center) shows plots of J_2 and J_{HS} for the optimized structure from Figure 5.9 (bottom-right) as a function of ε_r and Figure 5.10 (right) shows plots of J_2 and J_{HS} for the final structure as a function of the wave number k. In both plots, the vertical line (dotted magenta) shows the values for ε_r and k that we used for the optimization ($\varepsilon_r = 30$, $k = 1$). Both measures are monotonically increasing in ε_r. Moreover, the relative smooth measure J_{HS} has a local maximum for $k = 1$ and the relative chirality measure J_2 has a local maximum, which is close to $k = 1$. The sensitivities of both measures are more pronounced

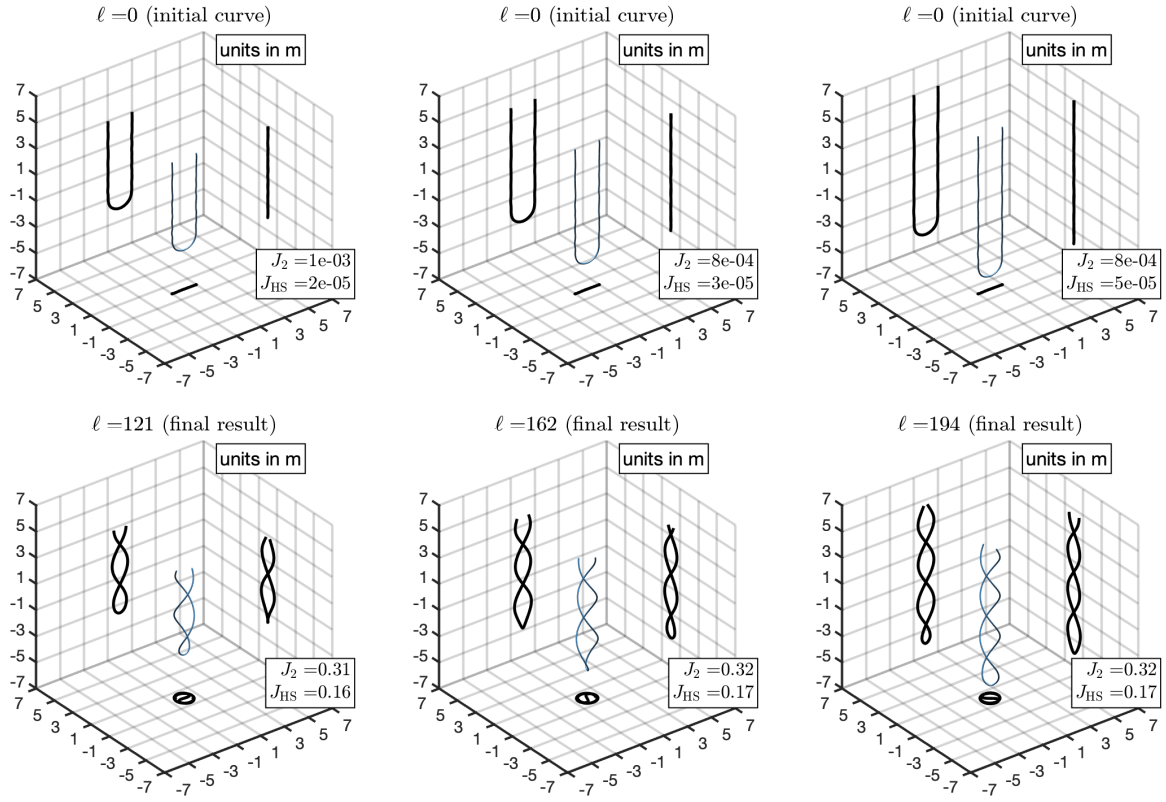

Figure 5.11: Optimized structures for the different length constraints $L = 15, 20, 25$m (left to right) from Example 5.23. Top row: Initial guesses. Bottom row: Final results.

than in Example 5.22. This is due to higher values of J_2 and J_{HS}, which, on the other hand, result from a larger ε_r than in Example 5.22. To study the dependency of the optimized center curve on the length constraint L, we repeat the shape optimization for the length constraints $L = 15$m and $L = 25$m instead of $L = 20$m. We construct the initial curves in the same way as described above and use the same perturbations for the straight lines. As in the previous example, this determines the orientation of the final double helix.

The initial center curves for this simulation are shown in Figure 5.11 (top-left and top-right). For reference, we included the initial curve corresponding to the length constraint $L = 20$m in the top-middle plot. For the length constraint $L = 15$m we choose $N = 5$, on the other hand, for the length constraint $L = 25$m we choose $N = 7$ as the maximal degree of vector spherical harmonics that is used in the basis representation of the operator $\boldsymbol{T}_\rho(\boldsymbol{p}_\triangle, V_{\boldsymbol{p}_\triangle})$ from (5.45) and of its Fréchet derivative $\boldsymbol{T}'_\rho[\boldsymbol{p}_\triangle, V_{\boldsymbol{p}_\triangle}]\boldsymbol{h}_\triangle$ from (5.55). In Figure 5.11 (bottom-left and bottom-right) we show the final results that are obtained by the BFGS method after 121 steps ($L = 15$m) and after 194 steps ($L = 25$m). We also included the final result for $L = 20$ in the bottom-center plot of Figure 5.11, for comparison. As we already observed in Example 5.22 for the helix, the diameters and the pitches of the three intertwined double helices that are found by the optimization algorithm are basically the same for the three different length constraints L. However, the number of turns of these helices increases with increasing length constraint L. In all of these simulations, the algorithm converges to objects that essentially attain the same values for J_2 and J_{HS}. For increasing total lengths of the center curve, the total interaction cross section also increases. This is not shown in our figures and is studied in more detail for metallic scattering objects in the next subsection.

5.6.2 Dual symmetric scatterers

As described Remark 5.5, the choice $\mu_r = \varepsilon_r$ is the condition for duality symmetry for the macroscopic Maxwell's equations and this implies preservation of helicity independent from the shape of the scatterer. For the leading order term of the asymptotic expansion of the far field operator T_ρ from (5.45) the property $\mu_r = \varepsilon_r$ implies $T_\rho^{+-} = T_\rho^{-+} = 0$, what can be easily seen by using the representations in (5.34). Accordingly, in our next numerical examples the condition $\mu_r = \varepsilon_r > 0$ guarantees preservation of helicity. For having a well defined derivative of χ_{HS} for $\mu_r = \varepsilon_r$, we replace the space X from (5.72) by

$$X' = \left\{ \mathcal{G} \in \mathrm{HS}(L_t^2(S^2)) \mid \chi_{\mathrm{HS}}(\mathcal{G}) \neq 0 \text{ and } \|\mathcal{G}^{pp}\|_{\mathrm{HS}} > 0,\ \|\mathcal{G}^{p\overline{p}}\|_{\mathrm{HS}} = 0,\ p \in \{+,-\} \right\},$$

where $\overline{p} = -p$, and find that for a given $\mathcal{G} \in X'$ and $\mathcal{H} \in \mathrm{HS}\left(L_t^2(S^2)\right)$, the derivative is given by

$$\left(\chi_{\mathrm{HS}}\right)'[\mathcal{G}]\,\mathcal{H} = \frac{\mathrm{Re}\langle \mathcal{G}, \mathcal{H}\rangle_{\mathrm{HS}} - \sum_{p\in\{+,-\}} \mathrm{Re}\langle \mathcal{G}^{pp}, \mathcal{H}^{pp}\rangle_{\mathrm{HS}} \frac{\|\mathcal{G}^{\overline{pp}}\|_{\mathrm{HS}}}{\|\mathcal{G}^{pp}\|_{\mathrm{HS}}}}{\chi_{\mathrm{HS}}(\mathcal{G})}, \tag{5.99}$$

where $\overline{p} = -p$. This replaces the derivative in (5.73). The fact that (5.99) is the Fréchet derivative of χ_{HS} on X' can be seen by using the same computations as in Lemma 5.19.

As in the previous subsection, the unit of length that we choose here is artificial.

Example 5.24. We consider thin tubular scattering objects with a circular cross-section and material parameters given by $k = 1\mathrm{m}^{-1}$ and $\mu_r = \varepsilon_r = 50$. As outlined before, this implies that throughout the iterations it holds that $\boldsymbol{T}_\rho^{+-}(\boldsymbol{p}_\triangle) = \boldsymbol{T}_\rho^{-+}(\boldsymbol{p}_\triangle) = 0$. We construct a U-shaped initial guess as in the previous Example 5.23, where we used the vertical side length 6m. The distance of these vertical lines is 2m. Thus, we use the length constraint $L = 14\mathrm{m}$. We discretize both vertical lines by using 10 nodal points. Furthermore, we use 5 nodal points to discretize the arc that connects both lines. This yields $n = 25$ discretization points in total. In order to obtain an initial guess that is not em-achiral, we perturb the x and y component of all nodes by adding random numbers between $-0.02\mathrm{m}$ and $0.02\mathrm{m}$. Moreover, we pick $M = 11$ on each spline segment to approximate integrals over K using the composite Simpson's rule. For the regularization parameters, we consider (as in Example 5.23) $\alpha_1 = 10$, $\alpha_2 = 0.005$ and $\alpha_3 = 0$. In accordance with Remark 5.9 and Remark 5.17, we use $N = 5$ as the maximal degree of vector spherical harmonics that is used in the basis representation of the operator $\boldsymbol{T}_\rho(\boldsymbol{p}_\triangle, V_{\boldsymbol{p}_\triangle})$ from (5.45) and of its Fréchet derivative $\boldsymbol{T}_\rho'[\boldsymbol{p}_\triangle, V_{\boldsymbol{p}_\triangle}]\boldsymbol{h}_\triangle$ from (5.55).

In Figure 5.12 we show the initial guess for our shape optimization (top-left), together with some intermediate results obtained after $\ell = 10, 20, 30, 40$ steps and the final result (bottom-right) after $\ell = 50$ iterations of the optimization scheme. Despite the different material parameters, the convergence history from Figure 5.12 is similar to the convergence history from Example 5.23 in Figure 5.9. However, we observe that both measures attain higher values, what also results from using larger material parameters.

In Figure 5.13 (left) we track the evolution of both measures J_2 and J_{HS} as the iteration number ℓ increases. Moreover, we study the sensitivity on the material parameters $\varepsilon_r = \mu_r$ (center) and the sensitivity on the wave number k (right). Comparing these data with the results from Example 5.23 shows that for the dual symmetric case, the measures are slightly higher. Finally, we study the dependency on the length constraint L by performing the same simulation with the length constraints $L = 10, 18\mathrm{m}$ instead of $L = 14\mathrm{m}$. As an initial guess we construct U-shaped curves by decreasing and increasing the lengths of the parallel vertical lines to 4m and 8m, respectively. The maximal degree of vector spherical harmonics is chosen to be $N = 4$ in the first simulation and $N = 6$ in the second experiment. The initial guesses corresponding to the lengths $L = 10, 14, 18\mathrm{m}$ can be found in the top row of Figure 5.14. The final result of the optimization is visualized below. Again, the diameter and pitch of the intertwined double helix remains constant. However, the total length and consequently the number of turns increases

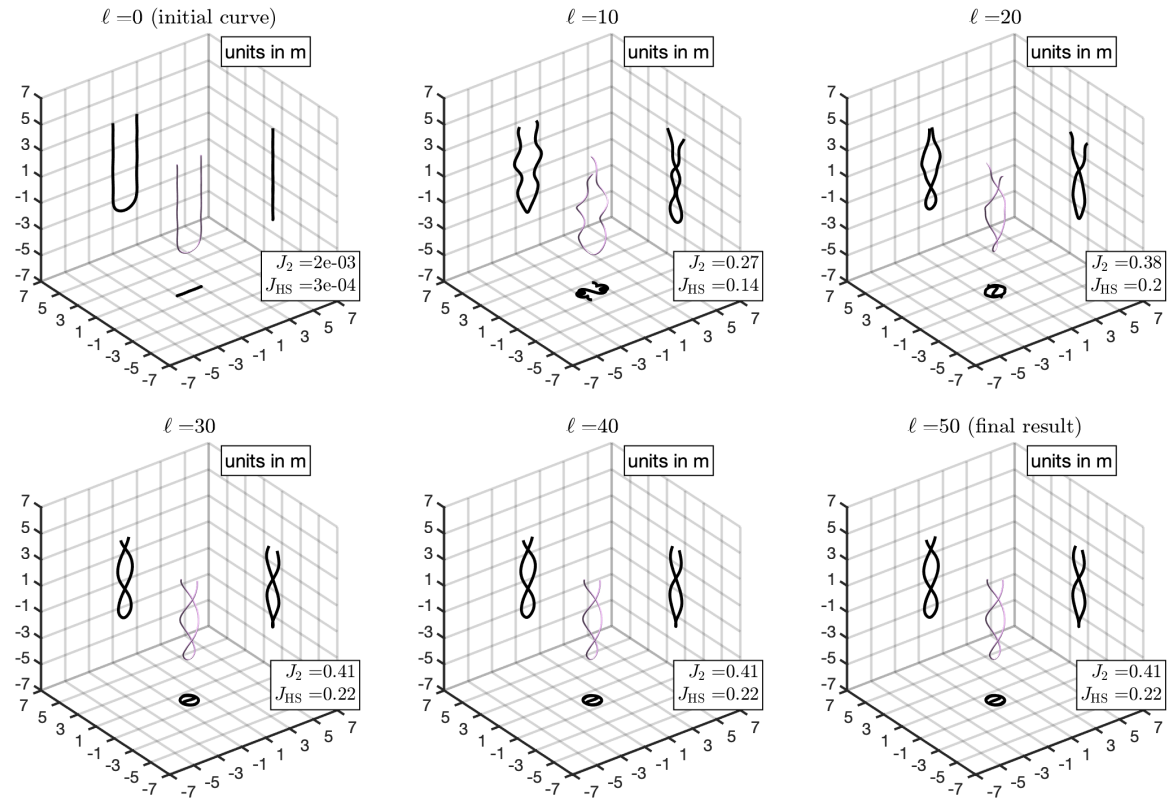

Figure 5.12: Convergence history for the dual symmetric scatterers from Example 5.24. Top-left: Initial guess. Bottom-right: Final result.

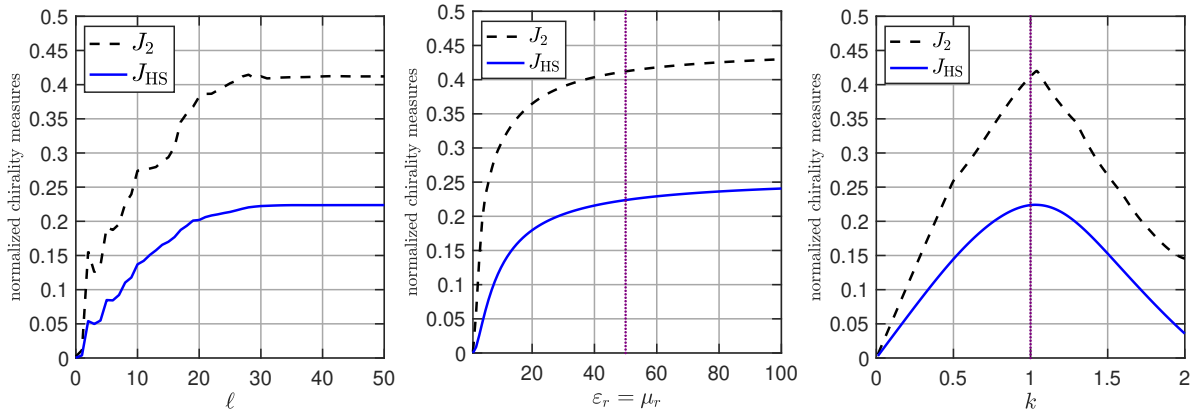

Figure 5.13: The relative measures J_{HS} and J_2 for Example 5.24 corresponding to the length constraint $L = 14$. Left: Evolution of both measures for increasing iterations ℓ. Center: Sensitivity with respect to the relative electric permittivity ε_r and relative magnetic permeability μ_r. Right: Sensitivity with respect to the wave number k.

with increasing length constraint L. This does not affect the measures corresponding to the final structures, as they almost keep the same values throughout the different lengths.

Example 5.25. In this example, we consider $k = 1\mathrm{m}^{-1}$ and $\varepsilon_r = \mu_r = 50$. As in the previous example we use the regularization parameters $\alpha_1 = 10$, $\alpha_2 = 0.005$ and $\alpha_3 = 0$ for the functional Φ in (5.85). For the initial guess we consider three parallel vertical line segments arranged in a common two-dimensional plane having a length of 6m, respectively. The distance from the outer vertical lines to the middle line is 1m. Furthermore, the first outer line is connected to the

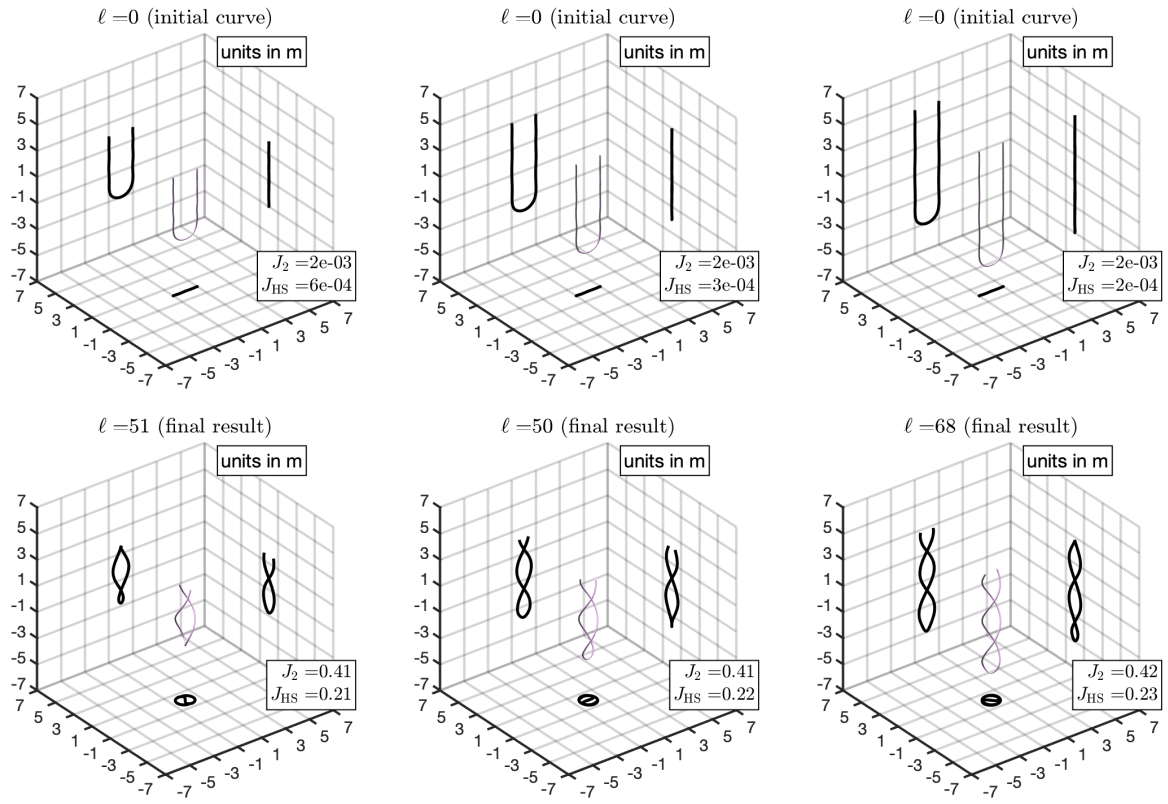

Figure 5.14: Optimized structures for the different length constraints $L = 10, 14, 18$ (left to right) from Example 5.24. Top row: Initial guesses. Bottom row: Final results.

middle line by a half circle at one end and the second outer line is connected to the middle line by a half circle at the other end. This gives an S-shaped initial curve completely lying in a two-dimensional plane. We discretize the vertical lines by using 10 nodes, respectively. Moreover, the half circles are discretized by 5 points. This yields $n = 40$ nodal points in total. As the initial curve is geometrically achiral, it is em-achiral and the aim functional is not differentiable for this center curve. Therefore, we perturb the center curve of the initial guess by adding random numbers between -0.02m and 0.02m to the x and y components of the nodal points. Moreover, we pick $M = 11$ on each spline segment to approximate integrals over K using the composite Simpson's rule. The length constraint for this numerical example is set to $L = 22$m. In accordance with Remark 5.9 and Remark 5.17 we use $N = 6$ as the maximal degree of vector spherical harmonics that is used in the basis representation of the operator $\boldsymbol{T}_\rho(\boldsymbol{p}_\triangle, V_{\boldsymbol{p}_\triangle})$ from (5.45) and of its Fréchet derivative $\boldsymbol{T}'_\rho[\boldsymbol{p}_\triangle, V_{\boldsymbol{p}_\triangle}]\boldsymbol{h}_\triangle$ from (5.55).

In Figure 5.15 we visualize the convergence history by showing the initial curve (top-left), some intermediate results obtained after $\ell = 10, 20, 30, 40$ (top-center - bottom-center) and the final result obtained after $\ell = 123$ steps of the BFGS method. Starting with an almost em-achiral center curve, the optimization algorithm turns the scatterer into a nonintuitive shape attaining relatively high values of both measures J_2 and J_{HS}. The final curve possesses remarkable symmetries when projecting it onto the three surrounding planes as seen in the bottom-right plot in Figure 5.15.

In Figure 5.16 (left) we show the evolution of both measures J_2 and J_{HS} during the optimization process. Both functionals increase by several orders of magnitude. Figure 5.16 (center) shows a sensitivity analysis of both measures J_2 and J_{HS} with respect to $\varepsilon_r = \mu_r$ and Figure 5.16 shows corresponding plots of J_2 and J_{HS} as a function of k. In both plots, the parameters that are used in the simulation are marked with a vertical line ($\varepsilon_r = \mu_r = 50$, $k = 1$). As before, both measures are monotonically increasing in $\varepsilon_r = \mu_r$. Moreover, the smooth relaxation J_{HS} reaches

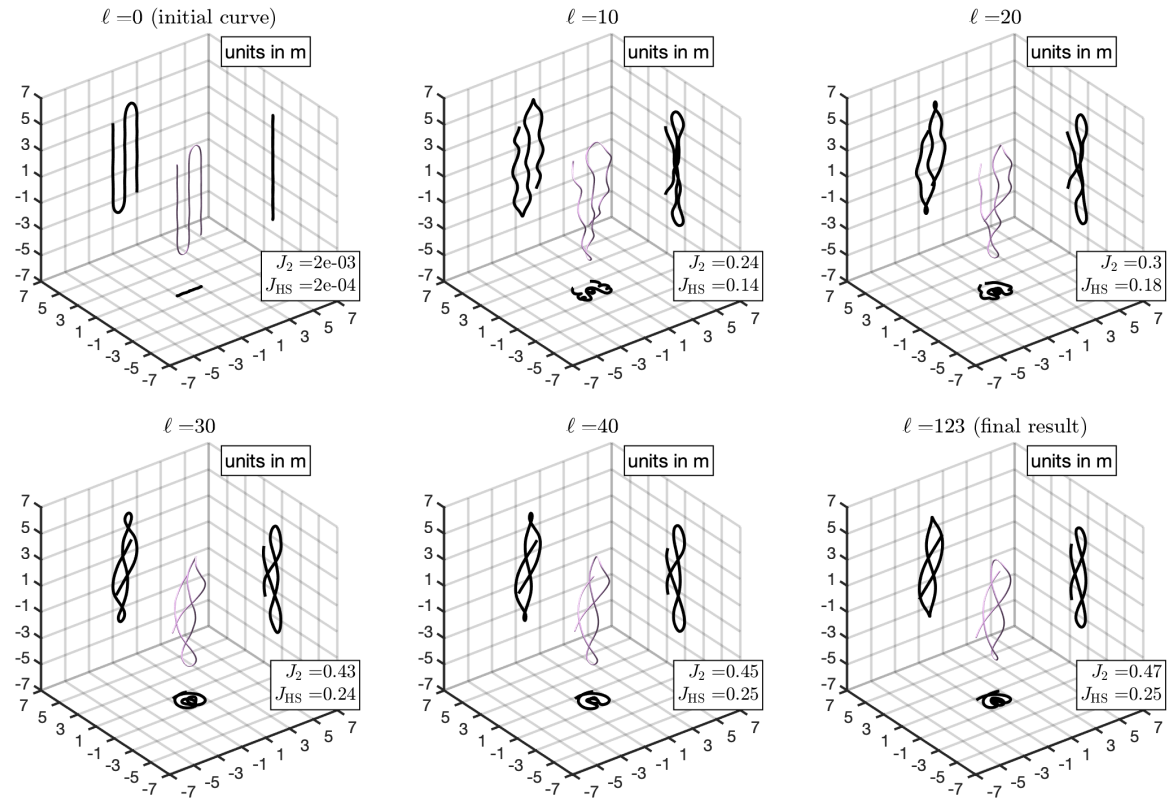

Figure 5.15: Convergence history for the dual symmetric scatterers from Example 5.25. Top-left: Initial guess. Bottom-right: Final result.

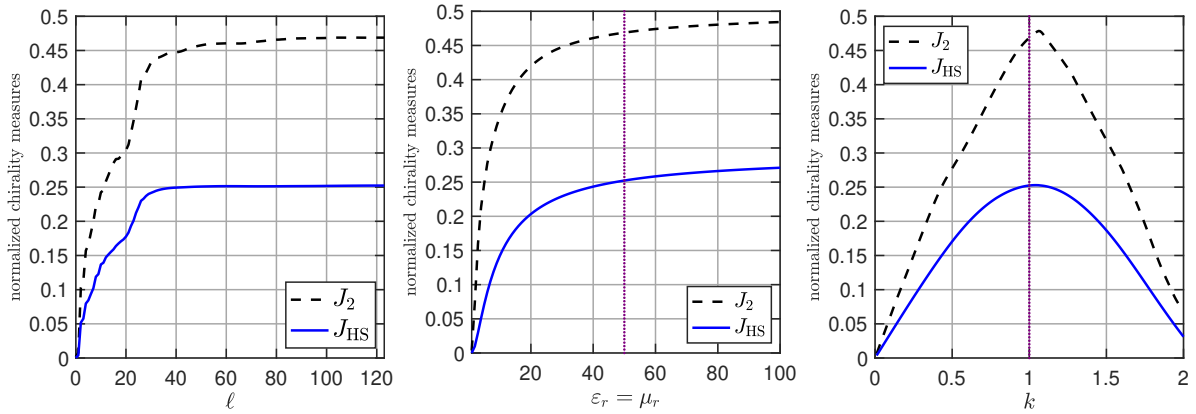

Figure 5.16: The relative measures J_{HS} and J_2 for Example 5.25 corresponding to the length constraint $L = 22$. Left: Evolution of both measures for increasing iterations ℓ. Center: Sensitivity with respect to the relative electric permittivity ε_r and relative magnetic permeability μ_r. Right: Sensitivity with respect to the wave number k.

a local maximum at $k = 1\mathrm{m}^{-1}$, which is the wave number for which we optimized the function Φ in (5.85). The original relative chirality measure has a local maximum near $k = 1$. The sensitivity with respect to k is more pronounced than in Example 5.24 (see Figure 5.13 (right)). Finally, we study the dependency of the optimized center curve on the length constraint L. For this purpose, we pick two more initial curves having the same vertical line distance as before but with a length of 4m and 8m instead of 6m.

This gives two more S-shaped initial curves for which (after a slight perturbation of the nodal points as before) we start the optimization by setting the length constraints to $L = 16\mathrm{m}$

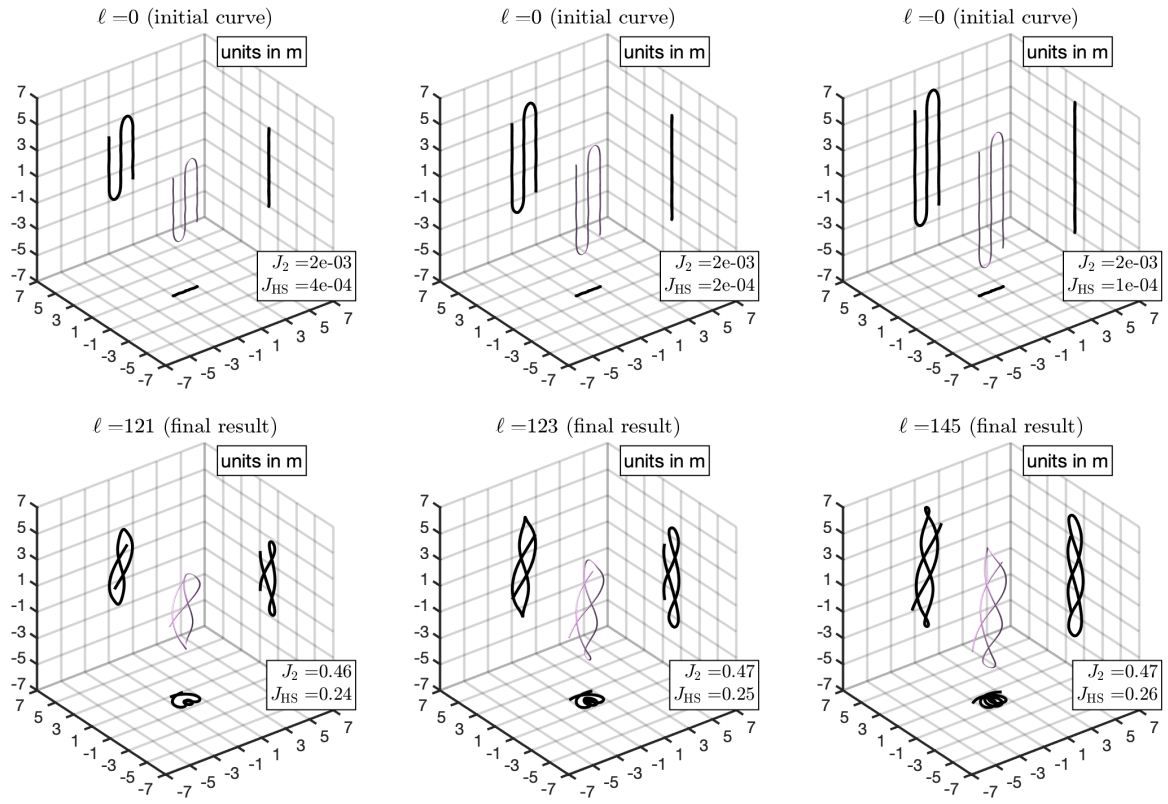

Figure 5.17: Optimized structures for the different length constraints $L = 16, 22, 28$m (left to right) from Example 5.25. Top row: Initial guesses. Bottom row: Final results.

and $L = 28$m, respectively. These curves can be found in the top row of Figure 5.17. For comparison, we included the initial curve for the length constraint $L = 22$m in the top-middle plot of Figure 5.17. In accordance with Remark 5.9, we choose $N = 4$ when $L = 16$m and $N = 6$ for $L = 28$m as the maximal degree of vector spherical harmonics that is used in the basis representation of the operator $\boldsymbol{T}_\rho(\boldsymbol{p}_\triangle, V_{\boldsymbol{p}_\triangle})$ from (5.45) and of its Fréchet derivative $\boldsymbol{T}'_\rho[\boldsymbol{p}_\triangle, V_{\boldsymbol{p}_\triangle}]\boldsymbol{h}_\triangle$ from (5.55). In Figure 5.17 (bottom-left and bottom-right) we visualize the final results that are found by the optimization scheme after $\ell = 121$ iterations (for $L = 16$m) and after $\ell = 145$ iterations (for $L = 28$m). In Figure 5.17 (bottom-middle) we included the final result for $L = 22$m for comparison. With increasing length constraint L the nonintuitive final structure becomes larger. However, both measures remain almost constant.

5.6.3 Metallic nanowires

In the previous two subsections we studied scattering objects with positive material parameters $\mu_1, \varepsilon_1 > 0$. The shape optimization scheme provides interesting thin tubular scatterers, however both measures J_2 and J_{HS} do not come close to their upper bound 1, which would give us a maximal em-chiral scattering object.

Now, we study shape optimization for metallic nanowires D_ρ with an elliptical cross-section $D'_\rho = \rho D'$ that possibly rotates along the center curve K. As we observed in Section 3.4, by tuning the semi axes lengths of the ellipse we can manipulate the appearance of plasmonic resonances. Thus, it is possible to shift local maxima and minima of the total interaction cross section $\|T_{D_\rho}\|^2_{\mathrm{HS}}$ along the optical band. Rather than working directly with the material parameters for gold and silver, we consider frequencies f in the optical band and obtain a corresponding frequency dependent electric permittivity $\varepsilon_r(f)$ by using the dataset provided in [83]. Intermediate values are obtained via interpolation. We use these experimental data as the

	Silver		Gold	
f	$\mathrm{Re}(\varepsilon_r)$	$\mathrm{Im}(\varepsilon_r)$	$\mathrm{Re}(\varepsilon_r)$	$\mathrm{Im}(\varepsilon_r)$
300 THz	-50.55	0.57	-41.78	2.94
350 THz	-36.23	0.48	-28.84	1.77
400 THz	-26.94	0.32	-20.11	1.24
450 THz	-20.57	0.44	-14.10	1.04
500 THz	-16.05	0.44	-9.36	1.53
550 THz	-12.62	0.42	-5.59	2.19
600 THz	-9.78	0.31	-2.54	3.65
650 THz	-7.64	0.25	-1.73	5.06
700 THz	-5.94	0.20	-1.69	5.66
750 THz	-4.41	0.21	-1.66	5.74
800 THz	-3.10	0.21	-1.50	5.63

Table 5.1: Relative electric permittivities ε_r of silver and gold at optical frequencies (from [83]).

Drude model provides inaccurate material parameters for optical frequencies (see Remark 2.7) and the appearance of a plasmonic resonance is highly sensitive with respect to the material parameters (see Section 3.4). We discuss three numerical examples, where we use the shape optimization scheme developed in Section 5.5 (see Algorithm 2) to design highly chiral thin silver and gold nanowires at four different frequencies in the optical band. We work at

- $f_{\mathrm{opt}} = 400\mathrm{THz}$, i.e., the wavelength is $\lambda_{\mathrm{opt}} = 749\mathrm{nm}$ (red light),
- $f_{\mathrm{opt}} = 500\mathrm{THz}$, i.e., the wavelength is $\lambda_{\mathrm{opt}} = 600\mathrm{nm}$ (orange light),
- $f_{\mathrm{opt}} = 600\mathrm{THz}$, i.e., the wavelength is $\lambda_{\mathrm{opt}} = 500\mathrm{nm}$ (green light),
- $f_{\mathrm{opt}} = 700\mathrm{THz}$, i.e., the wavelength is $\lambda_{\mathrm{opt}} = 428\mathrm{nm}$ (blue light).

The relative electric permittivities ε_r of silver and gold corresponding to these frequencies can be found in Table 5.1 (see also Figure 2.1). For the elliptical cross-sections $D'_\rho = \rho D'$ we denote the lengths of the semi axes of the rescaled cross-section D' by $0 < b \leq a < 1$. As introduced in Definition 3.24, a frequency f_{res} is called a plasmonic resonance frequency of such a thin metallic nanowire, if the aspect ratio a/b of its elliptical cross-section satisfies $a/b = -\mathrm{Re}(\varepsilon_r(f_{\mathrm{res}}))$, and if $\mathrm{Im}(\varepsilon_r(f_{\mathrm{res}})) > 0$ is sufficiently small. The total interaction cross section of the nanowire (i.e. the squared Hilbert-Schmidt norm of the associated far field operator) at a plasmonic resonance frequency is much larger than away from this frequency. Accordingly, thin metallic nanowires are strongly scattering at plasmonic resonance frequencies. Strongly scattering highly em-chiral nanowires would be very interesting for the design of novel chiral metamaterials (see e.g. [76, 80, 120]). Thus, we choose in our first two examples the aspect ratios of the elliptical cross-sections of the nanowires such that the frequency f_{opt}, where the shape optimization is carried out, is a plasmonic resonance frequency, i.e., $f_{\mathrm{opt}} = f_{\mathrm{res}}$. We show that strongly scattering thin metallic nanowires with fairly large em-chirality measures can be obtained. In our third example we then design thin metallic nanowires with even larger em-chirality measures, choosing the frequency f_{opt} to be around 100THz to 150THz below the plasmonic resonance frequency f_{res} of the nanowire, i.e., $f_{\mathrm{opt}} \neq f_{\mathrm{res}}$. However, in this case the total interaction cross section of the optimized nanowire is smaller than in the previous examples. For a metallic nanowire with circular cross-section, for instance, choosing $\rho = 0.1/k_{\mathrm{opt}}$ means that the radius ρ is between 6.8nm at $f_{\mathrm{opt}} = 700\mathrm{THz}$ and 11.9nm at $f_{\mathrm{opt}} = 400\mathrm{THz}$. Here, k_{opt} denotes the wave number corresponding to the frequency f_{opt}, i.e. $k_{\mathrm{opt}} = 2\pi/\lambda_{\mathrm{opt}}$. In our visualizations of the optimized nanowires with elliptical cross-sections and for the plots of the total interaction cross section of these optimized nanowires in the examples below, we choose ρ such that $k_{\mathrm{opt}}\rho\sqrt{ab} = 0.05$.

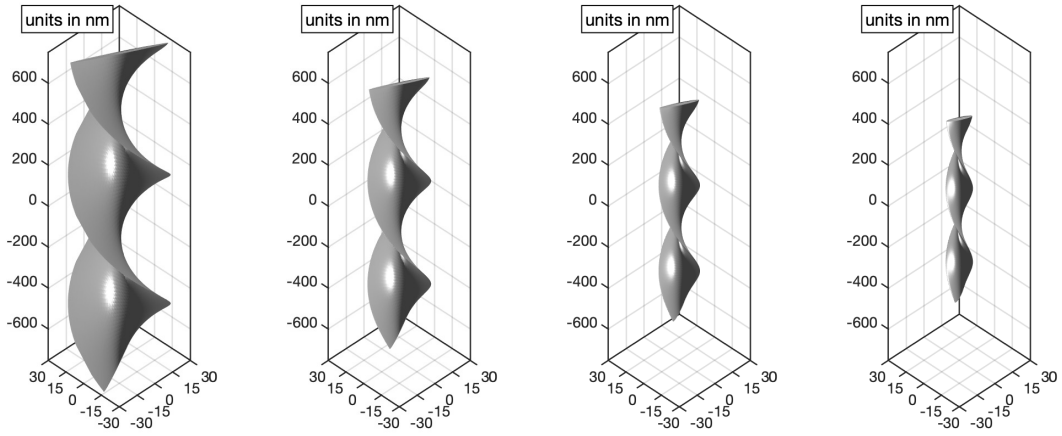

Figure 5.18: Optimized silver nanowires of length $L = 2\lambda_{\text{opt}}$ from Example 5.26 for $f_{\text{opt}} = 400, 500, 600, 700$ THz (left to right).

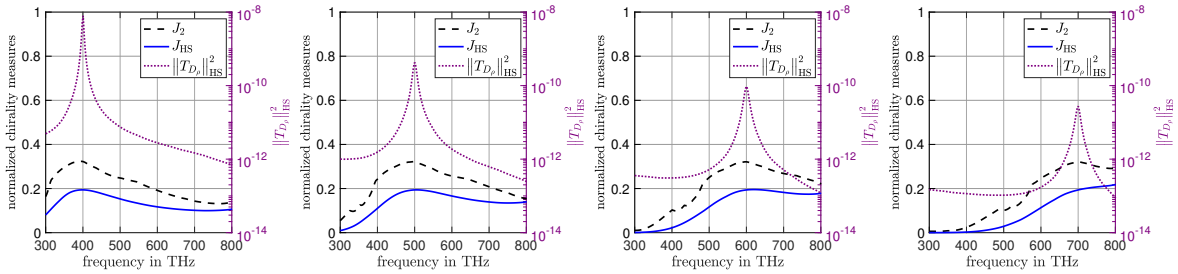

Figure 5.19: Frequency scans for optimized silver nanowires of length $L = 2\lambda_{\text{opt}}$ from Example 5.26 at $f_{\text{opt}} = 400, 500, 600, 700$THz (left to right).

Example 5.26. In our first numerical example we discuss thin straight silver and gold nanowires with elliptical cross-sections. We consider four different frequencies $f_{\text{opt}} = 400, 500, 600$, and 700THz, and for each of these frequencies we choose a different aspect ratio for the elliptical cross-section of the nanowire such that $f_{\text{opt}} = f_{\text{res}}$ is a plasmonic resonance frequency of the nanowire, i.e., $a/b = -\operatorname{Re}(\varepsilon_r(f_{\text{opt}}))$. We fix the spine curve of the nanowire to be a straight line segment and we optimize just the twist rate of the elliptical cross-section along the spine curve of the nanowire, i.e., the twist function θ that determines the rotation matrix in (3.4). For the regularization parameters in (5.85) we choose $\alpha_1 = \alpha_2 = 0$ and $\alpha_3 = 5 \times 10^{-5}$.

To discuss the influence of the length of the nanowire on the optimized shape of the nanowire, we consider four different values $L = j\lambda_{\text{opt}}/4$ with $j = 1, 2, 4, 8$ for the length constraint in (5.80). As before, λ_{opt} denotes the wavelength at the frequency f_{opt}. Accordingly, we choose the maximal degree N of circularly polarized vector spherical harmonics that is used in the discretization of the operator $\boldsymbol{T}_\rho(\boldsymbol{p}, V_{\boldsymbol{p},\theta})$ and of its Fréchet derivative $\boldsymbol{T}'_\rho[\boldsymbol{p}, V_{\boldsymbol{p},\theta}](\boldsymbol{h}, \phi)$ (see Remark 5.9 and Remark 5.17) to be $N = 2, 4, 6, 8$ for $L = j\lambda_{\text{opt}}/4$ with $j = 1, 2, 4, 8$, respectively.

We use cubic not-a-knot splines with $n = 10$ knots to describe the (fixed) spine curve K and the twist function θ and $M = 11$ quadrature points for the composite Simpson rule on each spline segment to approximate integrals over K. Since the em-chirality measure χ_{HS}, and thus also the objective functional Φ, are not differentiable at an em-achiral configuration, we choose an em-chiral initial guess for the shape optimization algorithm. To this end, we start with a rotation minimizing frame along the straight spine curve and add a small random twist. The same random twist is used for all frequencies and length constraints.

In Figure 5.18 we show the optimized twisted silver nanowires obtained by the shape op-

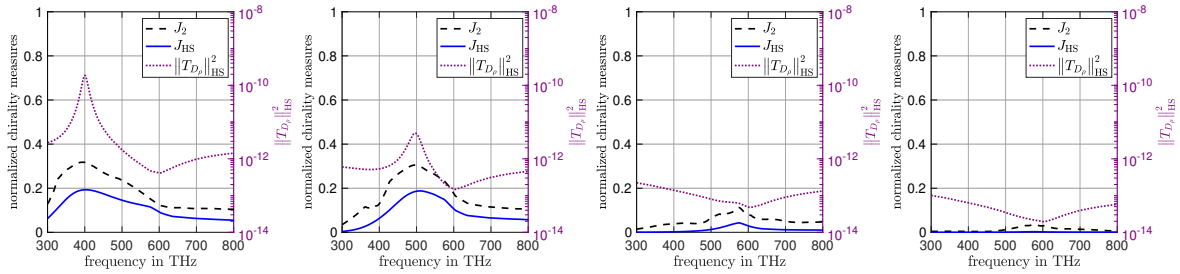

Figure 5.20: Frequency scans for optimized gold nanowires of length $L = 2\lambda_{\mathrm{opt}}$ from Example 5.26 at $f_{\mathrm{opt}} = 400, 500, 600, 700$THz (left to right).

		Silver					**Gold**				
	f_{opt} [THz]	400	500	600	700		f_{opt} [THz]	400	500	600	700
$L = \frac{\lambda_{\mathrm{opt}}}{4}$	J_2	0.26	0.26	0.26	0.26	$L = \frac{\lambda_{\mathrm{opt}}}{4}$	J_2	0.26	0.23	0.09	0.03
	J_{HS}	0.12	0.12	0.12	0.12		J_{HS}	0.12	0.12	0.02	0.003
$L = \frac{\lambda_{\mathrm{opt}}}{2}$	J_2	0.39	0.39	0.39	0.39	$L = \frac{\lambda_{\mathrm{opt}}}{2}$	J_2	0.39	0.37	0.17	0.06
	J_{HS}	0.17	0.17	0.17	0.17		J_{HS}	0.17	0.17	0.03	0.004
$L = \lambda_{\mathrm{opt}}$	J_2	0.37	0.37	0.37	0.37	$L = \lambda_{\mathrm{opt}}$	J_2	0.36	0.35	0.13	0.03
	J_{HS}	0.20	0.20	0.20	0.20		J_{HS}	0.20	0.19	0.04	0.003
$L = 2\lambda_{\mathrm{opt}}$	J_2	0.32	0.32	0.32	0.32	$L = 2\lambda_{\mathrm{opt}}$	J_2	0.32	0.30	0.08	0.01
	J_{HS}	0.19	0.19	0.19	0.19		J_{HS}	0.19	0.19	0.03	0.0008

Table 5.2: Normalized em-chirality measures J_2 and J_{HS} of optimized silver (left) and gold nanowires (right) from Example 5.26.

timization for $L = 2\lambda_{\mathrm{opt}}$ and $f_{\mathrm{opt}} = 400, 500, 600$, and 700THz (left to right). The direction of the twist of the optimized structure depends on the initial guess. The aspect ratios a/b of the elliptical cross-sections vary between 26.94 at $f_{\mathrm{opt}} = 400$THz and 5.94 at $f_{\mathrm{opt}} = 700$THz. The optimized twist rate per wavelength of the cross-sections of the four optimized twisted silver nanowires around the straight spine curve is almost constant and virtually the same for all frequencies.

In Table 5.2 we collect the values of the normalized em-chirality measures J_2 and J_{HS} from (5.70) and (5.69) of the optimized straight twisted silver and gold nanowires for the four different frequencies and the four different length constraints. Each pair of entries in these tables corresponds to a different optimized twisted silver or gold nanowire. For the silver nanowires we observe that the values of J_2 and J_{HS} that are reached for the different optimized structures are independent of the frequency. On the other hand, for the optimized gold nanowires these values change significantly with the frequency. While at $f_{\mathrm{opt}} = 400$THz and 500THz the normalized em-chirality measures of the optimized twisted gold nanowires are comparable to those of the optimized twisted silver nanowires, the normalized em-chirality measures of the optimized twisted gold nanowires quickly decrease at higher frequencies. This is a consequence of the increasing imaginary part of the relative electric permittivity of gold at higher frequencies (see Table 5.1). For the gold nanowires the aspect ratio a/b of the elliptical cross-section varies between 20.11 at $f_{\mathrm{opt}} = 400$THz and 1.69 at $f_{\mathrm{opt}} = 700$THz, i.e., the cross-section is somewhat rounder than for the corresponding silver nanowires. Finally, we study the frequency dependence of the normalized em-chirality measures for the optimized twisted silver and gold nanowires of length $L = 2\lambda_{\mathrm{opt}}$ that have been optimized at $f_{\mathrm{opt}} = 400, 500, 600$, and 700THz. In each of the plots in Figure 5.19 and 5.20 the optimized nanowire is fixed. However, it is illuminated with incident waves of different frequencies, and thus its frequency-dependent relative electric permittivity ε_r varies. In Figure 5.19 we plot the normalized em-chirality measures J_2 (dashed) and

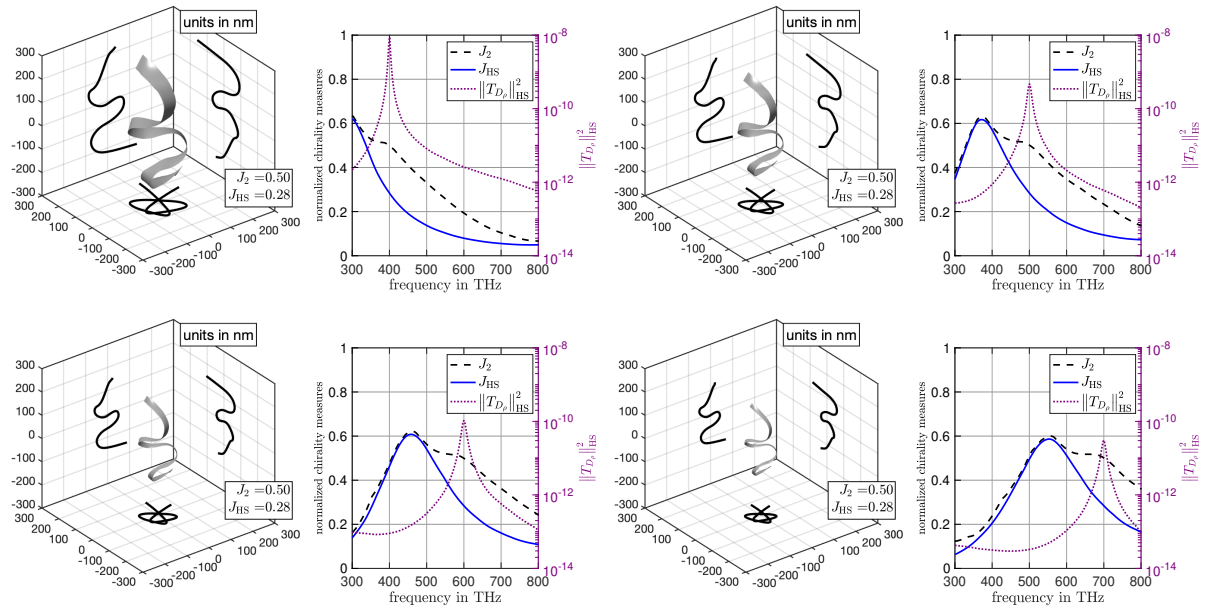

Figure 5.21: Optimized silver nanowires and corresponding frequency scans from Example 5.27 for $f_{\mathrm{opt}} = 400, 500\mathrm{THz}$ (top row) and $f_{\mathrm{opt}} = 600, 700\mathrm{THz}$ (bottom row).

J_{HS} (solid) and an approximation of the total interaction cross section (dotted) of the optimized thin twisted silver nanowires shown in Figure 5.18 over a frequency range between 300THz and 800THz. The approximation of the total interaction cross section is obtained by evaluating the Hilbert-Schmidt norm of the operator $\mathcal{T}_{D_\rho}$ from (5.25) with $\rho = 0.05/(k_{\mathrm{opt}}\sqrt{ab})$. The sharp peak in the total interaction cross section is exactly at the plasmonic resonance frequency f_{res} of the corresponding thin silver nanowire. It is important to note that, in contrast to the normalized em-chirality measures, the total interaction cross section is plotted in a logarithmic scale. We find that J_2 and J_{HS} have a peak at the plasmonic resonance frequency f_{res} as well. This is the frequency that has been used in the shape optimization, i.e., $f_{\mathrm{opt}} = f_{\mathrm{res}}$.

In Figure 5.20 we show the corresponding frequency scans for the optimized thin twisted gold nanowires. For the gold nanowires that have been optimized at $f_{\mathrm{opt}} = 400\mathrm{THz}$ and 500THz, the results are similar as for the silver nanowires that have been optimized at the same frequencies in Figure 5.19. On the other hand, for the gold nanowires optimized at $f_{\mathrm{opt}} = 600\mathrm{THz}$ and 700THz, the plasmonic resonance is no longer visible in the plots of the total interaction cross section. This is a consequence of the larger imaginary part of the electric permittivity of gold at $f_{\mathrm{opt}} = 600, 700\mathrm{THz}$ (see Table 5.1 and Figure 2.1). For these two higher frequencies, the values of the normalized em-chirality measures J_2 and J_{HS} are small across the entire frequency band. The plasmonic resonance seems to be required to obtain thin metallic nanowires that exhibit large normalized em-chirality measures.

Example 5.27. In our second example we consider a free-form shape optimization for the spine curve of thin silver and gold nanowires with elliptical cross-sections, but we do not optimize the twist rate of the cross-section of the nanowire along the spine curve. As in the first example, we consider four different frequencies $f_{\mathrm{opt}} = 400, 500, 600,$ and 700THz, and for each of these frequencies we again choose the aspect ratio of the elliptical cross-section of the nanowire such that $f_{\mathrm{opt}} = f_{\mathrm{res}}$ is a plasmonic resonance frequency for the nanowire. For the regularization parameters in (5.85) we choose $\alpha_1 = 5$, $\alpha_2 = 8 \times 10^{-3}$ and $\alpha_3 = 0$.

The length constraint for the nanowire is set to be $L = 3\lambda_{\mathrm{opt}}/2$, and, accordingly, we choose the maximal degree N of circularly polarized vector spherical harmonics that is used in the discretization of the operator $\boldsymbol{T}_\rho(\boldsymbol{p}, V_{\boldsymbol{p},\theta})$ and of its Fréchet derivative $\boldsymbol{T}'_\rho[\boldsymbol{p}, V_{\boldsymbol{p},\theta}](\boldsymbol{h}, \phi)$ (see Remark 5.9 and Remark 5.17) to be $N = 5$. We use cubic not-a-knot splines with $n = 20$ knots

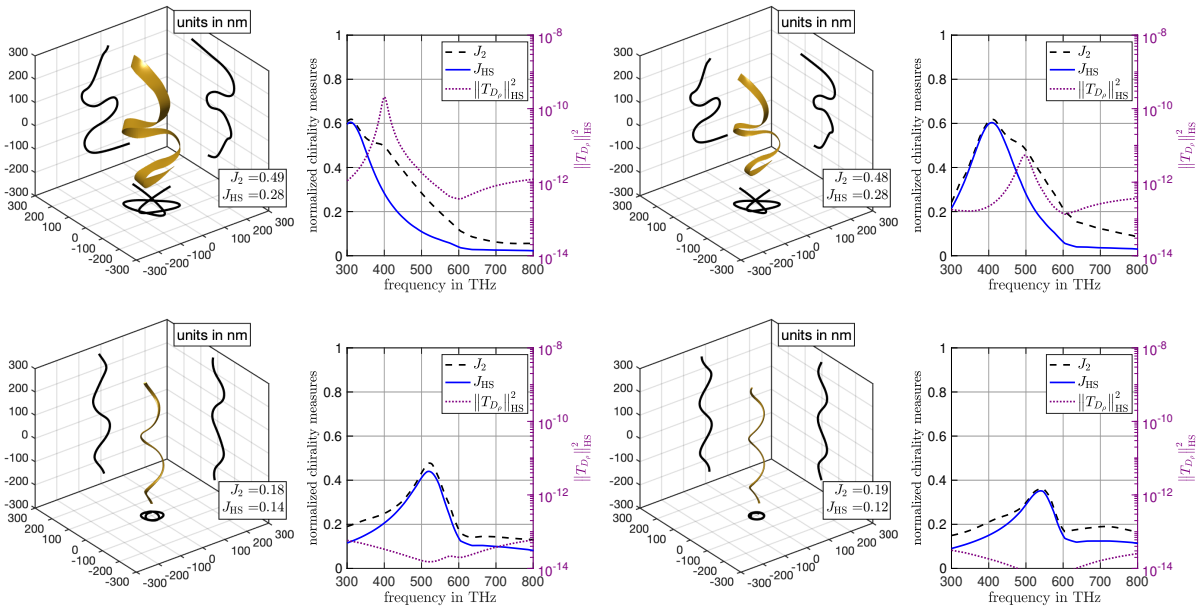

Figure 5.22: Optimized gold nanowires and corresponding frequency scans from Example 5.27 for $f_{\mathrm{opt}} = 400, 500\mathrm{THz}$ (top row) and $f_{\mathrm{opt}} = 600, 700\mathrm{THz}$ (bottom row).

to parametrize the spine curve K and the (fixed) twist function θ and $M = 11$ quadrature points on each spline segment to discretize line integrals over K.

For the initial guess for the spine curve we use a straight line of length $L = 3\lambda_{\mathrm{opt}}/2$, and we add a small random perturbation to obtain an em-chiral configuration. The same random perturbation is used for all frequencies. The initial geometry adapted frame is chosen to be rotation minimizing.

In Figure 5.21 we show the optimized silver nanowires that have been obtained by the shape optimization for $f_{\mathrm{opt}} = 400, 500, 600$, and 700THz. The aspect ratios a/b of the elliptical cross-sections are the same as in Example 5.26 and vary between 26.94 at $f_{\mathrm{opt}} = 400\mathrm{THz}$ and 5.94 at $f_{\mathrm{opt}} = 700\mathrm{THz}$. For a better three-dimensional impression, we also included the projections of the spine curves of the optimized nanowires on the three coordinate planes in these plots. During the optimization the straight initial guess bends into a rather irregular shape that is difficult to interpret. However, the optimized silver nanowires obtained at the four different frequencies have very similar shapes, which seem to be rescaled versions of each other with respect to the wavelength.

Figure 5.21 also contains plots illustrating the frequency dependence of the normalized em-chirality measures J_2 (dashed) and J_{HS} (solid) as well as of the total interaction cross-section (dotted) of the optimized silver nanowires. The maxima of the normalized em-chirality measures and the plasmonic resonances visible in the plots of the total interaction cross-section are rather localized. It is interesting to observe that, although the shape optimization has been carried out at the plasmonic resonance frequency, i.e., $f_{\mathrm{opt}} = f_{\mathrm{res}}$, the maximum of the normalized em-chirality measures J_2 and J_{HS} is attained around 100THz to 150THz below the plasmonic resonance frequency in all four examples. This is a common feature that we have observed in several other examples, and we will utilize this phenomenon in Example 5.28 below to design thin silver and gold nanowires with even higher em-chirality measures.

In Figure 5.22 we show the corresponding results of the shape optimization of thin gold nanowires for $f_{\mathrm{opt}} = 400, 500, 600$, and 700THz. The shapes of the gold nanowires that have been optimized at $f_{\mathrm{opt}} = 400, 500\mathrm{THz}$ are similar to those of the optimized thin silver nanowires in Figure 5.21. Also the frequency scans in Figure 5.22 show a similar behavior, although the plasmonic resonance is not as pronounced as for the silver nanowires. For $f_{\mathrm{opt}} = 600, 700\mathrm{THz}$

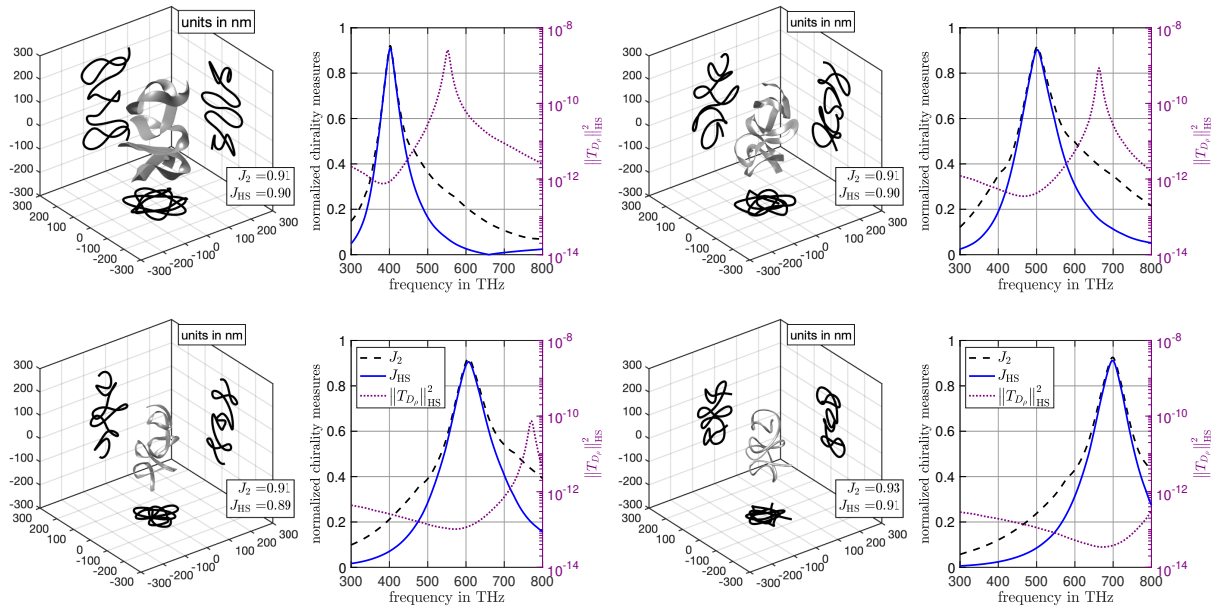

Figure 5.23: Optimized silver nanowires and corresponding frequency scans from Example 5.28 for $f_{\mathrm{opt}} = 400, 500\mathrm{THz}$ (top row) and for $f_{\mathrm{opt}} = 600, 700\mathrm{THz}$ (bottom row).

the results are different. The shapes of the optimized gold nanowires look similar to those obtained for dielectric thin tubes in Example 5.22. The optimized gold nanowires are helices, and no plasmonic resonances are visible in the plots of the total interaction cross-sections. This different behavior results from the larger imaginary part of the electric permittivity of gold at $f_{\mathrm{opt}} = 600, 700\mathrm{THz}$ (see Table 5.1 and Figure 2.1).

Example 5.28. The goal of our final example is to design thin silver and gold nanowires with elliptical cross-sections that possess normalized em-chirality measures J_2 and J_{HS} as close to 1 as possible at optical frequencies. We consider a free-form shape optimization for the spine curve of the nanowire, and we optimize the twisting of the elliptical cross-section of the nanowire along the spine curve. As in the previous examples, we discuss four different frequencies $f_{\mathrm{opt}} = 400, 500, 600$, and $700\mathrm{THz}$. For each of these frequencies we choose the aspect ratio of the elliptical cross-section of the nanowire such that its plasmonic resonance frequency f_{res} is around 100THz to 150THz above the frequency f_{opt} that is used in the shape optimization, i.e., we use $a/b = 12.5$ at $f_{\mathrm{opt}} = 400\mathrm{THz}$, $a/b = 7.14$ at $f_{\mathrm{opt}} = 500\mathrm{THz}$, $a/b = 3.85$ at $f_{\mathrm{opt}} = 600\mathrm{THz}$, and $a/b = 1.92$ at $f_{\mathrm{opt}} = 700\mathrm{THz}$. In particular, it holds that $f_{\mathrm{opt}} \neq f_{\mathrm{res}}$. This is different from the previous two examples, where we optimized the shape of the nanowires directly at the plasmonic resonance frequency. It is motivated by our observations at the end of Example 5.27. For the regularization parameters in (5.85) we choose $\alpha_1 = 5$, $\alpha_2 = 8 \times 10^{-3}$ and $\alpha_3 = 1 \times 10^{-6}$. The outcome of the shape optimization strongly depends on the initial guess for the spine curve. Thus, we consider in this example 100 different initial spine curves for the optimization scheme at each frequency. These are helices with four turns, where the total height and the radius of the helix are chosen randomly in $[0, 2\lambda_{\mathrm{opt}}/3]$ and in $[0, \lambda_{\mathrm{opt}}/2]$, respectively. As before, λ_{opt} denotes the wavelength at the frequency f_{opt}. We also add different random twists to these initial guesses. We use cubic not-a-knot splines with $n = 40$ knots to parametrize the spine curve and the twist function, and $M = 21$ quadrature points on each spline segment to discretize line integrals over K. We choose the maximal degree N of circularly polarized vector spherical harmonics that is used in the discretization of the operator $\boldsymbol{T}_\rho(\boldsymbol{p}, V_{\boldsymbol{p},\theta})$ and of its Fréchet derivative $\boldsymbol{T}'_\rho[\boldsymbol{p}, V_{\boldsymbol{p},\theta}](\boldsymbol{h}, \phi)$ (see Remark 5.9 and Remark 5.17) to be $N = 5$. This gives 100 different optimized silver and gold nanowires for each frequency f_{opt}, and we finally select those (for each frequency f_{opt}) that attain the highest normalized em-chirality measures.

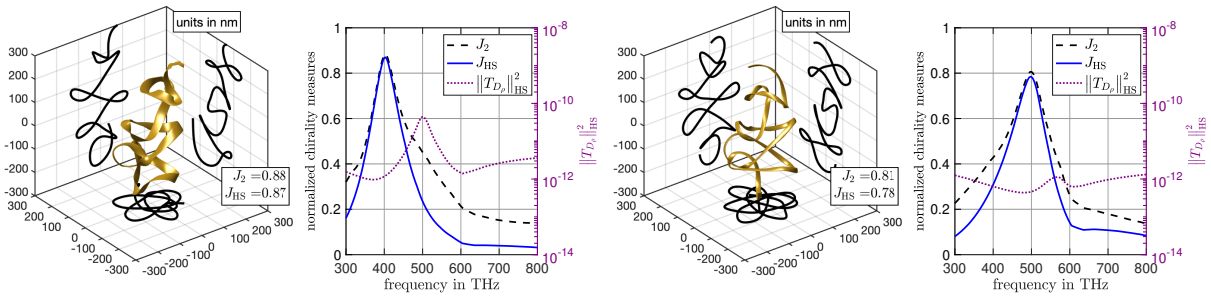

Figure 5.24: Optimized gold nanowires and corresponding frequency scans from Example 5.28 for $f_{\mathrm{opt}} = 400, 500\mathrm{THz}$.

In Figure 5.23 we show the optimized silver nanowires that have been obtained for $f_{\mathrm{opt}} = 400, 500\mathrm{THz}$ (top row) and for $f_{\mathrm{opt}} = 600, 700\mathrm{THz}$ (bottom row). The shapes of the optimized nanowires look complicated but they show similarities and seem to be scaled according to the wavelength, where the optimization has been carried out. Very high normalized em-chirality measures are being attained by the optimized structures at all four frequencies $f_{\mathrm{opt}} = 400, 500, 600,$ and $700\mathrm{THz}$, respectively. Figure 5.23 also shows plots of the normalized em-chirality measures J_2 (dashed) and J_{HS} (solid) as well as of the total interaction cross section (dotted) of the optimized thin silver nanowires as a function of the frequency of the incident waves. The maximal values of the normalized em-chirality measures appear at approximately the same frequency, where the total interaction cross-section of the nanowires has a local minimum. Directly at the plasmonic resonance frequency the normalized em-chirality measures are smaller, but on the other hand the total interaction cross section of the nanowire is much larger.

In Figure 5.24 we show the corresponding results for gold nanowires at $f_{\mathrm{opt}} = 400\mathrm{THz}$ and $500\mathrm{THz}$. The obtained normalized em-chirality measures are lower than for silver, which might be explained by the larger imaginary part of the relative electric permittivity of gold at these frequencies. Also the plasmonic resonances are not as pronounced as for the thin silver nanowires. As a consequence of the even larger imaginary part of the electric permittivity of gold at $f_{\mathrm{opt}} = 600\mathrm{THz}$ and $700\mathrm{THz}$, the normalized em-chirality measures obtained for thin gold nanowires optimized at these frequencies are rather small. Therefore, we do not show the results for these frequencies.

Appendix A

Results from linear functional analysis

The following theorem is about the partition of unity. We need this theorem to introduce Sobolev spaces of (vector-valued) functions on the boundary of a Lipschitz domain $\partial\Omega$. The formulation itself can be found in e.g. [88, Thm. A.9]. A proof for a more general setting can be found in [122, p. 61].

Theorem A.1. *Let $K \subset \mathbb{R}^3$ be a compact set. For every system of open sets $\{U_j \,|\, j = 1, \dots, m\}$ with $K \subset \bigcup_{j=1}^m U_j$ there exists a system of functions $\{\phi_j \,|\, j = 1, \dots, m\}$ with $\phi_j \in C^\infty(\mathbb{R}^3)$, $supp(\phi_j) \subset U_j$ for $j = 1, \dots, m$ and $\sum_{j=1}^m \phi_j(\boldsymbol{y}) = 1$ for all $\boldsymbol{y} \in K$. We call $\{\phi_j \,|\, j = 1, \dots, m\}$ a partition of unity on K with respect to the covering $\{U_j \,|\, j = 1, \dots, m\}$ and write $(U_j, \phi_j)_{j=1,\dots,m}$ in abbreviated form.*

The following definition can be found in e.g. [91, Def. 15.15, Thm. 15.16]. We need these definitions in Chapter 5, when studying norms and scalar products involving the far field operator.

Definition A.2. Let X and Y be Hilbert spaces, $A : X \to Y$ be a compact injective linear operator, and $A^* : Y \to X$ be its adjoint. The nonnegative square roots of the eigenvalues of the nonnegative self-adjoint compact operator $A^*A : X \to X$ are called singular values of A and are denoted by $(\mu_j)_{j\in\mathbb{N}}$. A singular system of A is a triple $(\mu_j, x_j, y_j)_{j\in\mathbb{N}}$ such that $(x_j)_{j\in\mathbb{N}}$ and $(y_j)_{j\in\mathbb{N}}$ are orthonormal bases in X and Y, respectively and

$$Ax_j \;=\; \mu_j y_j, \qquad A^* y_j = \mu_j x_j \quad \text{for all } j \in \mathbb{N}.$$

The next definition is found e.g. in [44, XI.6, Def. 1, Lem. 2, Def. 17].

Definition A.3. Let X be a separable Hilbert space with orthonormal basis $(x_j)_{j\in\mathbb{N}} \subset X$. A bounded linear operator $A : X \to X$ is said to be a Hilbert-Schmidt operator if the series

$$\|A\|_{\mathrm{HS}} \;=\; \Big(\sum_{j\in\mathbb{N}} \|Ax_j\|^2 \Big)^{1/2}$$

converges. In this case, $\|A\|_{\mathrm{HS}}$ is independent of the choice of the orthonormal basis $(x_j)_{j\in\mathbb{N}}$ and it holds that

$$\|A\|_{\mathrm{HS}} \;=\; \Big(\sum_{j\in\mathbb{N}} \langle A^*Ax_j, x_j\rangle \Big)^{1/2} \;=\; \mathrm{tr}(A^*A)^{1/2}\,.$$

For a singular system $(\mu_j, x_j, y_j)_{j\in\mathbb{N}}$ of A, it holds that $\|A\|_{\mathrm{HS}} = \|(\mu_j)_{j\in\mathbb{N}}\|_{\ell^2}$. The space of all Hilbert-Schmidt operators on X is a Hilbert space with scalar product

$$\langle A, B\rangle_{\mathrm{HS}} \;=\; \sum_{j\in\mathbb{N}} \langle Ax_j, Bx_j\rangle \;=\; \mathrm{tr}(B^*A).$$

The Lax-Milgram theorem is used to prove existence and uniqueness of the subproblems that arise by considering the Helmholtz decomposition of $H(\mathbf{curl}, B_R(0))$ in Chapter 2. The proof is similar to [45, Ch. 6.2.1, Thm. 1].

Theorem A.4 (Lax-Milgram)**.** *Let H be a Hilbert space and $a : H \times H \to \mathbb{C}$ a bounded sesquilinear form, i.e. there exists a constant $C > 0$ such that*

$$|a(u,v)| \leq C\|u\|\|v\| \quad \text{for all } u, v \in H.$$

Then there exists a uniquely determined, linear, bounded operator $A : H \to H$ such that

$$a(u,v) = \langle Au, v\rangle \quad \text{for all } u, v \in H.$$

Further, let a satisfy

$$\mathrm{Re}(e^{\mathrm{i}t}a(u,u)) \geq c\|u\|^2 \quad \text{for all } u \in H$$

for some $t \in \mathbb{R}$ and $c > 0$. Then, A has a bounded inverse with $\|A^{-1}\| \leq c^{-1}$ and the problem to find $u \in H$ such that

$$a(u,v) = \ell(v) \qquad \text{for all } v \in H,$$

where ℓ is a continuous, antilinear functional defined on H, is uniquely solvable.

Proof. Let $u \in H$. We define the linear and bounded functional

$$\ell_u : H \to \mathbb{C}, \qquad \ell_u(v) = \overline{a(u,v)}.$$

The Riesz representation theorem shows that there is a uniquely determined $w = w(u) \in H$ such that

$$\ell_u(v) = \langle v, w(u)\rangle \quad \text{for all } v \in H.$$

We define the operator $A : H \to H$ via $Au = w$. This operator is linear, bounded, uniquely determined and it holds that

$$a(u,v) = \langle Au, v\rangle \quad \text{for all } u, v \in H.$$

Further, it holds that

$$c\|u\|^2 \leq \mathrm{Re}(e^{\mathrm{i}t}a(u,u)) \leq |e^{\mathrm{i}t}a(u,u)| = |\langle Au, u\rangle| \leq \|Au\|\,\|u\|$$

and thus

$$c\,\|u\| \leq \|Au\|\,. \tag{A.1}$$

This immediately gives that A is injective. For $u \in A(H)^\perp$ we have that

$$0 = \langle Au, u\rangle \geq c\,\|u\|^2\,,$$

giving that $A(H)^\perp = \{0\}$. For $(v_n)_{n\in\mathbb{N}} \subset A(H)$ with $Au_n = v_n \to v \in \overline{A(H)}$, (A.1) shows that $(u_n)_{n\in\mathbb{N}} \subset H$ is a Cauchy sequence. Since H is a Hilbert space, we find $u \in H$ with $u_n \to u$. The continuity of A now gives that $Au = v$, proving that $H = A(H)$. This shows, that the operator A is invertible. The inequality (A.1) further gives that $\|A^{-1}\| \leq c^{-1}$. For the continuous and antilinear functional ℓ, the Riesz representation theorem shows the existence of a uniquely determined $f \in H$ such that

$$\ell(v) = \langle f, v\rangle \quad \text{for all } v \in H.$$

Consequently, the problem to find $u \in H$ with

$$a(u,v) = \ell(v) \quad \text{for all } v \in H,$$

is equivalent to find $u \in H$ with $Au = f$. Since A is proven to be boundedly invertible, we find that $u = A^{-1}f$. □

Appendix B

Some useful estimates

Lemma B.1. *Let D be a Lipschitz domain and let Ω be smooth (e.g. Ω with a boundary in C^3 in order to apply [63, Thm. 8.13.]) with $D \subset \Omega \subset \mathbb{R}^d$, $d = 2, 3$. Further, let $\gamma_0 > 0$ and either $\gamma_1 > 0$ or $\gamma_1 \in \mathbb{C}$ with $\operatorname{Re}(\gamma_1) < 0$ and $\operatorname{Im}(\gamma_1) > 0$. Define $\gamma \in L^\infty(\Omega)$ by*

$$\gamma = \begin{cases} \gamma_1, & x \in D, \\ \gamma_0, & x \in \Omega \setminus \overline{D}. \end{cases}$$

Given $\boldsymbol{F} \in L^\infty(\Omega)^d$, the problem to find $w \in H^1_0(\Omega)$ such that

$$\operatorname{div}(\gamma \nabla w) = \operatorname{div}(\chi_D \boldsymbol{F}) \quad \text{in } \Omega, \quad w = 0 \quad \text{on } \partial\Omega \tag{B.1}$$

has a unique (variational) solution. Moreover, there exist constants $C, C_p > 0$ such that

$$\|\nabla w\|_{L^2(\Omega)} \leq C\,|D|^{1/2}\,\|\boldsymbol{F}\|_{L^\infty(D)}\,, \tag{B.2}$$

$$\|w\|_{L^2(\Omega)} \leq C\,|D|^{3/4}\,\|\boldsymbol{F}\|_{L^\infty(D)}\,, \tag{B.3}$$

$$\|w\|_{W^{1,p}(\Omega)} \leq C_p\,|D|^{1/p}\,\|\boldsymbol{F}\|_{L^\infty(D)}\,, \quad 1 < p < 2. \tag{B.4}$$

Proof. The variational formulation is to find $w \in H^1_0(\Omega)$ such that

$$\int_\Omega \gamma \nabla w \cdot \overline{\nabla v}\,\mathrm{d}\boldsymbol{x} = \int_D \boldsymbol{F} \cdot \overline{\nabla v}\,\mathrm{d}\boldsymbol{x} \quad \text{for all } v \in H^1_0(\Omega). \tag{B.5}$$

If $\gamma_1 > 0$, the sequilinear form on the left hand side is bounded and coercive on $H^1_0(\Omega)$. If $\gamma_1 \in \mathbb{C}$ with $\operatorname{Re}(\gamma_1) < 0$ and $\operatorname{Im}(\gamma_1) > 0$, we consider $\beta \in \mathbb{R}$ such that $\operatorname{Re}(e^{\mathrm{i}\beta}\gamma) > 0$ and find for $w \in H^1_0(\Omega)$ that

$$\operatorname{Re}\left(e^{\mathrm{i}\beta} \int_\Omega \gamma |\nabla w|^2\,\mathrm{d}\boldsymbol{x}\right) \geq c\,\|\nabla w\|^2_{L^2(\Omega)} \geq c\,\|w\|^2_{H^1(\Omega)}\,.$$

The last step follows by the Poincaré inequality. Thus, in both cases, the Lax-Milgram theorem A.4 shows the existence of a unique variational solution $w \in H^1_0(\Omega)$ of (B.1). From the weak formulation in (B.5), we immediately find that

$$\|\nabla w\|^2_{L^2(\Omega)} \leq C\,|D|^{1/2}\,\|\boldsymbol{F}\|_{L^\infty(D)}\,\|\nabla w\|_{L^2(\Omega)}\,,$$

what gives (B.2). Now let $z \in H^1_0(\Omega)$ be the unique solution to

$$\operatorname{div}(\gamma_0 \nabla z) = -w \quad \text{in } \Omega, \quad z = 0 \quad \text{on } \partial\Omega. \tag{B.6}$$

Elliptic regularity results (see e.g. [63, Thm. 8.13.]) show that $\|z\|_{H^3(\Omega)} \leq C\,\|w\|_{H^1(\Omega)}$. Note that $\|z\|_{H^1(\Omega)} \leq C\,\|w\|_{H^1(\Omega)}$ due to the Lax-Milgram theorem A.4. The Sobolev embedding theorem (see e.g. [63, Cor. 7.11]) further gives that

$$\|\nabla z\|_{L^\infty(\Omega)} \leq C\,\|z\|_{H^3(\Omega)}\,.$$

Using the weak formulation of (B.6) and (B.1) gives that

$$\begin{aligned}\|w\|_{L^2(\Omega)}^2 &= \int_\Omega \gamma_0 \nabla z \cdot \overline{\nabla w}\,\mathrm{d}\boldsymbol{x} = \overline{\int_\Omega (\gamma_0-\gamma)\,\nabla w\cdot\overline{\nabla z}\,\mathrm{d}\boldsymbol{x}} + \overline{\int_\Omega \gamma\nabla w\cdot\overline{\nabla z}\,\mathrm{d}\boldsymbol{x}}\\ &= \overline{\int_\Omega (\gamma_0-\gamma)\,\nabla w\cdot\overline{\nabla z}\,\mathrm{d}\boldsymbol{x}} + \overline{\int_D \boldsymbol{F}\cdot\overline{\nabla z}\,\mathrm{d}\boldsymbol{x}}\\ &\le \left(\|\chi_D\boldsymbol{F}\|_{L^1(\Omega)} + \|(\gamma_0-\gamma)\,\nabla w\|_{L^1(\Omega)}\right)\|\nabla z\|_{L^\infty(\Omega)}\\ &\le C\left(|D|\,\|\boldsymbol{F}\|_{L^\infty(D)} + |D|^{1/2}\,\|\nabla w\|_{L^2(\Omega)}\right)\|w\|_{H^1(\Omega)}\end{aligned}$$

Using (B.2) and the Poincaré inequality finally gives (B.3). Moreover, we note that

$$\operatorname{div}(\gamma_0\nabla w) = \operatorname{div}(\chi_D\boldsymbol{F}) + \operatorname{div}((\gamma_0-\gamma)\,\nabla w)\,. \tag{B.7}$$

For $1<p<2$ it holds that Δ is an isomorphism from $W_0^{1,p}(\Omega)$ to $W^{-1,p}(\Omega)$ (see e.g. [17, p. 40]). The right hand side of (B.7) is in $W^{-1,p}(\Omega)$ as well and using Hölders inequality and (B.2) leads to

$$\begin{aligned}\|w\|_{W^{1,p}(\Omega)} &\le C_p\,\|\operatorname{div}(\gamma_0\nabla w)\|_{W^{-1,p}(\Omega)}\\ &\le C_p\left(\|\operatorname{div}(\chi_D\boldsymbol{F})\|_{W^{-1,p}(\Omega)} + \|\operatorname{div}((\gamma_0-\gamma)\,\nabla w)\|_{W^{-1,p}(\Omega)}\right)\\ &\le C_p\left(\|\chi_D\boldsymbol{F}\|_{L^p(\Omega)} + \|(\gamma_0-\gamma)\,\nabla w\|_{L^p(\Omega)}\right)\\ &\le C_p\left(|D|^{1/p}\,\|\boldsymbol{F}\|_{L^\infty(D)} + |D|^{1/p-1/2}\,\|\nabla w\|_{L^2(\Omega)}\right) \le C_p|D|^{1/p}\,\|\boldsymbol{F}\|_{L^\infty(D)}\,.\end{aligned}$$

The third inequality can be deduced by using that $\operatorname{div}: L^p(\Omega)\to W^{-1,p}(\Omega)$ is continuous. □

Lemma B.2. *Let $0<\rho<r/2$ and let $D'_\rho\subset B'_\rho(0)$ be open, where $B'_\rho(0)\subset\mathbb{R}^2$ denotes the disc of radius ρ around zero. Suppose that $A_0, A_1\in C^{0,1}(B'_r(0),\mathbb{R}^{2\times 2})$ are symmetric and*

$$c^{-1}|\boldsymbol{\xi}'|^2 \le \boldsymbol{\xi}'\cdot A_j(\boldsymbol{x}')\boldsymbol{\xi}' \le c|\boldsymbol{\xi}'|^2 \quad \text{for all } \boldsymbol{\xi}'\in\mathbb{R}^2,\ \boldsymbol{x}'\in B'_r(0) \quad \text{and } j=1,2$$

with some constant $c>0$ and let $\boldsymbol{F}\in C^{0,1}(B'_r(0),\mathbb{C}^2)$. Define A_ρ, $\widetilde{A}_\rho\in C^{0,1}(B'_r(0),\mathbb{R}^{2\times 2})$ by

$$A_\rho(\boldsymbol{x}') = \begin{cases} A_1, & \boldsymbol{x}'\in D'_\rho,\\ A_0, & \boldsymbol{x}'\in B'_r(0)\setminus\overline{D_\rho}, \end{cases} \qquad \widetilde{A}_\rho(\boldsymbol{x}') = \begin{cases} A_1(0), & \boldsymbol{x}'\in D'_\rho,\\ A_0(0), & \boldsymbol{x}'\in B'_r(0)\setminus\overline{D_\rho}. \end{cases}$$

Furthermore, let $\gamma_0>0$ and either $\gamma_1>0$ or $\gamma_1\in\mathbb{C}$ with $\operatorname{Re}(\gamma_1)<0$ and $\operatorname{Im}(\gamma_1)>0$. Define $\gamma_\rho\in L^\infty(\Omega)$ by

$$\gamma_\rho = \begin{cases} \gamma_1, & x\in D'_\rho,\\ \gamma_0, & x\in\Omega\setminus\overline{D'_\rho}. \end{cases}$$

The problems to find $w_\rho, \widetilde{w}_\rho\in H_0^1(B'_r(0))$ with

$$\operatorname{div}(\gamma_\rho A_\rho\nabla w_\rho) = \operatorname{div}(\chi_{D'_\rho}\boldsymbol{F}) \quad \text{in } B'_r(0), \qquad w_\rho = 0 \quad \text{on } \partial B'_r(0), \tag{B.8}$$

$$\operatorname{div}\left(\gamma_\rho\widetilde{A}_\rho\nabla\widetilde{w}_\rho\right) = \operatorname{div}(\chi_{D'_\rho}\boldsymbol{F}(0)) \quad \text{in } B'_r(0), \qquad \widetilde{w}_\rho = 0 \quad \text{on } \partial B'_r(0) \tag{B.9}$$

both have a unique solution. Furthermore, it holds that

$$\|\nabla w_\rho - \nabla\widetilde{w}_\rho\|_{L^2(B'_r(0))} = o(|D'_\rho|^{1/2}) \quad \text{as } \rho\to 0. \tag{B.10}$$

Proof. First, we prove that (B.8) and (B.9) both have a unique solution. For (B.8) we find that

$$\int_{B_r'(0)} \gamma_\rho \left(A_\rho \nabla w_\rho\right) \cdot \overline{\nabla v} \, \mathrm{d}\boldsymbol{x} = \int_{B_r'(0)} \chi_{D_\rho} \boldsymbol{F} \cdot \overline{\nabla v} \, \mathrm{d}\boldsymbol{x} \quad \text{for all } v \in H_0^1(B_r'(0)). \tag{B.11}$$

Moreover, we find that for all $u, v \in H_0^1(B_r'(0))$ it holds that

$$\begin{aligned}
\int_{B_r'(0)} \gamma_\rho \left(A_\rho \nabla u\right) \cdot \overline{\nabla v} \, \mathrm{d}\boldsymbol{x} &\leq C \int_{B_r'(0)} \left| \left(A_\rho \nabla u\right) \cdot \overline{\nabla v} \right| \mathrm{d}\boldsymbol{x} \\
&\leq C \left(\int_{B_r'(0)} |A_\rho \nabla u|^2 \, \mathrm{d}\boldsymbol{x} \right)^{1/2} \left(\int_{B_r'(0)} |\nabla v|^2 \, \mathrm{d}\boldsymbol{x} \right)^{1/2} \\
&\leq C \left\| u \right\|_{H^1(B_r'(0))} \left\| v \right\|_{H^1(B_r'(0))}.
\end{aligned}$$

Additionally, with $\beta \in \mathbb{R}$ such that $\mathrm{Re}(\mathrm{e}^{\mathrm{i}\beta}\gamma_\rho) > 0$, it holds that

$$\begin{aligned}
\mathrm{Re} \left(\int_{B_r'(0)} \mathrm{e}^{\mathrm{i}\beta} \gamma_\rho \left(A_\rho \nabla u\right) \cdot \overline{\nabla u} \, \mathrm{d}\boldsymbol{x} \right) \geq C \int_{B_r'(0)} A_\rho \nabla u \cdot \overline{\nabla u} \, \mathrm{d}\boldsymbol{x} &\geq C \int_{B_r'(0)} |\nabla u|^2 \, \mathrm{d}\boldsymbol{x} \\
&\geq C \left\| u \right\|_{H^1(B_r'(0))}.
\end{aligned}$$

Here, we used the Poincaré inequality for the last estimate. Since the right hand side in (B.11) is antilinear, the Lax-Milgram theorem A.4 shows that there is a unique solution $w_\rho \in H_0^1(B_r'(0))$ that solves (B.8). The uniqueness and existence of $\widetilde{w}_\rho \in H_0^1(B_r'(0))$, the solution to (B.9) can be shown analogously. Furthermore, it holds that

$$\begin{aligned}
\mathrm{div} \left(\gamma_\rho \widetilde{A}_\rho \nabla w_\rho \right) &= \mathrm{div} \left(\gamma_\rho \left(\widetilde{A}_\rho - A_\rho \right) \nabla w_\rho \right) + \mathrm{div} \left(\gamma_\rho A_\rho \nabla w_\rho \right) \\
&= \mathrm{div} \left(\chi_{D_\rho} \boldsymbol{F} \right) + \mathrm{div} \left(\gamma_\rho \left(\widetilde{A}_\rho - A_\rho \right) \nabla w_\rho \right) \\
&= \mathrm{div} \left(\chi_{D_\rho} \boldsymbol{F}(0) \right) + \mathrm{div} \left(\chi_{D_\rho} \left(\boldsymbol{F} - \boldsymbol{F}(0) \right) \right) + \mathrm{div} \left(\gamma_\rho \left(\widetilde{A}_\rho - A_\rho \right) \nabla w_\rho \right).
\end{aligned}$$

Introducing $\Omega' = B'_{\rho^{1/4}}(0)$ implies that $w_\rho = \widetilde{w}_\rho + v_1 + v_2 + v_3$, where v_1, v_2 and v_3 are the unique solutions to

$$\mathrm{div} \left(\gamma_\rho \widetilde{A}_\rho \nabla v_1 \right) = \mathrm{div} \left(\chi_{D_\rho} \left(\boldsymbol{F} - \boldsymbol{F}(0) \right) \right) \quad \text{in } B_r'(0), \quad v_1 = 0 \text{ on } \partial B_r'(0), \tag{B.12}$$

$$\mathrm{div} \left(\gamma_\rho \widetilde{A}_\rho \nabla v_2 \right) = \mathrm{div} \left(\chi_{\Omega'} \gamma_\rho \left(\widetilde{A}_\rho - A_\rho \right) \nabla w_\rho \right) \quad \text{in } B_r'(0), \quad v_2 = 0 \text{ on } \partial B_r'(0), \tag{B.13}$$

$$\mathrm{div} \left(\gamma_\rho \widetilde{A}_\rho \nabla v_3 \right) = \mathrm{div} \left(\left(1 - \chi_{\Omega'}\right) \gamma_\rho \left(\widetilde{A}_\rho - A_\rho \right) \nabla w_\rho \right) \quad \text{in } B_r'(0), \quad v_3 = 0 \text{ on } \partial B_r'(0). \tag{B.14}$$

In the following, we estimate the gradients of v_1, v_2 and v_3 to prove the claim. For v_1 we use (B.12), (B.2) and the Lipschitz continuity of $\boldsymbol{F}$ to see that

$$\left\| \nabla v_1 \right\|_{L^2(B_r'(0))} \leq C |D_\rho'|^{1/2} \left\| \boldsymbol{F} - \boldsymbol{F}(0) \right\|_{L^\infty(D_\rho')} \leq C |D_\rho'|^{1/2} \rho = o(|D_\rho'|^{1/2}). \tag{B.15}$$

For (B.13) we use (B.2) and the Lipschitz continuity of A_0 and A_1 to find that

$$\begin{aligned}
\left\| \nabla v_2 \right\|_{L^2(B_r'(0))} &\leq C \left\| \left(\widetilde{A}_\rho - A_\rho \right) \chi_{\Omega'} \right\|_{L^\infty(B_r'(0))} \left\| \nabla w_\rho \right\|_{L^2(B_r'(0))} \\
&\leq C \left(\left\| A_1 - A_1(0) \right\|_{L^\infty(D_\rho')} + \left\| A_0 - A_0(0) \right\|_{L^\infty(\Omega')} \right) |D_\rho'|^{1/2} \\
&\leq C(\rho + \rho^{1/4}) |D_\rho'|^{1/2} = o(|D_\rho'|^{1/2}).
\end{aligned} \tag{B.16}$$

Next, let $h_\rho \in C^1([0, r])$ be a cut-off function satisfying

$$\begin{aligned}
&0 \leq h_\rho \leq 1, \qquad \chi_{(0,\rho^{1/2})} h_\rho = 0, \\
&\chi_{(\rho^{1/4},r)} h_\rho = \chi_{(\rho^{1/4},r)}, \qquad \left\| \frac{\partial h_\rho}{\partial t} \right\|_{L^\infty((0,r))} \leq C \rho^{-1/4}
\end{aligned} \tag{B.17}$$

(see [19, Lem. 3.6] for a similar construction). With this function we find that

$$0 = \int_{D'_\rho} \boldsymbol{F} \cdot \nabla \left(h_\rho^2 \overline{w_\rho} \right) \mathrm{d}\boldsymbol{x}'.$$

Furthermore, using the weak formulation of (B.8) gives that

$$\begin{aligned} 0 &= \int_{B'_r(0)} \gamma_\rho A_\rho \nabla w_\rho \cdot \nabla (h_\rho^2 \overline{w_\rho}) \, \mathrm{d}\boldsymbol{x}' \\ &= \int_{B'_r(0)} \gamma_\rho A_\rho \nabla w_\rho \cdot (h_\rho \nabla (h_\rho \overline{w_\rho}) + h_\rho \overline{w_\rho} \nabla h_\rho) \, \mathrm{d}\boldsymbol{x}' \\ &= \int_{B'_r(0)} \gamma_\rho A_\rho \nabla (h_\rho w_\rho) \cdot \nabla (h_\rho \overline{w_\rho}) \, \mathrm{d}\boldsymbol{x}' - \int_{B'_r(0)} \gamma_\rho |w_\rho|^2 A_\rho \nabla h_\rho \cdot \nabla h_\rho \, \mathrm{d}\boldsymbol{x}' \\ &\quad + 2\mathrm{i} \int_{B'_r(0)} \gamma_\rho h_\rho (A_\rho \operatorname{Im} (\overline{w_\rho} \nabla w_\rho) \cdot \nabla h_\rho) \, \mathrm{d}\boldsymbol{x}'. \end{aligned} \tag{B.18}$$

Note that, since $\chi_{(0,\rho^{1/2})} h_\rho = 0$, the coefficient γ_ρ in (B.18) satisfies $\gamma_\rho = \gamma_0$. Therefore,

$$\|\nabla (h_\rho w_\rho)\|^2_{L^2(B'_r(0))} \leq C \|w_\rho\|^2_{L^2(B'_r(0))} \|\nabla h_\rho\|^2_{L^\infty(B'_r(0))}.$$

Thus, an application of (B.17) and (B.3) yields that

$$\|\nabla (h_\rho w_\rho)\|_{L^2(B'_r(0))} \leq C\rho^{-1/4} |D'_\rho|^{3/4} \leq C |D'_\rho|^{-1/8} |D'_\rho|^{3/4} = o(|D'_\rho|^{1/2}).$$

Here, we used that $D'_\rho \subset B'_\rho(0)$ and consequently $|D'_\rho| \leq \pi\rho^2$. Finally, we combine (B.14) with (B.2) to obtain that

$$\|\nabla v_3\|_{L^2(B'_r(0))} \leq C \|\nabla w_\rho\|_{L^2(B'_r(0) \setminus \overline{\Omega'})} \leq C \|\nabla (h_\rho w_\rho)\|_{L^2(B'_r(0))} = o(|D'_\rho|^{1/2}). \tag{B.19}$$

Combining (B.15),(B.16) and (B.19) yields (B.10). □

Appendix C

The PMCHWT formulation for the Maxwell transmission problem

In this appendix we derive a multitrace formulation for Maxwell's equations. We need these formulations in Chapter 3.3 and 4 to compute (reference) solutions using the boundary element library Bempp (see [115]). Similar formulations combined with numerical approximation using Bempp are studied in e.g. [16, 72, 73, 89, 90]. In this appendix we follow the presentation in [72, Sec. 6.1.2.] to derive the PMCHWT integral equation.

First, we adapt some notations to be consistent with the Bempp framework. In Proposition 3.9 we study the Maxwell single and double layer potentials and cite their mapping properties. In [113] the operator $\widetilde{M}$ is denoted by $\mathcal{H}$ and represents the magnetic potential. The electric potential $\mathcal{E}$ is often defined as $\mathcal{E} = -(\mathrm{i}k)^{-1}\widetilde{N}$ with $\widetilde{N}$ from Proposition 3.9 (see also [88, Thm. 5.52] to see the equality). Let $(\boldsymbol{E}, \boldsymbol{H}) \in (H_{\mathrm{loc}}(\mathbf{curl}, \mathbb{R}^3))^2$ be the unique solutions to (2.31) together with the radiation condition (2.32). As before, let D be a bounded Lipschitz domain representing the scattering object in the scattering problem. We say that a field $\boldsymbol{V}$ lies in $H(\mathbf{curl}^2, D)$ (or in $H_{\mathrm{loc}}(\mathbf{curl}^2, \mathbb{R}^3 \setminus \overline{D})$), if $\mathbf{curl}\, \boldsymbol{V} \in H(\mathbf{curl}, D)$ (or $\mathbf{curl}\, \boldsymbol{V} \in H_{\mathrm{loc}}(\mathbf{curl}, \mathbb{R}^3 \setminus \overline{D})$). We find that the Maxwell system in (2.31) can be equivalently formulated as the transmission problem to find $(\boldsymbol{E}_1, \boldsymbol{H}_1) \in (H(\mathbf{curl}^2, D))^2$ and $(\boldsymbol{E}_0, \boldsymbol{H}_0) \in (H_{\mathrm{loc}}(\mathbf{curl}^2, \mathbb{R}^3 \setminus \overline{D}))^2$ satisfying

$$\mathbf{curl}\, \boldsymbol{E}_1 - \mathrm{i}\omega\mu_1 \boldsymbol{H}_1 = 0\,, \qquad \mathbf{curl}\, \boldsymbol{H}_1 + \mathrm{i}\omega\varepsilon_1 \boldsymbol{E}_1 = 0 \qquad \text{in } D\,, \tag{C.1a}$$

$$\mathbf{curl}\, \boldsymbol{E}_0 - \mathrm{i}\omega\mu_0 \boldsymbol{H}_0 = 0\,, \qquad \mathbf{curl}\, \boldsymbol{H}_0 + \mathrm{i}\omega\varepsilon_0 \boldsymbol{E}_0 = 0 \qquad \text{in } \mathbb{R}^3 \setminus \overline{D}\,, \tag{C.1b}$$

$$\boldsymbol{\nu} \times \boldsymbol{E}_1|_{\partial D}^{-} = \boldsymbol{\nu} \times \boldsymbol{E}_0|_{\partial D}^{+}, \quad \boldsymbol{\nu} \times \boldsymbol{H}_1|_{\partial D}^{-} = \boldsymbol{\nu} \times \boldsymbol{H}_0|_{\partial D}^{+} \qquad \text{on } \partial D\,, \tag{C.1c}$$

$$\boldsymbol{E}_0^s = \boldsymbol{E}_0 - \boldsymbol{E}^i|_{\mathbb{R}^3 \setminus \overline{D}}, \qquad \boldsymbol{H}_0^s = \boldsymbol{H}_0 - \boldsymbol{H}^i|_{\mathbb{R}^3 \setminus \overline{D}} \quad \text{satisfy (2.32)}\,. \tag{C.1d}$$

Note that the transmission condition (C.1c) implies that $(\boldsymbol{E}, \boldsymbol{H}) \in (H_{\mathrm{loc}}(\mathbf{curl}, \mathbb{R}^3))^2$, where

$$\boldsymbol{E} = \begin{cases} \boldsymbol{E}_1 & \text{in } D\,, \\ \boldsymbol{E}_0 & \text{in } \mathbb{R}^3 \setminus \overline{D}\,, \end{cases} \qquad \boldsymbol{H} = \begin{cases} \boldsymbol{H}_1 & \text{in } D\,, \\ \boldsymbol{H}_0 & \text{in } \mathbb{R}^3 \setminus \overline{D}\,. \end{cases}$$

and vice versa. With $\mathcal{E}_j$ and $\mathcal{H}_j$ we define the electric and magnetic potential with wave number $k_j = \omega\sqrt{\varepsilon_j \mu_j}$ for $j = 0, 1$, respectively. The Stratton-Chu formula (see e.g. [88, Thm. 5.49]) in the interior reads

$$-\mathcal{H}_1(\boldsymbol{\nu} \times \boldsymbol{E}_1|_{\partial D}^{-}) - \frac{1}{\mathrm{i}k_1}\mathcal{E}_1(\boldsymbol{\nu} \times \mathbf{curl}\, \boldsymbol{E}_1|_{\partial D}^{-}) = \boldsymbol{E}_1 \quad \text{in } D\,. \tag{C.2}$$

Moreover, in the exterior we find that

$$\mathcal{H}_0(\boldsymbol{\nu} \times \boldsymbol{E}_0^s|_{\partial D}^{+}) + \frac{1}{\mathrm{i}k_0}\mathcal{E}_0(\boldsymbol{\nu} \times \mathbf{curl}\, \boldsymbol{E}_0^s|_{\partial D}^{+}) = \boldsymbol{E}_0^s \quad \text{in } \mathbb{R}^3 \setminus \overline{D}\,. \tag{C.3}$$

We note from the jump relations in (3.30) and by defining $\mathrm{E}_j^t = -(\mathrm{i}k_j)^{-1} N_j$, $\mathrm{H}_j^t = M_j$ with M_j, N_j from (3.29) with wave number k_j, $j = 0, 1$ in the fundamental solution Φ, that for

$\boldsymbol{a} \in H_{\mathrm{div}}^{-1/2}(\partial D)$ it holds that

$$\begin{aligned}
\boldsymbol{\nu} \times \mathcal{H}_j \boldsymbol{a}|_{\partial D}^{\pm} &= \pm\frac{1}{2}\boldsymbol{a} + \mathrm{H}_j^t \boldsymbol{a}\,, \qquad \boldsymbol{\nu} \times \mathcal{E}_j \boldsymbol{a}|_{\partial D}^{\pm} = \mathrm{E}_j^t \boldsymbol{a}\,,\\
\frac{1}{\mathrm{i}k_j}\boldsymbol{\nu} \times \mathbf{curl}\, \mathcal{H}_j \boldsymbol{a}|_{\partial D}^{\pm} &= -\mathrm{E}_j^t \boldsymbol{a}\,, \quad \frac{1}{\mathrm{i}k_j}\boldsymbol{\nu} \times \mathbf{curl}\, \mathcal{E}_j \boldsymbol{a}|_{\partial D}^{\pm} = \pm\frac{1}{2}\boldsymbol{a} + \mathrm{H}_j^t \boldsymbol{a}\,.
\end{aligned}$$

We apply the interior traces to (C.2) and find that

$$\begin{aligned}
\frac{1}{2}\boldsymbol{\nu} \times \boldsymbol{E}_1|_{\partial D}^{-} - \mathrm{H}_1^t(\boldsymbol{\nu} \times \boldsymbol{E}_1|_{\partial D}^{-}) - \frac{1}{\mathrm{i}k_1}\mathrm{E}_1^t(\boldsymbol{\nu} \times \mathbf{curl}\, \boldsymbol{E}_1|_{\partial D}^{-}) &= \boldsymbol{\nu} \times \boldsymbol{E}_1|_{\partial D}^{-}\,,\\
\mathrm{E}_1^t(\boldsymbol{\nu} \times \boldsymbol{E}_1|_{\partial D}^{-}) + \frac{1}{2}\frac{1}{\mathrm{i}k_1}\boldsymbol{\nu} \times \mathbf{curl}\, \boldsymbol{E}_1|_{\partial D}^{-} - \frac{1}{\mathrm{i}k_1}\mathrm{H}_1^t(\boldsymbol{\nu} \times \mathbf{curl}\, \boldsymbol{E}_1|_{\partial D}^{-}) &= \frac{1}{\mathrm{i}k_1}\boldsymbol{\nu} \times \mathbf{curl}\, \boldsymbol{E}_1|_{\partial D}^{-}\,.
\end{aligned}$$

This yields that

$$\begin{bmatrix} \boldsymbol{\nu} \times \boldsymbol{E}_1|_{\partial D}^{-} \\ \frac{1}{\mathrm{i}k_1}\boldsymbol{\nu} \times \mathbf{curl}\, \boldsymbol{E}_1|_{\partial D}^{-} \end{bmatrix} = \left(\frac{1}{2}I + A^{-}\right) \begin{bmatrix} \boldsymbol{\nu} \times \boldsymbol{E}_1|_{\partial D}^{-} \\ \frac{1}{\mathrm{i}k_1}\boldsymbol{\nu} \times \mathbf{curl}\, \boldsymbol{E}_1|_{\partial D}^{-} \end{bmatrix} \quad \text{with } A^{-} = \begin{bmatrix} -\mathrm{H}_1^t & -\mathrm{E}_1^t \\ \mathrm{E}_1^t & -\mathrm{H}_1^t \end{bmatrix}. \tag{C.4}$$

Moreover, we apply the traces from the exterior to (C.3) and see that

$$\begin{aligned}
\frac{1}{2}\boldsymbol{\nu} \times \boldsymbol{E}_0^s|_{\partial D}^{+} + \mathrm{H}_0^t(\boldsymbol{\nu} \times \boldsymbol{E}_0^s|_{\partial D}^{+}) + \frac{1}{\mathrm{i}k_0}\mathrm{E}_0^t(\boldsymbol{\nu} \times \mathbf{curl}\, \boldsymbol{E}_0^s|_{\partial D}^{+}) &= \boldsymbol{\nu} \times \boldsymbol{E}_0^s|_{\partial D}^{+}\,,\\
-\mathrm{E}_0^t(\boldsymbol{\nu} \times \boldsymbol{E}_0^s|_{\partial D}^{+}) + \frac{1}{2}\frac{1}{\mathrm{i}k_0}\boldsymbol{\nu} \times \mathbf{curl}\, \boldsymbol{E}_0^s|_{\partial D}^{+} + \frac{1}{\mathrm{i}k_0}\mathrm{H}_0^t(\boldsymbol{\nu} \times \mathbf{curl}\, \boldsymbol{E}_0^s|_{\partial D}^{+}) &= \frac{1}{\mathrm{i}k_0}\boldsymbol{\nu} \times \mathbf{curl}\, \boldsymbol{E}_0^s|_{\partial D}^{+}\,.
\end{aligned}$$

This shows that

$$\begin{bmatrix} \boldsymbol{\nu} \times \boldsymbol{E}_0^s|_{\partial D}^{+} \\ \frac{1}{\mathrm{i}k_0}\boldsymbol{\nu} \times \mathbf{curl}\, \boldsymbol{E}_0^s|_{\partial D}^{+} \end{bmatrix} = \left(\frac{1}{2}I - A^{+}\right) \begin{bmatrix} \boldsymbol{\nu} \times \boldsymbol{E}_0^s|_{\partial D}^{+} \\ \frac{1}{\mathrm{i}k_0}\boldsymbol{\nu} \times \mathbf{curl}\, \boldsymbol{E}_0^s|_{\partial D}^{+} \end{bmatrix} \quad \text{with } A^{+} = \begin{bmatrix} -\mathrm{H}_0^t & -\mathrm{E}_0^t \\ \mathrm{E}_0^t & -\mathrm{H}_0^t \end{bmatrix}. \tag{C.5}$$

The transmission condition (C.1c) yields that

$$\begin{bmatrix} \boldsymbol{\nu} \times \boldsymbol{E}_1|_{\partial D}^{-} \\ \frac{1}{\mathrm{i}k_1}\boldsymbol{\nu} \times \mathbf{curl}\, \boldsymbol{E}_1|_{\partial D}^{-} \end{bmatrix} = S \begin{bmatrix} \boldsymbol{\nu} \times \boldsymbol{E}_0^s|_{\partial D}^{+} \\ \frac{1}{\mathrm{i}k_0}\boldsymbol{\nu} \times \mathbf{curl}\, \boldsymbol{E}_0^s|_{\partial D}^{+} \end{bmatrix} + S \begin{bmatrix} \boldsymbol{\nu} \times \boldsymbol{E}^i|_{\partial D}^{+} \\ \frac{1}{\mathrm{i}k_0}\boldsymbol{\nu} \times \mathbf{curl}\, \boldsymbol{E}^i|_{\partial D}^{+} \end{bmatrix}, \tag{C.6}$$

where the matrix $S \in \mathbb{C}^{2\times 2}$ is given by

$$S = \begin{bmatrix} 1 & 0 \\ 0 & \frac{\sqrt{\mu_r}}{\sqrt{\varepsilon_r}} \end{bmatrix},$$

with $\mu_r = \mu_1/\mu_0$, $\varepsilon_r = \varepsilon_1/\varepsilon_0$. We define the operators $C^{\pm} = 1/2I \mp A^{\pm}$, with A^{-} from (C.4) and A^{+} from (C.5). Now, we apply (C.4), (C.6) and (C.5) and obtain

$$\begin{aligned}
C^{-} \begin{bmatrix} \boldsymbol{\nu} \times \boldsymbol{E}_1|_{\partial D}^{-} \\ \frac{1}{\mathrm{i}k_1}\boldsymbol{\nu} \times \mathbf{curl}\, \boldsymbol{E}_1|_{\partial D}^{-} \end{bmatrix} &= S \begin{bmatrix} \boldsymbol{\nu} \times \boldsymbol{E}_0^s|_{\partial D}^{+} \\ \frac{1}{\mathrm{i}k_0}\boldsymbol{\nu} \times \mathbf{curl}\, \boldsymbol{E}_0^s|_{\partial D}^{+} \end{bmatrix} + S \begin{bmatrix} \boldsymbol{\nu} \times \boldsymbol{E}^i|_{\partial D}^{+} \\ \frac{1}{\mathrm{i}k_0}\boldsymbol{\nu} \times \mathbf{curl}\, \boldsymbol{E}^i|_{\partial D}^{+} \end{bmatrix}\\
&= SC^{+} \begin{bmatrix} \boldsymbol{\nu} \times \boldsymbol{E}_0^s|_{\partial D}^{+} \\ \frac{1}{\mathrm{i}k_0}\boldsymbol{\nu} \times \mathbf{curl}\, \boldsymbol{E}_0^s|_{\partial D}^{+} \end{bmatrix} + S \begin{bmatrix} \boldsymbol{\nu} \times \boldsymbol{E}^i|_{\partial D}^{+} \\ \frac{1}{\mathrm{i}k_0}\boldsymbol{\nu} \times \mathbf{curl}\, \boldsymbol{E}^i|_{\partial D}^{+} \end{bmatrix}.
\end{aligned} \tag{C.7}$$

Applying S^{-1} to (C.7), and using (C.6) once again yields

$$\begin{aligned}
S^{-1}C^{-} \left(S \begin{bmatrix} \boldsymbol{\nu} \times \boldsymbol{E}_0^s|_{\partial D}^{+} \\ \frac{1}{\mathrm{i}k_0}\boldsymbol{\nu} \times \mathbf{curl}\, \boldsymbol{E}_0^s|_{\partial D}^{+} \end{bmatrix} + S \begin{bmatrix} \boldsymbol{\nu} \times \boldsymbol{E}^i|_{\partial D}^{+} \\ \frac{1}{\mathrm{i}k_0}\boldsymbol{\nu} \times \mathbf{curl}\, \boldsymbol{E}^i|_{\partial D}^{+} \end{bmatrix} \right)\\
= C^{+} \begin{bmatrix} \boldsymbol{\nu} \times \boldsymbol{E}_0^s|_{\partial D}^{+} \\ \frac{1}{\mathrm{i}k_0}\boldsymbol{\nu} \times \mathbf{curl}\, \boldsymbol{E}_0^s|_{\partial D}^{+} \end{bmatrix} + \begin{bmatrix} \boldsymbol{\nu} \times \boldsymbol{E}^i|_{\partial D}^{+} \\ \frac{1}{\mathrm{i}k_0}\boldsymbol{\nu} \times \mathbf{curl}\, \boldsymbol{E}^i|_{\partial D}^{+} \end{bmatrix}.
\end{aligned}$$

Rearranging these terms and using that

$$S^{-1}C^{-}S - C^{+} = S^{-1}A^{-}S + A^{+} \quad \text{and} \quad I - S^{-1}C^{-}S = \frac{1}{2}I - S^{-1}A^{-}S$$

yields the PMCHWT integral equation

$$(S^{-1}A^{-}S + A^{+}) \begin{bmatrix} \boldsymbol{\nu} \times \boldsymbol{E}_0^s|_{\partial D}^{+} \\ \frac{1}{\mathrm{i}k_0}\boldsymbol{\nu} \times \mathbf{curl}\, \boldsymbol{E}_0^s|_{\partial D}^{+} \end{bmatrix} = \Big(\frac{1}{2}I - S^{-1}A^{-}S\Big) \begin{bmatrix} \boldsymbol{\nu} \times \boldsymbol{E}^i|_{\partial D}^{+} \\ \frac{1}{\mathrm{i}k_0}\boldsymbol{\nu} \times \mathbf{curl}\, \boldsymbol{E}^i|_{\partial D}^{+} \end{bmatrix}. \tag{C.8}$$

We denote the operator on the left hand side of (C.8) with $\mathcal{P}$. Now, we apply the Calderón preconditioner $\mathcal{P} = (S^{-1}A^{-}S + A^{+})$ to both sides of (C.8) and obtain the Calderón preconditioned PMCHWT integral equation

$$\mathcal{P}^2 \begin{bmatrix} \boldsymbol{\nu} \times \boldsymbol{E}_0^s|_{\partial D}^{+} \\ \frac{1}{\mathrm{i}k_0}\boldsymbol{\nu} \times \mathbf{curl}\, \boldsymbol{E}_0^s|_{\partial D}^{+} \end{bmatrix} = \mathcal{P}\Big(\frac{1}{2}I - S^{-1}A^{-}S\Big) \begin{bmatrix} \boldsymbol{\nu} \times \boldsymbol{E}^i|_{\partial D}^{+} \\ \frac{1}{\mathrm{i}k_0}\boldsymbol{\nu} \times \mathbf{curl}\, \boldsymbol{E}^i|_{\partial D}^{+} \end{bmatrix}. \tag{C.9}$$

In [35] it is shown that this preconditioner yields a well-conditioned system matrix, when the left-hand side of (C.9) is discretized. A numerical approximation to the integral equation (C.9) can be simulated using the boundary element library Bempp. The multitrace operators $A^{\pm}$ from (C.4) and (C.5) and their discretization is discussed in [113]. Note that the different signs in front of the operators $\mathrm{E}_j^t, \mathrm{H}_j^t$ in the definition of the multitrace operators $A^{\pm}$ from (C.4) and (C.5) compared to [113, Eq. 31] result from a sign swap in the definition of the tangential traces. The implementation for the discretized multitrace operators $A^{\pm}$ from (C.4) and (C.5) that is provided by Bempp uses both the Rao-Wilton-Glisson basis functions of order 1 as well as the Buffa-Christiansen basis functions of order 1. This provides a stable discretization of the multitrace operators. For more details on these functions we refer to [26, 111, 113].

Appendix D

Derivatives of spherical vector wave functions

The explicit basis representation of the Fréchet derivative $\boldsymbol{T}'_\rho[\boldsymbol{p}_\Gamma]\boldsymbol{h}$ in Remark 5.16 contains derivatives of the circularly polarized spherical vector wave functions $\boldsymbol{P}_n^m$ and $\boldsymbol{Q}_n^m$, $m = -n, \dots, n$, $n = 1, 2, \dots$. Recalling the definition of $\boldsymbol{P}_n^m$ and $\boldsymbol{Q}_n^m$ in (5.29), we provide a detailed discussion of the derivatives of the spherical vector wave functions $\boldsymbol{M}_n^m$ and $\mathbf{curl}\, \boldsymbol{M}_n^m$ from (2.23). Both functions are best expressed in spherical coordinates,

$$\boldsymbol{x} \;=\; \begin{bmatrix} x_1 \\ x_2 \\ x_3 \end{bmatrix} \;=\; r \begin{bmatrix} \sin(\theta)\cos(\varphi) \\ \sin(\theta)\sin(\varphi) \\ \cos(\theta) \end{bmatrix} \;=\; \boldsymbol{\psi}(r, \theta, \varphi)\,, \qquad r > 0\,,\ \theta \in [0, \pi]\,,\ \varphi \in [0, 2\pi)\,,$$

and consist of terms of the form $\boldsymbol{F}(\boldsymbol{x}) = J(r)\boldsymbol{W}(\theta, \varphi)$, where $\boldsymbol{W}$ is one of the vector spherical harmonics $Y_n^m \widehat{\boldsymbol{x}}$, $\boldsymbol{U}_n^m$, or $\boldsymbol{V}_n^m$. Using the chain rule

$$(\boldsymbol{F} \circ \boldsymbol{\psi})' \;=\; (\boldsymbol{F}' \circ \boldsymbol{\psi})\boldsymbol{\psi}'$$

and observing that $(\boldsymbol{\psi}')^{-1}$ is known explicitly, it suffices to compute the partial derivatives of $\boldsymbol{M}_n^m$ and $\mathbf{curl}\, \boldsymbol{M}_n^m$ with respect to the spherical coordinates. More precisely, with the spherical unit coordinate vectors

$$\widehat{\boldsymbol{x}} \;=\; \begin{bmatrix} \sin(\theta)\cos(\varphi) \\ \sin(\theta)\sin(\varphi) \\ \cos(\theta) \end{bmatrix}, \qquad \widehat{\boldsymbol{\theta}} \;=\; \begin{bmatrix} \cos(\theta)\cos(\varphi) \\ \cos(\theta)\sin(\varphi) \\ -\sin(\theta) \end{bmatrix}, \qquad \widehat{\boldsymbol{\varphi}} \;=\; \begin{bmatrix} -\sin(\varphi) \\ \cos(\varphi) \\ 0 \end{bmatrix},$$

we obtain

$$\boldsymbol{\psi}'(r, \theta, \varphi) \;=\; \left[\widehat{\boldsymbol{x}} \,\middle|\, \widehat{\boldsymbol{\theta}} \,\middle|\, \widehat{\boldsymbol{\varphi}}\right] \begin{bmatrix} 1 & 0 & 0 \\ 0 & r & 0 \\ 0 & 0 & r\sin(\theta) \end{bmatrix},$$

and hence

$$\boldsymbol{F}' \circ \boldsymbol{\psi} \;=\; \left[\frac{\partial J}{\partial r}\boldsymbol{W} \,\middle|\, \frac{1}{r} J \frac{\partial \boldsymbol{W}}{\partial \theta} \,\middle|\, \frac{1}{r\sin(\theta)} J \frac{\partial \boldsymbol{W}}{\partial \varphi}\right] \begin{bmatrix} \widehat{\boldsymbol{x}}^\top \\ \widehat{\boldsymbol{\theta}}^\top \\ \widehat{\boldsymbol{\varphi}}^\top \end{bmatrix}. \tag{D.1}$$

Note that throughout this section, we will suppress the dependence on r, θ and φ of the unit coordinate vectors and most other functions.

We start with the factors in $\boldsymbol{M}_n^m$ and $\mathbf{curl}\, \boldsymbol{M}_n^m$ that depend only on the angular variables θ and φ and express their derivatives in terms of the spherical harmonics Y_n^m and the partial derivative of Y_n^m with respect to θ. First, we note that the derivatives of the unit coordinate vectors satisfy

$$\begin{aligned} \partial_\theta \widehat{\boldsymbol{x}} &= \widehat{\boldsymbol{\theta}}\,, & \partial_\theta \widehat{\boldsymbol{\theta}} &= -\widehat{\boldsymbol{x}}\,, & \partial_\theta \widehat{\boldsymbol{\varphi}} &= 0\,, \\ \partial_\varphi \widehat{\boldsymbol{x}} &= \sin(\theta)\widehat{\boldsymbol{\varphi}}\,, & \partial_\varphi \widehat{\boldsymbol{\theta}} &= \cos(\theta)\widehat{\boldsymbol{\varphi}}\,, & \partial_\varphi \widehat{\boldsymbol{\varphi}} &= -\sin(\theta)\widehat{\boldsymbol{x}} - \cos(\theta)\widehat{\boldsymbol{\theta}}\,. \end{aligned}$$

A particular choice of spherical harmonics Y_n^m, $m = -n, \dots, n$, $n = 0, 1, \dots$, is obtained from the definition

$$Y_n^m = C_n^m P_n^{|m|}(\cos(\theta)) \mathrm{e}^{\mathrm{i}m\varphi} \quad \text{with} \quad C_n^m = \sqrt{\frac{2n+1}{4\pi} \frac{(n-|m|)!}{(n+|m|)!}}, \tag{D.2}$$

where $P_n^m(t) = (1-t^2)^{m/2} (\mathrm{d}/\mathrm{d}t)^m P_n(t)$, $m = 0, \dots, n$, denote the associated Legendre functions (see e.g. [88, p. 41]). Derivatives of Y_n^m with respect to φ just amount to multiplications with powers of $\mathrm{i}m$. The first derivative of Y_n^m with respect to θ is calculated explicitly from

$$\begin{aligned} \frac{\mathrm{d}P_n^m}{\mathrm{d}t}(t) &= -mt(1-t^2)^{(m-2)/2} \frac{\mathrm{d}^m P_n}{\mathrm{d}t^m}(t) + (1-t^2)^{m/2} \frac{d^{m+1} P_n}{\mathrm{d}t^{m+1}}(t) \\ &= \frac{1}{(1-t^2)^{1/2}} P_n^{m+1}(t) - \frac{mt}{1-t^2} P_n^m(t), \qquad n \in \mathbb{N},\ m = 0, \dots, n, \end{aligned}$$

which gives

$$\partial_\theta Y_n^m = m \cot(\theta) Y_n^m - \frac{C_n^m}{C_n^{m+1}} \mathrm{e}^{-\mathrm{i}\varphi} Y_n^{m+1} \quad \text{and} \quad \partial_\theta Y_n^{-m} = \overline{\partial_\theta Y_n^m} \tag{D.3}$$

for $n \in \mathbb{N}$ and $m = 0, \dots, n$. Here, we use $P_n^{n+1} = 0$ and $Y_n^{n+1} = 0$ for convenience of notation.

As spherical harmonics are eigenfunctions of the Laplace-Beltrami operator on the unit sphere,

$$\frac{1}{\sin\theta} \partial_\theta \big(\sin(\theta) \partial_\theta Y_n^m \big) + \frac{1}{\sin^2(\theta)} \partial_\varphi^2 Y_n^m = -n(n+1) Y_n^m, \tag{D.4}$$

(see e.g. [88, p. 41]) we can compute the second derivative of Y_n^m with respect to θ as

$$\partial_\theta^2 Y_n^m = -\cot(\theta) \partial_\theta Y_n^m + \Big(\frac{m^2}{\sin^2(\theta)} - n(n+1) \Big) Y_n^m. \tag{D.5}$$

We apply these formulas to find expressions for the derivatives of the vector spherical harmonics $Y_n^m \widehat{\boldsymbol{x}}$, $\boldsymbol{U}_n^m$, and $\boldsymbol{V}_n^m$ with respect to θ and φ. For the radially oriented $Y_n^m \widehat{\boldsymbol{x}}$ we obtain

$$\partial_\theta (Y_n^m \widehat{\boldsymbol{x}}) = \partial_\theta Y_n^m \widehat{\boldsymbol{x}} + Y_n^m \widehat{\boldsymbol{\theta}}, \tag{D.6a}$$

$$\frac{1}{\sin(\theta)} \partial_\varphi (Y_n^m \widehat{\boldsymbol{x}}) = \frac{\mathrm{i}m}{\sin(\theta)} Y_n^m \widehat{\boldsymbol{x}} + Y_n^m \widehat{\boldsymbol{\varphi}}. \tag{D.6b}$$

From the definition (2.16) we find for $\boldsymbol{U}_n^m$ and $\boldsymbol{V}_n^m$ that

$$\boldsymbol{U}_n^m = \frac{1}{\sqrt{n(n+1)}} \Big(\partial_\theta Y_n^m \widehat{\boldsymbol{\theta}} + \frac{\mathrm{i}m}{\sin(\theta)} Y_n^m \widehat{\boldsymbol{\varphi}} \Big), \tag{D.7a}$$

$$\boldsymbol{V}_n^m = \frac{1}{\sqrt{n(n+1)}} \Big(\partial_\theta Y_n^m \widehat{\boldsymbol{\varphi}} - \frac{\mathrm{i}m}{\sin(\theta)} Y_n^m \widehat{\boldsymbol{\theta}} \Big). \tag{D.7b}$$

We further deduce

$$\partial_\theta \boldsymbol{U}_n^m = \frac{1}{\sqrt{n(n+1)}} \Big(-\partial_\theta Y_n^m \widehat{\boldsymbol{x}} + \partial_\theta^2 Y_n^m \widehat{\boldsymbol{\theta}} - \frac{\mathrm{i}m}{\sin(\theta)} (\cot(\theta) Y_n^m - \partial_\theta Y_n^m) \widehat{\boldsymbol{\varphi}} \Big), \tag{D.8a}$$

$$\frac{1}{\sin(\theta)} \partial_\varphi \boldsymbol{U}_n^m = \frac{1}{\sqrt{n(n+1)}} \Big(-\frac{\mathrm{i}m}{\sin(\theta)} Y_n^m \widehat{\boldsymbol{x}} + \frac{\mathrm{i}m}{\sin(\theta)} (\partial_\theta Y_n^m - \cot(\theta) Y_n^m) \widehat{\boldsymbol{\theta}} \tag{D.8b}$$

$$+ \Big(\cot(\theta) \partial_\theta Y_n^m - \frac{m^2}{\sin^2(\theta)} Y_n^m \Big) \widehat{\boldsymbol{\varphi}} \Big), \tag{D.8c}$$

$$\partial_\theta \boldsymbol{V}_n^m = \frac{1}{\sqrt{n(n+1)}} \Big(\frac{\mathrm{i}m}{\sin(\theta)} Y_n^m \widehat{\boldsymbol{x}} + \frac{\mathrm{i}m}{\sin(\theta)} (\cot(\theta) Y_n^m - \partial_\theta Y_n^m) \widehat{\boldsymbol{\theta}} + \partial_\theta^2 Y_n^m \widehat{\boldsymbol{\varphi}} \Big), \tag{D.8d}$$

$$\frac{1}{\sin(\theta)} \partial_\varphi \boldsymbol{V}_n^m = \frac{1}{\sqrt{n(n+1)}} \Big(-\partial_\theta Y_n^m \widehat{\boldsymbol{x}} + \Big(\frac{m^2}{\sin^2(\theta)} Y_n^m - \cot(\theta) \partial_\theta Y_n^m \Big) \widehat{\boldsymbol{\theta}} \tag{D.8e}$$

$$+ \frac{\mathrm{i}m}{\sin(\theta)} (\partial_\theta Y_n^m - \cot(\theta) Y_n^m) \widehat{\boldsymbol{\varphi}} \Big). \tag{D.8f}$$

The representations (D.3)–(D.8) contain several terms that are ill-suited to numerical evaluation for θ close to 0 or π. These are

$$\frac{1}{\sin(\theta)} Y_n^m\,, \qquad \frac{1}{\sin(\theta)}\big(\cot(\theta) Y_n^m - \partial_\theta Y_n^m\big)\,, \qquad \frac{m^2}{\sin^2(\theta)} Y_n^m - \cot(\theta)\partial_\theta Y_n^m\,. \tag{D.9}$$

Note that the first two expressions in (D.9) always appear in combination with a factor m in (D.3)–(D.8) and thus are only relevant for $m \neq 0$. We will only consider $m \geq 0$ in the following paragraphs, as the corresponding formulas for negative m can immediately be obtained by complex conjugation.

To rewrite the first term in (D.9), we use the recurrence relation

$$\frac{P_n^m(t)}{\sqrt{1-t^2}} = \frac{1}{2mt}\big(P_n^{m+1}(t) + (n+m)(n-m+1)P_n^{m-1}(t)\big), \qquad n \geq 2\,,\ m = 1, \dots, n-1\,,$$

for the associated Legendre functions (see e.g. [88, p. 35]). Inserting this into (D.2) gives

$$\frac{Y_n^m}{\sin(\theta)} = \frac{C_n^m}{2m\cos(\theta)}\Big(\frac{\mathrm{e}^{-\mathrm{i}\varphi}}{C_n^{m+1}} Y_n^{m+1} + \frac{(n+m)(n-m+1)\mathrm{e}^{\mathrm{i}\varphi}}{C_n^{m-1}} Y_n^{m-1}\Big) \tag{D.10}$$

for $n \geq 2$ and $m = 1, \dots, n-1$. Furthermore, differentiating Rodrigues' formula for the associated Legendre functions (see e.g. [88, Thm. 2.6]) n times shows that $P_n^n(\cos(\theta)) = \frac{(2n)!}{2^n n!}\sin^n(\theta)$. Therefore,

$$\frac{Y_n^n}{\sin(\theta)} = C_n^n \frac{(2n)!}{2^n n!}\sin^{n-1}(\theta)\mathrm{e}^{\mathrm{i}n\varphi}\,, \qquad n \in \mathbb{N}\,. \tag{D.11}$$

For the second term in (D.9), from (D.3) we have that

$$\frac{1}{\sin(\theta)}\big(\cot(\theta) Y_n^m - \partial_\theta Y_n^m\big) = \frac{C_n^m}{C_n^{m+1}}\mathrm{e}^{-\mathrm{i}\varphi}\frac{Y_n^{m+1}}{\sin(\theta)} - (m-1)\cos(\theta)\frac{Y_n^m}{\sin^2(\theta)}\,. \tag{D.12}$$

For $m = 1$, this can be evaluated using (D.10). For $n \geq 2$ and $m = 2, \dots, n$, expressions for $\sin^{-2}(\theta) Y_n^m$ are immediately obtained from (D.10) and (D.11).

Finally, the third term in (D.9) satisfies

$$\frac{m^2}{\sin^2(\theta)} Y_n^m - \cot(\theta)\partial_\theta Y_n^m = \frac{C_n^m}{C_n^{m+1}}\mathrm{e}^{-\mathrm{i}\varphi}\cos(\theta)\frac{Y_n^{m+1}}{\sin(\theta)} + \big(m^2 - m\cos^2(\theta)\big)\frac{Y_n^m}{\sin^2(\theta)}\,. \tag{D.13}$$

For n, $m \geq 2$, no new issues arise, and for $m = 1$, the last term on the right hand side of (D.13) reduces to Y_n^1. In (D.13) we also have to consider the case $m = 0$, where (D.2) gives

$$-\cot(\theta)\partial_\theta Y_n^0 = -C_n^0\cot(\theta)\partial_\theta P_n(\cos(\theta)) = C_n^0\cos(\theta)P_n'(\cos(\theta))\,. \tag{D.14}$$

For numerical implementations of (D.3), (D.5)–(D.8) we suggest to use the expressions directly when $\theta \in [\pi/4, 3\pi/4]$, and to replace the problematic terms with the expressions from (D.10)–(D.14) when $\theta \in [0, \pi/4)$ or $\theta \in (3\pi/4, \pi]$.

We continue with the factors in $\boldsymbol{M}_n^m$ and $\mathbf{curl}\,\boldsymbol{M}_n^m$ that depend only on the radial variable r, i.e.,

$$j_n(kr)\,, \qquad \frac{j_n(kr)}{r}\,, \qquad \frac{j_n(kr) + kr\,j_n'(kr)}{r}\,. \tag{D.15}$$

We require the derivatives

$$\begin{aligned}
\partial_r j_n(kr) &= k j_n'(kr)\,,\\
\partial_r \frac{j_n(kr)}{r} &= \frac{krj_n'(kr) - j_n(kr)}{r^2}\,,\\
\partial_r\left(\frac{j_n(kr) + krj_n'(kr)}{r}\right) &= \frac{(kr)^2 j_n''(kr) + krj_n'(kr) - j_n(kr)}{r^2}\,.
\end{aligned}$$

These may be simplified using the spherical Bessel differential equation

$$t^2 j_n''(t) + 2t j_n'(t) + (t^2 - n(n+1)) j_n(t) \;=\; 0$$

(see e.g. [88, p. 54]) and the recurrence relation

$$j_n'(t) \;=\; \frac{n}{t}\, j_n(t) - j_{n+1}(t)$$

(see e.g. [103, 10.51.2]) to obtain

$$\partial_r j_n(kr) \;=\; \frac{n}{r} j_n(kr) - k j_{n+1}(kr)\,, \tag{D.16a}$$

$$\partial_r \frac{j_n(kr)}{r} \;=\; \frac{(n-1) j_n(kr) - kr j_{n+1}(kr)}{r^2}\,, \tag{D.16b}$$

$$\begin{aligned} \partial_r \frac{j_n(kr) + kr j_n'(kr)}{r} \;&=\; \frac{-kr j_n'(kr) + (n(n+1) - 1 - (kr)^2) j_n(kr)}{r^2} \\ &=\; \frac{kr j_{n+1}(kr) + (n^2 - 1 - (kr)^2) j_n(kr)}{r^2}\,. \end{aligned} \tag{D.16c}$$

For small values of $r > 0$, the expansion of the spherical Bessel functions in powers of r (see e.g. [88, Def. 2.26]) should be inserted into (D.15) and (D.16) and being truncated to a finite sum for numerical evaluation. In particular, we note that for $n = 1$ negative powers of r seem to remain in (D.1) when the two summands in $\mathbf{curl}\, \boldsymbol{M}_n^m$ are inserted separately. However, some tedious calculations show that these terms cancel as expected when the sum is formed. Hence, for numerical evaluation in the case $n = 1$, all terms of order r^{-1} should be left out of the calculation to avoid cancellation effects.

Notation

Basic notation

$\mathbb{R}^d$	$d-$dimensional real Euclidean space	
$\mathbb{C}^d$	$d-$dimensional complex Euclidean space	
$\boldsymbol{x}$	point $\boldsymbol{x} = (x_1, x_2, x_3)^\top$ in $\mathbb{R}^3$	
$\boldsymbol{x} \cdot \boldsymbol{y}$	dot product of $\boldsymbol{x}, \boldsymbol{y}$	
$\boldsymbol{x} \times \boldsymbol{y}$	cross product of $\boldsymbol{x}, \boldsymbol{y}$	
$\lvert\boldsymbol{x}\rvert$	Euclidean norm of $\boldsymbol{x}$	
$B_R(\boldsymbol{x}_0)$	open ball in $\mathbb{R}^3$ of radius R centered at $\boldsymbol{x}_0$	
$\partial B_R(\boldsymbol{x}_0)$	boundary of $B_R(\boldsymbol{x}_0)$	
$\overline{B_R(\boldsymbol{x}_0)}$	closure of $B_R(\boldsymbol{x}_0)$	
$\boldsymbol{\nu}$	unit outward normal on $\partial B_R(0)$	
S^2	unit sphere in $\mathbb{R}^3$	
$B'_r(0)$	open ball in $\mathbb{R}^2$ centered at the origin	34
c	speed of light	13
ε_0	electric permittivity in free space	13
μ_0	magnetic permeability in free space	13
ε, ε_ρ	electric permittivity distribution (for D_ρ)	15, 34
μ, μ_ρ	magnetic permeability distribution (for D_ρ)	15, 34
ω	angular frequency	13
f	frequency	13
k	wave number	13
ε'_ρ	electric permittivity distribution for D'_ρ	50
μ'_ρ	magnetic permeability distribution for D'_ρ	50
Γ	exterior center curve including center curve K	33
$\boldsymbol{p}_\Gamma$	parametrization of Γ	33
$(\boldsymbol{t}_\Gamma, \boldsymbol{r}_\Gamma, \mathbf{s}_\Gamma)$	rotation minimizing frame	33
Ω_r	range of local coordinate system around $\boldsymbol{p}_\Gamma$	34
D_ρ	thin tubular scattering object with radius ρ	34
K	center curve of D_ρ	34
$\mathcal{P}$	set of admissible functions	80
$\triangle$	non-uniform partition	70, 84
$\mathcal{P}_\triangle$	set of not-a-knot splines on partition $\triangle$	84

Function spaces

$C^k(\Omega)$, $C^k(\partial\Omega)$	k times differentiable functions on Ω, $\partial\Omega$	7
$C^k(\overline{\Omega})$	functions in $C^k(\Omega)$ whose derivatives have continuous extensions to $\overline{\Omega}$	7
$L^p(\Omega)$	Lebesgue space on Ω	8
$W^{1,p}(\Omega)$	Sobolev space on Ω	8
$W_0^{1,p}(\Omega)$	closure of $C_0^1(\Omega)$ in $W^{1,p}(\Omega)$	8
$H^s(\Omega)$	Sobolev space on Ω	
$H^s_{\mathrm{loc}}(\Omega)$	functions that are in $H^s(\widetilde{\Omega})$ for all open and bounded $\widetilde{\Omega} \subset \Omega$	
$H(\mathbf{curl}, \Omega)$	function space of L^2-functions with weak **curl** in $L^2(\Omega)^3$	10
$H^{-1/2}_{\mathrm{div}}(\partial\Omega)$	trace space, range of γ_t	11
$H^{-1/2}_{\mathrm{curl}}(\partial\Omega)$	trace space, range of γ_T	11
$H^{-1/2}_{\mathrm{div},0}(\partial\Omega)$	subspace of $H^{-1/2}_{\mathrm{div}}(\partial\Omega)$	20
$\widetilde{S}$	$\nabla\widetilde{S}$ is the **curl** free part in the Helmholtz decomposition	23
$\widetilde{X}_0$	$\widetilde{X}_0$ is the div free part in the Helmholtz decomposition	26
$V^{\pm}$	eigenspaces of operator $\mathcal{C}$	97
$W^{\pm}$	Beltrami fields in Ω	98

Functions

Φ	fundamental solution of the Helmholtz equation	14
$\mathbb{G}$	fundamental solution of time-harmonic Maxwell's equation	14
Y_n^m	spherical harmonics	12
$\boldsymbol{U}_n^m, \boldsymbol{V}_n^m$	vector spherical harmonics	12
$\boldsymbol{M}_n^m, \mathbf{curl}\,\boldsymbol{M}_n^m$	entire solutions of time-harmonic Maxwell's equation	14
$\boldsymbol{N}_n^m, \mathbf{curl}\,\boldsymbol{N}_n^m$	radiating solutions of time-harmonic Maxwell's equation	14
$\boldsymbol{E}^i, \boldsymbol{H}^i$	incident electric and magnetic field	15
$\boldsymbol{E}^s, \boldsymbol{H}^s$	scattered electric and magnetic field	15
$\boldsymbol{E}, \boldsymbol{H}$	total electric and magnetic field	15
$\boldsymbol{E}^\infty, \boldsymbol{H}^\infty$	electric and magnetic far field	15
$\boldsymbol{E}^s_\rho$	scattered electric field corresponding to D_ρ	35
$\boldsymbol{E}^\infty_\rho$	electric far field corresponding to D_ρ	39
$\widetilde{\boldsymbol{E}^s_\rho}, \widetilde{\boldsymbol{E}^\infty_\rho}$	leading order term of the asymptotic perturbation formula	39, 44, 68, 80
$\boldsymbol{E}^i[\boldsymbol{A}], \boldsymbol{E}^s[\boldsymbol{A}]$, $\boldsymbol{E}[\boldsymbol{A}], \boldsymbol{E}^\infty[\boldsymbol{A}]$	incident, scattered, total, far field corr. to density $\boldsymbol{A}$	97
$\boldsymbol{e}_0, \boldsymbol{h}_0$	solution of homogeneous Maxwell's equation in $B_R(0)$	39
$\boldsymbol{e}_\rho, \boldsymbol{h}_\rho$	solution of inhomogeneous Maxwell's equation in $B_R(0)$	39
θ	rotation function	34
$\boldsymbol{q}_\Gamma$	local parametrization around $\boldsymbol{p}_\Gamma$	34
$\kappa, \kappa_{\max}$	(maximal) curvature of Γ	37
$V^{(j)}$	solution to boundary value problem without inclusion in $\mathbb{R}^3$	45

$v_\rho^{(j)}$	solution to boundary value problem with inclusion in $\mathbb{R}^3$	45
$V^{(\boldsymbol{\xi})}$	for $\boldsymbol{\xi} \in S^2$ given by $V^{(\boldsymbol{\xi})} = \sum_{j=1}^3 \xi_j V^{(j)}$	49
$v_\rho^{(\boldsymbol{\xi})}$	for $\boldsymbol{\xi} \in S^2$ given by $V^{(\boldsymbol{\xi})} = \sum_{j=1}^3 \xi_j v_\rho^{(j)}$	49
$\widetilde{v}_\rho^{(\boldsymbol{\xi})}$	modified potential satisfying $\widetilde{v}_\rho^{(\boldsymbol{\xi})} = V^{(\boldsymbol{\xi})}$ on $\partial B_R(0)$	49
$W_\rho^{(\boldsymbol{\xi})}$	three-dimensional corrector potential	49
$\mathbb{M}^\varepsilon, \mathbb{M}^\mu$	3×3 electric and magnetic polarization tensor corr. to D_ρ	45
μ	scaled Dirac measure on center curve K of D_ρ	38
μ'	Dirac measure in 0	
$w_\rho^{(\boldsymbol{\xi}')}$	two-dimensional corrector potential	50
$\widetilde{w}_\rho^{(R_\theta^{-1}\boldsymbol{\xi}')}$	modified corrector potential	55
m^ε, m^μ	2×2 electric and magnetic polarization tensor corr. to D'_ρ	50, 63
$z^{(j)}$	solution to boundary value problem without inclusion in $\mathbb{R}^2$	63
$z_\rho^{(j)}$	solution to boundary value problem with inclusion in $\mathbb{R}^2$	63
$\widetilde{w}_j$	solution to two-dimensional transmission problem	64
$\boldsymbol{E}^+, \boldsymbol{E}^-$	Riemann-Silberstein linear combinations	98
χ_2	chirality measure	100
χ_{HS}	smooth chirality measure	
J_2	relative chirality measure	115
J_{HS}	relative smooth chirality measure	115

Operators

γ_t	trace operator from $H(\mathbf{curl}, \Omega)$ to $H_{\mathrm{div}}^{-1/2}(\partial\Omega)$	11
γ_T	trace operator from $H(\mathbf{curl}, \Omega)$ to $H_{\mathrm{curl}}^{-1/2}(\partial\Omega)$	11
$\mathbf{curl}, \mathbf{curl}_{\mathrm{x}}, \mathbf{curl}_{\mathrm{y}}$	**curl** operator (w.r.t. $\boldsymbol{x}, \boldsymbol{y}$) acting on matrices columnwise	
Δ	Laplace operator	
Λ	electric to magnetic Calderón operator	19
$\widetilde{\Lambda}$	electric to magnetic Calderón operator with $k = \mathrm{i}$	20
Λ_1, Λ_2	$\Lambda = \Lambda_1 + \Lambda_2$	29
B	sesquilin. form in the weak formulation of the scat. problem	23
F	antilin. func. in the weak formulation of the scat. problem	23
a_1, a_2	$B = a_1 + a_2$	23
$\mathrm{div}'_{\eta,\zeta}$	divergence in local coordinates	37
$\nabla'_{\eta,\zeta}$	gradient in local coordinates	37
$\Lambda_{\rho_n}, \Lambda_0$	interior Calderón operators	42
T_{ρ_n}, T_0	resulting from $\boldsymbol{\nu} \times \cdot$ applied to Stratton-Chu formula	42
$\mathcal{F}_D$	far field operator	97
$\mathcal{C}$	used to define helicity for fields in $L_t^2(S^2)$	97

Index

P

R

S

T

U

V

W

Bibliography

[1] J. Aizpurua and R. Hillenbrand. Localized surface plasmons: Basics and applications in field-enhanced spectroscopy. In S. Enoch and N. Bonod, editors, *Plasmonics: From Basics to Advanced Topics*, pages 151–176. Springer Berlin Heidelberg, Berlin, Heidelberg, 2012.

[2] G. S. Alberti and Y. Capdeboscq. *Lectures on elliptic methods for hybrid inverse problems*, volume 25 of *Cours Spécialisés [Specialized Courses]*. Société Mathématique de France, Paris, 2018.

[3] H. Ammari, E. Beretta, and E. Francini. Reconstruction of thin conductivity imperfections. *Appl. Anal.*, 83(1):63–76, 2004.

[4] H. Ammari, E. Beretta, and E. Francini. Reconstruction of thin conductivity imperfections. II. The case of multiple segments. *Appl. Anal.*, 85(1-3):87–105, 2006.

[5] H. Ammari, Y. T. Chow, K. Liu, and J. Zou. Optimal shape design by partial spectral data. *SIAM J. Sci. Comput.*, 37(6):B855–B883, 2015.

[6] H. Ammari, Y. Deng, and P. Millien. Surface plasmon resonance of nanoparticles and applications in imaging. *Arch. Ration. Mech. Anal.*, 220(1):109–153, 2016.

[7] H. Ammari, K. Hamdache, and J.-C. Nédélec. Chirality in the Maxwell equations by the dipole approximation. *SIAM J. Appl. Math.*, 59(6):2045–2059, 1999.

[8] H. Ammari, E. Iakovleva, and S. Moskow. Recovery of small inhomogeneities from the scattering amplitude at a fixed frequency. *SIAM J. Math. Anal.*, 34(4):882–900, 2003.

[9] H. Ammari and H. Kang. *Reconstruction of small inhomogeneities from boundary measurements*, volume 1846 of *Lecture Notes in Mathematics*. Springer, Berlin, 2004.

[10] H. Ammari and H. Kang. *Polarization and moment tensors: With applications to inverse problems and effective medium theory*, volume 162 of *Applied Mathematical Sciences*. Springer, New York, 2007.

[11] H. Ammari, H. Kang, G. Nakamura, and K. Tanuma. Complete asymptotic expansions of solutions of the system of elastostatics in the presence of an inclusion of small diameter and detection of an inclusion. *J. Elasticity*, 67(2):97–129, 2002.

[12] H. Ammari, M. S. Vogelius, and D. Volkov. Asymptotic formulas for perturbations in the electromagnetic fields due to the presence of inhomogeneities of small diameter. II. The full Maxwell equations. *J. Math. Pures Appl. (9)*, 80(8):769–814, 2001.

[13] H. Ammari and D. Volkov. The leading-order term in the asymptotic expansion of the scattering amplitude of a collection of finite number of dielectric inhomogeneities of small diameter. *Int. J. Multiscale Comput. Eng.*, 3(3), 2005.

[14] T. Arens, R. Griesmaier, and M. Knöller. Maximizing the Electromagnetic Chirality of Thin Dielectric Tubes. *SIAM J. Appl. Math.*, 81(5):1979–2006, 2021.

[15] T. Arens, F. Hagemann, F. Hettlich, and A. Kirsch. The definition and measurement of electromagnetic chirality. *Math. Methods Appl. Sci.*, 41(2):559–572, 2018.

[16] T. Arens, X. Ji, and X. Liu. Inverse electromagnetic obstacle scattering problems with multi-frequency sparse backscattering far field data. *Inverse Problems*, 36(10):105007, 2020.

[17] A. Bensoussan, J.-L. Lions, and G. Papanicolaou. *Asymptotic analysis for periodic structures*, volume 5 of *Studies in Mathematics and its Applications*. North-Holland Publishing Co., Amsterdam-New York, 1978.

[18] E. Beretta, E. Bonnetier, E. Francini, and A. L. Mazzucato. Small volume asymptotics for anisotropic elastic inclusions. *Inverse Probl. Imaging*, 6(1):1–23, 2012.

[19] E. Beretta, Y. Capdeboscq, F. de Gournay, and E. Francini. Thin cylindrical conductivity inclusions in a three-dimensional domain: a polarization tensor and unique determination from boundary data. *Inverse Problems*, 25(6):065004, 22, 2009.

[20] E. Beretta and E. Francini. An asymptotic formula for the displacement field in the presence of thin elastic inhomogeneities. *SIAM J. Math. Anal.*, 38(4):1249–1261, 2006.

[21] I. Bialynicki-Birula and Z. Bialynicka-Birula. The role of the Riemann–Silberstein vector in classical and quantum theories of electromagnetism. *J. Phys. A: Math. Theor.*, 46(5):053001, 2013.

[22] R. L. Bishop. There is more than one way to frame a curve. *Amer. Math. Monthly*, 82:246–251, 1975.

[23] C. F. Bohren and D. R. Huffman. *Absorption and scattering of light by small particles*. New York: John Wiley, 1983.

[24] C. G. Broyden. The convergence of a class of double-rank minimization algorithms 1. general considerations. *IMA J. Appl. Math.*, 6(1):76–90, 1970.

[25] M. Brühl, M. Hanke, and M. S. Vogelius. A direct impedance tomography algorithm for locating small inhomogeneities. *Numer. Math.*, 93(4):635–654, 2003.

[26] A. Buffa and S. H. Christiansen. A dual finite element complex on the barycentric refinement. *Math. Comp.*, 76(260):1743–1769, 2007.

[27] A. Buffa and R. Hiptmair. Galerkin boundary element methods for electromagnetic scattering. In *Topics in computational wave propagation*, volume 31 of *Lect. Notes Comput. Sci. Eng.*, pages 83–124. Springer, Berlin, 2003.

[28] Y. Capdeboscq, R. Griesmaier, and M. Knöller. An asymptotic representation formula for scattering by thin tubular structures and an application in inverse scattering. *Multiscale Model. Simul.*, 19(2):846–885, 2021.

[29] Y. Capdeboscq and M. S. Vogelius. A general representation formula for boundary voltage perturbations caused by internal conductivity inhomogeneities of low volume fraction. *M2AN Math. Model. Numer. Anal.*, 37(1):159–173, 2003.

[30] Y. Capdeboscq and M. S. Vogelius. Pointwise polarization tensor bounds, and applications to voltage perturbations caused by thin inhomogeneities. *Asymptot. Anal.*, 50(3-4):175–204, 2006.

[31] D. J. Cedio-Fengya, S. Moskow, and M. S. Vogelius. Identification of conductivity imperfections of small diameter by boundary measurements. continuous dependence and computational reconstruction. *Inverse Problems*, 14(3):553–595, jun 1998.

[32] N. Chaulet and H. Haddar. Electromagnetic inverse shape problem for coated obstacles. *Adv. Comput. Math.*, 41(6):1179–1205, 2015.

[33] C. Clason. *Introduction to functional analysis*. Compact Textbooks in Mathematics. Birkhäuser/Springer, Cham, 2020.

[34] D. Colton and R. Kress. *Inverse acoustic and electromagnetic scattering theory, 4th ed.*, volume 93 of *Applied Mathematical Sciences*. Springer, Cham, 2019.

[35] K. Cools, F. P. Andriulli, and E. Michielssen. A Calderón multiplicative preconditioner for the PMCHWT integral equation. *IEEE Trans. Antennas Propag.*, 59(12):4579–4587, 2011.

[36] L. C. B. da Silva. *Differential geometry of rotation minimizing frames, spherical curves, and quantum mechanics of a constrained particle*. PhD thesis, Universidade Federal de Pernambuco, Recife, 2017.

[37] Y.-H. Dai. Convergence properties of the BFGS algorithm. *SIAM J. Optim.*, 13(3):693–701 (2003), 2002.

[38] Y.-H. Dai. A perfect example for the BFGS method. *Math. Program.*, 138(1-2, Ser. A):501–530, 2013.

[39] C. Dapogny. The topological ligament in shape optimization: a connection with thin tubular inhomogeneities. *SMAI J. Comput. Math.*, 7:185–266, 2021.

[40] C. de Boor. *A practical guide to splines*, volume 27 of *Applied Mathematical Sciences*. Springer, New York-Berlin, 1978.

[41] M. Decker, M. Klein, M. Wegener, and S. Linden. Circular dichroism of planar chiral magnetic metamaterials. *Opt. Lett.*, 32(7):856–858, 2007.

[42] J. E. Dennis, Jr. and R. B. Schnabel. *Numerical methods for unconstrained optimization and nonlinear equations*, volume 16 of *Classics in Applied Mathematics*. Society for Industrial and Applied Mathematics (SIAM), Philadelphia, PA, 1996. Corrected reprint of the 1983 original.

[43] M.-H. Ding, H. Liu, and G.-H. Zheng. Shape reconstructions by using plasmon resonances. *ESAIM Math. Model. Numer. Anal.*, 56(2):705–726, 2022.

[44] N. Dunford and J. T. Schwartz. *Linear operators. Part II.* Wiley Classics Library. John Wiley & Sons, Inc., New York, 1988.

[45] L. C. Evans. *Partial differential equations*, volume 19 of *Graduate Studies in Mathematics*. American Mathematical Society, Providence, RI, 1998.

[46] R. T. Farouki, C. Giannelli, M. L. Sampoli, and A. Sestini. Rotation-minimizing osculating frames. *Comput. Aided Geom. Design*, 31(1):27–42, 2014.

[47] I. Fernandez-Corbaton. *Helicity and duality symmetry in light matter interactions: Theory and applications*. PhD thesis, Macquarie University, Sydney, 2014.

[48] I. Fernandez-Corbaton, M. Fruhnert, and C. Rockstuhl. Dual and chiral objects for optical activity in general scattering directions. *ACS Photonics*, 2(3):376–384, 2015.

[49] I. Fernandez-Corbaton, M. Fruhnert, and C. Rockstuhl. Objects of maximum electromagnetic chirality. *Phys. Rev. X*, 6(3):031013, 2016.

[50] I. Fernandez-Corbaton, R. Griesmaier, M. Knöller, and C. Rockstuhl. Maximizing the electromagnetic chirality of thin metallic nanowires at optical frequencies. *J. Comput. Phys.*, 475:111854, 2023.

[51] I. Fernandez-Corbaton and G. Molina-Terriza. Role of duality symmetry in transformation optics. *Phys. Rev. B*, 88:085111, 2013.

[52] I. Fernandez-Corbaton, C. Rockstuhl, P. Ziemke, P. Gumbsch, A. Albiez, R. Schwaiger, T. Frenzel, M. Kadic, and M. Wegener. New twists of 3d chiral metamaterials. *Adv. Mater.*, 31(26):1807742, 2019.

[53] I. Fernandez-Corbaton, X. Zambrana-Puyalto, N. Tischler, X. Vidal, M. L. Juan, and G. Molina-Terriza. Electromagnetic duality symmetry and helicity conservation for the macroscopic Maxwell's equations. *Phys. Rev. Lett.*, 111:060401, 2013.

[54] R. Fletcher. A new approach to variable metric algorithms. *Comput. J.*, 13(3):317–322, 1970.

[55] G. B. Folland. *Introduction to partial differential equations, 2nd Ed.* Princeton University Press, Princeton, NJ, 1995.

[56] A. Friedman and M. Vogelius. Identification of small inhomogeneities of extreme conductivity by boundary measurements: a theorem on continuous dependence. *Arch. Ration. Mech. Anal.*, 105(4):299–326, 1989.

[57] M. Fruhnert, I. Fernandez-Corbaton, V. Yannopapas, and C. Rockstuhl. Computing the T-matrix of a scattering object with multiple plane wave illuminations. *Beilstein J. Nanotechnol.*, 8(1):614–626, 2017.

[58] M. Ganesh and S. C. Hawkins. Three dimensional electromagnetic scattering T-matrix computations. *J. Comput. Appl. Math.*, 234(6):1702–1709, 2010.

[59] J. K. Gansel, M. Latzel, A. Frölich, J. Kaschke, M. Thiel, and M. Wegener. Tapered gold-helix metamaterials as improved circular polarizers. *Appl. Phys. Lett.*, 100(10):101109, 2012.

[60] J. K. Gansel, M. Thiel, M. S. Rill, M. Decker, K. Bade, V. Saile, G. von Freymann, S. Linden, and M. Wegener. Gold helix photonic metamaterial as broadband circular polarizer. *Science*, 325(5947):1513–1515, 2009.

[61] X. García-Santiago. *Numerical methods for shape optimization of photonic nanostructures*. PhD thesis, Karlsruhe Institute of Technology (KIT), Karlsruhe, 2020.

[62] X. Garcia-Santiago, M. Hammerschmidt, J. Sachs, S. Burger, H. Kwon, M. Knöller, T. Arens, P. Fischer, I. Fernandez-Corbaton, and C. Rockstuhl. Toward maximally electromagnetically chiral scatterers at optical frequencies. *ACS Photonics*, 9(6):1954–1964, 2022.

[63] D. Gilbarg and N. S. Trudinger. *Elliptic partial differential equations of second order*. Grundlehren der Mathematischen Wissenschaften, Vol. 224. Springer, Berlin-New York, 1977.

[64] D. Goldfarb. A family of variable-metric methods derived by variational means. *Math. Comp.*, 24(109):23–26, 1970.

[65] J.-J. Greffet. Introduction to surface plasmon theory. In S. Enoch and N. Bonod, editors, *Plasmonics: From Basics to Advanced Topics*, pages 105–148. Springer Berlin Heidelberg, Berlin, Heidelberg, 2012.

[66] R. Griesmaier. An asymptotic factorization method for inverse electromagnetic scattering in layered media. *SIAM J. Appl. Math.*, 68(5):1378–1403, 2008.

[67] R. Griesmaier. Reconstruction of thin tubular inclusions in three-dimensional domains using electrical impedance tomography. *SIAM J. Imaging Sci.*, 3(3):340–362, 2010.

[68] R. Griesmaier. A general perturbation formula for electromagnetic fields in presence of low volume scatterers. *ESAIM Math. Model. Numer. Anal.*, 45(6):1193–1218, 2011.

[69] R. Griesmaier and N. Hyvönen. A regularized Newton method for locating thin tubular conductivity inhomogeneities. *Inverse Problems*, 27(11):115008, 22, 2011.

[70] R. Griesmaier and J. Sylvester. Uncertainty principles for inverse source problems for electromagnetic and elastic waves. *Inverse Problems*, 34(6):065003, 37, 2018.

[71] H. Haddar and R. Kress. On the Fréchet derivative for obstacle scattering with an impedance boundary condition. *SIAM J. Appl. Math.*, 65(1):194–208, 2004.

[72] F. Hagemann. *Reconstructing the shape and measuring chirality of obstacles in electromagnetic scattering*. PhD thesis, Karlsruhe Institute of Technology (KIT), Karlsruhe, 2019.

[73] F. Hagemann, T. Arens, T. Betcke, and F. Hettlich. Solving inverse electromagnetic scattering problems via domain derivatives. *Inverse Problems*, 35(8):084005, 20, 2019.

[74] F. Hagemann and F. Hettlich. Application of the second domain derivative in inverse electromagnetic scattering. *Inverse Problems*, 36(12):125002, 34, 2020.

[75] C. Hazard and M. Lenoir. On the solution of time-harmonic scattering problems for Maxwell's equations. *SIAM J. Math. Anal.*, 27(6):1597–1630, 1996.

[76] M. Hentschel, M. Schäferling, X. Duan, H. Giessen, and N. Liu. Chiral plasmonics. *Sci. Adv.*, 3(5):e1602735, 2017.

[77] F. Hettlich. Fréchet derivatives in inverse obstacle scattering. *Inverse Problems*, 11(2):371–382, 1995.

[78] F. Hettlich. Erratum: "Fréchet derivatives in inverse obstacle scattering" [Inverse Problems **11** (1995), no. 2, 371–382]. *Inverse Problems*, 14(1):209–210, 1998.

[79] F. Hettlich. The domain derivative of time-harmonic electromagnetic waves at interfaces. *Math. Methods Appl. Sci.*, 35(14):1681–1689, 2012.

[80] K. Höflich, T. Feichtner, E. Hansjürgen, C. Haverkamp, H. Kollmann, C. Lienau, and M. Silies. Resonant behavior of a single plasmonic helix. *Optica*, 6(9):1098–1105, Sep 2019.

[81] U. Hohenester. *Nano and quantum optics—an introduction to basic principles and theory*. Graduate Texts in Physics. Springer, Cham, 2020.

[82] J. D. Jackson. *Klassische Elektrodynamik*. De Gruyter, Berlin, Boston, 2006.

[83] P. B. Johnson and R. W. Christy. Optical constants of the noble metals. *Phys. Rev. B*, 6:4370–4379, Dec 1972.

[84] M. Kadic, G. W. Milton, M. van Hecke, and M. Wegener. 3d metamaterials. *Nat. Rev. Phys.*, 1(3):198–210, 2019.

[85] K. L. Kelly, E. Coronado, L. L. Zhao, and G. C. Schatz. The optical properties of metal nanoparticles: the influence of size, shape, and dielectric environment. *J. Phys. Chem. B*, 107(3):668–677, 2003.

[86] D. Khavinson, M. Putinar, and H. S. Shapiro. Poincaré's variational problem in potential theory. *Arch. Ration. Mech. Anal.*, 185(1):143–184, 2007.

[87] A. Kirsch. The domain derivative and two applications in inverse scattering theory. *Inverse Problems*, 9(1):81–96, 1993.

[88] A. Kirsch and F. Hettlich. *The mathematical theory of time-harmonic Maxwell's equations, Expansion-, integral-, and variational methods*, volume 190 of *Applied Mathematical Sciences*. Springer, Cham, 2015.

[89] A. Kleanthous, T. Betcke, D. P. Hewett, P. Escapil-Inchauspé, C. Jerez-Hanckes, and A. J. Baran. Accelerated Calderón preconditioning for Maxwell transmission problems. *J. Comput. Phys.*, 458:111099, 2022.

[90] A. Kleanthous, T. Betcke, D. P. Hewett, M. W. Scroggs, and A. J. Baran. Calderón preconditioning of PMCHWT boundary integral equations for scattering by multiple absorbing dielectric particles. *J. Quant. Spectrosc. Radiat. Transfer*, 224:383–395, 2019.

[91] R. Kress. *Linear integral equations, 3rd Ed.*, volume 82 of *Applied Mathematical Sciences*. Springer, New York, 2014.

[92] A. Lakhtakia. *Beltrami fields in chiral media*. World Scientific Series in Contemporary Chemical Physics. World Scientific, Singapore, 1994.

[93] M. Letz. Linear optical properties. In J. D. Musgraves, J. Hu, and L. Calvez, editors, *Springer Handbook of Glass*, pages 169–191. Springer International Publishing, Cham, 2019.

[94] D.-H. Li and M. Fukushima. On the global convergence of the BFGS method for nonconvex unconstrained optimization problems. *SIAM J. Optim.*, 11(4):1054–1064, 2001.

[95] R. A. Litherland, J. Simon, O. Durumeric, and E. Rawdon. Thickness of knots. *Topology Appl.*, 91(3):233–244, 1999.

[96] S. A. Maier. *Plasmonics: fundamentals and applications*. Springer New York, NY, 2007.

[97] W. McLean. *Strongly elliptic systems and boundary integral equations*. Cambridge University Press, Cambridge, 2000.

[98] M. I. Mishchenko, L. D. Travis, and A. Lacis. *Scattering, absorption, and emission of light by small particles*. Cambridge University Press, Cambridge, 1. publ. edition, 2002.

[99] P. Monk. *Finite element methods for Maxwell's equations*. Numerical Mathematics and Scientific Computation. Oxford University Press, New York, 2003.

[100] J. Nocedal and S. J. Wright. *Numerical optimization, 2nd Ed.* Springer Series in Operations Research and Financial Engineering. Springer, New York, 2006.

[101] A. A. Novotny and J. Sokołowski. *An introduction to the topological derivative method*. SpringerBriefs in Mathematics. Springer, Cham, 2020.

[102] L. Novotny and B. Hecht. *Principles of nano-optics, 2nd Ed.* Cambridge University Press, 2012.

[103] F. W. J. Olver, D. W. Lozier, R. F. Boisvert, and C. W. Clark, editors. *NIST handbook of mathematical functions*. U.S. Department of Commerce, National Institute of Standards and Technology, Washington, DC; Cambridge University Press, Cambridge, 2010.

[104] P. Pedregal. *Introduction to optimization*, volume 46 of *Texts in Applied Mathematics*. Springer, New York, 2004.

[105] J. Pendry. A chiral route to negative refraction. *Science*, 306(5700):1353–1355, 2004.

[106] L. A. Piegl and W. Tiller. *The NURBS Book, Second Edition*. Monographs in Visual Communication. Springer, 1997.

[107] E. Plum, J. Zhou, J. Dong, V. Fedotov, T. Koschny, C. Soukoulis, and N. Zheludev. Metamaterial with negative index due to chirality. *Phys. Rev. B*, 79(3):035407, 2009.

[108] R. Potthast. Fréchet differentiability of boundary integral operators in inverse acoustic scattering. *Inverse Problems*, 10(2):431–447, 1994.

[109] R. Potthast. Domain derivatives in electromagnetic scattering. *Math. Methods Appl. Sci.*, 19(15):1157–1175, 1996.

[110] R. Potthast. Fréchet differentiability of the solution to the acoustic Neumann scattering problem with respect to the domain. *J. Inverse Ill-Posed Probl.*, 4(1):67–84, 1996.

[111] S. Rao, D. Wilton, and A. Glisson. Electromagnetic scattering by surfaces of arbitrary shape. *IEEE Trans. Antennas Propag.*, 30(3):409–418, 1982.

[112] A. Rogacheva, V. Fedotov, A. Schwanecke, and N. Zheludev. Giant gyrotropy due to electromagnetic-field coupling in a bilayered chiral structure. *Phys. Rev. Lett.*, 97(17):177401, 2006.

[113] M. W. Scroggs, T. Betcke, E. Burman, W. Śmigaj, and E. van 't Wout. Software frameworks for integral equations in electromagnetic scattering based on Calderón identities. *Comput. Math. Appl.*, 74(11):2897–2914, 2017.

[114] D. F. Shanno. Conditioning of quasi-newton methods for function minimization. *Math. Comp.*, 24(111):647–656, 1970.

[115] W. Śmigaj, T. Betcke, S. Arridge, J. Phillips, and M. Schweiger. Solving boundary integral problems with BEM++. *ACM Trans. Math. Software*, 41(2):Art. 6, 40, 2015.

[116] J. Sokołowski and A. Żochowski. On the topological derivative in shape optimization. *SIAM J. Control Optim.*, 37(4):1251–1272, 1999.

[117] J. Sokołowski and J.-P. Zolésio. *Introduction to shape optimization*, volume 16 of *Springer Series in Computational Mathematics*. Springer, Berlin, 1992.

[118] M. Spivak. *A comprehensive introduction to differential geometry. Vol. I.* Publish or Perish, Inc., Wilmington, Del., second edition, 1979.

[119] K. Tapp. *Differential geometry of curves and surfaces*. Undergraduate Texts in Mathematics. Springer, Cham, 2016.

[120] V. K. Valev, J. J. Baumberg, C. Sibilia, and T. Verbiest. Chirality and chiroptical effects in plasmonic nanostructures: Fundamentals, recent progress, and outlook. *Adv. Mat.*, 25(18):2517–2534, 2013.

[121] W. Wang, B. Jüttler, D. Zheng, and Y. Liu. Computation of rotation minimizing frames. *ACM Trans. Graph.*, 27(1):1–18, 2008.

[122] K. Yosida. *Functional analysis*. Classics in Mathematics. Springer, Berlin, 1995. Reprint of the sixth (1980) edition.

[123] S. Yılmaz and M. Turgut. A new version of Bishop frame and an application to spherical images. *J. Math. Anal. Appl.*, 371(2):764–776, 2010.

[124] E. J. Zeman and G. C. Schatz. An accurate electromagnetic theory study of surface enhancement factors for silver, gold, copper, lithium, sodium, aluminum, gallium, indium, zinc, and cadmium. *J. Phys. Chem.*, 91(3):634–643, 1987.

[125] S. Zhang, Y.-S. Park, J. Li, X. Lu, W. Zhang, and X. Zhang. Negative refractive index in chiral metamaterials. *Phys. Rev. Lett.*, 102(2):023901, 2009.